ISSN 1983-4195

IBRACON

IBRACON Structures and Materials Journal

Revista IBRACON de Estruturas e Materiais

Volume 13, Number 6
December 2020

ISSN 1983-4195
Volume 13, Number 6
December 2020

IBRACON Structures and Materials Journal
Revista IBRACON de Estruturas e Materiais

Contents

Temperature influence on creep of reinforced concrete 13601
E. L. MADUREIRA and B. V. C. FONTES

Optimization of the structural system with composite beam and composite slab using genetic algorithm 13602
B. D. BREDA, T. C. PIETRALONGA and E. C. ALVES

Nonlinear finite element analysis of reinforced concrete shear walls 13603
J. R. B. SILVA and B. HOROWITZ

Synergic effects between mineral admixtures on strength and microstructure of concretes 13604
C. S. FELTRIN, G. C. ISAIA and A. LUBECK

Modelling of tension stiffening effect in reinforced recycled concrete........... 13605
M. P. MARTINS, C. S. RANGEL, M. AMARIO, J. M. F. LIMA, P. R. L. LIMA and R. D. TOLEDO FILHO

Influence of the cracking consideration in the displacements of a shallow tunnel lined in steel-reinforced concrete: numerical model................................. 13606
B. M. JENSEN, D. BERNAUD and A. CAMPOS FILHO

Numerical analysis on displacements of steel-fiber-reinforced concrete beams 13607
M. F. PONTES, W. M. PEREIRA JUNIOR and J. J. C. PITUBA

Reinforced concrete beams coated with fiberglass-reinforced polymeric profiles as partial substitutes for the transverse reinforcement................................. 13608
I. S. HOFFMAN, J. H. PIVA, A. WANDERLIND and E. G. P. ANTUNES

Numerical and experimental comparative of coupled neighboring buildings . 13609
L. A. P. PENA, G. N. DOZ and S. M. AVILA

Experimental analysis of the structural behavior of different types of shear connectors in steel-concrete composite beams 13610
J. G. RIBEIRO NETO, G. S. VIEIRA and R. O. ZOCCOLI

Metal magnesium industry waste for partial replacement of Portland cement 13611
M. L. F. MARTINS, R. R. BARRETO, P. R. R. SOARES JUNIOR, I. P. PINHEIRO and A. C. S. BEZERRA

Analysis of nodal stress on reinforced concrete two-pile caps supported on steel piles 13612
R. G. DELALIBERA, M. A. TOMAZ, V. F. GONCALVES and J. S. GIONGO

Concrete produced with recycled aggregate: a durability analysis for structural use 13613
L. L. PIMENTEL, G. F. RIZZO, A. E. P. G. A. JACINTHO and P. S. P. FONTANINI

Numerical analysis of reinforced concrete shear walls with rectangular cross section 13614
M. C. B. N. CAMPOS, P. M. V. RIBEIRO and R. A. OLIVEIRA

Design considerations on the influence of slab continuity on punching resistance of flat slabs................................. 13615
F. G. B. S. OLIVEIRA, L. F. S. SOARES and R. L. VOLLUM

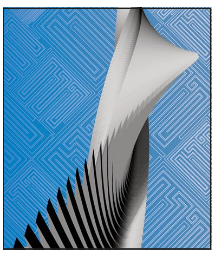

Cover: Parametric Tower

Courtesy: Marcela Noronha P. de O. e Sousa

IBRACON

Ibracon Structures and Materials Journal is published bimonthly
(February, April, June, August, October, and December) by IBRACON.

IBRACON
Instituto Brasileiro do Concreto Founded in 1972

Av. Queiroz Filho, nº 1700 — sala 407/408
Torre D — Villa Lobos Office Park
CEP 05319-000 — São Paulo, SP — Brazil
Phone: +55 11 3735-0202
Fax: +55 11 3733-2190
E-mail: riem@ibracon.org.br
Website: http://www.ibracon.org.br

Cover design & Layout: Editora Cubo
www.editoracubo.com.br

Aims and Scope

Aims and Scope

The IBRACON Structures and Materials Journal (in Portuguese: Revista IBRACON de Estruturas e Materiais) is a technical and scientific divulgation vehicle of IBRACON (Brazilian Concrete Institute), published every two months. Each issue has 12 to 15 articles and, possibly, a technical note and/or a technical discussion regarding a previously published paper. All contributions are reviewed and approved by professionals with recognized scientific competence in the area. The IBRACON Structures and Materials Journal is an open access Journal, free of charges for authors and readers.

Objectives

The IBRACON Structures and Materials Journal´s main objectives are:

- Present current developments and advances in concrete structures and materials.
- Make possible the better understanding of structural concrete behavior, supplying subsidies for a continuous interaction among researchers, producers, and users.
- Stimulate the development of scientific and technological research in the areas of concrete structures and materials, through papers peer-reviewed by a qualified Editorial Board.
- Promote the interaction among researchers, constructors and users of concrete structures and materials and the development of Civil Construction.
- Provide a vehicle of communication of high technical level for researchers and designers in the areas of concrete structures and materials.

Submission Procedure

The procedure to submit and revise the contributions, as well as the formats, are detailed in the Journal Website (ismj.org).

The papers and the technical notes are revised by at least two reviewers indicated by the editors. Discussions and replies are accepted for publication after a review by the editors and at least one member of the Editorial Board. In case of disagreement between the reviewer and the authors, the contribution will be sent to a specialist in the area, not necessarily linked to the Editorial Board. Conflict of interests is carefully handled by the Editors.

Contribution Types

The Journal will publish original papers, short technical notes, and paper discussions. Original papers will be accepted if they are in accordance with the objectives of the Journal and present quality of information and presentation. A technical note is a brief manuscript. It may present a new feature of research, development, or technological application in the areas of Concrete Structures and Materials, and Civil Construction. This is an opportunity to be used by industries, companies, universities, institutions of research, researchers, and professionals willing to promote their works and products under development.

A discussion is received no later than 3 months after the publication of the paper or technical note. The discussion must be limited to the topic addressed in the published paper and must not be offensive. The right of reply is granted to the Authors. The discussions and the replies are published in the subsequent issues of the Journal.

The submission file should be in accordance with the paper template available at the Journal Website. It is recommended that the length of the papers does not exceed 25 pages. Where available, URLs for the references should be provided.

The IBRACON Structures and Materials Journal will conduct the review process for manuscripts submitted in English. Titles, abstracts, and keywords are presented in English, and in Portuguese or Spanish. Articles and technical notes are peer-reviewed and only published after approval of the reviewers and the Editorial Board.

Once accepted, an article is typeset according to the journal layout. The author will be required to review and approve the galleys before publishing. At this stage only typesetting errors will be considered.

Internet Access

The IBRACON Structures and Materials Journal Webpage is available at http://ismj.org.

Sponsors

The funds for the maintenance of the Journal are currently obtained from the IBRACON. The Journal is not supposed to be maintained with funds from private sponsorship, which could diminish the credit of the publications.

Photocopying

Copyright

IBRACON

Av. Queiroz Filho, 1700 – sala 407/408 – Torre D
Villa Lobos Office Park
05319-000 – Vila Hamburguesa
São Paulo – SP
Phone: +55 (11) 3735-0202
E-mail: riem@ibracon.org.br

Disclaimer

Editorial Board

Reviewers List 2019-2020

Aguilar, Maria Teresa Paulino
Alax, Arthur
Albuquerque, M. da C. Fonseca de
Almeida Filho, Fernando Menezes
Almeida, Fernando do Couto Rosa
Almeida, Luiz Carlos de
Almeida, Saulo J. de Castro
Almeida, Sylvia
Almeida, Valério
Altoe, Silvia Paula Sossai
Alva, Gerson M. Sisniegas
Alves, Antônio Marcos de Lima
Alves, Elcio Cassimiro
Alves, Ricardo Valeriano
Amorim Júnior, Nilson
Amorim, David
Andrade, Jairo José de Oliveira
Andrade, Jorge
Ângulo, Sérgio
Antunes, Elaine Guglielmi
Arantes, João
Araújo, Daniel
Artigas, Laila Valduga
Assis, Wayne Santos de
Azevedo, Nuno
Balbo, José Tadeu
Baldassino, Nadia
Bandeira, Alex Alves
Banting, Bennett
Barbosa, Claudius de Sousa
Barbosa, Maria
Barbosa, Normando Perazzo
Barbosa, Paola
Barboza, Aline da Silva Ramos
Barros, Rodrigo
Baságlia, Cilmar
Batiston, Eduardo Roberto
Bauer, Elton
Beck, André Teófilo
Beeldens, Anne
Beraldo, Antônio
Bernardin, Adriano
Bernardo, Luis Filipe Almeida
Betioli, Andrea
Bianchi, Fernanda
Bitencourt Júnior, Luís A. Guimarães
Bolina, Cecília de Castro
Bolina, Fabrício
Bono, Giuliana Furtado Franca
Bonsembiante, Franciele Tiecher
Borges, Liana Jardim
Borges, Paulo Henrique
Bremer, Cynara Fiedler
Britez, Carlos Amado
Brito, Jorge de
Buchaim, Roberto
Bueno, Jeferson Rafael
Buratto, Caroline
Buttignol, Thomaz Eduardo Teixeira
Cabral, Kleber Cavalcanti
Caetano, Luciane Fonseca
Caldas, Rodrigo
Calixto, José Marcio
Camarini, Gladis
Camões, Aires
Campos, Heloisa Fuganti
Cardoso, Daniel
Cargnin, Andreia
Carneiro, Anselmo
Carneiro, Arnaldo Manoel Pereira
Carneiro, Ronaldson J. de F. Mendes
Carrazedo, Ricardo
Carrazedo, Rogério
Carvalho, Hermes
Carvalho, Roberto Chust
Castro, Alessandra Lorenzetti
Cervo, Tatiana Cureau
Chahud, Eduardo
Chen, Airong
Chen, Bing
Christ, Roberto
Christoforo, André
Cincotto, Maria Alba
Coelho, Antônio Carlos Vieira
Coelho, Luiz Herkenhoff
Colombo, Alberto Belotti
Cordeiro, Luciana de Nazare Pinheiro
Cordon, Heloísa Cristina Fernandes
Corrêa, Márcio Roberto Silva
Correia, José
Costa e Silva, Ramon Saleno Yure
Costa Neto, Murilo Limeira da
Coutinho, Joana Sousa
Couto, Douglas
Couto, Eduardo Costa
Dalfré, Gláucia
Damineli, Bruno Luís
De Nardin, Silvana
Delalibera, Rodrigo Gustavo
Di Mascio, Paola
Diaz, Benjamin Ernani
Diniz, Sofia Maria Carrato
Domingues, Aline Bensi
Doz, Graciela Nora
Ehrenbring, Hinoel
Einsfeld, Ricardo Amorim
El Debs, Ana Lúcia Homce de Cresce
Fabbri, Glauco
Fairbairn, Eduardo M. R.
Fakury, Ricardo Hallal
Feldman, Lisa
Felipe, Túlio Raunyr Cândido
Felix, Emerson
Fenu, Luigi
Fernandes, Juliana Ferreira
Fernandes, Robson da Silva
Ferrari, Vladimir José
Ferreira, Fernanda Giannotti da Silva
Ferreira, Gisleiva
Ferreira, Maurício de Pina
Ferreira, Régis de C.
Ferreira, Ruan
Figueiredo, Antônio Domingues de
Fonseca, Fernando
Fonseca, João
Fontanini, Patrícia Stella Pucharelli
Formagini, Sidiclei
Forti, Tiago Luís Duarte
França Filho, Wanderson Luiz
Futai, Marcos Massao
Gachet, Luísa Andréia
Gama, João Luiz Calmon N.
Garcez, Estela Oliari
Garcez, Mônica Regina
Garcia, Jean
Gaspar, Ricardo
Ghorbel, Elhem
Gidrão, Gustavo de Miranda Saleme
Gil, Augusto
Girardi, Ricardo
Gleize, Philippe Jean Paul
Gomes João Paulo
Gomes, Helder Pontes
Gomes, Henrique Campelo
Gomes, Ronaldo
Gouveia, Fernanda Pereira
Greco, Marcelo
Guimarães, Gilson Natal
Guimarães, Giuseppe
Guindani, Eduardo
Gumieri, Adriana
Haach, Vladimir Guilherme
Helene, Paulo R. L.
Hentges, Tatiane Isabel
Holanda, José Nilson Franca de
Hotza, Dachamir
Houmard, Manuel
Huespe, Alfredo
Jacintho, Ana Elisabete P. G. de Ávila
John, Vanderley Moacyr
Jordani, Bárbara
Justino Filho, Manoel Rodrigues
Kataoka, Marcela Novischi
Kautzmann, Vanessa
Kazmi, Syed
Kazmierczak, Cláudio de Souza
Kimura, Alio Ernesto
Kimura, Erica Fernanda Aiko
Koppe, Angélica
Krahl, Pablo
Kremer, Bruna Maria
Kulakowski, Marlova Piva
Ladeira, Luiz Orlando
Lages, Eduardo Nobre
Lautenschläger, Carlos
Lemes, Ígor
Lemonge, Afonso Celso de Castro
Leonel, Edson Denner
Liberati, Elyson
Lima, Flávio
Lima, Flávio Barboza de
Lima, Maria Cristina Vidigal
Lima, Paulo Roberto Lopes
Lima, Silvio de Souza
Lintz, Rosa Cristina Cecche
Liserre, Andréa Prado Abreu Reis
Longhi, Marlon
Lopes, Raduan Krause
Lopez, Rafael
Lubeck, André
Ludvig, Péter
Luz, Caroline Angulski da
Maedo, Michael
Magalhães, Aldo Giuntini de
Malite, Maximiliano
Mancio, Mauricio
Mappa, Paulo César
Marangon, Ederli
Mari, Antônio R.
Marin, Marcelo Cuadrado
Marques Filho, José
Marques, Marilia
Martins, Carlos Humberto
Marvila, Markssuel Teixeira

Reviewers List 2019-2020

Mata, Rodrigo da
Matos, Paulo de
Mazer, Wellington
Medeiros Júnior, Ronaldo A
Medeiros, Arthur
Medeiros, Marcelo
Meira, Gibson
Melges, José Luiz Pinheiro
Melo, Antônio Macário Cartaxo de
Melo, Guilherme
Melo, Weslley Imperiano Gomes de
Mendes, Julia Castro
Mendes, Paulo
Meneghetti, Leila Cristina
Mennucci, Marina Martins
Menon, Nara Villanova
Mesquita, Esequiel
Milani, Ana Paula da Silva
Mohamad, Gihad
Moita, Gray
Monte, Renata
Morsch, Inácio
Motta, Leila A. Castro
Moura, Márcio Wrague
Munaiar Neto, Jorge
Munhoz, Fabiana Stripari
Nascimento, Aderson
Neto, Joel
Neves Júnior, Alex
Noaman, Ahmed Tareq
Nóbrega, Petrus Gorgônio Bulhões da
Nogueira, Caio Gorla
Novais, Rui Miguel
Nunes, David Brandão
Oliveira Neto, Luttgardes de
Oliveira, Andrielli Morais de
Oliveira, Dênio Ramam Carvalho de
Oliveira, Luiz Antônio Pereira de
Oliveira, Marco Antônio Barbosa de
Oliveira, Marcos
Oliveira, Marcos Honorato de
Oliveira, Mateus Antônio
Oliveira, Romilde Almeida de
Oliveira, Tiago
Ortolan, Vinicius
Paccola, Rodrigo Ribeiro
Pachêco, Admilson da Penha
Pachêco, Alexandre Rodrigues
Pachêco, Fernanda
Paes, José Luiz Rangel
Pagnussat, Daniel
Palermo Júnior, Leandro
Paliga, Charlei Marcelo
Pantoja, João da Consta
Parente Júnior, Evandro
Parsekian, Guilherme
Passuello, Alexandra Cruz
Paula, Júnia de
Pauletti, Ruy Marcelo de Oliveira
Pavan, Roberto Carlos
Pavanello, Renato
Paz, Gumersinda Seara
Peixoto, Ricardo André Fiorotti
Pelisser, Fernando
Pellegrino Neto, Januario
Pereira, Eduardo
Pereira, Mauro Real
Pereira, Sebastião Salvador Real
Perlin, Lourenço
Pessôa, José Renato Castro
Pfeil, Michèle Schubert
Pieralisi, Ricardo
Pimenta, Roberval J.
Pimentel, Lia Lorena
Pimentel, Roberto
Pinto, Roberto Caldas de Andrade
Pituba, José Julio de Cerqueira
Portela, Enson de Lima
Positieri, Maria Ajosefina
Possan, Edna
Posterlli, Mariana
Pravia, Zacarias Martin Chamberlain
Proença, Sérgio Persival Baroncini
Quinino, Uziel Cavalcanti de Medeiros
Ramos, Antônio Pinho
Ramos, Violeta
Ranzi, Gianluca
Real, Mauro de Vasconcellos
Rebelo, Carlos
Ribeiro, Daniel Veras
Ribeiro, Diogo
Ribeiro, Paula de Oliveira
Ribeiro, Paulo Marcelo Vieira
Rocha, Fábio
Rocha, Janaíde Cavalcante
Rodrigues Júnior, Sandoval José
Rodrigues, Eduardo Alexandre
Rohden, Abrahão Bernardo
Romano, Roberto Desar Oliveira
Ruan, Xin
Ruthes, Heloiza Candeia
Sales, Almir
Sales, Mauricio Martines
Salles, Lúcio Salles de
Salvador Filho, José Américo Alves
Sanchez, Emil
Santos, Ana Carolina
Santos, Ana Carolina Parapinski dos
Santos, Antônio Carlos dos
Santos, Caio
Santos, Carol Ferreira Rezende
Santos, Daniel Miranda dos
Santos, Pablo Juan Lopes e Silva
Santos, Robson Arruda dos
Santos, Sérgio Hampshire de Carvalho
Santos, White José dos
Savaris, Gustavo
Sbrighi Neto, Cláudio
Scherer, Maílson
Schulz, Mauro
Scott, Allan
Seiffert, Henrique Luiz de Lima
Severi, Andrea Arantes
Shehata, Lidia
Shi, Jinjie
Shrive, Nigel
Siacara, Adrian Torrico
Silva Filho, José Neres
Silva, Adriano de Paula e
Silva, Arthur Leandro
Silva, Bruno do Vale
Silva, Fernando Artur Nogueira
Silva, Jordlly Reydson de Barros
Silva, José Guilherme Santos da
Silva, Maria Cecilia Amorim Teixeira
Silva, Matheus Fernandes de Araújo
Silva, Ricardo
Silva, Roberto Marcio da
Silva, Valdir Pignatta e
Silva, Wellington Andrade da
Simão, Tatiana Regina da Silva
Simonetti, Camila
Siqueira, Gustavo Henrique
Sousa Júnior, João Batista Marques de
Sousa, José
Souza, Alex Sander
Souza, Beatriz Ferreira
Souza, Diego Jesus de
Souza, Flávio Teixeira de
Souza, Rafael Alves de
Souza, Regina H.
Specht, Luciano
Strauss, Alfred
Tamashiro, Jacqueline Roberta
Tamayo, Jorge
Tanesi, Jussara
Tavares, Danusa
Teixeira, Ritermayer Monteiro
Thives, Liseane
Thomas, Carlos
Titotto, Silvia Lenyra Meirelles Campos
Toralles, Berenice
Torres, Ariela da Silva
Trautwein, Leandro Mouta
Trindade, Guilherme Höehr
Tsavdaridis, Konstantinos Daniel
Tutikian, Bernardo
Ulsen, Carina
Vellasco, Pedro Colmar G. da Silva
Veloso, Luis Augusto
Veríssimo, Gustavo
Vieira, Gregorio Sandro
Villegas, Noé
Vizotto, Isaias
Waimberg, Marcelo
Wally, Gustavo Bosel
Wolenski, Anderson
Xie, Tianyu (Anson)
Xin Lu, Jian
Yalcin, Omer
Yanez, Pablo Anibal Lopez
Zaccardi, Yury Andrés Villagrán
Zuchetti, Laís.

IBRACON Structures and Materials Journal
Revista IBRACON de Estruturas e Materiais
ISSN 1983-4195 ismj.org

ORIGINAL ARTICLE

Temperature influence on creep of reinforced concrete

Influência da temperatura na fluência do concreto armado

Edmilson Lira Madureira[a]
Brenda Vieira Costa Fontes[b]

[a]Universidade Federal do Rio Grande do Norte – UFRN, Centro de Tecnologia, Departamento de Engenharia Civil, Natal, RN, Brasil
[b]Universidade de Brasília - UnB, Departamento de Engenharia Civil e Ambiental, Programa de Pós-graduação em Estruturas e Construção Civil, Brasília, DF, Brasil

Received 25 September 2019
Accepted 17 March 2020

Abstract: The creep of concrete promotes strains over time in structural members kept under sustained load. It causes the stress decrease on the concrete and the steel stress increase in reinforced concrete members. The moisture content and temperature influence significantly such phenomenon. The creep strains model of the NBR 6118/2014 [1] is, applicable, solely, to those cases of constant stress magnitudes. Reinforced concrete members exhibit variations on the stress magnitudes and, in this way, requires the use of an alternative model for the prediction of the creep strains as the so known the State Model. This report refers itself to temperature influence analysis upon creep strains of reinforced concrete structural members. The results have revealed that temperature speeds up the creep effects and, in this way, the steel yielding caused by the stress increase on the reinforcement bars occurs at earlier ages.

Keywords: reinforced concrete, thin-walled column, creep, modelling, temperature.

Resumo: A Fluência do concreto promove deformações com o tempo em membros estruturais mantidos carregados permanentemente. Ela causa a redução das tensões no concreto e o aumento das tensões no aço em membros de concreto armado. A umidade e a temperatura influenciam significativamente a Fluência. O modelo de deformações por Fluência da NBR 6118/2014 [1] é, aplicável, apenas, aos casos de tensões constantes. Em membros de concreto armado as tensões variam exigindo o uso de modelo alternativo de cálculo de suas deformações a exemplo do modelo de estado. Este relato refere-se à análise da influência da temperatura na Fluência de membros estruturais de concreto armado. Os resultados revelaram que a temperatura acelera os efeitos de fluência e, assim, o escoamento do aço mediante o aumento de tensões nas barras da armadura ocorre precocemente.

Palavras-chave: concreto armado, pilares parede, fluência, modelagem, temperatura.

How to cite: E. L. Madureira and B. V. C. Fontes, “Temperature Influence on Creep of Reinforced Concrete”, *Rev. IBRACON Estrut. Mater.*, vol. 13, no. 6, e13601, 2020, https://doi.org/10.1590/S1983-41952020000600001

1 INTRODUCTION

The progressive strains over time developed on concrete structural members maintained under sustained load characterize the phenomenon known as material creep [1].

The creep strains are associated, mainly, to the viscous mechanical behavior of certain water coating that remains adsorbed at the surfaces of the cement Portland grains, inner to the sound concrete, even at high thermal levels [2].

Among the several relevant factors that influence the creep deformation they may be included the moisture content, the stresses field, the concrete strength, the reinforcement ratio and temperature [1].

The creep strains modify, significantly, the stresses fields in reinforced concrete members since they can promote the stresses reduction on the mass of the concrete and its increase in the reinforcement steel bars, which can induce those latter to the development of the yielding phenomenon [3]. It is known, including, that temperature speeds up the creep effects rates [1].

Corresponding author: Edmilson Lira Madureiras. E-mail: edmadurei@ct.ufrn.br
Financial support: PROPESQ – UFRN – Bolsa de Iniciação Científica.
Conflict of interest: Nothing to declare.

The creep of concrete numerical model recommended by the NBR 6118/2014 standard [4] is based on the traditional creep coefficient concept and, in this way, is applicable, directly, overall, to that cases for which the stress magnitudes upon the solid mass constituted of the referring material maintain itself unchanged over the phenomenon progress. Nevertheless, the calculus framework presented in that way may be modified to an alternative mode becoming it able to its application on those cases for which occur stress magnitude variations as, for instance, to creep strains analyses involving reinforced concrete structural members. The formulation of such a model depends on the adoption of simplified artifices from which result the Memory Models, that are named in this way, because they demand, in their application, the history of stresses storage [5]. The referring storage amount promotes a large-scale computational effort becoming the modelling unfeasible [6]. In order to overcome the difficulties related to such a computational memory storage, some models were developed from the integrating scheme changing, that provide the use, exclusively, of the stresses at the discrete instant of time previous to the one that is being considered. For that reason, such advanced formulation received the State Models designation [5].

The aim of this work is the numerical simulation analysis of the temperature effects on creep of Portland cement concrete based on a State Model, highlighting, above all, its consequences on the mechanical performance of reinforced concrete structural members.

The subjects of this paper are accomplished from the numerical analysis of thin walled columns presenting certain physical properties and loading condition and a diversity of thermal levels and moisture contents.

The expected results by this work is the better knowing with respect to the fashion from which the temperature effect upon the creep phenomenon influences the overall mechanical performance of reinforced concrete structural specimens.

The main scientific contribution of this product is to provide numerical results involving the repercussion of the creep, at a diversity of thermal levels, on the mechanical performance of reinforced concrete structural members, to the technical literature, considering that such kind of data are even scarcer.

2 MODELLING

The approximation from quadratic isoparametric formulation was adopted in the present analysis work.

2.1 Concrete Response to Loading

The plane state of stress orthotropic nonlinear framework proposed by Kwak and Filippou [7], upon an incremental iterative procedure and the finite element approach, were adopted in this work. In this way, the constitutive matrix elements were defined in a similar way to that one applied to the uniaxial state of stresses, taking as a reference, in its turn, the equivalent strains "$\boldsymbol{\varepsilon_{ei}}$", that are given for every principal directions by Equation 1.

$$\varepsilon_{ei} = \varepsilon_i + D_{ij}\varepsilon_j / D_{ii} \tag{1}$$

The "**i**" and "**j**" indexes refer to the principal plan directions. The "$\mathbf{D_{ij}}$" coefficients represent the constitutive matrix elements.

The concrete compressive mechanical performance was simulated from the constitutive relationships proposed by Hognestad [8], expressed in the form of Equation 2.

$$\sigma_i = \frac{2\sigma_{ip}}{\varepsilon_{ip}}\left(1 - \frac{\varepsilon_{ei}}{2\varepsilon_{ip}}\right)\varepsilon_{ei}, \quad for \varepsilon_{ip} < \varepsilon_{ei} < 0 \tag{2}$$

The "$\boldsymbol{\sigma_{ip}}$" and "$\boldsymbol{\varepsilon_{ip}}$" parameters represent the concrete peak stress and its corresponding strain, respectively, beyond every principal direction namely "**i**". The "$\boldsymbol{\varepsilon_{cu}}$" parameter, in turn, is the concrete ultimate strain in uniaxial compression. Equation 2 represents the hardening branch **OA** over the curve of Figure 1.

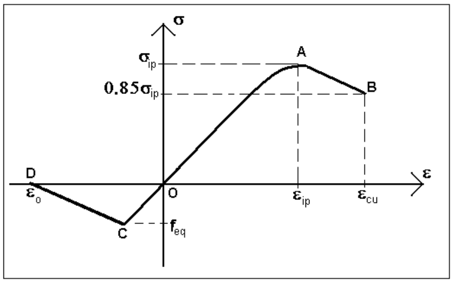

Figure 1. Stress strain curve for the concrete.

The concrete secant modulus recommended by [4] was adopted, that is expressed from Equation 3.

$$E_{cs} = 0.85 \times 5600\sqrt{f_{ck}} = 4760\sqrt{f_{ck}} \tag{3}$$

Such that the "$\mathbf{f_{ck}}$" parameter represents the concrete uniaxial compressive strength.

The concrete ultimate stresses were defined from the failure envelope proposed by Kupfer and Gerstle [9], Figure 2, whose analytical version in biaxial compression state is in Equation 4.

$$(\beta_1 + \beta_2)^2 - \beta_2 - 3.65\beta_1 = 0 \tag{4}$$

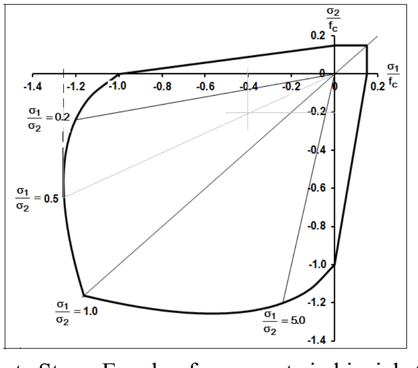

Figure 2. Ultimate Stress Envelop for concrete in biaxial state of stresses.

For which $\boldsymbol{\beta_i = \sigma_{ip}/f_{ck}}$. If $\alpha = \sigma_1/\sigma_2$, where the σ_1 and σ_2 are the principal stresses magnitudes such that $0 > \sigma_1 > \sigma_2$, from Equation 4 results in Equation 5.

$$\sigma_{2c} = \frac{1 + 3.65\alpha}{(1+\alpha)^2} f_{ck} \text{ and } \sigma_{1c} = \alpha\sigma_{2c} \tag{5}$$

The strains related to peak stresses in biaxial compression state, "$\boldsymbol{\varepsilon_{2p}}$" and "$\boldsymbol{\varepsilon_{1p}}$", according to [7], are obtained from Equation 6.

$$\varepsilon_{2p} = \varepsilon_{co}(3\beta_2 - 2) \text{ and } \varepsilon_{1p} = \varepsilon_{co}\left(-1.6\beta_1^3 + 2.25\beta_1^2 + 0.35\beta_1\right) \tag{6}$$

In which the "$\boldsymbol{\varepsilon_{co}}$" parameter is the deformation corresponding to the compressive peak stress referring to uniaxial state of stresses.

The concrete mechanical behavior referring to biaxial state of stresses was modelled from the incremental constitutive relationship proposed by Desai and Siriwardance [1]:

$$\begin{vmatrix} d\sigma_1 \\ d\sigma_2 \\ d\tau_{12} \end{vmatrix} = \frac{1}{1-v^2} \begin{vmatrix} E_1 & v\sqrt{E_1E_2} & 0 \\ v\sqrt{E_1E_2} & E_2 & 0 \\ 0 & 0 & \left(1-v^2\right)G \end{vmatrix} \begin{vmatrix} d\varepsilon_1 \\ d\varepsilon_2 \\ d\gamma_{12} \end{vmatrix} \tag{7}$$

The differentiations, "$d\sigma_1$", "$d\sigma_2$" e "$d\tau_{12}$", on Equation 7, represent the stress increments on the principal directions. The "**E_i's**" parameters are the concrete deformation modules relating to such directions and "**ν**" is the concrete Poisson's ratio. The "G" parameter, namely, the concrete transverse deformation module, may be expressed by the relationship in Equation 8.

$$\left(1-v^2\right)G = 0.25\left(E_1+E_2\right) - 2v\sqrt{E_1E_2} \tag{8}$$

The eight-nodded plane quadrilateral elements **Q8** were performed to represent the mass of concrete region, Figure 3a.

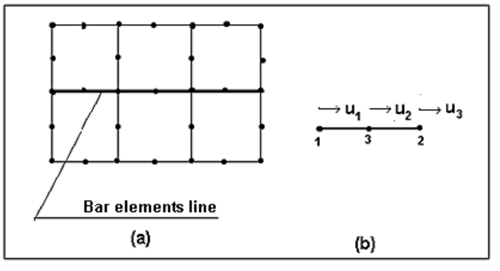

Figure 3. Finite elements: a) Plane Q8; b) bar L3.

2.2 Steel Response to Loading

The steel of the reinforcement was considered as an elastic perfectly plastic material. Due to the great reinforcement steel bars transverse flexibility, only its axial stiffness is taken in account in its mechanical performance, and then, they are simulated as three-nodded bar elements **L3**, Figure 3b. In this way, the referring stiffness matrix "**K**" is regarded according Equation 9.

$$K = \frac{2E_sA_s}{L}\begin{bmatrix} 1 & 0 & -1 \\ 0 & 1 & -1 \\ -1 & -1 & 2 \end{bmatrix} \tag{9}$$

where the "**E_s**" parameter represents the steel Young's modulus, which is considered equal to **210 GPa**. "**A_s**" is the reinforcement cross sectional area, while "**L**" represents the bar finite element length.

2.3 Creep Strains

The creep strains are simulated from the state model proposed by Kawano and Warner [5], Equation 10.

$$\varepsilon_c(t) = \varepsilon_{cd}(t) + \varepsilon_{cv}(t) \tag{10}$$

Where "**ε_{cd}(t)**" and "**ε_{cv}(t)**" are the deformation parcels due to hardening and visco-elastic effects, respectively, such that:

$$\varepsilon_{cd}(t) = -\frac{1}{E_o}\int_0^t \frac{d\Phi_d(t,\tau)}{d\tau}\sigma(\tau)d\tau \text{ and } \varepsilon_{cv}(t) = -\frac{1}{E_o}\int_0^t \frac{d\Phi_v(t,\tau)}{d\tau}\sigma(\tau)d\tau \tag{11}$$

In Equation 11, the "**ϕ_d(t,τ)**" and "**ϕ_v(t,τ)**" functions represent their respective creep coefficients. In their incremental versions, these parcels are presented from Equation 12 and Equation 13.

$$\Delta\varepsilon_{cd}(t_n) = \frac{\sigma(t_{n-1})}{E_o}\left[\Phi_d(t_n,t_o) - \Phi_d(t_{n-1},t_o)\right] \tag{12}$$

and,

$$\Delta\varepsilon_{cv}(t_n) = \left[\frac{\Phi_v^*\sigma(t_{n-1})}{E_o} - \varepsilon_{cv}(t_{n-1})\right]\left[1 - e^{-\Delta t_n/T_v}\right] \tag{13}$$

in which:

$$\Phi_d(t_n,t_o) = \frac{(t_n - t_o)^{0.6}}{10 + (t_n - t_o)^{0.6}}\Phi_d^* \tag{14}$$

In Equation 14, "**ϕ^*_d**" and "**ϕ^*_v**" are the asymptotic creep coefficients referring to those two parcels, and "**T_v**" is the retardation time. The "t_n" parameter is the instant of time for which the creep deformations are being calculated, "t_{n-1}" is the discrete instant, immediately preceding the instant "t_n", and "t_o" is the concrete age at the instant of loading. At every instant "**t_n**" the creep strains are described according to Equation 15.

$$\varepsilon_c(t_n) = \varepsilon_c(t_{n-1}) + \Delta\varepsilon_c(t_n) \tag{15}$$

where "$\Delta\varepsilon_c(t_n)$" is the incremental creep strain that is obtained from Equation 16.

$$\Delta\varepsilon_c(t_n) = \Delta\varepsilon_{cd}(t_n) + \Delta\varepsilon_{cv}(t_n) \tag{16}$$

The temperature effect upon the creep strains simulation was based on the NBR 6118/2014 proceedings [4] from which, the discrete observation time of the phenomenon must be fitted to fictitious concrete ages expressed by Equation 17.

$$t_n = \alpha\sum_i \frac{T_i + 10}{30}\Delta t_{ef,i} \tag{17}$$

where the "**α**" parameter is the cement hardening rate dependent coefficient, for which, the ABNT NBR 6118/2014 proceedings [[4]] recommends suitable typical values that may be applied if experimental results are not available. The "**T_i**" parameter represents the average daily environmental temperature that is expressed in Celsius Degrees (°C), while the "**Δt_{ef}**" term is the elapsed time along what the average daily environmental temperature, T_i, may be assumed as a constant value.

It is assumed in this work that, during each time interval, the stresses magnitudes remain constant, although they may present variation over all the phenomenon observation period, according a step kind function.

3 COMPUTATIONAL SUPPORT

With a view to the acquisition of the results aimed at the fulfilment of the objectives of this work, the software named "Análise Constitutiva Não-Linear" – ACNL [10] was used. Such program was structured according to incremental and iterative procedure and the Finite Elements Method (FEM), on a Nonlinear Orthotropic Formulation in plane state of stresses [7]. It even covers, in its algorithmic framework, the element formulations described in the Section 2 of this paper.

The images referring to the displacement fields were generated from the application NLPOS [11] while those corresponding to the stress fields were produced from the application PROJECT2, elaborated in DELPH 10.2 [12].

4 COMPUTATIONAL CODE VALIDATION

The adopted Code as the Computational Support for this paper was applied to perform the analysis of a rectangular cross-sectional concrete thin-walled column 3.00 m height, 0.20 m thick and 1.20 m width, in plane state of stresses, Figure 4, whose concrete slump test abatement was fixed from 0 cm up to 4 cm and the moisture content in 40%. It was considered two cases for which the reinforcement ratios were fixed as 0.63% and 1.58%. The results of such analysis were compared with their corresponding values obtained from a simplified model, based on the Solid Mechanic Postulates, under uniaxial state of stresses, as performed by Madureira at al [13]. The obtained results showed a good agreement, Figure 5.

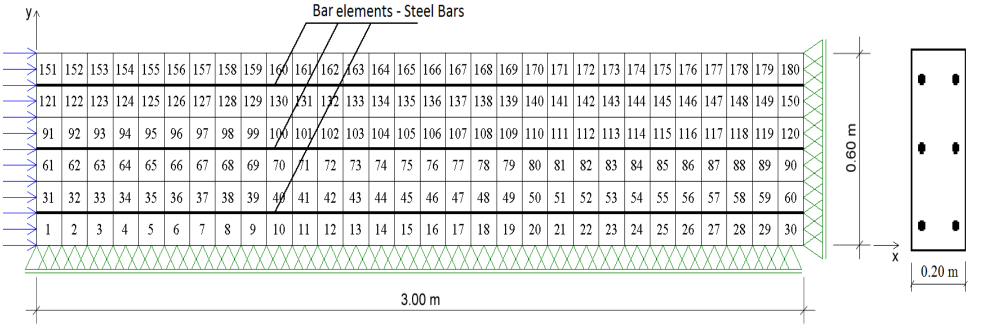

Figure 4. Basic model, Problem domain and finite element mesh.

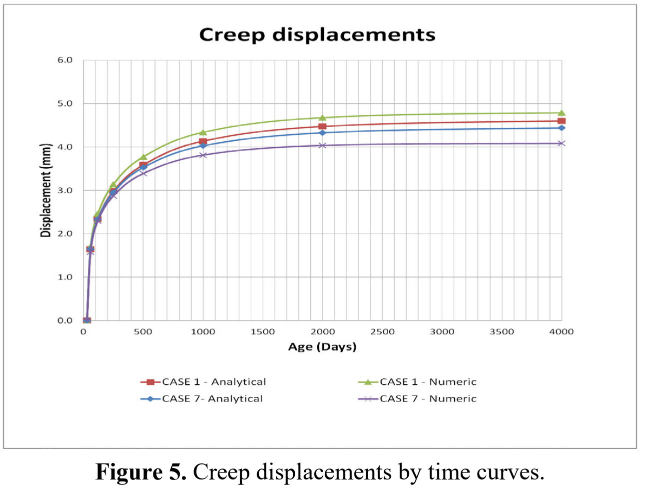

Figure 5. Creep displacements by time curves.

5 ANALYSED MODELS

The studied models are rectangular cross-sectional concrete thin-walled column, 3.00 m height, 0.20 m thick and 1.20 m width, cast both in **C30** or in **C40** concrete, reinforced by **CA-50** steel bars, Figure 4.

The structural members are subjected to a uniform load that is distributed on the column top section, whose magnitude progresses on a gradual mode from zero up to a final value fixed at 3750 kN and 4980 kN, for C30 and C40 concrete cases, respectively, promoting stresses whose magnitude are about 40% of the concrete ultimate compressive stress, the concrete f_{ck}, Table 1. Such load magnitudes are chosen under that pattern as a purpose to regard the NBR 6118/2014 proceedings creep model stresses limitation [4].

Table 1. Studied cases characterization.

Cases	f_{ck} (MPa)	Temperature (°C)	Moisture Content (%)	Φ_v^*
1	30	20	40	1.63
2	30	40	40	1.63
3	30	60	40	1.63
4	30	80	40	1.63
5	30	100	40	1.63
6	30	20	60	0.92
7	30	40	60	0.92
8	30	60	60	0.92
9	30	80	60	0.92
10	30	100	60	0.92
11	40	20	40	1.63
12	40	40	40	1.63
13	40	60	40	1.63
14	40	80	40	1.63
15	40	100	40	1.63
16	40	20	60	0.92
17	40	40	60	0.92
18	40	60	60	0.92
19	40	80	60	0.92
20	40	100	60	0.92

The analysis was performed upon twenty cases, differentiated among themselves by the concrete compressive strength, by the temperature and by the moisture content, as shown in columns 2, 3 and 4, respectively, of Table 1. It should be emphasized that the temperature levels were chosen in this way to simulate the predominant environmental conditions around the column surface during each season of the year.

Due to the column symmetry in terms of geometry, load, strains and stresses, along the column width the problem domain was defined from the rectangular area whose horizontal dimension is equal to the column height, and the vertical dimension is equal to its half width, Figure 4. In other words, the column width is represented by its half width. Its discretization was based on the plane and bar elements, both 0.10 m lengths, from which resulted the mesh composed by 180 plane elements and 90 bar elements, Figure 4. It is observed that in all column figures the structural member is being represented with its longitudinal axis coinciding with the "x" direction.

The age of the concrete at the instant of loading was set as 30 days. It was assumed that the overall column perimeter surface is exposed to the environment medium. The retardation time was fixed as $T_V = 600$ days. The asymptotic hardening creep coefficient was considered as being $\phi_d^* = 2.0$, as recommended by Kawano and Warner [5]. The asymptotic creep coefficient referring to viscous elastic effects, ϕ_v^*, exhibit distinct values, case to case, as shown on Table 1, column 5, that is obtained by the difference between the total asymptotic creep coefficient of NBR 6118/2014 [4] and the asymptotic hardening creep coefficient.

The analysis was performed according to the "Plane State of Stresses".

For the purposes of covering the creep phenomenon longevity, the maximum age limit of concrete was set as 2000 days, which corresponds to the age from which the creep displacements, virtually, stabilizes, Figure 5. Such an elapsed time was discretized from observation instants at 33, 39, 54, 90, 176, 379, 860 and 2000 days.

6 RESULTS AND DISCUSSION

According to the obtained results the fields of displacements and normal stresses took the morphologies shown in Figures 6 and 7, respectively, for the equilibrium configuration at the instant of loading. For those cases corresponding to C30 concrete the displacement magnitude at the column top and the stress on the mass of concrete, were about 2.0 mm and 15 MPa, respectively, for those one referring to C40 concrete such parameters have assumed magnitudes about 2.4 mm and 20 MPa, respectively, Table 2 and 3.

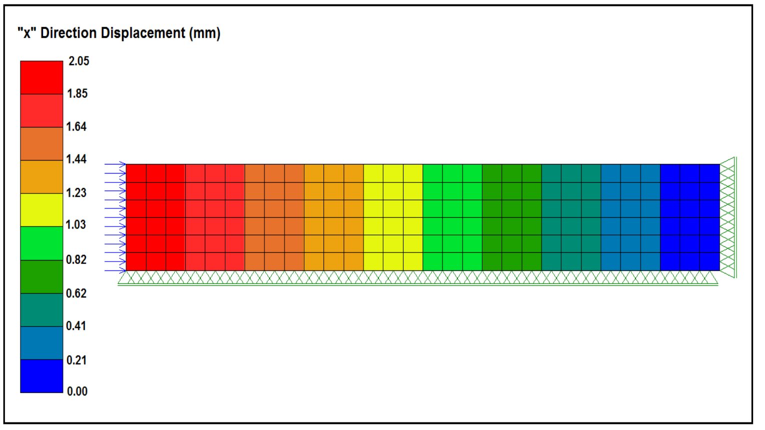

Figure 6. Field of axial displacement at the instant of loading – Case 1.

Table 2. Column top displacements.

Cases	Displacement (mm)			Final age (days)
	Immediate	Creep (90 days)	Final creep	
1	2.05	2.26	5.14	860
2	2.05	2.70	4.69	379
3	2.05	3.02	5.10	379
4	2.05	3.29	4.34	176
5	2.05	3.51	4.60	176
6	2.05	2.14	4.70	2000
7	2.05	2.50	4.80	2000
8	2.05	2.76	4.83	2000
9	2.05	2.96	4.85	2000
10	2.05	3.13	4.86	2000
11	2.37	2.64	4.76	379
12	2.37	3.16	4.23	176
13	2.37	3.54	4.72	176
14	2.37	3.85	3.85	90
15	2.37	4.11	4.11	90
16	2.37	2.50	4.10	379
17	2.37	2.93	4.63	379
18	2.37	3.23	4.09	176
19	2.37	3.47	4.35	176
20	2.37	3.66	4.56	176

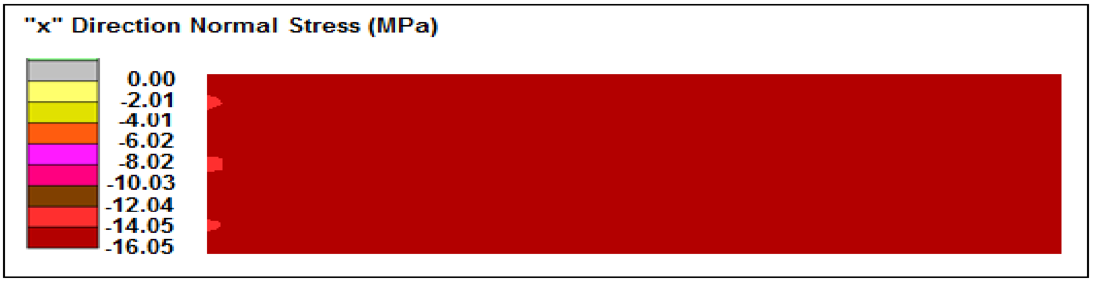

Figure 7. Field of normal stresses at the instant of loading – Case 1.

Table 3. Stresses on the mass of concrete.

Cases	Concrete Stress (MPa)			Final age (days)
	Immediate	Creep (90 days)	Final	
1	14.8	14.1	13.0	860
2	14.8	13.9	13.2	379
3	14.8	13.8	13.0	379
4	14.8	13.7	13.3	176
5	14.8	13.6	13.2	176
6	14.8	14.1	12.9	2000
7	14.8	14.0	12.8	2000
8	14.8	13.9	12.7	2000
9	14.8	13.8	12.7	2000
10	14.8	13.7	12.7	2000
11	19.8	18.9	18.2	379
12	19.8	18.8	18.4	176
13	19.8	18.6	18.2	176
14	19.8	18.5	18.5	90
15	19.8	18.4	18.4	90
16	19.8	19.0	18.3	379
17	19.8	18.8	18.1	379
18	19.8	18.7	18.3	176
19	19.8	18.6	18.2	176
20	19.8	18.5	18.2	176

At the instant of loading, the fields of stresses, Figure 7, have presented discrete stress changing, however, at the cross sections over the vicinity of the column top, namely, the loading introduction region, it may be observed tenuous disturbances.

The acquired results have revealed that the creep strains by time evolved according the curves showed in Figures 8 and 9 and the corresponding fields have stabilized themselves according the fashions of the Figures 10 and 11.

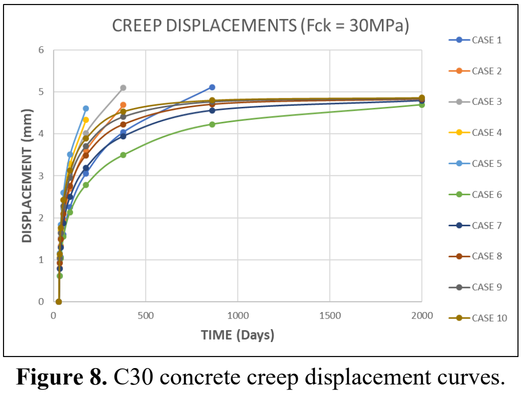

Figure 8. C30 concrete creep displacement curves.

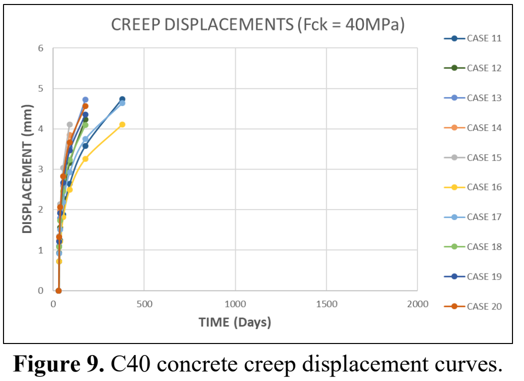

Figure 9. C40 concrete creep displacement curves.

As a result of the creep effect the stresses on the reinforcement steel bars evolved according the curves of Figures 12 and 13, noting up the increase occurrence in their magnitude. For every case associated to C40 concrete the overstress hit a value close to 200%, Table 4, inducing, in this way, the material yielding.

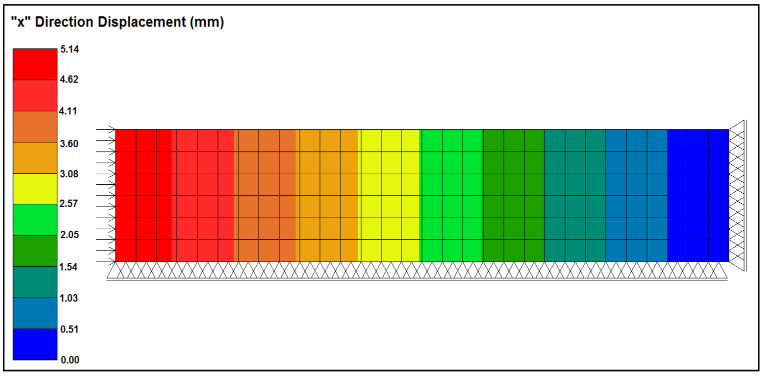

Figure 10. Field of creep longitudinal displacements: Day 860 - Case 1.

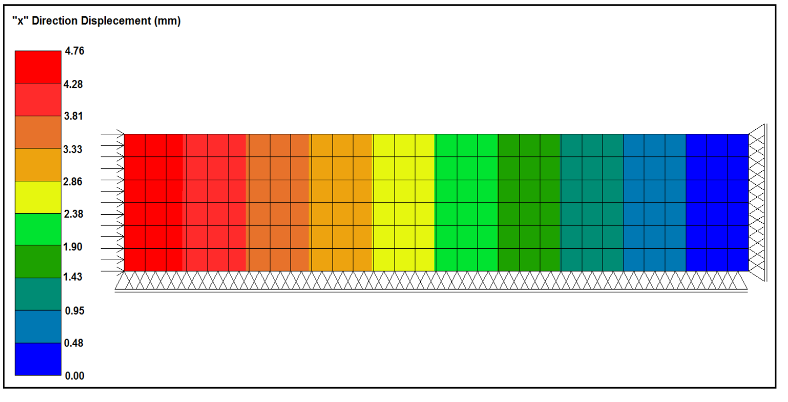

Figure 11. Field of creep longitudinal displacements: Day 379 - Case 11.

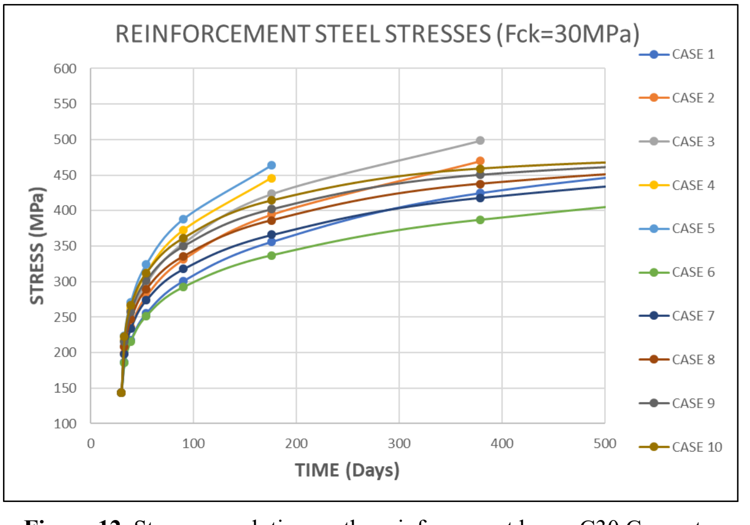

Figure 12. Stresses evolution on the reinforcement bars - C30 Concrete.

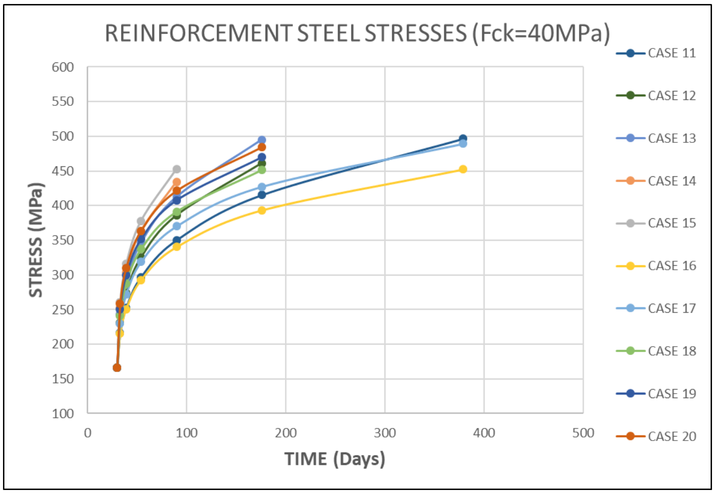

Figure 13. Stresses evolution on the reinforcement bars - C40 Concrete.

Table 4. Stresses on the reinforcement.

Cases	Reinforcement stresses (MPa)			Final age (days)
	Immediate	Creep (90 days)	Final	
1	143	301	499	860
2	143	331	470	379
3	143	354	498	379
4	143	372	446	176
5	143	388	464	176
6	143	292	470	2000
7	143	318	477	2000
8	143	336	479	2000
9	143	350	481	2000
10	143	361	482	2000
11	166	350	496	379
12	166	386	461	176
13	166	413	495	176
14	166	434	434	90
15	166	453	453	90
16	166	340	452	379
17	166	370	489	379
18	166	391	451	176
19	166	408	470	176
20	166	421	484	176

Although the observation time of the phenomenon discussed in this paper was fixed, at first, up to 2000 days of concrete age, due the precocity of the reinforcement bars steel yielding and the consequent lost of the column stability, as was already commented in the upper paragraph, in some studied cases the time-displacement curves and the time-stresses curves are being broken up. Due to that reason the 90 days of the age of concrete was considered as a reference for the relevant parameters' comparative analysis for all cases. Such age corresponds to the smallest among those one at which the steel yielding of all studied cases already has been triggered.

According to the obtained results the smallest creep displacement at the age of reference was about 2.1 mm, registered for case 6, Table 2, which refers itself to the smallest temperature, corresponding to 1.05 times the displacement recorded at the instant of loading. The largest one was about 4.1 mm, registered for case 15, which concerns itself to the highest temperature and corresponds to 1.7 times the displacement pointed at the instant of loading.

From more detailed analysis referring to C30 concrete, over the set of curves associated to moisture content by 40%, namely cases 1, 2, 3, 4 and 5, presented in Figure 8, it may be noted that as higher the temperature as higher the creep displacements. Nevertheless, for all cases of this group, the creep displacements after the phenomenon stabilization, present, in practice, similar magnitudes. In the same way, the set of curves associated to cases 6, 7, 8, 9 and 10, referring to the moisture content by 60%, exhibits a similar trend.

As to be expected from the fact that reinforcement bars stresses and the creep strains developed themselves on a similar pattern, the overstress was more significant and, therefore, the steel yielding was hit, as earlier as higher the temperature.

The gotten results indicate that the creep strains may promote the stress relief on the mass of concrete, Figure 14 and 15 and in some cases, the stresses fields stabilized themselves at 2000 days of concrete age according the aspect illustrated in Figure 16. In other cases, the relieving process was stopped prematurely, due to the yielding of reinforcement steel bars. The lowest stress relief at the reference age was about 4,7% and 4%, registered for cases 6 and 16, that are referred, to the lowest temperature, while, the largest one was about 8% and 7%, verified to the cases 5 and 15, referring to the highest temperature. However, it is worthwhile of note that was recorded stress relief of about 14% for cases 8, 9 and 10, when the stationary condition was reached.

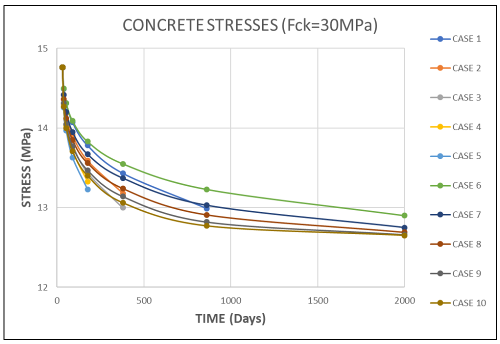

Figure 14. C30 Concrete stresses evolution by creep.

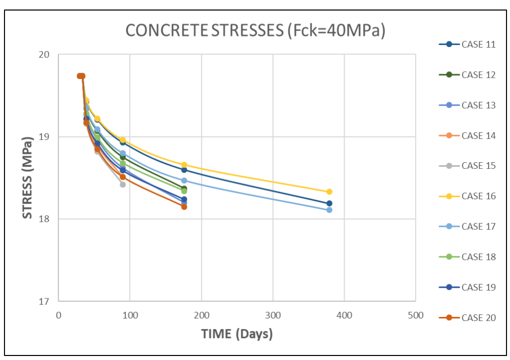

Figure 15. C40 Concrete stresses evolution by creep.

It was noticed, indeed, from the comparison between Figures 7 and 16, that the creep strains have intensified the stresses disturbance upon the mass of concrete over the region close to the top of column.

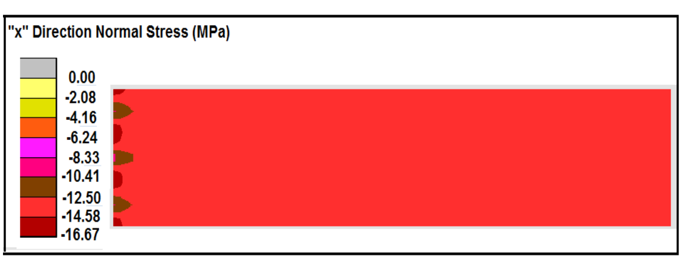

Figure 16. Field of the normal stresses on the mass of concrete: Day 860 – Case 1.

7 CONCLUSIONS

This work refers itself to the analysis of the temperature effects upon creep strains on reinforced concrete structural members based on a State Model from a non-linear orthotropic calculus framework and the finite element approximation.

Twenty cases involving thin-walled columns, differentiated among themselves by the temperature, by the concrete strength and by the moisture content, were studied.

The obtained results showed that, already at 2000 days from concrete cast, the creep displacement, virtually, reaches the stationary condition.

The analysis performed from the acquired results pointed out the occurrence of stresses increase on the reinforcement steel bars as it was reported in [14], that, especially for those cases referring to the highest temperature, it culminated to the material yielding condition, as reported in [13].

Because the yielding phenomenon commented in the last paragraph has occurred and, in this way, the column lost its structural stability, already, at 90 days from the concrete cast, even before the concrete creep strains had reached the stationary stage, such age was considered as the reference instant to the parameters comparative analysis performed in this work.

According to the obtained results, the creep displacement magnitudes at the reference age were as more pronounced as higher the temperature although, for those cases for which the deformation process was maintained up to the creep phenomenon stability, the final displacement values showed themselves temperature independent.

As a matter of fact, if the comparative analysis of the parameters corresponds to that age from which the steel yielding has triggered and that such an instant is earlier than the creep stabilization, the considered magnitudes of the concrete creep displacements in such a analysis are much lower than they would be if the steel yielding phenomenon had not occur.

From the acquired results it was noted the occurrence of stresses relief in the mass of concrete that, at the referring age, was as greater as higher the temperature, as it would be to expect.

ACKNOWLEDGEMENTS

This report is part of a research work on the numerical simulation of the creep strains on reinforced concrete members supported by the Fundação Coordenação de Aperfeiçoamento de Pessoal de Nível Superior – CAPES and by the Pró-Reitoria de Pesquisa da Universidade Federal do Rio Grande do Norte – UFRN. Their support is gratefully acknowledged.

REFERENCES

[1] A. M. Neville, *Properties of Concrete*. London, UK: Pearson, Prentice Hall, 2004.

[2] J. K. Wight and J. G. McGregor, *Reinforced Concrete – Mechanics & Design*. Boston, MA: Pearson, 2012.

[3] E. L. Madureira and L. A. Paiva, "Fresh concrete consistency effect on thin-walled columns creep phenomenon," *IBRACON Struct. Mater. J.*, vol. 11, no. 3, pp. 644–651, May/Jun. 2018, http://dx.doi.org/10.1590/s1983-41952018000300012.

[4] Associação Brasileira de Normas Técnicas *NBR 6118: Projeto de Estruturas de Concreto - Procedimento*. Rio de Janeiro, RJ, Brasil: ABNT, 2014.

[5] A. Kawano and R. F. Warner, "Model formulations for numerical creep calculations for concrete," *J Struct. Eng.*, vol. 122, no. 3, pp. 284–290, Mar. 1996. http://dx.doi.org/10.1061/(ASCE)0733-9445(1996)122:3(284).

[6] P. M. Pimenta and H. C. Santos, "Análise e Retro-análise de Estruturas de Concreto Sujeitas à Deformação Lenta," in IV Simpósio EPUSP sobre Estruturas de Concreto. São Paulo, SP, Brasil, Aug. 2000.

[7] H. G. Kwak and F. C. Filippou, *Finite Elements Analysis of Reinforced Concrete Structures Under Monotonic Loads* (Report UCB/SEMM-90/14). Berkeley, CA: University of California, 1990.

[8] E. Hognestad, *A Study of Combined Bending and Axial Load in Reinforced Concrete Members*. (Bolletin n. 399, Vol. 49, no. 22). Urbana, Illinóis: University of Illinois, Engineering Experiment Station, 1951.

[9] H. B. Kupfer and K. H. Gerstle, "Behaviour of Concrete under Biaxial Stresses," *J Eng Mech*, vol. 99, no. 4, pp. 853–866, Aug. 1973.

[10] E. L. Madureira, "Simulação numérica do comportamento mecânico de elementos de concreto armado afetados pela reação álcali-agregado," Ph.D. dissertation, Dept. Eng. Civil, Univ. Fed. Pernambuco, Recife, PE, 2007.

[11] R. L. S. Pitangueira and E. Parente Jr, *NLPOS – Programa para Visualização de Resultados de Analises Não Lineares de Modelos Bidimensionais de Elementos Finitos. Versão 1.0*, Rio de Janeiro: DEC/PUC-Rio, 1997.

[12] E. L. Madureira and A. L. A. Silva, *PROJECT1 – Programa para Visualização de Campos de Tensões Resultantes de Analises Não Lineares de Modelos Bidimensionais de Elementos Finitos. Versão 1.0*, Rio Grande do Norte: DEC/UFRN, 2013.

[13] E. L. Madureira, T. M. Siqueira, and E. C. Rodrigues, "Creep strains on reinforced concrete columns," *IBRACON Struct. Mater. J.*, vol. 6, no. 4, pp. 537–560, 2013., http://dx.doi.org/10.1590/S1983-41952013000400003.

[14] L. T. Kataota, M. A. S. Machado, and T. N. Bittencourt, "Análise numérica da transferência de carga do concreto para a armadura em pilares de concreto armado devida à fluência e retração," in *IBRACON*, Fortaleza: IBRACON, 2010.

[15] C. S. Desai and H. J. Siriwardance, *Constitutive Laws for Engineering Materials*. Englewood Cliffs, NJ: Prentice Hall, 1972.

Author contributions: ELM, BVCF conceptualization, conceptualization, formal analysis, methodology, writing; BVCF: data curation.

Editors: Bernardo Tutikian, José Luiz Antunes de Oliveira e Sousa, Guilherme Aris Parsekian.

IBRACON Structures and Materials Journal
Revista IBRACON de Estruturas e Materiais
ISSN 1983-4195 ismj.org

ORIGINAL ARTICLE

Optimization of the structural system with composite beam and composite slab using Genetic Algorithm

Otimização do sistema estrutural viga mista e laje mista com utilização de Algoritmo Genético

Breno Dias Breda[a]
Tiago Cetto Pietralonga[a]
Élcio Cassimiro Alves[a]

[a]Universidade Federal do Espírito Santo – UFES, Departamento de Engenharia Civil, Vitória, ES, Brasil

Received 05/Sep/2019
Accepted 25/Mar/2020

Abstract: The objective of this research is to create a software to optimize choice variables adopted by an engineer in a structural system with steel-concrete composite beams and steel decks, such as: beam shape, composite slab sheeting, number and spacing of beams, slab thickness and interaction ratio between beam and slab. To accomplish this, a program that uses the Genetic Algorithm optimization tool provided by Matlab R2015a was developed. To meet safety requirements, restrictions on the Ultimate Limit State were implemented in the code, following the normative requirements of ABNT NBR 8800: 2008. Case studies of a problem found in the literature and another of a real structure, are presented to serve as references for software evaluation. Results indicate that the use of optimization processes is fundamental to design increasingly cost-effective structures.

Keywords: optimization, genetic algorithm, composite beam, composite slab.

Resumo: O objetivo deste trabalho é apresentar uma formulação computacional que otimize as variáveis de escolha a serem adotadas pelo engenheiro em um projeto de viga mista metálica com *steel deck*. Para esse fim foi utilizado o programa Matlab R2015a que possui uma ferramenta de otimização que utiliza o AG. Para atender os requisitos de segurança, restrições considerando o ELU são consideradas no código do programa elaborado, seguindo as prescrições normativas da ABNT NBR 8800:2008. Estudos de casos de um problema encontrado na literatura e de uma estrutura real, uma laje de sala de aula em um edifício de dois pavimentos, são apresentados a fim de servirem de referência para aferição e avaliação do programa. Os resultados permitem concluir que a utilização de processos de otimização é fundamental para obtenção de projetos cada vez mais economicamente vantajosos.

Palavras-chave: otimização, algoritmo genético, viga mista, laje mista.

How to cite: B. D. Breda, T. C. Pietralonga, and E. C. Alves, "Optimization of the structural system with composite beam and composite slab using genetic algorithm," *Rev. IBRACON Estrut. Mater.*, vol. 13, no. 6, e13602, 2020, https://doi.org/10.1590/S1983-41952020000600002

1 INTRODUCTION

Structural optimization is a method aimed at reducing the construction cost of a given structural design as much as possible, without detriments to structural safety. A good optimization process is one in which the modelled structure and considerations regarding chosen design variables closely resemble actual service conditions. Examples of appropriate structural optimizations include the works conducted by Lazzari, Alves and Calenzani [1]; Lubke, Alves and Azevedo [2] and Breda et al. [3].

Among the optimization methods currently available, Genetic Algorithms (GA) stand out due to the possibility of working with discrete variables, making GA the recommended approach for optimizing structural systems featuring

Corresponding author: Breno Dias Breda. E-mail: breno.breda@hotmail.com
Financial support: None.
Conflict of interest: Nothing to declare.

steel-concrete composite beams and slabs, since these systems can be designed with the aid of tables provided by manufacturers.

In the 1960s, John Holland, regarded as the creator of the GA, relied on the principle of Mendelian inheritance and Darwin's natural selection to create the basis of the algorithm within the principles of meta-heuristics. In other words, Holland created an iterative process that uses random choices combined with knowledge of previous answers to achieve an overall optimal value, avoiding local instances of said value.

The system of composite beams combined with composite slabs with built-in steel sheeting, also known as steel deck (Figure 1), is a structural solution that stands out for reductions in construction time and usages of wooden formwork and shoring. The design of the composite slab is relatively complex; however, manufacturers of the steel formwork usually provide simplified design tables, making the design process easier and ideal for the implementation of GA.

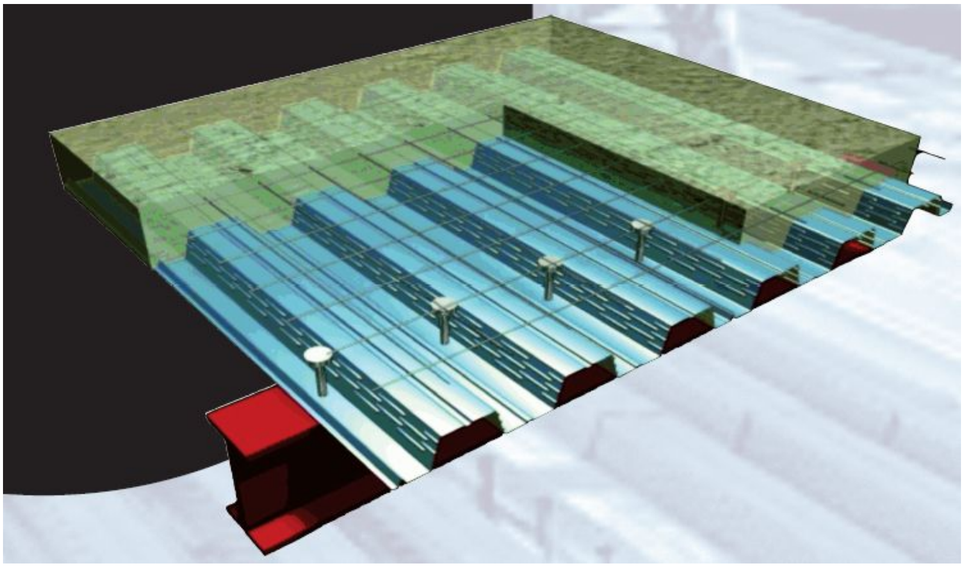

Figure 1 - Composite beam system with composite slab (Metform [4]).

Some of the different applications of GA in engineering are presented by Liu and Hammad [5]. In 1997, the authors performed an optimization study for bridge recovery using genetic algorithms, forming a model with multiple objective functions, and combining the different results with an approach based on the Pareto principle. The optimization study aimed to reduce the cost of bridge recovery and the degree of deterioration, concluding that GA presents excellent results even in a model with multiple objectives, and without requiring much time to perform calculations.

Cho, Min and Lee [6] carried out an optimization study in 2001 using GA to evaluate the life cycle cost of bridges with orthotropic steel deck systems, which consists of steel slabs with ribbed formwork reinforced longitudinally, transversely, or in both directions. In this life cycle analysis, building and maintenance costs were considered, with adjustments in structural resistance, deflection, and fatigue. The study concludes that optimization analyses lead to a more rational, economical, and safer design when compared to conventional design methods.

Kuan-Chen Fu, Zhai and Zhou [7] used GA in 2005 to find optimized solutions for bridges with steel beams. The main objective was to minimize the weight, and consequently the cost of the structure. Bridges with single span and continuous beams of various lengths were analyzed. The GA presented satisfactory results, emphasizing its proximity to actual service conditions when discrete variables are used.

Also, in 2005, Souza Junior [8] carried out a study that implemented GA on the global mechanical behavior of spatial steel tubular structures. This research assessed total steel consumption for several geometric configurations, focusing on solutions to minimize it.

In 2008, Câmara Neto, Landesmann and Batista [9] presented an application of GA on the design of steel-concrete composite beams in multi-story buildings. The study sought alternatives to lower costs while still abiding by safety criteria for room and fire temperatures, the latter prescribed in design standards EuroCode 4 and ABNT NBR 14323: 1999. Different laminated steel profiles were considered, combining different steel reinforcement rates and thicknesses of fire protection materials.

Still in 2008, Forti and Requena [10] developed a software to optimize the structural design of large steel roofs using GA, seeking to improve the structural design of single and multiplane trusses by varying specific parameters. Software tests concluded that GA optimization presents good results for this type of structure.

Lima [11] developed an optimization software in 2011 using GA applied to reinforced concrete beams, using discrete variables to better represent the variables of choice in each structural design. The use of GA provided significant improvements, especially in complex scenarios and with constant restrictions. Furthermore, in 85% of the cases, optimization procedures led to overall optimal solutions.

Kripakaran and Gupta [12] developed, also in 2011, a decision support system based on GA applied to steel frames, with various connection types. The study highlights the advantages of using discrete variables with GA. This feature is explored in the software later presented herein.

Kociecki and Adeli [13] and Prendes-Gero et al. [14] implemented GA for optimization of different steel structural systems in 2015 and 2018, respectively, and observed gains of around 10% when compared to non-optimized designs. Both studies also highlighted the ability to work with discrete variables when using GA as an important characteristic for obtaining good results.

Bilbao [15] presented in 2016 a study of optimal design of a tuned mass damper with GA in prefabricated slabs. Results proved to be valid when compared to existing design abacuses in the literature.

Bezerra [16] implemented, in 2017, a MATLAB code to optimize the cost of reinforced concrete beams using GA. Optimized variables included effective depth, beam width and the areas of longitudinal and transverse reinforcement steel. The author observed gains of around 2% when compared to other optimization methods.

Malveiro et al. [17] implemented GA in a 2018 study of bridges and viaducts using finite element models validated with experimental tests. The GA was used to perform a calibration of parameters, calculating the optimal values of the most significant physical properties to increase the correlation of numerical results with those obtained experimentally.

Studies addressing the optimization of composite structures are observed in Lima et al. [18]. As an example, in 2008 the authors used GA to assess design problems related to vibration in steel-concrete composite walkways, considering international criteria for assessing human comfort in structures of this type aimed at pedestrian use. The study sought to maximize allowable spans using said criteria along with standardized design recommendations concerning serviceability and ultimate limit states.

Pereira [19] conducted a 2016 study of optimization on composite beams used in bridges to reduce the dimensions of bridge decks. The optimization was implemented with Microsoft Excel and focused on resizing the support beams. Analyses yielded satisfactory results, indicating a reduction of 7.8% in the final cost of construction.

Papavasileiou and Charmpis [20] carried out, also in 2016, a study to optimize the costs of composite steel and concrete beams and columns in multi-story buildings, considering static and seismic loading. The authors implemented optimization via Evolution Strategies, a probabilistic method like the GA. The method proved to be efficient when applied to practical scenarios.

In 2018, Silva and Rodrigues [21] presented an optimization study of composite beams in which the structural design was performed using an iterative method of sequential linear programming as an optimization process. This approach sought to reduce consumption of materials via variation of parameters such as: cross-section geometry of the concrete slab and the beam, as well as the area of steel reinforcement.

Tormem et al. [22] published, in 2019, a research on the optimization of steel-concrete composite beams with welded steel profiles using the harmonic search optimization method. Profile geometries were selected as discrete variables and the design procedures followed standards such as ABNT 8800: 2008 and ABNT 5884: 2013. Overall, results proved to be quite efficient, minimizing costs.

The present research seeks to develop a computational tool that optimizes the choice variables adopted by engineers when designing structural systems featuring steel-concrete composite beams and slabs, such as: beam profile, slab profile sheeting, quantity and spacing of secondary beams, slab thickness and the degree of interaction between beam and slab.

The optimization is carried out in compliance with safety requirements, added to the software as restrictions considering Ultimate Limit State (ULS) design, according to design prescriptions from ABNT NBR 8800: 2008 [23].

Two problems are presented for validation and evaluation of the developed software. The first is an example of simplified optimization presented by Fakury, Silva and Caldas [24]. The second is a comparison with an existing structure that uses the steel deck as a floor system.

Furthermore, it is essential to emphasize the relevance of this work, considering the lack of optimization studies using the GA method applied to systems featuring composite slabs with profile sheeting in combination with steel-concrete composite beams.

2 METHODOLOGY

2.1 Genetic Algorithm

According to the Matlab R2015a documentation [25], the steps for solving an optimization problem via GA are as follows:

i. The algorithm creates an initial random population;
ii. A sequence of new populations is created. At each step, individuals of the current generation are used to create the next population. New populations, in turn, are obtained from the following steps:
   a. Evaluation of each individual within the population according to the value returned by the algorithm when calculating the objective function (fitness value);
   b. Application of a scale factor to the gross values from the previous step to convert them into a range that is easier to use;
   c. Selection of individuals, called parents, based on their fitness value;
   d. Some individuals in the current population who have better fitness values are chosen as the elite. These individuals are kept in the next population;
   e. Production of offspring from parents by making random changes to a single parent (mutation) or by combining vector input information from a pair of parents (crossing);
   f. Replacement of individuals in the current population with offspring, forming the next population.
iii. The algorithm stops when one of the stop criteria is met.

Thus, it can be understood that an individual is a possible answer to the problem studied and the population is a set of individuals.

The stopping criteria used by the GA are:

i. Number of generations (MaxGenerations), with a default value of 100 times the number of variables;
ii. Time limit (MaxTime), for which the default value is infinite;
iii. Optimal predetermined value reached (FitnessLimit), with a default value of negative infinity, that is, the lowest possible;
iv. Small or no variation in the best response between a given number of generations (MaxStallGenerations), with a default value of 50 generations;
v. Small or no variation in the best response over a period of time (MaxStallTime), with a default value of infinity;

The tolerance, or precision of the values, returned by the objective function is 10^{-6} and for the calculation of the restrictions, 10^{-3}.

2.2 Scope of the software

The software detailed in this paper was implemented in Matlab R2015a [25], the GA is native to the program, and is used here with its default parameters. The software uses the following underlying principles:

- Considers the slab as composite, supported by composite secondary beams, connected by stud-bolts;
- Optimizes the profile of the secondary beam using the table of laminated profiles from Gerdau [26];
- Optimizes the composite slab (steel deck thickness, maximum span, height of the concrete layer). The steel deck is selected from the Metform load-span table [4], which can be MF-50 or MF-75;
- Considers that the load is uniformly distributed over the slab.

Optimization of secondary composite beams is performed with the software developed by Breda et al. [3], changing only the way the variables to be optimized are treated, taken as discrete in this case. The restrictions regarding the beams are discussed in more detail in Breda et al. [3].

The initial population contains 120 individuals and the following, 60. The rate of elite individuals and crossing of the intermediate type are 0.05 and 0.8, respectively, whereas the mutation rate is random. The GA is performed primarily with an entirely random initial population, thereby obtaining an optimal local response. Then the algorithm is executed again with the previously obtained answer added to the initial population. More details can be found on the Matlab documentation.

2.3 Choice variables

The choice variables, or individuals, are represented by a 1x6 vector, where each element represents, respectively:

- The line number of Gerdau [26] profile table that represents the profile analyzed. The values are taken from the table for: profile height (d), flange width (b_f), web thickness (t_w) and flange thickness (t_f). This value ranges from 1 to 88 for the laminated profiles table;
- The line number of the table of values for the interaction ratio of the slab-beam analyzed. This value ranges from 1 to 100, the values in the table range from 0 to 1, with an accuracy of two decimal places;
- The line number of the Metform [4] table that represents the incorporated formwork for the composite slab analyzed. This value ranges from 1 to 24;
- The column number of the Metform [4] table, which represents the maximum span of the composite slab analyzed. This value ranges from 1 to 16;
- Value used to alternate the orientation of the secondary beams, between transversal and longitudinal. This value alternates between 1 and 2;
- Value used to switch between Metform sheeting types [4]. This element takes the value of 1 for MF-50 and 2 for MF-75.

By simple combinatorial analysis, the universe of possible responses, including viable and non-viable responses, has 13,516,800 possibilities.

2.4 Fitness function

The fitness function (*f*) determines the value to be optimized, which for the present case is the cost of the composite beam/slab structural system. The function f is given by Equation 1.

$$f = C_{beam} + C_{connector} + C_{formwork} + C_{concrete} + C_{mesh} \tag{1}$$

where: C_{beam} = total cost of the beams (R$), given by Equation 2; $C_{connector}$ = cost of the connectors (R$), given by Equation 3; $C_{formwork}$ = total cost of the steel profile sheeting (R$), given by Equation 4; $C_{concrete}$ = total cost of concrete used in the composite slab (R$), given by Equation 5; and C_{mesh} = total cost of the welded wire reinforcing mesh of the composite slab (R$), given by Equation 6.

$$C_{beam} = n_{beam} . \rho_{steel} . \left(A_{beam} . L_{beam} \right) . c_{beam} \tag{2}$$

where: n_{beam} = number of beams adopted in the solution (un.); ρ_{steel} = specific mass of profile steel, adopted as 0.00785 kg/cm^3; A_{beam} = cross section area of beam profile (cm^2); and L_{beam} = beam length (cm); and c_{beam} = unit cost of steel profile of the beam (R$/kg).

$$C_{connector} = n_{connector} . c_{connector} \tag{3}$$

where: $n_{connector}$ = number of shear connectors adopted in the solution (un.); and $c_{connector}$ = unit cost of the shear connector (R$/un).

$$C_{formwork} = A_{slab} . c_{formwork} \tag{4}$$

where: A_{slab} = rectangular slab area covered by profiled sheeting (cm^2); and $c_{formwork}$ = unit cost of the profile sheeting (R$/cm^2).

$$C_{concrete} = v_{concrete} . A_{slab} . c_{concrete} \tag{5}$$

where: $v_{concrete}$ = unitary concrete consumption, obtained from Metform's [4] load-span table (cm^3/cm^2); and $c_{concrete}$ = unit cost of concrete used in the slab (R$/cm^3).

$$C_{mesh} = p_{mesh}.A_{slab}.c_{mesh} \tag{6}$$

where: p_{mesh} unit consumption of slab welded wire reinforcement, obtained from Metform's [4] load-span table (kg/cm^2); and c_{mesh} = unit cost of welded wire reinforcement (R$/kg).

2.5 Restrictions

The constraint function (C), given by a system of equations, gathers the conditions that must be met for a given answer to be accepted as a solution to the problem. As such, restrictions are generally based on standardized requirements such as those prescribed in ABNT NBR 8800: 2008 [23]. For this case, function C is given by Equation 7.

$$C = \begin{cases} C_1 : \dfrac{h_w / t_w}{5.7\sqrt{E / f_{yk}}} - 1 \leq 0 \\ C_2 : \dfrac{\alpha_{min}}{\alpha} - 1 \leq 0 \\ C_3 : \dfrac{M_{sd}}{M_{rd}} - 1 \leq 0 \\ C_4 : \dfrac{V_{sd}}{V_{rd}} - 1 \leq 0 \\ C_5 : \dfrac{q_{sd}}{q_{rd}} - 1 \leq 0 \end{cases} \tag{7}$$

where:
C_1 prevents the use of profiles with slender webs in composite structures;
where: h_w = profile web height (cm); t_w = profile web thickness (cm); E = elasticity modulus of steel (kN/cm^2); and f_{yk} = characteristic value of yield strength of profile steel (kN/cm^2).
C_2 does not allow interaction ratios between beam and slab below the minimum value;
where: α_{min} = minimum interaction ratio between beam and slab given by ABNT NBR 8800: 2008 as a function of material, shape and length of the beam; and α = interaction ratio between beam and slab of the structure.
C_3 checks if the design bending moment is less than the resistant bending moment;
where: M_{sd} = design bending moment on the structure (kN.cm); and M_{rd} = resistant design bending moment (kN.cm).
C_4 checks if the design shear force is less than the resistant shear force;
where: V_{sd} = design shear force on the structure (kN); and V_{rd} = resistant design shear force (kN).
C_5 checks if the live load acting on the slab is less than the value allowed by the manufacturer;
where: q_{sd} = live load uniformly distributed on the slab (kN/cm^2); and q_{rd} = maximum live load (superimposed load) resisted by the composite slab depending on the span, type of formwork and height of the concrete layer, obtained from Metform's [4] load-span table (kN/cm^2).

2.6 Loading and resistance

The calculation of the design load adopted for the slab using the Metform [4] tables, does not consider resistance factors, that is, the characteristic values of the loads are adopted, disregarding dead load, in accordance to recommendations from the manufacturer.

Stresses on the beams are obtained considering resistance factors prescribed in ABNT NBR 8800: 2008 [23], with a value of 1.4 for gravitational loads (mainly due to concrete) and 1.5 for live loads. The design loads for slab and beam are given by equations 8 and 9 below:

$$q_{d,slab} = P_{p,surfacing} \cdot Q_{overload} \tag{8}$$

$$q_{d,beam} = 1.4\left(P_{p,structure} + P_{p,surfacing}\right) + 1.5\left(Q_{liveload} \cdot A_{influence}\right) \tag{9}$$

The loading on the slab is not calculated, since design is performed by comparing the load acting on the slab and the load resisted by the slab, according to the manufacturer. Alternatively, loads acting on the secondary beams are calculated considering these elements as simply supported, subjected to a uniformly distributed linear load. The calculation of the internal and resistant stresses of the beams is assessed in more detail by Breda et al. [3].

2.7 Input data

To begin the solution, specific parameters must be inserted into the software. These parameters are shown in Table 1, which also details the values adopted for the problems analyzed herein. The unit costs of the materials were taken from the sources mentioned in Table 1. The costs chosen are compatible with those usually practiced in the Brazilian market.

Table 1 - Input data.

Parameter	Unit	Value adopted
Slab - rectangular (axb)		
Slab Type		**Floor**
a	cm	See problem
b	cm	See problem
Uniformly distributed design load - q_d	kN/cm^2	See problem
Steel beam properties		
Characteristic yield strength of steel - f_{yk}	kN/cm^2	34.5
Resistance factor of steel - γ_a		1.1
Unit cost of steel – c_{beam} (SINAPI [27])	R$/kg	7.96
Concrete properties		
Type of agregate		**Granite**
Characteristic compressive strength of concrete - f_{ck}	kN/cm^2	3
Resistance factor of concrete strength - γ_c		1.4
Unit cost of concrete – $c_{concrete}$ (SINAPI [27])	R$/cm^3	0.000346
Shear connector properties		
Diameter - d_{cs}	cm	1.9
Ultimate tensile strength of the connector - f_{ucs}	kN/cm^2	41.5
Resistance factor of connector – γ_{cs}		1.25
Coefficient for considering the effect of connector grouping - R_g		1.0
Coefficient for considering the position of the connector - R_p		1.0
Connector unit cost – $c_{connector}$ (Cordeiro [28])	R$/un	11.40
Welded wire reinforcement		
Unit cost of welded mesh – c_{mesh} (SINAPI [27])	R$/kg	7.01
Built-in steel sheeting		
Sheeting unit cost – $c_{formwork}$ (MS Estruturas [29])		
MF-50, thickness 0.80 mm	R$/cm^2	0.007236
MF-50, thickness 0.95 mm	R$/cm^2	0.008096
MF-50, thickness 1.25 mm	R$/cm^2	0.010454
MF-75, thickness 0.80 mm	R$/cm^2	0.008329
MF-75, thickness 0.95 mm	R$/cm^2	0.009318
MF-75, thickness 1.25 mm	R$/cm^2	0.012031

3 RESULTS AND DISCUSSIONS

3.1 Proposed problem 1: simplified optimized design

In item 12.7.3, Fakury, Silva and Caldas [24] present a simulation of the most cost-efficient beam distribution for a given slab. Input data for the problem is given below and the answer suggested by the authors are shown in Figure 2.

- Slab dimensions (rectangular): 15 by 6 meters;
- Loading: 0.95 kN/m^2 from floor tiling, 0.65 kN/m^2 from underdeck ceiling and 6 kN/m^2 live load.

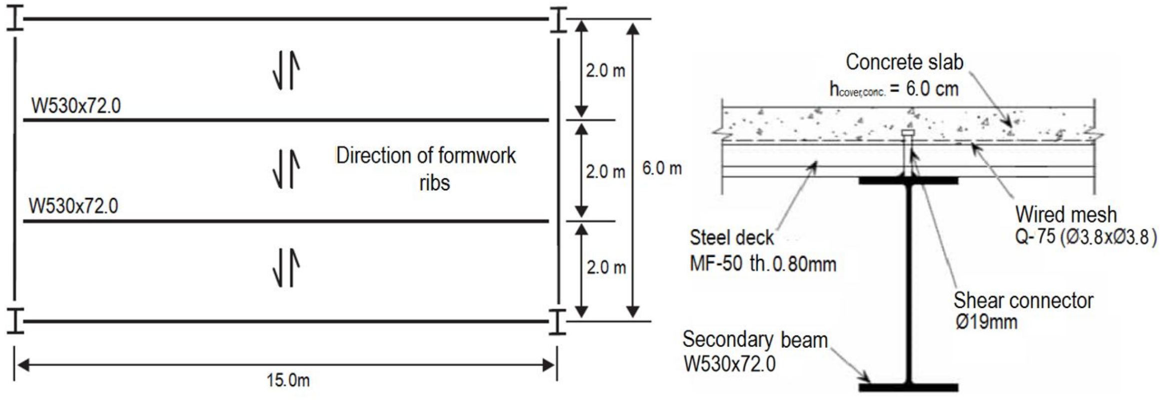

Figure 2 - Proposed problem 1 (Source: Fakury, Silva e Caldas [24], adapted).

To simplify the design optimization, Fakury, Silva and Caldas [24] adopt the lowest possible thickness of steel sheeting, that is, 0.8 mm and subsequently the following criteria:

1) use the shortest total beam length, regardless of the profiles to be adopted;
2) seek the lowest weight of the slab, which generally corresponds to the slab with the lowest concrete weight.

Table 2 shows the for combinations pertinent to ULS design used.

Table 2 - Loads for the proposed problem 1.

Load	Characteristic value [kN/m^2]	Resistance factor	Design load	
			Slab [kN/m^2]	Beam [kN/m^2]
Surfacing weight	0.95	$\gamma_g = 1.4$	0.95	1.33
Liner weight	0.65	$\gamma_g = 1.4$	0.65	0.91
Live load	6.00	$\gamma_q = 1.5$	6.00	9.00
Total			7.60	11.24

The answers proposed by Fakury, Silva and Caldas [24] and by the developed software are presented in Table 3, while beam disposition and cross section of the optimized answer found by the software are shown in Figure 3. Since the former does not present the optimal design of the secondary beams, their geometry was determined with the software, using the data of the slab analyzed in this problem.

Table 3 - Results for the proposed problem 1.

	Fakury, Silva e Caldas [24]	Developed software
Beam profile	W530x72.0*	W200x15.0
Number of secondary beams	2	6
Interaction Ratio	0.81*	0.84
Total number of connectors	76*	72
Length of each beam [cm]	1500	600
Total length of beams [cm]	3000	3600
Connector cost [R$]	866.40*	820.8

Table 3 – Continued…

	Fakury, Silva e Caldas [24]	Developed software
Beams cost [R$]	16931.96*	4173.44
Total cost of beams [R$]	17801.36*	4994.24
Sheeting type	MF-50 (th. 0.8 mm)	MF-50 (th. 0.80 mm)
Maximum slab span [cm]	200	220
Total slab height [cm]	11.0	13.0
Concrete slab cover height [cm]	6.0	8.0
Slab welded wired mesh	Q-75 (Φ3.8xΦ3.8 – 150x150)	Q-92 (Φ4.2xΦ4.2 – 150x150)
Sheeting cost [R$]	6512.40*	6512.40
Concrete cost [R$]	2650.19*	3273.76
Welded wired mesh cost [R$]	763.39*	933.73
Total slab cost [R$]	9925.98*	10719.9
Total cost of slab and beam [R$]	27724.33*	15714.14

* values obtained by the developed software.

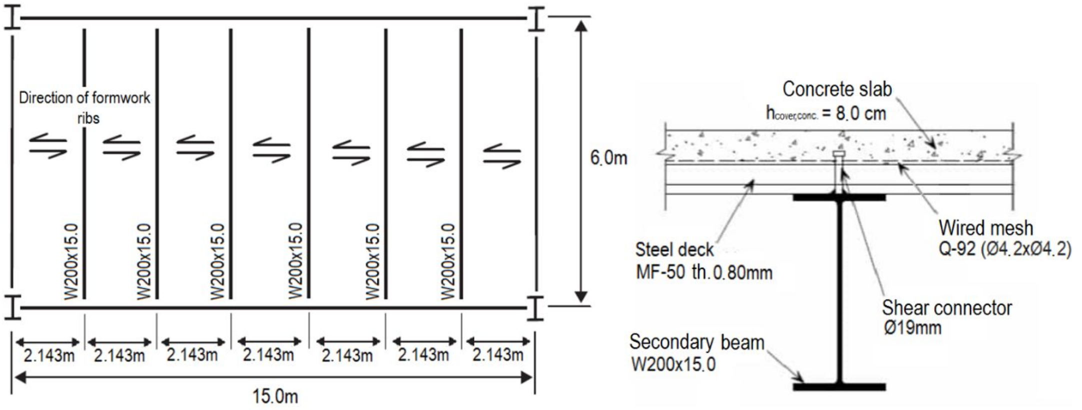

Figure 3 - Solution to the proposed problem 1.

In Figure 4, all the alternatives considered by the software are presented as a function of the total length of the beams and the weight of concrete, to analyze the aforementioned criteria. The pink dots represent the solutions for MF-50, while blue dots are associated with MF-75. The optimal solution is represented by the black crosses.

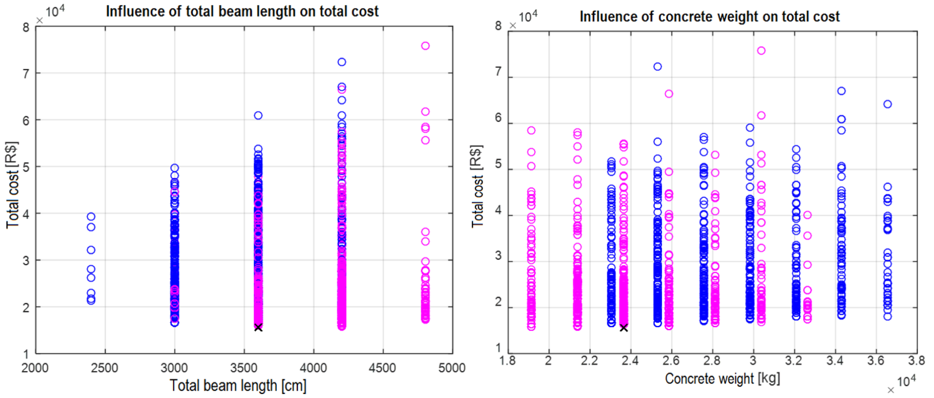

Figure 4 - Influence of beam length and weight of concrete on total cost.

It is noted that non-optimal answers for total length of the beams and concrete weight present solutions close to the optimal design. Figure 5 shows the influence of beam weight and sheeting thickness on total cost.

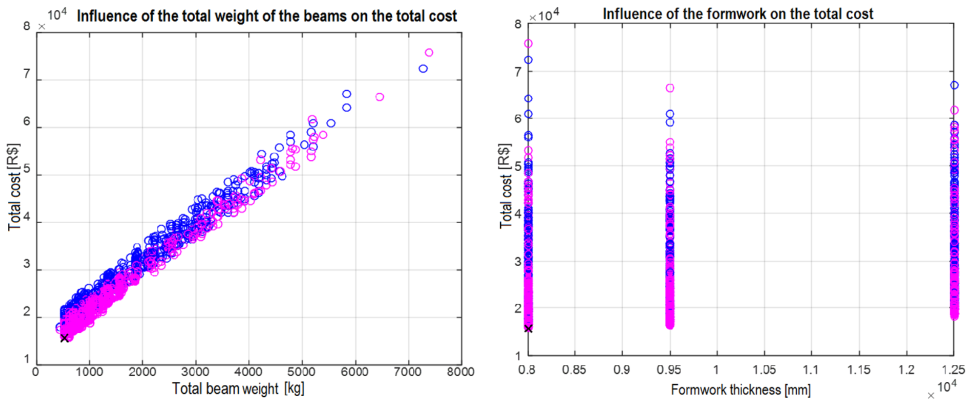

Figure 5 - Influence of the total weight of the beams and the thickness of the formwork on the total cost.

Analyzing the answers obtained as a function of the total weight of the beams (Figure 5) it is noted that the solutions with the lowest beam weight are close to the optimal solution. This would be a good criterion to be adopted in a simplified optimization. However, this information is only obtained after the design procedure.

Figure 4 and Figure 5 also show that, despite the use of MF-50 sheeting resulting in solutions with longer beam lengths, they also indicate lower concrete weights. The use of steel sheeting with thicknesses larger than 0.80 mm may also lead to answers that are not far from the optimal case.

The answer presented by the software leads to higher costs with concrete and welded wire reinforcement, but results in a set of beams 3.5 times lighter and, consequently, cheaper, making the software a more advantageous option in this case.

The difference observed is justified by the fact that Fakury, Silva and Caldas [24] place the secondary beams parallel to the largest dimension of the slab, thus increasing internal forces, as opposed to the optimal response presented by the software. It is worth mentioning that the differences between these two options can affect the design of the main beams, either decreasing or increasing their cost.

3.2 Proposed problem 2: Practical example

To assess the efficiency of the software, an existing building was chosen that uses the composite slab system supported by composite beams. The chosen structure was the headquarters of NEXEM - Nucleus of Excellence in Metallic Structures of UFES (Figure 6) - located in Vitória-ES, Brazil, with a constructed area of 264.98 m^2 and structural design by Engineer Pedro Sá and JP Engenharia Ltda. The construction was executed by Denenge - Dinelli Engenharia Ltda and the architectural project by the Architects Augusto Alvarenga, Adriane Alvarenga and Érica Márcia Leite Barros, according to Banco de Obras [30].

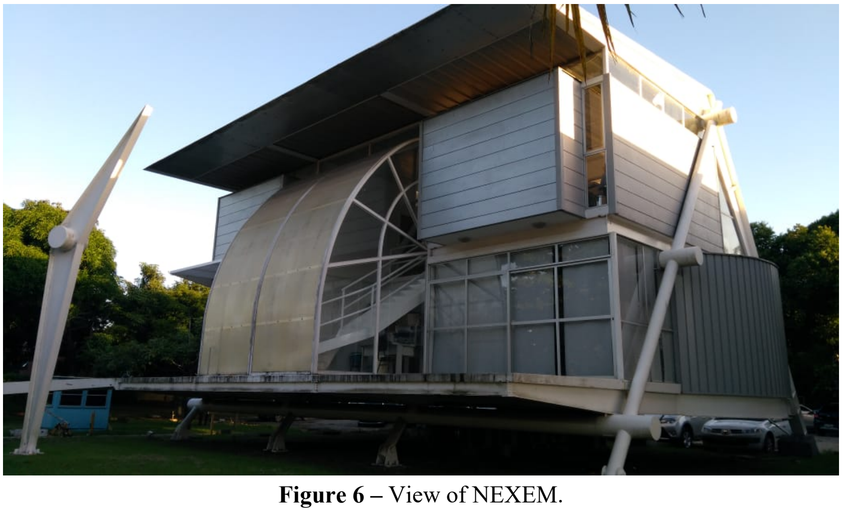

Figure 6 – View of NEXEM.

Structural parameters used to solve the problem were collected with field measurements. The analyzed slab is shown in its current position in Figure 7 and represented by the scheme of Figure 8. The slab is located on the first floor, used as a classroom, with plane dimensions of 10.5 m by 4.3 m, 15.0 cm in total height, MF-50 sheeting, 0.80 mm thickness and supported by two W200x31.3 secondary beams. The interaction ratio was taken as the minimum allowed value, which implies in the use of 24 shear connectors distributed along the two secondary beams and 30-MPa concrete.

Figure 7 - Detail of the slab analyzed in the proposed problem 2.

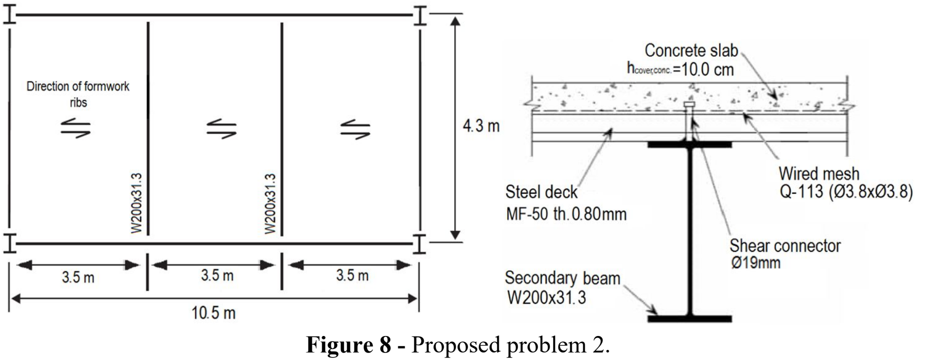

Figure 8 - Proposed problem 2.

Loading was adopted according to ABNT NBR 6120: 1980 [31], which prescribes a live load of 3.0 kN/m^2 for classrooms. A 0.4 kN/m^2 load is added to account for structural weight, which corresponds to a concrete slab with a thickness of 15 cm. Furthermore, a load of 1.35 kN/m^2 is added to account for the weight of surfacing and tiling.

Table 4 shows the combinations of forces used for ULS design.

Table 4 - Loads for the proposed problem 2.

Load	Characteristic value [kN/m^2]	Resistance factor	Design load	
			Slab [kN/m^2]	Beam [kN/m^2]
Surfacing weight	1.35	$\gamma_g = 1.4$	1.35	1.89
Liner weight	0.40	$\gamma_g = 1.4$	--	0.56
Live load	3.00	$\gamma_q = 1.5$	3.00	4.50
Total			4.35	6.95

Results obtained with the software are shown in Table 5 and illustrated in Figure 9, and indicate a cost reduction of 16% if compared with the actual structure. Once more, the optimal response does not correspond to the alternative with the shortest beam lengths. However, the software solution yielded the lowest possible concrete weight.

Table 5 - Results for the proposed problem 2.

	NEXEM	Developed software
Beam profile	W200x31.3	W150x13.0
Number of secondary beams	2	3
Interaction Ratio	0.40*	0.52
Total number of connectors	24*	18
Length of each beam [cm]	430	430
Total length of beams [cm]	860	1290
Connector cost [R$]	273.60**	205.20
Beams cost [R$]	2121.06**	1268.96
Total cost of beams [R$]	2394.66**	1474.16
Sheeting type	MF-50 (th. 0.8 mm)	MF-50 (th. 0.95 mm)
Maximum slab span [cm]	350	270
Total slab height [cm]	15	11
Concrete slab cover height [cm]	10	6
Slab welded wired mesh	Q-113 (Φ3.8xΦ3.8 - 100x100)*	Q-75 (Φ3.8xΦ3.8 - 150x150)
Sheeting cost [R$]	3267.05**	3655.34
Concrete cost [R$]	1955.16**	1329.51
Welded wired mesh cost [R$]	569.70**	382.97
Total slab cost [R$]	5791.92**	5367.82
Total cost of slab and beam [R$]	8168.58**	6841.99

* values adopted. ** values obtained by the developed software.

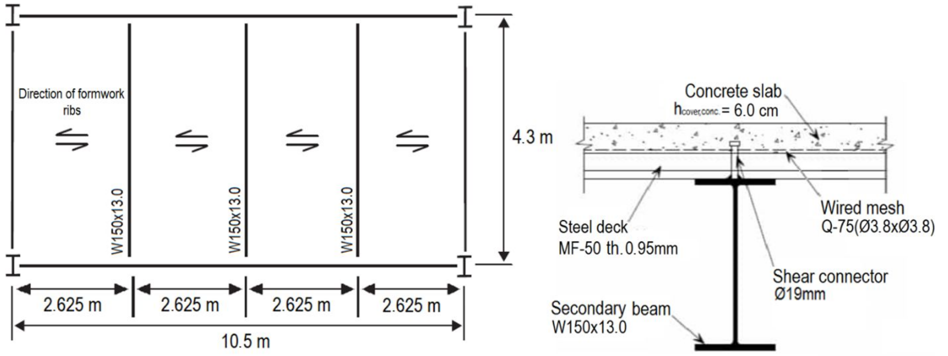

Figure 9 - Solution to the proposed problem 2.

Figure 10 shows a graph comparing the costs of each element of the optimized structural system.

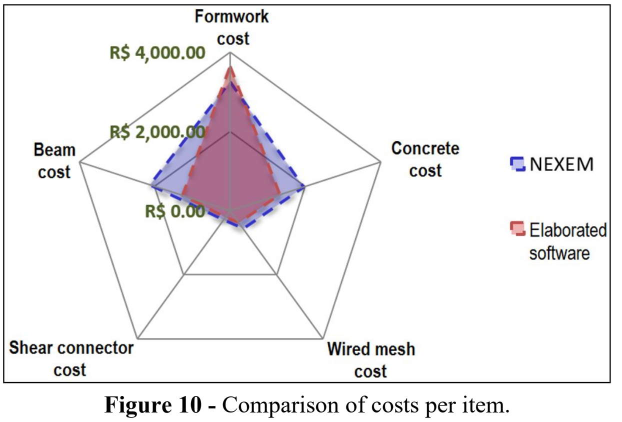

Figure 10 - Comparison of costs per item.

The graph shows that, even though the software presents a solution with the highest cost of steel sheeting, which is the most expensive item, lower expenses with remaining resources are observed. As such, even with the increased value to obtain the most expensive item in the system, overall cost is still reduced.

Geometric properties of the steel profiles were obtained disregarding the additional cross-sectional area associated with the radius of curvature between the web and the laminated profile flanges. This assumption aims to simplify calculations and it is a conservative determination. The properties of the steel profiles shown in this research are shown in Table 6.

Table 6 – Geometric properties of the beam profiles used.

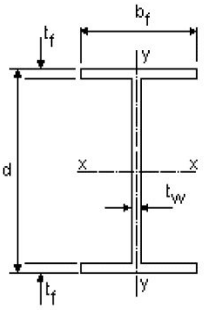

Profile	d [cm]	b_f [cm]	t_w [cm]	t_f [cm]	A* [cm²]	I_x* [cm⁴]	Z_x* [cm³]	W_x* [cm³]
W530x72.0	52.4	20.7	0.90	1.09	90.32	3.92 10^4	1725.2	1496.4
W200x15.0	20.0	10.0	0.46	0.52	19.12	1248.1	142.64	124.81
W200x31.3	21.0	13.4	0.64	10.2	39.47	3094.0	330.60	294.67
W150x13.0	14.8	10.0	0.43	0.49	15.74	596.48	90.651	80.605

* Calculated without considering the forming radius between flanges and web of the laminated profiles.

3.3 Time analysis

During the solution of the first problem proposed, the software spent an average of 0.627 seconds to analyze a generation with 60 individuals. Considering the universe of 13,516,800 individuals, the program would need 39.2 hours to analyze all possible alternatives and return the optimal answer. Using the GA, the developed software analyzed only 3120 individuals and found the optimal response in 32 seconds.

4 CONCLUSION

Results obtained from the application of the developed software to proposed problems indicate that the program is an efficient tool for optimization of structural systems composed of steel-concrete composite beams and slabs.

In Proposed Problem 1, although the criteria suggested by Fakury, Silva and Caldas [24] lead to a low-cost slab, the use of GA allowed for a more comprehensive optimization, and consequently, a better result.

In Proposed Problem 2, part of the difference observed may be a result of design considerations such as: additional loads, suitability for SLS, among others. Even so, the use of GA can lead to significant improvements, since the software solution indicated the possibility of using a lighter set of beams, in greater number, resulting in a smaller slab span and, consequently, reductions in cost and weight of concrete.

Results also show that the use of discrete variables obtained from commercial tables provided by the manufacturers, combined with knowledge of the actual market prices of each structural element and the use of GA as a method of optimization, lead to structural systems that are well optimized and close to practical scenarios.

Finally, the use of GA allows an alternative approach to structural design, perhaps even replacing the pre-design phase, since the algorithm itself can simulate an initial solution and, by an iterative process, converge to the optimal design.

REFERENCES

[1] J. A. Lazzari, E. C. Alves, and A. F. G. Calenzani “Optimum design of spatial steel frames according to ABNT NBR 8800:2008,” in *XIII SIMMEC*, Vitória, ES, Brasil, 2018.

[2] G. P. Lubke, E. C. Alves, and M. S. Azevedo “Optimum design and failure modes analysis of steel alveolar beams,” *REA - CBCA*, vol. 6, p. 1-20, 2017.

[3] B. D. Breda, N. G. P. Salgado, W. L. Siqueira, E. C. Alves, and A. F. G. Calenzani “Utilização de Algoritmo Genético na Otimização de Vigas Mistas Biapoiadas de Aço e Concreto,” in *XIII SIMMEC*, Vitória, ES, Brasil, 2018.

[4] METFORM. “Steel Deck: a solução definitiva em lajes.” http://www.metform.com.br/wordpress/wp-content/uploads/2015/05/steel_deck_metform.pdf (accessed May 13, 2019).

[5] C. Liu, A. Hammad, and Y. Itoh, "Multiobjective Optimization of Bridge Deck Rehabilitation Using a Genetic Algorithm," *Microcomputers Civ. Eng.*, vol. 12, pp. 431-443, 1997.

[6] H. Cho, D. Min, and K. Lee "Optimum Life-Cycle Design of Orthotropic Steel Deck Bridges," *Steel Struct.*, vol. 1, pp. 141-152, 2001.

[7] C. K. Fu, Y. Zhai, and S. Zhou "Optimum Design of Welded Steel Plate Girder Bridges Using a Genetic Algorithm with Elitism," *J. Bridge Eng.*, vol. 10, pp. 291-301, 2005.

[8] D. A. Souza Jr., "Otimização pelo método dos algoritmos genéticos e dimensionamento de estruturas tubulares metálicas espaciais com barras cruzadas para cobertura," Ph.D. thesis, DEC, UFU, Uberlândia, MG, 2005.

[9] J. Câmara Neto, A. Landesmann, and E. M. Batista "Aplicação de Algoritmos Genéticos para Dimensionamento de Vigas-Mistas Aço-Concreto," in *CONSTRUMETAL 2008 – Latin-American Congress on Steel Construction*, São Paulo, SP, 2008.

[10] T. L. D. Forti, M. G. Q. Souza, and J. A. V. Requena "Desenvolvimento de um Algoritmo Genético para Otimização de Grandes Estruturas de Aço para Coberturas," in *XXX Ibero-Latin-American Congress on Computational methods in Engineering*, Armação de Búzios, Rio de Janeiro, 2009, pp. 1-18.

[11] M. L. R. Lima, "Otimização topológica e paramétrica de vigas de concreto armado utilizando algoritmos genéticos," M.S. thesis, DEC, USP, São Paulo, SP, 2011.

[12] P. Kripakaran, B. Hall, and A. Gupta, "A genetic algorithm for design of moment-resisting steel frames," *Struct. Multidiscipl. Optim.*, vol. 44, no. 4, pp. 559–574, 2011.

[13] M. Kociecki and H. Adeli, "Shape optimization of free-form steel space-frame roof structures with complex geometries using evolutionary computing," *Eng. Appl. Artif. Intell. Elsevier*, vol. 38, pp. 168–182, 2015.

[14] M. B. Prendes-Gero, A. Bello-García, J. J. Coz-Díaz, F. J. Suárez Domínguez and P. J. G. Nieto, "Optimization of steel structures with one genetic algorithm according to three international building codes," *Rev. Constr.*, vol. 17, no. 1, pp. 47–59, 2018.

[15] H. F. X. A. Bilbao, "Dimensionamento de absorvedores de massa sintonizada para lajes duplo T pré-fabricadas em concreto por meio de algoritmo genético," Undergraduate thesis, UTFPR, Curitiba, PR, Brasil, 2016.

[16] L. A. Bezerra, "Emprego de algoritmos genéticos para otimização de vigas de concreto armado," Master's thesis, UFPE, Recife, PE, 2017.

[17] J. Malveiro, D. Ribeiro, C. Souza, and R. Calçada, "Model updating of a dynamic model of a composite steel-concrete railway viaduct based on experimental tests," *Eng. Struct.*, vol. 164, p. 40–52, 2018.

[18] N. L. A. Lima, J. G. S. Silva, F. J. C. P. Soeiro, L. Biondi No, and L. R. O. Lima, "Avaliação do conforto humano de passarelas mistas com o uso de algoritmos genéticos," *Engevista*, vol. 10, no. 1, pp. 59–70, 2008.

[19] R. P. B. C. Pereira, "Otimização de um projeto estrutural de ponte em viga mista," Undergraduate thesis, UniCEUB, Brasília, DF,Brasil, 2016.

[20] G. S. Papavasileiou and D. C. Charmpis "Seismic design optimization of multi–storey steel–concrete composite buildings," *Comput. Struct.*, vol. 170, p. 49–61, 2016.

[21] A. R. Silva, and T. A. Rodrigues, "Optimized dimensioning of steel-concrete composite beams," *Rev. IBRACON Estrut. Mater.*, vol. 12, no. 6, p. 1428-1453, Dec. 2019.

[22] A. F. Tormen, Z. M. C. Pravia, F. B. Ramires, and M. Kripka, "Optimization of steel concrete composite beams considering cost and environmental impact," *Steel Compos. Struct.*, vol. 34, no. 3, pp. 409–421, Feb 2020., http://dx.doi.org/10.12989/scs.2020.34.3.409.

[23] Associação Brasileira de Norma Técnicas, *Projeto de Estruturas de Aço e de Estruturas Mistas de Aço e Concreto de Edifícios – Procedimento, ABNT NBR 8800:2008*, Rio de Janeiro, 2008.

[24] R. H. Fakury, A. L. R. Silva, and R. B. Caldas, "*Dimensionamento de elementos estruturais de aço e mistos de aço e concreto*," 1. ed. São Paulo, Brasil: Pearson Education do Brasil, 2016.

[25] MATLAB. "Userguide R2015a." São Paulo, SP, Brasil: The Math Works Inc, 2015.

[26] GERDAU. "Perfil Estrutural." https://www2.gerdau.com.br/produtos/perfil-estrutural (accessed May 13, 2019).

[27] Sistema Nacional de Pesquisa de Custos e Índices da Construção Civil. http://www.caixa.gov.br/poder-publico/apoio-poder-publico/sinapi/Paginas/default.aspx (accessed Mar. 19, 2019).

[28] F. C. R. Cordeiro, "Análise de produtividade da mão-de-obra e composição de custos do serviço de execução da laje steel deck," Undergraduate thesis, UFSC, Florianópolis, SC, 2016.

[29] MS Estruturas Metálicas. "Painel Steel Deck." https://rms-estruturas-metalicas.webnode.com.pt/products/painel-steel-deck-apartir-de-r%24-46%2C35-m%C2%B2/. (accessed Mar. 15, 2019).

[30] CBCA. "Banco de Obras." http://www.cbca-acobrasil.org.br/banco-de-obras/obra/edificio-sede-do-nexem---vitoria/es. (accessed Mar. 18, 2019).

[31] Associação Brasileira de Norma Técnicas, *Associação Brasileira de Norma Técnicas. Cargas para o cálculo de estruturas de edificações – Procedimento, ABNT NBR 6120:1980*, Rio de Janeiro, 1980.

Author contributions: BDB: conceptualization, data curation, formal analysis, methodology, writing; TCP: conceptualization, writing; ECA: conceptualization, supervision, writing.

Editors: Bernardo Horowitz, José Luiz Antunes de Oliveira e Sousa, Guilherme Aris Parsekian.

IBRACON Structures and Materials Journal
Revista IBRACON de Estruturas e Materiais
ISSN 1983-4195 ismj.org

ORIGINAL ARTICLE

Nonlinear finite element analysis of reinforced concrete shear walls

Análise não-linear de pilares-parede de concreto armado via método dos elementos finitos

Jordlly Reydson de Barros Silva[a,b]
Bernardo Horowitz[b]

[a]Universidade Federal Rural de Pernambuco – UFRPE, Unidade Acadêmica do Cabo de Santo Agostinho – UACSA, Cabo de Santo Agostinho, PE, Brasil
[b]Universidade Federal de Pernambuco – UFPE, Programa de Pós-graduação em Engenharia Civil, Departamento de Engenharia Civil, Recife, PE, Brasil

Received 04 November 2019
Accepted 11 March 2020

Abstract: This paper deals with a fundamental issue for tall buildings safety: the structural analysis of reinforced concrete shear-walls that resist lateral loads. For two shear walls (simple planar and U-shaped), the results determined according to the Brazilian design code approximate procedure (NBR-6118:2014) and the grid method (CAD/TQS), presented in the literature, are compared with material and geometrically nonlinear finite shell element analysis (NL-FEA), performed by the software VecTor 4, based on the modified compression field theory (MCFT). In both cases NL-FEA analyses, besides the large computational cost, it was observed the significant influence of stress redistribution, and the Saint-Venant's principle, on the vertical normal stresses, and the consequent smoothing of the second order localized effects on the shear walls.

Keywords: shear walls, reinforced concrete, finite element, nonlinear analysis.

Resumo: O presente artigo trata de um tema fundamental para a segurança de edificações de altura elevada: a adequada avaliação do comportamento dos pilares-parede de concreto armado, que compõem a estrutura de contraventamento da construção. Para dois pilares-parede (simples e seção U), os resultados obtidos segundo o método simplificado (NBR-6118:2014) e o método da malha de barras (CAD/TQS), presentes na literatura, são comparados com análises não-lineares (física e geométrica) com elementos finitos de casca (MEF-NL), realizadas no software VecTor 4, o qual é baseado na teoria do campo de compressão modificada. Com isso, nos dois casos, nas análises via MEF-NL, além do considerável custo computacional, foi possível notar a significativa influência do efeito da redistribuição dos esforços, e do princípio de Saint-Venant, nas tensões normais verticais, o que contribuiu para a atenuação dos efeitos localizados de 2ª ordem nos pilares-parede, em relação ao observado na literatura.

Palavras-chave: pilares-parede, concreto armado, elementos finitos, análise não-linear.

How to cite: J. R. B. Silva and B. Horowitz, "Nonlinear finite element analysis of reinforced concrete shear walls," *Rev. IBRACON Estrut. Mater.*, vol. 13, no. 6, e13603, 2020, https://doi.org/10.1590/S1983-41952020000600003

1 INTRODUCTION

In the recent decades, it has become evident the increasing number of reinforced concrete tall-buildings. Although it's associated with an efficient occupation of the urban land, and consequently promotes economic benefits, it results in several technical challenges. These issues are been overcome due to scientific advances in several fields, such as concrete technology and structural analysis.

One of the main steps in the reinforced concrete tall-building design that has been influenced by this verticalization process is the global structural stability analysis, which is related to the building lateral loads, such as wind seismic loads.

Corresponding author: Jordlly Reydson de Barros Silva. E-mail: jordlly.silva@ufrpe.br
Financial support: None.
Conflict of interest: Nothing to declare.

According to Wight and MacGregor [1], in buildings up to 8 to 10 stories, the global stability can be guaranteed using a rigid frame system. On the other hand, when a building exceeds this limit, and especially when the structure is subject to earthquakes, the rigid system may not be enough, and shear walls can be used as lateral load-resisting system.

According to the Brazilian reinforced concrete design code, NBR-6118:2014 [2], in shear walls structural design, it's not necessary to calculate only global and local second order effects, as occur to conventional columns. It may also be necessary to take into account in the analysis the so-called second order localized effects. In the code's item 15.9.3, an approximate procedure for calculating these additional internal forces is presented. Although this model has been valid since NBR-6118:2003, it have not received general acceptance by the technical community, among other reasons, for not providing an adequate recommendation for shear walls transverse reinforcement. The code model limitations have motivated the development of alternative shear walls design procedures [3].

This paper presents, for two shear walls (simple planar and U-shaped), a comparative study between the structures behavior according to the Brazilian design code approximate procedure [2], the grid method [3], presented in the technical literature, and material and geometric nonlinear finite shell element analysis (NL-FEA), performed by VecTor 4 software, based on the Modified Compression Field Theory (MCFT) [4]. The U-shaped shear wall analysis was performed in order to consider the structure main buckling modes.

2 SHEAR WALLS AND SECORD ORDER LOCALIZED EFFECTS

NBR-6118:2014 [2] defines a shear wall as a vertical planar element mainly subjected to in-plane compression, where the structure cross-section dimensions have a relationship between the largest and the smallest dimensions greater than 5. Figure 1 illustrates the geometry and the use of a shear wall in a real reinforced concrete (RC) building [5].

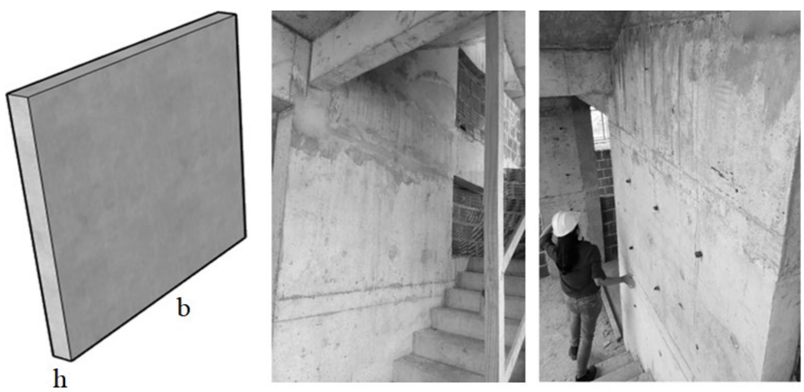

Figure 1. Simple planar shear wall geometry and its use in a RC building [5]

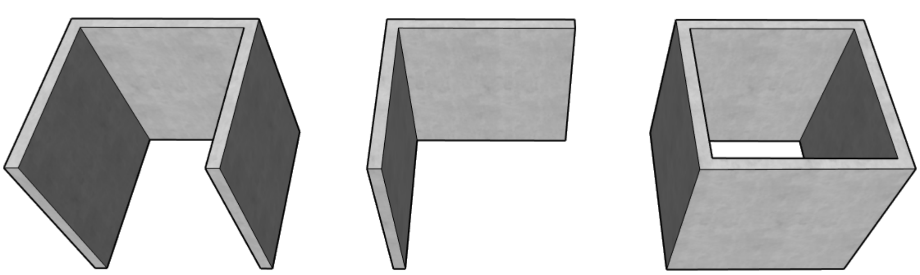

Figure 2. Assembled shear walls: U-shaped, L-shaped and closed cross-section shear walls

According to the case, in order to increase the system structural strength, it is usual to combine several planar wall segments, resulting in wall assemblies. Figure 2 shows three cases of wall assemblies, two open cross-sections (U-shaped and L-shaped) and a closed cross-section, usually used in bridge columns.

Due to the difficulty of allocate the shear walls in the building architectural project, these elements usually can be found around the elevator shaft or the stairs [1]. Figure 3 illustrates the arrangement of these elements in a structural project [6].

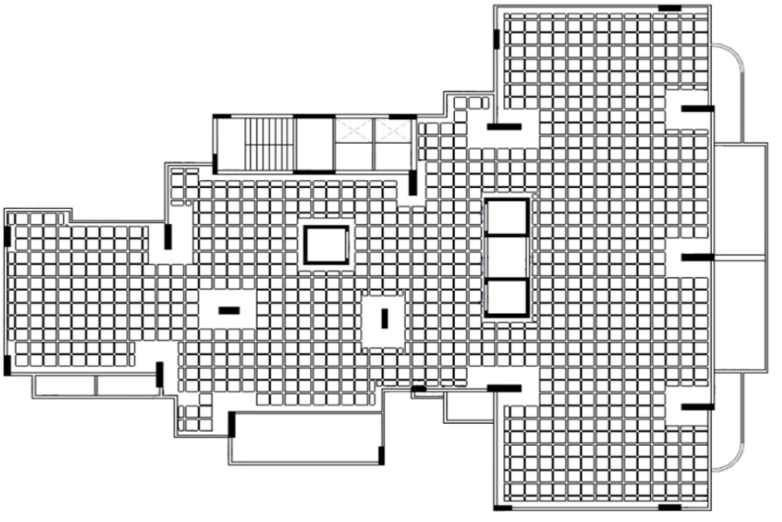

Figure 3. Shear walls arrangement on a building project [6]

2.1 Shear walls subjected to seismic loads

Currently, the structural analysis and design of reinforced concrete shear walls has become a usual object of scientific research around the world, especially after recent earthquakes that occurred in Chile (2010) and New Zealand (2011), which caused several structural damages in these elements [6].

However, according to relevant technical codes [7], the majority of the Brazilian territory, especially the most densely populated territories, with a larger number of tall buildings potentially subject to considerable horizontal forces, is located in a low seismic hazard region. Thus, unlike other countries, the main horizontal load acting in Brazilian buildings are wind loads, not seismic loads [6].

Thus, due to low seismic risk, in contrast to other parts of the world, there is a trend for shear walls to have thinner thickness than foreign ones, and, consequently, to be more susceptible to instabilities. This situation is aggravated by the concrete technology evolution, which allows the use of slender walls. Therefore, it becomes evident the necessity of research that reflect the Brazilian engineering situation.

2.2 Second order localized effects

As mentioned previously, in shear walls structural design, besides the global and local second order effects, common in the analysis of usual columns, it is also necessary evaluate the so-called second order localized effects, Figure 4. This phenomenon can be defined as a lateral instability, in certain regions of the shear wall, so that the resulting displacements cause additional second order internal forces in the structure.

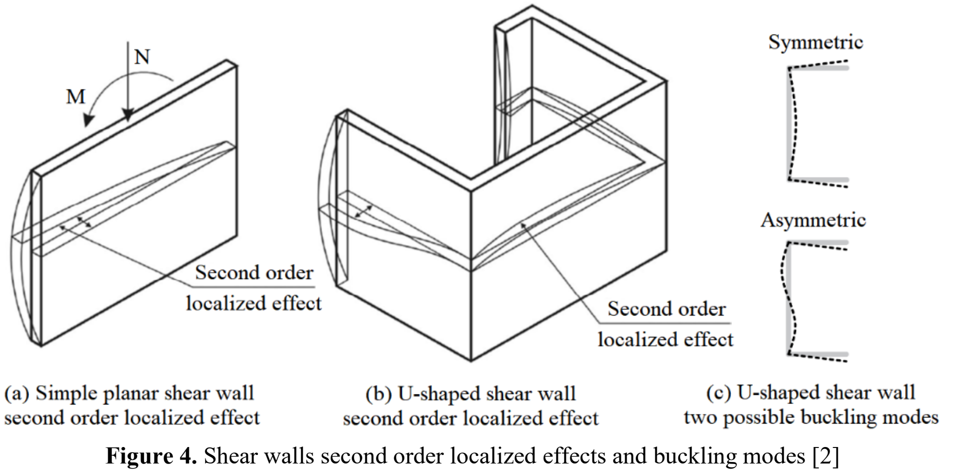

Figure 4. Shear walls second order localized effects and buckling modes [2]

The second order localized effect produces not only an increase in the wall longitudinal bending moment (tension in the vertical direction), but also a curvature in the horizontal direction, therefore, it's necessary to consider provision of reinforcement in that direction too (transverse reinforcement).

In addition, for a properly shear wall structural analysis, evaluating the second order localized effects, it's necessary to appropriately consider the structure buckling modes. This issue is of particular importance in the structural stability of thin-walled open sections, like U-shaped shear walls. Figure 4c illustrates two possible buckling modes for this kind of problem.

2.3 Brazilian code criteria for the consideration of second order localized effects

According to NBR-6118:2014 [2], the shear walls second order localized effects may be neglected if, for each of the planar segment that composes the shear wall, the following conditions are satisfied:

- The superior and inferior edge of each planar wall segments must be restrained by the slabs, which produces a horizontal diaphragm effect;
- The slenderness ratio of each planar segment λ_j must satisfy Equation 1.

$$\lambda_j = 3.46\frac{l_{ej}}{h_j} < 35 \tag{1}$$

where, h_j is the thickness of the wall j and l_{ej} is the wall equivalent length, which depends on the structure boundary conditions. Figure 5 illustrates some possible boundary conditions, where l and b are, respectively, the vertical free length and the wall largest cross-section dimension. Consulting Figure 5 and Table 1, it is possible to determine the equivalent length in each planar segment that composes the shear wall.

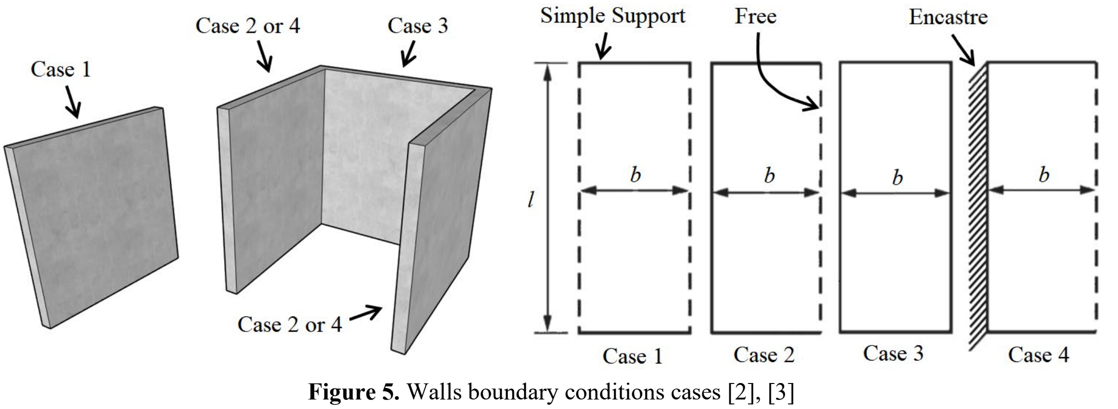

Figure 5. Walls boundary conditions cases [2], [3]

Table 1. Planar wall equivalent length.

Boundary conditions cases	Planar wall equivalent length equations
Case 1	$l_e = l$
Case 2	$l_e = \dfrac{l}{1+\left(\dfrac{l}{3b}\right)^2} \geq 0.3l$
Case 3	$l_e = \begin{cases} \dfrac{l}{1+\left(\dfrac{l}{b}\right)^2} sel \leq b \\ \dfrac{b}{2} sel > b \end{cases}$
Case 4	$l_e = 2b \leq l$

2.4 Brazilian code approximate procedure to second order localized effects analysis

According to NBR-6118:2014 [2], shear walls with slenderness ratios λ_j lower than 90, in each of their planar wall components, can be analyzed according to an approximate procedure. This model idealizes each wall as a set of i vertical frames and analyze the frames as independent columns subject to equivalent bending M_{ydi} and compression N_i loads, Figure 6. This procedure assumes that the equivalent width of each vertical frame a_i must satisfy the condition of Equation 2.

$$a_i = 3h < 100cm \tag{2}$$

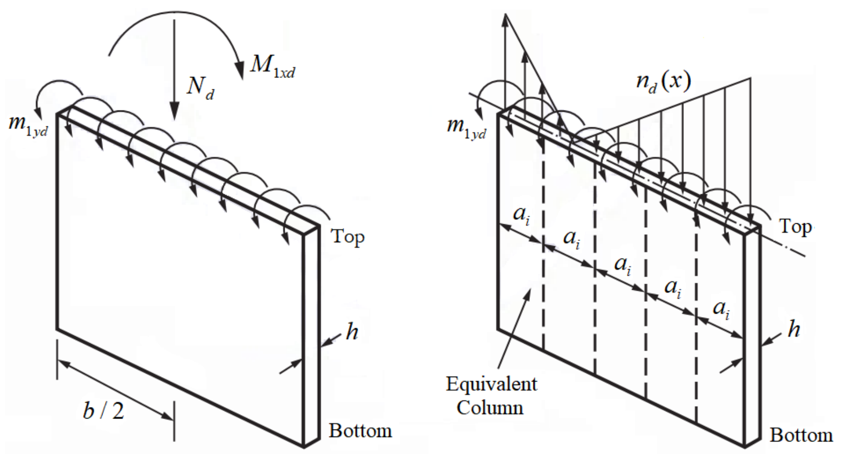

Figure 6. Brazilian code approximate procedure: wall discretization [2], [3]

The compression load N_i is calculated from the resulting compression stress over the wall largest dimension, Figure 6, and the moment M_{ydi} can be obtained according to the column width a_i and the bending moment m_{yd} in the smallest wall cross-section dimension, Equation 3.

$$M_{ydi} = m_{1yd} a_i \tag{3}$$

In addition, it must be ensured that the bending moment applied according to the frame smallest dimension must be greater than the first order minimum moment $M_{ydi} \geq M_{1d,min}$, when the latter is adopted in the geometric imperfections analysis. On the other hand, when $M_{ydi} < M_{1d,min}$, it is not necessary to adopt local analysis coefficients greater than 0.6, in the equivalent columns model [2], [6].

Based on this approximate procedure, the shear walls second order localized effects are evaluated using the equivalent columns second order local effects.

This approximate procedure is based on one of the structural analysis main principles: trying to understand the behavior of a complex construction based on the association of simpler elements. This principle is well known and used in the technical community, and it has resulted in several analysis procedures. Nevertheless, this procedure has been heavily criticized in the professional and academic fields [6], for example, according to Araújo [8], this procedure has no consistent experimental or theoretical justification, and leads the design to major increases in longitudinal reinforcement.

Other points that received criticism include:

- The Brazilian code does not specify what to do when the planar wall segments have slenderness ratios λ_j greater than 90;
- The code's item 18.5 recommends that if the wall transverse bending moment is not calculated (as the approximate procedure does), the wall transverse reinforcement should be greater that 25% of the wall longitudinal

reinforcement. According to França and Kimura [3], in some cases, this amount of reinforcement may be excessive, while in others it could be insufficient.

Thus, it is evident that the Brazilian code approximate procedure to shear wall second order localized effects analysis demands future contributions, so that it could be sufficiently precise and simple to apply, ideal for day-to-day work in project offices.

2.5 Grid method to second order localized effects analysis

In order to present an alternative procedure for shear wall second order localized effects analysis, França and Kimura [3] proposed a model, in which the shear wall is discretized in a bar mesh, like a grid. In this model, the physical nonlinearity is considered using the bars secant stiffnesses, according to axial-bending-curvature (N-M-1/r) diagrams. The geometric nonlinearity is evaluated through an iterative procedure, until displacement convergence.

One great advantage of the grid method in relation to the approximate procedure is that by providing bars in the horizontal direction, it can capture bending moments in this direction, which can be used in a more accurate design of the transverse reinforcement, instead of the arbitrary 25% of the longitudinal reinforcement, as indicated by the Brazilian code.

3 NONLINEAR FINITE ELEMENT ANALYSIS

3.1 Shear walls analyzed

As previously mentioned in this paper, two usual shear walls were selected for a comparative study between the two methods mentioned above and a nonlinear finite shell element analysis (NL-FEA). These two structures are a simple planar shear-wall (rectangular cross-section) and a U-shaped shear wall, both presented in the literature [3], [9], [10]. Figure 7 shows the structures geometry and loads. It was considered concrete C30, reinforcement cover equal to 30 mm and CA-50 steel reinforcement. In addition, all the planar wall segments were considered simply supported at the superior and inferior edges.

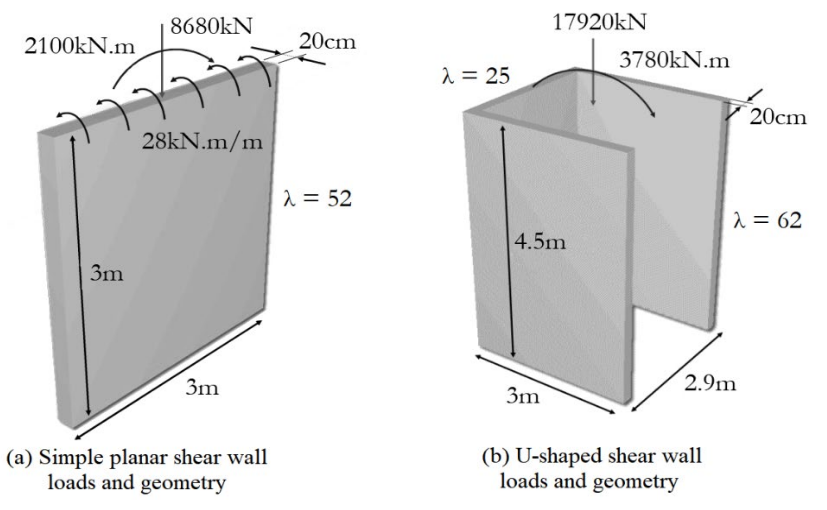

Figure 7. Shear walls loads and geometry [3], [9], [10]

3.2 Structural analysis software

In this paper, it was used the VecTor 4 structural analysis software (version 4.30, Jan. 2019). It is a nonlinear finite shell element analysis software of reinforced concrete structures such as shells, slabs, walls, in quasi-static and dynamic problems. This tool has been developed at the University of Toronto, Canada, since the 1980s and has received other previous names [4]. VecTor 4 can be used jointly with the software FormWorks+ and Janus, respectively, finite element analysis pre-processor and post-processor, both also developed at the same university. According to Hrynyk [4], VecTor

4 formulation uses a degenerated shell finite element, in other words, a shell element developed directly from three-dimensional elasticity equations, instead of using shell theories, and, that is one of the most common approaches in shell structures modeling. It is a quadrilateral 9-nodes shell, with a total of 42 degrees of freedom (3 translations in each direction, and two rotations, in the 8 edge nodes, Figure 8b). The element is also classified as a heterosis element because it uses in its formulation a combination of lagrangian and serendipity shape functions. In addition, this element is discretized in layers, so it could be possible to consider the variation in the internal stress along the thickness of the structure, both in thin and thick shells, Figure 8a. Further details about the 9-node heterosis degenerate shell element, implemented in VecTor 4, can be found in the literature [4], [11], [12].

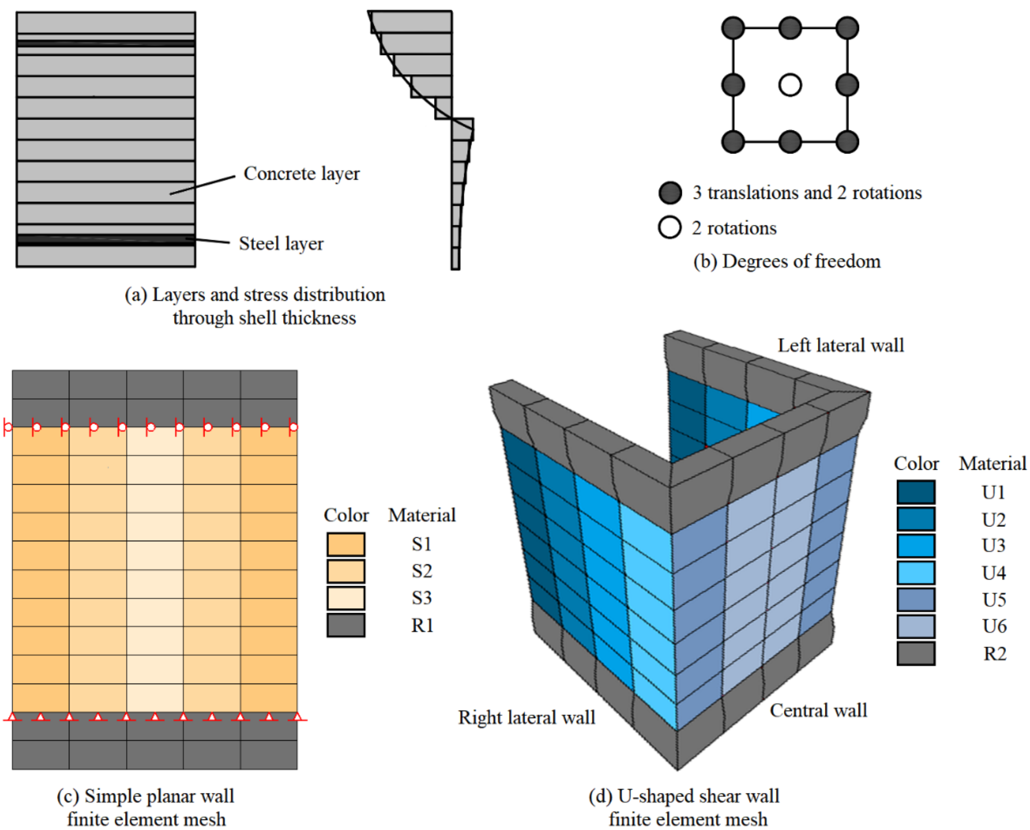

Figure 8. Shear walls finite element modeling [4]

One of the main factors that made VecTor 4 be chosen to this study was the constitutive modeling of reinforced concrete. As previously mentioned, this program is based on the well-known Modified Compression Field Theory (MCFT), one of the most accepted formulations by the technical community for reinforced concrete modeling. According to Hrynyk [4], the MCFT can be used to predict the behavior of reinforced concrete structures subjected to biaxial loads conditions. This formulation was published by Vecchio and Collins [13] in the 1980s, and has been studied since then. The MCFT idealizes cracked reinforced concrete as a new orthotropic material, with built-in reinforcement, subject to its own constitutive relationships. It considers the concrete compression softening and concrete tensile stiffening effects [4]. In addition, some of the main fundamentals of this model are:

- Transverse and longitudinal reinforcements are considered uniformly distributed throughout the element;
- The cracks are smeared across the concrete element and its orientation is free to rotate, according to variations in the applied loads and materials response;
- It is considered the average stresses and strains in regions containing several cracks;
- Independent constitutive relationships are used for concrete and steel;
- The principal stresses and strains axes are coincident.

In addition, according to Hrynyk [4], VecTor 4 also uses, in its formulation, the Disturbed Stress Field Model (DSFM). In general, the DSFM is an extension of the MCFT, which admits disagreements between the principal stresses and strains axes [4]. The DSFM was proposed by Vecchio [14] in order to solve some limitations of the MCFT in correctly predicting the behavior of high and low reinforcement rates element strength and stiffness.

Additional information and details about these two models and their implementation in VecTor 4 can be found in the technical literature [4], [11]–[14].

3.3 Finite element modeling criteria

This section details the main criteria used in the shear walls finite element modeling, using VecTor 4 and its preprocessor FormWorks+.

The external loads were applied as equivalent nodal forces and moments, concentrated at the nodes, in a similar way to what the Brazilian code approximate procedure indicates. The magnitudes of these nodal forces and moments were obtained considering the total loads indicated in Figure 7, the stress distribution, Figure 6, and each node influence area.

In addition to the external loads, in order to induce the behavior of the U-shaped shear wall to a specific buckling mode, two more nodal forces (induction loads) were applied in the midpoints of the two lateral planar wall segments free edges, perpendicular to the wall plan. When the symmetric buckling mode is analyzed, the two loads have opposite orientation (pointing towards the center of the structure). On the other hand, when the asymmetric buckling mode is analyzed, the two loads have the same orientation. The magnitude of these additional forces was defined in a way that it was sufficient to cause small transverse displacements in the lateral planar walls, equal to 1/20.000 of the wall height. In this evaluation, a 60 cm width strip of lateral planar wall was considered (3x wall thickness, as recommended by the Brazilian code approximate procedure). Thus, the magnitude of the induction loads was found about 1.5kN, approximately 0.3% of the lowest external nodal load. It is important to note that, if this or other similar criteria had not been adopted in the analysis, the lateral displacement pattern obtained could be significantly influenced by residual errors of the numerical solution procedure.

In order to avoid artificial stress concentration due to the load application process adopted, it was decided to use rigid elements on the loaded and supported edges, as an extension of the shear wall, in order to regularize the structure behavior in these regions. Figure 8 illustrates these rigid elements (R1 and R2), on the top and bottom edges of the structures.

As mentioned previously, the finite element meshes adopted heterosis degenerate elements. Figure 8c illustrates the first shear wall mesh geometry, which is composed of 5x14 square elements (elements dimensions = 60 x 30 cm). The top and the bottom elements consist of auxiliary rigid elements (R1), with thickness equal to 50 cm. According to Figure 8d, it is possible to notice that the U-shaped shear wall was discretized in the vertical direction in 6 elements and in two more rows, referring to rigid elements (R2), with thickness equal to 30 cm, at the superior and inferior edges. In the horizontal plane, 4 elements were applied in the central planar wall and 4 in each of the lateral planar walls. All elements on the lateral planar wall elements (including rigid ones) were 75 x 75 cm, while those in the central region were 72.5 x 75 cm.

In addition, due to the fact that the VecTor 4 finite element does not consider the drilling degrees of freedom (DOF), unlike other formulations, to ensure compatibility between the elements DOF at the connection between the laterals and the central walls, in the U-shaped shear wall, it was necessary to model this connection in a three-dimensional way, through a trapezoidal configuration of the elements involved, Figure 8d. This is a peculiarity of the software which despite modeling difficulties, reduces the number of degrees of freedom and contributes to computational efficiency.

It is important to note that, despite the symmetry of the U-shaped shear wall loads and geometry, it is not appropriate to consider this fact of the problem in the analysis, by modeling only half of the structure. Even if this meant a considerable reduction in the computational cost, the model would neglect the possible asymmetric buckling modes, Figure 4c, which can have considerable importance in the structure behavior.

As presented in section 3.1, the walls were considered simply supported. Thus, first and second shear walls were hinged supports at the lower edge (restricting all the translation degrees of freedom), and at the upper edge, the nodes translation degrees of freedom in the horizontal plane were restricted, Figure 8c.

In order to take into account the problem material non-linearity, it was necessary to consider the reinforcement presented in each shear wall. It was decided to adopt in this paper the reinforcement obtained in the literature [3], [10], using the Brazilian code approximate procedure [2]. According to the longitudinal reinforcement associated with the position of each finite element, an equivalent steel rate was defined in each of them, Figure 9. In both shear walls, the transverse reinforcement adopted was 25% of the longitudinal steel ratio, as recommended by NBR-6118:2014, respectively, 5.80 and 2.78 cm^2/m, per face, in the first and second shear wall. It is important to note that, due to the discretization of the layered shell element, the reinforcements could be arranged in the model in their appropriate positions, according to the cover and bar thickness. In the two structures, a total of 19 layers were adopted: 15 concrete, 2 longitudinal steel and 2 for the transverse steel layers.

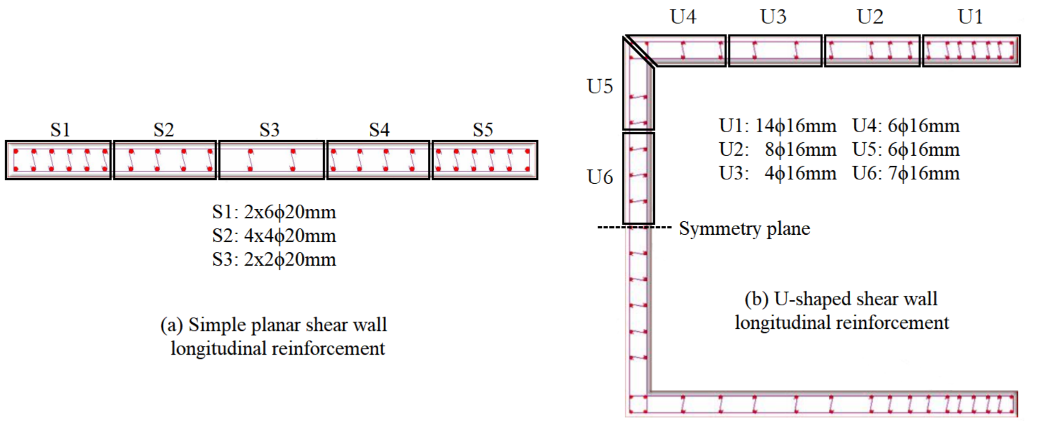

Figure 9. Shear walls longitudinal reinforcements [3], [10]

It was decided to adopt the software standard configurations for concrete and steel constitutive models, as recommended by Hrynyk [4], for most kind of problems analyzes in VecTor 4. Among these models, we can highlight:

- The well-known Hognestad parabola and the modified Park-Kent model [15], respectively, for pre-peak and post-peak concrete in compression;
- For the compression softening and the concrete tensile stiffening, in that order, the models known as Vecchio 1992-A and modified Bentz 2003, described in Wong et al. [16], and;
- Seckin's model [17], for the steel hysteretic behavior.

The development of appropriate constitutive models for each kind of problem is a current research field, given the significant influence they have on the accuracy of the results obtained. Thus, further studies are needed to verify which would be the most adequate constitutive relationships in the analysis of shear walls similar to those presented in this paper.

Finally, the iterative-incremental procedure adopted to solve the nonlinear finite element problems used 100 loading stages, with a load step increase equivalent to 1% of the total load. In addition, the load stage maximum number of iterations and the analysis convergence tolerance were defined, respectively, as 100 and 10^{-5}.

4 RESULTS AND DISCUSSIONS

This section is dedicated to presenting the main results obtained in the shear walls NL-FEA, as well as compare the internal forces obtained with their respective values according the Brazilian design code approximate procedure [2] and the grid method [3], [10].

In Figures 10, 11 and 12, it is possible to see the displacements and internal forces diagrams (without the rigid elements), respectively, of the simple planar and the U-shaped shear wall two buckling modes. In these illustrations, the displacements were obtained based on the VecTor 4 post-processor, Janus, while the diagrams were determined according to the internal forces provided by VecTor 4, at the Gauss points of each finite element, and a Python post-processing routine, written by the authors. In addition, Tables 2 and 3 compare the maximum bending moments obtained in the two structures, according to the three analyses procedure presented.

4.1 Simple planar shear wall analysis results

In the simple planar shear wall analysis, it was possible to observe that, close to the load application region (upper edge), the elements axial stress in the vertical direction N_{YY}, are practically the same values found according to the literature results. However, as the study point distances from the loads, the distribution of this stresses tends to become more uniform across the cross section, as described by the Saint-Venant principle, Figure 10d, a fact not observed in the grid model or in the Brazilian code approximate procedure.

The maximum longitudinal bending moment (tension in the vertical direction) M_{YY} is located in an element in the less vertically loaded side of the wall (left side), Figure 10e. This behavior disagrees with the literature models, which consider the maximum M_{YY} located on the right edge, due to the greater compression stress and the appearance of second order localized effects associated with it, Table 2. Thus, at first sight, the result obtained is counterintuitive. However, after investigations, the following possible justifications can be highlighted:

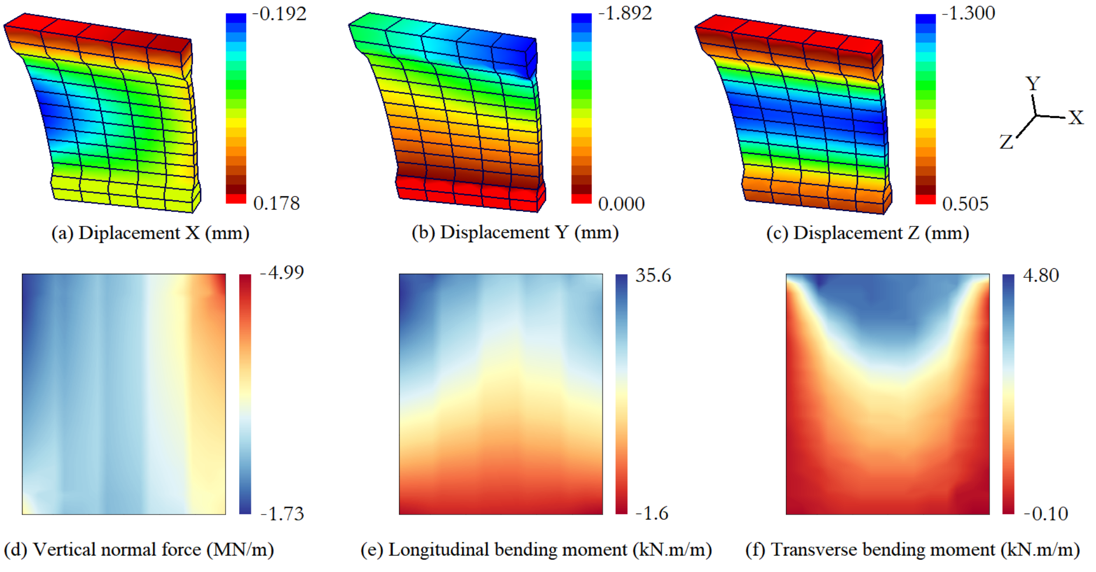

Figure 10. Simple planar shear wall displacements and internal forces diagrams

Table 2 Simple planar shear wall maximum bending moments (kN·m/m).

	Longitudinal bending moment M_{YY} (left edge)	**Longitudinal bending moment M_{YY} (right edge)**	**Transverse bending moment M_{XX}**
Brazilian code approximate procedure [3]	-	55.2 *	-
Grid method [3], [10]	33.6 *	48.8 *	1.7
VecTor 4 NL-FEA	35.6	27.9	4.8

* Approximate value obtained according to a quadratic variation of the second order moments.

- With the load application, the most requested side (right one) tends to experience a greater loss of stiffness, due to material nonlinearities, such as concrete cracking, for example, and with this, a stress redistribution effect to less loaded, more integrated and more rigid regions (left edge), occurs;
- In the shear wall NL-FEA, it can be observed that the maximum displacement, perpendicular to the structure plane, Figure 10a, was located in a node close to the center of the most loaded edge (right one). Consequently, after this translation, associated with a wall lateral instability, it is expected that there will be an effect of forces redistribution to the left edge, relative to geometric non-linearity;
- In addition, as seen earlier, the Saint-Venant's principle tends to smooth the compression stress distribution, and thereby mitigate the second order localized effects on the structure.

This behavior is observed comparing the maximum moments at the midpoints of the two lateral edges, in the 100 load steps. In the initial steps, when nonlinearities are negligible, the two bending moments were practically the same, however, with the load increasing, there is a trend for the maximum bending moment in the left edge (less loaded) to be 27.6% higher than the same internal moment in the right edge. In the last load steps, the bending moment M_{YY} on the left edge was equal to 35.6 kN·m/m, while in the right one was 27.9 kN·m/m, Table 2.

In addition, the internal forces redistribution effect is also influenced by the higher reinforcement ratio on the shear wall lateral sides, which causes the trend of internal forces migrate from the center to the lateral elements. To verify this behavior, the simple planar wall was reanalyzed considering a uniformly distributed longitudinal reinforcement ratio (23 cm^2/m per face). Thus, it was possible to observe that, even in this new situation, there is still a concentration of moments on the left edge, with intensity close to the original problem (+28.0%). However, the magnitude of the internal forces is attenuated, being, in the last load step, a maximum equal to 33.8 kN·m/m on the left edge, and 26.4 kN·m/m on the right one.

A finite shell element linear-elastic analysis of this problem was realized using the SAP 2000 software [18], without considering the structure geometric non-linearity, and, assuming mesh and other criteria similar to those previously presented. In this study, it is also possible to see that there is a certain trend of bending moments concentrate in the two free lateral edges. This can also be verified analyzing uniformly loaded linear-elastic plates, and somehow, it agrees with item 20.2 of NBR-6118/2014 [2], which, in its figure 20.1, recommends the positioning of steel bars at the ends of free edges, in reinforced concrete slabs.

On the other hand, it is possible to observe that the transverse bending moment (tension in the horizontal direction) M_{XX} is concentrated in the upper edge central region, Figure 10f, a behaviour that was also observed in the SAP 2000 linear-elastic analysis. The NL-FEA maximum moment M_{XX} (4.8 kN·m/m) is higher than the result provided by the grid method (1.7 kN·m/m) [3], Table 2. However, even so, M_{XX} was less than 13.5% of M_{YY} Thus, although the transverse and longitudinal reinforcements design are different, respectively, flexural design and combined axial load and bending design, and, N_{YY} has a crucial role in the latter, the difference obtained between M_{XX} and M_{YY} strengthens the thought that the Brazilian code recommendation that considers the transverse reinforcement as 25% of the longitudinal one can be exaggerated in certain situations, as presented by França and Kimura [3].

Finally, the computational cost of the simple planar shear wall NL-FEA, according to the criteria adopted for the iterative-incremental method, had an average processing time of approximately equal to 40 min, using a computer with an Intel Core i7-5500U CPU @ 2.40GHz processor. The computational cost observed can be considered high and makes this type of analysis less attractive for day-to-day work in the design office. However, it allows another perspective of the behavior of the structure and has fundamental importance for the engineering profession.

4.2 U-shaped shear wall analysis results

In the U-shaped shear wall, as well as in the previous problem, the stress redistribution effect, and the Saint-Venant principle, proved to be quite relevant, both in the symmetric and asymmetric buckling mode patterns. As can be seen in Figures 11d and 12d, although the maximum compression loading is located in the elements of the upper corners of the lateral planar wall free edges, the normal stress along the shear wall height tends to be concentrated close to the central-lateral walls connections (the greatest stiffness structure region).

Similarly to what can be found in the literature [3], the transverse bending moment M_{XX}, in the two buckling modes, is practically negligible at the lateral planar walls lateral free edge, and gradually increases as the study point approaches the central-lateral walls connection, Figures 11f and 12f. However, the bending moments found were less than the literature ones [3] (approximately 22.9%), and had the opposite sign, in some regions, Figures 11f and 12f. This behavior inversion was also noticed in the structure displacements, Figures 11c and 12c. Based on the bending moments M_{XX} found, in the two buckling modes, neglecting the minimum flexural reinforcement, a very small transverse reinforcement ratio, in the order of 0.7 cm^2/m, can be obtained, approximately 6.3% of the longitudinal reinforcement. Again, the results obtained strengthen the thought that the shear wall minimal transverse reinforcement presented in the Brazilian code may be exaggerated in some cases.

With respect to the longitudinal bending moment M_{YY}, in addition to the fact that no internal forces concentration was observed on the lateral planar walls free edge, in the two buckling modes, in disagreement to what is reported in the literature [3], the moments found in this region had a negligible magnitude, Figures 11e and 12e, and the maximum moment was located close to the central-lateral walls connection, Table 3. A possible justification for the difference between this result and the literature comes from the smallest transverse displacement in the lateral walls, obtained in the two buckling modes (0.064 mm), Figures 11c and 12c, which results in irrelevant second order localized effects. Again, it is presumed that the stress redistribution effect and the Saint-Venant's principle had a major role in smoothing of these nonlinear effects.

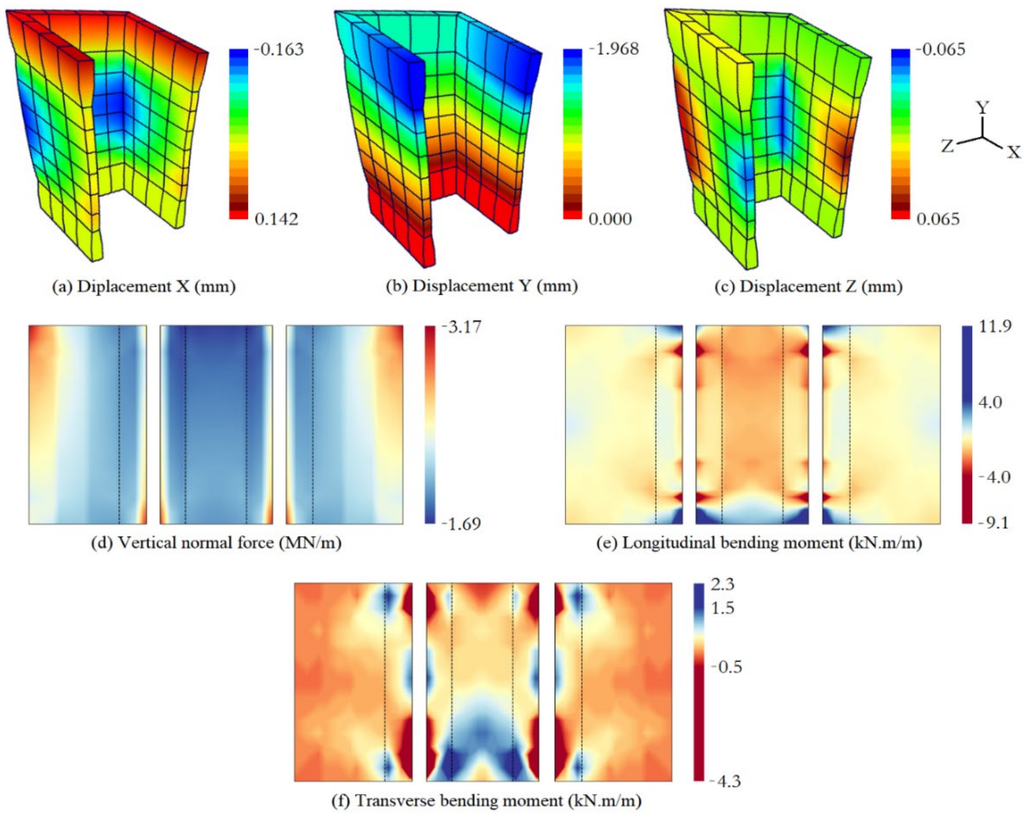

Figure 11. U-shaped shear wall displacements and internal forces diagrams (symmetric)

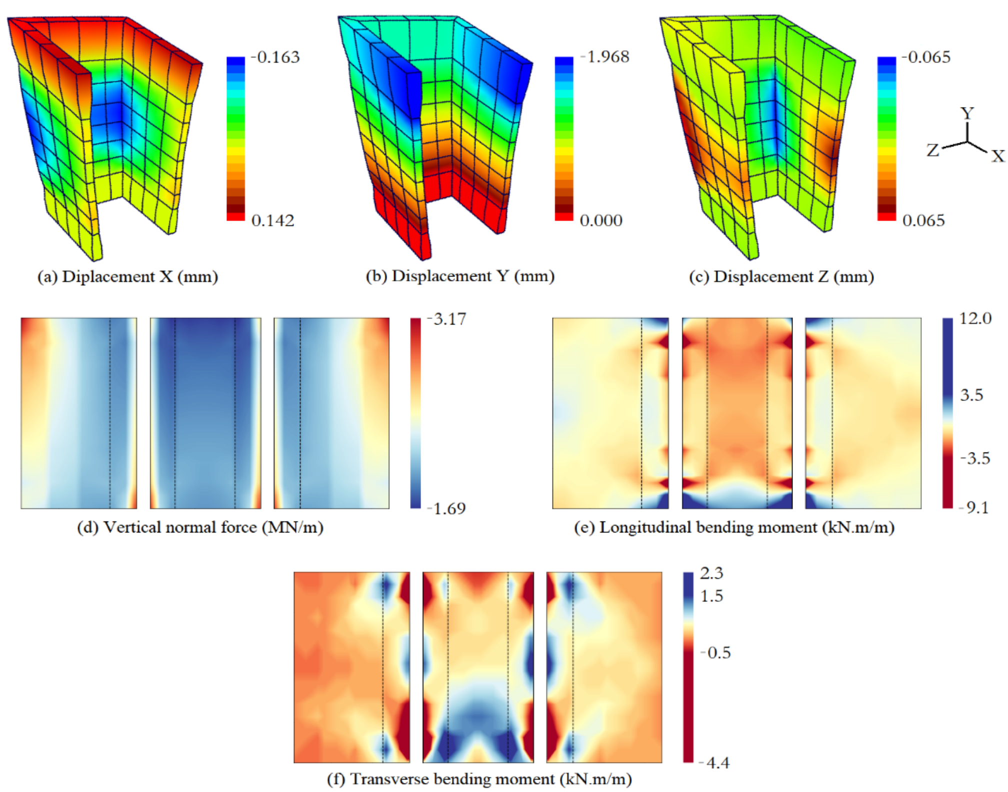

Figure 12. U-shaped shear wall displacements and internal forces diagrams (asymmetric)

In addition, it was observed irregular internal forces distributions in M_{XX} and M_{YY}, in the elements that form the central-lateral walls connection, Figures 11e and 11f. This atypical behavior can be associated with a way that the connection was modeled. Further studies are necessary to verify this structure modeling feature.

Table 3. U-shaped shear wall maximum bending moments (kN·m/m).

	Longitudinal bending moment M_{YY}	**Transverse bending moment** M_{XX}
Brazilian code approximate procedure [3]	76.7 *	-
Grid method [3], [10]	16.7 *	19
VecTor 4 NL-FEA (Symmetric Buckling Mode)	11.9 **	-4.3
VecTor 4 NL-FEA (Asymmetric Buckling Mode)	12.0 **	-4.4

* Located on the wall free edge. ** Located on the central-lateral walls connection.

In order to verify the results accuracy, analogous to the previous problem, a linear-elastic FEA was developed, using SAP 2000 software [18], assuming mesh and other modeling criteria similar to that presented previously. Thus, despite the simplicity of the model, it was possible to observe a qualitative behavior close to the NL-FEA, not only with respect to the displacements Z, Figures 11c and 12c, but also to the other degrees of freedom. This corroborates to the reasonableness of the results obtained in the NL-FEA.

In addition, the SAP 2000 model was subjected to a buckling modes analysis, where it was possible to verify that the two modes studied in this paper are actually the structure most likely behaviors. The buckling factors (buckling load/real load ratio), for the symmetric and asymmetric modes were, respectively, 24.87 and 25.37. The other buckling modes proved to be of little practical interest, for example, the third mode (symmetrical buckling with double curvature) had a much higher buckling factor than the first two, about 46.6. The relatively high buckling factors obtained in SAP 2000 help to justify the absence of major structural instabilities in the VecTor 4 results.

Somehow, the response observed in the shear wall NL-FEA is similar to the behaviour of cold-formed steel frames subject to local buckling [19], [20]. According to Yu and LaBoube [21], it is possible to observe in this type of problem a stress redistribution from free edges to region with relatively greater stiffness (central-lateral connections). This apparent similarity between the two problems behaviors is a promising opportunity for scientific investigation.

As in the previous example, based on the iterative-incremental analysis criteria presented, it was possible to observe in this case a high processing time, approximately equal to three hours. Again, a computer with an Intel Core i7-5500U CPU @ 2.40GHz processor was used. Nevertheless, this type of analysis remains relevant due to the fact that it allows the shear wall behavior evaluation considering complex and important effects.

4.3 Slender shear walls

Finally, in order to evaluate the behavior of shear walls composed by slender planar segments, the two structures analyzed in this paper had some dimensions modified to obtain planar walls components with a slenderness ratio ($\lambda = 90$), NBR-6118: 2014 [2]. The first simple planar shear wall height was changed from 3 to 5.2 meters, while in the U-shaped shear wall, in addition to the height having been increased from 4.5 to 6.5 m, it was necessary to expand the wall width from 3 to 4.3 m, since, according to Case 2 of Table 1, the wall equivalent, and consequently its slenderness ratio, depends on both dimensions. The other structure geometric parameters, reinforcement ratios, external loads, finite element mesh, among other criteria, remained unchanged. With respect to the first shear wall, in general, as can be seen comparing Figures 10 and 13, the behavior in both situations is very close. However, with the increase of the shear wall length, and, consequently, of the element slenderness ratio, a growth can be observed both in the longitudinal and transverse bending moments, as well as in the displacements, mainly in the Z axis, as expected.

Regarding the second shear wall, comparing, respectively, Figures 11 and 14, and, Figures 12 and 15, as well as in the first shear wall, one can observe the similarity between the two situations. However, although the height of the element has been increased, and this contributes to increasing the wall slenderness, as the width of these elements has also been increased (keeping the external loads constant), a considerable decrease in internal forces can be observed in the structure, although the wall slenderness in this new situation is greater than in the previous case.

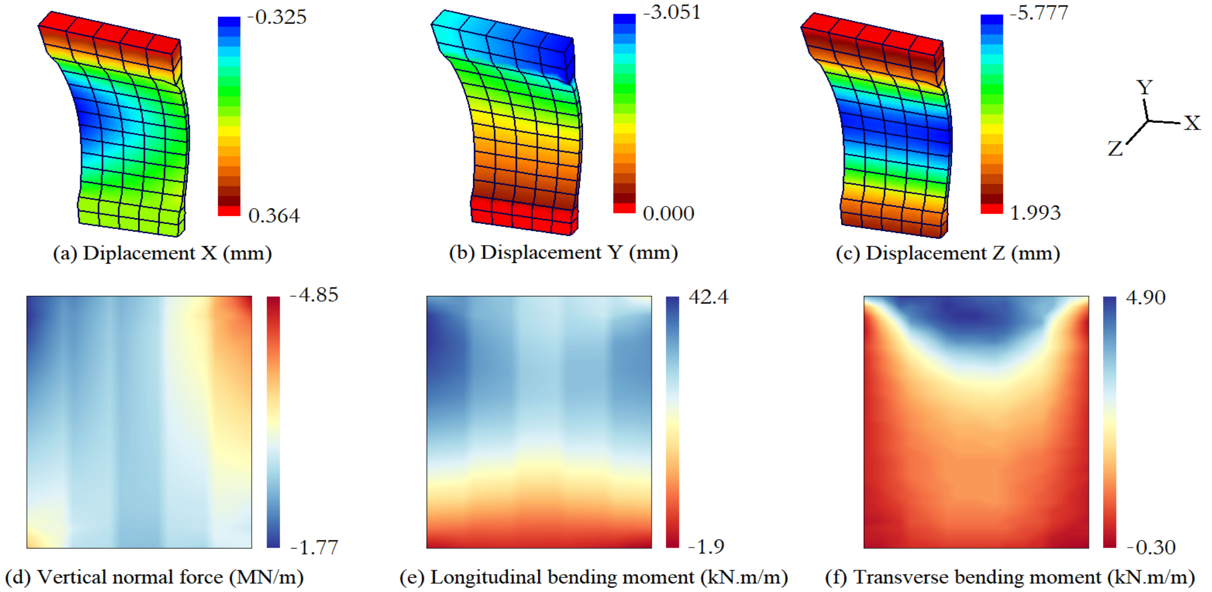

Figure 13. Simple planar shear wall displacements and internal forces diagrams, λ = 90

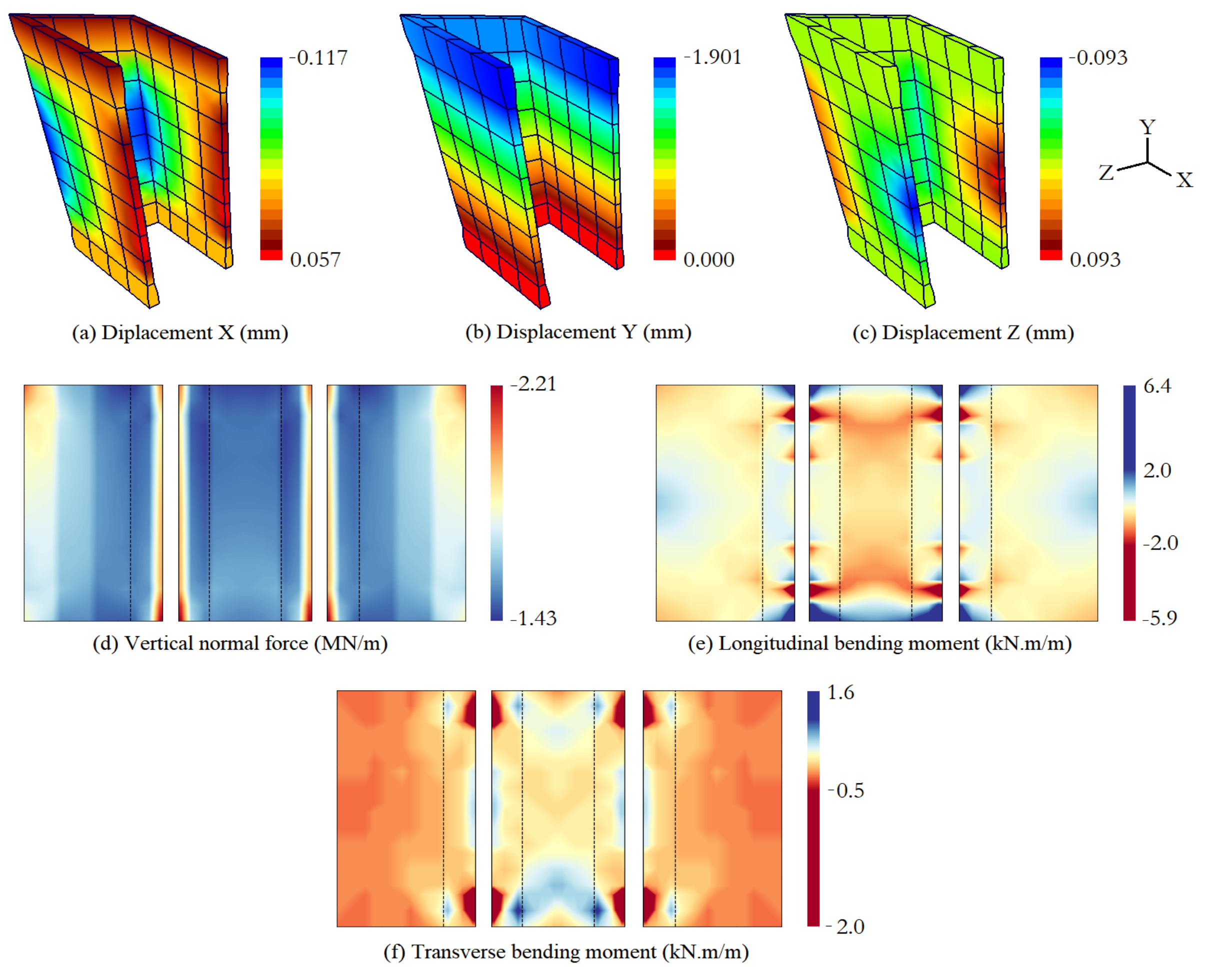

Figure 14. U-shaped shear wall results (symmetric), lateral planar wall segment λ = 90

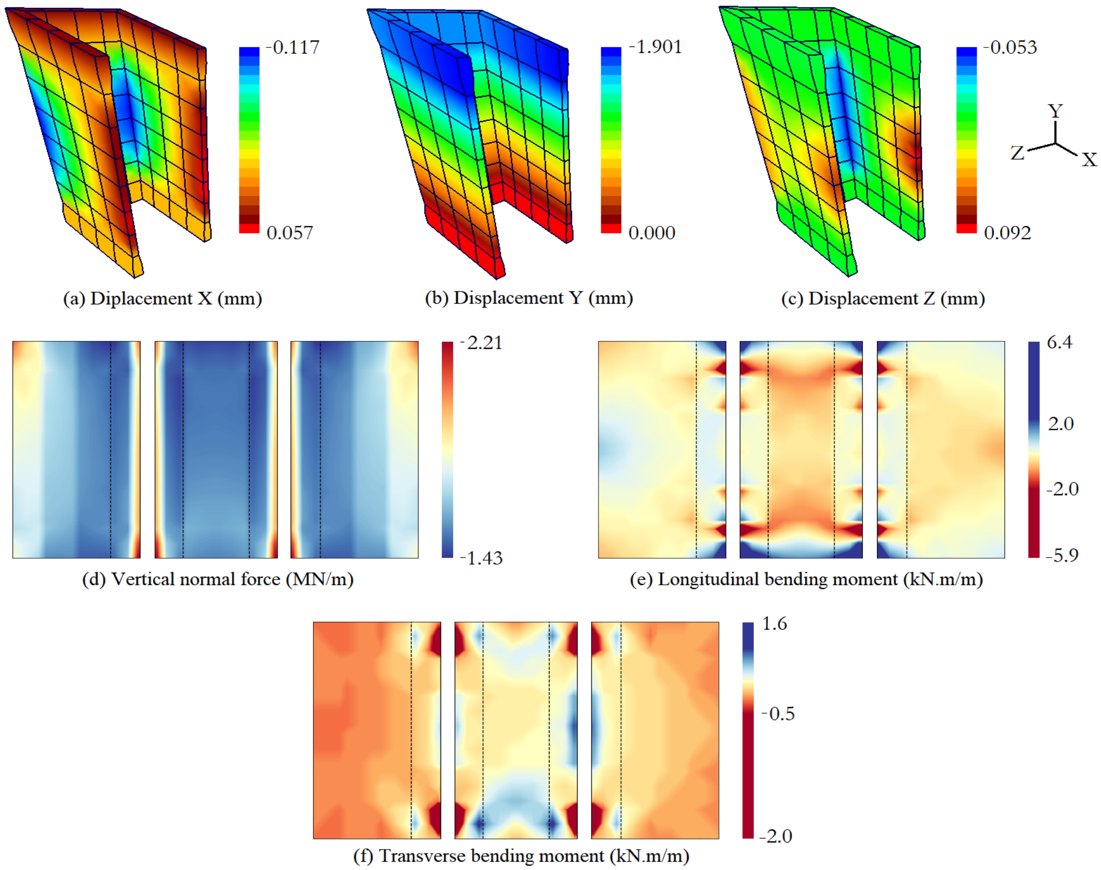

Figure 15. U-shaped shear wall results (asymmetric), lateral planar wall segment λ = 90

These last results demonstrate the need to development of parametric studies of this problem, varying dimensions, reinforcement ratios, among other properties, in order to verify the practical design limits.

5 CONCLUSIONS

In this article, for two usual shear walls (simple planar and U-shaped), a comparative study between the structures behavior according to the Brazilian code approximate procedure [2], the grid method [3], and a material and geometric nonlinear finite shell element analysis (NL-FEA), performed in VecTor 4 software, based on the Modified Compression Field Theory (MCFT) [4]. In addition, the U-shaped shear wall NL-FEA was made considering the structure main buckling modes displacement patterns. The following can be highlighted:

- The stress redistribution effect and the Saint-Venant's principle proved to be an analysis main issue, being responsible for smoothing the shear walls second order localized effects, a fact that was not observed in the grid method or in the Brazilian code approximate procedure;
- In these analyses, the bending moments obtained led to relationships between the transverse and longitudinal reinforcements below 25%, which suggests that the Brazilian code recommendation may be excessively conservative in some cases, as reported in the literature [3];
- With respect to the NL-FEA computational cost, according to the iterative-incremental method presented criteria, it was possible to observe an average processing time approximately equal to 40 min, for the simple planar shear wall, and, three hours, for the U-shaped shear wall. However, despite the high cost make this methodology less attractive for day-to-day work in design offices, this type of approach allows another perspective with regard to structure behavior and has fundamental importance for the engineering profession.
- Finally, the apparent similarity between the behavior of U-shaped shear wall and cold-formed steel frames subjected to local buckling may represent an opportunity for scientific investigation.

REFERENCES

[1] J. K. Wight and J. K. MacGregor, *Reinforced Concrete: Mechanics & Design*, 6th ed. Upper Saddle River: Pearson, 2012.

[2] Associação Brasileira de Normas Técnicas, *Projeto de Estruturas de Concreto – Procedimento,* NBR 6118, 2014.

[3] R. L. S. França and A. E. Kimura, "Resultados de recentes pesquisas para o dimensionamento das armaduras longitudinal e transversal em pilares-parede," in: *An. 9° Enc. Nac. Eng. Consult. Estrut.*, 2006.

[4] T. D. Hrynyk, "Behaviour and modelling of reinforced concrete slabs and shells under static and dynamic loads," Ph.D. dissertation, Dep. Civ. Eng., Univ. Toronto, Toronto, 2013.

[5] V. B. Almeida, "Dimensionamento, detalhamento e execução de pilares-parede," B.S. thesis, Dep. Eng. Civ., Univ. Fed. Pernambuco, Recife, 2018.

[6] M. C. B. N. Campos, "Análise numérica de pilares-parede de concreto armado com seção retangular," DSc. thesis, Prog. Pós-grad. Eng. Civ., Dep. Eng. Civ., Univ. Fed. Pernambuco, Recife, 2016.

[7] Associação Brasileira de Normas Técnicas, *Projeto de Estruturas Resistentes a Sismos – Procedimento*, NBR 15421, 2006.

[8] J. M. Araújo, "Flambagem local dos pilares-parede de concreto armado," *Rev. Teor. Prat. Eng. Civ.*, no. 9, pp. 29–37, 2006.

[9] Instituto Brasileiro do Concreto, *Comentários e Exemplos de Aplicação da ABNT NBR 6118:2014*, 2015.

[10] A. E. Kimura, *Cálculo de Pilares de Concreto Armado – Introdução, Visão Geral & Exemplos*. São Paulo: Associação Brasileira de Engenharia e Consultoria Estrutural, 2016.

[11] T. J. R. Hughes and M. Cohen, "The Heterosis finite element for plate bending," *Comput. Struc.*, vol. 9, pp. 445–450, 1978.

[12] D. R. J. Owen and J. A. Figueiras, "Ultimate load analysis of reinforced concrete plates and shells," *In Finite Element Software for Plates and Shells*, E. Hilton, D. R. J. Owen, Eds., Swansea, UK: Pineridge Press, 1984, pp. 403.

[13] F. J. Vecchio and M. P. Collins, "The modified compression field theory for reinforced concrete elements subjected to shear," *ACI Struct. J.*, vol. 83, no. 6, pp. 925–933, 1986.

[14] F. J. Vecchio, "Disturbed stress field model for reinforced concrete: formulation," *J. Struct. Eng.*, vol. 126, no. 9, pp. 1070–1077, 2000.

[15] R. Park, M. J. N. Priestley, and W. D. Gill, "Ductility of square-confined concrete columns," *J. Struct. Div.*, vol. 108, pp. 929–950, 1982.

[16] P. S. Wong, H. Trommels, and F. J. Vecchio, *VecTor2 and FormWorks User's Manual, Technical Report*, 2nd ed. Toronto: Dep. Civ. Eng., Univ. Toronto, 2012.

[17] M. Seckin, "Hysteretic behaviour of cast-in-place exterior beam-column-slab subassemblies," Ph.D. thesis, Dep. Civ. Eng., Univ. Toronto, Toronto, 1981.

[18] *SAP 2000 v21*. Computers and Structures, Inc., Walnut Creek, California, USA, 2000. [Online]. Available: csiamerica.com/products/sap2000.

[19] Associação Brasileira de Normas Técnicas, *Projeto de Estruturas de Aço e de Estruturas Mistas de Aço e Concreto de Edifícios, NBR 8800*, 2008.

[20] W. Pfeil and M. Pfeil, *Estruturas de Aço – Dimensionamento Prático de Acordo com a NBR 8800:2008*, 8th ed. Rio de Janeiro: LTC, 2009.

[21] W. Yu and H. LaBoube, *Cold-Formed Steel Design*, 4th ed. Hoboken: Wiley, 2010.

Author contributions: Jordlly Reydson de Barros Silva: conceptualization, methodology, numerical analysis, writing. Bernardo Horowitz: conceptualization, methodology, writing, supervision.

Editors: Osvaldo Luís Manzoli, José Luiz Antunes de Oliveira e Sousa, Guilherme Aris Parsekian.

Rev. IBRACON Estrut. Mater., vol. 13, no. 6, e13604, 2020

IBRACON Structures and Materials Journal
Revista IBRACON de Estruturas e Materiais

ISSN 1983-4195 ismj.org

ORIGINAL ARTICLE

Synergic effects between mineral admixtures on strength and microstructure of concretes

Efeitos sinérgicos entre adições minerais na resistência e microestrutura de concretos

Cristina Silva Feltrin[a]
Geraldo Cechella Isaia[a]
André Lübeck[a]

[a]Universidade Federal de Santa Maria – UFSM, Programa de Pós-Graduação em Engenharia Civil – PPGEC, Santa Maria, RS, Brasil

Received 22 August 2018
Accepted 03 March 2020

Abstract: The present research aims at evaluating the physical, chemical and synergistic effects of substitution 25% cement in mass by limestone filler (LF), fly ash (FA) and rice husk ash (RHA), in similarity of physical condition (near grain size curves), and to compare the different binary and ternary mixtures of concrete after 28 days of wet curing, keeping the ratio water/cement (w/c) constant. The concrete samples were characterized in relation to the axial compressive strength and their microstructure using TG/DTA and MEV/EDS techniques. The CCA in the binary mixture was the one that obtained bigger compressive strength among the investigated mixtures, but when combined with a less reactive mineral addition in ternary mixtures, an overlap of chemical and physical effects occurred which resulted in better resistance and higher C-S-H formation in the hardened cement paste.

Keywords: synergistic effect, limestone filler, fly ash, rice husk ash, concrete.

Resumo: A presente investigação tem o propósito de avaliar os efeitos físicos, químicos e sinérgicos da substituição de 25% de cimento em massa por fíler calcário (FC), cinza volante (CV) e cinza de casca de arroz (CCA), em similaridade de condição física (curvas granulométricas próximas), e comparar as diferentes misturas binárias e ternárias de concreto após 28 e 91 dias de cura úmida, mantendo-se constante a relação água/aglomerante (ag/agl.). As amostras de concreto foram caracterizadas em relação à resistência à compressão axial e quanto à sua microestrutura com uso de técnicas de TG/DTA e MEV/EDS. Os resultados indicam que uma adição mineral mais reativa como a CCA quando aliada à uma adição mineral menos reativa em uma mistura ternária, proporciona uma sobreposição de efeitos químicos e físicos que se traduz em melhores resistências e maior formação de C-S-H na pasta de cimento endurecido.

Palavras-chave: efeito sinérgico, fíler calcário, cinza volante, cinza de casca de arroz, concreto.

How to cite: C. S. Feltrin, G. C. Isaia, and A. Lübeck, “Synergic effects between mineral admixtures on strength and microstructure of concretes,” *Rev. IBRACON Estrut. Mater.*, vol. 13, no. 6, e13604, 2020, https://doi.org/10.1590/S1983-41952020000600004

1 INTRODUCTION

In recent years, climate change has concerned society and has been the subject of negotiations among world leaders to restrict greenhouse gas emissions. According to the The Intergovernmental Panel on Climate Change (IPCC) Synthesis Report [1], it is likely that the Earth's surface temperature will increase by more than 1.5 °C throughout the 21st century if pollution levels do not stop growing.

In the construction industry, the replacement of cement by mineral admixtures remains a solution with great potential for reducing the environmental impacts from the production of Portland cement. The consequence of this substitution is not negative in the sense that these additions generally improve technical properties, such as mechanical strength and durability of concrete, especially at more advanced ages. Scrivener and Nonat [2] point to the future importance of seeking an understanding of the factors that control the reaction rate of Supplementary Cementitious

Corresponding author: Cristina Silva Feltrin. E-mail: cristina.feltrin2@gmail.com
Financial support: CNPq; CAPES; FAPERGS; BASF Company.
Conflict of interest: Nothing to declare.

Materials (SCM), as well as the changes that occur in the calcium silicate hydrates (C-S-H), aiming at a higher use of these materials when replacing the use of Portland cement in ternary mixtures.

SCM are generally silica rich materials, largely present in the amorphous state, which influences the kinetics of cement hydration, the amount and type of hydrates formed, and consequently the volume, porosity and durability of cementitious systems [3].

These materials result in concrete physical, chemical and synergistic effects when used in ternary mixtures. The physical effect is characterized by the provision of additional nucleation points for the products of cement hydration and a change in particle packing [4]. The chemical effect is dependent on the type of mineral admixture used in the cementitious mixture and the mineralogical composition (crystalline and amorphous phases) [5].

The synergistic effect occurs when two pozzolans are combined, or when a pozzolan is combined with an inert material together with the cement in a ternary mixture, characterized by the overlapping of physical and chemical effects of one or another admixture resulting in better mechanical and microstructure properties. Isaia et al. [6] found that mixing a less reactive pozzolan with a more reactive pozzolan produces a synergistic effect between these two, which translates into a greater compressive strength. Antiohos et al. [7] carried out a study on pastes and mortars and found that the effect of ternary mixtures of different fly ash improved the mechanical properties of the mixtures compared to binary mixtures (with only one type of fly ash) due to the synergistic effect between them. Ha et al. [8] studied the synergic effect between FA and RHA in self-compacting and high performance concretes (with water/cement ratio 0,26), and observed that those pozzolans combination in ternary mixtures increased the compressive strength at the most advanced ages (56 days) in relation to the reference mixture (only Portland cement) and to the binary mixture with FA.

Limestone filler (LF) is a material considered practically inert, with little chemical activity; its preponderant effect on the concrete is the physical nucleation of new sites of hydration and closure of the pores. The presence of LF in the hydrated cement paste leads to the presence of monocarbonates in the system, which promotes the transformation of monosulfoaluminates into monocarboaluminates, inducing the conversion of monosulfoaluminate into ettringite due to the release of the sulfate during the carbonate replacement in the reaction [9]. The stabilization of ettringite in the presence of calcite leads to an increase in the total volume of hydrated phases, reducing the porosity of the system [10]. This active presence of the LF in the hydration process leads to an increase in initial compressive strength in concretes [10], [11].

Fly ash (FA) is SiO_2 rich material in its chemical composition but may also contain significant amounts of Al_2O_3. According to Lothenbach et al. [3], the mixture of Portland cement with FA results in a reduction in the amount of Portlandite (CH) and, if Class F ash (containing between 15 and 35% alumina [12]) is used, the greater are the amounts of hydrated phases rich in alumina. Under normal conditions of cure, these ashes are known to have little influence on the initial strength (up to 28 days), but they provoke a development of strength at more advanced ages, above 28 days [13].

In relation to the rice husk ash (RHA), both the low silica content (content less than 20%) and the high silica content (content higher than 80%) have a strong consumption of $Ca(OH)_2$ due to the pozzolanic reactions leading to the reduction of the C/S ratio in the C-S-H of the cementitious compound [14]. In terms of mechanical strength, RHA is known to have similar performance to silica fume, increasing mechanical strength at early ages [15]. The higher reactivity of RHA is due to the high content of amorphous silica and high specific surface of its grains [16].

A synergistic effect occurs between LF and FA that leads to better mechanical properties in the ternary concretes, attributed to the interaction of the limestone with the aluminates of the cement hydration, leading to the formation of carboaluminates. These additional aluminates brought to the system by fly ash during their pozzolanic reaction amplify the aforementioned effect of the limestone filler [17]. The bonding of LF with the RHA in the ternary mixture improves chemical and morphological properties that lead to greater compression strength and reduction of permeability in the cementitious system [18]. Vance et al. [19] studied hydration and strength increase in cement binary and ternary mixtures with LF, FA and metakaolin and verified that, for a certain substitution rate (20%), ternary mixtures (containing fly ash or metakaolin with limestone filler) had greater strengths than their correspondent binary mixtures.

The aim of this study was to analyze the behavior of ternary concrete mixtures containing LF, FA and RHA up to 28 days of wet curing, and to compare them with the respective binary mixtures at levels up to 25% cement mass replacement. The concrete samples were analyzed by means of axial compressive strength, scanning electron microscopy (SEM/EDS) and thermogravimetry (TGA/DTA).

2. MATERIALS AND EXPERIMENTAL PROGRAM

2.1 Binder materials

The type of cement used in the preparation of the mixtures was the CPV-ARI 32 [20] manufactured by a Brazilian industry. In order to replace the cement, a limestone filler (LF) from the region of Santa Maria (RS, Brazil), a fly ash (FA) from the Candiota thermoelectric plant, RS, Brazil, class C [21], and a rice husk ash (RHA) from rice industries also in the region of Santa Maria, burned without temperature control, class E [21].

The grain size distributions were approximated in order to allow admixtures to be compared to each other in the binary and ternary mixtures, without the physical effect influencing the synergic effect, that is, in similarity of physical condition. Thus, the three admixtures were milled in a ball mill at different milling times, being the LF milled for three hours, the FA for two hours and the RHA for one hour. The grain size distribution curves of the mineral admixtures obtained in the laser granulometer, using the PO-GT-1043 method, with dispersed using anhydrous alcohol and ultrasound for 60 seconds are presented in Figure 1. In Table 1 are shown the average diameters of the mineral admixtures.

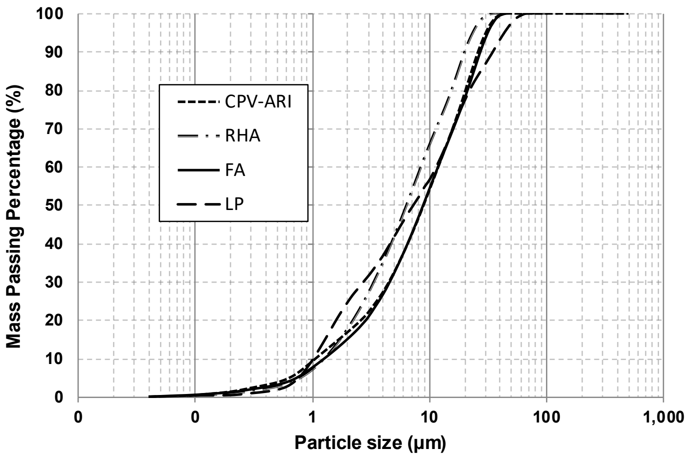

Figure 1. Particle size distribution of cement and mineral admixtures.

The mineral admixtures were statistically compared to the particle sizes (Table 1), with a 22.5% dispersion for larger grains (diameter < 90%) and a trend towards lower values for the finer grains, respectively, of 17.8% for diameters less than 50% and 10.7% for diameters smaller than 10%, which are the ones that most influence the physical effect of the reactions, the synergy and the packaging of the particles. Thus, it can be considered that, in relation to grain size, the mineral admixtures are fairly close, with a dispersion classified as medium to low, according to the granulometry range considered.

Table 1. Average Diameters of Mineral Admixtures.

Material	10% Diameter (µm)	50% Diameter (µm)	90% Diameter (µm)	Average Diameter (µm)
CPV-ARI 32 Cement	1.07	8.9	26.01	11.54
RHA (1h milled)	1.26	6.35	19.98	8.73
FA (2h milled)	1.25	8.74	26.93	11.75
LF (3h milled)	1.02	9.89	34.72	7.28
Average	1.15	8.5	26.91	9.83
Standard Deviation	0.123	1.512	6.051	2.185
Variation Coef. (%)	10.7	17.8	22.5	22.2

In Table 2 it is shown the results of the tests of the physical and chemical characteristics of the binder materials.

Table 2. Physical, mechanical and chemical characteristics of binders.

Physical properties	CP-V	LF	FA	RHA
Specific mass (g/cm^3)	3.09	2.92	2.36	2.18
Specific area BET (m^2/g)	1.14	2.64	1.04	19.67
Residual #0.075 mm (%)	0.82			
Initial setting time (min)	234			
End setting time (min)	270			
Normal consistency (%)	29.0			
Performance index with cement Portland	-	85	92	107
Compressive strength				
3 days (MPa)	27.6			
7 days (MPa)	36.2			
28 days (MPa)	42.8			
Chemical (%)				
Loss on the ignition	3.16	34.44	0.10	0.25
SiO_2	20.40	14.18	68.81	94.84
Al_2O_3	4.37	1.54	23.51	0.39
Fe_2O_3	2.64	0.87	4.70	2.58
CaO	62.90	28.89	1.00	1.32
MgO	2.70	18.28	2.16	0.40
SO_3	2.20	-	-	0.01
Na_2O	0.13	0.34	-	0.11
K_2O	0.95	0.39	0.39	1.45
MnO	0.05	-	0.68	-
TiO_2	0.29	-	0.16	-
P_2O_5	2.05	-	-	-

In the case of pozzolans tested, FA and RHA reached the chemical requirements given by the Brazilian standard NBR 12653 [21]. In relation to the performance index with Portland cement (evaluation of pozzolanic activity) at 28 days (Table 2), executed with mortars according to Brazilian standard NBR 5752 [22], it can be observed that the RHA obtained an index greater than 100%, that is, the compressive strength of the mortars with RHA were greater than the strength of the control mortar at 28 days of age, indicating good chemical activity through the pozzolanic reactions in the early ages. In spite of reaching the chemical parameters, FA did not achieve a performance of more than 90% in the performance index, as recommended by NBR 12653 [21]. It is observed that the LF with 3 hours of milling had a performance index of 85%, an index considered satisfactory since the material is an inert fine.

In relation to the specific BET surface of the cement, it is verified that the value of 1140 m^2/kg is in the expected range, considering that the cement used is a thin and low porous material. RHA presented a high BET specific surface area of 19670 m^2/kg, reflecting its highly porous internal structure with a large specific surface area, with the presence of voids, resulting in a higher demand for water (or chemical admixtures) when partial replacement of cement by this mineral admixture in the concrete. FA and LF presented values close to that of cement in the BET specific surface analysis, 1040 and 2640 m^2/kg, respectively, indicating a more spherical structure and smaller specific surface area of this admixture.

In Figure 2 it is shown the pozzolans, FA and RHA, and limestone filler (LF) diffractograms. The X-ray diffractogram of the LF shows calcite peaks ($CaCO_3$), and large peaks of dolomite carbonate ($CaMg(CO_2)_2$). The RHA X-ray diffractogram exhibits few crystalline peaks of cristobalite revealing predominantly amorphous silicon oxides in the composition. The behavior with some crystalline peaks of cristobalite and quartz indicates that the RHA was burned without temperature control. In the FA diffractogram it is observed the presence of quartz (Q), mullite (M) and hematite (H). In the comparison between the pozzolans, it is verified that the amorphization halo (between 15 and 30º 2Θ) of the RHA is broader than that of the FA, configuring greater pozzolanic activity.

2.2 Aggregates

Aiming at better packaging, the composite particles, four natural river sands with different granulometries were used, named: sand 1, sand 2, sand 3 and sand 4. The selected sands were strained in a 6,30 mm mesh strainer for the removal of stone grains, washed, taking the necessary measures in order to avoid wasting the fine grains, leaving it to decant before draining the water, and dried in an oven at 110 °C and then stored in an appropriate place (in closed boxes). Two types of diabase stones were used as coarse aggregates: gravel 0, with maximum characteristic size (MCS, [23]) of 12.5 mm, and gravel 1 with MCS of 19.0 mm. The coarse aggregate was washed, air dried and finally stored in closed boxes. The granulometric size distribution of the aggregates is shown in Figure 3. In Table 3 it is presented a summary of the characterization results of the aggregates.

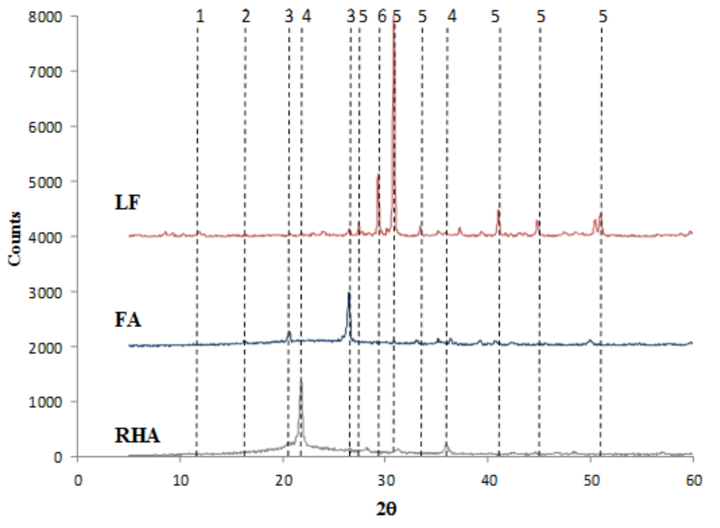

Figure 2. FA, RHA and LF diffractograms. (1) – Kaolinite; (2) – Mullite; (3) - Quartz; (4) – Cristobalite; (5) – Dolomite; (6) – Calcite.

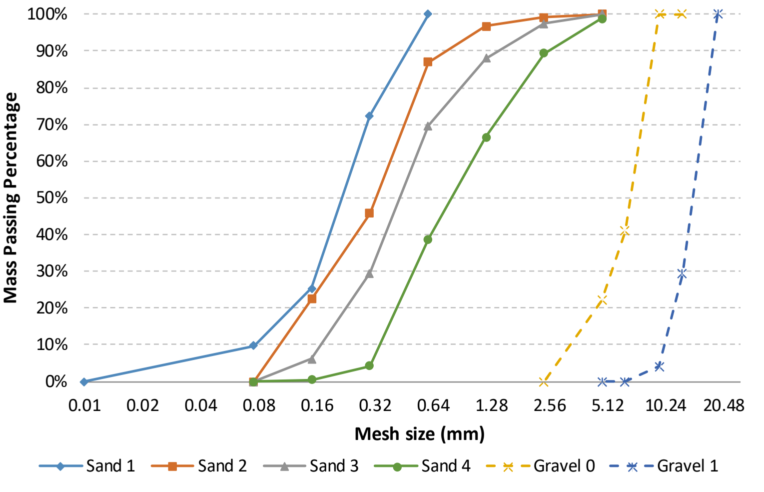

Figure 3. Particle size distribution of aggregates.

Table 3. Physical properties of aggregates.

Properties	Sand 1	Sand 2	Sand 3	Sand 4	Gravel 0	Gravel 1
Modulus of fineness	1.14	1.49	2.04	3.02	5.75	6.96
Characteristic maximum diameter (mm)	0.60	1.20	2.40	4.75	12.50	19.00
Specific mass (g/cm^3)	2.65	2.65	2.66	2.66	2.44	2.50
Unit mass (g/cm^3)	1.53	1.63	1.65	1.69	1.36	1.46
Loss of mass in Los Angeles abrasion (%)	-	-	-	-	11.04	15.20
Form index	-	-	-	-	-	2.80
Water absorption (%)	0.33	0.35	0.38	0.40	3.16	2.36
Powdery material (%)	5.50	3.00	2.80	-	-	-

2.3 Mixtures tested

The ideal mortar content was determined according to the method proposed by Helene and Terzian [23], the content of 51% was found for the chosen materials and kept constant in all mixtures. In the mixtures with mineral admixtures, the increase in paste volume was counterbalanced by reducing the volume of sand. The correction of sand amount for maintaining the paste volume in binary and ternary mixtures ensured a constant binder volume between the mixtures.

After the materials were prepared and the mortar content established, the water/binder ratio (w/b) was defined as 0.50 and cement substitution content as 25%, the best composition among the smaller amount of voids, through the analysis of the packing of particles of the constituent materials of the concrete. Thus, the binary and ternary mixtures had the aggregates varied so as to result in maximum packing. Figure 4 exemplifies the packing curve of the materials constituting Mixture 3 (binary) with 25% RHA. The attempt was to approximate the curve of the mixtures with the modified Andreasen Curve [24] by means of the variation in sand and coarse aggregate proportions. The coefficient of distribution used was 0.25, as it favors the densification of composite ceramic materials [25].

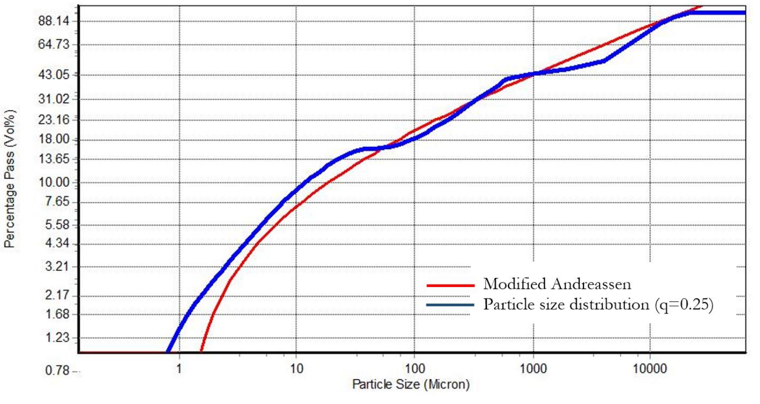

Figure 4. Example of packing curve, RHA25 mixture.

In Table 4 it is shown the unitary proportions for mixtures tested, and in Table 5 it is presented the material consumption per cubic meter of concrete. The correction in the amount of sand to maintain the paste volume in the binary and ternary mixtures ensured a constant volume of cement for all the mixtures.

For the axial compressive strength test on concrete, four cylindrical specimens were molded for each age, with a diameter of 10 cm and a height of 20 cm, according to Brazilian standard NBR 5738 [26]. The mixtures were performed in conventional inclined-axis concrete mixer, and the consistency of the concrete was kept constant for all mixtures, adopting a slump between 100 ± 20 mm. The chemical admixture used was a hyperplasticizer based on ether polycarboxylate, compatible with Portland cement. In general, the chemical admixture content remained between 0.1 and 0.2% of the mass of the binder. The specimens were densified on a vibrating table and held in the molds in a humid chamber (relative humidity of 100% and temperature of 23 ± 1 °C) for 24 hours, after which they were demolded and cured in a tank filled with lime-saturated water at a temperature of 23 ± 2 °C to date of the tests.

For the axial compressive strength data, an Analysis of Variance (ANOVA) was conducted in order to verify the statistical significance in the axial compressive strength results obtained for 7, 28 and 91 days. As a complementation of the analysis, a *post hoc* Tukey's Test was conducted, for comparing, two to two, the normal distribution data averages. The significance level adopted was 95% ($\alpha = 5\%$).

The samples for SEM were obtained after the removal of slices from the cylindrical test specimen after 28 days of curing. The slices were reduced to a maximum size of 5 mm in thickness and 20 mm in diameter. The concrete fragments were immersed in isopropanol for 7 days to stop the hydration reactions, and dried in an oven at 45 °C for a period of 48 hours. After drying, the samples were separated in closed containers and identified until they were taken to the laboratory, where they were analyzed by SEM with backscattered electrons (BSE) to shot images with the approximation of 3000x of the transition zone (ITZ) also, in the energy dispersive X-ray detector (EDS).

For each zone delimited in the BSE image, three EDS determinations were made, and with these three determinations average it was possible determine the amounts of Si, Ca e Al. It was settled that the sum of the Si, Ca and Al amounts of each of the samples correspond to the C-S-H amount, for that it was possible to accomplish a more effective comparison between the samples, basing such analysis in the studies of Durdzinski et al. [27] and Jung et al. [18].

Table 4. Unitary proportion of the studied mixtures.

Mixtures	w/b	Cement	LP	FA	RHA	Sand	Gravel	Chemical admixture
REF	0.50	1.00	-	-	-	2.06	2.94	0.0005
LF25	0.50	0.75	0.25	-	-	2.05	2.94	0.0010
RHA25	0.50	0.75	-	-	0.25	1.98	2.94	0.0030
FA25	0.50	0.75	-	0.25	-	2.00	2.94	0.0006
LF10FA15	0.50	0.75	0.10	0.15	-	2.02	2.94	0.0010
LF10RHA15	0.50	0.75	0.10	-	0.15	2.00	2.94	0.0020
FA12.5RHA12.5	0.50	0.75	-	0.125	0.125	1.98	2.94	0.0025

Table 5. Consumption of materials per m^3 of concrete (kg/m^3).

Mixture	Portland cement	LF	RHA	FA	Sand 1	Sand 2	Sand 3	Sand 4	Gravel 0	Gravel 1	Water	Chemical Admixture	Slump
1	358	-	-	-	-	-	737	-	-	1053	179	0.2	120
2	358	90	-	-	183	183	183	183	526	526	179	0.4	105
3	358	-	90	-	177	177	177	177	526	526	179	1.1	110
4	358	-	-	90	179	179	179	179	526	526	179	0.2	120
5	358	36	-	54	181	181	181	181	526	526	179	0.4	100
6	358	36	54	-	179	179	179	179	526	526	179	0.4	110
7	358	-	45	45	177	177	177	177	526	526	179	0.7	120

For the TG tests, the paste samples were prepared separately in a mechanical mixer and, after 28 days of wet curing, were ground and strained in the strainer #100 (0.15 mm mesh). For the stoppage of the hydration reactions, the paste powder was immersed in isopropanol for 15 minutes, and then filtered and washed with diethyl ether. Soon after, the samples were dried in an oven at 40 ºC for 10 minutes and stored in closed containers. During the test, portions of 15 ± 1 mg were placed in alumina melting pot and heated under inert nitrogen atmosphere, at a flow rate of 50 mL/min. Heating started from natural temperature and increased until reaching the temperature of 1000 °C, at a heating rate of 20 °C/min.

The curves resulting from the TG/DTA test on hydrated cement paste samples can be separated into bands or zones. Up to 105 ºC, evaporable water is lost, and between 105 ºC and 300 ºC, chemically combined water (BW) is lost from the decomposition of C-S-H and hydrated carboaluminates [28]. The amount of portlandite ($Ca(OH)_2$) can be calculated based on the loss of mass between the temperatures of 400 ºC and 500 °C and the calcite ($CaCO_3$) through the loss of mass above 600 °C [29].

3. RESULTS

3.1 Axial compressive strength

In Figure 5 it is presented the results of axial compression strength of the different mixtures at the initial ages, at 7, 28 and 91 days. The standard deviations resulted from each sample were indicated by the columns. The strength increased with the curing period, as expected, and at 7 days only the CCA25 mixture had a higher strength than the reference concrete, and at 28 days most of the mixtures with cement substitution by mineral additions had strength close or higher that of reference concrete. At 91 days, only the strength of the FC25 mixture was not higher than that of the reference concrete.

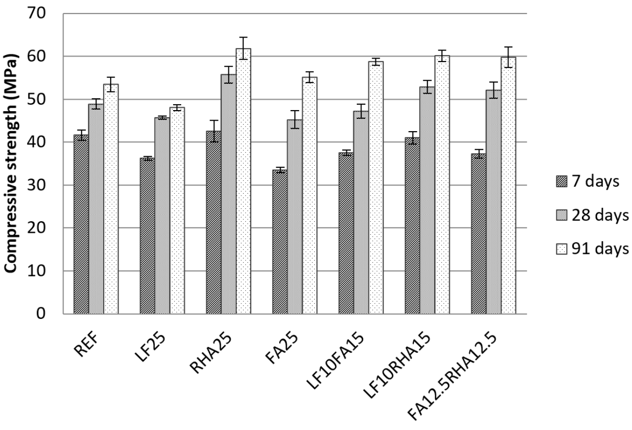

Figure 5. Compressive strength results for 7, 28 and 91 days.

Based on the Analysis of Variance *(*ANOVA*)* of the compression strength results at 7, 28 and 91 days (Table 6), it was possible to verify that there was a substantial strength difference between the evaluated mixtures. The "p" values smaller than 0,05, or $F_{calculated}$ values bigger than $F_{critical,}$ indicate that the relation between variables is statistically significant for 7, 28 and 91 days for a 95% significance level. The higher the F value, the more significant is the difference, thus at 91 days the difference was more significant than at 7 and 28 days.

In Tables 7, 8 and 9 it is presented the "p" values results obtained from the Tukey's test of comparison of compression strengths averages between mixtures at the ages of 7, 28 and 91 days, respectively. "p" values result smaller than 0,05 indicates that the strength variation between the two analyzed mixtures was significant. In those tables the significant differences were hatched with gray to facilitate identification.

Table 6. ANOVA analysis for compressive strength results at 7, 28 and 91 days.

Compressive strength at 7 days						
Variation source	**SQ***	**DF****	**AS*****	**$F_{calculated}$**	**P-value**	**$F_{critical}$**
Between mixtures	260.33	6	43.39	25.57	0.00000001	2.572712
Inside mixtures	35.63	21	1.70			
Total	295.96	27				
Compressive strength at 28 days						
Variation source	SQ	DF	AS	$F_{calculated}$	P-value	$F_{critical}$
Between mixtures	416.83	6	69.47	27.52	0.00000001	2.572712
Inside mixtures	53.01	21	2.52			
Total	469.84	27				
Compressive strength at 91 days						
Variation source	SQ	DF	AS	$F_{calculated}$	P-value	$F_{critical}$
Between mixtures	554.40	6	92.40	32.53	0.00000000	2.572712
Inside mixtures	59.65	21	2.84			
Total	614.05	27				

*SQ = the sum of the squares; **DF = degree of freedom; ***AS = average of the squares.

Table 7. Tukey's test results (p-value) for compressive strength at 7 days.

	REF	**LF25**	**RHA25**	**FA25**	**LF10FA15**	**LF10RHA15**	**FA12.5RHA12.5**
REF		0.0001	0.9454	0.0000	0.0038	0.9955	0.0020
LF25	8.2610		0.0000	0.0878	0.7842	0.0006	0.9044
RHA25	1.4320	9.6920		0.0000	0.0004	0.6667	0.0002
FA25	12.4600	4.2030	13.9000		0.0040	0.0000	0.0074
LF10FA15	6.2490	2.0110	7.6810	6.2150		0.0153	1.0000
LF10RHA15	0.8714	7.3890	2.3030	11.5900	5.3780		0.0083
FA12.5RHA12.5	6.6330	1.6280	8.0650	5.8310	0.3839	5.7620	

Table 8. Tukey's test results (p-value) for compressive strength at 28 days.

	REF	LF25	RHA25	FA25	LF10FA15	LF10RHA15	FA12.5RHA12.5
REF		0.1454	0.0001	0.0126	0.8017	0.0226	0.0896
LF25	3.8270		0.0000	0.8934	0.8364	0.0001	0.0002
RHA25	8.9160	12.7400		0.0000	0.0000	0.1521	0.0413
FA25	5.4980	1.6710	14.4100		0.2094	0.0000	0.0000
LF10FA15	1.9640	1.8630	10.8800	3.5340		0.0010	0.0044
LF10RHA15	5.1230	8.9500	3.7920	10.6200	7.0870		0.9935
FA12.5RHA12.5	4.1890	8.0160	4.7270	9.6870	6.1520	0.9347	

The Tukey's Test results confirm that cement substitution for mineral admixtures in binary and ternary mixtures may result in significant strength variations at the early ages. In the binary mixtures at 7 days (Table 7), only the 25% RHA substitution (*RHA25*) did not result in a significant compression strength decrease, but in an increase, showing the excellent performance in the early ages of CCA. In the ternary mixtures, the *LF10FA15* and *FA12.5RHA12.5* also resulted in significantly smaller strengths than the *REF* mixture at 7 days.

From the results presented in Table 8 it is noticed that cement substitution for 25% of RHA (*RHA25*) resulted in a significant compression strength increase at 28 days. The mixtures that exceeded 50 MPa at 28 days were binary with 25% RHA (*RHA25*) and the ternaries LF with RHA and FA with RHA, mixtures *LF10RHA15* and *FA12.5RHA12.5*, respectively. These were the same mixtures that outperformed the reference concrete (*REF*), yet only in the *RHA25* and *LF10RHA15* they resulted in a significant compressive strength increase. The 25% cement substitution for fly ash *(25FA)* resulted in a significant compressive strength decrease at 28 days in relation to the reference concrete. The other mixtures did not result in significant variations in relation to the reference mixture.

The binary concretes of LF (*LF25*) and FA (*FA25*) obtained very close compressive strengths. The mixture with 25% FA reached 45.2 MPa at 28 days and at 25% LF reached 45.7 MPa, indicating that the FA acts predominantly through the physical effect in the early ages, since the mixture with the limestone filler resulted in almost the same strength, that is, there was no significant difference between results.

At 91 days (Table 9), the increase in compressive strength in relation to the reference concrete was significant for most mixtures with mineral admixtures: *RHA25*, *LF10FA15*, *LF10RHA15* and *FA12.5RHA12.5*, which reached strengths of 61.8 MPa, 58.7 MPa, 60.1 MPa and 59.7 MPa, respectively. In the case of the LF25 mixture, there was a significant reduction in strength, with an average value of 48.0 MPa, and the reference concrete had an average strength of 53.4 MPa.

Table 9. Tukey's test results (p-value) for compressive strength at 28 days.

	REF	LF25	RHA25	FA25	LF10FA15	LF10RHA15	FA12.5RHA12.5
REF		0.0028	0.0000	0.9995	0.0036	0.0003	0.0050
LF25	6.4320		0.0000	0.0011	0.0000	0.0000	0.0000
RHA25	9.9650	16.4000		0.0000	0.1736	0.7753	0.1346
FA25	0.5844	7.0160	9.3810		0.0093	0.0006	0.0127
LF10FA15	6.2780	12.7100	3.6880	5.6930		0.8982	1.0000
LF10RHA15	7.9300	14.3600	2.0350	7.3460	1.6520		0.8403
FA12.5RHA12.5	6.0790	12.5100	3.8860	5.4940	0.1988	1.8510	

Figure 6 shows the average compressive strength indexes at 7, 28 and 91 days for the tested mixtures. The strength index is the relationship between the strength of the mixture with SCM and the reference mixture, for equal age and ag/agl ratio. From these results, it is possible to note, with greater evidence, the effects of mineral admixtures in the increase of the compressive strengths of the investigated mixtures with increasing age, based on the evolution of the average strength indexes.

In the comparison between binary and ternary mixtures it is noticed that the *LF10FA15* mixture achieved a slightly higher compressive strength than the respective binary mixtures *LF25* and *FA25*, as also verified by De Weerdt et al. [17], significantly higher at 91 days. For the *LF10RHA15* the strength increase was significant at 91 days in relation to the mixtures REF, *25LF* and *25FA* and ternary, *LF10FA15,* which demonstrated that there is sinergy between those two mineral admixtures, as also observed by Jung et al. [18]. In the case of the *FA12.5RHA12.5* mixture, it obtained significantly greater strength than the respective binary mixture with FA.

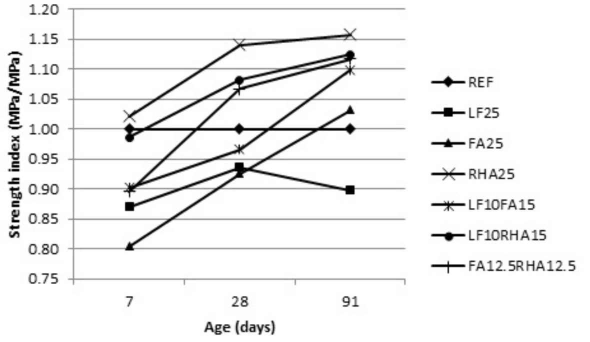

Figure 6. Strength index of the investigated mixtures.

The mixtures *RHA25*, *LF10RHA15* and *FA12.5RHA12.5* were the ones that obtained the best performances in the studied conditions in relation to the reference concrete, showing that the use of a more mineral admixture like RHA together with a less reactive one like LF or FA is effective for strength gain.

Assuming that mineral admixtures were analyzed in similarity of physical conditions, that is, with little difference between curves in all size ranges (Figure 1), so that it enables a more homogenous analysis between the binary and ternary mixtures with regards to their chemical and synergic effects, it is possible to observe a better performance of ternary mixtures in relation to the respective binary mixtures with less reactive mineral additions (LF e FA), indicating an overlapping of chemical effects (synergic effect) of those less reactive additions when they are used together with a more reactive addition (RHA) in ternary cementitious systems.

3.2 Scanning Electron Microscopy (SEM/EDS)

The microscopy images collected by BSE and EDS characterize the compounds formed in the hydrated cement paste in the concrete samples. These results allowed to make a qualitative analysis of the transition zone (ITZ) based on the images collected in the BSE with a 3000x approximation, and a quantitative analysis in terms of percentage of the compounds (Si, Ca, Al and C-S-H) present in the fragments of concrete with EDS after 28 days of wet curing. In the images presented in Figures 7, 8, 9 and 10, a region corresponding to the square indicated on the image was selected for collecting the EDS spectra shown next to each image.

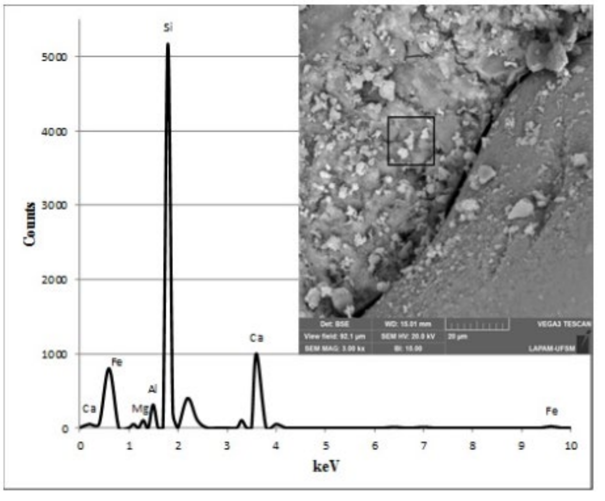

Figure 7. SEM/EDS image for REF mixture.

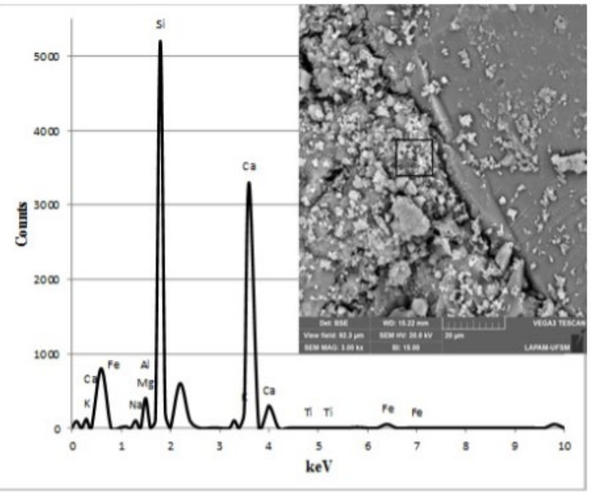

Figure 8. SEM/EDS image for LF10FA15 mixture.

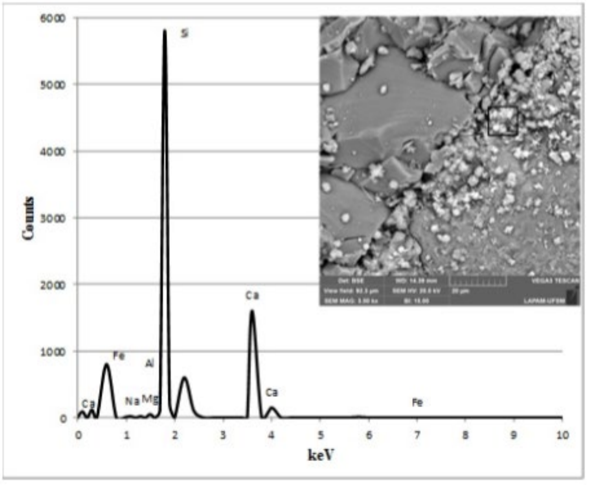

Figure 9. SEM/EDS image for LF10RHA15 mixture.

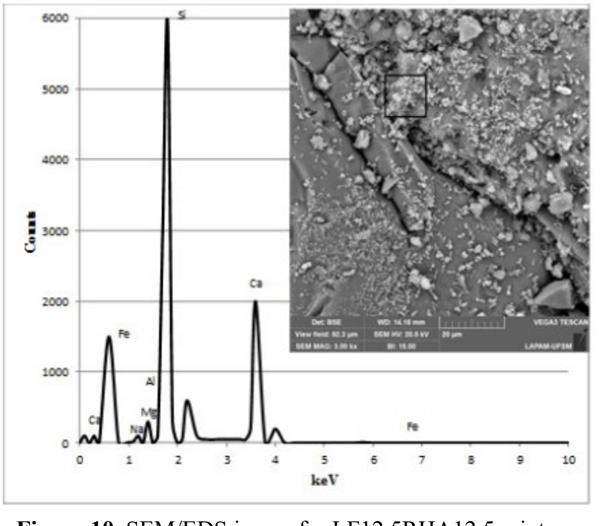

Figure 10. SEM/EDS image for LF12.5RHA12.5 mixture.

It can be seen in Figure 7 that the reference concrete (*REF*) has a porous transition zone and with fewer C-S-H microcrystals. In contrast, in Figures 8 (*LF10FA15*), 9 (*LF10RHA15*) and 10 (*FA12.5RHA12.5*), it is notable the increase in the amount of C-S-H agglomerates around the aggregate in the transition zone and a less porous and more uniform concrete in ternary mixtures than in the reference one (*REF*), as pointed by Mohammed et al. [30].

In Figure 11, it is possible to observe the mass percentages of Si, Ca, Al and C-S-H, and the value of C-S-H corresponds to the sum of the three compounds found in the EDS of the concrete samples.

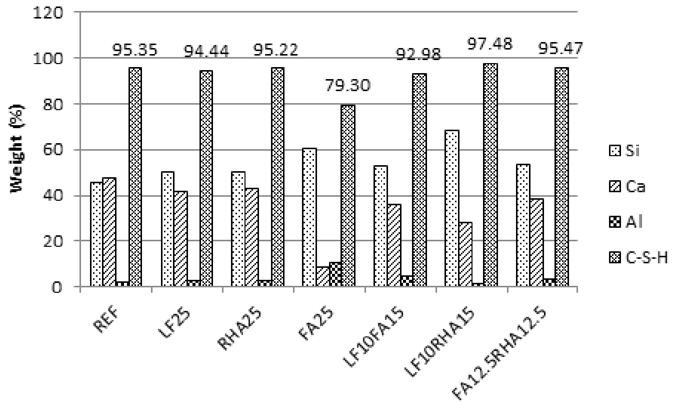

Figure 11. Percentage of weight of Ca, Si, Al and C-S-H obtained from the EDS spectrum.

The sample with the lowest amount of Ca and Si was with 25% FA (*FA25*), and the one with the highest Ca and Si amount was the ternary mixture of LF with RHA (*LF10RHA15*), revealing a synergy between these two additions in cementitious mixtures. All the mixtures with mineral admixtures showed higher Si contents than the reference concrete (*REF*). The mixture with higher presence of Al was the binary *FA25*, due to the chemical composition of the FA class F, with high content of alumina. The mixture that presented the highest content of C-S-H was *LF10RHA15*, evidencing a higher formation of hydrated calcium silicates in the ternary mixtures with LF and RHA.

3.3 Thermogravimetric analysis (TGA/DTA)

In Figures 12 and 13 it is shown the thermogravimetric curves TGA and DTA of the seven mixtures studied, respectively. A summary of the mass losses corresponding to the compounds formed in the cement paste is in Table 10.

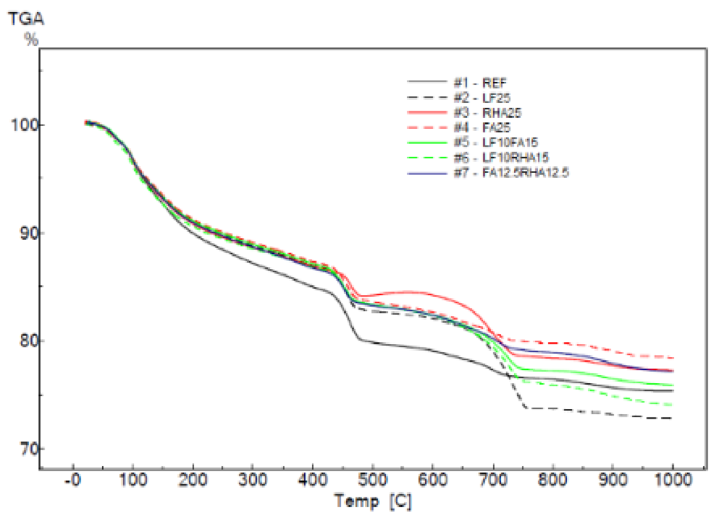

Figure 12. TGA curves for concrete mixtures tested.

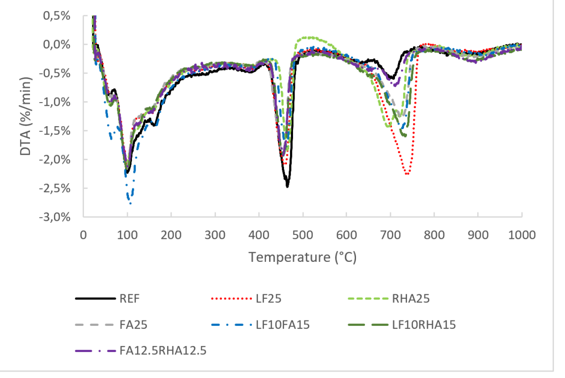

Figure 13. DTA curves for concrete mixtures tested.

Table 10. TGA/DTA results.

Mixture	BW (%)	Ca(OH)$_2$ (%)	CaCO$_3$ (%)
REF	8.91	5.16	0.78
LF25	7.46	4.23	8.38
RHA25	7.50	2.67	5.84
FA25	7.35	3.73	2.85
LF10FA15	7.34	3.79	5.14
LF10RHA15	7.16	3.48	6.37
FA12.5RHA12.5	7.54	3.47	3.47

The results of the thermogravimetric analysis at 28 days indicate that there was reduction of the remaining calcium hydroxide (CH) with the use of mineral admixtures in concrete. The mixture in which there was the highest consumption of CH was the binary mixture with 25% of RHA (*RHA25*), and in the ternary mixtures of LF and RHA (*LF10RHA15*) and FA and RHA (*FA12.5RHA12.5*), there was a very approximate consumption of CH of 3.48% and 3.47%, respectively. The reduction of the percentage of portlandite in the binary and ternary mixtures indicates the consumption of CH in the pozzolanic reaction and consequent formation of the secondary C-S-H [3].

The water content was lower in the mixtures with mineral admixtures than the reference concrete. In the mixtures with admixtures the values were very close, between 7 and 7.5%. In mixtures with 100% cement (*REF*) and *LF25* there is clearly a higher peak around 180 ºC relative to the formation of monosulfate e hemicarbonate [31]. On the other hand, there is a greater formation of CaCO$_3$ in all mixtures with mineral admixtures in comparison to the pure-cement mixture.

A better evaluation of the relative performance of the mineral additions is done through a unitary analysis, i.e., relating the results with the consumption of cement (per kg of cement) for each mixture. Thus, it was possible to obtain a comparative graph (Figure 14) between the unitary compressive strength and the contents of calcium hydroxide (CH), bind water (BW) and calcite (CaCO$_3$). The unitary contents are obtained by calculating the result by mass of cement of the mixtures.

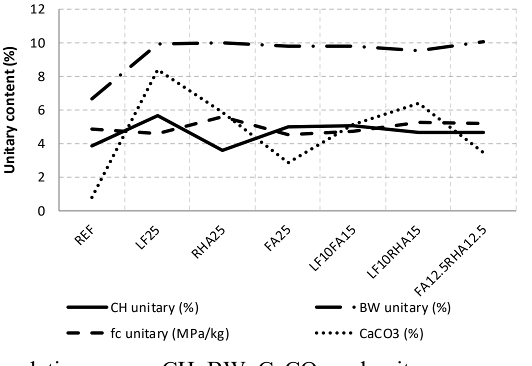

Figure 14. Correlation among CH, BW, CaCO$_3$ and unitary compressive strength.

In relation to the unitary content of CH, the inversely proportional relation between the axial compression strength and the CH amount is evident. The consumption of CH and consequent formation of secondary C-S-H in mixtures with mineral admixtures resulted in increased strength at 28 days of age.

There was a higher formation of calcium carbonate ($CaCO_3$) in the binary and ternary mixtures with LF. There is also a correlation between carbonate formation in the presence of RHA, in both binary (*RHA25*) and ternary (*LF10RHA15*) mixtures. There was a higher carbonate formation in the mixtures with the presence of mineral admixtures than in the reference mixture (*REF*), and the presence of the carbonate is directly proportional to the compressive strength in the ternary mixtures (Mixtures *LF10FA15* and *LF10RHA15*). The same occurred for unit bind water, which was higher in mixtures with mineral admixtures than in the reference mixture.

4 CONCLUSIONS

The conclusions based on the results of compressive strength and analysis of the microstructure of concrete samples with substitution of cement by LF, FA and RHA in binary and ternary mixtures, are as follows:

1. The use of RHA in binary and ternary mixtures increases the compressive strength of concrete mixtures in relation to the reference concrete, mainly at 91 days.
2. RHA is the most reactive mineral admixtures in the study, due to the presence of amorphous silica in its composition and the high specific surface of its particles. RHA was also the mineral admixture that resulted in the highest CH consumption and the highest unitary combined water content (per kg of cement).
3. The ternary mixture with LF and RHA (*FC10CCA15*) resulted in bigger compressive strength and formation of C-S-H compared to the reference mixture and the other mixtures with LF and FA, evidencing a synergic effect between these two mineral admixtures. The synergistic effect on ternary mixtures with LF is directly related to the higher carbonate formation in these mixtures.
4. When a less reactive pozzolan, such as FA, or even a non-reactive addition, such as LF, is used together with a more reactive one, such as RHA, a synergy occurs between them due to a chemical interaction, resulting in an increase in secondary C-S-H content and lower porosity at the paste-aggregate interface zone.

REFERENCES

[1] Intergovernmental Panel on Climate Change, *Climate Change 2014: Synthesis Report*, 2014.

[2] K. L. Scrivener and A. Nonat, "Hydration of cementitious materials, present and future," *Cement Concr. Res.*, vol. 41, no. 7, pp. 651–665, 2011.

[3] B. Lothenbach, K. Scrivener, and R. D. Hooton, "Supplementary cementitious materials," *Cement Concr. Res.*, vol. 41, no. 12, pp. 1244–1256, 2011.

[4] F. Deschner et al., "Hydration of Portland cement with high replacement by siliceous fly ash," *Cement Concr. Res.*, vol. 42, no. 10, pp. 1389–1400, 2012.

[5] P. K. Mehta, "Pozzolanic and cementitious by-products in concrete – another look," in *Int. Conf. Fly Ashs, Silica Fume, Alg, and Nat. Pozzolans Concr.*, 1989, pp. 1–44.

[6] G. C. Isaia, A. L. G. Gastaldini, and R. Moraes, "Physical and pozzolanic action of mineral additions on the mechanical strength of high-performance concrete," *Cement Concr. Compos.*, vol. 25, pp. 69–76, 2003.

[7] S. K. Antiohos, V. G. Papadakis, E. Chaniotakis, and S. Tsimas, "Improving the performance of ternary blended cements by mixing different types of fly ashes," *Cement Concr. Res.*, vol. 37, pp. 877–885, 2007.

[8] L. T. Ha, K. Siewert, and H. M. Ludwig, "Synergistic of rice husk ash and fly ash on properties of self-compacting high performance concrete", in *Ultra-High Performance Concrete and Nanotechnology in Construction*, M. Schmidt, E. Fehling, C. Glotzbach, S. Fröhlich, and S. Piotrowski, Eds. Kassel: Kassel University Press, 2012, pp. 187–195.

[9] V. L. Bonavetti, V. F. Rahhal, and E. F. Irassar, "Studies on the carboaluminate formation in limestone filler-blended cements," *Cement Concr. Res.*, vol. 31, pp. 853–859, 2001.

[10] B. Lothenbach, G. Le Sauout, E. Gallucci, and K. Scrivener, "Influence of limestone on the hydration of Portland cements," *Cement Concr. Res.*, vol. 38, pp. 848–860, 2008.

[11] V. Tydlitát, T. Matas, and C. Robert, "Effect of w/c and temperature on the early-stage hydration heat development in Portland-limestone cement," *Constr. Build. Mater.*, vol. 50, pp. 140–147, 2014.

[12] American Society for Testing and Materials, *Standard Specification for Coal Fly Ash and Raw or Calcined Natural Pozzolan for Use as a Mineral Admixture in Concrete*, ASTM C618, 1978.

[13] I. Jawed, "Hardened mortar and concrete with fly ash," in *Fly Ash in Concrete – Properties and Performance* (Rilem Report 7), K. Wesche, Ed. London: Chapman & Hall, 1991, pp. 42–159.

[14] J. H. S. Rêgo, A. A. Nepomuceno, E. P. Figueiredo, and N. P. Hasparyk, "Microstructure of cement pastes with residual rice husk ash of low amorphous silica content," *Constr. Build. Mater.*, vol. 80, pp. 56–68, 2015.

[15] F. Zunino and M. Lopez, "Decoupling the physical and chemical effects of supplementary cementitious materials on strength and permeability – a multi-level approach," *Cement Concr. Compos.*, vol. 65, pp. 19–28, 2016.

[16] P. K. Mehta, "Rice husk ash – a unique supplementary cementing material," in *Advances in Concrete Technology*, 2nd ed., V. M. Malhotra, Ed. Ottawa: Canmet, 1992, pp. 407–431.

[17] K. De Weerdt, M. Ben Haha, G. Le Saout, K. O. Kjellsen, H. Justnes, and B. Lothenbach, "Hydration mechanisms of ternary Portland cements containing limestone powder and fl y ash," *Cement Concr. Res.*, vol. 41, no. 3, pp. 279–291, 2011.

[18] S. Jung, V. Saraswathy, S. Karthick, P. Kathirvel, and S.-J. Kwon, "Microstructure characteristics of fly ash concrete with rice husk ash and lime stone powder," *Int. J. Concr. Struct. Mater.*, vol. 12, no. 1, pp. 17, 2018.

[19] K. Vance, M. Aguayo, T. Oey, G. Sant, and N. Neithalath, "Hydration and strength development in ternary portland cement blends containing limestone and fly ash or metakaolin," *Cement Concr. Compos.*, vol. 39, pp. 93–103, 2013.

[20] Associação Brasileira de Normas Técnicas, *Cimento Portland de Alta Resistência Inicial*, NBR 5733, 1991, pp. 1–5.

[21] Associação Brasileira de Normas Técnicas, *Materiais Pozolânicos – Requisitos*, NBR 12653, 2014.

[22] Associação Brasileira de Normas Técnicas, *Materiais Pozolânicos: Determinação do Índice de Desempenho com Cimento Portland aos 28 Dias*, NBR 5752, 2014, p. 1–8.

[23] P. Helene and P. Terzian, *Manual de Dosagem e Controle do Concreto.* São Paulo: PINI, 1992.

[24] J. E. Funk and D. R. Dinger, "Particle packing, part III: discrete versus continuous particles sizes," *Interceram*, vol. 41, pp. 332–334, 1992.

[25] A. L. Castro and V. C. Pandolfelli, "Revisão : Conceitos de dispersão e empacotamento de partículas para a produção de concretos especiais aplicados na construção civil," *Ceramica*, vol. 55, pp. 18–32, 2009.

[26] Associação Brasileira de Normas Técnicas, *Concreto – Procedimento para Moldagem e Cura de Corpos-de-Prova de Concreto,* NBR 5738, 2015, pp. 1–6.

[27] T. Durdzinski, C. F. Dunant, M. Ben, and K. L. Scrivener, "A new quantification method based on SEM-EDS to assess fl y ash composition and study the reaction of its individual components in hydrating cement paste," *Cement Concr. Res.*, vol. 73, pp. 111–122, 2015.

[28] L. Alarcon-Ruiz, G. Platret, E. Massieu, and A. Ehrlacher, "The use of thermal analysis in assessing the effect of temperature on a cement paste," *Cement Concr. Res.*, vol. 35, no. 3, pp. 609–613, 2005.

[29] B. Lothenbach, P. Durdzinski, and K. De Weerdt, "Thermogravimetric analysis," in *A Practical Guide to Microstructural Analysis of Cementitious Materials*, K. Scrivener, R. Snellings, and B. Lothenbach, Eds., Boca Raton: CRC Press, 2016, p. 177–211.

[30] M. K. Mohammed, A. R. Dawson, and N. H. Thom, "Production, microstructure and hydration of sustainable self-compacting concrete with different types of filler," *Constr. Build. Mater.*, vol. 49, pp. 84–92, 2013.

[31] V. S. Ramachandran, "Thermal analyses of cement components hydrated in the presence of calcium carbonate," *Thermochim. Acta*, vol. 127, pp. 385–394, 1988.

Author contributions: GCI: conceptualization, funding acquisition, supervision; AL: conceptualization, data curation, formal analysis, writing.

Editors: José Luiz Antunes de Oliveira e Sousa, Guilherme Aris Parsekian.

IBRACON Structures and Materials Journal
Revista IBRACON de Estruturas e Materiais
ISSN 1983-4195 ismj.org

ORIGINAL ARTICLE

Modelling of tension stiffening effect in reinforced recycled concrete

Modelagem do efeito do enrijecimento à tração em concreto armado reciclado

Maurício Prado Martins[a]
Caroline Santana Rangel[b]
Mayara Amario[b]
José Mario Feitosa Lima[a]
Paulo Roberto Lopes Lima[a]
Romildo Dias Toledo Filho[b]

[a]Universidade Estadual de Feira de Santana – UEFS, Departamento de Tecnologia, Programa de Pós-graduação em Engenharia Civil e Ambiental, Feira de Santana, BA, Brasil
[b]Universidade Federal do Rio de Janeiro – UFRJ, Programa de Engenharia Civil, Instituto Alberto Luiz Coimbra de Pós-Graduação e Pesquisa de Engenharia, Rio de Janeiro, RJ, Brasil

Received 24 July 2019
Accepted 30 March 2020

Abstract: Concrete with recycled aggregate is a fragile material under tensile stresses. However, like conventional concrete, it is possible that its contribution is relevant in the design of reinforced concrete elements under tension or bending, even after cracking. The objective of this work is to evaluate the application of the analytical models used to predict the effect of tension stiffening on recycled reinforced concrete. Tests of reinforced concrete under tensile were performed using conventional concrete and concrete containing 25% and 50% replacement of the natural aggregate with recycled aggregate. From the experimental results of reinforced concrete, the contribution of the concrete was isolated and a parametric study was carried out to identify which analytical model in the literature may be more appropriate. The models proposed by Carreira and Chu (1986), Vecchio and Collins (1986) and Hsu and Mo (2010) were evaluated. A numerical analysis, based on the finite element method, was implemented to model the mechanical behavior of the reinforced concrete under tensile using the analytical models already adjusted to concrete with recycled aggregate. The stress distribution in steel and concrete and the cracking mode were evaluated numerically. The results indicate that the parameters used in the analytical models for conventional concrete cannot predict the behavior of concrete with recycled aggregate and need to be modified to obtain a more accurate answer.

Keywords: tension stiffening, damage, plasticity, finite elements.

Resumo: O concreto com agregado reciclado é um material frágil sob tensões de tração, no entanto, assim como o concreto convencional, é possível que, mesmo após sua fissuração, a sua contribuição seja relevante no dimensionamento de elementos de concreto armado sob tração ou flexão. O objetivo deste trabalho é avaliar a aplicação dos modelos analíticos usados na previsão do efeito do enrijecimento a tração (tension stiffening) ao concreto armado reciclado. Ensaios de tirantes de concreto armado foram realizados utilizando concreto convencional e concreto contendo 25% e 50% de substituição do agregado natural por agregado reciclado. A partir dos resultados experimentais, a contribuição do concreto foi isolada e um estudo paramétrico foi realizado para identificar qual modelo analítico existente na literatura pode ser mais apropriado. Foram avaliados os modelos propostos por Carreira e Chu (1986), Vecchio e Collins (1986) e Hsu e Mo (2010). Uma análise numérica baseada no método dos elementos finitos foi implementada para modelar o comportamento mecânico do tirante de concreto armado utilizando os modelos analíticos já ajustados ao concreto com agregado reciclado. A distribuição de tensões no aço e no concreto e o modo de fissuração foram avaliados numericamente. Os resultados indicam que os parâmetros utilizados nos modelos analíticos para concreto convencional não conseguem prever o comportamento do concreto com agregado reciclado e precisam ser modificados para se obter uma resposta mais precisa.

Palavras-chave: tirante de concreto armado, modelo de dano, plasticidade, método dos elementos finitos.

Corresponding author: Paulo Roberto Lopes Lima. E-mail: lima.prl@pq.cnpq.br
Financial support: CNPq (303931/2016-7)
Conflict of interest: Nothing to declare.

How to cite: M. P. Martins, C. S. Rangel, M. Amario, J. M. F. Lima, P. R. L. Lima, and R. D. Toledo Filho, "Modelling of tension stiffening effect in reinforced recycled concrete," *Rev. IBRACON Estrut. Mater*., vol. 13, no. 6, e13605, 2020, https://doi.org/10.1590/S1983-41952020000600005

1 INTRODUCTION

The great success obtained by reinforced concrete as a structural material is due to the excellent bond between the reinforcement and the concrete, which allows the redistribution of stresses between the materials after the cracking of the concrete. Due to this bond, the concrete, considered as a fragile material under tensile stress, can contribute to the increase of the strength and stiffness of the reinforced concrete even after the formation of cracks, in an effect called "tension stiffening". The tension stiffening effect has been defined as the contribution of intact concrete between cracks to the stiffness of the structural element or even by the ability of intact concrete between cracks to resist part of the resulting tensile forces. This contribution of cracked concrete has been identified as responsible for increasing the flexural strength [1], increasing the shear strength of reinforced concrete structures [2], increasing the stiffness of reinforced concrete slabs [3] and for the non-linear response of reinforced concrete under stress [4].

Due to the importance of this phenomenon, several studies have been carried out to determine theoretical models of the tension stiffening effect, as a way of incorporating it into the design standards for reinforced concrete structures. In this context, two different approaches have been used to determine the constitutive models: i) change in the constitutive equation associated with steel [1], [5], [6]; ii) or modification of the constitutive law of concrete, after the opening of the first crack [2], [7], [8]. Despite the good results obtained with the theoretical models for determining the tension stiffening effect, the parameters obtained for the design have been validated through experimental results of conventional reinforced concrete elements, which may limit its applicability to structures produced with recycled concrete aggregate.

The use of concrete with recycled aggregate in reinforced concrete structures is allowed by several design standards [9] and, as a result, some studies [10], [11] and practical applications [12] have reported the inherent gains in economic or sustainability terms of this material. However, the cracking mode of recycled concrete is different from conventional concrete, either under tensile [13] or compression [14] stresses, due to the lower strength and stiffness of the recycled aggregate, which may limit the use of some established and validated standard equations for conventional concrete.

The structural behavior evaluation of reinforced concrete beams with recycled aggregates, carried out by Etxeberria et al. [15], identified that the design standards overestimate the shear strength of reinforced concrete beams produced with recycled aggregate. According to Ignjatović et al. [16], the deflection in service of reinforced concrete beams containing recycled aggregate may be higher than the deflection of beams with conventional reinforced concrete. Xiao et al. [10] evaluated the bond between steel bars and recycled concrete and, after verifying the reduction in bond with the increase of the content of recycled aggregate in the concrete, established a new empirical law to determine the steel-recycled concrete bond. The drying shrinkage measures of concrete with recycled aggregate also indicate that the equations currently used by the structural design standards cannot predict the shrinkage behavior of recycled concrete [17]. Considering all these aspects and the important effect that drying shrinkage has on the tension stiffening effect of concrete [18], [19], it is believed that the use of normative models of the tension stiffening effect, calibrated for conventional concrete [20], are not valid for recycled reinforced concrete. Due to such particularities of recycled concrete, Kosior-Kazberuk and Grzywa [21] indicate that the special properties of concrete with recycled aggregate need to be considered in the design of reinforced concrete structures.

The objective of this work is to evaluate the tension stiffening effect of recycled concrete on the mechanical behavior of elements of reinforced concrete under tensile stress. For this, changes were made to the theoretical tension stiffening models proposed by Carreira and Chu [22], Vecchio and Collins [2] and Hsu and Mo [23] to fit the experimental results of concrete containing 0%, 25% and 50% of recycled aggregate. Subsequently, the elements were numerically modeled, using the finite element method, to evaluate the most appropriate theoretical model for the design of recycled concrete elements. The cracking pattern of the elements and the level of stress in the concrete and in the reinforcement were also numerically obtained and discussed.

2 ANALYTICAL MODELS OF THE TENSION STIFFENING EFFECT

The tension stiffening effect can be seen in Figure 1a, in which an element is subjected to tensile stress. The typical curve of this element subjected to tensile can be subdivided into 3 phases.

The first phase is represented by the elastic region, where the stresses and strains of the element follow the Hooke's Law, and there are no cracks in the concrete. The second phase is initiated by the primary cracking of the concrete and the appearance of new cracks, as the stresses in the concrete (between cracks already formed) reach the tensile strength of the concrete. Thus, phase 2 is marked by instability in the test due to gradual cracking. At the end of phase 2, all the cracks have already appeared and a reduction in the stiffness of the element is verified. At the crack opening site, the force is resisted almost exclusively by the steel bar, while in the region between cracks some tensile force is transferred (by bond) from the bar to the surrounding concrete, which results in a reduction of stresses and deformations in the reinforcement. At the beginning of cracking, the tension stiffening effect reaches its maximum value (see Figure 1b) and gradually decreases with the evolution of the deformation. In the third phase, there is a stable cracking, with the opening of existing cracks and loss of bond between steel and concrete. In this phase, the contribution of concrete between cracks is reduced to zero as the reinforcement steel tends to yielding phase.

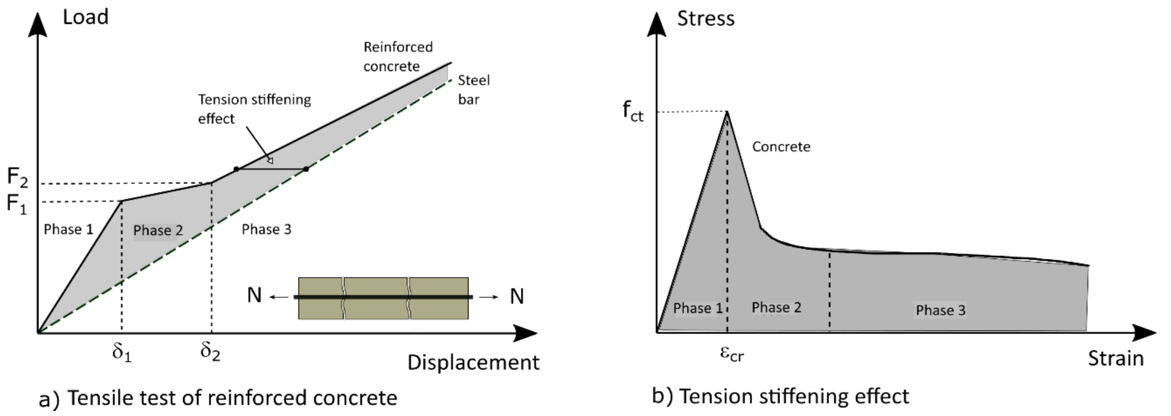

Figure 1. Stages of typical load-strain behavior of a tension stiffening element (a) and region where new cracks appear (b).

The prescription of the load-displacement behavior of reinforced concrete elements can be performed by standard specifications such as CEB [1]. To determine the tension stiffening effect, several models have been proposed over the years, being differentiated by the complexity and number of variables involved in the equations. In this study, the constitutive equations proposed by Carreira and Chu [22], Vecchio and Collins [2] and Hsu and Mo [23] were used, which were based on experimental studies and used in different applications.

2.1 Tension stiffening Model by CEB [1]

A classic model for evaluated the behavior of reinforced concrete elements is presented by CEB [1], as illustrated in Figure 2.

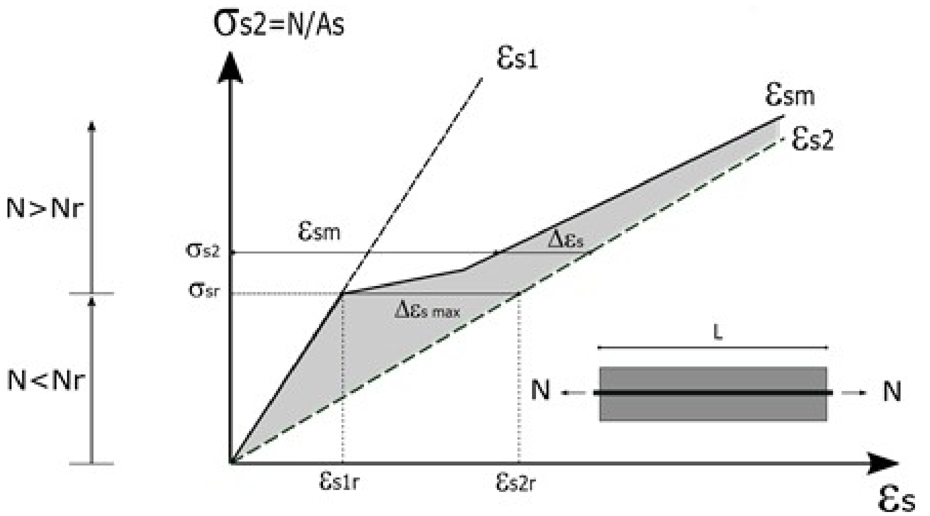

Figure 2. Relative strain of the reinforcement in the tension stiffening element.

In this model, the objective is to determine the average relative deformation of the reinforcement ε_{sm} of an element of length L subjected to an axial load N. Until reaching the total elongation ΔL, the element goes through an elastic phase (Phase 1 in Figure 1a) until reaching the crack load N_r. For values greater than N_r, the average strain of the reinforcement is given by:

$$\varepsilon_{sm} = \frac{\Delta L}{L} = \varepsilon_{s2} - \Delta\varepsilon_s \tag{1}$$

Where $\Delta\varepsilon_s$ represents the contribution of the concrete between cracks (tension stiffening effect), which was established experimentally as:

$$\Delta\varepsilon_s = \Delta\varepsilon_{smax}\left(\sigma_{sr} / \sigma_{s2}\right) = \left(\varepsilon_{s2r} - \varepsilon_{s1r}\right)\left(\sigma_{sr} / \sigma_{s2}\right) \tag{2}$$

By substituting Equation 2 in Equation 1, it is obtained:

$$\varepsilon_{sm} = \varepsilon_{s2}\left[1 - \left(\sigma_{sr} / \sigma_{s2}\right)^2\right] + \varepsilon_{s2}\left(\sigma_{sr} / \sigma_{s2}\right)^2 \tag{3}$$

That can be written in the form:

$$\varepsilon_{sm} = \left[1 - \zeta\right]\varepsilon_{s1} + \zeta\varepsilon_{s2} \tag{4}$$

Where ζ is a distribution coefficient given by:

$$\zeta = \begin{cases} 1 - \left(\sigma_{sr} / \sigma_{s2}\right)^2, & para\, \sigma_{s2} \geq \sigma_{sr} \\ 0, & para\, \sigma_{s2} < \sigma_{sr} \end{cases} \tag{5}$$

In the Equation 1 to Equation 5, σ_{s2} is the stress of the reinforcement in a cracked section; σ_{sr} is stress in the reinforcement at the moment of cracking, that is, when the stress in the concrete reaches the tensile strength; ε_{s1} is the deformation in the reinforcement in Phase 1; ε_{s2} is the deformation in the reinforcement after cracking the concrete, not considering the contribution of the concrete between cracks; ε_{s1r} is the strain in the reinforcement corresponding to the stress σ_{sr}, in Phase 1; ε_{s2r} is the strain in the reinforcement corresponding to the stress σ_{sr}, not considering the contribution of concrete between cracks.

To consider the quality of the bond of the reinforcement bars and the influence of the duration and repetition of the load application, the CEB Model Code 1990 [24] introduced, respectively, the coefficient β_1 and the coefficient β_2 in Equation 5:

$$\zeta = \begin{cases} 1 - \beta_1 \cdot \beta_2 \cdot \left(\sigma_{sr} / \sigma_{s2}\right)^2, & para\, \sigma_{s2} \geq \sigma_{sr} \\ 0, & para\, \sigma_{s2} < \sigma_{sr} \end{cases} \tag{6}$$

Where $\beta_1 = \frac{1}{2,5\kappa 1}$, with $\kappa_1 = 0.4$ for ribbed bars and $\kappa_1 = 0.8$ for smooth bars, and $\beta_2 = 1.0$ for load applied for a short time and $\beta_2 = 0.5$ for load applied for a long time or for a large number of load cycles.

2.2 Model by Carreira and Chu [22]

The equation proposed by Carreira and Chu [22] was adapted from a model for the behavior of concrete under compression and it is given by:

$$\sigma_t = \frac{\beta_t \cdot f_{ct}\left(\dfrac{\varepsilon_{ct}}{\varepsilon_{cr}}\right)}{\beta_t - 1 + \left(\dfrac{\varepsilon_{ct}}{\varepsilon_{cr}}\right)^{\beta_t}} \tag{7}$$

where σ_t and ε_{ct} correspond, respectively, to the normal tensile stress and the specific linear strain in the stress-strain diagram; ε_{cr} is the deformation corresponding to the maximum tensile stress. The parameter β_t combines the effect of cracking and the loss of bond between the reinforcement and the concrete and it must be obtained from experimental tests.

Equation 7 was used by the authors [22] to determine the tension stiffening effect in concrete elements reinforced with different ratios of reinforcement, and values for β_t ranging between 1.45 and 1.70 were adopted.

2.3 Model by Hsu and Mo [23]

The model presented by Hsu and Mo [23] was obtained based on experiments carried out on reinforced concrete panels submitted to uniaxial tensile stress. The equation that correlates the tensile stress in the concrete σ_t with the axial strain ε_{ct} is given by:

$$\sigma_t = f_{ct}\left(\frac{\varepsilon_{cr}}{\varepsilon_{ct}}\right)^{\mu} \tag{8}$$

Where the exponent μ is an adjustment parameter, initially adopted as equal to 0.4 by the authors [21]; f_{ct} is the tensile strength of concrete and ε_{cr} is the deformation corresponding to this stress, being adopted by Hsu and Mo [23] as $\varepsilon_{cr} = 0.00008$, based on the experimental results for conventional concrete.

Equation 8 was used by Wang and Hsu [25] and by Dede and Ayvaz [26], obtaining good results.

2.4 Model by Vecchio and Collins [2]

The model proposed by Vecchio and Collins [2] was based on the experiments carried out on reinforced concrete panels subjected to pure shear stress and it is given by:

$$\sigma_t = \frac{f_{ct}}{1 + \sqrt{\eta \varepsilon_1}} \tag{9}$$

Where η is an experimental parameter, adopted equal to 200 for conventional concrete, and ε_1 is the tensile strain of the concrete in direction 1 (axial).

Equation 9 is present in the Modified Compression-Field Theory (MCFT) [2], in which the authors reported the importance of considering the tension stiffening effect in the analysis of structures subjected to shearing force predominantly to flexion.

3 EXPERIMENTAL PROGRAM

3.1 Materials

The coarse recycled aggregate used in this study, with a maximum diameter of 9.5 mm, was obtained by demolishing concrete beams produced in laboratory for this purpose. The coarse natural aggregate was granite gravel with a maximum diameter of 9.5 mm. The water absorption test indicated that the natural aggregate has a total absorption of 1.2% while the recycled aggregate has a total absorption of 8.0%. Quartz sand with a maximum diameter of 4.75 mm, CPV-ARI cement and polycarboxylate-based superplasticizer with a solids content of 30% were used.

The concretes were composed according to the Compressible Packing Model (CPM), described in Rangel [27], to achieve a compressive strength of 25 MPa and an slump value of 75 mm. Three types of concrete were produced, R0, R25 and R50, with the replacement of 0%, 25% and 50% of natural aggregate by recycled aggregate, respectively. Table 1 shows the consumption of materials for the production of the concrete mixtures, as well as the results of mechanical tests at 28 days after curing in a humid chamber. The superplasticizer content was about 3 kg/m^3 for all mixtures. The concretes were produced in an air-conditioned room at 21ºC ± 1ºC, using a planetary mixer.

Table 1. Composition and properties of the concrete mixtures.

Mixture	Composition (kg/m^3)				Mechanical properties		
	Cement	Coarse aggregate	Fine aggregate	Water	f_c (MPa)	E (GPa)	F_{td} (MPa)
R0	304	922.9	841.1	205.7	27.5(±4.2%)	20.8(±7.4%)	2.98(±7.7%)
R25	301.4	695.0	844.5	211.0	26.9(±4.0%)	21.9(±3.9%)	2.88(±7.9%)
R50	293.8	467.6	852.3	213.4	26.5(±4.8%)	21.8(±5.5%)	3.02(±5.6%)

In the tension stiffening elements, CA 50 steel bars with 20 mm of diameter were used, which were subjected to tensile test and the bars presented a yield stress of 540 MPa, a rupture stress of 705 MPa and an elastic modulus of 232.9 GPa. This diameter bar was adopted so that a larger post-cracking region could be investigated before the bar begins the yielding phase.

3.2 Tension stiffening test

Metallic molds with dimensions of 15 x 15 x 80 cm were used to produce the tension stiffening elements. The steel bar was positioned in the center of the cross section of the mold before casting the concrete, as shown in Figure 3.

The tests were performed in a servo-controlled press with a capacity of 1000 kN, in three samples for each concrete mixture. The loading of the test was applied continuously, with a constant speed of 0.3 mm/min. Two electric transducers (LVDT) were used to measure longitudinal displacements in the central region of the specimens (0.7 m).

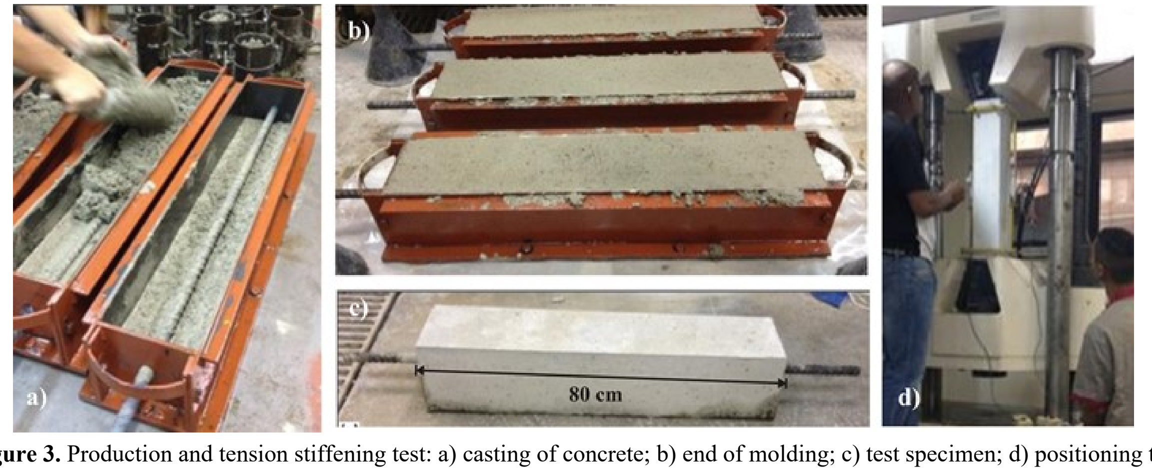

Figure 3. Production and tension stiffening test: a) casting of concrete; b) end of molding; c) test specimen; d) positioning the testing machine.

4 CALIBRATION OF ANALYTICAL MODELS

From the experimental result of the tension stiffening test, the contribution of the matrix to the overall load-strain behavior of the element was isolated. For this, it was evaluated the difference between the result obtained for the element and the individually contribution of the steel bar.

The analytical models of tension stiffening represented by Equation 7 to Equation 9 were calibrated in comparison with the experimental result, from the variation of the values of the parameters β_t , μ and η , respectively. To determine the parameter that best fits the theoretical model to the experimental curve, the regions under the curves were then compared up to a deformation of 3.5/1000 and the errors were calculated. The error rate was established as the relation between the area under the obtained curve with the theoretical model, divided by the area under the curve obtained from the experimental test.

The analytical stress-strain ratio that corresponded to the smallest error was then used in the numerical modeling of the reinforced concrete element.

5 NUMERICAL MODELING OF THE TENSION STIFFENING ELEMENT

The computational numerical modeling of the reinforced concrete element was performed using the finite element method with application of the plasticity model to the concrete. The ABAQUS software was used.

5.1 Discretization of the tension stiffening element

A three-dimensional mesh was modeled in finite elements using the solid element C3D8R, with eight nodes, with three degrees of freedom per node (displacements in the X, Y and Z directions) and reduced integration. The C3D8R element has 6 faces and four integration points per face, as shown in Figure 4. In the tension stiffening element mesh, 44400 thousand elements were used, with 47315 nodes, as shown in Figure 5.

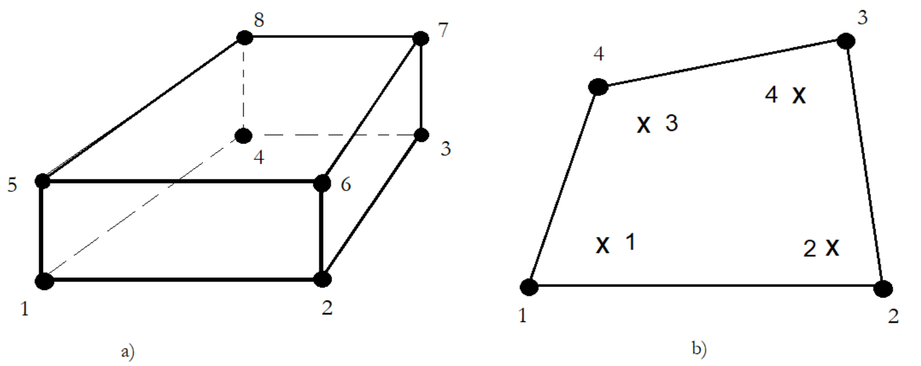

Figure 4. Finite element C3D8R used in the mesh: a) numbering of nodes; b) integration points.

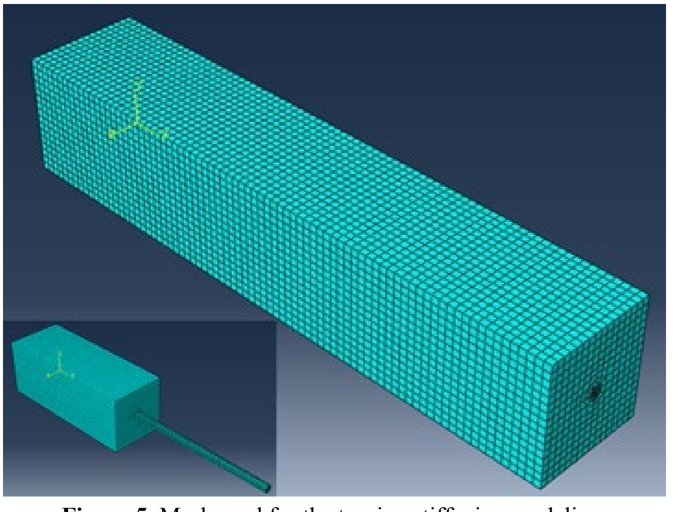

Figure 5. Mesh used for the tension stiffening modeling.

The computer simulation was performed by applying axial displacements, according to the experimental test performed, shown in Figure 6a. Despite the finite element mesh having 80 cm in length, it were monitored the difference between the axial displacements, referring to the U_1 direction, of points A and B spaced 70 cm apart and located 5 cm from the upper and lower faces, respectively, as shows Figure 6b. These points correspond to the places where the LVDTs were fixed for measuring the axial displacement during the experimental test.

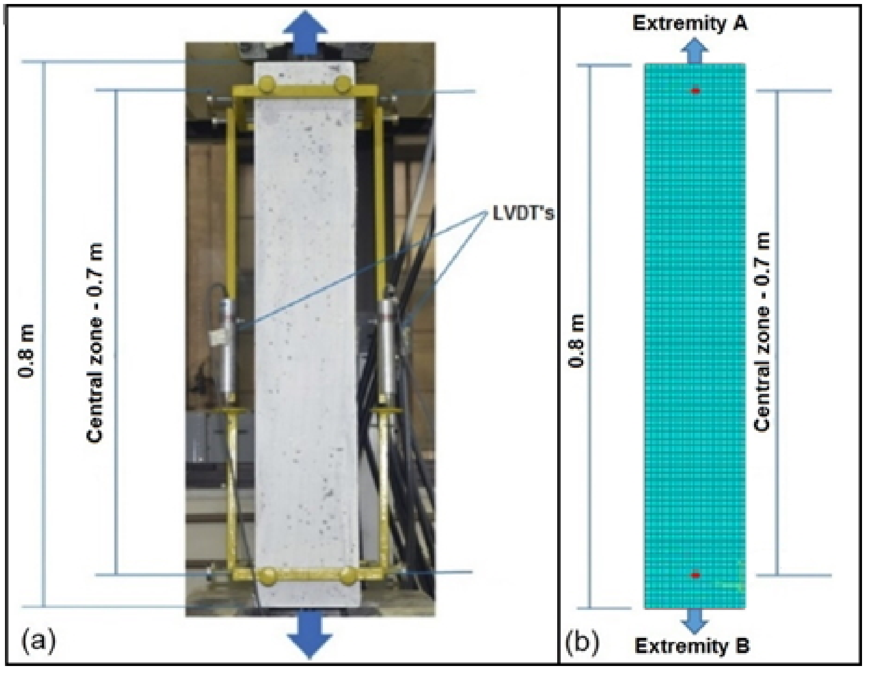

Figure 6. Representation of the reinforced concrete tension stiffening test: a) experimental configuration; b) numerical representation.

The numerical analysis was implemented by gradually applying a displacement at point A of 0.0096 m in the U_1 direction, with $U_2 = U_3 = 0$. In point B, displacement restrictions were applied in the three directions, $U_1 = U_2 = U_3 = 0$. Thus, the values referring to axial deformations were obtained through the application of Equation 10:

$$\varepsilon = \frac{U_{1\ ponto\ A}}{L_{inicial}} \tag{10}$$

where $U_{1\ ponto\ A}$ is the displacement in the U_1 direction of point A and $L_{inicial}$ is the initial distance of 0.70 m, between point A and point B.

The modeling was performed considering a static problem. Thus, it was decided to use the Static General tool, available at ABAQUS, which uses the direct method for solving systems of equations using the Full Newton solution technique or pure Newton. The automatic increment was chosen, in which the user determines the initial, maximum and minimum increment size. An initial increment of 1E-007 m was used. Concrete and steel were modeled separately and, for concrete-steel interaction, perfect bond was considered, so that the tension stiffening effect on the response was isolated.

5.2 Plasticity Model

To model the tension of the elements, the Concrete Damaged Plasticity (CDP) model was used, in which the nonlinear behavior of the concrete is based on the concept of isotropic elastic damage, which aims to represent the stiffness degradation associated with the irreversible damage that it occurs during the fracture process, in combination with isotropic plasticity, to describe the damage mechanisms, called "softening" in tensile and "crushing" in compression. In this context, local damage models assume that nonlinear behavior is different in relation to tensile and compression [28], [29].

On the contrary of the concrete models based on smeared crack, the CDP does not present a tool that can capture the development of the crack at the point of integration of the material. However, it is possible to introduce the concept of an effective crack direction in order to obtain a graphic visualization of crack patterns in the concrete structure. It is assumed that the cracking starts at points where the plastic strain, ε^{pl}, equivalent to tensile is greater than zero and the maximum main plastic strain is positive. The direction of the vector normal to the crack plane is assumed to be parallel to the direction of the maximum main plastic stress [30].

To use the CDP model, it is necessary to define some parameters of plasticity, described in Table 2, which, in this study, were chosen based on the values used by several researchers, such as Jankowiak and Lodygowski [33], Birtel and Mark [34] and Ors et al. [35]. Regarding the dilatation angle, ψ, it is usually used between 30° and 40° to describe the behavior of the concrete [36], [37].

Table 2. Plasticity parameters of the CDP model.

Parameters	Values	Denotation
ψ	30°	Dilatation angle (Lee and Fenves [31])
ϵ	0.1	Potential flow function parameter
$\frac{f_{b0}}{f_{c0}}$	1.16	Relation between biaxial compressive strength and uniaxial compressive strength (Kupfer et al. [32])
k_c	0.667	Rate of the second stress invariant
Viscosity	0	Viscosity

5.2.1 Constitutive laws

As the CDP model allows to insert a table with the behavior of the concrete related to the tensile, the analytical models of tension stiffening were introduced after being calibrated with the experimental results.

For the behavior under compression, the model proposed by Hognestad [38] and Kent and Park [39], represented by Equation 11, was used, applying the peak stress and the peak strain values obtained from experimental tests.

$$\sigma_c = \sigma_{cu}\left[\frac{2\varepsilon_c}{\varepsilon_0} - \left(\frac{\varepsilon_c}{\varepsilon_0}\right)^2\right] \tag{11}$$

where σ_{cu} is peak stress in compression, adopted as the compressive strength value experimentally obtained, and ε_0 of the strain related to peak stress.

For the steel of the reinforcement bar, a perfect elastoplastic model was adopted, considering the experimental results.

6 RESULTS AND DISCUSSION

6.1 Experimental results

The experimental load-strain curves of the tests of reinforced concrete elements for mixtures R0, R25 and R50 are shown in Figure 7. The experimental curve of the direct tensile test of the isolated steel bar is also presented.

It appears that all tension stiffening elements, with conventional concrete or recycled concrete, exhibit a behavior similar to that predicted in Figure 1, with a linear phase followed by a baseline of constant force in which multiple cracking occurs. After this phase, the elements showed an increase in loading, with a stiffness lower than that initially verified, and close to the stiffness presented by the isolated steel bar. It appears that after cracking, the force in the element is greater than the force in the isolated bar, demonstrating the contribution of concrete between cracks to the mechanical behavior of the reinforced concrete element.

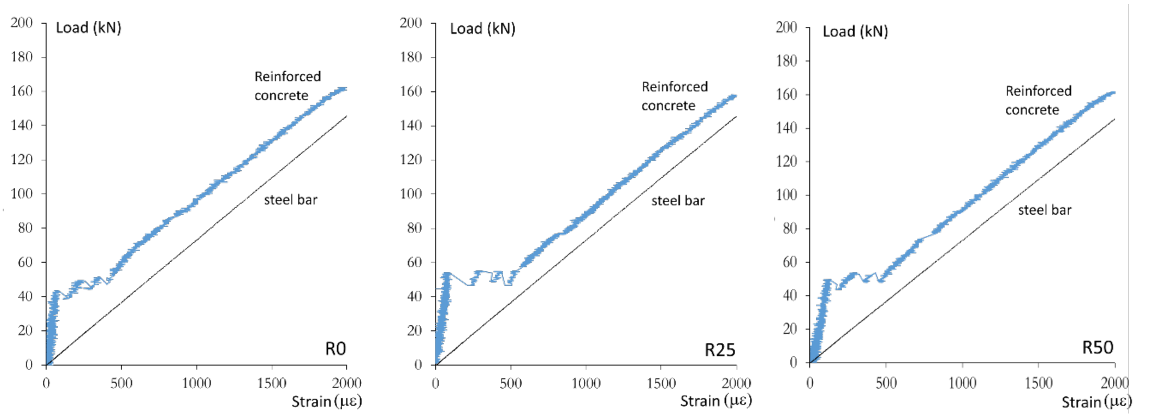

Figure 7. Experimental results for tension stiffening elements without recycled aggregate (R0) and with substitution of 25% (R25) and 50% (R50) of natural aggregate for recycled aggregate.

The average results of the properties of the concrete elements under tensile test, before and after the cracking phase, are presented in Table 3. It is verified that the presence of the recycled aggregate affected the behavior of the tension stiffening element, with an increase of up to 15% in the cracking stress (F_1) and 19.4% increase in deformations ($\Delta\varepsilon$) during the multiple cracking process (phase 2, Figure 1). The stiffness of the element, before and after cracking, was less influenced by the recycled aggregate since the steel stiffness affects these properties more strongly.

Table 3. Experimental results of tension stiffening tests.

Element	F_1(kN)	ε_1(με)	ε_2(με)	Δε	E_1(GPa)	E_2(GPa)
R0	44.4 (±6.6%)	92.8 (±1.4%)	384.7 (±9.2%)	291.9	23.0 (±6.3%)	3.03 (±2.5%)
R25	49.3 (±6.8%)	96.0 (±4.6%)	442.4 (±7.5%)	346.4	22.9 (±7.5%)	3.04 (±6.5%)
R50	51.1 (±3.4%)	103.3 (±6.4%)	451.8 (±8.6%)	348.5	22.0 (±2.9%)	3.13 (±1.6%)

From the difference between the load value on the element and the load value on the steel bar, the contribution of the concrete matrix to the behavior of the element (tension stiffening effect) was obtained, as shown in Figure 8 to Figure 10. Assessing the stress-strain behavior of concrete elements, it appears that, after the appearance of the first crack, when the stress reaches the tensile strength shown in Table 4, there is a sudden reduction in the resistant strength of the material (softening), followed by the maintenance of this strength until deformations of the order of 3.5/1000. The substitution of the natural aggregate for recycled aggregate contributed to an increase in the peak stress in tensile, in the strain corresponding to the peak stress and in the elastic modulus of about 15%, 33% and 10%, respectively.

Table 4. Concrete properties obtained in the tension stiffening test.

Concrete	f_{ct} (MPa)	ε_{cr}	E (MPa)
R0	1.97	7.5E-05	20700
R25	2.19	1.0E-04	21900
R50	2.27	1.0E-04	22700

6.2 Parametric study of analytical models to determine the tension stiffening effect

To calibrate the analytical models, a parametric study was carried out in which several values of the parameters β_t , μ and η were tested in the models proposed by Carreira and Chu [22], Hsu and Mo [23] and Vecchio and Collins [2], respectively, and compared with the experimental results. The results are shown in Figure 8 to Figure 10 for conventional concrete, concrete with 25% recycled aggregate and concrete with 50% recycled aggregate, respectively. The values obtained for the parameters and the prediction errors of each model, when compared with the experimental results, are shown in Table 5.

The model by Vecchio and Collins [2] was initially tested with a value of η equal to 200, as proposed by the authors, however the theoretical values of stresses, after the peak, were much higher than the values obtained in the experimental result. Values varying between 1500 and 3000 were then tested. For conventional concrete, investigated in this study, a value of η equal to 1500 was the one that best adjusted the theoretical curve to the experimental result, with an error of less than 1%. For concrete with recycled aggregate, values of η equal to 1800 and 2700 were obtained, with errors of about 1%.

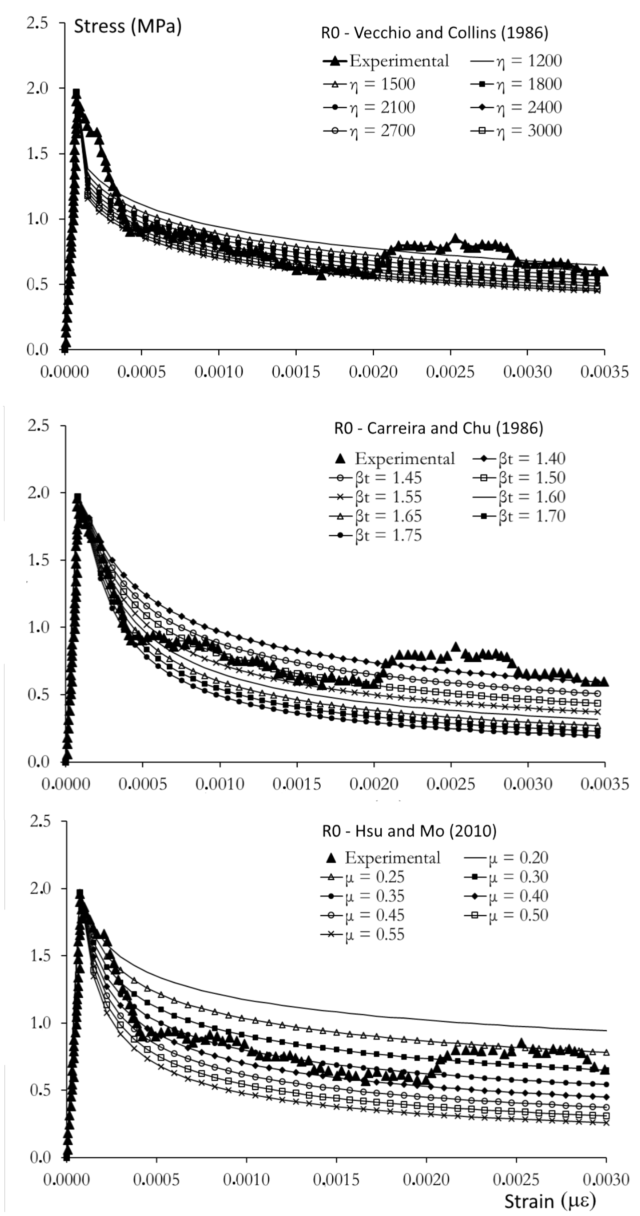

Figure 8. Parametric study of analytical models for the R0 tension stiffening element.

Although the model by Vecchio and Collins [2] does not fit well with the modeling of the tension stiffening behavior, especially in the second phase of the curve, immediately after the peak, it appears that the parameter used for conventional concrete does not fit in the modeling of the concrete with recycled aggregate. This fact was also identified in the other models used.

Compared with the model used previously, it appears that the Carreira and Chu model [22] has greater versatility with respect to the ability to model the stress-strain curves, as well as the model presented by Hsu and Mo [23], as can be seen in Figures 8, Figure 9 and Figure 10. For small variations in the experimental adjustment parameters βt and μ, presented in Equation 7 and Equation 8, respectively, a significant variation in the tension stiffening behavior was verified. The parameter βt ranged from 1.45 to 1.70, while the parameter μ ranged from 0.25 to 0.50.

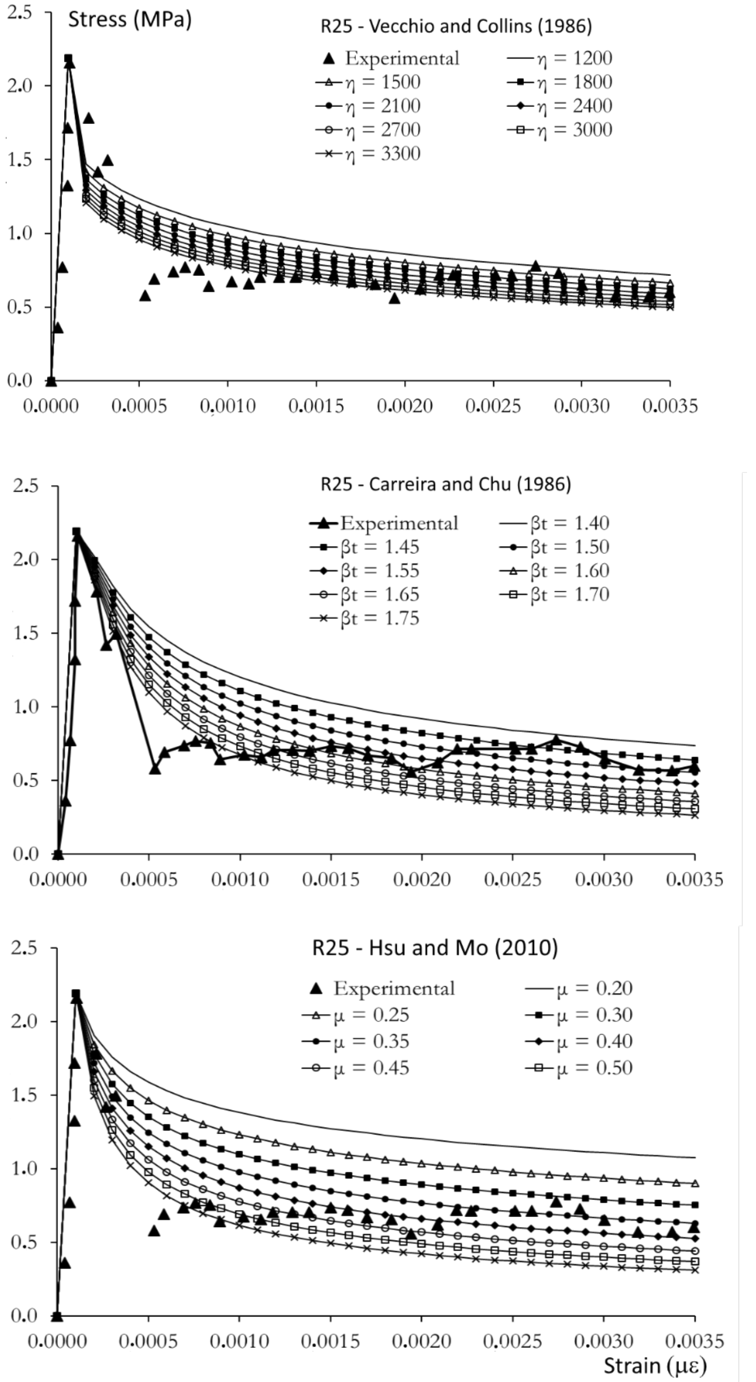

Figure 9. Parametric study of analytical models for the R25 tension stiffening element.

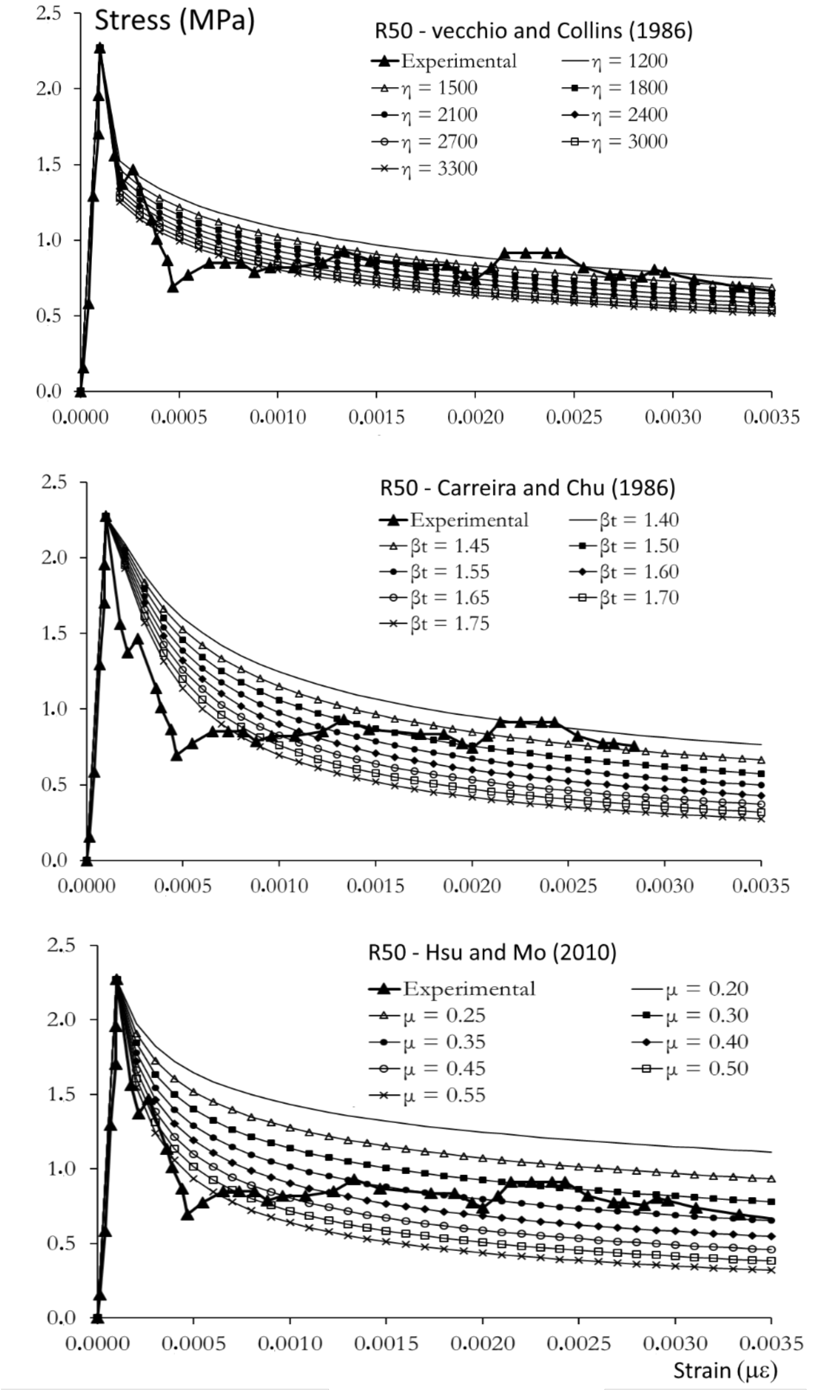

Figure 10. Parametric study of analytical models for the R50 tension stiffening element.

Table 5 indicates the values of adjustment parameters that best suit the experimental results, considering each model and each type of concrete. The comparison between these parameters indicates that the analytical models obtained to predict the behavior of conventional concrete do not apply to recycled concrete, even when using the 25% substitution content, whose effect on mechanical strength is not so relevant. This proves the initial hypothesis established in this study that, the mathematical relations already established in the design standards for conventional concrete structures can be used to predict the structural behavior of recycled reinforced concrete, there must be an adjustment in the parameters used or a modification of the models.

Table 5. Parameter values obtained for tension stiffening models.

Mix	Theoretical model	Parameter		Theoretical area (MPa.mm/mm)	Experimental area (MPa.mm/mm)	Relative error rate (%)
		Symbol	Value			
R0	Carreira and Chu (1986)	βt	1.45	0.00281	0.00283	-0.71
	Hsu and Mo (2010)	μ	0.30	0.00294	0.00283	3.89
	Vecchio and Collins (1986)	η	1500	0.00286	0.00283	1.06
R25	Carreira and Chu (1986)	βt	1.60	0.00273	0.00268	1.87
	Hsu and Mo (2010)	μ	0.40	0.00277	0.00268	3.36
	Vecchio and Collins (1986)	η	2700	0.00265	0.00268	-1.12
R50	Carreira and Chu (1986)	βt	1.55	0.00307	0.00306	0.26
	Hsu and Mo (2010)	μ	0.35	0.00322	0.00306	5.23
	Vecchio and Collins (1986)	η	1800	0.00310	0.00306	1.31

6.3 Modeling of the reinforced concrete elements

Figure 8, Figure 9 and Figure 10 show the experimental results of the tension stiffening test compared to the numerical models. In the numerical models, the stress-strain diagrams used for concrete under tensile were obtained from appropriate tension stiffening models, using the parameters presented in Table 5. For the purpose of comparison with design standards, the analytical model presented by CEB [1] is also shown in Figure 11, Figure 12 and Figure 13. It appears that the numerical model was able to predict the overall behavior of the tension stiffening element with an acceptable approximation. To prediction the load and the strain of the first crack of the element, shown in Table 6, the greatest differences between the numerical value and the experimental value, of the order of 19% for the force F_I and 39% for the strain ε_I, were verified when the Vecchio and Collins [2] model was used to determine the tension stiffening effect. The Hsu and Mo [23] model was the one that best fitted to conventional concrete, with an error of 3.1% in the predicted F_I, and the Carreira and Chu model [22] resulted in a maximum error of 6.85% in predicted F_I for recycled concrete.

Table 6. Tension stiffening test properties at the cracking start.

Models	R0		R25		R50	
	$F_I(kN)$	$\varepsilon_I(\mu\varepsilon)$	$F_I(kN)$	$\varepsilon_I(\mu\varepsilon)$	$F_I(kN)$	$\varepsilon_I(\mu\varepsilon)$
Experimental	44.4	92.8	49.3	96.0	51.1	103.3
Carreira and Chu (1986)	46.1	72.7	47.6	73.2	47.6	74.5
Hsu and Mo (2010)	45.8	72.1	47.3	71.6	46.8	72.5
Vecchio and Collins (1986)	35.8	56.6	45.2	67.3	45.8	70.3

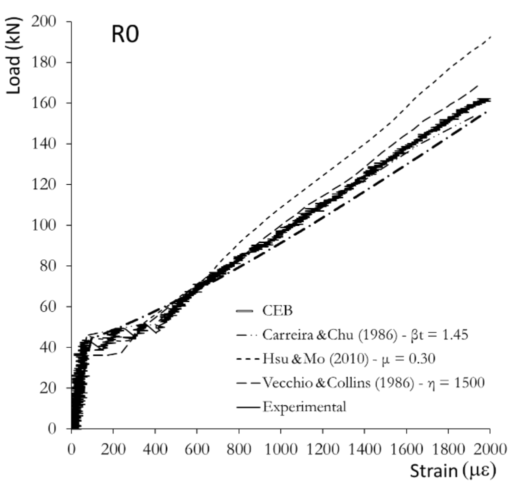

Figure 11. Comparison between numerical models, analytical model and experimental result for the tension stiffening element with conventional concrete R0.

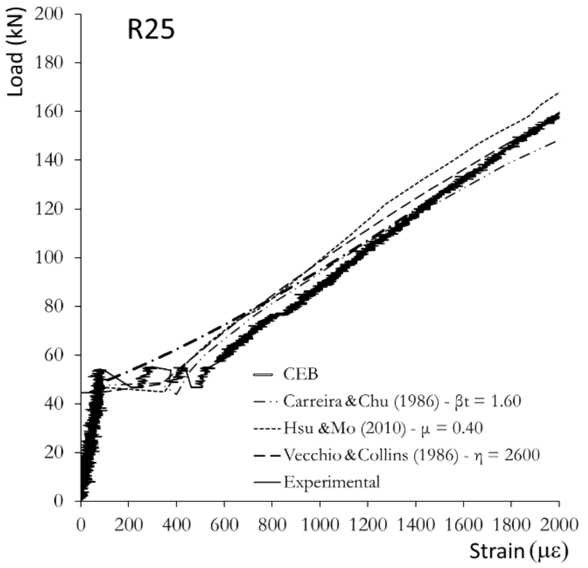

Figure 12. Comparison between numerical models, analytical model and experimental result for the tension stiffening element with recycled concrete R25.

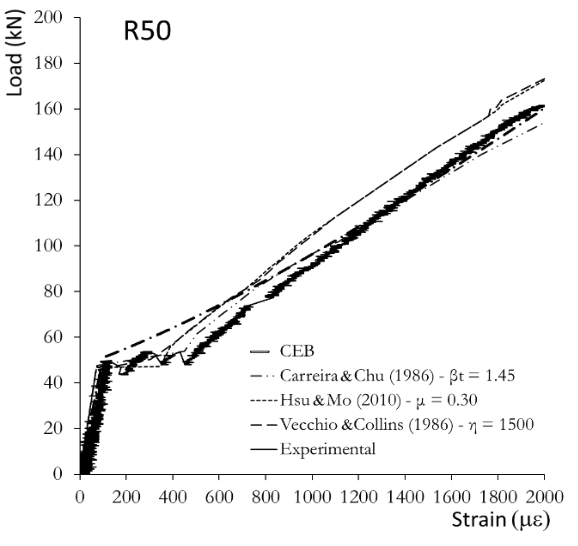

Figure 13. Comparison between numerical models, analytical model and experimental result for the tension stiffening element with recycled concrete R50.

To evaluate the numerical modeling in the prediction of the post-cracking behavior of the tension stiffening element, the areas under the load-strain curves (numerical, analytical and experimental), up to the 2000 με deformation, were calculated and the error was calculated by the relation between these areas. The results are shown in Table 7.

The maximum error obtained by the numerical models was about 14% when the Hsu and Mo model [23] was used in the analytical modeling of the tension stiffening of conventional concrete. In fact, evaluating Figure 9, it is observed that, after the multiple cracking phase, the ascending phase of this numerical curve is more rigid than the other models and then the experimental result. For this phase, the numerical model with the Vecchio and Collins [2] curve presents the best approximation for conventional concrete, with an error of 0.77%, while the model with the Carreira and Chu [22] curves more adequately model the element with recycled concrete, with a maximum error of 0.82%.

Regarding the analytical model proposed by CEB [1], it appears that the main difference concerns the load-strain behavior in Phase 2 (see Figure 1). While the numerical models and the experimental result indicate a baseline on the curve, with constant load during the multiple cracking process, the CEB model shows an increase in load during this phase. However, the maximum prediction error using the normative prescription was 5.24%, which shows a potential for predicting the behavior of tension stiffening elements with conventional or recycled concrete.

Table 7. Comparison between numerical, analytical and experimental results of reinforced concrete tension stiffening elements.

Element	Theoretical model	Parameter		Simulation area (kN·με)	Experimental area (kN·με)	Error (%)
		Symbol	Value			
R0	Carreira and Chu (1986)	βt	1.45	190861	188567	1.21
	Hsu and Mo (2010)	μ	0.30	215484		14.27
	Vecchio and Collins (1986)	η	1500	190033		0.77
	CEB	-	-	186224		-1,24
R25	Carreira and Chu (1986)	βt	1.60	183680	183574	0.05
	Hsu and Mo (2010)	μ	0.40	198222		7.92
	Vecchio and Collins (1986)	η	2700	188121		2.47
	CEB	-	-	193206		5,24
R50	Carreira and Chu (1986)	βt	1.55	189327	187780	0.82
	Hsu and Mo (2010)	μ	0.35	205180		9.26
	Vecchio and Collins (1986)	η	1800	205678		9.53
	CEB	-	-	195334		4,02

6.3.1 Monitoring the distribution of stresses and strains in the tension stiffening element

According to the theory of tension stiffening element cracking [1], after the appearance of the first crack, there is a variation on the distribution of stresses inside the element and, at the crack region, there is a reduction in the concrete stress (which can go to zero) and an increase in tension in the reinforcement. Using the numerical model, it was possible to monitor the development of element cracking and map the level of stresses and strains in concrete and steel.

The experimental results of the tension stiffening test indicate the appearance of three or four main cracks spaced along its length, as shown in Figure 14. The numerical models managed to capture this behavior indicating the appearance of three cracks in all analyzed elements, as shows Figure 15. Despite the appearance of the first crack being in a random region, changing according to the type of concrete, it appears that the final spacing between cracks remained equal to 20 cm. The experimental results indicate an average spacing of 11.3 cm, since in some specimens a greater number of cracks appeared.

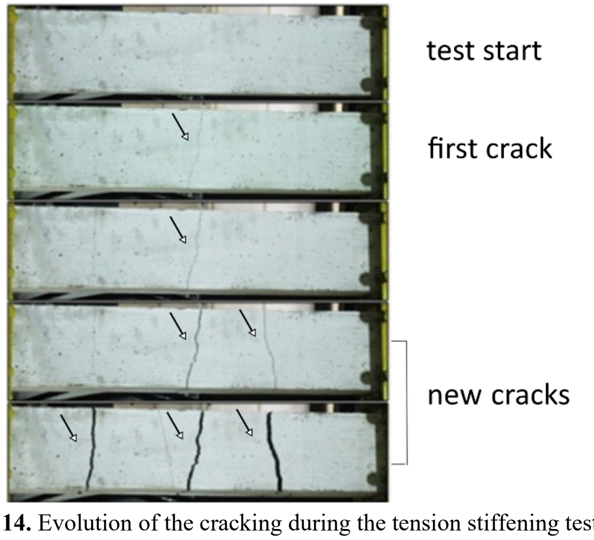

Figure 14. Evolution of the cracking during the tension stiffening test of R0.

The variation of stresses in the steel bar and in the concrete were monitored along the length of the element during the multiple cracking phase and it is shown in Figure 15. The tension was obtained in a node located inside the concrete, halfway between the face of the element and the reinforcement bar, that is, at a distance of 37.5 mm from the external face.

With the appearance of the first crack (Figure 15a), at the crack region, there is a reduction in the stress in the concrete and an increase in the steel stress, since there is a transfer of stresses between the two components. A similar fact is observed when there is the appearance of the second (Figure 15b) and third (Figure 15c) cracks. It is possible to observe, however, that the stresses in the concrete between cracks remain high, indicating the occurrence of the tension stiffening effect, with the contribution of the concrete between cracks to the total strength.

Throughout the cracking process, it appears that, with the appearance of a new crack, there is a redistribution of stresses, and at the point where the crack appears, the steel bar becomes more tensioned and the concrete has a reduction in the capacity to transmit efforts. However, different from what is proposed in the classic tension stiffening cracking model [1], which proposes that in the crack region the stresses in the concrete go to zero, it is realized in the computational model that the concrete, even in the cracked region, can transmit a small portion of efforts. This phenomenon, called interlocking, is predicted by Prado and Van Mier [40] for conventional concrete, and corresponds to the friction that the crack faces impose on the relative displacement and which is influenced by the type of aggregate.

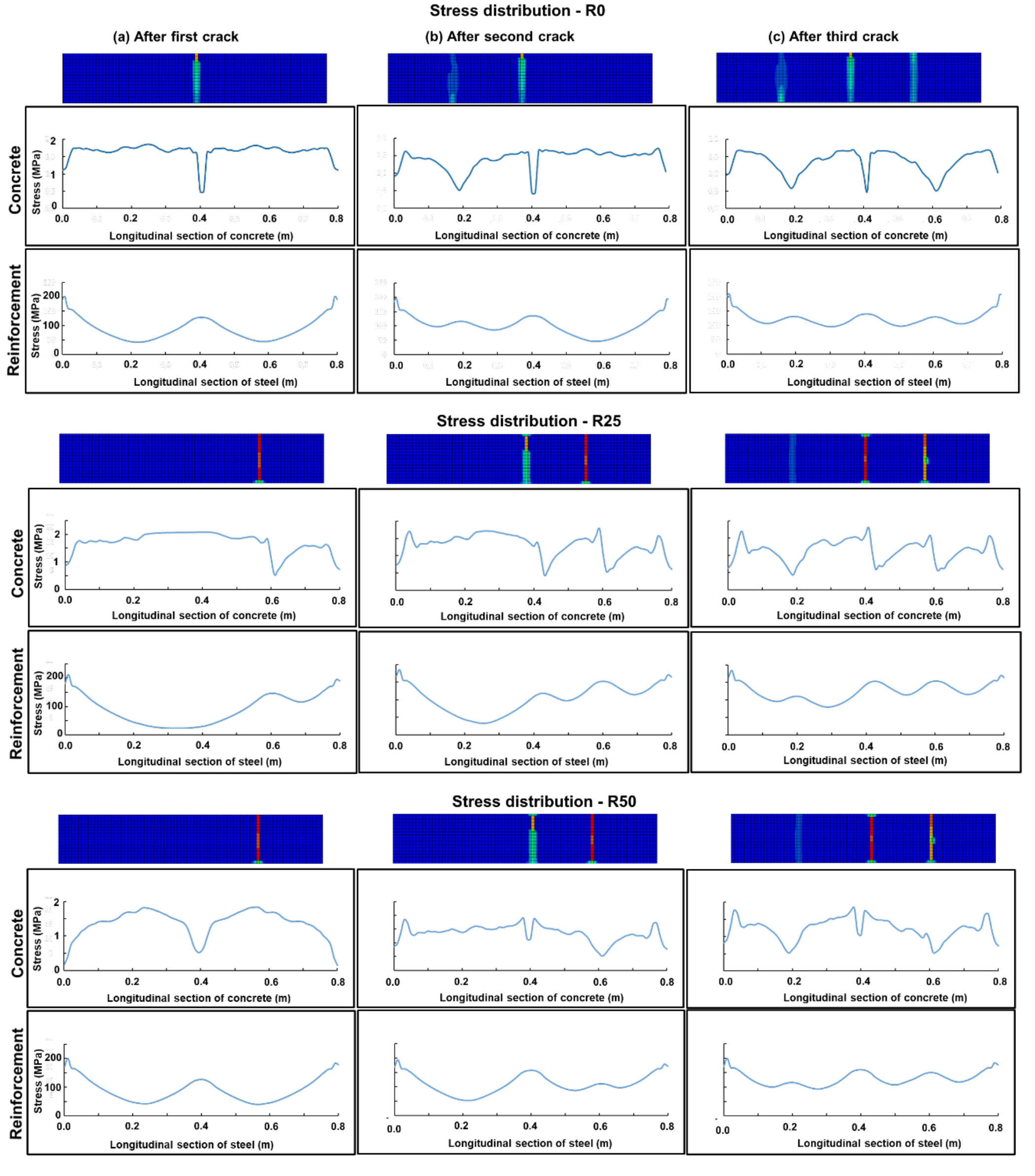

Figure 15. Stress distribution in concrete and in reinforcement along the elements after: a) first crack; b) second crack and c) third crack.

In addition to the variation in stresses along the length of the element, it is expected that the stresses in the concrete will vary along the cross section, since the transfer of stresses, after cracking, is made from the steel bar to the concrete. Using numerical simulation, it was possible to monitor the development of stresses at two points in the concrete cross section, as shown in Figure 16: close to the surface and inside the concrete. Evaluating the non-cracked concrete, it appears that the stresses measured inside the concrete (Point P2) are practically constant while the stresses measured on the surface (Point P1) have a parabolic shape along the length of the element.

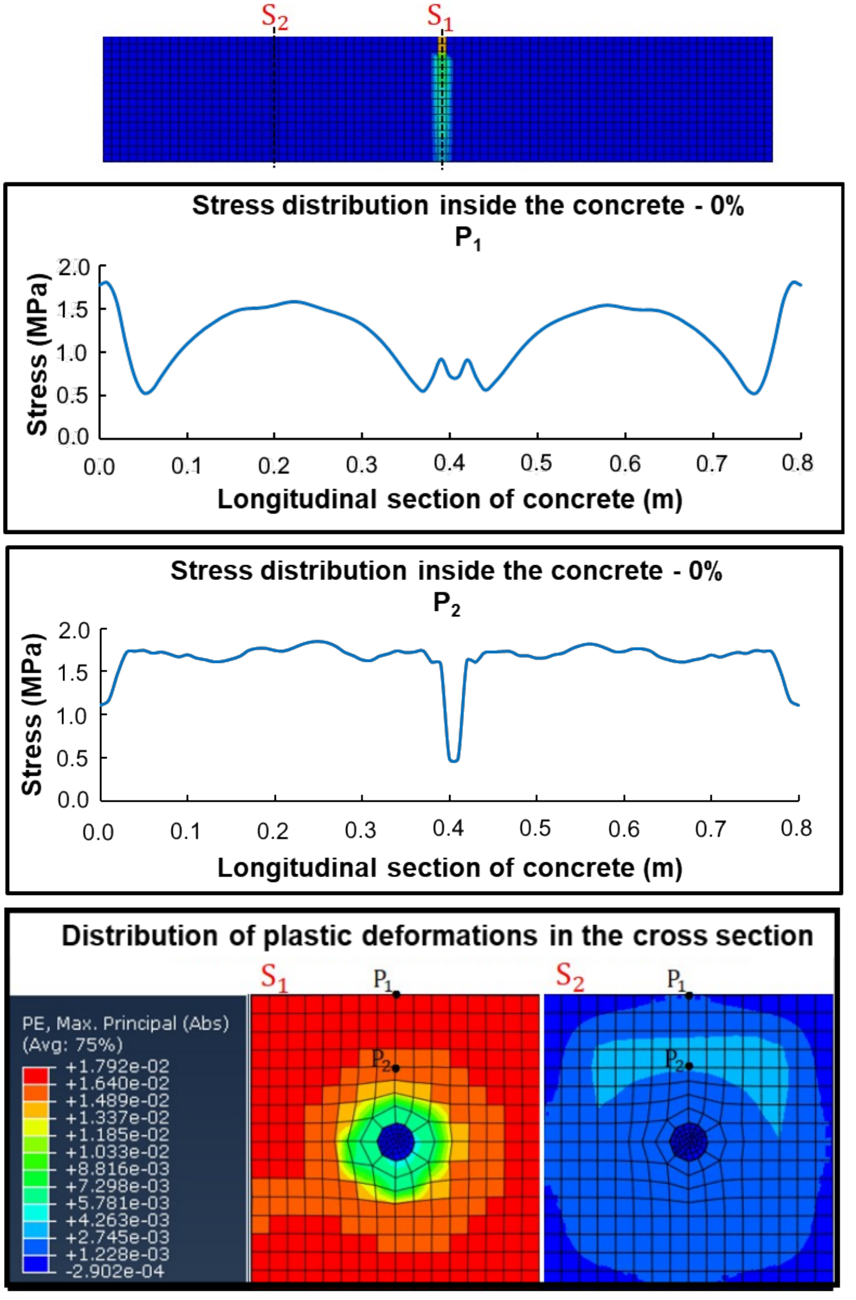

Figure 16. Stress and strain distribution in concrete and in reinforcement for R0 element.

Assessing the distribution of plastic deformations inside the concrete (Figure 16), it appears that there is a variation along the cross section. In the cracked section (S1), it can be seen that the deformation of the concrete is greater on the external surface and it decreases as it approaches the steel bar, indicating the maintenance of a certain level of bond that allows the development of stresses in the concrete. In the section S2, formed of intact concrete, a difference is also verified between the deformation in the surface and the deformation inside the concrete, but with less intensity, which is compatible with the level of stresses observed in this section.

7 CONCLUSIONS

Reinforced concrete elements produced with normal concrete and recycled concrete, containing 25% and 50% of recycled aggregate in substitution to the conventional aggregate, were experimentally evaluated under direct tensile and analyzed through numerical and analytical models.

All tension stiffening elements showed multiple cracking under uniaxial tensile. After the cracking process, the observed load values remained higher than the values observed in the steel bar tested separately, confirming the contribution of concrete between cracks (tension stiffening effect) for the strength of the reinforced concrete element. The recycled concrete element presented higher cracking stress and greater deformations in the multiple cracking phase than the conventional concrete element, confirming the influence of the addition of recycled aggregate on the mechanical behavior.

Three analytical models of tension stiffening, with different mathematical equations, were compared with the experimental stress-strain diagrams obtained for the isolated matrix. It is verified that the values obtained for modeling of conventional concrete cannot adequately predict the tension stiffening behavior of concrete with recycled aggregate. For that, new parameters had to be obtained. The mathematical model proposed by Carreira and Chu (1986) obtained better approximations with the experimental results for the behavior of conventional concrete and for concrete with 50% recycled aggregate, but with different adjustment parameters equal to 1.45 and 1.55, respectively.

The numerical evaluation of reinforced concrete elements indicates that the type of analytical model adopted for tension stiffening affects the prediction of structural behavior, both in the approximation of curves and in the determination of crack loads. Comparing the models used, it can be seen that, for conventional concrete elements, the tension stiffening model proposed by Vecchio and Collins managed to approximate the areas under the curve (0.77% of error), but does not present as good approximation in the post-cracking behavior regarding the model proposed by Carreira and Chu, who managed to predict the behavior of the elements with conventional and recycled concrete with reasonable precision, provided that the appropriate parameters for each type of concrete were used. Despite presenting an error of 5.24% in the prediction of the element behavior, the analytical model proposed by CEB showed a good approximation, especially when it is considered that it did not change the original parameters proposed by the standard.

The monitoring of the stress distribution along the element, during the loading and cracking processes, demonstrated that there is a stress redistribution as new cracks appear in the concrete, making it possible to identify the tension stiffening effect, that is, the contribution of the concrete between cracks. At the crack region, it is possible to identify that the concrete stresses reduce, but do not reach zero, also contributing to the strength of the tension stiffening element.

The numerical results indicate that, in the same section of the element, there is a variation of plastic deformations and stresses along the cross section. This variation affects the form of stress distribution in the concrete along the length of the element, which is no longer uniform when measured inside the section, and becomes parabolic when measured on the concrete surface.

ACKNOWLEDGMENTS

The authors acknowledge the support from CAPES and CNPq for this study.

REFERENCES

[1] Comité Euro-International du Béton, *Design Manual on Cracking and Deformation* (Bulletin d'Information 158). 1985.

[2] F. J. Vecchio and M. P. Collins, "The modified compression-field theory for reinforced concrete elements subjected to shear," *ACI J. Proc.*, vol. 83, no. 2, pp. 219–231, Oct 1986.

[3] R. Ian Gilbert, "Tension stiffening in lightly reinforced concrete slabs," *J. Struct. Eng.*, vol. 133, no. 6, pp. 899–903, Jun 2007, http://dx.doi.org/10.1061/(ASCE)0733-9445(2007)133:6(899).

[4] S. Khalfallah and D. Guerdouh, "Tension stiffening approach in concrete of tensioned members," *Int. J. Adv. Struct. Eng.*, vol. 6, no. 1, pp. 1–6, Jan 2014, http://dx.doi.org/10.1007/s40091-014-0051-8.

[5] R. Ian Gilbert and R. F. Warner, "Tension stiffening in reinforced concrete slabs," *J. Struct. Div.*, vol. 104, no. 2, pp. 1885–1900, 1978.

[6] C. K. Choi and S. H. Cheung, "Tension stiffening model for planar reinforced concrete members," *Comput. Struc.*, vol. 59, no. 1, pp. 179–190, Apr 1996, http://dx.doi.org/10.1016/0045-7949(95)00146-8.

[7] A. Scanlon and D. Murray, "Time-dependent reinforced concrete slab deflections," *J. Struct. Div.*, vol. 100, no. 8, pp. 1911–1924, Sep 1974.

[8] A. K. Gupta and S. R. Maestrini, "Tension-stiffness model for reinforced concrete bars," *J. Struct. Eng.*, vol. 116, no. 3, pp. 769–790, Mar 1990, http://dx.doi.org/10.1061/(ASCE)0733-9445(1990)116:3(769).

[9] P. C. M. Gonçalves, "Betão com agregados reciclados – análise comentada da legislação existente," M.S. thesis, Inst. Sup. Téc., UTL, Lisboa, 2007.

[10] J. Xiao, Y. Sun, and H. Falkner, "Seismic performance of frame structures with recycled aggregate concrete," *Eng. Struct.*, vol. 28, no. 1, pp. 1–8, Jan 2006, http://dx.doi.org/10.1016/j.engstruct.2005.06.019.

[11] V. Corinaldesi, V. Letelier, and G. Moriconi, "Behaviour of beam-column joints made of recycled-aggregate concrete under cyclic loading," *Constr. Build. Mater.*, vol. 25, no. 4, pp. 1877–1882, Apr 2011, http://dx.doi.org/10.1016/j.conbuildmat.2010.11.072.

[12] J. Xiao, W. Li, Y. Fan, and X. Huang, "An overview of study on recycled aggregate concrete in China (1996–2011)," *Constr. Build. Mater.*, vol. 31, pp. 364–383, Jun 2012, http://dx.doi.org/10.1016/j.conbuildmat.2011.12.074.

[13] C. S. Rangel, M. Amario, M. Pepe, Y. Yao, B. Mobasher, and R. D. Toledo Fo., "Tension stiffening approach for interface characterization in recycled aggregate concrete," *Cement Concr. Compos.*, vol. 82, pp. 176–189, Sep 2017., http://dx.doi.org/10.1016/j.cemconcomp.2017.06.009.

[14] J. A. Carneiro, P. R. L. Lima, M. B. Leite, and R. D. Toledo Filho, "Compressive stress–strain behavior of steel fiber reinforced-recycled aggregate concrete," *Cement Concr. Compos.*, vol. 46, pp. 65–72, Feb 2014, http://dx.doi.org/10.1016/j.cemconcomp.2013.11.006.

[15] M. Etxeberria, A. R. Marí, and E. Vázquez, "Recycled aggregate concrete as structural material," *Mater. Struct.*, vol. 40, no. 5, pp. 529–541, Jun 2007, http://dx.doi.org/10.1617/s11527-006-9161-5.

[16] I. S. Ignjatović, S. B. Marinković, Z. M. Mišković, and A. R. Savić, "Flexural behavior of reinforced recycled aggregate concrete beams under short-term loading," *Mater. Struct.*, vol. 46, no. 6, pp. 1045–1059, Jun 2013, http://dx.doi.org/10.1617/s11527-012-9952-9.

[17] R. V. Silva, J. Brito, and R. K. Dhir, "Prediction of the shrinkage behavior of recycled aggregate concrete: a review," *Constr. Build. Mater.*, vol. 77, pp. 327–339, Feb 2015, http://dx.doi.org/10.1016/j.conbuildmat.2014.12.102.

[18] P. H. Bischoff, "Effects of shrinkage on tension stiffening and cracking in reinforced concrete," *Can. J. Civ. Eng.*, vol. 28, no. 3, pp. 363–374, 2001., http://dx.doi.org/10.1139/l00-117.

[19] G. Kaklauskas, V. Gribniak, D. Bacinskas, and P. Vainiunas, "Shrinkage influence on tension stiffening in concrete members," *Eng. Struct.*, vol. 31, no. 6, pp. 1305–1312, Jun 2009, http://dx.doi.org/10.1016/j.engstruct.2008.10.007.

[20] S. M. Allam, M. S. Shoukry, G. E. Rashad, and A. S. Hassan, "Evaluation of tension stiffening effect on the crack width calculation of flexural RC members," *Alex. Eng. J.*, vol. 52, no. 2, pp. 163–173, Jun 2013, http://dx.doi.org/10.1016/j.aej.2012.12.005.

[21] M. Kosior-Kazberuk and M. Grzywa, "Recycled aggregate concrete as material for reinforced concrete structures," *J. Sustain. Archit. Civ. Eng.*, vol. 7, no. 2, pp. 60–66, Jun 2014, http://dx.doi.org/10.5755/j01.sace.7.2.7135.

[22] D. J. Carreira and K. H. Chu, "Stress-strain relationship for reinforced concrete in tension," *ACI J.*, vol. 83, no. 1, pp. 21–28, Jan 1986.

[23] T. T. C. Hsu and Y. L. Mo, *Unified Theory of Concrete Structures.* Chichester, UK: Wiley, 2010.

[24] Comité Euro-International du Béton. Fédération Internationale de la Précontrainte, *CEB-FIP Model Code 1990: Design Code*, 1993.

[25] T. Wang and T. T. C. Hsu, "Nonlinear finite element analysis of concrete structures using new constitutive models," *Comput. Struc.*, vol. 79, no. 32, pp. 2781–2791, Dec 2001, http://dx.doi.org/10.1016/S0045-7949(01)00157-2.

[26] T. Dede and Y. Ayvaz, "Nonlinear analysis of reinforced concrete beam with/without tension stiffening effect," *Mater. Des.*, vol. 30, no. 9, pp. 3846–3851, Oct 2009, http://dx.doi.org/10.1016/j.matdes.2009.02.003.

[27] C. S. Rangel, "Influência de agregados graúdos reciclados nas propriedades estruturais de concretos de resistência normal e de alto desempenho," M.S. thesis, Univ. Fed. Rio de Janeiro, Rio de Janeiro, 2015.

[28] D. S. Simulia, *Abaqus 6.11 Theory Manual.* Providence, RI, USA: DS Simulia Corp., 2011.

[29] L. M. D. S. Soares, "Análise numérica não linear de ligações pilares laje fungiforme," M.S. thesis, Univ. Nova, Lisboa, 2016.

[30] D. S. Simulia, *Abaqus 6.12 Analysis User's Manual*. Providence, RI, USA: DS Simulia Corp., 2012.

[31] J. Lee and G. L. Fenves, "Plastic-damage model for cyclic loading of concrete structures," *J. Eng. Mech.*, vol. 124, no. 8, pp. 892–900, Aug 1998., http://dx.doi.org/10.1061/(ASCE)0733-9399(1998)124:8(892).

[32] H. Kupfer, H. K. Hilsdorf, and H. Rusch, "Behavior of concrete under biaxial stresses," *ACI J. Proc.*, vol. 66, no. 8, pp. 656–666, Jan 1969.

[33] T. Jankowiak and T. Lodygowski, "Identification of parameters of concrete damage plasticity constitutive model," *Found. Civ. Environ. Eng.*, vol. 6, no. 1, pp. 53–69, 2005.

[34] V. Birtel and P. Mark, "Parameterised finite element modelling of RC beam shear failure," in *ABAQUS Users'conf.*, May 2006, pp. 95–108.

[35] D. M. F. Ors, H. O. Okail, and A. H. Zaher, "Modeling of shear deficient beams by the mixed smeared/discrete cracking approach," *HBRC J.*, vol. 12, no. 2, pp. 123–136, Aug 2016, http://dx.doi.org/10.1016/j.hbrcj.2014.11.002.

[36] W. S. A. Nana, T. T. Bui, A. Limam, and S. Abouri, "Experimental and numerical modelling of shear behaviour of full-scale RC slabs under concentrated loads," *Structures*, vol. 10, pp. 96–116, May 2017, http://dx.doi.org/10.1016/j.istruc.2017.02.004.

[37] R. Malm, *Shear Cracks in Concrete Structures Subjected to In-Plane Stresses*. Stockholn: Department of Civil and Architectural Engineering, KTH, 2006.

[38] E. Hognestad, *Study of Combined Bending and Axial Load in Reinforced Concrete Members* (Bulletin Series 399). Champaign: University of Illinois Urbana-Champaign, 1951.

[39] D. C. Kent and R. Park, "Flexural members with confined concrete," *J. Struct. Div.*, vol. 97, no. 7, pp. 2703–2722, Aug 1971.

[40] E. P. Prado and J. G. M. Van Mier, "Effect of particle structure on mode I fracture process in concrete," *Eng. Fract. Mech.*, vol. 70, no. 14, pp. 1793–1807, Sep 2003., http://dx.doi.org/10.1016/S0013-7944(03)00125-5.

[41] C. S. Lin and A. C. Scordelis, "Nonlinear analysis of RC shells of general form," *J. Struct. Div.*, vol. 101, no. 3, pp. 523–538, 1975.

Author contributions: MPM: methodology, numerical modelling, investigation, formal analysis, writing - original draft; CSR and MA: experimental analysis, investigation, data curation, formal analysis; JMFL: conceptualization, formal analysis, supervision; PRLL: conceptualization, formal analysis, supervision, writing - review & editing; RDTF: conceptualization, supervision, project administration.

Editors: Vladimir Guilherme Haach, José Luiz Antunes de Oliveira e Sousa, Guilherme Aris Parsekian.

Rev. IBRACON Estrut. Mater., vol. 13, no. 6, e13606, 2020

IBRACON Structures and Materials Journal
Revista IBRACON de Estruturas e Materiais
ISSN 1983-4195 ismj.org

ORIGINAL ARTICLE

Influence of the cracking consideration in the displacements of a shallow tunnel lined in steel-reinforced concrete: numerical model

Influência da fissuração nos deslocamentos de um túnel superficial revestido em concreto armado: modelo numérico

Betina Mariano Jensen[a]
Denise Bernaud[a]
Américo Campos Filho[a]

[a]Universidade Federal do Rio Grande do Sul – UFRGS, Departamento de Engenharia Civil, Programa de Pós-graduação em Engenharia Civil, Porto Alegre, RS, Brasil

Received 12 December 2019
Accepted 11 April 2020

Abstract: The study of shallow tunnels introduces different aspects when compared to deep tunnels analysis. Among these characteristics can be emphasized the non-uniform shape of the deformed cross-section and the impossibility of some simplifications such as the consideration of homogeneous stresses around the excavation. Since the tunnel lining is subject to combined bending and compression, shallow tunnels are more susceptible to the development of final tensile stresses (not founded in deep tunnels) and the consequent concrete cracking. This paper presents a numerical simulation in finite elements with the ANSYS software. The purpose of the study is to analyze the cracking influence in the displacements of shallow tunnels, treating the concrete behavior by three different models: elastic, viscoelastic and viscoelastic with cracking effects.

Keywords: shallow tunnels, cracking, finite element method, concrete, viscoelasticity.

Resumo: O estudo de túneis superficiais apresenta peculiaridades se comparado à análise de túneis profundos. Dentre estes aspectos, pode-se enfatizar o formato não uniforme da seção deformada e a impossibilidade de adotar algumas simplificações, como a consideração de tensões uniformes ao redor da escavação. Uma vez que o revestimento do túnel está sujeito à flexo-compressão, túneis superficiais são mais suscetíveis ao desenvolvimento de tensões finais de tração (não encontradas em túneis profundos) e a consequente fissuração do concreto. Este artigo apresenta uma simulação numérica pelo método dos elementos finitos, realizada com o *software* ANSYS. O estudo tem o objetivo de analisar a influência da fissuração nos deslocamentos de túneis superficiais, ao tratar o comportamento do concreto por meio de três diferentes modelos: elástico, viscoelástico e viscoelástico com fissuração.

Palavras-chave: túneis superficiais, fissuração, método dos elementos finitos, concreto, viscoelasticidade.

How to cite: B. M. Jensen, D. Bernaud, and A. Campos Filho, "Influence of the cracking consideration in the displacements of a shallow tunnel lined in steel-reinforced concrete: numerical model," *Rev. IBRACON Estrut. Mater.*, vol. 13, no. 6, e13606, 2020, https://doi.org/10.1590/S1983-41952020000600006

1 INTRODUCTION

The strains resulting from an excavation process reduce the existing stresses in the soil mass and induce forces in the lining that correspond to a part of this initial geostatic pressures [1], [2]. So, the design of underground facilities requires the correct evaluation of both the soil mass deformations and the lining stress levels. The magnitude of these

Corresponding author: Betina Mariano Jensen. E-mail: betina.jensen@ufrgs.br
Financial support: Scolarship provided by Coordenação de Aperfeiçoamento de Pessoal de Nível Superior (CAPES).
Conflict of interest: Nothing to declare.

solicitations depends on several factors, such as the excavation method, the lining type, the material characteristics and, mainly, the interaction of the lining and the soil mass.

In tunnel engineering, there is a distinction between treating a tunnel as a shallow or as a deep one, since they present different characteristics. Stress and strain fields are the main aspects that distinguish then. Dealing with shallow tunnels, located at a small depth compared with their cross-section size, the complexity of the problem increases, since this type of tunnel is influenced by the free ground surface above it. Shallow tunnels present, then, an ovalized cross-sectional deformed shape, different from the uniform deformed shape usually seen in deep tunnels [3].

Since shallow tunnel linings are subjected to lower compression levels than deep tunnels, it is important to consider the actual coefficient of earth pressure at rest (K), which modifies the value of the horizontal pressures in relation to the vertical pressures, considering a relation value different from one. On the other hand, treating the horizontal pressure acting on the soil as equal to the vertical pressure (simplification often adopted in deep tunnels analysis) may have a significant impact on the results. The actual K coefficient causes some cross-sectional regions less compressed than others. As the lining is subject to bending-compressive stresses, a shallow tunnel becomes more susceptible to the development of tensile stresses and consequent concrete cracking, which may reduce its stiffness and induce higher strains.

This paper presents a finite element model elaborated with ANSYS software. The tunnel excavation and lining placement processes are simulated with the tool of activation and deactivation of elements, step by step. Soil mass behavior is represented by an elastoplastic model with the Mohr-Coulomb plasticity criterion. Three different models represent the concrete behavior: linear elastic, viscoelastic and viscoelastic considering the cracking effects. Since these two last-mentioned models are not previously available in the software chosen, ANSYS's User Programmable Features (UPF) tool is used, based on the studies of Quevedo [4] and Schmitz [5]. Additionally, the steel reinforcement is represented by an embedded reinforcement element, with perfect elastoplastic behavior.

The purpose of the performed analysis is, thereby, to determine the difference between the consideration of concrete behavior with the help of the three mentioned models. In these analyses, tunnel depth is also varied to establish its influence. Furthermore, the impact of other involved parameters (unlined length (d_0), concrete strength (f_{ck}) and soil mass Young modulus (E_m)) is studied by considering a given depth value and the concrete behavior as viscoelastic with cracking.

2 MECHANICAL BEHAVIOR OF TUNNELS

In the study of mechanical and structural behavior of a tunnel, it is particularly important to consider in the analysis the constructive phases, related to the soil mass excavation. During the excavation process, the region near the tunnel advancing cross-section (called excavation face) is subjected to higher stresses and strains gradients. Hence, this part of the tunnel consists of an influence zone that starts from a cross-section located inside the unexcavated soil mass, where the radial displacements are small, to another section located in the excavated part, where the displacements reach maximum values [6]–[8].

The radial displacements (u_r) define the so-called tunnel convergence (U_i), shown in Equation 1. This parameter is described by the relation between these displacements in each section and the tunnel radius (R_e).

$$U_i = \frac{-u_r\left(r = R_e\right)}{R_e} \tag{1}$$

Figure 1 shows the convergence curve of a circular tunnel, relative to the excavation sections. From it, we can observe that the displacement values are null in a region of the unexcavated soil mass far from the excavation face (undisturbed). They present a maximum gradient in the region around the excavation face and show the greatest magnitudes in an excavated region far from the front (in which the tunnel reached the equilibrium).

Numerical methods based on the finite element method (FEM) are an important tool to determine soil mass displacements and to design the tunnel lining, since they present several advantages over analytical and empirical methods. The numerical methods allow the use of nonlinear and distinct constitutive models for the soil and the lining, the modeling of complex geometries and the consideration of boundary and loading conditions like those found in the field. Additionally, numerical simulations can reproduce the excavation process and the lining installation by the activation and deactivation method, as done in the studies of Bernaud [9], Fiore et al. [10] and Quevedo [4].

In this model, the excavation and lining placement sequences are simulated by changing the stiffness value of the affected elements (soil or concrete) at each excavation step (face advance). To represent the soil mass removal, the stiffness of the excavated elements is reduced. In order to simulate the lining placement (at a specified distance d_0 from the advancing face), the mechanical characteristics of the respective elements, which were previously related to the soil, are replaced to those of the concrete lining [11]. The typical mesh employed in the models which are used in the construction stages analysis is shown in Figure 2 (illustrative).

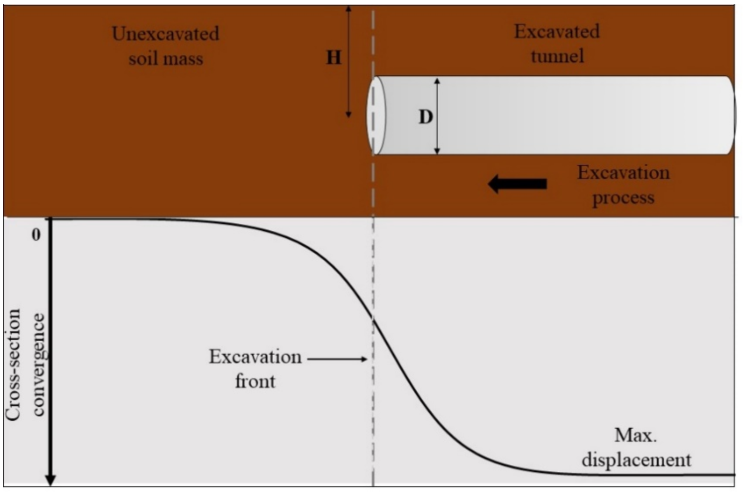

Figure 1. Tunnel convergence along the longitudinal section to the excavated and unexcavated parts.

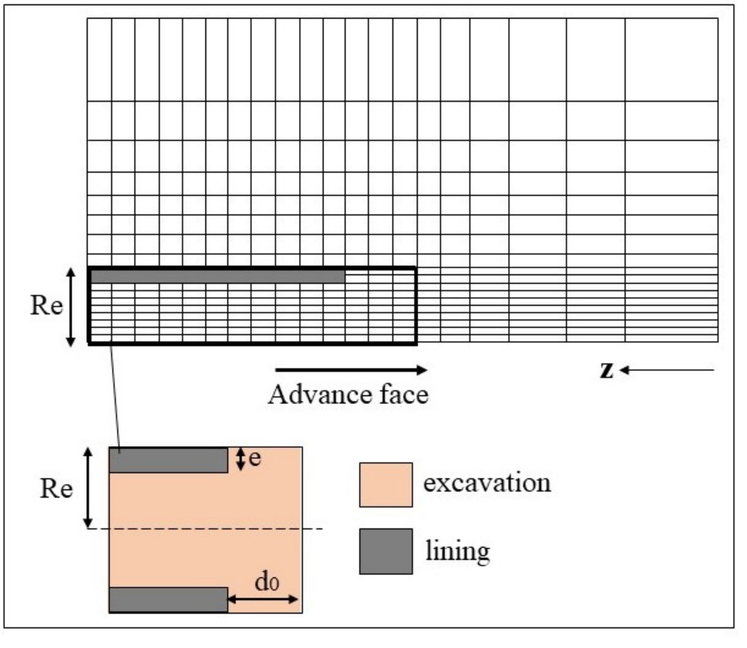

Figure 2. Typical mesh for tunneling simulation (illustrative).

2.1 Tunnel lining

The lining is the structural system installed to provide the necessary support to the tunnel. Thus, it confers stiffness and assists the soil mass in the stabilization of strains during the construction and the different structural stages. It acts also with other functions such as limiting water infiltration and representing the basis for the final inner tunnel surface [12]. In general, this is a hyperstatic problem, since the forces acting in the lining, the stresses resulting from these actions, and the resulting displacements are interdependent and related to the soil-lining interaction.

Several factors are associated with the stresses developed in a tunnel lining as, for example, the lining stiffness. For a better understanding of stiffness influence, Peck [13] suggests that two main situations should be assumed, both for a circular tunnel with lining. If the tunnel lining is perfectly flexible but able to withstand the radial compressive pressures, tangential and shear stresses would not appear, neither bending moments. On the other hand, assuming this lining to be perfectly rigid, the pressures would cause bending moments due to the lining resistance to the imposed forces. In practice, however, the actual lining stiffness is acting between the two proposed conditions. In this way, the tunnel equilibrium cannot be reached only by changing its cross-section size, and this distortion may induce the development of bending moments.

The different structural behavior of a tunnel lining can be explained as a case of bending-compressive stresses. For deep tunnels, the resulting main stresses are purely compressive and more uniform than those found in shallow tunnels. As a result, the bending causes essentially areas with a higher concentration of stresses (usually compressive ones). On the other hand, in shallow tunnels, due to the smaller magnitude of the compressive forces, this bending can cause final tensile stresses.

2.2 Shallow tunnel conditions

The distribution of stresses in the soil mass, the magnitude order of the displacements on the ground surface and the degree of displacements symmetry above and below the tunnel cross-section present some aspects that distinguish the tunnels between shallow or deep. In practice, it is possible to differentiate these two tunnel types through the relationship between their depth (H) and their diameter (D) and, although there is no accordance about the limit value, the adoption of the relation $H / D < 10$ (as in Benamar [14] and Ferrão [15] studies) seems appropriate to consider the tunnel as a shallow one.

The stresses field developed around a shallow tunnel is not purely radial like in deep tunnels, due to the influence of the proximity to the free ground surface. Consequently, the cross-sectional deformation of a shallow tunnel is not merely uniform and is not related only to the cavity volume change. Actually, in accordance with Pinto and Whittle [3], two other components define the final deformed state: distortion (or ovalization) and vertical translation. The difference in the deformed shape from shallow to deep tunnels is shown in Figure 3.

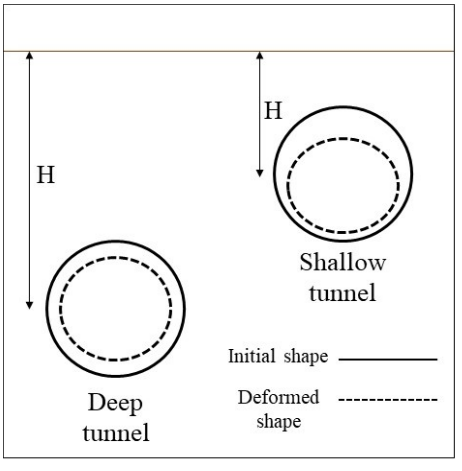

Figure 3. Difference in the shape of deep and shallow tunnels deformed cross-section.

Moreover, regarding shallow tunnel analysis, it is most adequate to consider as acting in the soil mass the actual variable pressures than the geostatic-hydrostatic ones, taking into account the value of the coefficient of earth pressure at rest (K), which is actually different from the unit. This coefficient modifies the value of the horizontal pressures in relation to the vertical ones, causing non-uniform displacements and stresses, which vary along the tunnel cross-section (causing zones of stress concentration and relaxation) and bending moments in the tunnel lining [16]. As the soil weight is smaller at lower depths, the compression level at the lining is, consequently, lower. Then, the anisotropy induced by K can cause the development of tensile stresses.

Jensen [17] carried out analysis concerning circular shallow tunnels lined in concrete (soil mass and lining with linear elastic behavior), in which the influence of both depth and earth pressure coefficient in the appearance of tension stresses were studied. The obtained results indicated that tunnels with a smaller H/D relation present more areas of tensile stresses compared to deeper tunnels. The same conclusion was obtained on the variation of the K coefficient: the smaller and distant from the unit, more tensile areas tended to form.

In shallow tunnels, the change in the stress state caused by the excavation also induces another displacement type, called surface settlement. Among the methods of analysis and evaluation of surface settlements, is cited the empirical method given by Peck [13], which indicates that the shape of these displacements resembles a reversed Gaussian curve. Thus, the maximum displacement is precisely on the axis of the tunnel cross-section and the magnitude is greater the closer the tunnel is to the surface.

3 CONSTITUTIVE MODELS OF MATERIALS

This item aims to describe the constitutive models chosen to represent the materials that compose the tunnels: the soil mass and the steel-reinforced concrete lining.

3.1 Soil mass

To represent the soil mass behavior, it is employed the constitutive model of Mohr-Coulomb, often adopted as a resistance criterion in the geotechnical engineering. A version of this model is provided by ANSYS [18] and can be applied by the insertion of the soil parameters as the friction angle (φ), the cohesion (C) and the dilatancy angle (ψ) of the material.

3.1 Lining: steel-reinforced concrete

This research aimed to contemplate two behaviors presented by the concrete: one model represents the time-dependent strains and the other one represents the low resistance to tensile stresses. Thus, to implement a viscoelastic model with the consideration of cracking effects, it was necessary to use the ANSYS customization tool, the User Programmable Features - UPF, through the UserMat subroutine, specific to customize material behavior. For this, the procedures presented by Quevedo [4], Schmitz [5], Lazzari [19] and Quevedo et al. [20] were followed. Further details on formulations and solution features can be found in the studies cited above.

The time-dependent behavior of the concrete can be explained in terms of the creep and shrinkage phenomena. The first one concerns the continuous and gradual strains increase under constant stresses and can be separated, as in the case of the Solidification Theory proposed by Bazant and Prasannan [21], in a portion dependent on the loading age and another part dependent on the concrete age, the same distinction made by the formulation given by the Comité Euro-International du Béton (CEB-FIP MC90) [22]. The second phenomenon, called shrinkage, refers to the material volume reduction given by the gradual water loss remaining in the capillary vessels inside the concrete, which it has not been completely used in the cement hydration reactions.

The Comité Euro-International du Béton [22] evaluates the total strain in the age t of a concrete element uniaxially loaded at age t_0 with uniform stress $\sigma_c(t_0)$ by the Equation 2:

$$\varepsilon_c(t) = \varepsilon_{ci}(t_0) + \varepsilon_{cc}(t) + \varepsilon_{cs}(t) + \varepsilon_{cT}(t) = \varepsilon_{c\sigma}(t) + \varepsilon_{cn}(t) \tag{2}$$

in which $\varepsilon_{ci}(t_0)$ = initial elastic and linear strain (immediate); $\varepsilon_{cc}(t)$ = creep strain; $\varepsilon_{cs}(t)$ = the shrinkage strain; and $\varepsilon_{cT}(t)$ = thermal strain.

Therefore, the total strain is composed of a dependent on the stress part ($\varepsilon_{c\sigma}(t)$), where the elastic and the creep strains are included, and an independent on the stress part ($\varepsilon_{cn}(t)$), that comprises the shrinkage and the thermal strains. The thermal strains are not addressed in this paper.

The strain depending on the stress can be expressed by Equation 3:

$$\varepsilon_{c\sigma}(t,t_0) = \sigma_c(t_0)\left[\frac{1}{E_c(t_0)} + \frac{\phi(t,t_0)}{E_{ci}}\right] = \sigma_c(t_0)J(t,t_0) \tag{3}$$

In Equation 3, $J(t,t_0)$ is the creep function and refers to the terms given by the Equation 4:

$$J(t,t_0)=\frac{1}{E_c(t_0)}+\frac{\phi(t,t_0)}{E_{ci}} \tag{4}$$

The other terms of Equation 3 are: $\sigma_c(t_0)$ = stress applied at the initial time (MPa); $E_c(t_0)$ = concrete tangent elasticity modulus at the initial time (MPa); $\phi(t,t_0)$ = creep coefficient; E_{ci} = Young modulus at the age of 28 days (MPa).

To the shrinkage strain, the Comité Euro-International du Béton [22] defines the relation below (Equation 5):

$$\varepsilon_{cs}(t,t_s)=\varepsilon_{cs0}\beta_s(t-t_s) \tag{5}$$

where t_s = concrete age (in days) when shrinkage starts; ε_{cs0} = shrinkage factor (dependent on concrete composition); and $\beta_s(t-t_s)$ = factor that depends on the shrinkage age $(t-t_s)$.

It is worth noting that, in accordance with Quevedo et al. [20], the use of the Comité Euro-International du Béton [22] formulation is due to the fact that the creep model fits into the Bazant and Prasannan [21] Solidification Theory. This facilitates the numerical solution of the concrete time-dependent behavior considering aging as an isolated factor (related only to the solidified concrete volume over time).

In turn, the concrete characteristic of not resisting tensile stresses well, since its tensile strength is much lower than its compressive strength, can result in cracking even at low stress levels (to which shallow tunnels are generally subjected, for example). To verify if cracking occurs, the stress level of the integration points is evaluated by two procedures. It is verified whether the integration point stresses reached the yield surface, which in this research is defined by Ottosen [23]. Then, it is also evaluated if cracking or crushing failure occurs (the cracking failure occurs if the first principal stress of the sample point is equal or greater than the half of the concrete average tension strength).

The cracking consideration (for the points which have reached the mentioned criteria) is evaluated through a model of distributed cracks. So, only material properties are modified, without being necessary to change the finite element mesh. In this case, as in Schmitz [5] and Lazzari [19] studies, the crack is considered to be formed in a perpendicular plane to the main stress direction. Furthermore, the longitudinal and transverse elasticity modulus are reduced, in addition to neglecting the Poisson effect.

Dealing with reinforced concrete, when cracking occurs, the concrete between cracks continues to resist certain tensile stresses. The adherence effects between the concrete and the steel bars contribute to the total structure stiffness. This phenomenon is known as tension stiffening effect. One of the ways to represent this behavior in the model is to modify the stress-strain curve of the concrete, which becomes linear with softening, as shown in Figure 4. A constitutive relation, proposed by Martinelli [24], describes this behavior and is given by Equation 6:

$$\sigma_c=0.6E_{ci}\varepsilon_t\left(1-\frac{\varepsilon_c}{\varepsilon_{cTU}}\right)=0.6\sigma_t\left(1-\frac{\varepsilon_c}{0.001}\right) \tag{6}$$

in which σ_c = concrete stress; E_{ci} = tangent elasticity modulus; ε_t = tensile nominal strain in the cracked zone; ε_c = concrete strain; σ_t = tensile stress in the cracked zone; and ε_{cTU} = tensile strain limit which defines the end of the softening portion.

In addition to the tension stiffening effect consideration, a gradual reduction of shear stresses in the crack plane is also evaluated, as suggested by Hinton [25]. To represent this phenomenon in an approximate way, the material transverse elasticity modulus is multiplied by a reducing factor.

The described formulations considering both the viscoelastic behavior and the cracking effects in the concrete are then added to the UserMat subroutine, which is called by ANSYS iterative procedure for each integration point. The main program computes the total stresses, deformations, and increments of total deformations in the current time increment and the subroutine returns the update stresses according to the implemented instructions [20]. Shortly, within the subroutine, after stress determination considering the time-dependent effects, the cracking checking is done. If it is reached, the mentioned modifications are considered, and the stresses are updated again. If it is not reached, the subroutine saves the results and the program goes on to the next point of the iteration procedure.

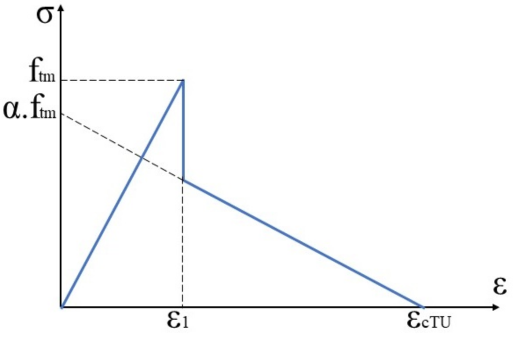

Figure 4. Stress-strain curve for the tensile concrete.

Finally, the behavior of the steel reinforcement bars of the lining, which resist only axial forces, can be described by a uniaxial model. Thus, the steel is represented by a bilinear stress-strain diagram and has a perfect elastoplastic behavior, although a small hardening factor is applied to avoid numerical errors, as recommended by Schmitz [5].

4 NUMERICAL ANALYSIS

This item presents details about the numerical modeling, describing the finite elements chosen, the mesh adopted and other characteristics of the model. Afterward, the results of the performed simulations are shown.

4.1 ANSYS numerical modeling

The solid finite element adopted in the model to represent both soil and concrete is the SOLID185, which has eight nodes with three degrees of freedom per node (translation in X, Y and Z). To represent the steel bars, the element chosen is the REINF264, an embedded reinforcement element which has only axial stiffness and could be placed in any orientation within the base element. In the modeling, the rebars (two layers) are positioned in the middle of the base element, both on longitudinal and circumferential directions.

The numerical simulation of the tunnel construction process is done by 37 excavation steps, with the length, each one, of one-third of the external tunnel radius, so that the final model has an excavated part (more refined mesh) and an unexcavated part. The model has 15678 finite elements. The excavation process, simulated by the element's activation and deactivation tool, is done with the ANSYS Birth and Death commands. First, it is generated a duplicate mesh in the lining region; then, the elements that represent the concrete are soon disabled. Finally, step by step, the soil mass elements are deactivated, as those of the lining are reactivated.

It is important to emphasize that, as a simplification, the speed and the length of the excavation are equal in each step, disregarding possible time intervals without excavation (that occurs in practice) and other variations. The soil mass, in turn, is treated as a single material, homogeneous and isotropic, without the presence of heterogeneous layers.

Figure 5 shows the (a) 3D mesh and their respective (b) longitudinal and (c) transverse sections. The boundary conditions (restriction to the displacement in Y in the lower face and in Z in the front face) and loads ($P_v = \gamma H$ and $P_h = KP_v$, with γ the soil specific weight, H the tunnel height, and K the earth pressure coefficient) are also indicated. Moreover, it is applied a symmetry condition in the ZY plane. Consequently, only half of the model is simulated.

In addition to the external loads, it is necessary to apply an initial stress condition with the same values of P_v and P_h , as the soil elements weight. This procedure is done to assign a null initial strain state, with no deformations before the excavation. At the same time, the stress state will be the geostatic one.

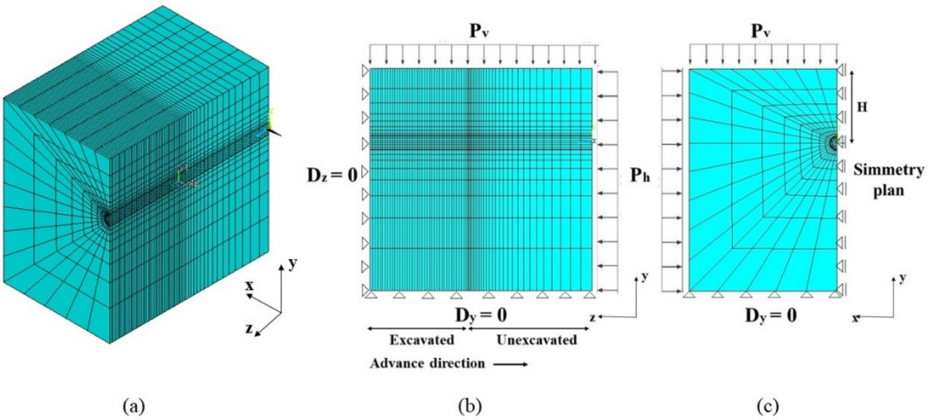

Figure 5. (a) 3D mesh, (b) longitudinal section and (c) transverse section of the model.

4.2 Results

Some simulations are carried out to compare the results obtained by altering the behavior models of the lining material. Thus, it is expected to analyze the influence of considering or not the cracking of the concrete rather than contemplating only an elastic or viscoelastic behavior. The objective is to obtain the displacements in a region far from the excavation face, in three points of the tunnel cross-section: at 90º, 180º and 270º, for three distinct lining constitutive models.

For the soil mass, a plastic behavior is admitted by assuming the Mohr-Coulomb criterion, as already explained in item 3.1. For the lining, it is expected to evaluate the evolution of the tunnel convergence as the model changes between elastic, viscoelastic, and viscoelastic with cracking (all these with steel reinforcement). The tunnel depth will also be varied so that its influence on the results can be analyzed.

In order to intensify the solicitations undergone by the lining, which can contribute to the cracking occurrence in the concrete, the distance of the lining placement to the excavation front (or unlined length) is considered null in the examples. This means that the lining is placed immediately after the soil mass excavation.

The required parameters for the analysis of a circular tunnel are shown in Table 1. It is worth to mention that the examples consider a fictitious tunnel, with reduced dimensions. Thus, the results represent only an assessment of the procedures adopted and an indication of behavior.

Table 1. Geometry and material parameters.

Parameter	Nomenclature	Unit	Value
	Tunnel parameters		
Outer radius	Re	m	1
Inner radius	Ri	m	0.9
Height	H	m	20 - 16 - 10
	Soil parameters		
Specific weight	γ	N/m^3	20000
Poisson ratio	ν	dimensionless	0.3
Young modulus	E	MPa	30
Earth pressure coefficient	K	dimensionless	0.5
Cohesion	C	MPa	0.5
Friction angle	φ	°	30
Dilatancy angle	ψ	°	10
	Lining parameters: concrete		
Poisson ratio	ν	dimensionless	0.2
Young modulus	E	MPa	30000
Compressive strength	f_{ck}	MPa	30
	Lining parameters: steel		
Poisson ratio	ν	dimensionless	0.3
Young modulus	E	MPa	210000
Yield stress	f_{ya}	MPa	500
Reinforcement ratio (two layers)	ρ	%	0.173

The analysis results, for three H/D relations (5, 8 e 10) are exhibit in Tables 2, 3 e 4, where the convergence, in %, is given in three points of the tunnel cross-section, for each concrete behavior model.

Table 2. Results of the convergence (%) in the analysis with H/D = 5 for each concrete behavior model.

H/D = 5		**Model**	
Point (º)	**Elastic**	**Viscoelastic**	**Viscoelastic with cracking**
90	0.2701	0.3069	0.3072
180	0.0539	0.0744	0.0746
270	0.2343	0.2662	0.2663

Table 3. Results of the convergence (%) in the analysis with H/D = 8 for each concrete behavior model.

H/D = 8		**Model**	
Point (º)	**Elastic**	**Viscoelastic**	**Viscoelastic with cracking**
90	0.5048	0.5637	0.5822
180	0.1314	0.1644	0.1784
270	0.4840	0.5378	0.5598

Table 4. Results of the convergence (%) in the analysis with H/D = 10 for each concrete behavior model.

H/D = 10		**Model**	
Point (º)	**Elastic**	**Viscoelastic**	**Viscoelastic with cracking**
90	0.6226	0.6959	0.7377
180	0.1658	0.2076	0.2414
270	0.6103	0.6782	0.7165

By analyzing the results shown in Tables 2, 3 and 4, it can be noted that the found displacements for the tunnels with $H/D=8$ and $H/D=10$ grow from the elastic model to the viscoelastic one, and also increase when considering cracking. In the example with $H/D=5$, however, the difference only occurred from the elastic model to the viscoelastic, without considerable changes in the displacements when considering cracking. This occurs due to the lower pressure levels at which the tunnel is subjected in this smaller depth ($H=10m$), not causing sufficient tensile stresses for the concrete to crack. In the same way, it can be seen that this difference considering cracking is greater when the tunnel is at a higher depth and subjected to higher pressures (tunnel case with $H=20m$ compared with $H=16m$). This consideration is important, since tunnels with larger diameters than the studied ($D=2m$) may be located at higher depths than those analyzed and still be considered as a shallow tunnel.

The relative difference, from the elastic model to the viscoelastic model and from the viscoelastic model to the viscoelastic model with cracking, for each relation example in the three analyzed positions, is shown in Table 5.

Table 5. Relative difference in the convergence values for each model of concrete material.

Point (º)	**From elastic to viscoelastic model**	**From viscoelastic to viscoelastic with cracking model**
	H/D = 5	
90	13.64%	0.08%
180	37.98%	0.37%
270	13.59%	0.05%
	H/D = 8	
90	11.67%	3.27%
180	25.11%	8.48%
270	11.12%	4.09%
	H/D = 10	
90	11.76%	6.01%
180	25.23%	16.27%
270	11.13%	5.65%

Another example of the influence of the concrete behavior model can be observed in the surface settlement results. Figure 6 shows the transverse settlement basin for the tunnel with $H/D=8$. Since this tunnel has not a considerable ground cover above it, the magnitude of the settlement is small in the three models of concrete behavior. However, it is still possible to visualize the difference in the results according to the model (in terms of maximum settlement: 27.07% from the elastic to the viscoelastic model and 7.07% from the viscoelastic to the viscoelastic with cracking).

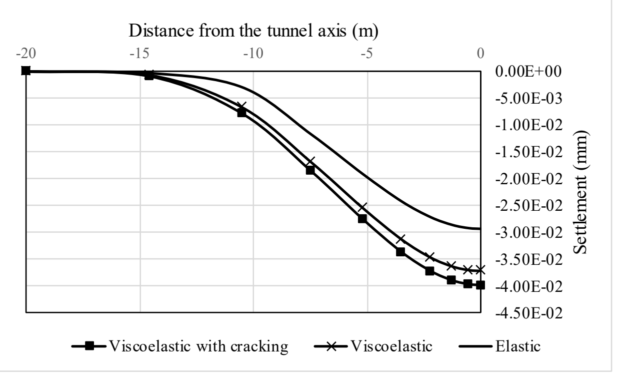

Figure 6. Variation of the surface settlements according to the concrete behavior model (tunnel with H/D=8).

The tunnel with $H/D=8$ is considered again. By varying the concrete model from elastic to viscoelastic and then viscoelastic with cracking, the changes in stress behavior can be also observed. First, when shrinkage and creep effects are considered instead of an elastic behavior, the maximum stress values decrease, both in compression and tension. The strains are greater from the first model to the other.

Regarding cracking effects, it is possible to contemplate the concrete behavior in tension, defined previously by Equation 6 and Figure 4. Before cracking, stresses increase linearly with strains. Then, once cracked the concrete, these stresses decrease for greater strains. Hence, the tendency for the cracked model is lower stresses for the lining points with greater strains, which cracks first than others.

Figures 7, 8 and 9 illustrate the circumferential stresses ($\sigma_{\theta\theta}$) in the tunnel lining, from the elastic, viscoelastic and viscoelastic with cracking models, respectively. The stresses in this direction have the highest magnitudes. From the figures, the aspects highlighted above can be observed. In elastic and viscoelastic models, the stress distribution is the same, but the magnitudes change. Regarding tension, the maximum value decrease from $3.87MPa$ to $2.72MPa$. On the other hand, from viscoelastic to viscoelastic with cracking model, in addition to the maximum value going from $2.72MPa$ to $1.54MPa$, the location of this maximum value also changes. This is because in the previous location of the maximum tensile stress (exactly at $90°$), the concrete has already cracked, and its tensile behavior is in the descending part of the curve of Figure 4.

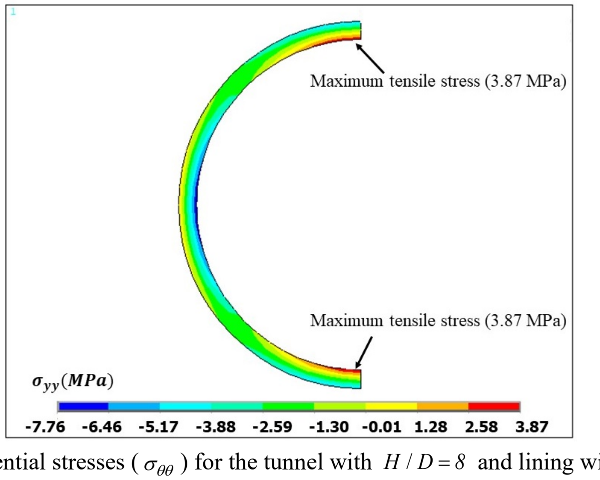

Figure 7. Circumferential stresses ($\sigma_{\theta\theta}$) for the tunnel with $H/D=8$ and lining with elastic behavior.

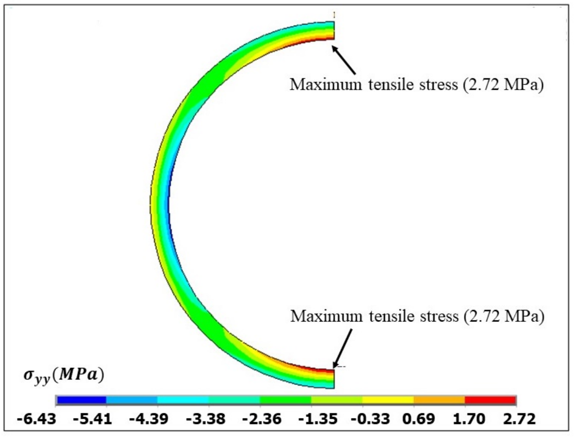

Figure 8. Circumferential stresses ($\sigma_{\theta\theta}$) for the tunnel with $H / D = 8$ and lining with viscoelastic behavior.

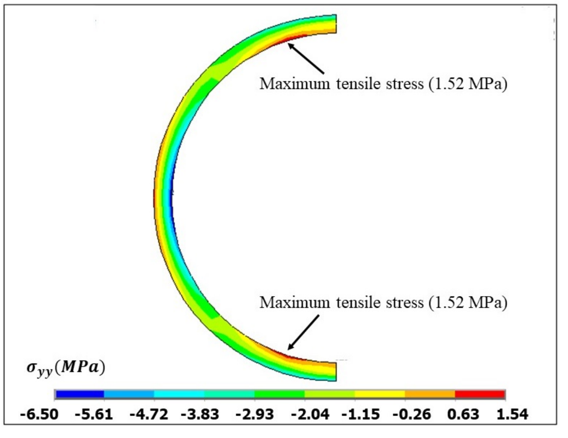

Figure 9. Circumferential stresses ($\sigma_{\theta\theta}$) for the tunnel with $H / D = 8$ and lining with viscoelastic with cracking behavior.

For better understanding the changes, Figure 10 schematically illustrates the tensile concrete behavior for a general section. First, the tensile part behaves linearly, with the maximum tensile stress at the bottom of the section. Upon reaching the concrete tensile strength and, therefore, the deformation referring to the beginning of crack formation, this stress decreases. The decline remains until it reaches the maximum deformation to consider the collaboration of concrete between cracks, equal to 0.001.

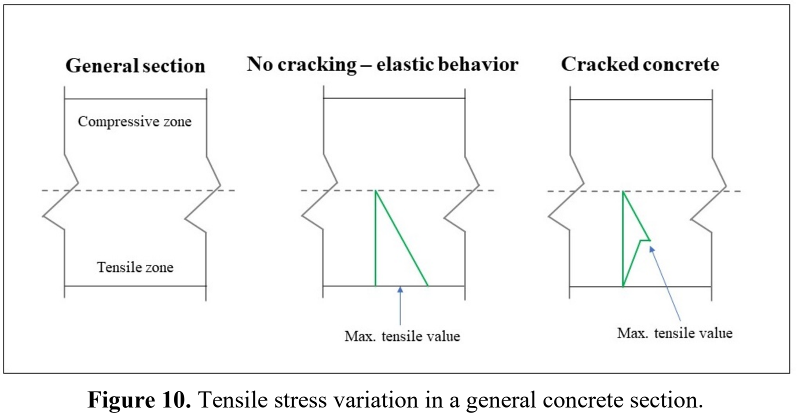

Figure 10. Tensile stress variation in a general concrete section.

In order to elucidate the difference of behavior for the tunnel with $H / D = 5$ in relation to the others, the stresses ($\sigma_{\theta\theta}$) according to the model are shown also for this example of tunnel (Figures 11, 12 and 13). From the results, it can be verified the change only from the elastic to viscoelastic model, with the stresses decreasing. Considering cracking in concrete behavior does not cause variation in stresses (there is only a residual difference). Since in this depth the tunnel is submitted to low levels of stresses, the lining does not crack.

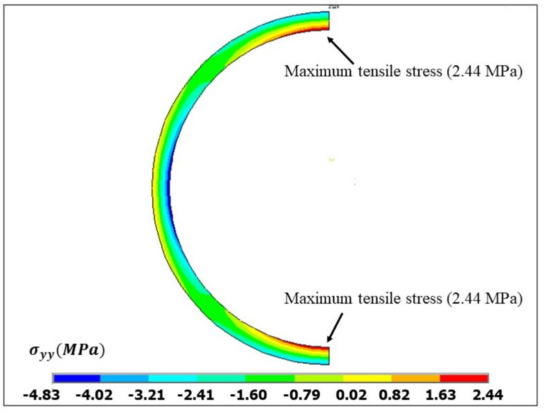

Figure 11. Circumferential stresses ($\sigma_{\theta\theta}$) for the tunnel with $H / D = 5$ and lining with elastic behavior.

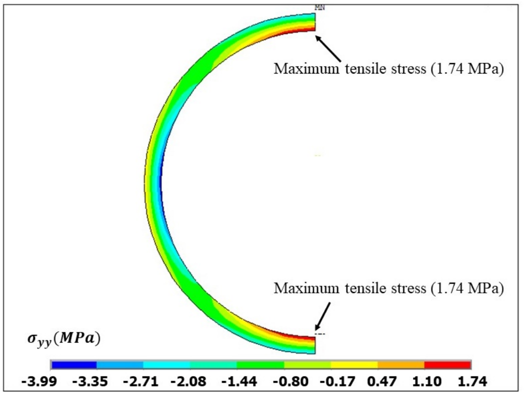

Figure 12. Circumferential stresses ($\sigma_{\theta\theta}$) for the tunnel with $H / D = 5$ and lining with viscoelastic behavior.

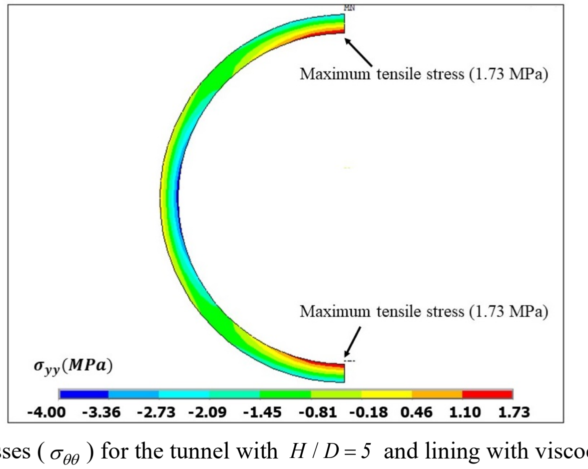

Figure 13. Circumferential stresses ($\sigma_{\theta\theta}$) for the tunnel with $H / D = 5$ and lining with viscoelastic with cracking behavior.

A simplified parametric analysis is also performed with the aim to study the influence of some parameters in the final convergence magnitude when considering the cracking in the lining model. The properties of the tunnel and the materials are the same employed in the previous simulations and shown in Table 1. The height is fixed as $16m$ and variations are applied in the following properties: the unlined length (d_0), the characteristic compressive strength of the concrete (f_{ck}) and the Young modulus of the soil mass (E_m). The results are presented in Figures 14, 15 and 16.

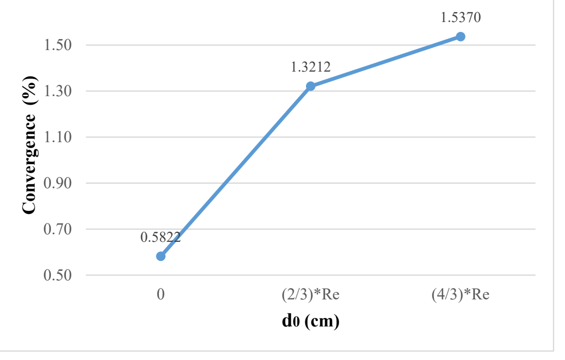

Figure 14. Variation of the final convergence according to the unlined length (d_0).

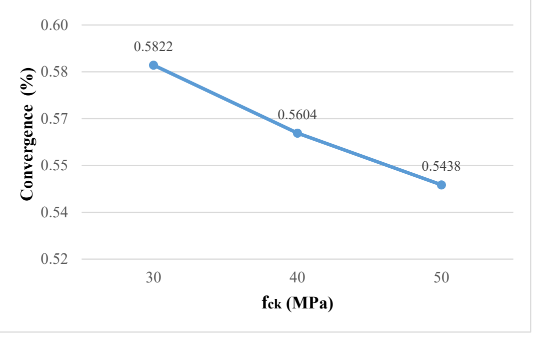

Figure 15. Variation of the final convergence according to the compressive strength of the concrete.

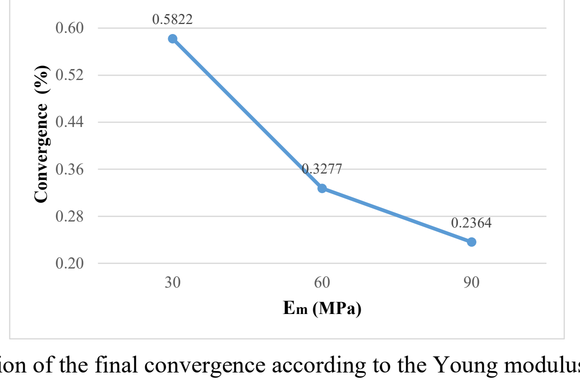

Figure 16. Variation of the final convergence according to the Young modulus of the soil mass.

As exposed by the results shown in the figures above, the convergence is greater for larger unlined lengths. This is related to the contribution of the lining to the tunnel support: the longer it takes to place the lining, the more the tunnel deforms. On the other hand, this greater strain of the soil mass implies smaller pressures acting on the lining, which attenuates the appearance of cracking.

Furthermore, the convergence values decrease when both concrete and soil mass stiffness increase. When the material is stiffer, it can support more pressure and, as a result, fewer displacements are found in the cross-section. Cracking also presents consequences: the smaller the f_{ck} , for example, the concrete tensile strength is also smaller, and, accordingly, this concrete is more propitious to crack, causing greater displacements. However, the influence of these parameters is correlated, since the relative stiffness between the soil mass and the lining also affects the stress distribution, so that the greater the concrete stiffness in comparison to the ground, the higher tensile stresses may form.

5 CONCLUSIONS

There are several peculiarities of tunnels closest to the ground surface. Among these characteristics, is the great unevenness of the stress field around the excavation and the possibility of the appearance of tensile stresses in the lining, that could induce the concrete to crack. So, the present research deals with the structural behavior of the reinforced concrete lining of shallow tunnels, with emphasis on the cracking analysis and the impact obtained on the displacement results when considering its effects.

From the results obtained, it was possible to observe that the consideration of cracking affects the behavior of reinforced concrete tunnel linings, causing larger displacements in the tunnel cross-section than those calculated considering the concrete with elastic or viscoelastic behavior. For the example with greater depth ($H/D=10$) and, therefore, submitted to larger loads, this difference reached 16.3% in one of the cross-section points, analyzing the final convergence at a point distant from the excavation face. The maximum surface settlement value was also modified by changing the model: 7.07% greater when considering cracking.

Changes in stress behavior were also demonstrated. The tunnel with $H/D=8$ shown a decrease in the maximum value of stresses by varying the concrete model. In addition, when considering cracking, the maximum stress location also changes, indicating lower stresses for the lining points with greater strains, which cracks first than others. For the tunnel with $H/D=5$, the stresses are the same regarding or not the cracking in the model, since the loads in this depth are not enough to the concrete to crack.

By setting other parameters and changing the unlined length (d_0), the characteristic compressive strength of concrete (f_{ck}) and the Young modulus of the soil mass (E_m), convergence results were higher for larger unlined lengths and smaller values of f_{ck} and E_m . It is worth noting that these influences are interdependent because, while they interfere directly in the magnitude of the displacements, they also interfere in the crack formation. Cracking, in turn, causes greater strains and, consequently, greater displacements.

ACKNOWLEDGEMENTS

The authors recognize and would like to thank the support of the Federal University of Rio Grande do Sul (UFRGS), as well as the scholarship provided by the Coordenação de Aperfeiçoamento de Pessoal de Nível Superior (CAPES).

REFERENCES

[1] ITA, "Guidelines for the design of tunnels," *Tunn. Undergr. Space Technol.*, vol. 3, no. 3, pp. 237–249, 1988., http://dx.doi.org/10.1016/0886-7798(88)90050-8.

[2] F. El-Nahhas, F. El-Kadi, and A. Ahmed, "Interaction of tunnel linings and soft ground," *Tunn. Undergr. Space Technol.*, vol. 7, no. 1, pp. 33–43, Jan 1992, http://dx.doi.org/10.1016/0886-7798(92)90111-T.

[3] F. Pinto and A. J. Whittle, "Ground movements due to shallow tunnels in soft ground. I – analytical solutions," *J. Geotech. Geoenviron*, vol. 140, no. 4, 2013, http://dx.doi.org/10.1061/(ASCE)GT.1943-5606.0000948.

[4] F. P. M. Quevedo, "Comportamento a longo prazo de túneis profundos revestidos com concreto: modelo em elementos finitos", M.S. Thesis, Dep. Eng. Civ., Univ. Fed. Rio Grande do Sul, Porto Alegre, 2017.

[5] R. J. Schmitz, "Estrutura mista aço-concreto: análise de ponte composta por vigas de alma cheia", M.S. Thesis, Dep. Eng. Civ., Univ. Fed. Rio Grande do Sul, Porto Alegre, 2017.

[6] P. Lunardi, *Design and Construction of Tunnels: Analysis of Controlled Deformations in Rock and Soils (ADECO-RS*). Milano: Springer, 2008.

[7] A. M. T. Gomes, "Túneis urbanos sujeitos a solicitações não uniformes: o túnel do Largo do Carregal na cidade do Porto", M.S. Thesis, Univ. Porto, Porto, 1998.

[8] E. C. Couto, "Um modelo tridimensional para túneis escavados em rocha reforçada por tirantes passivos", Ph.D. dissertation, Dep. Eng. Civ., Univ. Fed. Rio Grande do Sul, Porto Alegre, 2011.

[9] D. Bernaud, “Tunnels profonds dans les milieux viscoplastiques: approches expérimentale et numérique”, Ph.D. dissertation, Ec. Natl. Ponts et Chaussées, France, 1991.

[10] P. V. Fiore, D. B. Maghous, and A. Campos Fo., "A tridimensional finite element approach to model a tunnel with shotcrete and precast concrete," *Ibracon Struct. Mater. J.*, vol. 9, no. 3, pp. 403–413, Jun 2016, http://dx.doi.org/10.1590/S1983-41952016000300005.

[11] D. Bernaud and G. Rousset, "The ‘new implicit method’ for tunnel analysis," *Int. J. Numer. Anal. Methods Geomech.*, vol. 20, no. 9, pp. 673–690, 1996, http://dx.doi.org/10.1002/(SICI)1096-9853(199609)20:9<673::AID-NAG845>3.0.CO;2-9.

[12] K. J. Bakker, "Structural design of linings for bored tunnels in soft ground," *Heron*, vol. 48, no. 1, pp. 33–64, 2003.

[13] R. B. Peck, “Deep excavations and tunneling in soft ground,” in *Proc. 7th Int. Con. SMFE, State of the Art*, 1969, pp. 225-290.

[14] I. Benamar, “Étude des effets différés dans les tunnels profonds”, Ph.D. dissertation, Ec. Natl. Ponts et Chaussées, France, 1996.

[15] W. C. Ferrão, “Estudo de túneis superficiais: influência na convergência e no perfil de assentamento”, M.S. Thesis, Dep. Eng. Civ., Univ. Fed. Rio Grande do Sul, Porto Alegre, 2018.

[16] A. Mitelman and D. Elmo, "Analysis of tunnel-support interaction using an equivalent boundary beam," *Tunn. Undergr. Space Technol.*, vol. 84, pp. 218–226, 2019, http://dx.doi.org/10.1016/j.tust.2018.11.021.

[17] B. M. Jensen, “Modelagem tridimensional em elementos finitos de túneis superficiais revestidos em concreto armado”, M.S. Thesis, Dep. Eng. Civ., Univ. Fed. Rio Grande do Sul, Porto Alegre, 2019.

[18] *ANSYS Element Reference – Release 12.0*. (2009).

[19] P. M. Lazzari, “Simulação numérica das etapas construtivas de pontes estaiadas através do método dos elementos finitos”, Ph.D. dissertation, Dep. Eng. Civ., Univ. Fed. Rio Grande do Sul, Porto Alegre, 2016.

[20] F. P. M. Quevedo, R. J. Schmitz, I. B. Morsch, A. Campos Fo., and D. Bernaud, "Customization of a software of finite elements to analysis of concrete structures: long-term effects," *Ibracon Struct. Mater. J.*, vol. 11, no. 4, pp. 696–718, 2018., http://dx.doi.org/10.1590/s1983-41952018000400005.

[21] Z. P. Bazant and S. Prasannan, "Solidification theory for aging creep," *Cement Concr. Res.*, vol. 18, no. 6, pp. 923–932, 1988, http://dx.doi.org/10.1016/0008-8846(88)90028-2.

[22] Comité Euro-International du Béton, *CEB-FIP Model Code 1990*, 1993.

[23] N. S. Ottosen, "A failure criterion for concrete," *J. Eng. Mech. Div. ASCE*, vol. 103, no. 4, pp. 527–535, 1977.

[24] M. Martinelli, “Modelagem de situações de punção em lajes de concreto armado através do Método dos Elementos Finitos”, M.S. Thesis, Dep. Eng. Civ., Univ. Fed. Rio Grande do Sul, Porto Alegre, 2003.

[25] E. Hinton, *Numerical Methods and Software for Dynamic Analysis of Plates and Shells*. Swansea: Pineridge Press, 1988.

Author contributions: Conceptualization, methodology: B. M. Jensen, D. Bernaud and A. Campos Filho. Formal analysis, data curation, writing: B. M. Jensen. Supervision: D. Bernaud and A. Campos Filho.

Editors: Sérgio Hampshire de Carvalho Santos, José Luiz Antunes de Oliveira e Sousa, Guilherme Aris Parsekian.

IBRACON Structures and Materials Journal
Revista IBRACON de Estruturas e Materiais
ISSN 1983-4195 ismj.org

ORIGINAL ARTICLE

Numerical analysis on displacements of steel-fiber-reinforced concrete beams

Análise numérica da deformabilidade de vigas de concreto armado reforçado com fibras

Mateus Fereira Pontes[a]
Wanderlei Malaquias Pereira Junior[a]
José Júlio de Cerqueira Pituba[a]

[a]Universidade Federal de Catalão – UFCAT, Departamento de Engenharia Civil, Catalão, GO, Brasil

Received 19 June 2018
Accepted 15 March 2020

Abstract: This work deals with parametric analyses of the structural behaviour of steel-fiber-reinforced concrete using a Damage Constitutive Model and homogenization technique. This approach is contemporary once Brazil has not a standard procedure for the design of this type of material. The present study performs a parametric analysis of rectangular beams subjected to flexion at four points, with height variations (h), reinforcement area (As) and span (L) are used to verify the influence of each parameter on the numerical study of the deformability of beams composed by this material. Fiber volume concentrations of 2.00% and 2.50% have been used on the modelling. It is observed that the obtained results were mainly affected by height and span. It is noticeable that the inclusion of steel fibers leads to an increase in the maximum load and ductility of the analyzed beams in this work.

Keywords: steel-fiber-reinforced concrete, damage mechanics, non-linear analysis, parametric analysis.

Resumo: Este trabalho aborda uma análise numérica paramétrica do comportamento estrutural do concreto armado reforçado com fibras metálicas utilizando um modelo constitutivo de Mecânica do Dano e técnica de homogeneização. Essa abordagem ainda é recente, visto que o Brasil não possui nenhuma normatização em relação ao procedimento de cálculo desse tipo de material. O presente estudo realiza uma análise paramétrica de vigas de seção retangular submetidas à flexão em quatro pontos com variações de altura (h), área de aço (As) e o vão (L) de forma a verificar a influência de cada parâmetro no estudo numérico da deformabilidade de vigas compostas por esse material. Foram utilizados percentuais de 2,00% e 2,50% de fibras metálicas na modelagem. Observa-se que os resultados obtidos foram afetados principalmente pela altura e pelo vão da peça. Também se percebe que a inclusão de fibras proporciona aumento da carga máxima da estrutura além de promover uma boa ductilidade.

Palavras-chave: concreto reforçado com fibras de aço, mecânica do dano, análise não-linear, identificação paramétrica.

How to cite: M. F. Pontes, W. M. Pereira Junior, and J. J. C. Pituba, "Numerical analysis on displacements of steel-fiber-reinforced concrete beams," *Rev. IBRACON Estrut. Mater.*, vol. 13, no. 6, e13607, 2020, https://doi.org/10.1590/S1983-41952020000600007

1 INTRODUCTION

Concrete is one of the most used materials as a constituent of structural elements [1], [2] and due to its great importance, several numerical models are developed to simulate its mechanical behaviour [3].

In several situations there is a need for the concrete to resist tensile and bending loads, making it necessary to use longitudinal and transverse reinforcements. However, new ways of using this material have been developed, as example, the use of metallic fibers in simple and reinforced concrete. Salvador et al. [4] says that metal fibers have

Corresponding author: Wanderlei Malaquias Pereira Junior. E-mail: wanderlei_junior@ufg.br
Financial support: The authors wish to thank CNPq (National Council for Scientific and Technological Development) grant numbers 304281/2018-2 and 409970/2016-6 and FAPEG (Goias Research Foundation) grant number 201710267000521.
Conflict of interest: Nothing to declare.

been used for a long time and can be considered a kind of traditional reinforcement for concrete. Despite this, there are several technical aspects of this kind of reinforcement that still need a better study.

In Brazil, fiber reinforced concrete is still a material not so used in civil construction and it deserves more studies for understanding its behaviour. Only two Technical Standards address the theme: (a) NBR 15530 "Steel fibers for concrete - specification" [5]; and (b) NBR 8890 "Circular section concrete pipe for rainwater and sanitary sewerage systems - Requirements and test methods" [6]. Despite this national reality, in other countries this material already has great applicability in Structural Engineering, for example, in shotcrete for tunnels, earthquakes regions, slender repairs, pavements subjected to dynamic loads, in the area of structural recovery, rigid pavements subjected to cyclic loads [7]–[11] including technical standards which guide tests and design steps, such as the following codes: ACI 544.1R-96 [12], ACI 544.2R-89 [13], ACI 544.3R-93 [14], ACI 544.4R-88 [15], ACI 318 [16], RILEM TC 162-TDF [17], Model Code 2010 [18] and EN 14651 [19]. The study of this material is still an open research field, especially concerning the computational modelling line of structural parts composed of this material.

Banthia and Trottier [20] recommend the use of fibers in order to improve the mechanical properties of composite materials. Therefore, in this context, the incorporation of fibers of different natures into concrete deserves to be highlighted. However, in this work, the goal is to contribute on the understanding of the mechanical behaviour of concrete beams reinforced with steel fibers. In this context yet [21], made an analysis of the recent advances in the area of Ultra High-Performance Fiber-Reinforced Concrete (UHPFRC) leading to the conclusion that the current regulations are not valid to be used in the design of structural elements composed of this kind of material. Also Buttignol et al. [21], discusses some normative issues related to its properties, such as bending, compression, stress-strain relations, design criteria, etc. In Błaszczyński and Falek [22], the addition of short metal fibers in concrete samples subjected to uniaxial compression tests has been investigated. The experimental tests indicated that for additions of 0.50% and 3.00% there was an increasing of tension strength on the tested samples. Specifically, the control concrete with 0.00% of fibers showed a peak tension of 35.88 MPa while the samples with 3.00% of fiber reached values about 41.99 MPa. In Yoo et al. [23], concrete beams with Ultra High-Performance Concrete (UHPC) have been investigated numerically and experimentally. Beams with a fiber ratio between 0.00% (beam with control concrete) and 1.71% fibrous reinforcement were tested. It has been concluded that for steel fiber reinforced beams, an increasing in the post-peak region as well as a toughness gain have been observed.

In this context, the intention of the present work is to contribute for understanding the mechanical behaviour of steel-fiber-reinforced concrete beams the influence of a cementitious matrix and fibers in the load peak of beams. Therefore, the present work can be justified due to importance of the theme and the need of more researches about.

Regarding the investigation of the applicability of constitutive models for cracked concrete, there are several numerical tools which stand out, including the following: (a) Continuum Damage Mechanics (CDM) Models [3], [24]–[30]; (b) Concentrated Damage Model [31]–[36]; (c) Cracking distributed [37]–[40]; (c) Multi-scale models [41]; (d) Models based on failure or rupture criteria [28], [42]; and (e) Fracture models [28], [43]. On the other hand, the models can be called phenomenological models, which are intended to model the mechanical behaviour of materials based on dissipative processes which occur in the microscale. On the other hand, the so-called multiscale models have been gaining attention in recent years. In this case, the mechanical behaviour of the macroscale is a consequence of the dissipative processes of the microscale leading to a more realistic representation of the nonlinear physical behaviour of materials. This modelling is possible due to the use of homogenization techniques. However, the computational cost is still a limiting factor in some more complex analyses. Within this context, it can be cited some works that deals with concrete with fibers [44]–[46].

The constitutive damage model developed by Pituba and Fernandes [26] together with a homogenization process proposed by La Borderie [47] are used in the present work to consider the incorporation of steel fibers into the concrete. This method has already been applied and discussed initially in Pereira et al. [3].

In this paper, the model will be used to investigate the mechanical behaviour of steel-fiber-reinforced concrete (SFRC) beams focusing on the deformability aspects in order to contribute to a proposal for estimating displacements in SFRC beams in a future expansion of NBR 6118 [48] dealing with SRFC.

On the other hand, CDM is a constitutive theory that simulates the degradation of the elastic properties of the material as a cause of the cracking processes. Therefore, it is a properly theory for materials which present the cracking process as an important phenomenon of physical non-linearity, such as concrete. CDM seeks to describe a local constitutive relationship that changes the material stiffness from an early stage, considering a situation without defects, to the situation of complete damage of the Representative Volume Element (RVE).

Therefore, this work aims to contribute for understanding the mechanical behaviour of concrete with fibers and to identify parameters which support a discussion on the context of a future proposal for the standardization of this material.

This work is divided into 5 sections. In the first one, a brief introduction to the topic is presented. In section 2, the formulation of the damage model employed is briefly addressed, as well as the concepts of the proposed homogenization are presented. The presentation of the object of study of the numerical analyses ends section 2. The numerical examples are presented in section 3. Finally, sections 4 and 5 present the obtained results as well as the conclusions and suggestions for further work.

2 CONSTITUTIVE MODEL FOR CONCRETE AND CONCRETE WITH FIBERS

In this section, the necessary tools to perform the numerical analyses are presented, as well as the finite element models of the objects of study in this work. Initially, the damage model for concrete and the homogenization model are briefly addressed for the consideration of steel fibers incorporated into concrete. Then, the finite element model and the numerical analyses performed are presented.

2.1 Constitutive Damage Model

Concrete is understood here as a material that belongs to the category of initially isotropic media that starts to present transverse isotropy and bimodular response induced by damage. The formulation of the model for concrete is based on the energy equivalence principle and the formalism has been presented in Pituba and Fernandes [26]. In what follows, the proposed model is briefly described, starting with the presentation of the damage tensor for predominant states of traction, whose expression is given in the form:

$$D_T = f_1\left(D_1, D_4, D_5\right)(A \otimes A) + 2 f_2\left(D_4, D_5\right) \left[\left(A \overline{\underline{\otimes}} I + I \overline{\underline{\otimes}} A\right) - (A \otimes A)\right] \tag{1}$$

where $f_1(D_1, D_4, D_5) = D_1 - 2 f_2(D_4, D_5)$ and $f_2(D_4, D_5) = 1 - (1\text{-}D_4)(1\text{-}D_5)$.

The damage tensor has two scalar variables in its composition (D_1 and D_4) and a third damage variable D_5, activated only if there has been a previous compression with corresponding damage. The variable D_1 represents the damage in the direction perpendicular to the local plane of transversal isotropy of the material and D_4 is the variable representing the damage generated by the shear between the edges of the cracks belonging to that plane.

In Equation 1, tensor ***I*** is the second order identity tensor and tensor ***A*** is, by definition, formed by the tensor product of the versor perpendicular to the transverse isotropy plane itself. The tensor product operations between second order ***I*** and ***A*** tensors that appear in Equation 1 and that will be used throughout the formulation are described in Pituba and Fernandes [26].

For predominant states of compression, the relation for the damage tensor is proposed:

$$D_C = f_1\left(D_2, D_4, D_5\right)(A \otimes A) + f_2\left(D_3\right) \left[\left(I \overline{\otimes} I\right) - (A \otimes A)\right] + 2 f_3\left(D_4, D_5\right)\left[\left(A \overline{\underline{\otimes}} I + I \overline{\underline{\otimes}} A\right) - (A \otimes A)\right] \tag{2}$$

where $f_1(D_2, D_4, D_5) = D_2 - 2 f_3(D_4, D_5)$, $f_2(D_3) = D_3$ and $f_3(D_4, D_5) = 1 - (1\text{-}D_4)(1\text{-}D_5)$.

There are three scalar variables in its composition: D_2, D_3, and D_5, in addition to D_4, related to pre-existing traction effects. The variable D_2 (damage perpendicular to the local plane of transversal isotropy of the material) penalizes the elastic modulus in this direction, and together with D_3 (representative of damage in the transversal isotropy plane) penalizes the Poisson's ratio in planes perpendicular to the transversal isotropy one.

Finally, the resulting constitutive tensors are described by:

$$E_T = \lambda_{11}\left[I \otimes I\right] + 2\mu_1\left[I \overline{\underline{\otimes}} I\right] - \lambda_{22}^{+}(D_1, D_4, D_5)\left[A \otimes A\right] - \lambda_{12}^{+}(D_1)\left[\mathbf{A} \otimes \mathbf{I} + \mathbf{I} \otimes \mathbf{A}\right] - \mu_2(D_4, D_5)\left[A \overline{\underline{\otimes}} I + I \overline{\underline{\otimes}} A\right] \tag{3}$$

$$E_C = \lambda_{11}[I \otimes I] + 2\mu_1[I \underline{\overline{\otimes}} I] - \lambda_{22}^{-}(D_2, D_3, D_4, D_5) - \lambda_{12}^{-}(D_2, D_3)$$
$$[\mathbf{A} \otimes \mathbf{I} + \mathbf{I} \otimes \mathbf{A}] - \lambda_{11}^{-}(D_3)[\mathbf{I} \otimes \mathbf{I}] - \frac{(1-2\nu_0)}{\nu_0}\lambda_{11}^{-}(D_3)[\mathbf{I} \otimes \mathbf{I}] - \mu_2(D_4, D_5)[A \underline{\overline{\otimes}} I + I \underline{\overline{\otimes}} A] \tag{4}$$

where $\lambda_{11} = \lambda_0$ and $\mu_1 = \mu_0$. The other parameters exist only for non-zero damage, thus showing the anisotropy and bimodularity induced by the damage, and are defined by:

$$\lambda_{22}^{+}(D_1, D_4, D_5) = (\lambda_0 + 2\mu_0)\left(2D_1 - D_1^2\right) - 2\lambda_{12}^{+}(D_1) - 2\mu_2(D_4, D_5) \quad \lambda_{12}^{+}(D_1) = \lambda_0 D_1;$$
$$\mu_2(D_4, D_5) = 2\mu_0[1 - (1-D_4)^2\left(1-D_5\right)^2\Big] + \frac{(\nu_0 - 1)}{\nu_0}\lambda_{11}^{-}(D_3) - 2\mu_2(D_4, D_5) \tag{5}$$

$$\lambda_{12}^{-}(D_2, D_3) = \lambda_0\Big[\left(1-D_3\right)^2 - \left(1-D_2\right)\left(1-D_3\right)\Big] \; \lambda_{11}^{-}(D_3) = \lambda_0\left(2D_3 - D_3^2\right); \; \mu_2(D_4, D_5) = 2\mu_0[1-(1-D_4)^2\left(1-D_5\right)^2\Big] \tag{6}$$

Moreover, Pituba and Fernandes [26] defines a hypersurface in the space of stresses or deformations. This hypersurface is used as a criterion for the identification of the constitutive responses of compression or tension. In this model, a particular shape is adopted for the hypersurface in the deformation space: a hyperplane g(ε), characterized by its unitary normal N (||N|| = 1). For this model, the following relation is valid:

$$g(\mathbf{e}, \mathbf{D_T}, \mathbf{D_C}) = \mathbf{N}\left(\mathbf{D_T}, \mathbf{D_C}\right).\mathbf{e_e} = g_1(D_1, D_2)\varepsilon_V^e + g_2(D_1, D_2)\varepsilon_{11}^e \tag{7}$$

where $\gamma_1(D_1,D_2)=\{1+H(D_2)[H(D_1)-1]\}\eta(D_1)+\{1+H(D_1)[H(D_2)-1]\}\eta(D_2)$ and $\gamma_2(D_1,D_2) = D_1+D_2$.

The Heaveside functions employed in the last relation are given by:

$$H(Di) = 1 \text{ for } Di > 0;\ H(Di) = 0 \text{ for } Di = 0 \ (i = 1,\ 2) \tag{8}$$

The functions $\eta(D_1)$ and $\eta(D_2)$ are defined, respectively, for traction cases, assuming that there is no prior damage to compression, and compression, assuming that there was no prior damage to traction.

$$\eta(D_1) = \frac{-D_1 + \sqrt{3 - 2D_1^2}}{3}; \quad \eta(D_2) = \frac{-D_2 + \sqrt{3 - 2D_2^2}}{3} \tag{9}$$

Regarding the damage criterion, it is convenient to separate it into a criterion for the beginning of damage, when the material is no longer isotropic; and criteria for loading and unloading, being understood here in the sense of evolution or not of the damage variables when the material is already presented as transversely isotropic.

The criterion for initial damage processes activation in tension or compression is given by:

$$f_{T,C}(s) = W_e^* - Y_{0T,0C} < 0 \tag{10}$$

where W_e^* is the complementary elastic deformation energy considering the initially intact, isotropic and purely elastic environment and $Y_{0T} = \frac{\sigma_{0T}^2}{2E_0}$ ou $Y_{0C} = \frac{\sigma_{0C}^2}{2E_0}$ is a reference value obtained from uniaxial tensile or compression tests, respectively, where σ_{0T} and σ_{0C} stresses of the elastic limits.

Therefore, D_T=0 (that is, D_1=D_4=0) for predominant states of traction or $D_C=0$ (that is, $D_2=D_3=D_5=0$) for compression states, where the material response regime is linear elastic and isotropic.

For $g(\varepsilon, D_T, D_C) > 0$, the complementary elastic energy of the damaged environment is given by the relation:

$$W_{e+}^{*} = \frac{\sigma_{11}^{2}}{2E_0(1-D_1)^2} + \frac{\left(\sigma_{22}^{2}+\sigma_{33}^{2}\right)}{2E_0} - \frac{\nu_0\left(\sigma_{11}\sigma_{22}+\sigma_{11}\sigma_{33}\right)}{E_0\left(1-D_1\right)} - \frac{\nu_0\sigma_{22}\sigma_{33}}{E_0} + \frac{\left(1+\nu_0\right)}{E_0(1-D_4)^2(1-D_5)^2}\left(\sigma_{12}^{2}+\sigma_{13}^{2}\right) + \frac{\left(1+\nu_0\right)}{E_0}\sigma_{23}^{2} \tag{11}$$

On the other hand, for predominant states of compression ($g(\varepsilon, D_T, D_C) < 0$), the complementary elastic energy is expressed by:

$$W_{e-}^{*} = \frac{\sigma_{11}^{2}}{2E_0(1-D_2)^2} + \frac{(\sigma_{22}^{2}+\sigma_{33}^{2})}{2E_0(1-D_3)^2} - \frac{\nu_0(\sigma_{11}\sigma_{22}+\sigma_{11}\sigma_{33})}{E_0(1-D_2)(1-D_3)} - \frac{\nu_0\sigma_{22}\sigma_{33}}{E_0(1-D_3)^2} + \frac{(1+\nu_0)}{E_0(1-D_4)^2(1-D_5)^2}(\sigma_{12}^{2}+\sigma_{13}^{2}) + \frac{(1+\nu_0)}{E_0}\sigma_{23}^{2} \tag{12}$$

Considering, then, a general situation of a damaged medium in a predominant traction regime, the damage increases identification criterion is represented by the following relation:

$$f_T\left(\sigma\right) = W_{e+}^{*} - Y_{0T}^{*} \leq 0 \tag{13}$$

Where the reference value Y_{0T}^* is defined by the maximum complementary elastic energy determined during the damage process up to the current state. For the damaged medium in a predominant compression regime, analogous relationships to the case of traction are valid.

In cases where loading is configured, that is, where $D_T \neq 0$ and/or $D_C \neq 0$, it is necessary to update the values of the damage scalar variables that appear in the D_T and D_C, tensors, considering their evolution laws.

Limiting the analysis to the case of increasing monotonic loading and uniaxial version of the model, the proposed laws of evolution for scalar damage variables are the result of adjustments on experimental results. The general form proposed is:

$$D_i = 1 - \frac{1+A_i}{A_i + \exp\left[B_i(Y_i - Y_{0i})\right]} \qquad \text{with } i = 1,\ 2 \tag{14}$$

Where Ai, Bi, and $Y0i$ are parameters to be identified. The parameters Y0i are understood as initial limits for the activation of the damage, the same used in Equation 10.

There is still a need to define the location of the material local plane of transversal isotropy, therefore, the following statement is accepted as valid: “In the space of the main deformations, if two of the three deformation rates are elongation, shortening or null, the plane defined by them will be the material local plane of transversal isotropy.”

Both in the case of uniaxial traction and uniaxial compression, it turns out that the transverse isotropy plane is perpendicular to the direction of the tension or compression stress.

This one-dimensional version of the model was implemented in a finite element code for the analysis of bar structures with layered finite elements. For concrete, the damage model is valid, and for longitudinal reinforcement bars, an elastoplastic behaviour is admitted. In the discretized reinforced concrete cross section, a certain layer may contain steel and concrete. The related layer contains an equivalent elastic modulus and an equivalent inelastic deformation, using the homogenization rule.

On the other hand, adopting direction 1 as the longitudinal direction of the bar, the model relationships in its one-dimensional version are summarized below and they are implemented in the computational code described in item 3.

$$E := \begin{cases} E_C & \text{if} \quad g(\varepsilon, D_T, D_C) < 0, \\ E_T & \text{if} \quad g(\varepsilon, D_T, D_C) > 0, \end{cases} \tag{15}$$

$$E_T = E_0(1-D_1)^2(1-D_2)^2 \tag{16}$$

$$E_C = E_0(1-D_2)^2 \tag{17}$$

$$W_{e+}^* = \frac{\sigma_{11}^2}{2E_0(1-D_1)^2(1-D_2)^2}\ ;\ W_{e-}^* = \frac{\sigma_{11}^2}{2E_0(1-D_2)^2} \tag{18}$$

$$Y_T = \frac{\partial W_{e+}^*}{\partial D_1} = Y_1; \quad Y_C = \frac{\partial W_{e-}^*}{\partial D_2} = Y_2 \tag{19}$$

$$Y_1 = \frac{\sigma_{11}^2}{E_0(1-D_1)^3(1-D_2)^2}\ ;\ Y_2 = \frac{\sigma_{11}^2}{E_0(1-D_2)^3} \tag{20}$$

2.2 Mechanical behaviour of fibers and the homogenization model for considering steel fibers

The crack evolution process in concrete or any other brittle material occurs because of changing the tension lines and, consequently, the accumulation of stress in the crack tip region. The addition of steel fibers mitigates this effect, as they act as a transfer bridge for internal stresses in the solid leading to a reduced stress concentration at the crack tip and, consequently, the crack propagation speed.

Throughout the loading process due to the increasing of the load level, the debonding process between fiber and matrix takes place leading to changes of the internal forces transfer mechanics by adhesion to friction. These changes occur when the tangential stresses at the interface of the materials exceed its adhesion strength promoting sliding between the faces. This debonding process causes relative displacements between fiber and matrix (see Figure 1).

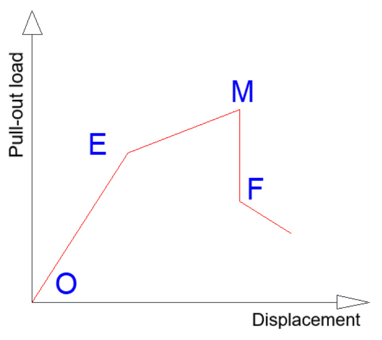

Figure 1. Experimental mechanical behaviour of the fiber/matrix interface behaviour (adapted from Bartos [49]).

In Figure 1, the OE section characterizes all the stress transfers due to adhesion which occur between fiber and concrete, i. e., the displacement of the fiber/matrix interface. At certain loading level, the debonding process represented by EM section is initiated. In this last stage, the process incorporates frictional stresses due to the sliding of the fiber until to the complete debonding represented by MF section. From the F point, the presence of the friction transfer mechanism is remarkable leading to the gradual strength decreasing until the complete pull-out of the steel fiber from the matrix.

A complete analysis of the behaviour should consider the various phenomena related to the mechanical behaviour of the fibers, concrete, and interface. According to La Borderie [47], there are no difficulties in modelling the mechanical behaviour of fibers or concrete. However, the behaviour of the fiber/concrete interface is different from the isolated behaviour of the fiber or concrete.

[47] focused his study on the behaviour of the interface evidenced in pull-out tests of steel fibers from a cementitious matrix. From the observations of the test results, the proposal for uniaxial modelling of the homogenization of the fiber/cement matrix interface behaviour is shown in Figure 2. This proposal was implemented in the finite element code used in Pereira et al. [3].

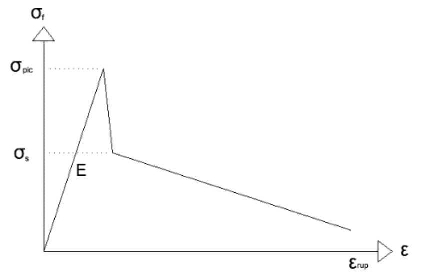

Figure 2. Model for the fiber/matrix interface behaviour (La Borderie [47]).

Figure 2 shows the parameters peak stress (σ_{pic}), post-peak residual stress (σ_s) and limit strain (ε_{rupt}) proposed to represent the fiber/matrix interface behaviour.

On the other hand, using Voigt's kinematic homogenization method [47], proposed the following expression to obtain the homogenized stress:

$$\sigma_{SFRC} = (1 - C).\sigma_m + C.\sigma_f \tag{21}$$

Where: σ_{SFRC}: the homogenized material stress; C: steel fibers concentration; σ_m: cementitious matrix stress; σ_f: Stress at the fiber/matrix interface.

In Equation 21, the cementitious matrix stress σ_m is the result of applying the damage model to the existing concrete in the layers of finite elements, whereas the stress σ_f is obtained by applying the model proposed by [47] considering that in the given layer there are fibers immersed in the concrete, this model showed in Figure 2. Finally, applying the homogenization model given by Equation 21, the homogenized material (fibers and concrete) stress for the given layer is obtained.

It is observed that a simplifying hypothesis was introduced: the deformation is assumed to be identical for the matrix and interface. Besides, the fiber orientation, that is random and not aligned to the load direction, is not considered in the proposed modelling. However, for the purposes of this work, it is believed that such limitations have little interference in the numerical results of the concrete structures modelling as the analyses performed are in one-dimensional version.

3 FINITE ELEMENT MODEL

This item describes the finite element models of beams used to verify the influence of structural element parameters such as height (*h*), span (*L*) and the longitudinal reinforcement area (*As*) on the estimative of displacements.

The one-dimensional version of the damage model is implemented in a computational code written in FORTRAN language based on the Finite Element Method for the analysis of layered bar elements. The hypothesis of non-consideration of the distortion deformation is assumed [3]. The mechanical behaviour of the concrete layers is governed by the damage model [26], while the reinforcement inside any layer is governed by a classic bilinear elastoplastic model. If the concrete layer contains fibers (layer characterized as SFRC), the homogenization model proposed by La Borderie [47] is used. Perfect bond between the different materials is assumed with an equivalent longitudinal elastic module and an equivalent inelastic deformation for each layer. For details, see [3], [24]–[26].

The results obtained in this work are based on numerical tests of beams with a rectangular section, where the focus is the analysis of the deformability considering the behaviour of the load versus displacement relationships aiming to contribute to estimate percentages of reduction and/or expansion of the loads and displacements caused by the variation of the geometric parameters of the SFRC beams. The procedure consists in changing parameters of the structural element such as: height (h), span (L) and the longitudinal reinforcement area (As).

The experimental model developed in Lopes [50] has been taken as a reference model for the present work. The initial data of the constitutive models are the same obtained in Pereira et al. [3]. It is important to note that the proposed modelling was used in Pereira et al. [3] to simulate the experimental behaviour obtained by Lopes [50]. Therefore, the modelling of the reference model was validated by Pereira et al. [3] as well as the parametric identifications of the damage and homogenization models. In the present work, the proposed modelling is used varying the geometric parameters of the analysed beams.

First of all, Figure 3 shows the structural model of the reference beam, when $L = 200.00$ cm, $Lc = 70.00$ cm, $b_w = 12.50$ cm, $h = 25.00$ cm and $A_s = 4.022$ cm^2. However, these parameters will be varied during the analyses. On the other hand, Figure 4 illustrates the adopted finite element model with 50 finite bar elements and the cross section discretized into 25 layers. In the work [3], a mesh objectivity study was performed, but the finite model does not need finer meshes. Also, the computational cost is considerably low for performing numerical analyses. The reinforcement bars are indicated in Figure 4.

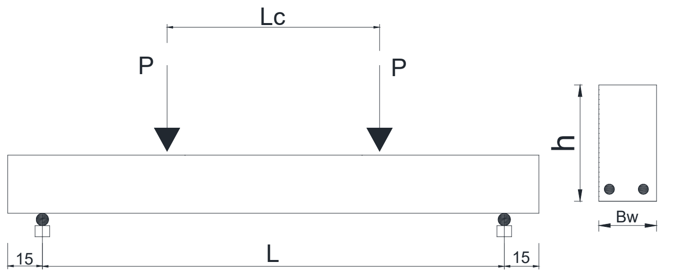

Figure 3. Structural model of the beam proposed for the numerical simulations.

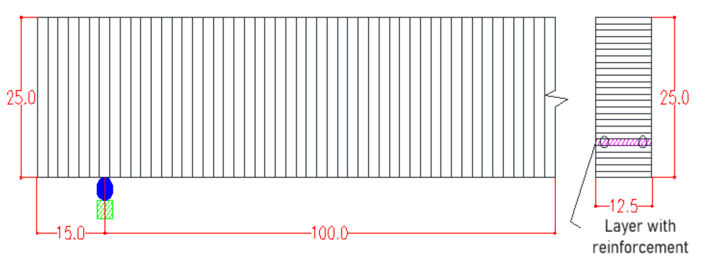

Figure 4. Proposal of finite element mesh for numerical simulations.

Tables 1 and 2 present the values for parameters of the damage and homogenization models considering metallic fibers. The longitudinal reinforcement is CA-50 and its mechanical properties can be seen in Table 3. The results in Tables 1 and 2 have been obtained through retro analysis of four points bending tests performed by Lopes [50] in 100 mm x 100 mm x 400 mm specimens with free span of 300 mm. For details, see Pereira et al. [3].

Table 1. Parameters for the damage model proposed in Pituba and Fernandes [26].

E (MPa)	A_t	A_c	B_t *(MPa^{-1})*	B_c *(MPa^{-1})*	Y_{0t} *(MPa)*	Y_{0c} *(MPa)*	β_t	β_c
31900	15	0.70	1290	2.50	0.000086	0.00455	0.00000045	0.000030

Table 2. Variables of the homogenization model proposed by La Borderie [47] for the consideration of metallic fibers.

Fiber volume percentage V_f (%)	Peak Stress (MPa)	Yield stress (MPa)	Ultimate strain (m/m)
2.00	525.00	420.00	0.025
2.50	550.00	440.00	0.025

Table 3. Parameters values of the elastoplastic model for CA-50 steel for reinforcement.

Model properties	Value	Unit
Young's Modulus	210.000,00	MPa
Yield strength	500,00	MPa
Peak stress	550,00	MPa
Specific mass	7850,00	kg/m^3
Ultimate strain	1,00	%

Note that the numerical analyses have been performed in [24]–[26], [3] validating the use of the proposed damage and homogenization models. On the other hand, the geometric characteristics of the finite element models used in this work are shown in Tables 4 to 6. Considering the “zero” situation as the reference model illustrated in Figure 3, the sequence used in this work is described as follows: (*i*) Height variation (*h*) (Table 4); (*ii*) Variation of the reinforcement area (*As*) (Table 5); and (*iii*) Free span variation (*L*) (Table 6), respectively.

Table 4. Height variation proposal (*h*).

Test	h (cm)	b (cm)	L (cm)	As (cm^2)	h/b
h0	25.00	12.50	230	4.022	2.00
h1	26.25	12.50	230	4.022	2.10
h2	28.13	12.50	230	4.022	2.25
h3	31.25	12.50	230	4.022	2.50
h4	34.38	12.50	230	4.022	2.75
h5	37.50	12.50	230	4.022	3.00

The reinforcement reductions (As) are between 10.00% and 50.00% of the initial value given in the reference model.

Table 5. Proposed variation for the reinforcement area (A_s).

Test	h (cm)	b (cm)	L (cm)	As (cm^2)	Reinforced area reduction (%)
as0	25.00	12.50	230.00	4.02	-
as1	25.00	12.50	230.00	3.62	10%
as2	25.00	12.50	230.00	3.22	20%
as3	25.00	12.50	230.00	2.82	30%
as4	25.00	12.50	230.00	2.41	40%
as5	25.00	12.50	230.00	2.01	50%

Test 3 is performed changing the free span (L) of the beam. As mentioned in and Pereira and Pituba [51], it is important to note that in this simulation the distance between the bending loads at 4 points was always maintained in a range close to *L/3* ensuring that the test always has the same pattern as the previous ones. This procedure allows the comparison of load versus displacement to be done properly. The reinforcement area is kept constant at $As = 4.022\ cm^2$.

Table 6. Span variation proposal (*L*).

Test	*h* (cm)	*bw* (cm)	*L* (cm)	*As* (cm^2)	Reinforcement area reduction (%)	1st load position (cm)	Distance between loads (cm)
L0	25.00	12.50	230.00	200.00	4.022	80.00	70.00
L1	26.25	12.50	280.00	250.00	4.022	97.50	85.00
L2	25.13	12.50	330.00	300.00	4.022	115.00	100.00
L3	31.25	12.50	380.00	350.00	4.022	130.00	120.00
L4	34.38	12.50	430.00	400.00	4.022	147.50	135.00
L5	37.50	12.50	480.00	450.00	4.022	165.00	150.00

The analyses are based on the verification of load versus displacement curves of the numerical models generated by the finite element code. two volumetric fibers concentrations of 2.00% and 2.50% are used. Note that the numerical analyses are performed using displacement control taking the node localized in the middle span as reference. Therefore, the load versus displacement graphs presented in this work characterize the loading P + P (represented in Figure 3) and the displacement in the middle of the beam span.

4 RESULTS AND DISCUSSIONS

In this section, the results of numerical simulations are presented. These results intend to compare the simulations for 2.00% and 2.50% of fiber volume. The results will be presented in the following sequence: (*i*) height variation (*h*);

(*ii*) reinforcement area variation (*As*); and (*iii*) span length variation (*L*). Note that in Figures 5, 6 and 7, the curves on the left axis referring to tests with 2.50% of fiber volume and on the right axis the curves referring to tests with 2.00% of fiber volume.

The first simulation compares the obtained results for the beam with volumes of steel fibers of 2.00% and 2.50% considering height variation (*h*) of the beams. The results are presented in Figure 5.

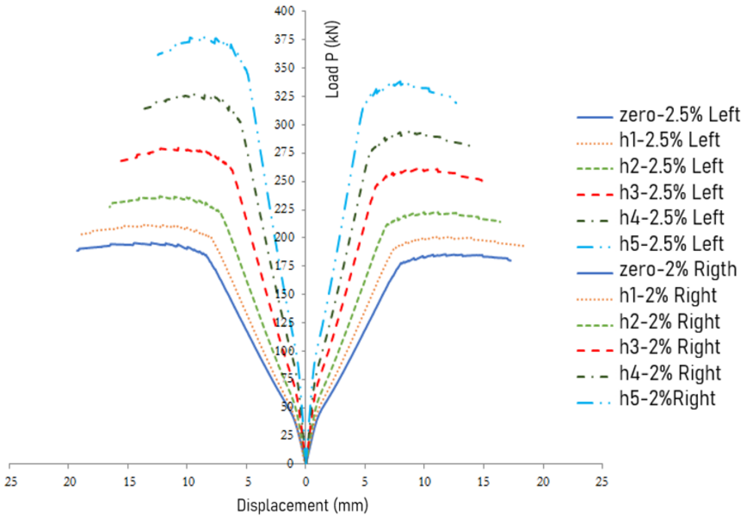

Figure 5. Load-displacement in the middle of the span for height variation (Table 4).

Observe that the gains in strength and stiffness have been evidenced for height increases in both situations (for 2.00% and 2.50% of fiber volume). It is possible to note that the height increasing leads to a gain of mechanical strength since from the region of the Serviceability Limit State (SLR) to the collapse regime of the beam. For a concentration of 2.00% of fibers, the increase in the ultimate load of the structure for the case h5 is up to 81.56% when compared to the h0 case (the reference model). For 2.50% of fiber volume, the increase is up to 93.31%. For details, Table 7 presents the total gain in each performed test. Besides, it is possible to note that when h4 and h5 tests are compared, the gains are about 7.00% and 12.00% for 2.00% and 2.50% of fiber volume cases, respectively.

Table 7. Maximum loads and loads in the SLS for tests with height variation (*h*).

Test	Maximum load (kN)	SLS Load (kN)	Increasing of SLS load (kN)	Increasing of SLS load (%)
h0-2.0%	186.17	74.46	----	----
h1-2.0%	200.42	80.16	14.25	7.66%
h2-2.0%	223.02	89.20	36.85	19.79%
h3-2.0%	262.35	104.94	76.18	40.92%
h4-2.0%	294.47	117.79	108.30	58.18%
h5-2.0%	338.00	135.20	151.83	81.56%
h0-2.5%	195.38	78.15	----	----
h1-2.5%	211.38	84.55	15.99	8.19%
h2-2.5%	236.59	94.63	41.21	21.10%
h3-2.5%	280.67	112.26	85.29	43.65%
h4-2.5%	327.76	131.10	132.38	67.76%
h5-2.5%	377.69	151.07	182.31	93.31%

In order to capture the contribution of steel fibers to the ultimate load of the analysed beams, Table 7 compares the situations h0-2.0% and h0-2.5%. For these situations it is possible to note that only the change in fiber volume represents an increasing of 9.21 kN on the ultimate load. Regarding h5-2.0% and h5-2.5%, there is an increase of 39.69 kN. If the two strength gains previously mentioned are compared, there is a total of 30.48 kN for an increasing in section height from 25 cm (case h0) to 37.50 cm (case h5). It can be concluded that the increasing in fiber volume leads to a higher strength gain for high values for h/b ratio.

Table 8 presents the comparison of the load according to specific displacement measurement points in order to evaluate the load versus displacement behaviour. For theses analyses, it has been investigated the states of the beams for 4 mm, 8 mm and 12 mm displacement cases.

Table 8. Comparative study about load versus displacement for 4, 8 and 12 mm for all simulations with height variation (*h*).

Test	Load at 4 mm (kN)	Load at 8 mm (kN)	Load at 12 mm (kN)
h0-2.0%	99.50	178.42	185.24
h1-2.0%	112.76	193.42	199.72
h2-2.0%	134.86	217.36	221.62
h3-2.0%	177.09	258.02	258.18
h4-2.0%	214.35	290.77	285.80
h5-2.0%	269.41	334.93	324.97
h0-2.5%	97.68	177.79	193.73
h1-2.5%	111.30	199.52	211.06
h2-2.5%	133.98	226.77	235.82
h3-2.5%	177.59	274.22	279.33
h4-2.5%	228.45	324.22	321.53
h5-2.5%	288.17	374.58	363.91

Looking at Table 8, it is possible to state that for the cases of h0-2.0% and h0-2.5%, in a displacement of 12 mm, the higher fiber volume implies an increasing in the corresponding load of 8.49 kN (185.24 kN to 193.73 kN) equivalent to an increasing of 4.58%. This gain is more evident in the comparison of cases h5-2.0% and h5-2.5% in the displacement of 12 mm, with 38.94 kN (an increase of 11.98%). Therefore, it can be concluded that in situations with more damaged states, the greater will be the contribution of the reinforcement and steel fiber set to the stiffness of the structural element.

The second simulation compares the obtained results for beams with fiber volumes of 2.00% and 2.50% considering a reinforcement variation. As previously mentioned, this simulation shows reductions in the original reinforcement. Figure 6 presents the results for such simulation.

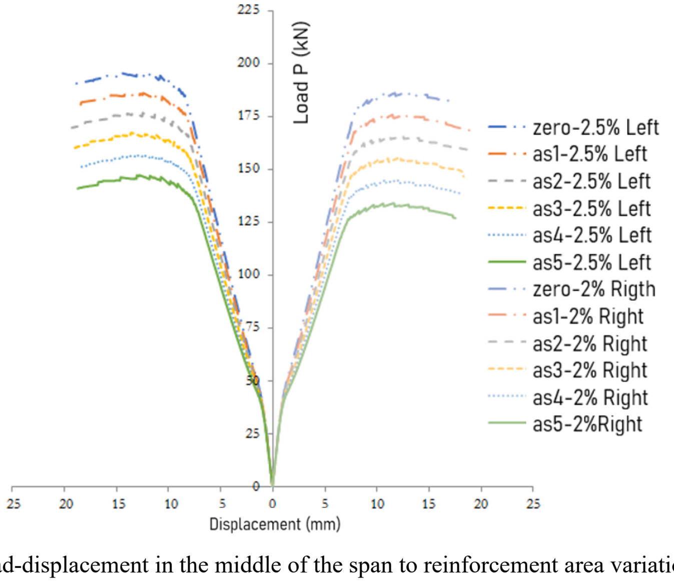

Figure 6. Load-displacement in the middle of the span to reinforcement area variation(Table 5).

As expected, as the total area of the longitudinal reinforcement is reduced, the peak load of the structural element is reduced. However, it is worth mentioning that between the as0 and the as5 tests with 50.00% decreasing in the reinforcement, it is observed that in none of the scenarios there was a load reduction more than 28.00% within the analyses for the same fiber volume showing the effective role of steel fibers on the structural element. Besides, it is observed a reduction in the load of 4.66 kN (load in the SLS) regarding to the test as4-2.50% for the test as4 -2.00%. For more details, Table 9 presents each test performed and comparative analyses of the variations of the steel fibers concentrations.

Table 9. Maximum loads and loads in the SLS for the tests with reinforcement area variation (*As*).

Test	Maximum load (kN)	SLS load (kN)	Decreased load on SLS (kN)	Decreased load on SLS (%)
as0-2.0%	186.17	74.46	----	----
as1-2.0%	176.34	70.53	3.93	5.28%
as2-2.0%	165.71	66.28	8.18	10.99%
as3-2.0%	155.75	62.30	12.16	16.34%
as4-2.0%	144.96	57.98	16.48	22.14%
as5-2.0%	134.21	53.68	20.78	27.91%
as0-2.5%	195.38	78.15	----	----
as1-2.5%	185.89	74.35	3.79	4.86%
as2-2.5%	176.47	70.58	7.56	9.68%
as3-2.5%	167.13	66.85	11.30	14.46%
as4-2.5%	156.62	62.64	15.50	19.84%
as5-2.5%	147.19	58.87	19.27	24.66%

Table 10 presents a comparative study of loads according to points of displacement measurements. For theses analyses, it has been investigated the states of the beams for 4 mm, 8 mm and 12 mm displacement cases.

Table 10. Comparative study about load versus displacement for 4, 8 and 12 mm for all simulations with reinforcement area variation (*As*).

Test	Load at 4 mm (kN)	Load at 8 mm (kN)	Load at 12 mm (kN)
as0-2.0%	99.50	178.43	185.24
as1-2.0%	95.60	168.76	175.06
as2-2.0%	91.65	158.40	165.16
as3-2.0%	87.61	148.68	155.35
as4-2.0%	83.31	139.58	144.67
as5-2.0%	78.91	129.15	132.97
as0-2.5%	97.68	177.79	193.73
as1-2.5%	94.28	170.35	184.85
as2-2.5%	90.80	163.88	175.36
as3-2.5%	87.28	156.24	166.13
as4-2.5%	83.44	146.81	155.95
as5-2.5%	79.60	137.37	145.77

As previously mentioned, it is possible to observe that the steel fibers have influenced the nonlinear behaviour of the structural element not allowing that a reduction in the reinforcement rate would lead to a massive impact on the ultimate load value. It can be seen that in the 8 mm displacement situation, in cases of loading with as5-2.50% to as5-2.00% there was a total reduction in the maximum load value of 8.22 kN (137.37 kN to 129.15 kN), i. e., just a reduction of 5.98%. Obviously, the focus in this work is the use of simplified models to practical applicability [27], but to study the non-linear aspect of the performed analyses in more details, two and three-dimensional analyses with more complex damage models have to be applied in order to better understand the dissipative phenomena involved.

The third simulation compares the results obtained for the beam with steel fiber volumes of 2.00% and 2.50% considering a span variation. Each simulation has an increasing of 50 cm in the effective span as shown in Table 6. Figure 7 presents the results for such simulation.

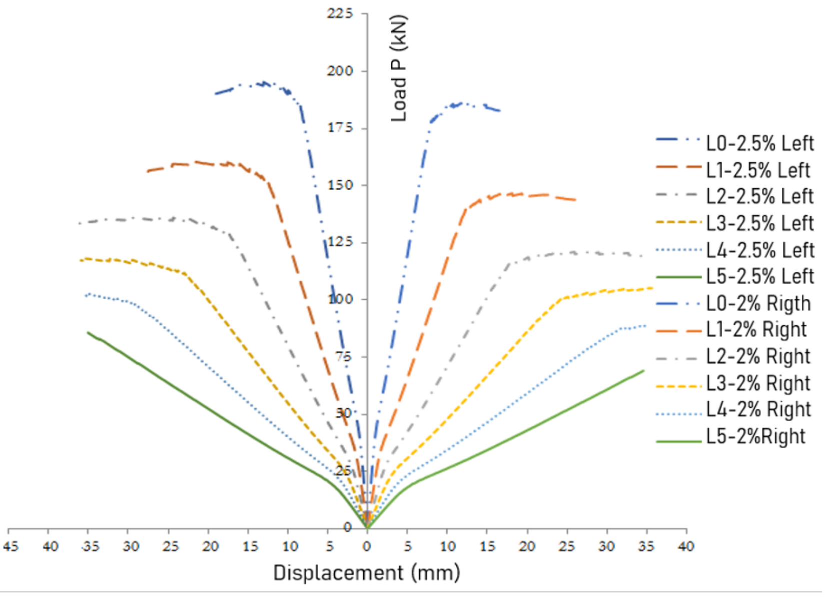

Figure 7. Load-displacement in the middle of the span to span length variation (Table 6).

For the L5 standard test, there is an increasing of approximately 24.00% in the peak load comparing L5-2.00% to L5-2.50%. Table 11 presents all tests.

Table 11. Maximum loads and loads in the SLS for tests with span length variation (*L*).

Test	Maximum load (kN)	SLS load (kN)	Decreased load on SLS (kN)	Decreased load on SLS (%)
L0-2.0%	186.17	74.47	----	----
L1-2.0%	146.66	58.66	15.81	21.23%
L2-2.0%	121.03	48.41	26.06	34.99%
L3-2.0%	105.20	42.08	32.39	43.49%
L4-2.0%	88.84	35.54	38.93	52.28%
L5-2.0%	69.01	27.61	46.86	62.93%
L0-2.5%	195.38	78.15	----	----
L1-2.5%	160.51	64.20	13.95	17.85%
L2-2.5%	136.17	54.47	23.68	30.30%
L3-2.5%	118.27	47.31	30.85	39.47%
L4-2.5%	102.66	41.06	37.09	47.46%
L5-2.5%	85.71	34.28	43.87	56.13%

It is possible to verify that the simulations L1-2.00% and L1-2.50% have a difference of 13.85 kN representing a reduction of 8.63% in the load value (160.51 kN to 146.66 kN). For the L5-2.00% and L5-2.50% simulations, this difference reached 19.48%. When the results of span reduction (*L*) are compared with the results of reinforcement reduction (*As*), it is noted that the span reduction (*L*) is always preponderant concerning to the reinforcement area (*As*) because in the simulations L5 the reductions reach values higher than 56.00% while the reduction of the reinforcement provides a decreasing in load in the SLS lower than 28.00%.

Table 12 shows the comparative study of the load decreasing as a function of displacement measurement points. For theses analyses, it has been investigated the states of the beams for 4 mm, 8 mm and 12 mm displacement cases.

In Table 12, it is possible to notice that the load reductions are approximately 39.44 kN for a displacement of 4 mm regarding to reference test 1 (2.0% of fiber volume) when compared to reference test 0 (2.0% of fiber volume). For the same tests with 2.5% of fiber volume, the reduction is about 38.33 kN. Table 13 shows the load reductions compared to the reference zero model.

Table 12. Comparative study about load versus displacement for 4, 8 and 12 mm for all simulations with variation of the effective span length (L).

Test	Load at 4 mm (kN)	Load at 8 mm (kN)	Load at 12 mm (kN)
L0-2.0%	95.50	178.43	185.24
L1-2.0%	56.06	97.02	136.98
L2-2.0%	37.27	59.32	83.2
L3-2.0%	27.52	40.8	55.36
L4-2.0%	20.57	30.03	39.18
L5-2.0%	15.35	23.32	29.5
L0-2.5%	97.68	177.79	193.73
L1-2.5%	59.35	103.65	147.09
L2-2.5%	40.74	66.47	94.02
L3-2.5%	30.18	46.29	63.98
L4-2.5%	23.28	34.50	46.16
L5-2.5%	17.95	27.09	34.99

Table 13 Comparison study about load reduction with displacements of 4, 8 and 12 mm.

Test	Load at 4 mm (kN)	Load reduction (kN)	Load at 8 mm (kN)	Load reduction (kN)	Load at 12 mm (kN)	Load reduction (kN)
L0-2.0%	95.50	---	178.43	---	185.24	---
L1-2.0%	56.06	39.44	97.02	81.41	136.98	48.26
L2-2.0%	37.27	58.23	59.32	119.10	83.20	102.00
L3-2.0%	27.52	67.98	40.80	137.63	55.36	129.88
L4-2.0%	20.57	74.93	30.03	148.40	39.18	146.06
L5-2.0%	15.35	80.15	23.32	155.11	29.50	155.74
L0-2.5%	97.68	--	177.70	---	193.70	---
L1-2.5%	59.35	38.33	103.65	74.14	147.09	46.64
L2-2.5%	40.74	56.94	66.47	111.30	94.02	99.71
L3-2.5%	30.18	67.50	46.29	131.50	63.98	129.70
L4-2.5%	23.28	74.40	34.50	143.29	46.16	147.57
L5-2.5%	17.95	79.73	27.09	150.70	34.99	158.74

It is possible to verify that the loading decreased considerably at 4 mm, 8 mm and 12 mm, showing the loss of the strength when the span length is increased. When analysing the displacement points and their respective forces, it is noticed that for 4.00 mm of displacement the load reduces from 35 kN to 80 kN approximately in both fiber volumes. For displacements of 8 mm and 12 mm, this value ranges from approximately 46 kN to 158 kN.

Another important issue to be evaluate is the non-linear aspect of the load versus displacement behaviour which, in the case of span reduction, implied in a sharp drop in bending stiffness of the structural element when compared with the reinforcement area variation showed in Figure 6, for example.

5 CONCLUSIONS

In the context of studies performed in this work, it was evidenced that the steel fibers have a great potential to improve the mechanical properties of the concrete, which can promote gains in the ductility of the structural elements. This information is also found by experimental analyses presented in [21]–[23], [50], [52]–[54]. The regions of beams which behave in State II (section with cracks, the contribution of the concrete submitted to tension stress is not considered for the equilibrium of the transversal section) evidence the improving of stiffness when the results are compared between models with the same characteristics and different concentrations of fiber volume (2.00% and 2.5%) in Figures 5, 6 and 7, despite the predominant influence in strength gain when analyzing the increase in the height of the cross section (Figure 5).

The results obtained in this work confirm that height and span length are perhaps the most influential properties on the deformability process of damaged structural elements. This influence is evidenced quantitatively in the present work by simulations which pointed out that when increasing the height of the cross section increases more than 90.00% in the ultimate load are observed. On the other hand, for the span length, the change is sensitive in the sense of reducing the ultimate load. For example, for beams with 2.00% of fiber concentration, the reduction obtained was between approximately 21.00% to 63.00%. For simulations involving beams with a concentration of 2.50%, the ultimate load reduction also occurred, and it was in the range of 17.00% to 56.00%.

Regarding the tests dealing with variation of the longitudinal reinforcement, reductions between 10.00% and 50.00% of the bending reinforcement have been performed (both for 2.00% and 2.50% of fiber concentration). However, in none of the cases, a reduction higher than 25.00% of the ultimate load has occurred. This fact is possibly attributed, in part, to the strength promoted by the griping effect of steel fibers. It is also observed that the presence of fibers in the cementitious matrix reduces the level of displacement on the structural elements, even if there is a significant reduction in the reinforcement area. Therefore, it is observed that the present work contributes to visualize an estimative of percentages of reduction and/or increasing of the displacements and internal efforts caused by the geometric parameter variations of the SFRC beams analyzed so far.

Another important issue to be observed in this work is that the addition of a volume of steel fibers in the structural system have allowed a reduction in the reinforcement without significant loss of flexural stiffness (Figure 6) in the service loading situations. In the context of structural design, this situation is interesting since the opening cracks and displacements of the structural elements are related to this flexural stiffness. Thus, it is possible to state that the use of fibers will allow a reduction in the reinforcement density without detriment to the bending strength properties, mainly in parts with high h/b_w ratio. Another issue is the improvement in the effectiveness of using fibers in structural elements with larger span lengths, where the cracking process is more intense, and the number of cracks is high.

More experimental and numerical tests must be performed to obtain answers with the possibility of statistical treatment and contribute to obtaining a methodology for estimating displacements in SFRC beams. It is also worth mentioning the importance of numerical analyses, as experimental analyses have high costs involved, unlike numerical analyses that allow different structural elements to be analyzed without higher costs. Therefore, this work contributes to the understanding and dissemination of the use of SRFC in Brazil.

ACKNOWLEDGEMENTS

The authors wish to thank to CNPq (National Council for Scientific and Technological Development) and FAPEG (Goias Research Foundation).

REFERENCES

[1] A. Medeiros, “Estudo do comportamento à fadiga em compressão do concreto com fibras,” Ph.D. dissertation, Pontif. Univ. Catol. Rio de Janeiro, 2012.

[2] S. Khan, S. Islam, and Z. Rizvi, "Innovation in steel fibre reinforced concrete – a review," *Int. J. Res. Eng. Appl. Sci.*, vol. 3, pp. 21–33, 2014.

[3] W. M. Pereira Jr., J. J. C. Pituba, and D. L. Araújo, "Numerical analysis of steel fiber rein-forced concrete beams using damage mechanics," *IBRACON Struct. Mater. J.*, vol. 9, no. 2, pp. 153–191, 2016, http://dx.doi.org/10.1590/S1983-41952016000200002.

[4] R. P. Salvador, J. F. Fernandes, and A. D. Figueiredo, "Assessment of concrete reinforced with low content of fibres for structural purposes according to standard EN 14651-2007," *Rev. Materia*, vol. 20, pp. 961–974, 2015, http://dx.doi.org/10.1590/S1517-707620150004.0100.

[5] Associação Brasileira de Normas Técnicas, *Fibras de Aço para Concretos – Especificação – Procedimento*, NBR 15530, 2007.

[6] Associação Brasileira de Normas Técnicas, *Tubo de Concreto Armado de Seção Circular para Esgoto Sanitário*, NBR 8890, 2007.

[7] J. Katzer, "Steel fibers and steel fiber reinforced concrete in civil engineering," *Pac. J. Sci. Technol.*, vol. 7, no. 1, pp. 53–58, 2006.

[8] A. M. Brandt, "Fibre reinforced cement-based (FRC) composites after over 40 years of development in building and civil engineering," *Compos. Struct.*, vol. 86, no. 1-3, pp. 3–9, 2008, http://dx.doi.org/10.1016/j.compstruct.2008.03.006.

[9] A. N. Ali and M. V. Mohod, "A review on effect of fiber reinforced concrete on rigid pavement," *Int. J. Res. Eng. Sci. Technol.*, vol. 1, pp. 222–227, 2015.

[10] V. Gribniak, V. Tamulenas, P.-L. Ng, A. K. Arnautov, E. Gudonis, and I. Misiunaite, "Mechanical behavior of steel fiber-reinforced concrete beams bonded with external carbon fiber sheets," *Pac. J. Sci. Technol.*, vol. 10, no. 6, pp. 1–18, 2017.

[11] E. A. Latifa, R. Aguswari, and P. H. Wardoyo, "Performance of steel fiber concrete as rigid pavement," *Adv. Mat. Res.*, vol. 723, pp. 452–458, 2013, http://dx.doi.org/10.4028/www.scientific.net/AMR.723.452.

[12] American Concrete Institute, *State-of-the-Art Report on Fiber Reinforced Concrete*, ACI 544.1R-96, 2006.

[13] American Concrete Institute, *Measurement of Properties of Fiber Reinforced Concrete – Manual of Concrete Practice*, ACI 544.2R-89, 2006

[14] American Concrete Institute, *Guide for Specifying, Proportioning, Mixing, Placing and Finishing Steel Fiber Reinforced Concrete*, ACI 544.3R-93, 2006.

[15] American Concrete Institute, *Design Considerations for Steel Fiber Reinforced Concrete*, ACI 544.4R-88, 2006.

[16] American Concrete Institute, *Building Code Requirements for Structural Concrete*, ACI 318, 2006.

[17] International Union of Laboratories and Experts in Construction Materials, Systems and Structures, "RILEM TC 162-TDF – test and design methods for steel fiber reinforced concrete: bending test - final recommendation," *Mater. Struct.*, vol. 35, no. 253, pp. 579–582, 2002.

[18] International Federation for Structural Concrete, *Model Code for Concrete Structures 2010*, 2013.

[19] European Committee for Standardization, *Test Method for Metallic Fibered Concrete – Measuring the Flexural Tensile Strength (Limit of Proportionality (LOP), Residual*, EN 14651, 2005.

[20] N. Banthia and J. F. Trottier, "Test methods for flexural toughness characterization of fiber rein-forced concrete: some concerns and a proposition," *ACI Mater. J.*, vol. 92, no. 2, pp. 48–57, 1995.

[21] T. E. T. Buttignol, J. L. A. O. Sousa, and T. N. Bittencourt, "Ultra high-performance fiber-reinforced concrete (UHPFRC): a review of material properties and design," *IBRACON Struct. Mater. J.*, vol. 10, no. 4, pp. 957–971, 2017.

[22] T. Błaszczyński and M. P. Falek, "Steel fiber reinforced concrete as a structural material," *Procedia Eng.*, vol. 122, pp. 282–289, 2015.

[23] D.-Y. Yoo, N. Banthia, and Y. S. Yoon, "Experimental and numerical study on flexural behavior of ultra-high-performance fiber reinforced concrete beams with low reinforcement ratios," *Can. J. Civ. Eng.*, vol. 44, no. 1, pp. 18–28, 2017.

[24] J. J. C. Pituba, "Sobre a formulação de um modelo de dano para concreto," Ph.D. dissertation, Esc. Eng. São Carlos, Univ. São Paulo, São Carlos, 2003.

[25] J. J. C. Pituba, "Validação de um modelo de dano para a análise não-linear de estruturas em concreto armado," *Acta Scientiarum*, vol. 32, no. 3, pp. 251–259, 2010.

[26] J. J. C. Pituba and G. R. Fernandes, "An anisotropic damage model for concrete," *J. Eng. Mech.*, vol. 137, no. 9, pp. 610–624, 2011.

[27] M. M. S. Lacerda and J. J. C. Pituba, "Simplified damage models applied in the numerical analysis of reinforced concrete structures," *IBRACON Struct. Mater. J.*, vol. 5, pp. 26–37, 2012.

[28] L. A. F. Souza and R. D. Machado, "Numerical-computational analysis of reinforced concrete structures considering the damage, fracture and failure criterion," *IBRACON Struct. Mater. J.*, vol. 6, no. 1, pp. 101–120, 2013.

[29] J. J. C. Pituba and R. G. Delalibera, "Evaluation of deflection in reinforced concrete structures using damage mechanics," *IBRACON Struct. Mater. J.*, vol. 7, pp. 68–99, 2014.

[30] J. J. C. Pituba and W. M. Pereira Jr., "A bi-dissipative damage model for concrete," *IBRACON Struct. Mater. J.*, vol. 8, no. 1, pp. 49–65, 2015.

[31] C. G. Nogueira, "Modelo mecânico para estruturas lineares em concreto armado – uma abordagem acoplada entre a mecânica do dano e algoritmos de otimização," *Eng. Estudo Pesqui.*, vol. 12, no. 2, pp. 14–27, 2012.

[32] G. M. S. Alva, A. L. H. C. El Debs, and J. Kaminski Jr., "Nonlinear analysis of reinforced concrete structures in design procedures: application of lumped dissipation models," *IBRACON Struct. Mater. J.*, vol. 3, pp. 149–178, 2010.

[33] A. Cipollina, A. López-Inojosa, and J. Flórez-López, "A simplified damage mechanics approach to nonlinear analysis of frames," *Comput. Struc.*, vol. 54, no. 6, pp. 1113–1126, 1995, http://dx.doi.org/10.1016/0045-7949(94)00394-I.

[34] M. G. Santoro and S. K. Kunnath, "Damage-based RC beam element for nonlinear structural analysis," *Eng. Struct.*, vol. 49, pp. 733–742, 1995.

[35] J. Flórez-Lópes, "Simplified model of unilateral damage for RC frames," *J. Struct. Eng.*, vol. 121, no. 12, pp. 1765–1772, 1995.

[36] K. O. Coelho and E. D. Leonel, "Modelo de dano concentrado aplicado à modelagem mecânica de estruturas em concreto armado," in *XXXVII Iber. Lat. Am. Congr. Comput. Methods Eng.*, Brasília, 2016.

[37] R. C. G. Menin, L. M. Trautwein, and T. N. Bittencourt, "Smeared crack models for reinforced concrete beams by finite element methods," *IBRACON Struct. Mater. J.*, vol. 2, no. 2, pp. 166–200, 2009.

[38] S. S. Penna, R. L. S. Pitangueira, and J. S. Fuina, "Estudo Comparativo de modelos de fissuração distribuída para estruturas de concreto," *Semin. Ciênc. Exatas Tecnol.*, vol. 34, no. 2, pp. 211–228, 2013.

[39] T. M. Pacheco, J. M. F. Lima, and P. Lima, "R L. Influence of cracking models on numerical analysis of reinforced concrete beam," *Sci. Eng. J.*, vol. 22, pp. 57–63, 2013.

[40] D. S. Oliveira, R. Barros, and J. S. Giongo, "Six pile caps reinforced concrete: numerical simulation and design by the strut and tie method," *IBRACON Struct. Mater. J.*, vol. 7, pp. 1–23, 2014.

[41] D. C. Borges, W. M. G. Quaresma, G. R. Fernandes, and J. J. C. Pituba, "Evaluation of a proposed model for concrete at mesoscopic scale," *IBRACON Struct. Mater. J.*, vol. 10, no. 5, pp. 1087–1112, 2017.

[42] T. E. T. Buttignol and L. C. Almeida, "Three-dimensional analysis of two-pile caps," *IBRACON Struct. Mater. J.*, vol. 5, no. 2, pp. 252–283, 2012.

[43] A. Carpinteri and M. Corrado, "Nonlinear Fracture Mechanics investigation on the ductility of reinforced concrete beams," *IBRACON Struct. Mater. J.*, vol. 3, no. 2, pp. 137–148, 2010.

[44] X. Ren and J. Li, "Multi-scale based fracture and damage analysis of steel fiber reinforced concrete," *Eng. Fail. Anal. China*, vol. 35, pp. 253–261, 2013.

[45] V. F. P. Dutra, S. Maghous, and A. Campos Fo., "A homogenization approach to macroscopic strength criterion of steel fiber reinforced concrete," *Cement Concr. Res.*, vol. 44, pp. 34–45, 2013.

[46] J. Oliver, D. F. Mora, A. E. Huespe, and R. Weyler, "A micromorphic model for steel fiber reinforced concrete," *Int. J. Solids Struct.*, vol. 49, no. 21, pp. 2990–3007, 2012.

[47] C. La Borderie, "Phenomenes unilateraux dans un materiau endommageable: modelisation et application a l'analyse de structures en beton," Ph.D. dissertation, Univ. Paris 6, Paris, 1991.

[48] Associação Brasileira de Normas Técnicas, *Projeto de Estruturas de Concreto – Procedimento*, NBR 6118, 2014.

[49] P. Bartos, "Analysis of pull-out tests on fiber embedded in brittle matrices," *J. Mater. Sci.*, vol. 15, no. 12, pp. 3122–3128, 1980.

[50] M. M. Lopes, "Substituição parcial de armadura de flexão por fibras de aço em vigas de concreto," M.S. thesis, Dep. Eng. Estrut., Univ. Fed. Rio de Janeiro, Rio de Janeiro, 2005.

[51] W. M. Pereira Jr. and J. J. C. Pituba, "Análise paramétrica de vigas de concreto com fibras metálicas, in: *Tecnologias em Pesquisa: Engenharias*, J. J. C. Pituba and M. H. Stoppa, Eds., São Paulo: Blucher, 2017, pp. 349-364.

[52] D. L. Araújo, L. C. Carmo, F. G. T. Nunes, and R. D. Toledo Fo., "Computational modeling of steel fiber reinforced concrete beams subjected to shear," *IBRACON Struct. Mater. J.*, vol. 3, pp. 68–94, 2010.

[53] A. R. Barros, P. C. C. Gomes, and A. S. R. Barboza, "Steel fibers reinforced self-compacting concrete – behavior to bending," *IBRACON Struct. Mater. J.*, vol. 4, pp. 49–78, 2011.

[54] R. P. A. F. Pinto Lima, "Utilização de fibras metálicas com funções estruturais em estruturas de betão," M.S. thesis, Fac. Eng. Porto, Porto, 2012.

Author contributions: J. J. C. Pituba: conceptualization, funding acquisition, supervision, writing, methodology, formal analysis; M. F. Pontes: writing, data curation, formal analysis; W. M. Pereira Junior: conceptualization, writing, methodology, data curation, formal analysis.

Editors: José Luiz Antunes de Oliveira e Sousa, Guilherme Aris Parsekian.

IBRACON Structures and Materials Journal
Revista IBRACON de Estruturas e Materiais
ISSN 1983-4195 ismj.org

ORIGINAL ARTICLE

Reinforced concrete beams coated with fiberglass-reinforced polymeric profiles as partial substitutes for the transverse reinforcement

Vigas de concreto armado revestidas com perfis de polímeros reforçados com fibras de vidro como substituto parcial das armaduras transversais

Igor Souza Hoffman[a]
Jorge Henrique Piva[b]
Augusto Wanderlind[b]
Elaine Guglielmi Pavei Antunes[b]

[a]Universidade Federal do Rio Grande do Sul – UFRGS, Programa de Pós-graduação em Engenharia Civil – PPGEC, Porto Alegre, RS, Brasil
[b]Universidade do Extremo Sul Catarinense – UNESC, Grupo de Pesquisa em Desempenho de Estruturas e Construção Civil – GPDECC, Curso de Eng. Civil, Criciúma SC, Brasil

Received 02 November 2019
Accepted 27 Março 2020

Abstract: The use of GFRP (Glass Fiber Reinforced Polymers) structural profiles in the construction sector is growing due to their attractive properties, such as high mechanical strength and durability in aggressive environments. With this, it is necessary to conduct studies that deepen the knowledge about the performance of these materials in structural applications. Therefore, this work aims to analyze the mechanical performance of reinforced concrete beams coated with GFRP profiles, in comparison to reinforced concrete beams, by analyzing groups with different spacing between transversal reinforcement. In all groups there was no change in the longitudinal reinforcement, and the D and Q groups were, respectively, made up of transverse reinforcement spaced twice and quadruple the one calculated for the reference beams, and presented the GFRP profiles in their constitution. All beams were tested at four-point bending, and strain gauges were installed in one of the beams of each group studied. The results obtained in the tests showed an increase in strength of 83.67% in the beams of group D, and 79.91% for group Q, in relation to the references. The analysis of longitudinal deformations made it possible to verify increases in stiffness and the moment of cracking in composite beams. Thus, based on this study, the composite structures studied may constitute future solutions for constructions exposed to aggressive environmental conditions, in order to increase their durability and also to contribute to the design of such structural elements with lower reinforcement rates.

Keywords: GFRP profile, composite beams, transverse reinforcement, pultrusion.

Resumo: A utilização de perfis estruturais de GFRP (Glass Fiber Reinforced Polymers) no setor da construção civil vem crescendo devido as suas propriedades atrativas, como altas resistências mecânicas e a durabilidade em ambientes agressivos. Com isso, faz-se necessário a realização de estudos que aprofundem o conhecimento sobre o desempenho desses materiais em aplicações estruturais. Sendo assim o presente trabalho tem por objetivo analisar o desempenho mecânico de vigas de concreto armado revestidas com perfis de GFRP, em comparação a vigas de concreto armado, através da análise de grupos com distintos espaçamentos entre armaduras transversais. Em todos os grupos não houve alteração nas armaduras longitudinais, e os grupos D e Q eram constituídos, respectivamente, por armaduras transversais espaçadas conforme o dobro e o quadruplo do calculado para as vigas referência, e apresentavam os perfis de GFRP em sua constituição. Todas as vigas foram ensaiadas a flexão quatro pontos, e strain gauges foram instalados em uma das vigas de cada grupo estudado. Os resultados obtidos nos ensaios apresentaram um aumento de resistência de 83.67% nas vigas do grupo D, e de 79.91% para o grupo Q, em relação as referências. A análise de deformações longitudinais possibilitou verificar aumentos de rigidez e o momento de fissuração nas vigas mistas. Sendo assim, com base nesse estudo, as estruturas mistas estudadas podem constituir futuras soluções para construções expostas a

Corresponding author: Elaine Guglielmi Pavei Antunes. E-mail: elainegpa@unesc.net / eelainegpa@gmail.com
Financial support: None.
Co'nflict of interest: Nothing to declare.

condições ambientais agressivas, com o intuito de aumentar a sua durabilidade e, também, contribuir para o dimensionamento de tais elementos estruturais com menores taxas de armadura.

Palavras-chave: Perfil de GFRP, vigas mistas, armaduras transversais, pultrusão.

How to cite: I. S. Hoffman, J. H. Piva, A. Wanderlind, and E. G. P. Antunes, "Reinforced concrete beams coated with fiberglass-reinforced polymeric profiles as partial substitutes for the transverse reinforcement," *Rev. IBRACON Estrut. Mater.*, vol. 13, no. 6, e13608, 2020, https://doi.org/10.1590/S1983-41952020000600008

1 INTRODUCTION

The composite materials are defined as a compound substance of two or more materials, combined on a macroscopic scale, insoluble among themselves, to form a useful engineering material with certain properties that are not found in its constituents when in isolation [1], [2]. The use of composites, especially materials formed by fiber-reinforced polymers (FRP- Fiber Reinforced Polymer), has been wide and competitive in some engineering areas [3].

The attractive properties of fiber-reinforced polymers are: durability, corrosion resistance to marine environments; mechanical strength, particularly at low temperatures; ability to resist vibrations and absorb energy under seismic loads; electromagnetic transparency; low coefficient of thermal expansion; pigmentation and decorative characteristics; in addition to an excellent stiffness by weight and strength by weight, therefore, reducing transportation and assembly costs [4], [5]. Due to such properties, its use has been widely studied as a viable substitute for steel of the reinforcement of concrete structures, especially in structures exposed to aggressive environments, which require constant maintenance due to corrosion problems [3], [6], [7]. Although the characteristics and properties of GFRP are also affected in the long term, mainly by the diffusion of humidity through the resin layer and between the fiber and matrix interfaces [8], GFRP, facing more severe exposure conditions, still exhibits greater durability when compared to steel [9], [10]. The GFRP can be commonly seen in civil construction, either in structures made entirely of structural profiles [6] or as a substitute for steel bars in reinforced concrete structures [11] or even in hybrid structures formed by reinforced concrete and GFRP profiles. Hybrid structures formed by bonding GFRP profiles to reinforced concrete elements have been proven to provide a virtually efficient interaction in the short term [12].

The association of GFRP profiles by bonding, through adhesives, in reinforced concrete structural elements, brings economic and mechanical advantages [12], [13]. The GFRP profiles have a low elasticity module [7], therefore, they can demonstrate instability phenomena due to their deformation and, to overcome such limitations, the combined use of GFRP profiles with reinforced concrete, originates a structural solution [3], [13], [14]. Applications of reinforced polymer profiles with externally connected fiberglass play a fundamental role in guaranteeing the strength and stiffness of buildings, mainly due to the bold designs of modern buildings [13].

In addition to the strength requirements, GFRP also serves as a protective shield for structural elements against adverse environmental and meteorological conditions, such as, for example, the penetration of carbon chloride ions [15]. In view of these notes, the present work aims to analyze the mechanical performance of composite reinforced concrete beams with GFRP profiles, in comparison to reinforced concrete beams commonly used in civil construction, through the analysis of groups with different spacing between transverse reinforcement. Therefore, the samples of each group are submitted to bending moment and shear forces, to study the behavior of the composite structure, and to analyze the performance of the profiles used as partial substitutes for the transverse reinforcement.

2 MATERIALS AND METHODS

2.1 Methodology

In order to fulfill the objectives of this study, three different groups of beams were performed, group REF, D and Q, consisting of three samples each. For all groups, the structural elements had a total length of 160 cm, and an effective span of 150 cm, as can be seen in Figure 1.

The GFRP profiles constitute a collaborative structural form, which serves as a formwork for the execution of the beams and as a structural element. The longitudinal reinforcements were kept constant in all groups, being composed of a pair of 12.5 mm diameter ribbed CA-50 steel bars, totaling a steel area of 2.50 cm^2.

The verification of the rupture mode for the reference beams was carried out by determining the depth of the neutral line (NL) for the ultimate limit state (ULS), according to the recommendations of NBR 6118 [16], considering the balance of the tension forces in the reinforcement and compression in concrete according to the stress distributions for Stadium 3 deformations. With the determination of the depth of the neutral line, it is possible to evaluate the deformation domain that will characterize the rupture mode of these structural elements, by considering the Bernoulli hypothesis for flat sections. The final theoretical strength moment for the reinforced concrete reference beams can be determined through Equation 1.

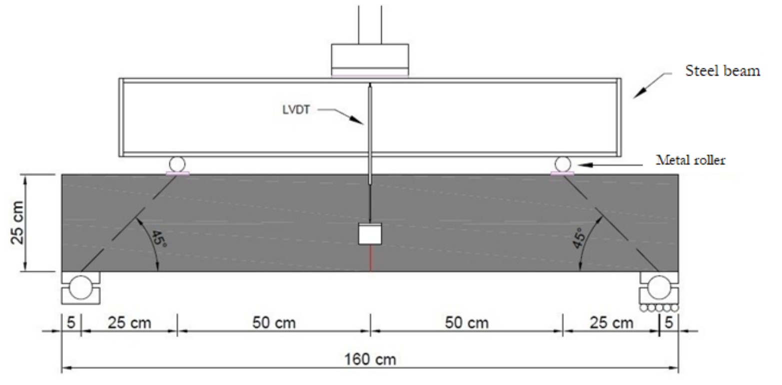

Figure 1. Schematic of the four-point bending test carried out on the beams.

$$M_u = \left(f_{yk} / \gamma_s\right) \cdot A_s \cdot \left(d - 0,4x\right) \tag{1}$$

Where:
M_u – last resistant moment for the beam in the ULS; A_s – total steel area of the main longitudinal reinforcements; d – useful beam height; x – depth of the neutral line; f_{yk} – characteristic steel yield strength; γ_s – coefficient for the reduction of steel strength. In this work $\gamma_s = 1.0$.

The calculation of the predicted moment for the beginning of the cracking in the reference beams due to the tensile efforts in the concrete was carried out according two methodologies: Approximate method, according to NBR 6118 [16], and the homogenized sections method. According to NBR 6118 [16], the moment of cracking in reinforced concrete beams is given by Equation 2.

$$M_r = \frac{\alpha \cdot f_{ctk,inf} \cdot I_c}{y_t} \tag{2}$$

Where:
M_r – expected cracking moment of the structural element; $\alpha = 1.5$ for rectangular cross sections; I_c – moment of inertia of the concrete section; $f_{ctk,inf}$ – lower tensile strength of concrete given by $f_{ctk,inf} = 0.21 \cdot f_{ck}^{2/3}$; y_t – distance from the center of gravity to the most strained fiber.

The homogenized section methodology considered the transformation of the reinforced concrete cross section into an equivalent theoretical section of concrete. The beginning of cracking in the tensioned concrete is characterized by the passage from Stadium 1 to Stadium 2 of deformations. Therefore, when the stresses acting on the stretched concrete fibers reach the lower tensile strength ($f_{ctk,inf}$), the cracking process begins. The position of the neutral line in Stadium I of deformations is given by Equation 3.

$$x_h = \frac{-B}{A} \tag{3}$$

Where:
x_h - position on the neutral line in Stadium I of deformations considering the homogenized section, measured from the upper end of the beam; Coefficients A and B in Equation 3 are given by Equations 4 and 5.

$$A = b_w \cdot h + A_s \cdot (\eta - 1) \tag{4}$$

$$B = \frac{-b_W}{2} \cdot h^2 - A_s \cdot d \cdot (\eta - 1) \tag{5}$$

Where:
b_w – width of the cross section; h - total beam height; A_s – total steel area of the main longitudinal reinforcements; d – useful beam height; The homogenization coefficient of sections η is given by Equation 6.

$$\eta = \frac{E_s}{E_{cs}} \tag{6}$$

Where:
E_s – modulus of elasticity of steel. For this work E_s = 210 MPa; E_{cs} – secant elasticity modulus predicted for concrete. $E_{cs} = \alpha_i \cdot E_{ci}$; the value of $\alpha_i = 0.90$ for $f_{ck} = 40$ MPa, and $E_{ci} = \alpha_E \cdot 5600 \cdot \sqrt{f_{ck}}$; $\alpha_E = 1.20$.

The theoretical cracking moment for the homogenized concrete section will be given by Equation 7.

$$M_{rh} = \frac{f_{ctk,inf} \cdot I_{ch}}{y_t} \tag{7}$$

Where:
M_{rh} - cracking moment in concrete section; I_{ch} – moment of inertia of the section; $f_{ctk,inf}$ – lower tensile strength of concrete; y_t – Position of the most strained fiber in relation to the neutral line, given by $y_t = h - x_h$.

Through the four-point bending test model considered for this work, presented in Figure 1, it is possible to describe the equation that relates the moment applied at the center of the effective span to the loads measured in the HBM U10M load cell. Once the moments of cracking and collapse are known, obtained theoretically, one can predict the loading observed in the load cell for each of these cases through Equations 8 and 9.

$$P = \left(M + \frac{\rho_{ca} \cdot A_C}{2} \cdot \left(-\frac{1}{4} \cdot L_{ef}^2 \right) \right) / l_{ap} \tag{8}$$

$$P_{CC} = 2 \cdot P \tag{9}$$

Where:
P – point load applied in the test; P_{CC} – expected loading in the load cell; M – moment observed in the center of the theoretical span of the beams; ρ_{ca} – specific weight considered for reinforced concrete, being $\rho_{ca} = 25\,kN/m^3$; A_C – cross-sectional area of the rectangular reinforced concrete beam; L_{ef} – effective span of the beam considered, being $L_{ef} = 1.50\,m$; l_{ap} - distance from the point of application of the test loads, measured from the model supports, being $l_{ap} = 0.25\,m$.

The transverse reinforcement was determined using the methodology of model I and II of calculation, according to NBR 6118 [16], considering for the second model the angle of the compression rod ϴ = 45º (as indicated in the structure of the tests shown in Figure 1), and the angle of the transverse reinforcement of α = 90º. In addition, the necessary spacing was verified by considering the ultimate limit state for the plastification of the transverse reinforcement, disregarding the calculation parcels referring to the complementary resistance mechanisms, such as the effects of aggregate gearing and the effect of reinforcement pins between cracks. All calculations were performed considering that the transverse reinforcement was composed of simple branches with ribbed CA-50 steel bars of 6.30 mm in diameter. Equation 10 [17] was used to determine the longitudinal spacing between the reinforcements.

$$s = \frac{A_{sw} \cdot d \cdot (f_{yk} / \gamma_s)}{1.10 \cdot V_s} \tag{10}$$

Where:
s – longitudinal spacing of transverse reinforcement; A_{sw} – cross sectional area of shear reinforcement; f_{yk} – characteristic yield strength steel, being $f_{yk} = 500\,MPa$; γ_s – coefficient for the reduction of steel strength. In this work $\gamma_s = 1.0$; V_s – active shear force.

Table 1 presents the longitudinal spacing calculated for each design methodology considered in this work.

Table 1. Longitudinal spacing of transverse reinforcement, for 6.30 mm diameter bars.

Methodology	Longitudinal spacing (s)
Model I	11.43 cm
Model II	9.58 cm
Calculation using Equation 10	6.07 cm

All the beams of the groups (Ref, D and Q) were made with a concrete cross section of 15 x 25 cm and in groups D and Q GFRP profiles were used. The longitudinal reinforcement for all groups were two bars of 12.5 mm diameter (2 Φ12.5 mm). Spacing of transverse reinforcement used in groups Ref, Q and D was 7 cm, 14 cm and 28 cm, respectively.

The collaborative form of GFRP, if treated as a structural reinforcement, can add mechanical strength to both shear and bending. The American standard ACI 440 2R-*08 Guide for the Design and Construction of Externally Bonded FRP Systems for Strengthening Concrete Structures* [18] has recommendations and analytical formulas capable of quantifying these reinforcements. Following the ACI 440 2R-08 standard [18], the shear strength can be calculated with Equation 11.

$$\varnothing V_n = \varnothing \cdot \left(V_c + V_s + \varphi_f \cdot V_f \right) \tag{11}$$

Where:
$\varnothing$ - lessening strength factor; V_n - nominal shear strength; V_c - shear strength related to concrete; V_s - shear strength related to steel: φ_f - coefficient of reduction of reinforcement efficiency; V_f - shear strength related to reinforcement.

For the study of this work, the factor Ø was adopted as 1.0, in order to compare with the experimental responses and the coefficient φ_f was adopted with the value of 0.85, which is recommended when the reinforcement has a "U" geometry. The strengths V_c and V_s were calculated with Equations 12 and 13, taken from the American standard ACI 318-05 *Building Code Requirements for Structural Concrete and Commentary* [19].

$$V_c = 2 \cdot \sqrt{f'_c} \cdot b_w \cdot d \tag{12}$$

$$V_s = \frac{A_v \cdot f_{yt} \cdot d}{s} \tag{13}$$

Where:
f'_c - characteristic compressive strength of concrete; b_w - width of the cross section of the concrete beam; d - distance from the most compressed face to the centroid of the longitudinal steel reinforcement; A_v - area of steel transverse reinforcement with spacing s;
f_{yt} - yield strength of the transverse reinforcement; s - spacing between transverse reinforcements.

In Equation 12 the unit of psi for f'_c should be used. The other equations in the article are adapted to use the units of the international system. The equation for obtaining the strength V_f contained in that standard is based on spaced reinforcements. However, the collaborative form characterizes a continuous reinforcement, thus the shear strength offered by it was computed assuming that the two webs of the GFRP profile act integrally. Equations 14 and 15 are used for its calculation.

$$V_f = A_{fv} \cdot f_{fe} \tag{14}$$

$$A_{fv} = 2 \cdot t_f \cdot d_{fv} \tag{15}$$

Where:
A_{fv} - shear reinforcement area from GFRP; f_{fe} - effective tensile strength of GFRP; t_f - web thickness of the collaborative form GFRP; d_{fv} - web height of the collaborative form of GFRP.

In order to obtain f_{fe} acting against the shear, the linear relationship by Hooke's law can be used, but an effective deformation (ε_{fe}) must be considered, which experimentally obtains values lower than those of the concrete fracture, characterizing a fracture by disconnection of the reinforcement with concrete [20]. Equations 16, 17, 18, 19, 20 and 24 lead to characterize the behavior of the shear reinforcement until obtaining ε_{fe}, which is a function of the strength of the concrete, the cross section of the reinforcement and the stiffness of the reinforcement [21].

$$\varepsilon_{fe} = k_v \cdot \varepsilon_{fu} \tag{16}$$

$$k_v = \frac{k_1 \cdot k_2 \cdot L_e}{11900 \cdot \varepsilon_{fu}} \tag{17}$$

$$k_1 = \left(\frac{f'_c}{27} \right)^{2/3} \tag{18}$$

$$k_2 = \frac{d_{fv} - L_e}{d_{fv}} \tag{19}$$

$$L_e = \frac{23300}{\left(n_f \cdot t_f \cdot E_f \right)^{0.58}} \tag{20}$$

Where:
k_v - reduction coefficient of the shear deformation efficiency; ε_{fu} - limit deformation for rupture of the GFRP; k_1 - reduction factor due to the influence of concrete strength; k_2 - reduction factor due to the influence of the "U" type transverse section of the reinforcement; n_f - number of reinforcement layers; E_f - longitudinal elastic modulus of the GFRP; L_e - active length of the connection of the GFRP with the concrete over which most of the shear tension is maintained.

According to the ACI 440 2R-08 [18] standard, the flexural strength of the reinforced beam can be calculated with the collaborating formwork. Considering only the plate on the underside of the U profile as an active reinforcement, Equation 21 was used for the calculation.

$$M_n = A_s \cdot f_s \cdot \left(d - \frac{\beta_1 \cdot c}{2} \right) + \varphi_f \cdot A_f \cdot f_{fe} \cdot \left(h - \frac{\beta_1 \cdot c}{2} \right) \tag{21}$$

Where:
M_n - nominal moment strength considering the bending reinforcement; A_s - steel area of longitudinal reinforcement; f_s - stress resisted by steel bars; A_f - bottom plate area of GFRP; h - total beam height; β_1 - ratio between the depth of the equivalent rectangular stress block and the depth of the neutral axis taken as the values associated with the Whitney stress block; c - distance from the most compressed face to the neutral axis.

The other terms of Equation 21 have been previously described, with the φ_f coefficient also being adopted as 0.85. The term c must be calculated iteratively, to produce the compatibility of the deformations in the materials and the equivalence of the internal forces. For this, the deformations are calculated with Equations 22 and 23 arbitrating the value of c. Equations 24 and 25 are used to obtain the stresses. After obtaining the deformations and stresses, Equation 26 is used to carry out the internal balance of forces and thus verify that the dimension c adopted satisfies the conditions of compatibility and balance.

$$\varepsilon_{fe} = \varepsilon_{cu} \cdot \left(\frac{d_f - c}{c} \right) \leq \varepsilon_{fd} \tag{22}$$

$$\varepsilon_s = \varepsilon_{fe} \cdot \left(\frac{d - c}{d_f - c} \right) \tag{23}$$

$$f_{fe} = E_f \cdot \varepsilon_{fe} \tag{24}$$

$$f_s = E_s \cdot \varepsilon_s \leq f_y \tag{25}$$

$$c = \frac{A_s \cdot f_s + A_f \cdot f_{fe}}{\alpha_1 \cdot f'_c \cdot \beta_1 \cdot b_w} \tag{26}$$

Where:
ε_{fe} - effective deformation of the GFRP; ε_{cu} - ultimate deformation of the concrete obtained by the stress-strain graph at the point equal to $0.85 \cdot f_c$ or equal to 0.003; ε_{fd} - limit deformation to disconnect the GFRP from the concrete; ε_s - deformation of steel; E_s - modulus of elasticity of steel; f_y - yield stress of steel; α_1 - multiplication factor to determine the stress intensity in the concrete using the rectangular distribution.

The other terms can be seen in Figure 2a, which shows the transverse section adopted for the flexural reinforcement model. Figures 2b and 2c present, respectively, the diagram of the distribution of deformations and the diagram of the balance of internal forces.

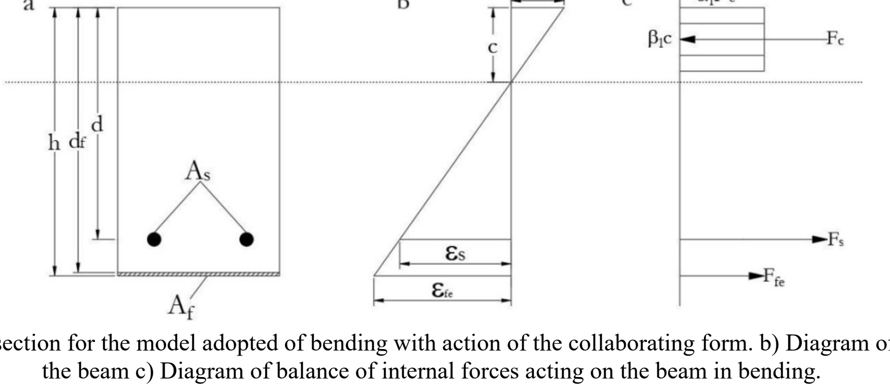

Figure 2. a) Cross section for the model adopted of bending with action of the collaborating form. b) Diagram of deformations of the beam c) Diagram of balance of internal forces acting on the beam in bending.

However, if Equation 22 presents ε_{fe} greater than ε_{fd}, the concrete does not reach ε_{cu} thus the failure is characterized by the disconnection of the GFRP with the concrete [22]. In the work (Teng et al [23]) an equation was developed based on experimental data and fracture mechanics. This equation was adapted by the ACI 440 2R-08 [18] standard from a committee that evaluated a significant number of experimental data on beams subjected to bending, which suffered failure due to disconnection of the reinforcement. Equation 27 is then used to calculate ε_{fd} based on the equation proposed by (Teng et al [23]), calibrated by the coefficient equal to 0.41 proposed by the standard.

$$\varepsilon_{fd} = 0.41 \cdot \sqrt{\frac{f'_c}{n_f \cdot E_f \cdot t_f}} \tag{27}$$

In this case, the deformation in the concrete will be less than its ultimate deformation and will need to be calculated, which can be obtained by similarity of triangles, as provided by Equation 28.

$$\varepsilon_c = \varepsilon_{fe} \cdot \left(\frac{c}{d_f - c} \right) \tag{28}$$

After the concreting activities, shown in Figure 3, the beams were covered with tarpaulins, in order to avoid water losses in the concrete mixture, and the specimens were placed in a tank with water and calcium hydroxide solution, according to the specification of NBR 5738 [24].

Figure 3. a) Composite concrete beams in GFRP profiles. b) Concreting of composite concrete beams in GFRP profiles.

The tests were carried out 28 days after the concreting of the elements, thus respecting the curing time. All beams were subjected to four-point bending tests, following the model of ASTM C78 / C78M [25] with adaptations in relation to the height of the beams, definitions of supports and load application positions, as these were positioned close to the supports, forming an angle of 45º in relation to the support, in order to increase the shear forces in the tested beams. The tests were carried out with the use of a hydraulic piston with a maximum capacity of 500kN, supported under a reaction frame. To obtain the values of vertical deflections, a LVDT of 100 mm was used. The four-point bending test scheme, as well as the orientations of the load application positions and LVDT positioning already presented in Figure 1.

The strain gauges were inserted in the upper concrete face in beams “REF-1”, “D-1” and “Q-1”, Figure 4a, and in the lower part in beams “D-1 ”and“ Q-1 ”, in GFRP forms, Figure 4b. In addition to these, a strain gauge was inserted in one of the bars that make up the lower longitudinal reinforcement in beams “REF-1”, “D-1” and “Q-1”, Figure 4c.

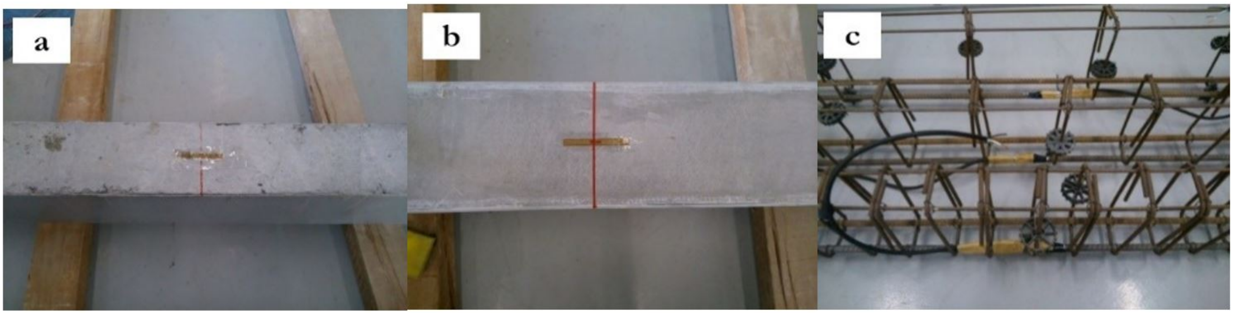

Figure 4. a) Strain gauge in concrete. b) Strain gauge in GFRP profile. c) Strain gages in REF, D and Q group reinforcement.

All sensors were positioned at the center of the theoretical span. The sensors used in the tests were connected to a Quantum X MX840 data acquisition module of the HBM brand, and the software used for receiving, recording and synchronizing data was Catman 3.0.

The axial compression tests were performed according to NBR 5739 [26], on a hydraulic press model EMIC PC200I, with a maximum capacity of 2000 kN. The elasticity modules were obtained through tests carried out according to NBR 8522 [27], in a hydraulic press model EMIC PC200CS, with a maximum capacity of 2000 kN.

2.2 Materials

The GFRP profiles were consisted of an electro-gutter profile with the dimensions of 15.00 x10.00x0.32 cm (width x height x thickness), and two plates of 25.00x0.32 cm (width x thickness), which were glued on both sides of the walls of the electro-gutter profile using polyurethane glue. Then, a transverse section was obtained with the final dimensions of 15.00 x 25.00 cm (width x height), 0.32 cm thick and a total length of 160 cm, maintained in all forms used, as shown in Figure 5.

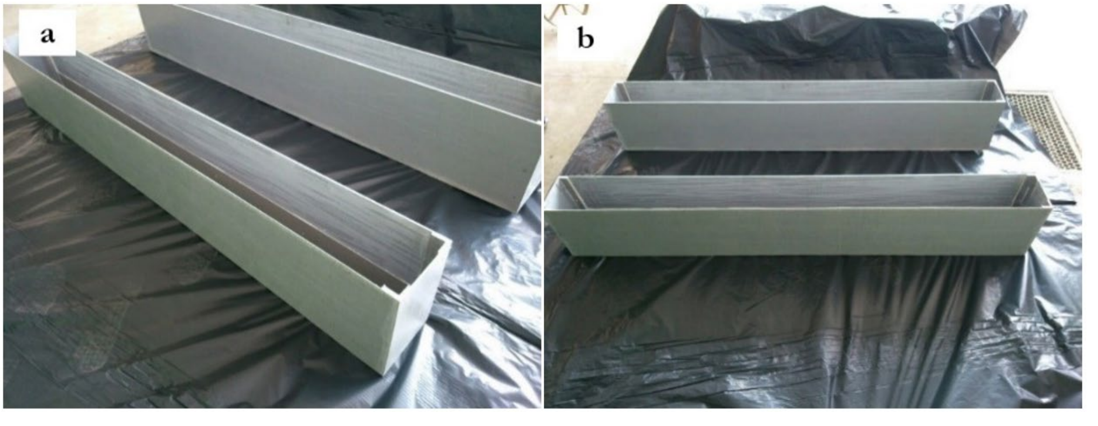

Figure 5. GFRP profiles used in groups D and Q.

The profiles are pultruded and have a minimum fiber/resin ratio of 55%. The mechanical properties of interest for using the collaborative form as reinforcement, longitudinal modulus of elasticity (E_f), the tensile strength (f_{fu}) and the deformation at rupture (ε_{fu}), were measured by uniaxial tensile testing performed on a universal testing machine of EMIC brand, model DL30000 with the aid of a clip-gauge, with the following results respectively; 21358 ± 524.74 MPa, 265.2 ± 1.48 MPa and 0.011717 ± 0.000957 mm/mm.

Stress-strain behavior presented by the specimens can be seen in the graph of Figure 6, these were linear until their rupture, which was fragile. The GFRP profiles generally have a specific mass of 1800 kg/m^3, as indicated by the material supplier company.

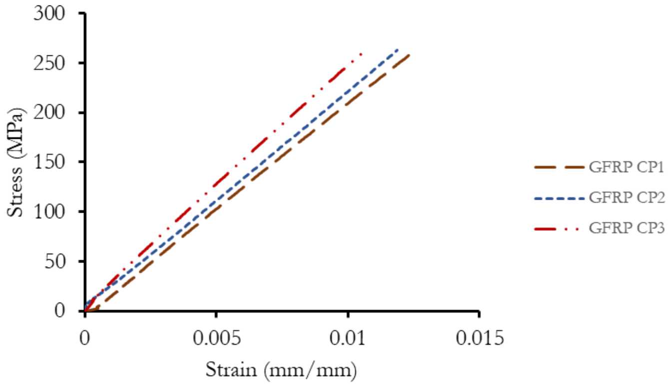

Figure 6. Stress versus strain graph obtained by the uniaxial tensile test on 3 GFRP specimens.

The yield stress (f_y) and the tensile strength limit stress (f_u) for the CA-50 steel used were determined by uniaxial tensile testing performed on the same universal testing machine. In this test it was not possible to use an extensometer, a fact that made the correct measurement of the longitudinal elastic modulus (E_s) impossible, which was adopted equal to 210 GPa, a value recommended by NBR 6118: 2014 [16].

The concrete used in the beams was dosed to present a compressive strength of 40 MPa after 28 days. The cement used was of the CPIV-32 type with property resistant to aggressive environments, mainly to the attack of sulfides. The unitary mix was executed in mass in the following proportion, 1: 2.87: 2.13 with water/cement ratio of 0.48 and addition of polypropylene fiber equal to 0.90 kg/m^3 of concrete. The reduction of the cone trunk on the slump test, according to NBR NM 67 [28] was 70 ± 20 mm. The aggregates used in the concrete were characterized according to NBR NM 248 [29]. The concrete was reinforced with the use of multifilament polypropylene fibers, in order to reduce the risk of plastic cracking (effect of shrinkage in the concrete) [30], thus improving the performance of the profile/concrete adhesion, which was accomplished through the use of an epoxy resin.

The fiber content used was 0.9 kg/m^3, since low fiber contents between 0.9 to 2.7 kg/m^3 do not influence the increase in concrete strength [31].

The connection between the GFRP profile and the concrete was carried out with the use of a bicomponent thixotropic epoxy resin. The application was carried out on the walls of the profile, in the areas close to the supports of the beams (region of greater shear force) and in the area of the bottom of the profiles, which comprise the places that present the greatest bending moments. The regions where the resin was applied are shown in the areas indicated in Figure 7.

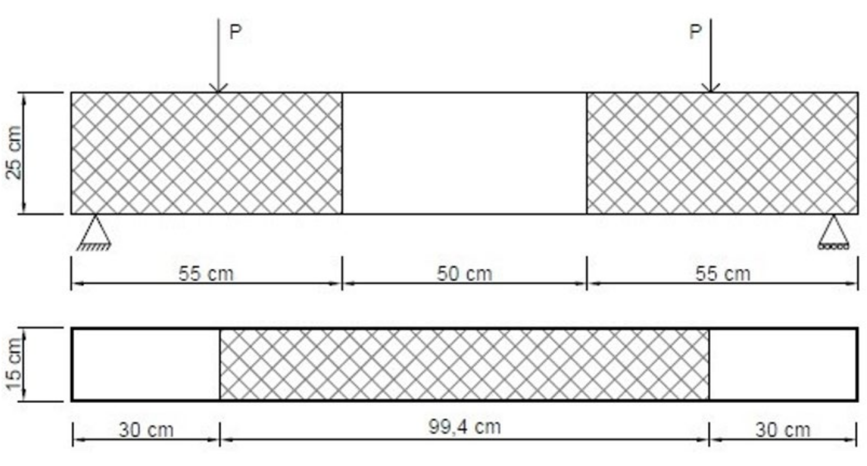

Figure 7. Regions of application of resin on the walls and bottom of the moulds, respectively.

The application of the resin was carried out manually, using spatulas, with a thickness of approximately 2 mm of glue, as indicated manufacturer.

3 RESULTS AND DISCUSSIONS

3.1 Efforts and acting requests on the beams theoretically obtained

Table 2 presents the results of the theoretical efforts calculated according to the equations presented in section 2 of this work. The results obtained are regarding the reinforced concrete beams.

Table 2. Results of the theoretical efforts calculated according to the equations presented in section 2

Useful beam height - d	**21.875 cm**
Depth of the neutral line in the ULS - x	2.56 cm
x/d ratio	0.12
Domains of deformations in the ULS	2
Deformations of reinforcements in the ULS	10 ‰
Deformations of concrete in the ULS	1.32 ‰
Last resistant moment - M_u	25.59 kN·m
Load measured in the load cell in the ULS - P_{CCu}	202.61 kN
Cracking moment predicted by NBR 6118 - M_r	5.76 kN·m
Load measured in the load cell for cracking - P_{CCr}	43.94 kN
Cracking moment predicted through the homogenized concrete section- M_{rh}	4.11 kN·m
Load measured in the load cell for cracking - P_{CCrh}	30.78 kN

Through the methodologies for checking the deformation domains for the ultimate limit state, according to NBR 6118 [16], it was found that the rupture of the reinforced concrete beams meets the ductility recommendations, with no fragile rupture in the bending elements. The rupture mechanism foreseen for the tested reinforced concrete beams will be the flow of the drawn longitudinal reinforcements, and the deformations in the most compressed concrete fibers do not reach the deformation limit for the beginning of plasticization, given as $\varepsilon_{c2} = 2.00‰$ by NBR 6118 [16], for concretes com $f_{ck} \leq 50\,MPa$. The theoretical shear strength (V_n) for beam group D is 185 kN and for beam group Q 158 kN, while the theoretical M_n for reinforced beams was 45.6 kN·m.

3.2 Axial compression and modulus of elasticity of concrete

The average axial compression strength and elasticity modulus results obtained for the respective groups Ref, D and Q were, 45.27 ± 1.88 MPa; 41.80 ± 2.29 MPa; 43.55 ± 1.33 MPa and elasticity modulus 44.70 ± 2.08 GPa; 44.38 ± 2.05 GPa; 45.58 ± 1.81 GPa.

Through the results obtained, the concrete used for molding the beams presented axial compression strength close to the pre-established for this work.

3.3 Analysis of loads and vertical displacements of beams

During the tests, limits were set in relation to the load applied by the hydraulic piston on the beams, in order to avoid damage to the equipment used, for that purpose the application of up to 450 kN was kept as a limit. Figure 8 presents the graph with the results of the loads and vertical displacements obtained for the reference beams (REF), beams of group D and Q.

The average maximum load for the beams of group D was 439.03 kN, an increase of 83.67% in relation to the structural elements of the REF group, which had an average maximum load of rupture of 239.03 kN. For the beams of group Q, the average maximum load was 430.04 kN, an increase of 79.91% in relation to the elements of the REF group, and a difference of 2.05% in relation to the average maximum load of group D beams.

Table 3 presents the mechanical results for each tested beam, as well as the load obtained for the maximum vertical service displacement, which according to NBR 6118 [16] is L/250, with L being the effective span of the beam considered. To calculate the maximum shear forces and maximum bending moments, the specific weight of reinforced concrete was used as $\rho = 25\,kN / m^3$.

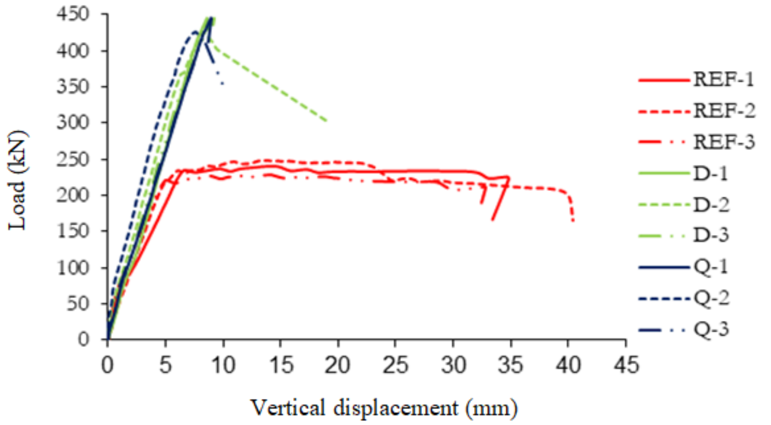

Figure 8. Graph of loads and vertical displacements for each tested beam.

Table 3. Mechanical results for each tested beam

Group	Beams	L/250 = 6 mm Load in L/250 (kN)	Maximum load (kN)	Displacement vertical in maximum load (mm)	Maximum shear force (kN)	Maximum bending moment (kN·m)
REF	REF-1	223.31	240.61	14.27	121.01	30.34
	REF-2	234.30	248.31	13.50	124.86	31.30
	REF-3	216.92	228.17	14.02	114.79	28.78
	Average	224.84	239.03	13.93	120.22	30.14
	S.D.	8.79	10.16	0.39	5.08	1.27
D	D-1	320.25	445.50	8.58	223.46	55.95
	D-2	356.55	426.05	8.31	213.73	53.52
	D-3	330.83	445.54	9.23	223.48	55.96
	Average	335.88	439.03	8.71	220.22	55.14
	S.D.	18.67	11.24	0.47	5.62	1.41
Q	Q-1	315.14	446.20	8.90	223.81	56.04
	Q-2	381.69	425.09	7.57	213.25	53.40
	Q-3	315.27	418.83	8.25	210.12	52.62
	Average	337.37	430.04	8.24	215.73	54.02
	S.D.	38.39	14.34	0.67	7.17	1.79

The vertical displacements observed experimentally during the tests of the beams, were obtained at the moment of the maximum applied load. For the elements of group D, the average vertical displacement was 8.71 mm, which is 37.50% less than the average vertical displacement obtained for beams in the REF group, which was 13.93 mm. Among the samples in group Q, the average vertical displacement was 8.24 mm, a difference of 40.85% in relation to the beams in the REF group, and a difference of 5.36% in relation to the elements in group D.

It can be seen through the graph in Figure 8 that the vertical displacements obtained of the REF group are contained in the Stadium III deformations, when the beams were in state collapse. And the values found for the samples of group D and Q were obtained while the elements were in the Stadium II of deformations, before the collapse of the structures.

3.4 Analysis of loads and longitudinal deformations in the materials

Figure 9 presents the results of deformations of the materials during the four-point bending tests, in relation to the resulting bending moment in the center of the theoretical span.

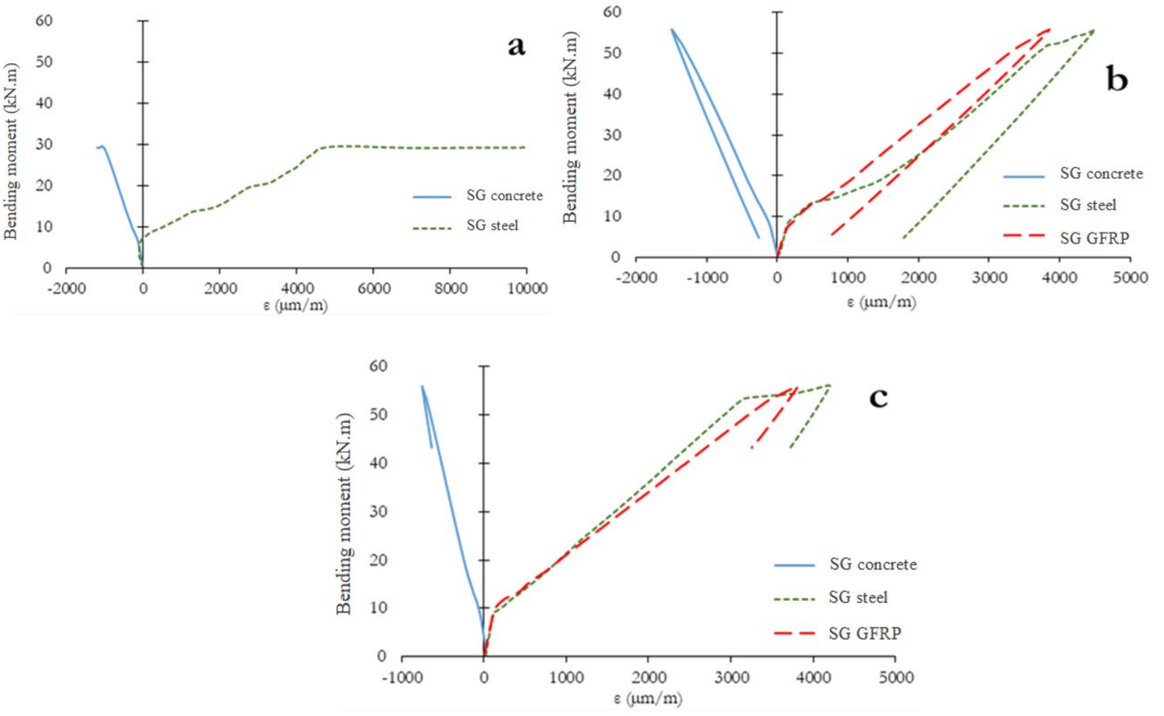

Figure 9. Graph of bending moment and longitudinal strain of the materials for the beams a) REF-1; b) D-1; c) Q-1.

The curves shown in Figure 9 demonstrate through the values of longitudinal deformations, that the steel and the GFRP profiles were, together, responsible for the resistance to the tensile stresses in the structural elements tested in groups D and Q. note that the beams of the reference group presented, in their collapsed state, plastification deformations in the tensioned reinforcements, while the concrete remained in linear-elastic behavior, thus corroborating the theoretical model predicted for the deformation domain 2, according to NBR 6118 [16].

It is also possible to observe the elastic-linear behavior of the GFRP profiles throughout the test, as well as for the concrete in the compressed region, which in all samples did not present a compression rupture at the moment of collapse, and the measured deformations did not reach the values foreseen for the beginning of the appearance of plastic deformations.

The results obtained for the longitudinal deformations of the steel bars in the beams REF-1, D-1 and Q-1 show, through the first change in the inclination of the lines in the graphs, the cracking moments in the structural elements, when the beams pass Deformation Stadium I for Stadium II. This increase in deformations in the bars, shown in the graphs by the sudden increases in deformations for a small variation in the bending moments, reflects the increase in stresses in the tensioned bars due to the appearance of cracks in the adhesion regions [32]. At these high points, adhesion stresses arise due to the difference in deformations between steel bars and concrete, which result in loss of adhesion due to adhesion, which in the case of ribbed bars give rise to transversal cracks in these regions.

It is also observed that after the moment of cracking, all the materials that make up the beams demonstrate changes in the inclination of the straight lines that characterize them. This variation is characteristic of structural elements in Stadium II of deformations, when the beams do not have constant stiffness, resulting from the change in the stiffness of the materials that constitute them [32].

The groups of beams REF-1, D-1 and Q-1 presented the following results of the cracking moment 6.24 kN·m, 8.3 kN·m and 8.82 kN·m, respectively.

3.5 Support load and self-weight ratio

The ratio between the support load obtained experimentally and the proper weight estimated for each beam was carried out to determine the efficiency of the structures. The results of the efficiency factors found for all groups of beams tested (REF, D and Q) were respectively: 159.35 ± 6.78; 285.67± 7.31; 279.82± 9.33.

3.6 Rupture mode

The rupture mode of the reference beams (REF) in relation to the samples of groups D and Q were different, however the behavior observed in the beams of groups D and Q were similar. All the structural elements that made up the REF group showed, at the beginning of the collapse state due to bending stresses, longitudinal reinforcement flow characterized by the opening of large cracks in the tensioned region, without breaking in the compressed concrete area due to the last deformations at compression. This behavior is characteristic of structural elements in domain 2 of deformations in the ELU, according to ABNT NBR 6118 [16]. Figure 10 shows the beams of the reference group (REF) after the mechanical tests performed.

Figure 10. Beams of the reference group (REF) after four-point bending tests a) REF-1. b) REF-2. c) REF-3.

The M_n calculated with the reinforcement was equal to 45.6 kN·m, this explains the change from rupture mode to shear.

Among the samples that made up group D, two of them (D-1 and D-3) did not show rupture until the maximum application loads established for the tests were reached. The beam D-2 presented a rupture close to the support, due to the shear in the GFRP profile at the bottom, which led to the subsequent rupture in the beam due to the shear efforts. Figure 11 shows the beams of group D after the four-point bending tests.

Figure 11. Beams of the group D after four-point bending tests. a) D-1. b) D-2. c) D-3.

The beams of group Q showed a similar behavior in relation to the elements of group D, and the sample Q-1 did not rupture until reaching the maximum load stipulated for the tests. The beams Q-2 and Q-3, on the other hand, showed rupture close to the supports due to the shear of the GFRP profile in the lower part, which subsequently caused the rupture in the beams in this region, due to the acting shear forces.

Beams D-2 and Q-3 showed unevenness in the supports, due to errors during their execution, and due to this, the rupture of the profiles in these elements occurred in the region where the beam was not fully supported, consequently reducing the contact area, that favored the collapse in these regions.

4 CONCLUSIONS

After the tests performed, and through the results obtained, it appears that the GFRP profiles showed considerably increasing their mechanical strength, and their use as a partial substitute for transverse reinforcement proved to be effective.

The results show that there was no significant difference for the results of the samples of the groups that had the profiles of GFRP, therefore it is inferred that the spacing used for the transverse reinforcement in each group was not a relevant factor to justify the mechanical performance of the beams, but the presence of the profiles, and that the different spacing did not generate loss or gain of mechanical resistance in the analyzed samples.

Through the tests and the results obtained, the epoxy resin used to adhere the reinforced concrete structure to the GFRP profiles showed satisfactory performance.

The presence of GFRP profiles in the beams contributed to the increase of their stiffness, in relation to the structural reference elements (REF).

The strength gains obtained in the samples that had the GFRP profiles were the result of the joint action of the profiles and the tensioned longitudinal reinforcement.

The presence of GFRP profiles in the beams contributed to the increase in cracking moments, it can be deduced that such increase occurred due to the tensile stress resisted by these structures.

The theoretical results of cracking moments, last moments of resistance, and deformation domains predicted for the ultimate limit state in the reference beams showed a good correlation with the experimental results obtained.

The theoretical results of the reinforced beams, on the other hand, presented conservative predictions, with all tests on reinforced beams obtaining results superior to those calculated.

The graphical results of longitudinal deformation of the materials that make up the beams showed that the GFRP profiles worked together with the reinforced concrete structure, so the composite design structure showed satisfactory behavior.

The presence of GFRP profiles in the beams significantly increased the efficiency of the structures, when comparing the maximum loads obtained experimentally in relation to the estimated weight of the beams, and the presence of the GFRP profiles did not contribute significantly to the increase of the weight of the samples analyzed.

REFERENCES

[1] American Society for Testing and Materials. *ASTM D3878 – 16: Standard Terminology for Composite Materials*. United States: ASTM, 2016, 6 p.

[2] G. M. Santos, C. A. Gomes, and F. K. Arakaki, “Análise da propriedade mecânica de tração em perfis estruturais pultrudados em fibra de vidro e resina termofixa,” in *XIII INIC IX EPG*, São José dos Campos, São Paulo, 2009, pp. 1-6. Accessed: Dec. 2016. [Online]. Available: www.inicepg.univap.br/cd/INIC_2009/anais/arquivos/0980_0572_01.pdf

[3] J. A. Gonilha et al., “Durability of GFRP-concrete adhesively bonded connections: Experimental and numerical studies,” *Eng. Struc.*, v. 168, p.784-798, maio 2018. http://dx.doi.org/10.1016/j.engstruct.2018.05.018.

[4] A. S. Mosallam “Composites in construction,” in *Handbook of Materials Selection*, M. Kutz, et al., New York, NY, John Wiley & Sons, Inc., 2002. ch. 45, pp. 1369-1420. Accssed: Set. de 2019. [Online]. Available: https://www.researchgate.net/publication/260834646.

[5] V. Mara, R. Haghani, and P. Harrysin, “Bridge decks of fibre reinforced polymer (FRP): a sustainable solution,” *Constr. Build. Mater.*, vol. 50, pp. 190-199, Jan. 2014. http://doi.org/10.1016/j.conbuildmat.2013.09.036.

[6] H. Xin et al., “Analytical and experimental evaluation of flexural behavior of FRP pultruded composite profiles for bridge deck structural design,” *Constr. Build. Mater.*, vol. 150, pp. 123-149, Set. 2017. http://dx.doi.org/10.1016/j.conbuildmat.2017.05.212.

[7] J. R. Correia, *Utilização de Perfis Pultrudidos de Fibra de Vidro (GFRP) na Construção*. Porto, Portugal: Fac. Eng., Univ. do Porto, 2006. 20 p.

[8] H. Fergani et al., "Durability and degradation mechanisms of GFRP reinforcement subjected to severe environments and sustained stress,” *Constr Build Mater*, vol. 170, pp. 637–648, May 2018. http://dx.doi.org/10.1016/j.conbuildmat.2018.03.092.

[9] A. El-nemr et al., “Evaluation of the flexural strength and serviceability of concrete beams reinforced with different types of GFRP bars,” *Eng Struc*, v. 173, pp. 606–619, Oct. 2018. http://dx.doi.org/10.1016/j.engstruct.2018.06.089.

[10] M. C. Pearson, T. Donchev, and M. Limbachiya, “An investigation into the sustainability of frp reinforcement bars,” in *CDCC-11 4th Intern. Conf. Durability Sustainability of Fibre Reinforced Polymer (FRP) Composites for Construction and Rehabilitation*, Quebec City, Canada, Jul. 2011, pp. 71–80.

[11] M. Najm, “Investigating the use of fiber-reinforced polymer bars in concrete,” Master thesis, Dept. Civ. Environ. Eng, Massachusetts Inst. Technol., Cambridge, MA, USA, 2012. [Online]. Available: https://dspace.mit.edu/handle/1721.1/74409.

[12] J. R. Correia, F. A. Branco, and J. Ferreira, "GFRP-concrete hybridcross-sections for floorsofbuildings," *Eng Struc*, vol. 31, no. 6, pp. 1331–1343, June 2009. http://dx.doi.org/10.1016/j.engstruct.2008.04.021.

[13] X. Sha, and J. S. Davidson, "Analysis of interfacial stresses in concrete beams strengthened by externally bonded FRP laminates using composite beam theory," *Compos Struct*, vol. 19, pp. 2020, 2020., http://dx.doi.org/10.1016/j.compstruct.2020.112235.

[14] A. Koaik, S. Bel, and B. Jurkiewiez, "Experimental tests and analytical model of concrete-GFRP hybrid beams under flexure," *Compos Struct*, vol. 180, pp. 192-210, Nov. 2017. https://doi.org/10.1016/j.compstruct.2017.07.059.

[15] A. A. Mohammed et al., "State-of-the-art of prefabricated FRP composite jackets for structural repair," *Eng Sci Technol,* vol. 19, pp. 2020, 2020., http://dx.doi.org/10.1016/j.jestch.2020.02.006.

[16] Associação Brasileira de Normas Técnicas. *NBR 6118: Projeto de Estruturas de Concreto - Procedimento*. Rio de Janeiro, RJ: ABNT, 2014. 236 p.

[17] R. C. Carvalho, and J. R. Filho, "Cálculo e detalhamento de estruturas usuais de concreto armado: segundo NBR 6118:2014," 4. ed. São Carlos: Editora EdUFSCar, 2014.

[18] American Concrete Institute, *ACI 440.2R-08: Guide for the Design and Construction of Externally Bonded FRP Systems for Strengthening Concrete Structures*. Farmington Hills, MI, USA: ACI, 2008. 80 p

[19] American Concrete Institute, *ACI 318-05: Buildingcoderequirements for Structural Concrete and Comentary*. Farmington Hills, MI, USA: ACI, 2005, 1445 p.

[20] Y. H. Mugahed Amran et al., "RC beam strengthening using hinge and anchorage approach," *Resul. Mater.*, vol. 5, no. 10047. Nov. 2020, p. 1–17. http://dx.doi.org/10.1016/j.rinma.2019.100047.

[21] A. Khalifa et al., "Contribution of externally bonded FRP to the Shear Capacity of RC Flexural Members," *J Compos Constr*, vol. 2, no. 4, pp. 195–203. https://doi.org/10.1061/(ASCE)1090-0268(1998)2:4(195).

[22] J. G. Teng et al. "Recent research on intermediate crack induced debonding in FRP Strengthened Beams," in *Proc. 4th Int. Conf. Adv. Comp. Mater. Brid. Struc.*, 2004, Calgary, AB, Canada.

[23] J. G. Teng et al., "Intermediate crack induced debonding in RC beams and slabs," *Construction and Building Materials*, vol. 17, no 6-7, pp. 447–462, Sept./Out. 2003. http://dx.doi.org/10.1016/S0950-0618(03)00043-6

[24] Associação Brasileira de Normas Técnicas, *NBR 5738: Concreto – Procedimento para Moldagem e Cura de Corpos de Prova*. Rio de Janeiro, RJ: ABNT, 2015, 9 p.

[25] American Society for Testing and Materials, *ASTM C78/C78 – 16: Standard Test Method for Flexural Strength of Concrete. Using Simple Beam with Third-Point Loading*. United States: ASTM, 2016. 4 p.

[26] Associação Brasileira de Normas Técnicas, *NBR 5739: Concreto – Ensaio de compressão de corpos-de-prova cilíndricos*. Rio de Janeiro, RJ: ABNT, 2007, 9 p.

[27] Associação Brasileira de Normas Técnicas, *NBR 8522: Concreto – Determinação do módulo estático de elasticidade à compressão*. Rio de Janeiro, RJ: ABNT, 2008, 16 p.

[28] Associação Brasileira de Normas Técnicas, *NBR NM 67: Concreto – Determinação da consistência pelo abatimento do tronco de cone*. Rio de Janeiro, RJ: ABNT, 1996, 8 p.

[29] Associação Brasileira de Normas Técnicas, *NBR NM 248: Agregados - Determinação da composição granulométrica*. Rio de Janeiro, RJ: ABNT, 2003, 6 p.

[30] I. C. Canalli "Estudo de comportamento de estrutura mista de concreto e perfil pultrudado de PRFV sob flexão," M.S. thesis, Civil Eng. Grad. Prog., Univ. Fed. de Santa Catarina, Florianópolis, 2010. [Online]. Available: https://repositorio.ufsc.br/handle/123456789/94068.

[31] A. D. Figueiredo, J. Tanesi, and A. A. Nince, "Concreto com fibras de polipropileno (CFP)," Téchne, vol. 10, no. 66, pp. 48-51, 2002.

[32] F. Leonhardt, *Construções de concreto Vol. 4: Verificação da Capacidade de Utilização: Limitação da Fissura, Deformações, Redistribuição de Momentos e Teorias das Linhas de Ruptura em Estruturas de Concreto Armado*, 1. Ed. Rio de Janeiro, RJ: Interciência, 1979. 210 p.

Author contributions: ISH: proposed the research, performed the literature review, the experimental campaign and wrote this article; JHP: handled and review data and writing; AW: performed the literature review, implemented the GFRP reinforcement theoretical calculus, wrote this article and handled its review; EGPA: proposed the research, supervised the student ISH, proposed the experimental campaign, wrote this article and handled its review.

Editors: José Marcio Calixto, José Luiz Antunes de Oliveira e Sousa, Guilherme Aris Parsekian.

IBRACON Structures and Materials Journal
Revista IBRACON de Estruturas e Materiais
ISSN 1983-4195 ismj.org

ORIGINAL ARTICLE

Numerical and experimental comparative of coupled neighboring buildings

Comparativo numérico e experimental de edificações vizinhas acopladas

Luis Alejandro Perez Peña[a]
Graciela Nora Doz[b]
Suzana Moreira Avila[c]

[a]Universidade de Brasília – UnB, Faculdade de Arquitetura e Urbanismo, Brasília, DF, Brasil
[b]Universidade de Brasília – UnB, Faculdade de Tecnologia, Brasília, DF, Brasil
[c]Universidade de Brasília – UnB, Faculdade de Engenharia do Gama, Brasília, DF, Brasil

Received 07 August 2019
Accepted 28 April 2020

Abstract: In recent years a vibration control technique, called structural coupling, has been studied. This technique consists on linking two neighboring buildings, through a coupling device, with the purpose of reducing dynamic response. It is possible to control both structures response simultaneously, which is precisely the attractiveness of this technique. Given the potential of the structural coupling technique, this work evaluates numerically and experimentally the performance of the structural coupling technique in simple plane frames when subjected to an oscillatory movement in at base caused by a shaking table, designed and built in the Structure Laboratory of University of Brasilia. Initially, the model numerical dynamic responses, without and with coupling, were obtained. Then, experimentally, the plane frames were fixed to the shaking table and subjected to a base movement uncoupled and coupled in order to obtain the acceleration registers and its frequency spectra. Finally, numerical and experimental frequency spectra were compared. The results obtained showed the efficiency of the control method through coupling, which depends mainly on the mechanical properties of adjacent buildings and connecting devices.

Keywords: seismic analysis, structural dynamics, structural control, coupled building.

Resumo: Nos últimos anos têm sido implementada uma técnica de controle de vibrações chamada de acoplamento estrutural. Essa técnica consiste em ligar duas edificações vizinhas por meio de um dispositivo de acoplamento, com o objetivo de diminuir os efeitos dinâmicos em função das propriedades mecânicas de cada estrutura. Ao fazê-lo, em princípio, é possível controlar a resposta de ambas as estruturas simultaneamente, o que é precisamente a atratividade da técnica. Dado o seu potencial, este trabalho tem como objetivo avaliar numérica e experimentalmente a eficácia dela utilizando pórticos planos simples quando submetidos a um movimento oscilatório na base provocado por uma mesa vibratória, projetada e construída no Laboratório de Estruturas da Universidade de Brasília. Inicialmente, foram calculadas as respostas dinâmicas numéricas dos modelos com e sem acoplamento. Em seguida, experimentalmente, os pórticos planos foram fixados na mesa vibratória e foram submetidos a um movimento na base quando desacoplados e acoplados a fim de obter os registros de acelerações e assim obter seus espectros de frequência. Finalmente, foram comparados os espectros obtidos experimentalmente com os obtidos numericamente. Os resultados apresentados mostraram a eficiência do método de controle por meio do acoplamento, a qual foi afetada principalmente pelas propriedades mecânicas dos edifícios adjacentes e dos elementos de conexão.

Palavras-chave: análise sísmica, dinâmica estrutural, controle estrutural, acoplamento estrutural.

How to cite: L. A. Perez Peña, G. N. Doz, and S. M. Avila, "Numerical and experimental comparative of coupled neighboring buildings," *Rev. IBRACON Estrut. Mater.*, vol. 13, no. 6, e13609, 2020, https://doi.org/10.1590/S1983-41952020000600009

Corresponding author: Luis Alejandro Perez Peña. E-mail: alejandrop@unb.br
Financial support: CNPq Brazilian Council of National Scientific and Technological Development and Federal District Research Support Foundation (FAPDF).
Conflict of interest: Nothing to declare.

INTRODUCTION

With the cities development there is a tendency of population increase in large urban centers, causing thus a shortage of spaces and making tall buildings a characteristic of modern cities. These types of buildings because of their height and high mass concentration characteristics are very vulnerable to collapse in the presence of one of the most destructive phenomena of nature: the earthquake. These vibrations are undesirable from the point of view of both comfort and safety.

To work avoiding this problem, medium- and high-rise structures started employing control techniques such as tuned mass dampers (TMDs) to help mitigate excessive vibrations and deformations when subjected to dynamic loads. According to Watanabe et al. [1], one of the drawbacks when a single TMD is used in flexible structures is its sensitivity to any discrepancy in the natural frequency of the structure and the TMD damping. As a solution for this problem, multiple tuned mass dampers with different dynamic characteristics are used. However, the control system becomes expensive.

Thus, a control technique called structural coupling, which consists of connecting two or more neighboring buildings through coupling devices to provide reaction control forces, showed to be a viable alternative for the protection of adjacent flexible structures. This technique can be applied to a wide variety of structural systems and can incorporate various types of control strategies including passive, active, or semiactive control [2], [3].

The application of the coupling technique to civil structures has received much attention from the 90's since it was first proposed by Klein et al. [4] and Kunieda [5]. Theoretical, numerical and experimental approaches of coupled structures were performed in order to demonstrate the viability of this technique [6]–[34]. These studies showed that the efficiency of the coupling technique depends on the mechanical and geometrical properties of the neighboring buildings, as well as on the mechanical properties of the connecting device.

In addition to these analytical and experimental research, a few full-scale applications of coupled building control have been undertaken. In 2001, the Triton Square office complex, located on the Tokyo waterfront on Harumi Island, completed construction. The complex is a cluster of three buildings, 195, 175, and 155 m high, respectively. The three buildings are coupled with two active control actuators for wind and seismic protection [35], [36]. In 2013, between the Chiesa del Sacro Cuore (Florence - Italy) and R/C bell tower, passive viscofluid shock absorbers were installed in order to reduce the pounding between them [37].

It should be noted that most researches on the coupling technique were performed in countries located in areas with a high risk of seismicity and high economic development. In Latin American countries, research related to this technique are still incipient. Thus, this work evaluates numerically and experimentally the performance of the structural coupling technique in simple plane frames when subjected to an oscillatory base movement caused by a shaking table, designed and built in the Structure Laboratory of University of Brasilia. It should also be noted that, even using steel plane frames, the results can be extended to concrete or other materials frames.

METHODOLOGY

In a previous stage, numerical preliminary models were developed to set material type and dimensions of the plane frames to be tested. Then, the shear building frames were constructed and tested to identify dynamic properties such as frequencies, vibration modes and damping factors using the ARTeMIS Modal software [38]. It should be noted that in the shear building model a degree of freedom per floor is considered, therefore, for each of these degrees a frequency value is associated.

Subsequently, numerical models were validated using the correlation of the natural frequencies and the vibrational modes, numerical and experimental, using the percentage of variation of the frequency (FER) and the Modal Assurance Criterion (MAC) [39], [40]. This validation is important to ensure that the numerical models represented the actual physical behavior of the tested plane frames.

Once validation was done, an optimization study was performed using the particle swarm optimization (PSO) [41] in a way to set the connecting device properties. Next, the device that was used in the experimental tests was built.

Then, a numerical and experimental analysis were performed to evaluate the performance of the coupling technique in reducing the amplitudes of the dynamic responses of the adjacent shear frames. For this purpose, the acceleration records and the frequency spectra of each structure were obtained and compared. All numerical analysis, as well as the treatment of experimental data, were performed using MATLAB [42].

MATHEMATICAL FORMULATION

Coupled models

In Figure 1, two plane frames are shown, the structure 1 with $n + m$ floors and the structure 2 with n floors. Each of these buildings has mass, stiffness, and damping properties m_i^j, c_i^j, k_i^j known beforehand, where i indicates the floor number and j the building number. The strategy of passive coupling control involves the placement of springs and dampers between the two buildings, whose mechanical properties are k_n^3 and c_n^3, here n indicates the position of these elements.

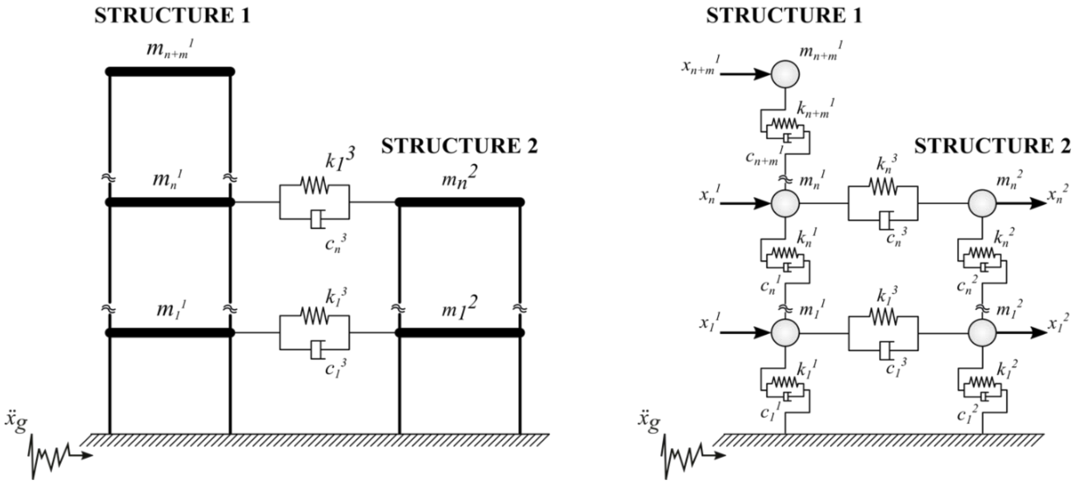

Figure 1. Coupled system with multiple degrees of freedom.

The coupled system motion equation, when submitted to a seismic base acceleration $\ddot{\mathbf{x}}_g\,(t)$ is given by:

$$\boldsymbol{M}_{ss}\,\ddot{\boldsymbol{x}}_{ss}(t)+\left(\boldsymbol{C}_{ss}+\boldsymbol{C}^3\right)\dot{\boldsymbol{x}}_{ss}(t)+\left(\boldsymbol{K}_{ss}+\boldsymbol{K}^3\right)\boldsymbol{x}_{ss}(t)=-\boldsymbol{M}_{ss}\begin{Bmatrix}1\\1\end{Bmatrix}\ddot{\boldsymbol{x}}_g(t) \tag{1}$$

where $\mathbf{M}_{ss}$, $\mathbf{C}_{ss}$ and $\mathbf{K}_{ss}$ are the mass, damping and stiffness matrices of the coupled system respectively; $\mathbf{C}^3$ and $\mathbf{K}^3$ are the matrices that contains the damping and stiffness coefficients of the linking system k_n^3 and c_n^3; $\mathbf{x}_{ss}(t)$, $\dot{\mathbf{x}}_{ss}(t)$ and $\ddot{\mathbf{x}}_{ss}(t)$ are the vectors containing the displacements, velocities and accelerations of the two structures relative to the ground.

Mass, stiffness and damping matrices, $\mathbf{M}_{ss}$, $\mathbf{K}_{ss}$ and $\mathbf{C}_{ss}$, of the coupled structure are defined as follows:

$$\boldsymbol{M}_{ss}=\begin{bmatrix}\boldsymbol{m}^1_{(n+m,n+m)} & 0_{(n+m,n)}\\ 0_{(n,n+m)} & \boldsymbol{m}^2_{(n,n)}\end{bmatrix} \tag{2}$$

$$\boldsymbol{C}_{ss}=\begin{bmatrix}\boldsymbol{c}^1_{(n+m,n+m)} & 0_{(n+m,n)}\\ 0_{(n,n+m)} & \boldsymbol{c}^2_{(n,n)}\end{bmatrix} \tag{3}$$

$$\boldsymbol{K}_{ss}=\begin{bmatrix}\boldsymbol{k}^1_{(n+m,n+m)} & 0_{(n+m,n)}\\ 0_{(n,n+m)} & \boldsymbol{k}^2_{(n,n)}\end{bmatrix} \tag{4}$$

where: $\mathbf{m}^j$ is the diagonal mass matrix of the jth building; $\mathbf{c}^j$ and $\mathbf{k}^j$ are a block diagonal matrix corresponding to the internal damping and stiffness of the jth building. These matrices can be written as:

$$\boldsymbol{m}^j = \begin{bmatrix} m_1^j & & \\ & \ddots & \\ & & m_i^j \end{bmatrix} \tag{5}$$

$$\boldsymbol{c}^j = \begin{bmatrix} c_1^j + c_2^j & -c_2^j & & & & \\ -c_2^j & c_2^j + c_3^j & -c_3^j & & & \\ & -c_3^j & \ddots & & & \\ & & & -c_{i-1}^j & c_{i-1}^j + c_i^j & -c_i^j \\ & & & & -c_i^j & c_i^j \end{bmatrix} \tag{6}$$

$$\boldsymbol{k}^j = \begin{bmatrix} k_1^j + k_2^j & -k_2^j & & & & \\ -k_2^j & k_2^j + k_3^j & -k_3^j & & & \\ & -k_3^j & \ddots & & & \\ & & & -k_{i-1}^j & k_{i-1}^j + k_i^j & -k_i^j \\ & & & & -k_i^j & k_i^j \end{bmatrix} \tag{7}$$

where j indicates the structure number, m_i^j, c_i^j and k_i^j are the mass, damping and stiffness value of the ith story in the jth building. The matrix that contains the damping coefficients of the linking system $\mathbf{C}^3$ is:

$$\boldsymbol{C}^3 = \begin{bmatrix} \hat{\boldsymbol{c}}^1_{(n+m,n+m)} & -\hat{\boldsymbol{c}}_{(n+m,n)} \\ -\hat{\boldsymbol{c}}_{(n,n+m)} & \hat{\boldsymbol{c}}^2_{(n,n)} \end{bmatrix} \tag{8}$$

where

$$\hat{\boldsymbol{c}}^1_{(n+m,n+m)} = \begin{bmatrix} c_1^3 & & & \\ & \ddots & & \\ & & c_n^3 & & \\ & & & \ddots & \\ & & & & 0 \end{bmatrix}, \hat{\boldsymbol{c}}^2_{(n,n)} = \begin{bmatrix} c_1^3 & & \\ & \ddots & \\ & & c_n^3 \end{bmatrix} \tag{9}$$

$$\hat{\boldsymbol{c}}_{(n,n+m)} = \begin{bmatrix} c_1^3 & & & \cdots & 0 \\ & \ddots & & \cdots & 0 \\ & & c_n^3 & \cdots & 0 \end{bmatrix}, \hat{\boldsymbol{c}}_{(n+m,n)} = \begin{bmatrix} c_1^3 & & \\ & \ddots & \\ & & c_n^3 \\ \vdots & \vdots & \vdots \\ 0 & 0 & 0 \end{bmatrix} \tag{10}$$

where c_n^3 is the damping coefficient of the nth passive linking element. The matrix that contains the stiffness coefficients of the linking system $\mathbf{K}^3$ can be obtained from Equation 8, replacing the damping coefficients c_n^3 by the corresponding stiffness coefficients k_n^3.

From the second-order model (Equation 1), a first-order state-space model can be derived:

$$\begin{cases} \dot{z}(t) = \boldsymbol{A}z(t) + \boldsymbol{E}\,\ddot{\boldsymbol{x}}_g(t) \\ \boldsymbol{y}(t) = \boldsymbol{C}_y z(t) \end{cases} \tag{11}$$

with state vector:

$$z(t) = \begin{Bmatrix} \boldsymbol{x}(t) \\ \dot{\boldsymbol{x}}(t) \end{Bmatrix} \tag{12}$$

The state and disturbance input matrices, **A** and **E**, in Equation 11 have, respectively, the following form:

$$\boldsymbol{A} = \begin{bmatrix} 0 & \boldsymbol{I} \\ -\boldsymbol{M}^{-1}\boldsymbol{K} & -\boldsymbol{M}^{-1}\boldsymbol{C} \end{bmatrix}, \boldsymbol{E} = \begin{Bmatrix} 0 \\ -1 \end{Bmatrix} \tag{13}$$

Obtained the state vector $\mathbf{z}(t)$ and using the output matrix $\mathbf{C}_y$ shown in Equation 14, the vector $\mathbf{y}(t)$ (Equation 15) can be obtained, which contains the responses in terms of displacement and velocity relative to the ground, as well as the absolute acceleration of the two buildings.

$$\boldsymbol{C}_y = \begin{bmatrix} \boldsymbol{I} & 0 \\ 0 & \boldsymbol{I} \\ -\boldsymbol{M}_{ee}^{-1}\boldsymbol{K}_{ee} & -\boldsymbol{M}_{ee}^{-1}\boldsymbol{C}_{ee} \end{bmatrix} \tag{14}$$

$$\boldsymbol{y}(t) = \begin{Bmatrix} \boldsymbol{x}_{ee}(t) \\ \dot{\boldsymbol{x}}_{ee}(t) \\ \ddot{\boldsymbol{x}}_{ee}(t) \end{Bmatrix} \tag{15}$$

Correlation between numerical and experimental data

Correlation methods are some techniques to compare the analytical modal data with the experimental modal data. Among the most used correlation techniques are the FER frequency variation and the Modal Assurance Criterion (MAC) [39], [40].

The correlation between natural frequencies is calculated using the FER frequency variation. The FER index for the g experimental mode is calculated using Equation 16, where λ_h and λ_g are the numerical and experimental natural frequency of the h and g mode, respectively.

$$FER = \left| \frac{\lambda_h - \lambda_g}{\lambda_g} \right| \tag{16}$$

The agreement between numerical and experimental modes of vibration is obtained through the Modal Assurance Criterion (MAC) index [39], [40]:

$$MAC(g,h) = \frac{\left|\boldsymbol{\Phi}_g^T \boldsymbol{\Phi}_h\right|^2}{\left(\boldsymbol{\Phi}_h^T \boldsymbol{\Phi}_h\right)\left(\boldsymbol{\Phi}_g^T \boldsymbol{\Phi}_g\right)} \tag{17}$$

where $\mathbf{\Phi}_g$ and $\mathbf{\Phi}_h$ are the test modal and analytical modal vectors, respectively. The MAC index takes values between 0 (representing no consistent correspondence) and 1 (representing a consistent correspondence). Values larger than 0.9 indicate consistent correspondence whereas small values indicate poor resemblance of the two shapes [43].

Numerical and experimental models

Six modules were constructed as shown in Figure 2a and represent a common floor of a residential building. Each of these modules consists of two stainless steel columns (ferritic alloy 430 – E = 210 GPa) with a rectangular section (1.5×25.4 mm) and rigid aluminum beams with a rectangular section (25.4×9.8 mm). The height of the columns was considered of 200 mm [31].

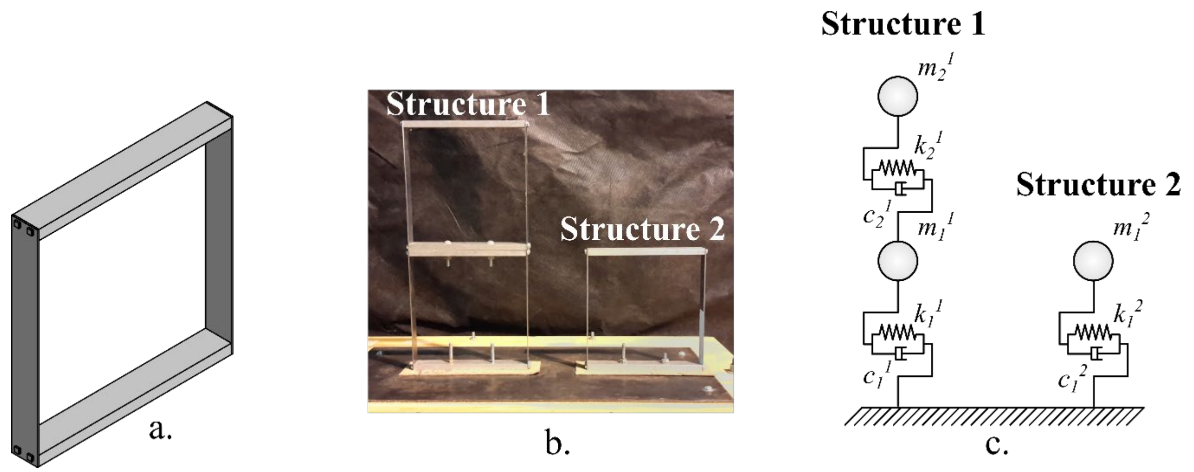

Figure 2. a) module of the plane frame; b) experimental model of adjacent uncoupled plane frames; c) numerical model of adjacent uncoupled plane frames.

By joining several of these modules, it is possible to simulate more pavement structures as if they were a shear building (Figure 2b), since the stiffness of the aluminum bars, which constitute the floors, is much higher in relation to the stainless- steel plates stiffness, which represent the columns of the experimental models. In Figure 2c, the numerical models of adjacent uncoupled plane frames are presented.

The mass and stiffness matrices of the models showed in the Figure 2c are defined in the following Equations 18 and 19. In the mass matrices, besides the mass of the elements that make up the modules, the masses of the screws, nuts and washers used to join them were considered. In the case of stiffness matrices, it was considered that the stiffness of the modules is given by the columns fixed at the base.

$$\boldsymbol{m}^1 = \begin{bmatrix} 0,3912 & 0 \\ 0 & 0,1826 \end{bmatrix} kg \qquad m_1^2 = 0,1830\ kg \tag{18}$$

$$\boldsymbol{k}^1 = \begin{bmatrix} 9740,27 & -4885,93 \\ -4885,930 & 4885,93 \end{bmatrix} \frac{N}{M} \qquad k_1^2 = 5236,19 \frac{N}{M} \tag{19}$$

To assemble the stiffness matrices, the Caughey or extended Rayleigh method [44] (Equation 20) was used to construct these matrices from data obtained from experimental modal analysis of both buildings, that is, from a natural frequency ω_i and its corresponding modal damping ξ_i of the ith mode.

$$\boldsymbol{c} = \boldsymbol{m} \sum_{i=0}^{N-1} \alpha_i \left(\boldsymbol{m}^{-1} \boldsymbol{k} \right)^i \tag{20}$$

In Equation 20: N is the number of degrees of freedom of the system; **m** and **k** are the mass and stiffness matrices of the building, respectively; α_i are real and positive constants which are calculated by:

$$\xi_n = \frac{1}{2} \sum_{i=0}^{j-1} \alpha_i \left(\omega_n \right)^{2i-1} \tag{21}$$

where ξ_n e ω_n are the natural frequencies and damping factors for the n modes of the system. Thus, the equation above becomes a set of equations, one for each ω_n and ξ_n, where α_i is the constant to be calculated.

Shaking Table

In order to simulate the movement at the base of the small-scale models, the unidirectional shaking table shown in Figure 3 was designed and constructed in the Laboratory of Structures of the University of Brasilia according to the safety conditions of the Brazilian technical standards.

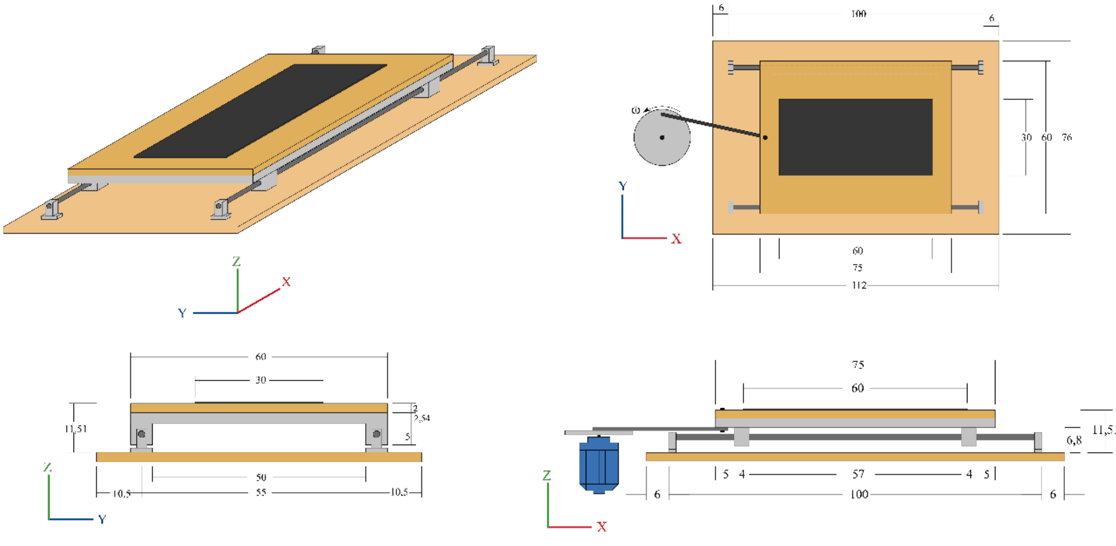

Figure 3. Unidirectional shaking table. Dimensions in centimeters.

The oscillating motion of the table is generated by a rod-crank system, which can transform the circular movement into a translational movement. The crank describes the flat rotational movement, the rod pushes the main platform which, by means of the four linear bearings located in its corners, has rectilinear translation motion in the orthogonal direction X. The rotation movement of the crank is promoted by a motor whose angular rotation speed ω is controlled by a frequency inverter. The constructed model and mechanical and electronic components of the Shaking table can be observed in Figure 4.

Instrumentation

To obtain the accelerations in the plane frames, as well as their modal identification, PCB Piezotronics model 353B01 accelerometers were used, which have an approximate mass of 10*g* and sensitivity of ±5% 20 mV/g (2.04 mV/(m/s^2)). These accelerometers were connected to the IPC Model 482A22 unit gain signal conditioner from the same company and which translates the vibration of the structure into electrical pulses and sends them to the ADS2000 signal receptor, manufactured by Lynx Tecnologia Eletrônica. Finally, the acceleration registers are monitored and recorded using AqDados 7 software [45].

The acquisition equipment was configured to capture records from 1 to 3 channels, at time instants of 0.005s, resulting in a 200 Hz sampling frequency. Consequently, the Nyquist frequency was half the sampling frequency, in this case, 100Hz.

Figure 4. Shaking table built and mechanical and electronic components.

RESULTS

Plane frame modal identification

Table 1 shows the natural frequencies obtained from the acceleration records acquired in the laboratory for each plane frame model (Figure 2b), as well as the FER frequency variation and the damping factor ξ for each vibration mode. The comparison of the numerical and experimental vibration modes of Structure 1 (Figure 2b), as well as the matrix of the MAC index correlation, are shown in Figure 5.

It can be seen in the Table 1 that the first frequencies in both plane frames presented a FER index lower than 1%. However, there was a low value for the second frequency, with differences of more than 7%. On the other hand, it is observed in Figure 5 that the MAC indexes presented diagonal values approximately equal to 1, which indicates a good agreement between the modal forms.

It is interesting to note that, as expected, the damping factors presented very low values as seen in the Table 1 [46]. Thus, having the frequencies and damping factors and using Equations 20 and 21, the damping matrices of the structures shown in Figure 2b can be assembled.

Finally, it is worth noting that the 1% error between the numerical and experimental frequencies for the first mode (fundamental mode) is acceptable due to the possible differences that the shear building model or plane frame are unable to represent, besides the possible instrumental errors. Thus, it was decided to not be updating the models.

Connection Device

An optimization study was performed using the particle swarm optimization (PSO) [41] in a way to set the mechanical properties k_n^3 and c_n^3 of the connection device (Figure 1). The summation of coupled model rms (Root Mean Square) accelerations was used as an objective function. Once these mechanical properties were obtained, the damper that was used in the experimental tests was built. Table 2 presents the results of the optimization.

It can be observed in Table 2 that k^3 and c^3 had a very little variation. It also can be noticed that to control dynamic response on both structures, it is necessary to use a connection device with c^3 = 9.48 Ns/m and k^3 = 0. It can be said that the best connection device to the analyzed model is using only a viscofluid damper

Table 1. Averages values of experimental vibration natural frequencies and damping factors of the plane frames, as well as the FER index.

Structure	*Mode*	*ξ*	*Exp. Frequency [Hz]*	*Num. Frequency [Hz]*	*FER [%]*
1	*1*	*0.40*	*13.90*	*13.84*	*0.45*
	2	*0.20*	*36.18*	*33.42*	*7.62*
2	*1*	*0.20*	*27.34*	*27.11*	*0.84*

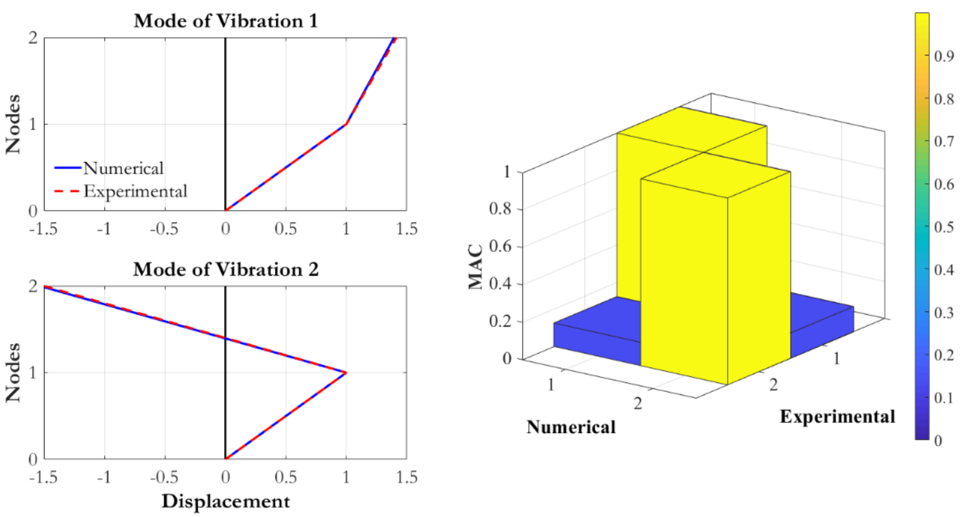

Figure 5. Comparison of numerical and experimental vibration modes and MAC correlation matrix – Structure 1 Uncoupled.

Table 2. Optimal connection device properties obtained with PSO.

c_n^3 [Ns/m]	*k_n^3 [N/m]*	*$f_{objetivo}$ [m/s²]*
9.4799	*9.58930×10⁻⁷*	*1.7197*
9.4798	*8.58930×10⁻⁷*	*1.7197*
9.4788	*9.18925×10⁻⁷*	*1.7197*

Viscofluid damper construction

The connecting element used in this work was of the viscofluid type ($c^3 \neq 0$, $k^3 = 0$) as shown in Figure 6. In this type of shock absorber, the energy dissipation occurs due to the rub of the piston in crossing the fluid generated by the viscous fluid, defined as viscous friction. The piston restricts the flow of oil through holes when it moves, causing a dissipation of mechanical energy in the form of heat.

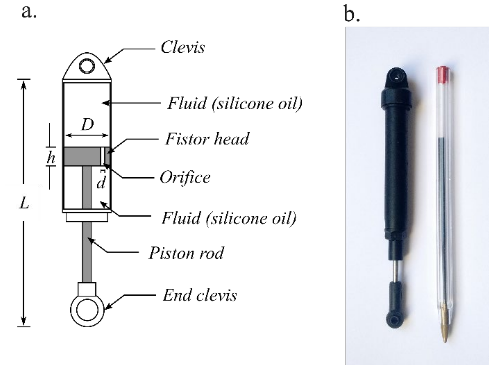

Figure 6. a) Components of a viscofluid damper; b) Viscofluid damper used in the experimental analyses.

As the piston rod moves within the cylinder (Figure 6a), the fluid exerts a resistive force proportional to the velocity. The simplest mathematical modeling of the damping force, adopted in this work, is given by Equation 22, where F_d is the viscous resistance or damper force, c^3 is the viscous damping coefficient of the connecting element and $\dot{x}$ is the relative velocity.

$$F_d = c^3 \dot{x} \tag{22}$$

For the calculation of the coefficient c^3, it is generally used Equation 23 proposed by Rao [47]:

$$c^3 = \mu \frac{3\pi D^3 h}{d^3}\left(1 + \frac{2d}{D}\right) \tag{23}$$

where: μ is the dynamic viscosity of the fluid; D and h are the diameter and height of the fistor head, respectively; d is the diameter of the orifice in the fistor head. For the construction of this device, the measurements listed in Table 3 were employed.

Table 3. Geometric properties of the fluid viscous damper.

L [mm]	*D [mm]*	*d [mm]*	*h [mm]*
200	10	1	3

Having calculated the optimal c^3 value of the connection element and using the geometric properties of the fluid viscous damper (Table 3) as well as Equation 23, it is possible to obtain the dynamic viscosity μ of the fluid to be placed in the device. Thus, μ = 0.279 Pa.s was obtained.

In this work, silicone oils were used, which are common in the manufacture of shock absorbers for RC cars. However, an oil with dynamic viscosity slightly higher than that calculated was used due to the unavailability on the market for the purchase of oils. Therefore, it was used a 47V350 silicone oil [48] of 0.97 g/cm^3 density and a dynamic viscosity μ = 0.350 Pa.s. Table 4 shows the mechanical properties, ideal and used, of the viscofluid damper.

Table 4. Mechanical properties of the viscofluid damper.

μ_{ideal} *[Pa.s]*	c^3_{ideal} *[Ns/m]*	μ_{used} *[Pa.s]*	c^3_{used} *[Ns/m]*
0.279	9.48	0.350	11.519

Dynamic responses

This section presents the comparison between the experimental and numerical responses of the plane frames shown in Figure 7, without and with coupling, when submitted to base movement. For each case, ten tests were performed, five for the uncoupled system and five for the coupled system, in order to calculate an average of the responses and decrease the error tendency.

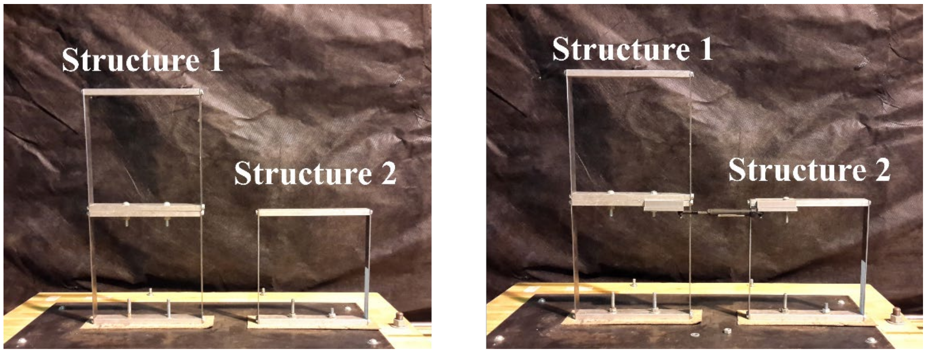

Figure 7. a) Uncoupled frames; b) Coupled frames.

Generally, in the study of the coupling technique, the acceleration records of El Centro, Kobe and Northridge earthquakes are used, which present the highest values of peak ground acceleration (PGA) in a frequency range between 2 and 5 Hz. Thus, in this work, a movement in the base with an oscillation frequency of 3 Hz was used (Figure 8), which represents the average of these frequency range. This simplification is necessary to be able to compare numerical and experimental results.

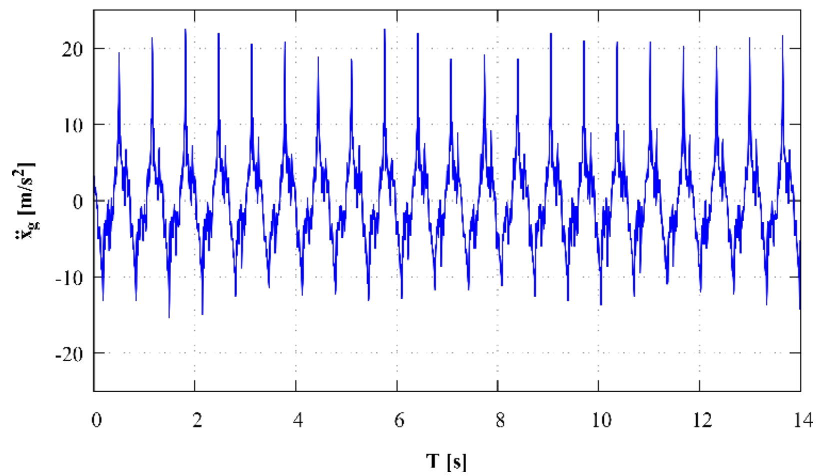

Figure 8. Acceleration records measured at the base of the adjacent experimental plane frames.

Figures 9 and 10 show the acceleration records at different points calculated using Equation 11 and those obtained in experimental tests, respectively. With the acceleration register it was possible to calculate the rms responses (Table 5), which, when compared, gives an indication of the effectiveness of the coupling technique in reducing dynamic responses [10]. Likewise, using these acceleration registers it was possible to obtain the frequency spectra, shown in Figures 11 and 12. It should be noted that these frequency spectra and the rms values listed in Table 5 show the mean of the data collected from all tests.

It can be seen from Figures 9 and 10 and Table 5 that, by coupling the structures with the viscofluid damper, it was possible to considerably decrease the accelerations in Structure 1 (red lines) compared to the uncoupled structure (gray lines). On the other hand, in Structure 2, even having a fundamental frequency (27.34 Hz) well above the value of the excitation frequency (3 Hz), the coupling technique managed to slightly decrease the accelerations compared to the uncoupled structure.

It can be seen in Figures 11 and 12 that the numerical and experimental spectra were almost identical, displaying differences only in the amplitude values at the peak frequency of the structures. Similarly, it is observed that the frequency spectra of the coupled system (red lines) decreased in the peaks where the fundamental frequency of each structure appears without increasing or decreasing the frequency of the structures.

In the case of the frequency spectra of Structure 2 (Figures 11 and 12), it is observed that in some ranges of the frequency spectrum there is an increase of the amplitudes when this building is coupled, however, these peaks correspond to harmonics associated to the movement of the shake table.

Finally, it is noteworthy that even without updating the numerical models, it was obtained response values close to those reached experimentally, and the structure 1 presented the closest approximation between the results.

Table 5. Mean of rms experimental and numerical responses in terms of acceleration.

Coupling Configurations	*Structure 1 – rms [m/s²]*				*Structure 2 – rms [m/s²]*	
	Numerical		*Experimental*		*Numerical*	*Experimental*
	1st floor	*Top*	*1st floor*	*Top*	*Top*	*Top*
Uncoupled	*36.93*	*48.36*	*31.35*	*44.36*	*11.49*	*11.11*
Coupled	*9.18*	*13.49*	*9.85*	*15.21*	*9.89*	*10.03*
% Reduction	*75.1*	*72.1*	*68.6*	*65.7*	*13.9*	*9.7*

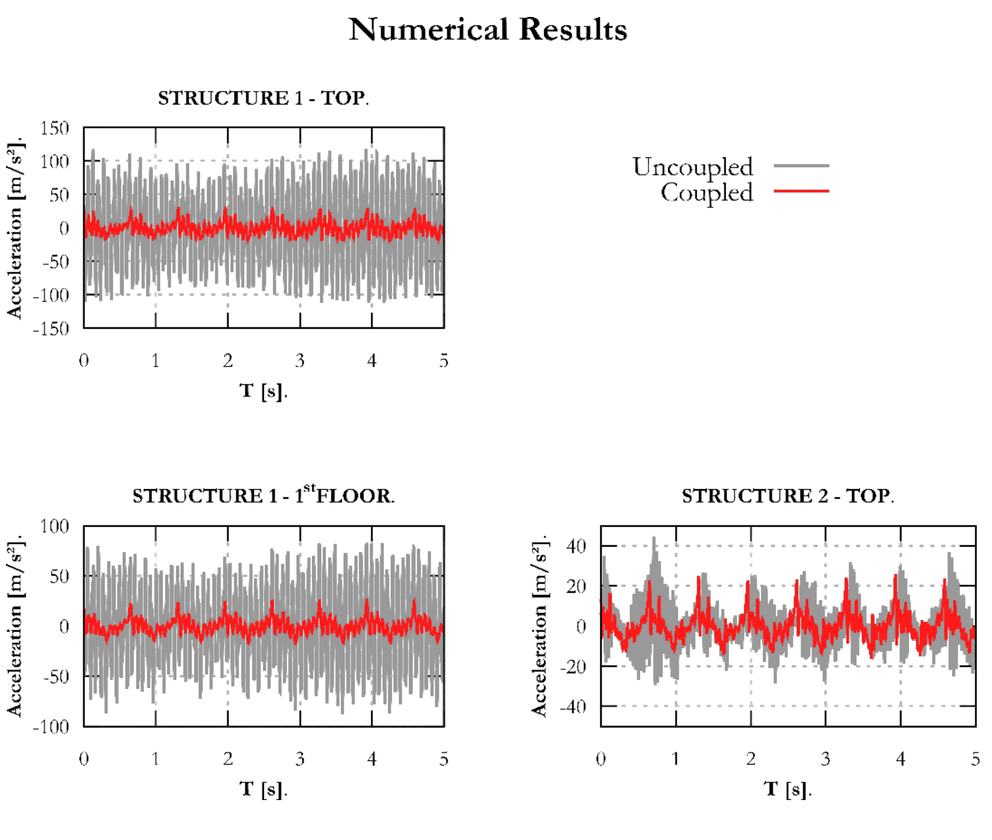

Figure 9. Comparison of the numerical acceleration records of the adjacent frames.

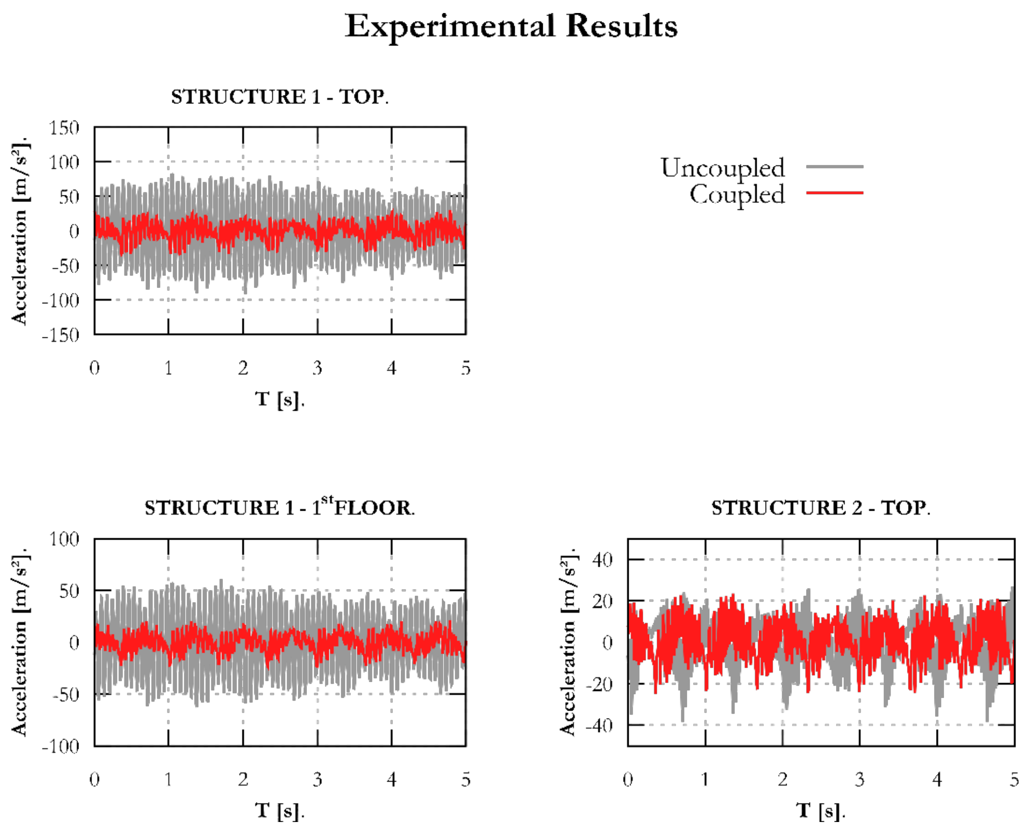

Figure 10. Comparison of the experimental acceleration records of the adjacent frames.

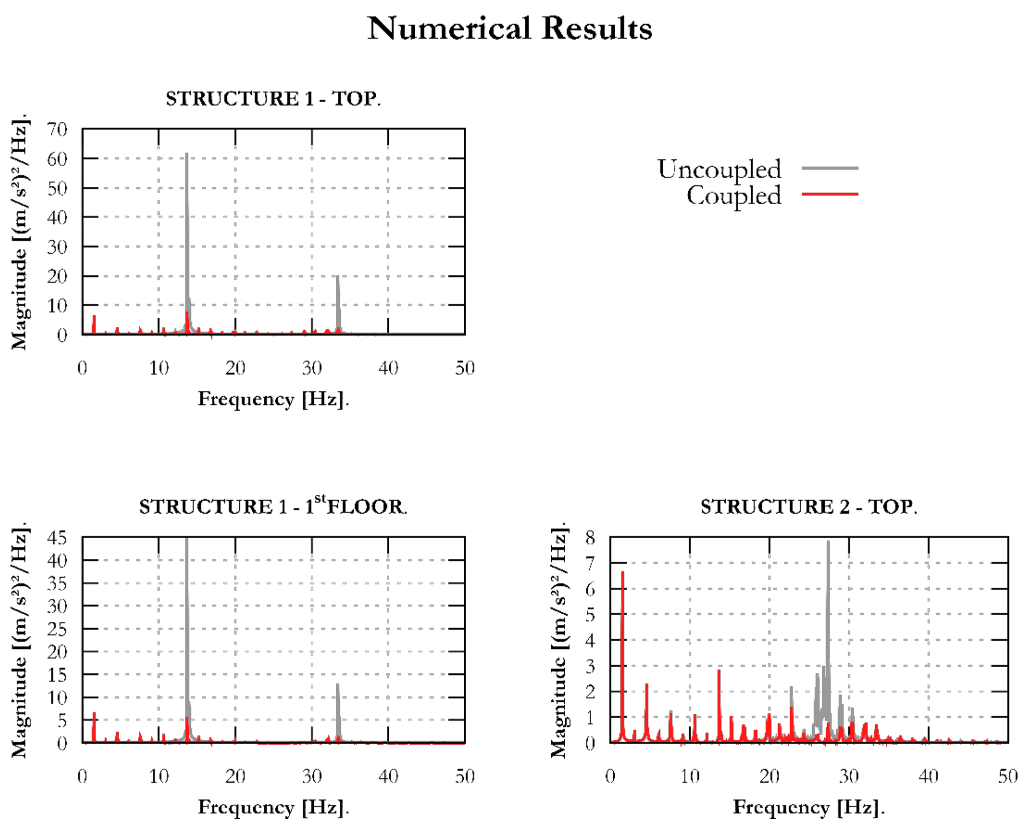

Figure 11. Comparison of the numerical frequency spectra of the adjacent frames.

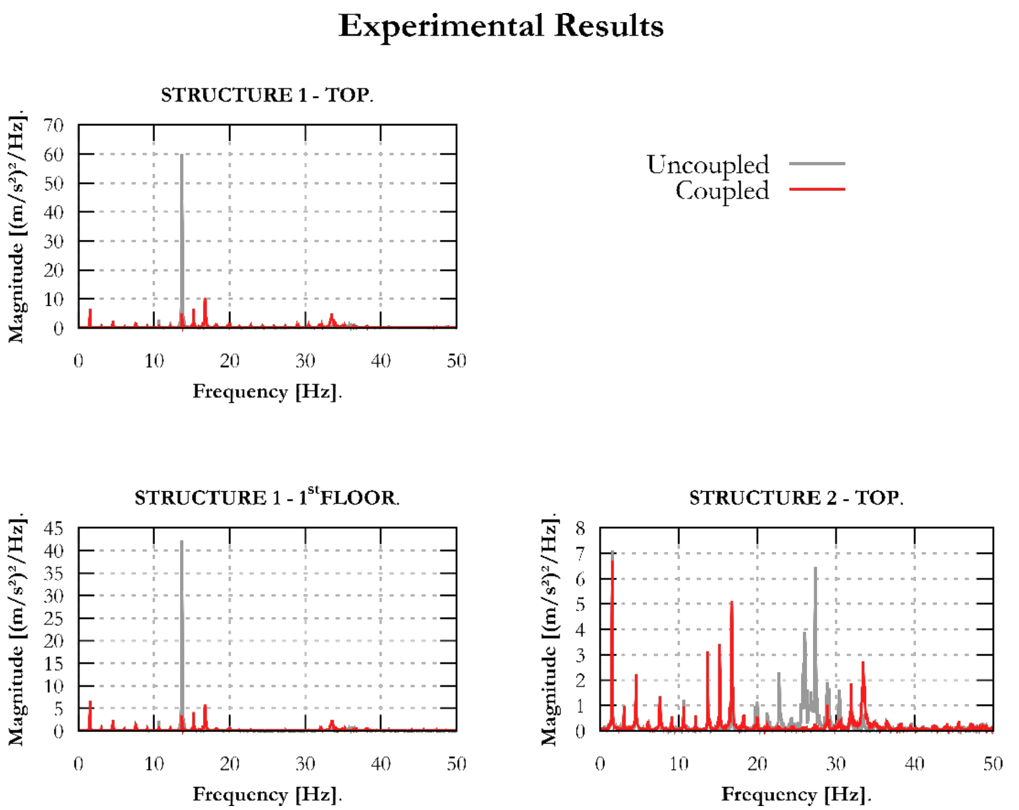

Figure 12. Comparison of the experimental frequency spectra of the adjacent frames.

CONCLUSION

The structural coupling technique consists of connecting two or more neighboring buildings by means of coupling devices in order to provide reaction control forces and thus, reduce the dynamic effects. Doing that, at first, it is possible to control the response of both structures simultaneously, which is precisely the attractiveness of the technique.

It is important to note that in this work, a base movement with an oscillation with only one frequency component (3 Hz) was used that represents the average of the frequencies range of the earthquakes most considered in research on the coupling technique.

Based on the results obtained in this work, several conclusions can be drawn. The optimization results showed that the fluid viscous damper is the ideal connection device, since increases the damping of the coupled structures and did not interfere in the values of the frequencies of the coupled system.

Another aspect to mention is that, even though the oil with the optimum dynamic viscosity was not used due to the unavailability of the material (common situation in civil construction), there was a decrease in the peak values of the acceleration records as well as in the amplitude peaks in the frequency spectra.

Finally, it is important to note that this research can be adapted for concrete or steel buildings [1], [15], [36]. The mathematical formulation would be the same, however, it would change the values of the mechanical properties of the structures.

ACKNOWLEDGEMENTS

The authors acknowledge CNPq Brazilian Council of National Scientific and Technological Development and Federal District Research Support Foundation (FAPDF) for the financial support of this research.

REFERENCES

[1] T. Watanabe, K. Seto, H. Toyoda, and T. Takano, "Bidirectional connected control method applied to an experimental structural model split into four substructures," *J. Phys. Conf. Ser.*, vol. 744, no. 1, pp. 12–35, Sep 2016., http://dx.doi.org/10.1088/1742-6596/744/1/012035.

[2] K. Seto "Vibration control method for flexible structures arranged in parallel," in *Proc. 1st World Conf. Struct. Control, vol. 2*, 1994, FP3-62-71.

[3] K. Fujimura, K. Makita, T. Watanabe, and K. Seto, "Vibration control using connected control device for two identical structures arranged in parallel," in *Proc. ASME 2005 Int. Des. Eng. Tech. Conf. Comput. Inf. Eng.Conf.*, 2005, pp. 2357–2364, http://dx.doi.org/10.1115/DETC2005-85194.

[4] R. E. Klein, C. Cusano, and J. Stukel, "Investigation of a method to stabilize wind induced oscillations in large structures," in *1972 ASME Winter Annu. Meeting* (Paper 72), 1972.

[5] M. Kunieda, "Earthquake prevent design and earthquake proof design for structures," *J. JSME*, vol. 79, no. 689, pp. 86–91, 1974.

[6] B. D. Westermo, "The dynamics of interstructural connection to prevent pounding," *J. Earthq. Eng. Struct. Dyn.*, vol. 18, no. 5, pp. 687–699, 1989., http://dx.doi.org/10.1002/eqe.4290180508.

[7] M. C. Graham, "Design strategies for coupling buildings," M.S. thesis, Dept. Civ. Environ. Eng., Inst. Technol., Massachusetts, 1994.

[8] J. E. Luco and C. P. Barros, "Optimal damping between two adjacent elastic structures," *J. Earthq. Eng. Struct. Dyn.*, vol. 27, no. 7, pp. 649–659, 1998., http://dx.doi.org/10.1002/(SICI)1096-9845(199807)27:7<649::AID-EQE748>3.0.CO;2-5.

[9] Y. Xu, Q. He, and J. M. Ko, "Dynamic response of damper-connected adjacent buildings under earthquake excitation," *J. Eng. Struct.*, vol. 21, no. 2, pp. 135–148, 1999., http://dx.doi.org/10.1016/S0141-0296(97)00154-5.

[10] R. E. Christenson, "Semiactive control of civil structures for natural hazard mitigation: analytical and experimental studies," Ph.D. dissertation, Dept. Civ. Eng. Geol. Sci., Univ. Notre Dame, Indiana, 2001.

[11] S. H. Kim, S. W. Lee, and H. S. Mha, "Dynamic behaviors of the bridge considering pounding and friction effects under seismic excitation," *J. Struct. Eng. Mech.*, vol. 10, no. 6, pp. 621–633, 2001, http://dx.doi.org/10.12989/sem.2000.10.6.621.

[12] H. Zhu, Y. Wen, and H. Iemura, "A study on interaction control for the seismic response of parallel structures," *J. Comp. Struct.*, vol. 79, no. 1, pp. 231–242, 2001., http://dx.doi.org/10.1016/S0045-7949(00)00119-X.

[13] Y. L. Xu, Z. Yang, and X. L. Lu, "Inelastic seismic response of adjacent buildings linked by fluid dampers," *J. Struct. Eng. Mech*, vol. 15, no. 5, pp. 513–534, 2003., http://dx.doi.org/10.12989/sem.2003.15.5.513.

[14] C. G. Karayannis and M. J. Favvata, "Inter-story pounding between multistory reinforced concrete structures," *J. Struct. Eng. Mech.*, vol. 20, no. 5, pp. 505–526, 2005., http://dx.doi.org/10.12989/sem.2005.20.5.505.

[15] K. Makita, R. E. Christenson, K. Seto, and T. Watanabe, "Optimal design strategy of connected control method for two dynamically similar structures," *J. Eng. Mech.*, vol. 133, no. 12, pp. 1247–1257, 2007., http://dx.doi.org/10.1061/(ASCE)0733-9399(2007)133:12(1247).

[16] G. P. Cimellaro and D. Lopez-Garcia, "Algorithm for design of controlled motion of adjacent structures," *J. Struct. Control Health Monit.*, vol. 18, no. 2, pp. 140–148, 2009, http://dx.doi.org/10.1002/stc.357.

[17] H. Roh, G. P. Cimellaro, and D. Lopez-Garcia, "Seismic response of adjacent steel structures connected by passive device," *Adv. Struct. Eng.*, vol. 14, no. 13, pp. 499–517, 2011, http://dx.doi.org/10.1260/1369-4332.14.3.499.

[18] S. Naserkhaki, A. Aziz, and N. A. Farah, "Pourmohammad, H. Parametric study on earthquake induced pounding between adjacent buildings," *J. Eng. Mech.*, vol. 43, no. 4, pp. 503–526, 2012, http://dx.doi.org/10.12989/SEM.2012.43.4.503.

[19] F. Palacios-Quiñonero, J. M. Rossell, J. Rubió-Masseguú, and H. R. Karimi, "“Structural vibration control for a class of connected multistructure mechanical systems”, *J*," *Math. Probl. Eng.*, vol. 12, no. 1, pp. 1–23, 2012, http://dx.doi.org/10.1155/2012/942910.

[20] E. Tubaldi, M. Barbato, and S. Ghazizadeh, "A probabilistic performance-based risk assessment approach for seismic pounding with efficient application to linear systems," *J. Struct. Saf.*, vol. 36–37, pp. 14–22, May 2012., http://dx.doi.org/10.1016/j.strusafe.2012.01.002.

[21] M. Barbato and E. Tubaldi, "A probabilistic performance-based approach for mitigating the seismic pounding risk between adjacent buildings," *J. Earthq. Eng. Struct. Dyn.*, vol. 42, no. 8, pp. 1203–1219, Oct 2012., http://dx.doi.org/10.1002/eqe.2267.

[22] C. C. Patel and R. S. Jangid, "Seismic response of dynamically similar adjacent structures connected with viscous dampers," *IES J. Part A Civ. Struct. Eng.*, vol. 3, no. 1, pp. 1–13, Feb 2010, http://dx.doi.org/10.1080/19373260903236833.

[23] H.-S. Kim and J.-W. Kang, "Seismic response control of adjacent buildings using shared tuned mass damper," *J. Korean Assoc. Spat. Struct.*, vol. 14, no. 3, pp. 75–84, Sep 2014, http://dx.doi.org/10.9712/KASS.2014.14.3.075.

[24] S. Naserkhaki, M. El-Rich, F. N. A. A. Aziz, and H. Pourmohammad, "Pounding between adjacent buildings of varying height coupled through soil," *J. Struct. Eng. Mech.*, vol. 52, no. 3, pp. 573–593, Nov 2014, http://dx.doi.org/10.12989/sem.2014.52.3.573.

[25] L. A. Pérez, S. Avila, and G. Doz, "Seismic response control of adjacent buildings connected by viscous and hybrid dampers", in *Dynamics of Civil Structures, vol. 4, no. 1*, F. N. Catbas, Ed., Cham: Springer, 2014, pp. 433–440.

[26] K. Bigdeli, W. Hare, J. Nutini, and S. Tesfamariam, "Optimizing damper connectors for adjacent buildings," *J. Opt. Eng.*, vol. 17, no. 1, pp. 47–75, Nov 2015, http://dx.doi.org/10.1007/s11081-015-9299-5.

[27] E. Tubaldi, "Dynamic behavior of adjacent buildings connected by linear viscous/viscoelastic dampers," *J. Struct. Control Health Monit.*, vol. 22, no. 8, pp. 1086–1102, Feb 2015, http://dx.doi.org/10.1002/stc.1734.

[28] H. M. Faridani and A. Capsoni, "A modified replacement beam for analyzing building structures with damping systems," *J. Struct. Eng. Mech.*, vol. 58, no. 5, pp. 905–929, Jun 2016, http://dx.doi.org/10.12989/sem.2016.58.5.905.

[29] M. Abdeddaim, A. Ounis, M. K. Shrimali, and T. K. Datta, "Retrofitting of a weaker building by coupling it to an adjacent stronger building using MR dampers," *J. Struct. Eng. Mech.*, vol. 62, no. 2, pp. 197–208, Apr 2017, http://dx.doi.org/10.12989/sem.2017.62.2.197.

[30] Z. Guenidi, M. Abdeddaim, A. Ounis, M. K. Shrimali, and T. K. Datta, "Control of Adjacent Buildings Using Shared Tuned Mass Damper," *Procedia Eng.*, vol. 199, pp. 1568–1573, 2017, http://dx.doi.org/10.1016/j.proeng.2017.09.059.

[31] L. A. Pérez Peña, "Resposta dinâmica de edificações adjacentes acopladas: considerações sobre a interção solo – estrutura," Ph.D. dissertation, Dep. Eng. Civ., Univ. Brasília, Brasília, 2017.

[32] S. Rahimi and M. Soltani, "Expected extreme value of pounding force between two adjacent buildings," *J. Struct. Eng. Mech.*, vol. 61, no. 2, pp. 183–192, Jan 2017, http://dx.doi.org/10.12989/sem.2017.61.2.183.

[33] J. Song, K. T. Tse, G. Hu, S. Liang, and L. Zou, "Dynamic properties of wind-excited linked tall buildings considering both intrabuilding and interbuilding structural couplings," *J. Struct. Eng.*, vol. 144, no. 1, pp. 6017007, Jan 2018, http://dx.doi.org/10.1061/(ASCE)ST.1943-541X.0001928.

[34] P. Pippi, P. Bernardes Jr., S. Avila, M. Morais, and G. Doz, "Dynamic response to different models of adjacent coupled buildings," *J. Vib. Eng. Tech.*, vol. 8, no. 1, pp. 247–256, Apr 2019., http://dx.doi.org/10.1007/s42417-019-00102-7.

[35] M. Asano, Y. Yamano, K. Yoshie, Y. Koike, K. Nakagawa, and T. Murata, "Development of active-damping bridges and its application to triple high-rise buildings," *JSME Int. J. Ser. C*, vol. 46, no. 3, pp. 854–860, 2003., http://dx.doi.org/10.1299/jsmec.46.854.

[36] K. Yoshie, Y. Koike, H. Shiraki, M. Asano, and Y. Yamano, "Active-damping bridges for buildings of Harumi Island Triton Square (Part 5, Control effect evaluation using performance records)," in *Summaries of Tech. Papers Annu. Meeting Architectural Inst. Japan, B-2 Struct. Struct. Dyn. Nuclear Power Plants*, 2003, pp. 717–718.

[37] F. Pratesi, S. Sorace, and G. Terenzi, "Analysis and mitigation of seismic pounding of a slender R/C bell tower," *J. Eng. Struct.*, vol. 71, pp. 23–34, Jul 2014, http://dx.doi.org/10.1016/j.engstruct.2014.04.006.

[38] *ARTeMIS Modal Analysis – Structural Vibration Analysis (v4.0.6 – 2015)*, Aalborg, Denmark, 2015.

[39] R. J. Allemang, "Investigation of some multiple input/output frequency response function experimental modal analysis techniques," Ph.D. dissertation, Dept. Mech. Eng., University of Cincinnati, 1980.

[40] R. J. Allemang and D. L. Brown, "A correlation coefficient for modal vector analysis," in *Proc. Int. Modal Analysis Conf.*, 1982, pp. 110–116.

[41] J. Kennedy and R. Eberhart, "Particle swarm optimization," in *Proc. of IEEE Int. Conf. on Neural Networks*, 1995, pp. 1942–1948.

[42] *MATLAB – Matrix Laboratory (R2009b)*. MathWorks - MATLAB and Simulink for Technical Computing, Massachusetts, U.S.A., 2009.

[43] S. Braun, D. Ewins, and S. S. Rao, *Encyclopedia of Vibration*. San Diego: Academic Press, 2002.

[44] R. W. Clough and J. Penzien, *Dynamics of Structures*. New York, USA: McGraw Hill, 2003.

[45] *AqDados 7.02, Acquisition Program Signals: User Manual, Ver. 7*. Lynx Electronic Technology Ltd., São Paulo, 2003.

[46] J. Franceschini and H. M. Gomes, "Avaliação de amortecimento estrutural usando-se o método do 'Random Decrement'," *Rev. Eng. Estudo Pesqui.*, vol. 10, no. 1, pp. 39–48, 2010.

[47] S. S. Rao, *Mechanicals Vibrations*. USA: Prentice Hall Pearson, 2010.

[48] Quimidrol. "Empresa de importação de produtos químicos e farmacêuticos." http://www.quimidrol.com.br/quimica (accessed July 1, 2016).

Author contributions: Peña developed the theoretical formalism, performed the analytic calculations, and performed the numerical simulations and experimental tests. Doz and Avila supervised the project and contributed to the design and implementation of the research, to the analysis of the results and to the writing of the manuscript. Luis Alejandro Perez Peña & Graciela Nora Doz – conceptualization, supervision, writing, data curation, formal analysis. Suzana Moreira Avila – conceptualization, supervision, writing;, data curation, formal analysis.

Editors: Bernardo Horowitz, José Luiz Antunes de Oliveira e Sousa, Guilherme Aris Parsekian.

IBRACON Structures and Materials Journal
Revista IBRACON de Estruturas e Materiais
ISSN 1983-4195 ismj.org

ORIGINAL ARTICLE

Experimental analysis of the structural behavior of different types of shear connectors in steel-concrete composite beams

Análise experimental do comportamento estrutural de diferentes tipos de conectores de cisalhamento em vigas mistas de aço-concreto

Juliano Geraldo Ribeiro Neto[a]
Gregório Sandro Vieira[b]
Rogers de Oliveira Zoccoli[c]

[a]Remy Consulting Engineers Toronto, Ontario, Canada
[b]Universidade Federal de Uberlândia – UFU, Faculdade de Engenharia Civil, Uberlândia, MG, Brasil
[c]Centro Universitário Cathedral, Barra do Garças, MT, Brasil

Received 15 September 2019
Accepted 30 March 2020

Abstract: The present work aims to compare the structural behavior of steel-concrete composite-section beams for three types of shear connectors made of U hot rolled section and cold-formed sections of U and L. Experimental tests were performed with the three types of connectors associated with I section laminated steel beams and reinforced concrete slabs. For each type of connector, three push-out tests were performed, as well as six simple supported beam tests to evaluate the positive bending moment region. The results indicated that the direct shear behavior among the different types of connectors presents significant differences, however they do not significantly influence the average flexural strength of the composite beams. These, however, present considerable differences in deflections and deformations due to the stiffness differences of the connectors.

Keywords: push-out test, shear connectors, composite beans of steel and concrete.

Resumo: O presente trabalho tem como objetivo comparar o comportamento estrutural de vigas com seção mista de aço-concreto, para três tipos de conectores de cisalhamento, confeccionados em perfil laminado de seção U e em perfis metálicos formados a frio de seções U e L. Para tal, foram realizados ensaios experimentais com os três tipos de conectores associados a vigas metálicas em perfil laminado de seção I e lajes de concreto armado maciças. Para cada tipo de conector foram realizados três ensaios de cisalhamento direto, além de dois ensaios em vigas mistas simplesmente apoiadas para avaliação da região de flexão simples. Os resultados obtidos indicaram que o comportamento ao cisalhamento direto dos conectores apresenta diferenças expressivas a depender do modelo adotado, entretanto, não influenciam significativamente na capacidade resistente média à flexão das vigas mistas. Estas, contudo, apresentam diferenças consideráveis de deslocamento vertical e deformações em virtude das diferenças de rigidez dos conectores.

Palavras-chave: ensaio de cisalhamento, conectores de cisalhamento, vigas mistas aço-concreto.

How to cite: J. G. Ribeiro Neto, G. S. Vieira, and R. O. Zoccoli, “Experimental analysis of the structural behavior of different types of shear connectors in steel-concrete composite beams,” *Rev. IBRACON Estrut. Mater.*, vol. 13, no. 6, e13610, 2020, https://doi.org/10.1590/S1983-41952020000600010

1 INTRODUCION

In several countries over the last few decades, steel-concrete composite structures have been increasingly used by engineering. In order to take advantage of the benefits of each material, both in structural and constructive terms, the composite steel-concrete elements arbe constituted by the combination of steel sections and concrete elements. The

Corresponding author: Juliano Geraldo Ribeiro Neto. E-mail: julianogeraldo.eng@gmail.br
Financial support: CNPq and Funape/UFG.
Conflict of interest: Nothing to declare.

advantages of composite systems result from the fact that the steel and concrete elements can work subjected to tensile and compression efforts, respectively, a situation in which it is possible to explore the main mechanical properties of each material [1].

The search for more economical structural systems by reducing material consumption and the self-weight, without affecting their safety and durability, is one of the main objectives of structural engineering. The combination of steel and concrete in composite sections allows the complementation of the characteristics regarding both materials [2], which makes it possible to obtain elements of higher rigidity and smaller dimensions, providing a reduction in costs related to the foundation, resulting in performance and economy gains [3].

The interaction between the concrete elements and steel sections used in composite steel-concrete systems can be achieved by mechanical means (connectors, cavities, rebounds), by both friction and adhesion [4]. Although the natural adhesion between the two materials generates remarkably high friction forces, these are not usually considered when calculating the resistant capacity of some elements, such as composite beams [5].

The composite beams, in particular, are constituted by the association of a steel section located in a predominantly traction region with a concrete slab located in a prevalently compressed region. The mechanical connection among the materials is made by steel devices called shear connectors [4] whose main functions are: to allow the slab-beam elements to work together [3], to restrict longitudinal slipping and vertical displacement at the interface elements, in addition to absorbing shear forces [6].

The sizing of composite beams submitted to bending efforts depends on the characterization of the behavior at the level of the steel-concrete connection. Two situations are considered in this case: the complete and the partial interactions. When it comes to complete interaction, it is considered that there is a perfect connection between steel and concrete. In this case, there is no relative longitudinal slip between both elements. When slipping relative to the level of the steel-concrete connection occurs, there is a discontinuity regarding the deformation diagram characterizing the partial interaction [7].

The connection between steel and concrete is dimensioned according to the diagram of longitudinal shear forces per unit of length (q), known as longitudinal shear flow. In the case of complete interaction, the resultant of the longitudinal shear flow diagram (Vh) is given as a function of the maximum shear force that can be transferred through the connection, which is limited by the maximum tensile and compression resulting that may act on the steel beam and concrete slab, respectively. The number of connectors, when it comes to complete interaction, must then be determined to resist the resulting Vh [7].

When the resistant capacity of the connectors is higher or equal than the one of the components from the composite structure, (flow by tensile of the steel section or crushing by compression of the collaborative portion of the concrete slab), the degree of connection is total, in this case the connectors do not directly influence the flexural performance of the composite beam. If the resistance capacity of the connectors is less than the lowest resistance offered by either element, there is a partial connection, in which the connectors control the flexural strength of the composite beam [8].

In this context, it is known that the structural behavior of the connecting elements that acts on composite steel-concrete beams is a significantly important work, since their performance can directly compromise the safety and stability of the structures. The main idea of this article is to experimentally evaluate the efficiency of the connectors, checking the equivalence or the difference of the resistant capacity among the types of connectors analyzed.

By means of experimental tests, the work assessed the structural behavior of shear connectors made with three different steel sections associated with steel beams in laminated I section, connecting this to a reinforced concrete slab.

2 MATERIALS AND EXPERIMENTAL PROGRAM

The work consisted of analyzing the behavior of composite steel and concrete beams, double-based, subjected to forces applied at two points so that the central region was subjected to pure bending. All models with theoretical span equal to 2800 mm and two forces concentrated at a distance of 900 mm from each end, slab 800 mm wide and 100 mm thick (Figure 1).

Three different types of shear connectors were used, one in hot rolled U section and two in cold formed U and L sections, all welded to steel beams (Table 1).

For each type of shear connector, two identical parts were tested, differentiated by the nomenclatures “A”, instrumented with electrical strain gauge, and “B”, a reference piece.

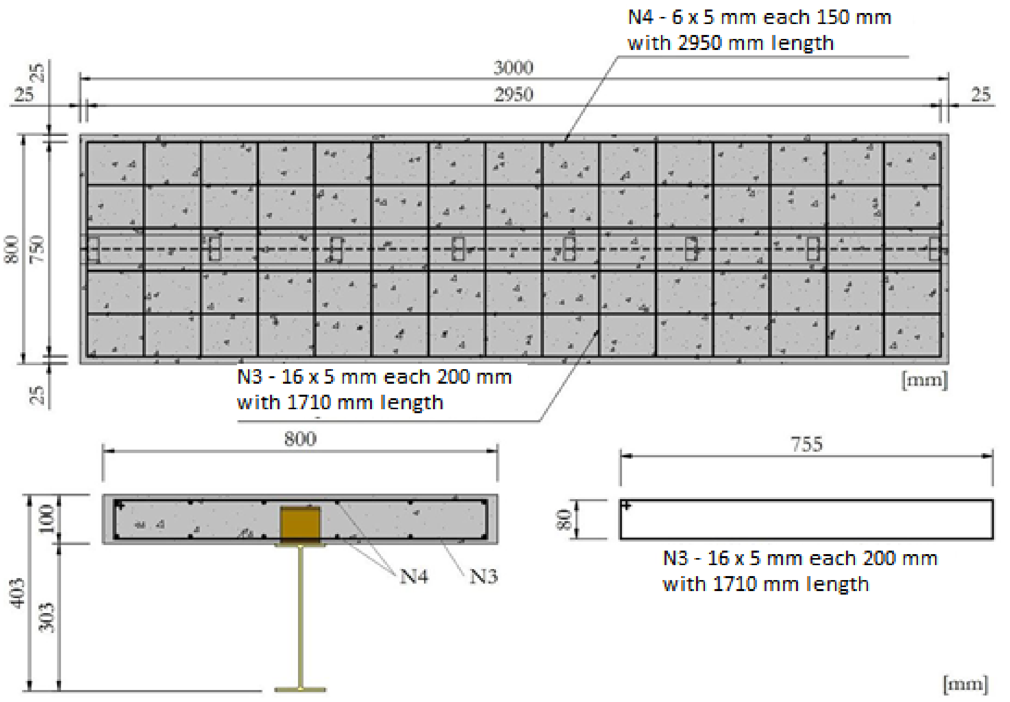

Figure 1. Beam dimensions and concrete slab reinforcement detail.

Table 1. Characterization of composite beam models

Beam	Steel beam section	Connector types	Connector
V1A*	W 310x21 (303x101x5.1x5.7)	U 3"x6.1	
V1B	W 310x21 (303x101x5.1x5.7)	U 3"x6.1	
V2A*	W 310x21 (303x101x5.1x5.7)	U 76x36x4.32	
V2B	W 310x21 (303x101x5.1x5.7)	U 76x36x4.32	
V3A*	W 310x21 (303x101x5.1x5.7)	L 76x36x4.32	
V3B	W 310x21 (303x101x5.1x5.7)	L 76x36x4.32	

* Beam and connectors instrumented with electrical strain gauges.

2.1 Materials Characterization

Two specimens were extracted from each type of section in order to obtain the mechanical properties of the steel from both the connectors and the beam. The ASTM A572-GR50, ASTM A36 and SAE 1020 steel specifications were used to make the beam, the hot rolled U section and for the cold formed U and L sections, respectively. The dimensions of the specimens met the minimum prescribed by the standard [9] (Figure 2). The elongation of the specimen was measured in accordance with the standard [10].

(a) (b) (c)

Figure 2. Steel specimen: (a) dimensions; (b) specimen; (c) on the testing machine.

The concrete used was machined and had a target value of 30 MPa with slump 12. All the slabs were concreted in a single step. After concreting, the strength gain of the concrete was monitored through tests to determine the compressive strength in twelve cylindrical specimens, measuring 10 x 20 cm (Figure 3), at 3, 7, 14 and 28 days. The modulus of elasticity and the tensile strength were also evaluated, all following the criteria of the respective standards [11]–[13].

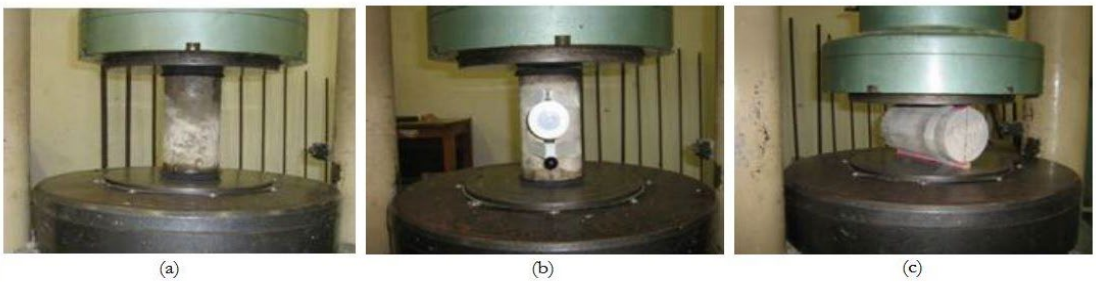

Figure 3. Concrete strength characterization test: (a) compression; (b) elastic modulus; (c) tension by diametral compression.

2.2 Connector testing (Push-out)

Three pieces were made for each type of shear connector, (Table 2), and only one of them was instrumented with electrical strain gauge. The dimensional characteristics and the arrangement of the reinforcements were in accordance with the criteria defined in the European standard [13] (Figures 4 and 5).

Table 2. Characterization of push-out test models

Model	Connector type	Length (mm)	Slab thickness[1] (mm)	$f_{c28,m}$[2] (MPa)
CD11	U 3”x6.1	80	100	30
CD12	U 3”x6.1	80	100	30
CD13*	U 3”x6.1	80	100	30
CD21	U 76x36x4.75	80	100	30
CD22	U 76x36x4.75	80	100	30
CD23*	U 76x36x4.75	80	100	30
CD31	L 76x36x4.75	80	100	30
CD32	L 76x36x4.75	80	100	30
CD33*	L 76x36x4.75	80	100	30

* Connectors instrumented with electrical strain gauges. [1] Concrete slab. [2] Target strength of concrete at 28 days

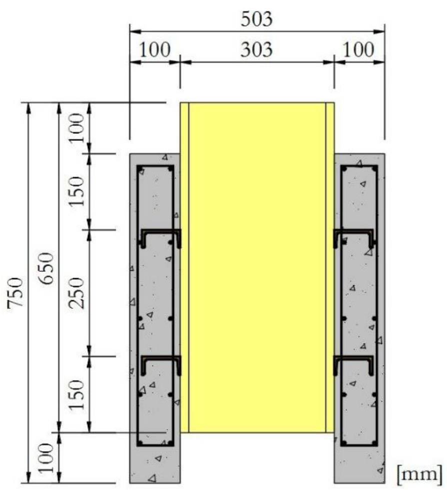

Figure 4. Push-out test models with shear connectors.

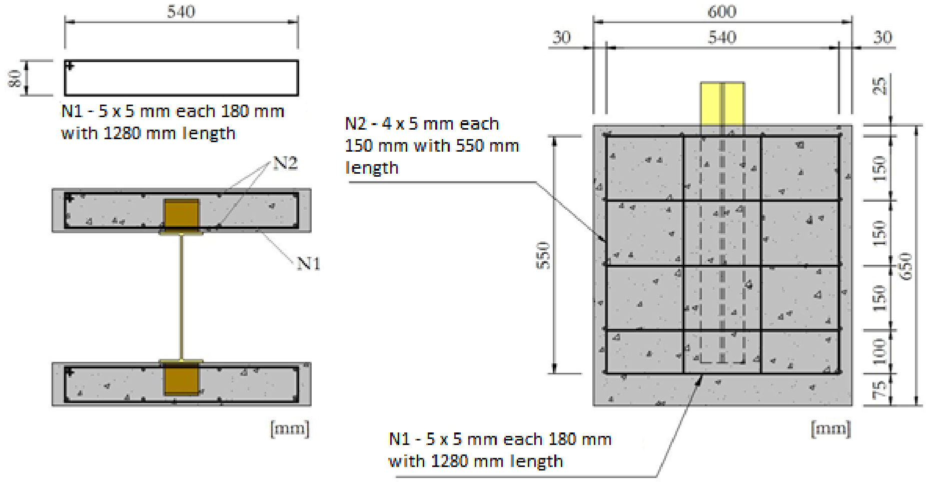

Figure 5. Concrete slab dimensions for push-out test models.

In order to measure the relative displacements between the beam and the slab, in addition to the distance between them, digital displacement meters were installed for this purpose (Figure 6). Steel uniaxial strain gauge was also installed in each connector (Figure 7), to measure the deformations and calculate the stresses.

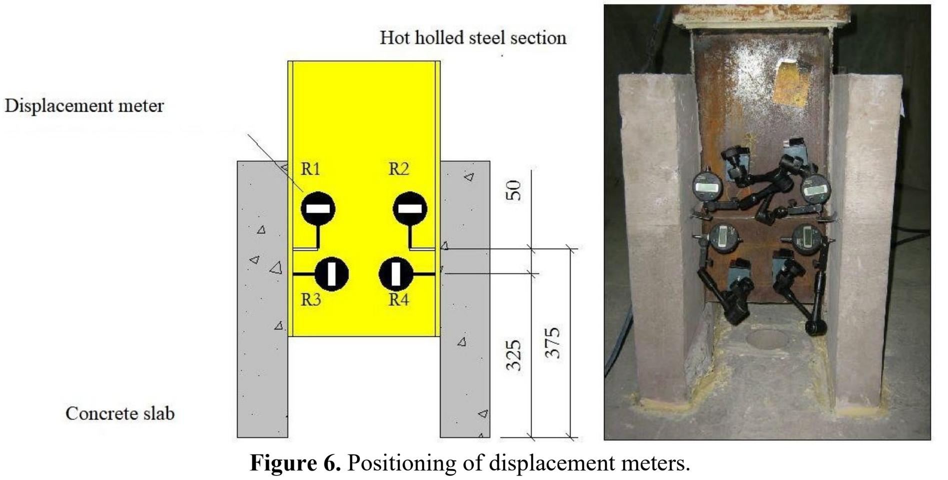

Figure 6. Positioning of displacement meters.

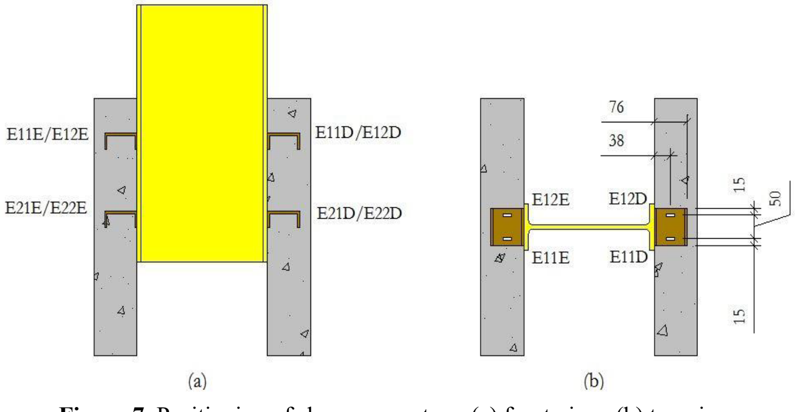

Figure 7. Positioning of shear connectors: (a) front view; (b) top view.

The force was applied directly to the steel section (Figure 8), with manual control of its application.

Figure 8. Test scheme for push-out.

2.3 Bending test on beams

Aiming to verify the structural behavior of the connectors acting directly at the interface of the steel beam with the concrete slab, two identical composite beams were made for each type of connector, where each pair differed from each other only by the presence of electrical strain gauge. The connectors were, except for those near the end of the beam, equally spaced respecting the maximum distance recommended by the standard [14] (Figure 9).

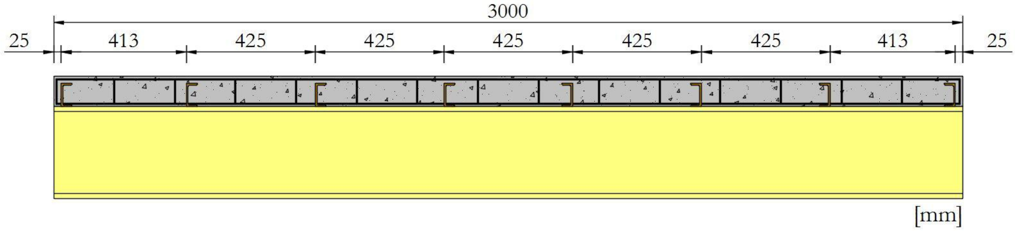

Figure 9. Positioning of shear connectors on the beam.

All beams tested for simple bending were instrumented by means of digital displacement meters, positioned in the middle and a quarter of the span (Figure 10). Such meters provided the information of relative horizontal displacement at the interface of the steel beam with the concrete slab, the same positioning points of the shear connectors (R1 to R4), and of the vertical displacement of the beam (R5 and R6).

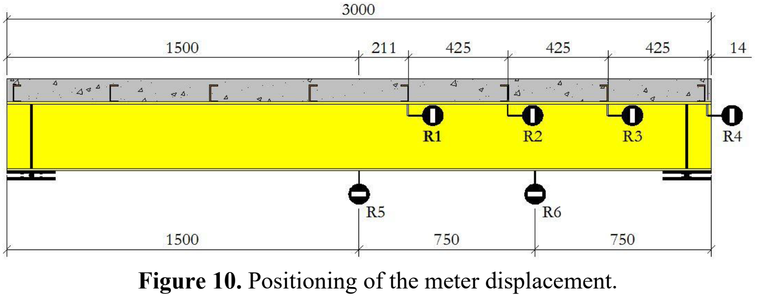

Figure 10. Positioning of the meter displacement.

The electrical strain gauge, uniaxial and rosettes, were positioned in order to obtain the deformations and to be able to calculate the stresses in both materials (Figures 11 and 12).

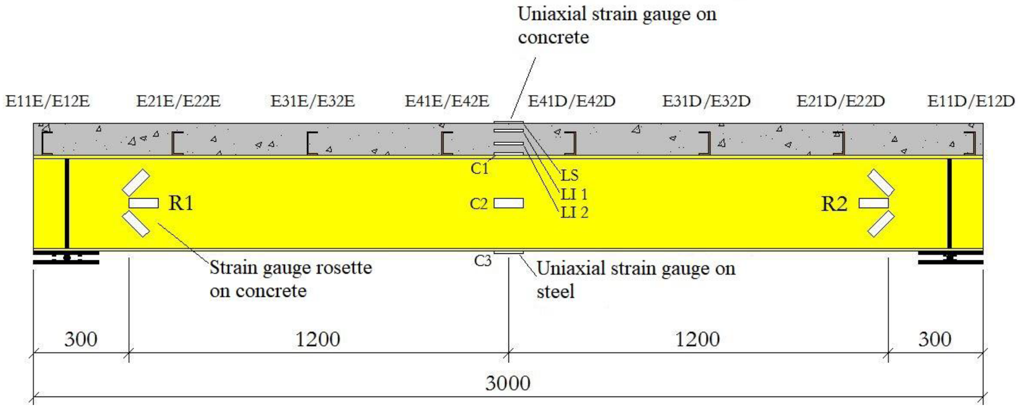

Figure 11. Side view of the positioning of the strain gauges on the beam.

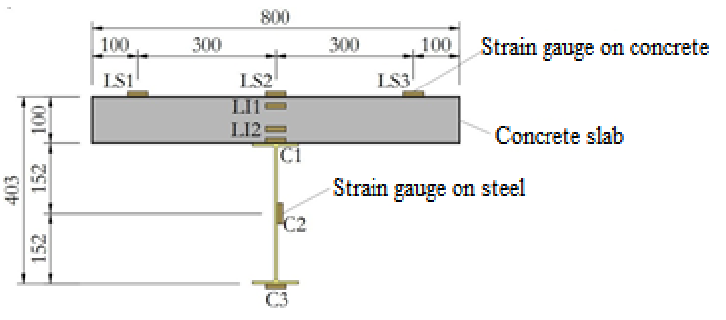

Figure 12. Cross section of the positioning of the strain gauges on the beam.

For flexural tests on composite beams, the same equipment used in the direct shear test was used (Figure 13).

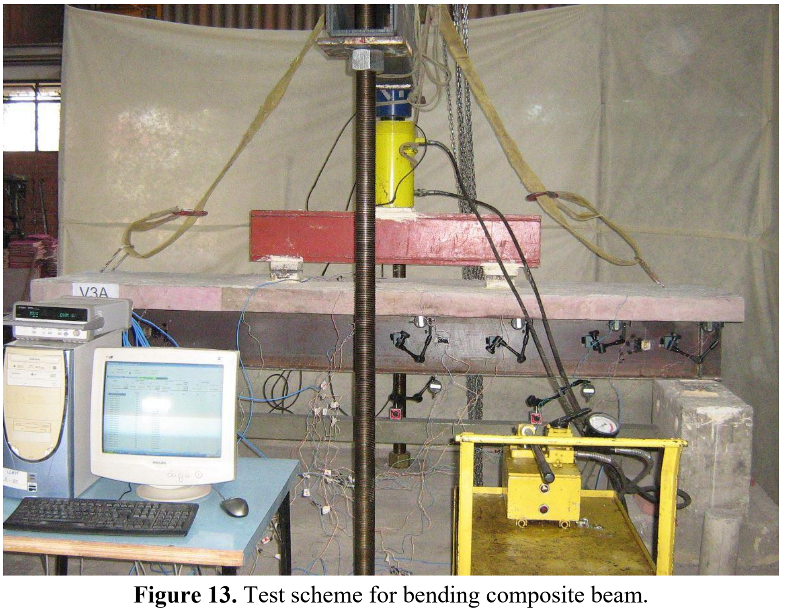

Figure 13. Test scheme for bending composite beam.

To guarantee the free displacement in the horizontal direction regarding the composite beam and the power transmission beam, by avoiding the appearance of efforts in this direction, steel plates and rollers were used (Figures 14 and 15).

Figure 14. Composite beam support.

Figure 15. Load transmission beam support.

3 RESULTS AND DISCUSSIONS

After testing the specimens, the values regarding the strength of the steel were used in the beams and connectors (Table 3).

Table 3. Steel Characterization

Specimen		Loads		Nominal (min.)		Experimental		A (%)
		Yield (kN)	Ultimate (kN)	f_y (MPa)	f_u (MPa)	f_y (MPa)	f_u (MPa)	
U 3”x6.1 connector	CP1	37.4	58.3	250	400-550	306	478	26
	CP2	38.5	59.1			316	484	29
	Average	38.0	58.7			311	481	28
U 76x36x4.75 and L 76x36x4.75 connectors	CP3	22.0	40.1	210	380	231	422	28
	CP4	22.7	39.8			239	419	31
	Average	22.3	39.9			235	420	30
W310x21 steel beam	CP5	41.4	53.6	345	450	406	525	32
	CP6	42.4	54.2			416	531	28
	Average	42.0	53.9			411	528	30

The strength of the concrete over time until the day 28th after concreting as well as the values of resistance to compression, tensile and the modulus of elasticity of the concrete were obtained (Table 4). Apart from the compressive strength value, where the highest value was adopted, the tensile strength and the modulus of elasticity were obtained by averaging the results of three specimens.

Table 4. Concrete characterization

Compressive strength ABNT NBR-5739:2007 f_{cm} (MPa)				Tensile strength ABNT NBR-7222:1994 f_{ctm} (MPa)				Elastic modulus ABNT NBR-8522:2008 E_{cs} (GPa)			
Specimen			Higher	Specimen			Higher	Specimen			Higher
CP1	CP2	CP3		CP1	CP2	CP3		CP1	CP2	CP3	
32.7	33.9	35.0	35.0	3.2	3.2	3.1	3.2	33.1	34.5	32.6	33.4

3.1 Results of direct shear strength

In terms of the results about the push-out tests, the presented force refers to a connector.

Regarding the maximum resistant capacity per connector (Qmax) measurement, the lowest value obtained in the experiments was disregarded due to the significant variability that can occur among the values for the same type of connector. The average of the two highest experimental values has been adopted as a reference aiming to reduce the influence of possible spurious results in the analysis of the results, and the characteristic slip (δuk) was also evaluated. In order to measure the experiment, the results found were compared with the model proposed in the standard [15] for cold-formed and hot rolled U section, in addition to the model proposed by [16] for cold-formed U sections (Table 5).

From the results presented there is a significant variation in the resistant capacity among the different types of connectors. The laminated U sections connector presents a behavior similar to that already observed in other works [16]–[18]. The cold-formed U (CD2 series) and L (CD3 series) connectors have a lower resistant capacity when compared to the laminated U connector (CD1 series). This can also be observed by comparing the relative slip between the beam and the slab for each type of connector tested (Figure 16).

In almost all specimens it was observed that the cracks originated from the center of the slabs, propagating in two compression struts in relation to the largest dimension of the slab to the base (Figure 17).

3.2 Results of composite beams

Concerning the composite beams, the results are presented in graphs and tables, where the experimental values are compared with those analytically obtained. The mechanical properties considered for the analytical studies common to all beams are: concrete elastic modulus (Ec) equal to 33.4 GPa, characteristic concrete strength (fc) equal to 35.01 Mpa, steel elastic modulus (Ea) equal to 200 GPa, steel yield stress (fy) equal to 411 MPa and moment of inertia in relation to the beam flexion axis (Ia) equal to 3,776 cm4. Due to the variation of the connector type, the following parameters were obtained: beams V1A and V1B sum of resistance of the connectors (∑Qn) equal to 540 kN and degree of interaction (η) equal to 0.46, beams V2A and V2B summation resistance of connectors (∑Qn) equal to 360 kN and degree of interaction (η) equal to 0.32, beams V3A and V3B sum of resistance of connectors (∑Qn) equal to 290 kN and degree of interaction (η) equal to 0.26.

From the experimental values of the material properties, the elastic and plastic moments were calculated for comparison with the respective analytical values (Table 6). It is observed that, apart from beams with L section connectors, the others present an elastic experimental moment and coincide with the expected analytical values. Regarding plastic moment values, it is noted that the experimental values, although close, were lower than the analytical ones. However, this difference, below 5%, does not represent problems from the structural point of view, which is covered by the coefficients of safety indicated in the design standards.

In terms of maximum forces (Table 7), beams V1A and V1B, with connectors in laminated U-section and with an interaction degree equal to 0.46, cracked with 380 and 403 kN, respectively. The failure mode occurred due to concrete rupture in the region close to the point of the strength application, associated with the local buckling of the section (Figure 18). This is due to the increase in compression stresses in the upper region from the web section, after the loss of part regarding the contribution of slab in the resistant capacity of the component, because of its rupture.

Table 5. Maximum force and relative displacement for the different connectors

Connector	Model	$Q_{máx.}$ (kN)	δ_{uk} (mm)	$Q_{R.NBR}$ (kN)	$Q_{R.DAVID}$ (kN)	$\frac{Q_{max}}{Q_{R.NBR}}$	$\frac{Q_{max}}{Q_{R.DAVID}}$	Rupture mode
U 3”x6,1	CD11	120.0	5.3	236	-	0.51	-	1
	CD12	135.0	2.7	236	-	0.57	-	1
	CD13	107.6	7.6	236	-	0.46	-	2
	Adopted	127.5	6.4	236		0.54		
U 76x36x4,75	CD21	87.6	4.1	184	166	0.47	0.53	1
	CD22	82.6	7.8	184	166	0.45	0.50	1
	CD23	92.5	8.8	184	166	0.50	0.56	3
	Adopted	90.1	8.3	184	166	0.49	0.54	
L 76x36x4,75	CD31	75.8	6.7	-	-	-	-	1
	CD32	69.3	2.0	-	-	-	-	1
	CD33	52.7	6.1	-	-	-	-	1
	Adopted	72.5	6.4					

-: not applicable

1: excessive displacement

2: weld failure

3: weld failure near to shear connector area

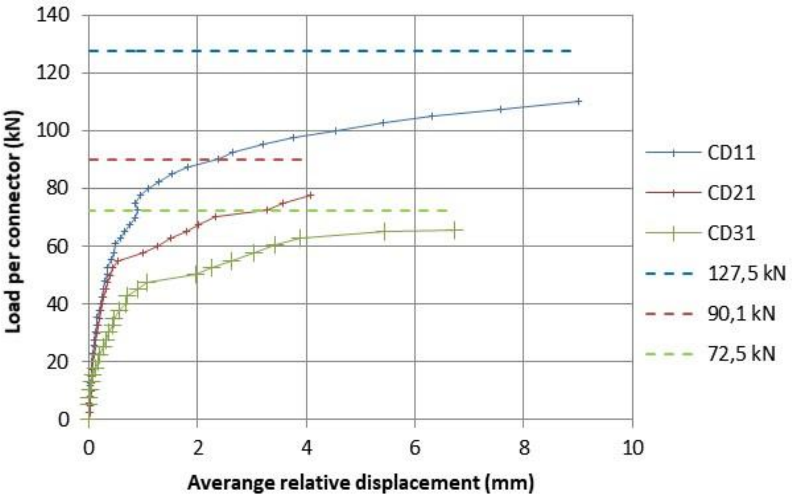

Figure 16. Curve load x average relative displacement per connector comparative between connectors.

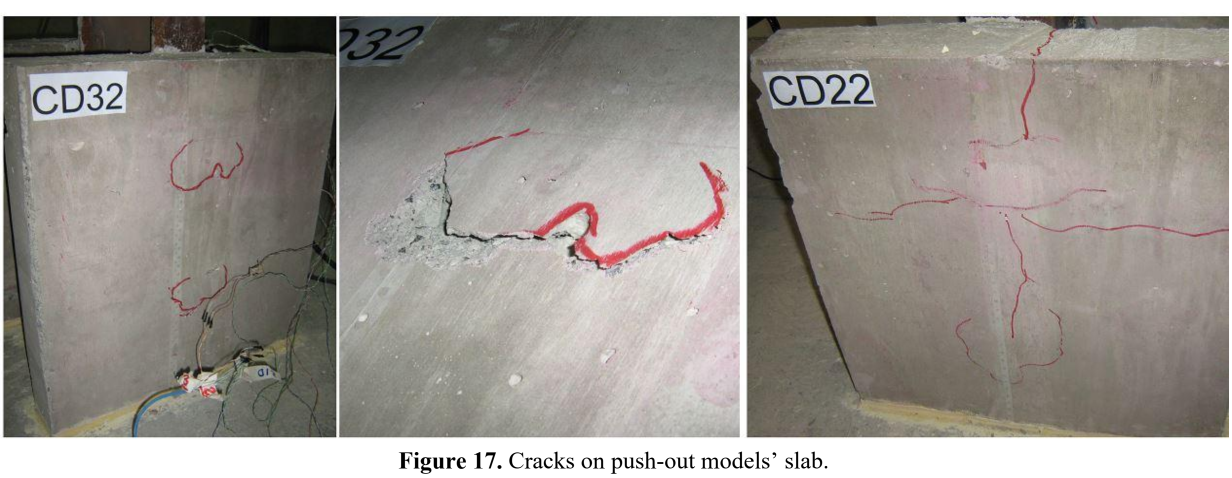

Figure 17. Cracks on push-out models’ slab.

Table 6. Resistant moments Experimental and analytical.

Beam	Experimental Elastic Moment $(\mathrm{kN \cdot cm})$ (1)	Experimental Plastic Moment $(\mathrm{kN \cdot cm})$ (2)	Analytical Elastic Moment $(\mathrm{kN \cdot cm})$ (3)	Analytical Plastic Moment $(\mathrm{kN \cdot cm})$ (4)	(1)/(3)	(2)/(4)	Rupture mode
V1A	15,607	17,407	15,568	18,232	1.00	0.95	1
V1B	15,697	18,442	15,568	18,232	1.01	1.01	1
V2A	14,707	17,407	14,718	17,717	1.00	0.98	2
V2B	14,797	17,182	14,718	17,717	1.01	0.97	2
V3A	12,142	14,437	14,259	16,816	0.85	0.86	3
V3B	13,357	15,652	14,259	16,816	0.94	0.93	3
Rupture mode:							
1 – Concrete slab break with local web buckling							
2 – Concrete slab break and steel beam yield							
3 – Connector break and steel beam yield							

Table 7. Experimental and analytical maximum load obtained for the beams.

Beams	Experimental maximum load (kN) - (1)	Analytical maximum load (kN) - (2)	$\frac{(1)}{(2)}$
V1A	380	405	0.94
V1B	403	405	1.00
V2A	380	394	0.96
V2B	375	394	0.95
V3A	314	374	0.84
V3B	341	374	0.91

Figure 18. Beam V1A rupture configuration.

For beams V2A and V2B, with U-shaped connectors formed by cold and the interaction degree of 0.32, rupture forces of 380 and 375 kN were obtained, respectively. The failure mode occurred due to the rupture of the concrete slab at the strength application point and the steel beam yield.

In the V3A and V3B beams, with cold-formed L- section connectors and 0.26 interaction degree, rupture forces of 314 and 340 kN were obtained (Figure 19). It was observed that the failure mode was characterized by the rupture of the connector, perceived during the test due to crackles heard inside the slab, followed by excessive vertical displacements due to the steel yield. Although a vertical separation between steel and concrete is not observed, this behavior suggests that the failure mode was characterized by the loss of the resistant capacity from the connectors, since the efforts are transferred to the steel beam and there is no collaboration of the concrete table.

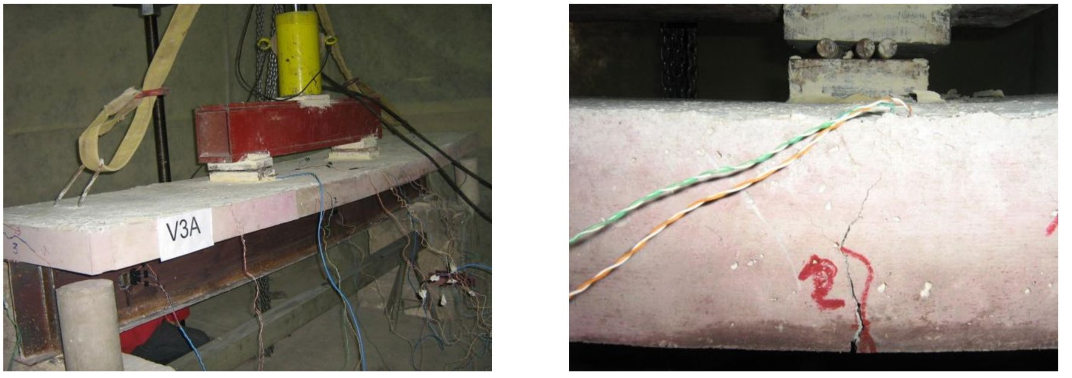

Figure 19. Beam V3A rupture configuration.

There was an attempt to analyze the relationship between the applied force and the deformation in the cross section in the middle of the span for four different loading values of 25, 50, 75 and 100% from the maximum force reached for the composite beams V1A to V3A (Figures 20 to 22).

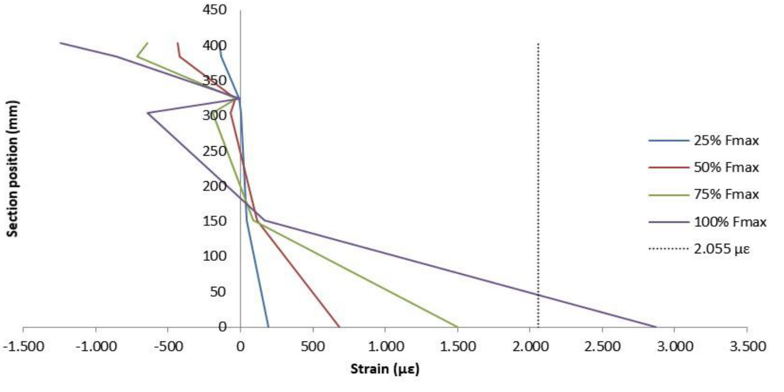

Figure 20. Strain distribution curve – V1A.

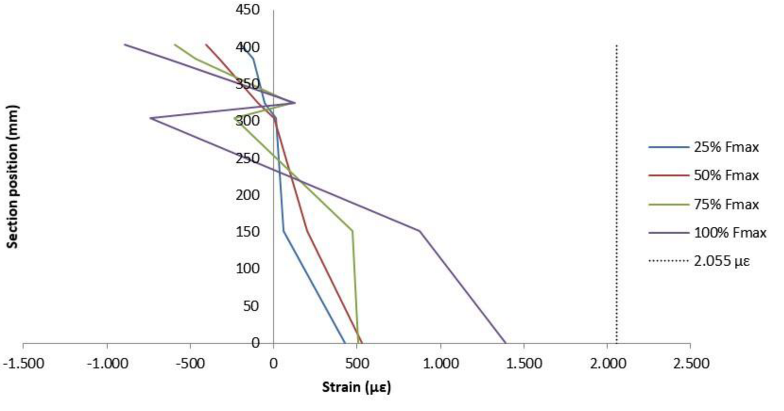

Figure 21. Strain distribution curve – V2A.

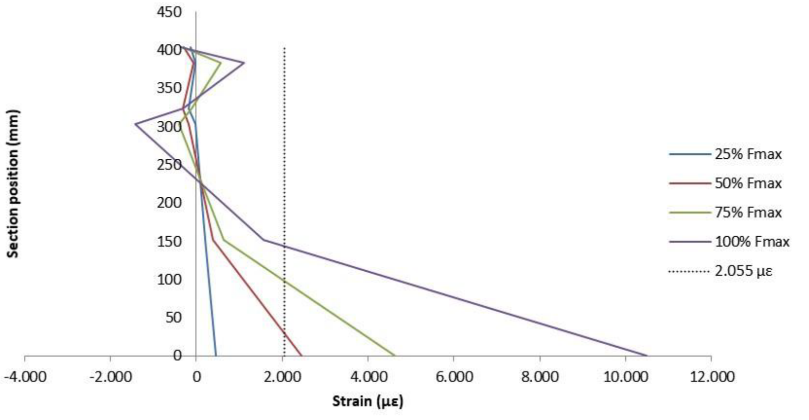

Figure 22. Strain distribution curve – V3A.

By analyzing the diagrams, the beam V1A (Figure 20) shows the existence of two neutral lines, one on the slab and one on the section, confirming the consideration of partial interaction. It is also verified that in the steel section the neutral line is in the web, confirming the theoretical analysis where the upper table of the section should be compressed.

The beam V2A (Figure 21) presents a behavior similar to the one of V1A, except for the fact that the most strained fiber of the steel section, represented by the point C3, does not reach the flow deformation. From the analysis of this beam, it is observed that after loading 180 kN, a stretch of decreasing deformations up to the force of 320 kN begins. It can be assumed that in this loading interval there was a loss of adhesion between the electrical strain gauge and the steel beam with later resumption of deformation growth. Thus, if we imagine that, contrary to what is shown by the measurements, in this stretch the deformations would continue to increase, it can be assumed that they would exceed the yield strength.

In beam V3A (Figure 22) it is observed that after 50% of the maximum load, a great loss of interaction occurs, which is possible to verify that the beam and the slab start to behave as if they were working in isolation. It is also observed that the deformations in the most stretched region of the steel section exceed considerably the yield deformation.

Another analyzed parameter was the relative displacement between the steel beam and the concrete slab, measured using digital displacement meters (Figure 10). These relative displacements were obtained by force readings at each 40 kN increment (Figures 23 to 25).

It was noted that the relative sliding between the slab and the section was practically null, while there was a bond between them. The force for which this bond was ruptured varied from beam to beam.

For beam V1A (Figure 23) the sliding measured by "R3" was higher than the sliding readings of other meters. This indicates a behavior of total interaction, considering that the interaction degree of this beam is 0.46, where the sliding in the region before the supports is much higher than the others.

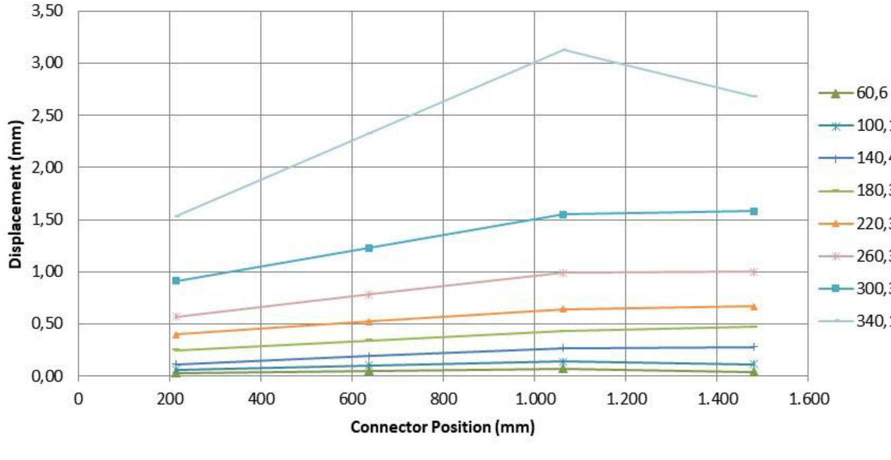

Figure 23. Relative displacement – V1A.

For the initial phase of the experiment, it is observed that the behavior of beams V2A (Figure 24) and V3A (Figure 25) is similar, with increasing displacements starting from the center towards the end, where the shear yield is higher. In the final phase of the experiment, close to the rupture, there is a change in the behavior of V3A, where it starts to present higher relative displacements in the center of the beam, a region where the shear yield is lower. Such behavior can be associated with the rupture of the connectors, generating a redistribution of efforts and a consequent increase in sliding.

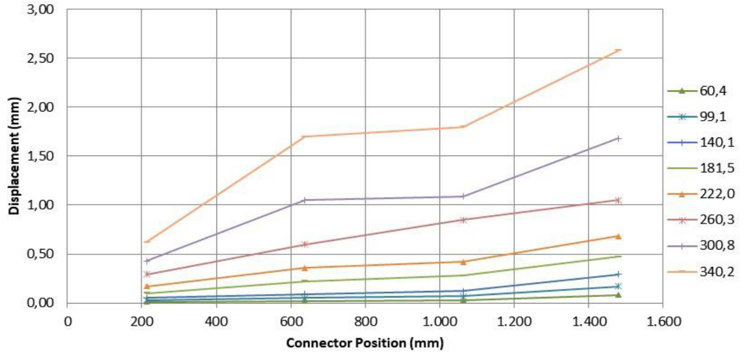

Figure 24. Relative displacement – V2A.

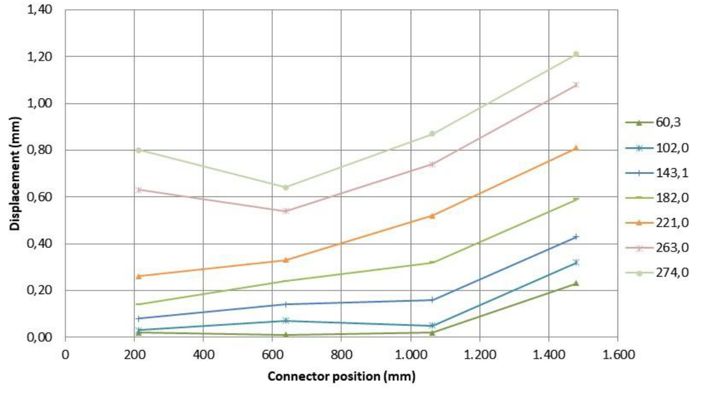

Figure 25. Relative displacement – V3A.

Comparing the relative sliding observed in the test of beams V1A, V2A and V3A (Figure 26), it is noted that the slides in the interface of the composite beams V2A and V3A present a similar behavior, although the beam V3A reached a lower force than V2A.

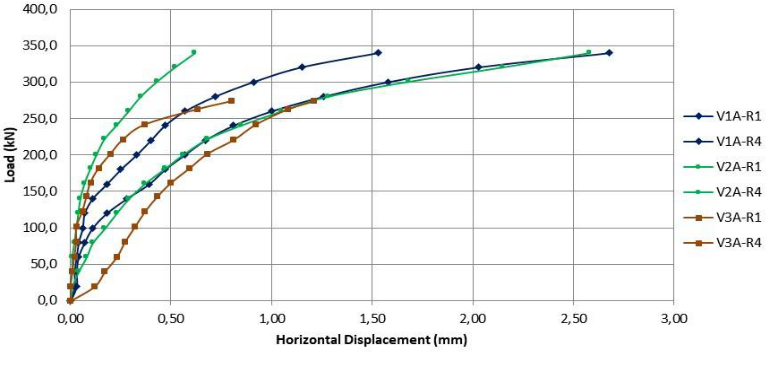

Figure 26. Comparative relative displacement curve – V1A, V2A e V3A.

Finally, the stress distribution in the connectors of the composite beams was analyzed (Figures 27 to 29). In general, the pairs of connectors positioned in symmetrical positions presented similar deformations.

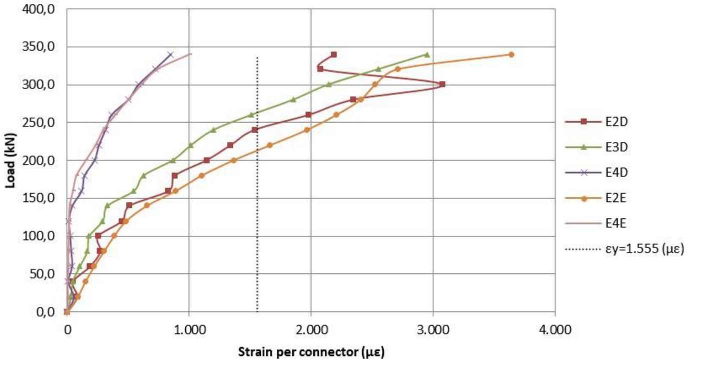

Figure 27. Load *x* strain per connector curve – V1A.

For some connectors, at the place where the strain gauges were bonded, the deformations at the rupture moment of the beams were lower than the steel yield deformation (1555 με for cold rolled U connectors and 175 με for cold formed U and L). However, as noted by [16], the concentration of voltages in the connectors is higher at the base and it is approximately twice the voltage in the center of the connector. Thus, it can be concluded that even though the strain gauges bonded in the central region of some connectors have not registered deformations superior to the yield in the region with the highest concentration of stresses, along with the weld, probably there was the steel yield.

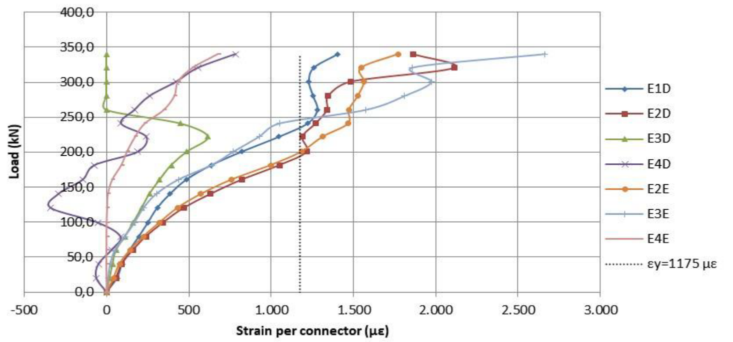

Figure 28. Load *x* strain per connector curve – V2A.

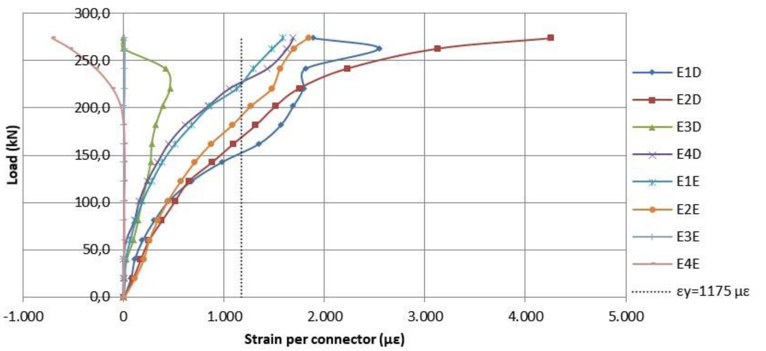

Figure 29. Load *x* strain per connector curve – V3A.

It can also be seen that the highest deformations occurred in the connectors located in the symmetrical positions "2E" and "2D", decreasing towards the central direction. Similarly, to the connectors of the push-out tests, those associated with the composite beams also showed deformations above the yield strength.

4 CONCLUSIONS

Motivated by the observation that in the execution of steel structures, the section replacement specified in the project with other equivalents is a common practice, as well as the fact that this replacement does not always meet a satisfactory equivalence of structural behavior, this research aimed to make a comparative study between the connectors in hot rolled U3 "x6.1 and the cold formed U and L 76x36x4.75. For this purpose, push-out tests were performed to characterize the connectors, and also bending tests in composite beams to analyze the behavior of the connectors in a situation closer to the real one.

It was found that the U 3"x6.1 connector has a 46% higher resistant capacity than the U 76x36x4.75; and this in turn is 24% more resistant than the L 76x36x4.75. Comparing the hot rolled U and cold formed L sections, there is a 76% variation in the resistant capacity. The variation in stiffness between the sections proved to be directly associated with its resistant capacity, where the more resistant the section the more rigid it is, and smaller the relative sliding between the concrete slab and the steel section will be.

In almost all specimens, it was observed that the cracks originated in the center of the slabs, propagating in two compression struts compared with the largest dimension of the slab to the base. Some failure modes were not truly clear, suggesting that the concrete rupture may have occurred after excessive sliding of the connector.

It was also found that the resistant capacities obtained experimentally for hot rolled and cold formed U sections correspond to approximately half of the expected theoretical value. No justifications were found for this difference in resistant capacities, so these results are not conclusive about the application of such formulations since they have already been satisfactory in other studies [16], [18].

The relative sliding has a huge influence on the stiffness of the composite beams. For the beam with a higher degree of interaction, it was observed that the theoretical displacement was slightly higher than the experimental one. For beams with an interaction degree close to 0.3, the experimental displacements were, on average, close to the theoretical ones.

The relative sliding at the interface between the concrete slab and the steel section is null while there is a chemical bond between them and the force at which this bond is disrupted differs from beam to beam. It was also possible to verify that, despite the normative recommendation for uniform distribution of the shear connectors along the beam, the stress distribution is not constant and is concentrated at the ends.

Through the deformation diagram, the position of the neutral lines was obtained according to the loading steps, and it was possible to verify the influence of the interaction degree on the behavior of the composite beam and the plasticization of the cross section. For the L-type connector, it is noteworthy that, due to its higher flexibility and less resistance, there was less efficiency of the behavior as a composite beam with higher displacements and less resistance.

Regarding the composite beams, the relationship between the experimental resistant moment and the theoretical resistant moment ranged from 0.86 to 1.01, whose average was 0.95. This shows that the experimental outcomes of the beams presented results close to what was expected, suggesting that the experimental resistant capacities obtained for the connectors are corresponding to their behavior when associated with composite beams, although they are below the expected theoretical values.

Therefore, it is concluded that cold formed U and L sections can be used as shear connectors in composite beams, nonetheless their lower resistant capacities and stiffness, when compared to laminated U sections, must be taken into account in the project process. In situations of composite beams with high loading values or the need for high stiffness, as in structural systems subjected to dynamic actions, it is suggested that their use should be avoided. However, this study is not entirely conclusive, suggesting that more research needs to be carried out in order to better understand the behavior of the L section as shear connectors.

ACKNOWLEDGMENTS

The authors of this work would like to thank the CNPq funding agency, CAPES for the financial support. They also thank the extinct post-graduate program CMEC-UFG and UFG for laboratory support.

REFERENCES

[1] G. S. Veríssimo, J. L. R. Paes, I. Valente, P. J. S. Cruz, and R. H. Fakury, “Design and experimental analysis of a new shear connector for steel and concrete composite structures,” in *Proc. 3rd Int. Conf. Bridg. Maintenance, Saf. Manag. Bridg. Maintenance, Safety, Manag. Life-Cycle Perform. Cost*, 2006, p. 807–809.

[2] M. D. A. Fabrizzi and R. M. Gonçalves, “Contribuição para o projeto e dimensionamento de edifícios de múltiplos andares com elementos estruturais mistos aço-concreto,” M.S. thesis, Univ. São Paulo, São Carlos, 2008.

[3] L. D. Kirchhof, “Uma contribuição ao estudo de vigas mistas aço-concreto simplesmente apoiadas em temperatura ambiente e em situação de incêndio,” M.S. thesis, Univ. São Paulo, São Carlos, 2004.

[4] L. R. Marconcin, R. D. Machado, and M. A. Marino, "Modelagem numérica de vigas mistas aço-concreto," *Rev. IBRACON Estrut. Mater.*, vol. 3, no. 4, pp. 449–476, 2010, http://dx.doi.org/10.1590/S1983-41952010000400006.

[5] J. G. R. Neto, “Análise teórico-experimental do uso de parafuso estrutural como conector de cisalhamento em pilar misto composto de perfil tubular preenchido com concreto,” Ph.D. dissertation, Univ. Fed. Ouro Preto, Ouro Preto, 2016.

[6] G. M. S. Alva and M. Malite, "Comportamento estrutural e dimensionamento de elementos mistos aço-concreto," *Cad. Eng. Estrut.*, vol. 7, pp. 51–84, 2005.

[7] S.-H. Kim, S.-J. Park, W.-H. Heo, and C.-Y. Jung, "Shear resistance characteristic and ductility of Y-type perfobond rib shear connector," *Steel Compos. Struct.*, vol. 18, no. 2, pp. 497–517, 2015, http://dx.doi.org/10.12989/scs.2015.18.2.497.

[8] D. J. Oehlers and M. A. Bradford, *Composite Steel and Concrete Structural Members – Fundamental Behaviour*, 1st ed. New York: Pergamon, 1995.

[9] American Society for Testing and Materials, *Standard Test Methods and Definitions for Mechanical Testing of Steel Products,* A370, 1992.

[10] Associação Brasileira de Normas Técnicas, *Materiais Metálicos – Ensaio de Tração à Temperatura Ambiente,* NBR ISO 6892, 2002, pp. 34.

[11] Associação Brasileira de Normas Tecnicas, *Concreto – Ensaios de Compressão de Corpos de Prova Cilíndricos,* NBR 5739, 2007, pp. 14.

[12] Associação Brasileira de Normas Tecnicas, *Concreto – Determinação dos Módulos Estáticos de Elasticidade e De Deformação à Compressão,* NBR 8522, 2008, pp. 16.

[13] Associação Brasileira de Normas Tecnicas, *Concreto e Argamassa – Determinação da Resistência à Tração por Compressão Diametral de Corpos de Prova Cilíndricos,* NBR 7222, 2011, pp. 8.

[14] European Committee for Standardization, *Eurocode 4 – Design of Composite Steel and Concrete Structures – Part 1-1 – General Rules and Rules for Buildings*, 2004, pp. 118.

[15] Associação Brasileira de Normas Técnicas, *Projeto de Estruturas de Aço e de Estruturas Mistas de Aço e Concreto de Edifícios*, NBR 8800, 2008, pp. 237.

[16] D. L. David, “Análise teórica e experimental de conectores de cisalhamento e vigas mistas constituídas por perfis de aço formados a frio e laje de vigotas pré-moldadas,” Ph.D. dissertation, Univ. São Paulo, São Carlos, 2007.

[17] M. Malite, “Análise do comportamento estrutural de vigas mistas aço-concreto constituídas por perfis de chapa dobrada,” Ph.D. dissertation, Univ. São Paulo, São Carlos, 1993.

[18] I. A. Chaves, “Viga mista de aço e concreto constituída por perfil formado a frio preenchido,” M.S. thesis, Univ. São Paulo, São Carlos, 2009.

Author contributions: JGRN: conceptualization, experimental study conduction, analysis and writing; GSV: experimental study conduction, analysis and writing; ROZ: analysis and writing.

Editors: Vladimir Guilherme Haach, José Luiz Antunes de Oliveira e Sousa, Guilherme Aris Parsekian.

Rev. IBRACON Estrut. Mater., vol. 13, no. 6, e13611, 2020

IBRACON

IBRACON Structures and Materials Journal
Revista IBRACON de Estruturas e Materiais
ISSN 1983-4195 ismj.org

SciELO

ORIGINAL ARTICLE

Metal magnesium industry waste for partial replacement of Portland cement

Rejeito da indústria de magnésio metálico para substituição parcial do cimento Portland

Maysa Lorena Figueiredo Martins[a]
Richard Rodrigues Barreto[b]
Paulo Roberto Ribeiro Soares Junior[c]
Ivete Peixoto Pinheiro[b]
Augusto Cesar da Silva Bezerra[d]

[a]Centro Federal de Educação Tecnológica de Minas Gerais – CEFET-MG, Programa de Pós-graduação em Engenharia de Materiais, Belo Horizonte, MG, Brasil
[b]Centro Federal de Educação Tecnológica de Minas Gerais – CEFET-MG, Departamento de Engenharia de Materiais, Belo Horizonte, MG, Brasil
[c]Centro Federal de Educação Tecnológica de Minas Gerais – CEFET-MG, Programa de Pós-graduação em Engenharia Civil, Belo Horizonte, MG, Brasil
[d]Centro Federal de Educação Tecnológica de Minas Gerais – CEFET-MG, Departamento de Engenharia de Transportes, Belo Horizonte, MG, Brasil

Received 01 July 2019
Accepted 07 May 2020

Abstract: The high demand for concrete has triggered studies on the mitigation of Portland cement production impacts, such as greenhouse gas emissions and energy demands, in addition to enabling cost reduction. Partial replacement of cement with other materials has been employed as an alternative to minimize the damage caused by the cement industry. In this regard, it is necessary to use materials that efficiently replace cement clinker. This study uses waste generated from the production of metallic magnesium as a partial replacement for Portland cement. The substitution is aimed at reducing the amount of clinker used, as its production necessitates high energy consumption and results in emission of large quantities of CO_2 into the atmosphere. The tailings were characterized via X-ray fluorescence (XRF), X-ray diffraction (XRD), scanning electron microscopy (SEM), and granulometric analysis. For evaluating the mechanical behavior and porosity, 25% of the cement (by mass) was replaced with tailings, and the resulting composite was molded into cylindrical specimens. After curing for 28 and 91 days, all specimens underwent compression testing. The results of the physical characterization showed that more than 65% of the tailing grain was lesser than 45 μm in size, which contributes to the packaging effect. In terms of the chemical and mineralogical composition, the tailing had high levels of calcium, and the predominant phases could be identified. The compressive strength of the mortar with substitution was higher than 40 MPa. The convergence observed between the results of the different characterization techniques demonstrates the efficiency of using the waste as a supplementary cementitious material.

Keywords: cementitious composite, industrial reject, mechanical behavior, filler effect.

Resumo: A alta demanda por concreto faz com que estudos sejam desenvolvidos para amenizar os impactos causados pela produção do cimento Portland, como emissões de gases do efeito estufa e demanda energética, além de viabilizar a redução de custos. A utilização de materiais em substituição parcial do cimento vem sendo empregada como alternativa para minimizar os danos causados pela indústria do cimento. Nesse escopo, se faz necessário utilizar materiais que consigam substituir de maneira eficiente o clínquer de cimento. O presente trabalho utilizou o rejeito resultante da produção de magnésio metálico como substituição parcial do cimento Portland. A substituição visa diminuir a quantidade de clínquer utilizada, tendo em vista que sua produção requer um elevado consumo de energia e emite grandes quantidades de CO_2 na atmosfera. A caracterização do rejeito foi feita por meio de fluorescência de raios X (FRX), difração de raios X (DRX), microscopia eletrônica de varredura (MEV) e análise granulométrica. Com intuito de avaliar o comportamento

Corresponding author: Maysa Lorena Figueiredo Martins. E-mail: maysa.lfm@gmail.com
Financial support: This work was supported by the Minas Gerais State Research Foundation (FAPEMIG) [grant number APQ-03739-16]; and the Brazilian Federal Agency for Support and Evaluation of Graduate Education (CAPES) [grant number 001].
Conflict of interest: Nothing to declare.

mecânico e a porosidade, a dosagem do compósito resultante foi realizada com substituição parcial do cimento pelo rejeito no teor de 25% em massa, e foram moldados corpos de prova cilíndricos. Após a cura de 28 e 91 dias, todos os corpos de prova foram ensaiados à compressão. Os resultados da caracterização física mostraram que mais de 65% dos grãos do rejeito são menores que 45 μm, o que contribui para o efeito de empacotamento. Quanto à composição química e mineralógica, o rejeito possui altos teores de cálcio e foi possível identificar as fases predominantes. A resistência mecânica à compressão da argamassa com substituição apresentou valores superiores a 40 MPa. A convergência entre os resultados de diferentes técnicas de caracterização evidencia a eficiência do rejeito para uso como material cimentício suplementar.

Palavras-chave: compósito cimentício, rejeito industrial, comportamento mecânico, efeito filer.

How to cite: M. L. F. Martins, R. R. Barreto, P. R. R. Soares Junior, I. P Pinheiro, and A. C. S. Bezerra, "Metal magnesium industry waste for partial replacement of Portland cement," *Rev. IBRACON Estrut. Mater.*, vol. 13, no. 6, e13611, 2020, https://doi.org/10.1590/S1983-41952020000600011

1 INTRODUCTION

Climate change is directly linked to greenhouse gas concentration, which modifies the average temperature of the planet; in recent years, this has increased. Current climate change is correlated with anthropogenic activities and is considered one of the most significant problems of humanity in the current century, compromising natural resources and life. Among greenhouse gases, CO_2 has a relatively high global warming potential, which makes it predominantly responsible for climate change [1], [2].

The main emission sources of polluting gases are the burning of fossil fuels and industrial processes. It is estimated that the cement industry is responsible for up to 7% of global carbon dioxide emissions, as cement is the most consumed material. Significant CO_2 emissions are related to population and economic growth, which requires more prominent and better structures and thus the demand for concrete is growing exponentially; it is estimated that the worldwide demand for concrete will reach 66.3 Gt by 2022. As a result, CO_2 emission rates are increasing, along with the demand for concrete. The decarbonization of limestone for the formation of silicates and aluminates in the clinker releases approximately 0.53 t of CO_2 per ton of clinker. Decarbonization contributes to approximately 60% of the total CO_2 emission in cement industries [3]–[6].

Clinker production is the main cause of high CO_2 emission levels owing to the need for high temperatures to burn the raw material under oxidizing conditions and calcinate it. The clinker process occurs at high temperatures of 1400 – 1500 °C, at which the reaction of calcium oxide with silica, alumina, and iron oxide occurs; this forms silicates, aluminates, and iron aluminates. The final stage in the process is to grind the clinker together with additives; it is thus vital to research new technological solutions to control CO_2 emissions and energy expenditure [7]–[9].

Among the materials already used to partially replace cement and subsequently decrease the amount of clinker used, silica fume, volcanic ash, and granulated slag from the kiln are notable. Research indicates that industrial waste presents a high potential for substitution, mainly owing to its availability and physicochemical properties [10]–[12].

Noteworthy partial clinker replacements include alkali-activated binders and binders based on reactive calcium silicates, magnesium oxides, precipitated calcium carbonates, and phosphates. Studies have demonstrated the significant feasibility of incorporating various cementitious materials into the clinker to produce more sustainable binders, preserving performance. The consumption of fly ash currently represents 70% of the volume of supplementary cement materials, totaling \$75 billion in sales, and it is estimated to reach \$98 billion in 2020 as a result of the high demand for materials that can partially replace clinker, reducing energy consumption and the emission of carbon dioxide. Industrial by-products are potential materials for partial replacement; these are environmentally viable, and they are considered as waste owing to their low cost [13]–[15]. In recent decades, some types of binders based on magnesium silicates, amorphous calcium carbonates, and phosphates have been used in the production of cementitious materials, encouraging interest in the use of industrial residues of mineral and vegetal origin. Studies show significant results regarding the mechanical performance and durability of cementitious materials composed of industrial by-products [16]–[25].

1.1 Justification

The use of materials as a substitute for clinker is gaining ground in cement production. The percentage of cement replacement is growing as it contributes to lower CO_2 emission and reduces energy expenditure, without impairing the performance of composites. At present, there is a search for materials that meet the ideal requirements for partially replacing cement. Studies on industrial waste indicate that they are a feasible substitute material. Hence, the focus of this study was to investigate the chemical, physical, and microstructural characteristics of tailings from the metal magnesium industry as a partial substitute for Portland cement, in addition to the compressive strength and porosity of the composite. Finally, this study established the efficacy of the waste as a new cementitious material.

2 MATERIALS AND EXPERIMENTAL PROGRAM

The waste used is a by-product of the metal magnesium industry, where dolomite is calcined in a rotary kiln as a raw material, mixed with silicon iron, and then processed under high vacuum—a process referred to as silicotherm. Resultantly, crude magnesium appears in the form of crystals, which are then melted and refined until reaching the characteristics of the final product, metallic magnesium, according to Rima Industrial S.A. The amount of by-product generated by the unit in Bocaiuva/MG is approximately 120 t/month. The waste was characterized and its composition quantified, following which it was used to partially replace Portland cement in the production of mortar. The tailings are light in color and have fine granulometry.

The tailings sample was used as received, without processing, owing to its small particle size and previous calcination performed in the industry. The tailings were characterized via X-ray fluorescence (XRF), X-ray diffraction (XRD), scanning electron microscopy (SEM), particle size analysis, and laser particle size. The XRF was performed using the ZSX/Primus II spectrometer, manufactured by RIGAKU, with the use of pressed powder tablets. The XRD results were obtained using the SHIMADZU diffractometer, model XRD-7000, with the emission of Cu k-alpha radiation (40 kV/30 mA), under a 2θ scan of 40˚ and 90˚ and a reading of 2˚ per min. The SEM images were captured using a Hitachi low-vacuum scanning electron microscope, model TM3000, with an electron acceleration of 15 kV. The granulometry was verified using the Cilas 1090 Laser Particle Size Analyzer laser granulometer, with obscuration of around 13–18%.

2.1 Obtaining the specimens

In the process of molding the specimens, Portland cement with a high initial strength was used as per the NBR 16697 standard [26]; containing a low percentage of additions, the cement was composed of clinker with calcium sulfate (90 to 100%) and carbonate material (0 to 10%). The choice of cement is related to the low levels of carbonate materials, i.e., the one that best approaches a cement that contains only the clinker. This alternative allows verification of the substitution efficiency.

The aggregate used was quartz sand, with four different granulometric fractions, according to NBR 7214 [27]. The local supply system supplied the mixing water. The replacement adopted was 25% by weight of Portland cement for industrial waste. The replacement content was chosen to verify the upper limit of the NBR 16697 standard [26], which establishes strength classes for Portland cement. This allowed for evaluation of the replacement at the maximum value, in consideration of carbonate materials.

The mortar was established using NBR 7215 and in consideration of previous studies [28]–[30]. A 1: 3 ratio between binder and aggregates was defined, with a water/binder factor of 0.48, as presented in Table 1. Two types of cementitious composites were fabricated; the first was a reference using Portland cement without replacement and the second had 25% cement replacement by tailings. The duly quantified materials, according to the established line, passed through the mechanical mixing process and were placed in cylindrical steel molds, with a diameter of 50 mm and a height of 100 mm, according to the NBR 7215 standard [30].

Table 1. Established proportions for molding

	Proportions in weight (kg)			Water/binder factor
	Portland cement	**Tailing**	**Sand**	
Composition I (Reference)	1.0	-	3.0	0.48
Composition II (Replacement)	0.75	0.25	3.0	0.48

After undergoing 24 hours of molding, the specimens were placed in a submerged cure in water saturated with calcium hydroxide for a period of 28 and 91 days. The compressive strength test was performed at 28 and 91 days, with four specimens for each line by age.

The results of the same trait were averaged; if any result showed a deviation more significant than 6%, the furthest value was excluded and the average recalculated. If the deviation was more significant than 6%, the test was to be repeated; however, this did not happen during this study. For determining the water absorption, the same number of specimens, test age, and procedure for eliminating results were used.

2.2 Mechanical testing and water absorption

The compression test was performed after 28 and 91 days of curing, using universal mechanical testing equipment, with a capacity of 300 kN. The specimens were inserted into the equipment at a constant loading rate of 0.25 MPa/s to promote an almost-static condition for the test and to facilitate consistency of the results. The accommodation of stresses on the upper and lower faces of the specimens was performed with the use of neoprene discs, coupled in metallic supports.

The water absorption test aims to verify the porosity present in the specimens, identifying the presence of pores in the material. The test was conducted using a hydrostatic scale, with an attached basket to hold the sample during weighing; this was inserted into a container containing water. The specimens were weighed under three conditions: (i) saturated, (ii) submerged in water, and (iii) dried for 24 hours, in an electric oven at a temperature of 100 °C, after the mass constancy was verified. Porosity was established by the relationship between permeable pore volume and total volume; the difference between the mass of the saturated and dry specimen was divided by the difference between the mass of the saturated and submerged specimen and the result multiplied by 100 to obtain the percentage of voids.

3 RESULTS AND DISCUSSIONS

3.1 Chemical and mineralogical

The X-ray fluorescence test allowed the chemical composition of the waste to be determined. The results are presented in terms of oxides (Table 2) owing to the semi-quantitative analysis. As the waste is obtained from the metal magnesium industry, the presence of magnesium oxide, silicon oxide, and calcium oxide was expected due to the silicothermal process involved in obtaining magnesium.

Table 2. Chemical composition of tailings.

Oxides	Na_2O	MgO	Al_2O_3	SiO_2	P_2O_5	SO_3	CaO	Fe_2O_3
%	0.04	6.9	0.2	29.5	0.04	0.15	59.7	3.2

The XRD analysis (Figure 1) allowed for the detection of the predominant mineralogical phases, the mineral Calcio-Olivine (COD 9012681), indicative of the polymorphism of the structures of Ca2.SiO4 and the periclase (COD 9005513). Calcium silicate is present owing to the calcination processes, whereas the presence of periclase or periclase is expected as it is a material derived from dolomite; this also justifies the presence of MgO in the chemical analysis of the material.

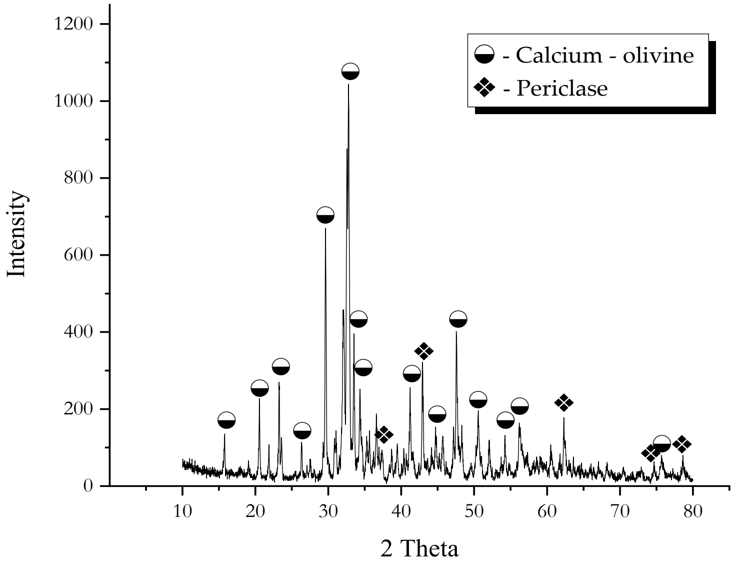

Figure 1. Diffractogram of tailings from the production of metallic magnesium.

3.2 Granulometry

The results of the laser granulometry indicate that 90% of the material had a granulometry smaller than 39.76 µm, which confirms the visual analysis and the fine, powdery characteristic of the residue; this can be confirmed by Figure 2, which presents the particle distribution as a histogram of the cumulative passing.

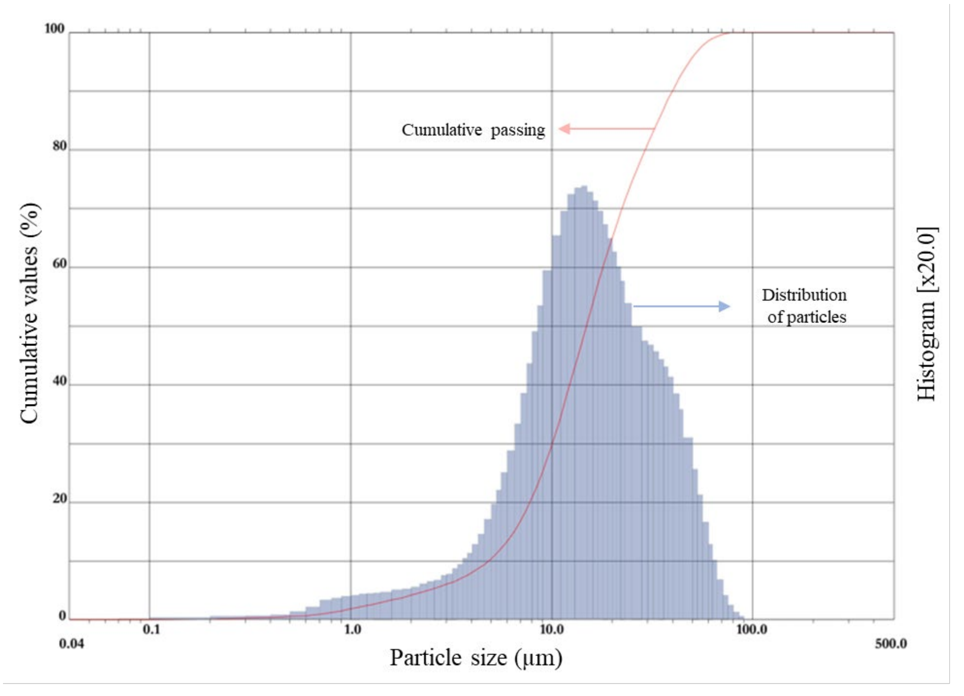

Figure 2. Laser particle size of the tailings.

Materials that present a very fine inert mineral load contribute to the density and strength of the cementitious composite owing to the finer fraction, which contributes to the hardening and filling of the voids; known as the filler effect. The effect occurs due to adhesion of the binder paste in the particulate interface, favoring the chemical and mechanical resistance of the composites, and decreasing the porosity. Adding materials with a filler effect improves performance, reducing voids and permeability, and increasing workability and strength [31]–[33].

3.3 Microstructural research

SEM allows observation of the morphology and topography and helps to elucidate the physical characteristics of the material under study [34]–[37]. The micrographs obtained via SEM (Figure 3) allowed for observation of the morphological characteristics of the tailings, which comprise micrometric particles with an approximate variation of 3 – 80 µm; these particles account for the majority of fragments with dimensions around 19 µm, which is in agreement with the image scale generated via SEM.

In general, it is observed that the particles are heterogeneous, considering the various existing forms. The grains have irregular geometry (Figure 3a), features with a rough surface (Figure 3b), are porous (Figure 3c), and smooth (Figure 3d); observed according to the increase in resolution of 500x to 2K in Figure 3. Lamellar structures are revealed at some points, indicating the presence of kaolinite.

3.4 Mechanical behavior

The compression test defines the ability of the material to withstand the forces applied directly. Research on using cementitious materials as a substitute for cement has evaluated the strength over time, and a strength of approximately 32 – 45 MPa has been determined [38]–[41]. The compression test was performed on reference specimens (without replacement) and specimens with a 25% replacement of cement by tailings. The results showed that the two types of materials were above 40 MPa at 28 days, a satisfactory result when compared to the literature. There was also an increase in resistance over the healing ages (Figure 4).

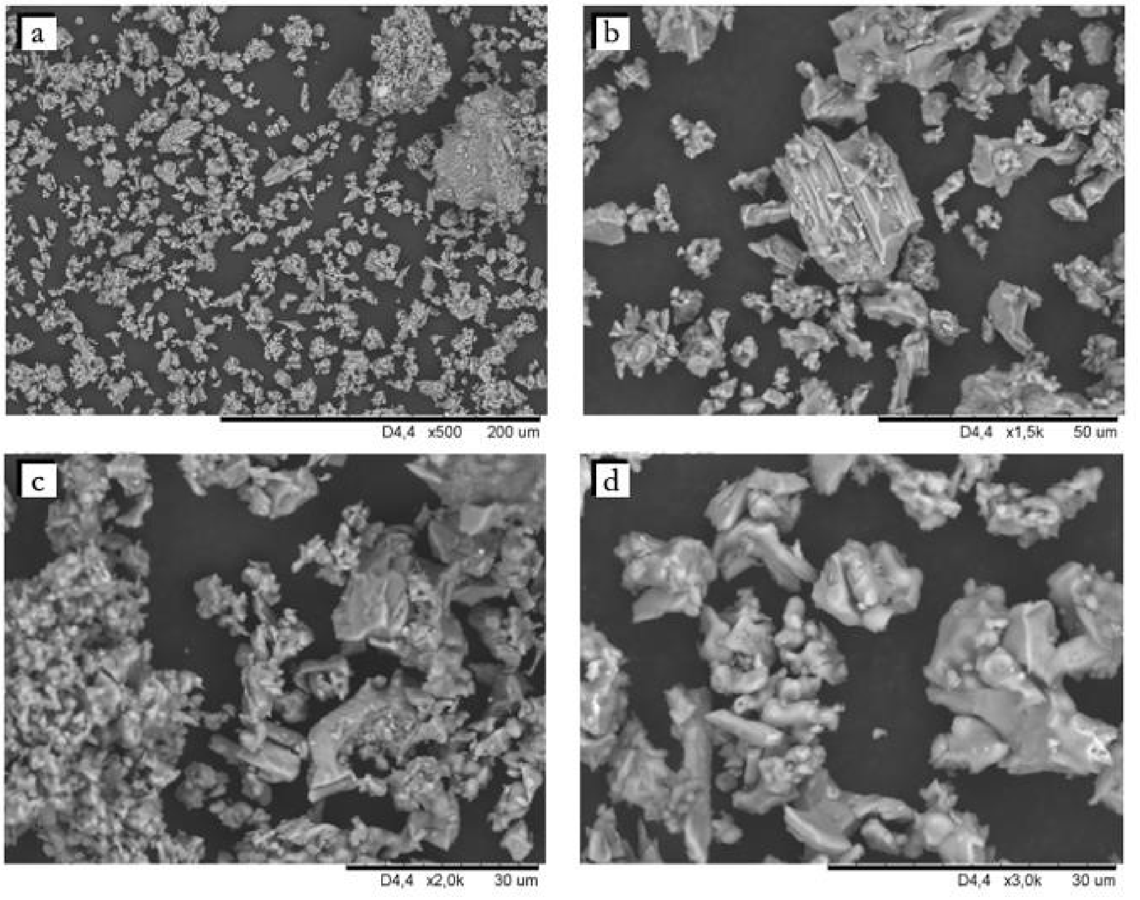

Figure 3. Tailing images obtained by SEM with different resolutions to observe the morphology of the material under study. (a) 500x resolution, (b) 1.5K resolution, (c) 2.0K resolution, and (d) resolution of 3.0K.

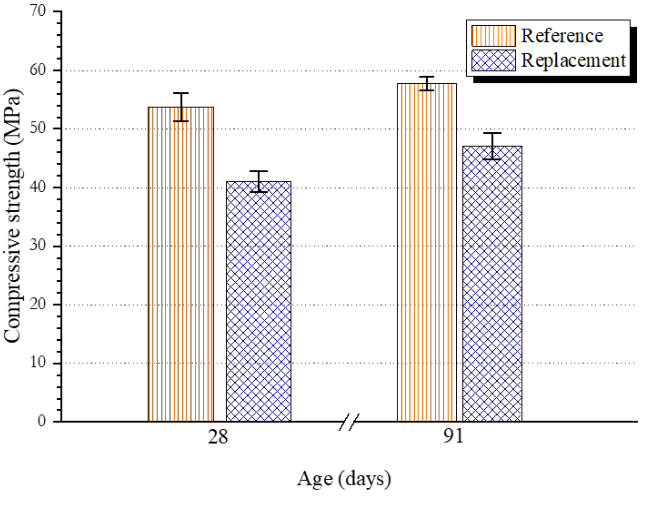

Figure 4. Results of the compressive strength test at 28 and 91 days.

The substituted material showed results above 40 MPa in the first 28 days and an increase in strength of 14.63% at 91 days; these values are higher than those established by NBR 16697 [26]. This result demonstrates that the material was efficient in partially replacing Portland cement. The variation in results, considering the deviation for both 28 and 91 days, demonstrated that the values obtained follow the values established in the norm and are compatible with similar studies [26], [38]–[41].

3.5 Porosity

The water absorption test demonstrated that the porosity of the replaced material decreased in the first 28 days when compared to the reference. At 91 days, the porosity values are close, as shown in Figure 5.

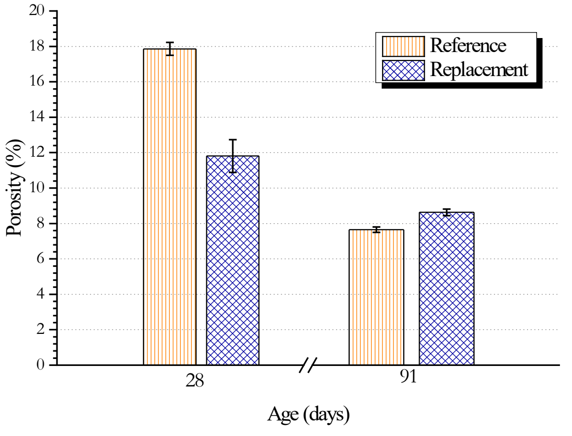

Figure 5. Results of the water absorption test after 28 and 91 days of curing.

The smaller number of voids indicates the occurrence of a filler effect, caused by the fine granulometry of the residue; this contributed to improved filling of the spaces between the mortar constituents and, consequently, the production of a material with less porosity. Furthermore, the formation of new cement hydration products and additions is assessed over time, with denser and more consistent structures filling the voids.

At 28 days, the variation in results was more significant than at 91 days, for the two evaluated traits. Despite the higher deviation at 28 days, the trace with residue showed a considerably lower number of voids than that of the reference trace. In contrast to the initial occurrences, where grain growth and emptying takes place at an accelerated rate, grain growth becomes stable and there are fewer voids after a period of time [42]. Thus, at 91 days, the deviation is significantly less than at 28 days.

4 CONCLUSIONS

The studies and tests carried out indicate the feasibility of using waste from the metal magnesium industry as a partial substitute for Portland cement. The material under analysis demonstrated chemical, structural, morphological, and granulometric characteristics, which contributed to the performance of the cementitious composite. In addition, the potential to promote the filler effect was evident owing to the fine granulometry, decreasing the porosity, and promoting the densification of the cement matrix. The mechanical behavior results demonstrated values higher than those established by the norm and in analogous studies. In this scope, the evaluated waste is eligible for partial replacement of Portland cement, contributing to the production of binders with less environmental impact, reducing CO_2 emissions, and reducing energy demand, with a view to sustainable development.

ACKNOWLEDGEMENTS

This work was supported by the Minas Gerais State Research Foundation (FAPEMIG) [grant numbers APQ-03739-16], the Brazilian Federal Agency for Support and Evaluation of Graduate Education (CAPES) [grant number 001], and Rima Industrial S.A. via donation of research material.

REFERENCES

[1] N. J. L. Lenssen et al., "Improvements in the uncertainty model in the Goddard Institute for Space Studies Surface Temperature (GISTEMP) analysis," *J. Geophys. Res. Atmos.*, vol. 124, 2019.

[2] D. Krekel, R. C. Samsun, R. Peters, and D. Stolten, "The separation of CO_2 from ambient air – a techno-economic assessment," *Appl. Energy*, vol. 218, pp. 361–381, 2018., http://dx.doi.org/10.1016/j.apenergy.2018.02.144.

[3] K. L. Scrivener, V. M. John, and E. M. Gartner, "Eco-efficient cements: potential economically viable solutions for a low-CO_2 cement-based materials industry," *Cement Concr. Res.*, vol. 114, pp. 2–26, 2018.

[4] A. Nazari, J. G. Sanjayan, and J. S. J. Van Deventer, "Progress in the adoption of geopolymer cement," in A. Nazari, Ed., *Handbook of Low Carbon Concrete*. Amsterdam: Academic Press, 2017, pp. 217–262.

[5] E. Benhelal, G. Zahedi, E. Shamsaei, and A. Bahadori, "Global strategies and potentials to curb CO2emissions in cement industry," *J. Clean. Prod.*, vol. 51, pp. 142–161, 2013.

[6] L. Evangelista and J. D. Silvestre, "Equivalent functional unit in recycled aggregate concrete," in J. Brito and F. Agrela, Eds., *New Trends in Eco-efficient and Recycled Concrete*. Duxford: Elsevier, 2019, pp. 293–327.

[7] N. Mahasenan, S. Smith, and K. Humphreys, "The cement industry and global climate changecurrent and potential future cement industry CO_2 emissions," in *Greenh. Gas Control Technol. 6th Int. Conf.*, 2003, pp. 995–1000.

[8] R. Kajaste and M. Hurme, "Cement industry greenhouse gas emissions e management options and abatement cost," *J. Clean. Prod.*, vol. 112, pp. 4041–4052, 2016.

[9] P. Singh, "Waste handling in liquid absorbent-based post-combustion capture processes," in *Absorption-Based Post-combustion Capture of Carbon Dioxide*, P. H. M. Feron, Ed., Duxford: Woodhead Publishing, 2016, pp. 505–517.

[10] J. Armengaud, M. Cyr, G. Casaux-Ginestet, and B. Husson, "Durability of dry-mix shotcrete using supplementary cementitious materials," *Constr. Build. Mater.*, vol. 190, pp. 1–12, 2018.

[11] M. Wu, Y. Zhang, G. Liu, Z. Wu, Y. Yang, and W. Sun, "Experimental study on the performance of lime-based low carbon cementitious materials," *Constr. Build. Mater.*, vol. 168, pp. 780–793, 2018.

[12] S. Ruan and C. Unluer, "Comparative life cycle assessment of reactive MgO and Portland cement production," *J. Clean. Prod.*, vol. 137, pp. 258–273, 2016.

[13] E. Gartner and T. Sui, "Alternative cement clinkers," *Cement Concr. Res.*, vol. 114, pp. 27–39, 2018.

[14] P. C. Aïtcin, "Supplementary cementitious materials and blended cements," in *Science and Technology of Concrete Admixtures*, P. C. Aïtcin and R. J. Flatt, Eds., Cambridge: Woodhead Publishing, 2016, pp. 53–73.

[15] L. L. Sutter and D. P. Bentz, "Assessing ash quality and performance," in *Coal Combustion Products (CCP's) – Characteristics, Utilization and Beneficiation*, T. Robl, A. Oberlink, and R. Jones, Eds., Oxford: Woodhead Publishing, 2017, pp. 225–254.

[16] M. Frías, R. Vigil de la Villa, R. García, S. Martínez, E. Villar, and I. Vegas, "Effect of a high content in activated carbon waste on low clinker cement microstructure and properties," *Constr. Build. Mater.*, vol. 184, pp. 11–19, 2018.

[17] S. Kim, A. Hanif, and I. Jang, "Incorporating Liquid Crystal Display (LCD) glass waste as Supplementary Cementing Material (SCM) in cement mortars – rationale based on hydration, durability, and pore characteristics," *Materials*, vol. 11, no. 12, pp. 2538, 2018.

[18] Y. C. Li et al., "Utilization of red mud and Pb/Zn smelter waste for the synthesis of a red mud-based cementitious material," *J. Hazard. Mater.*, vol. 344, pp. 343–349, 2018.

[19] G. Medina, I. F. Sáez del Bosque, M. Frías, M. I. Sánchez de Rojas, and C. Medina, "Granite quarry waste as a future eco-efficient supplementary cementitious material (SCM): Scientific and technical considerations," *J. Clean. Prod.*, vol. 148, pp. 467–476, 2017.

[20] M. Nasir and W. Al-Kutti, "Performance of date palm ash as a cementitious material by evaluating strength, durability, and characterization," *Buildings*, vol. 9, no. 1, pp. 6, 2018.

[21] A. A. Ramezanianpour, R. Mousavi, M. Kalhori, J. Sobhani, and M. Najimi, "Micro and macro level properties of natural zeolite contained concretes," *Constr. Build. Mater.*, vol. 101, pp. 347–358, 2015.

[22] K. Ramakrishnan, G. Pugazhmani, R. Sripragadeesh, D. Muthu, and C. Venkatasubramanian, "Experimental study on the mechanical and durability properties of concrete with waste glass powder and ground granulated blast furnace slag as supplementary cementitious materials," *Constr. Build. Mater.*, vol. 156, pp. 739–749, 2017.

[23] M. A. A. Sherir, K. M. A. Hossain, and M. Lachemi, "Self-healing and expansion characteristics of cementitious composites with high volume fly ash and MgO-type expansive agent," *Constr. Build. Mater.*, vol. 127, pp. 80–92, 2016.

[24] M. Sumesh, U. J. Alengaram, M. Z. Jumaat, and K. H. Mo, "Microstructural and strength characteristics of high-strength mortar using nontraditional supplementary cementitious materials," *J. Mater. Civ. Eng.*, vol. 31, no. 4, pp. 4019017, 2019.

[25] H. Wang, H. Li, X. Liang, H. Zhou, N. Xie, and Z. Dai, "Investigation on the mechanical properties and environmental impacts of pervious concrete containing fly ash based on the cement-aggregate ratio," *Constr. Build. Mater.*, vol. 202, pp. 387–395, 2019.

[26] Associação Brasileira de Normas Técnicas, *Cimento Portland – Requisitos,* NBR16697, 2018.

[27] Associação Brasileira de Normas Técnicas, *Areia Normal para Ensaio de Cimento – Especificação,* NBR 7214, 2015, pp. 4.

[28] P. Mehta and P. Monteiro, *Concreto: Microestrutura, Propriedades e Materiais*. São Paulo: IBRACON, 2014.

[29] P. Helene and B. F. Tutikian, "Dosagem dos concretos de cimento Portland," in *Concreto: Ciência e Tecnologia*, G. C. Isaia, Ed., São Paulo: IBRACON, 2011.

[30] Associação Brasileira de Normas Técnicas, *Cimento Portland – Determinação da Resistência à Compressão,* NBR 7215, 2019.

[31] İ. B. Topçu and A. Uğurlu, "Effect of the use of mineral filler on the properties of concrete," *Cement Concr. Res.*, vol. 33, no. 7, pp. 1071–1075, 2003.

[32] J. G. Speight, "Asphalt technology," in *Asphalt Materials Science and Technology*. Amsterdam: Elsevier, 2016, pp. 361-408.

[33] S. Ebnesajjad and S. Ebnesajjad, "Adhesion promoters," in *Surface Treatment of Materials for Adhesion Bonding*. Amsterdam: William Andrew, 2014, pp. 301–329.

[34] Z. Liu et al., "A review of fine structures of nanoporous materials as evidenced by microscopic methods," *Microscopy*, vol. 62, no. 1, pp. 109–146, 2013.

[35] S. Stevens et al., "An appraisal of high resolution scanning electron microscopy applied to porous materials," *JEOL News*, vol. 44, pp. 17–22, 2009.

[36] B. W. Jo, C. H. Kim, and J. H. Lim, "Characteristics of cement mortar with nano-SiO 2 particles," *ACI Mater. J.*, vol. 104, pp. 404–407, 2007.

[37] A. Sharif, "Review on advances in nanoscale microscopy in cement research," *Micron*, vol. 80, pp. 45–58, 2016.

[38] L. R. Steiner, A. M. Bernardin, and F. Pelisser, "Effectiveness of ceramic tile polishing residues as supplementary cementitious materials for cement mortars," *Sustain. Mater. Technol.*, vol. 4, pp. 30–35, 2015.

[39] L. Rodier and H. Savastano Jr., "Use of glass powder residue for the elaboration of eco-efficient cementitious materials," *J. Clean. Prod.*, vol. 184, pp. 333–341, 2018.

[40] P. R. Matos, L. R. Prudêncio Jr., A. L. Oliveira, F. Pelisser, and P. J. P. Gleize, "Use of porcelain polishing residue as a supplementary cimentitious material in self-compacting concrete," *Constr. Build. Mater.*, vol. 193, pp. 623–630, 2018.

[41] D. Dodoo-Arhin, R. A. Nuamah, B. Agyei-Tuffour, D. O. Obada, and A. Yaya, "Awaso bauxite red mud-cement based composites: characterization for pavement applications," *Case Stud. Constr. Mater.*, vol. 7, pp. 45–55, 2017.

[42] K. Scrivener, A. Ouzia, P. Juilland, and A. Kunhi Mohamed, "Advances in understanding cement hydration mechanisms," *Cement Concr. Res.*, vol. 124, pp. 105823, 2019.

Author contributions: All authors contributed to the research. M.L.F.M: conceptualization, methodology, investigation, data curation, writing - original draft preparation and editing. R.R.B: software and validation. P.R.S.J: conceptualization, methodology, writing - review and editing. I.P.P: funding acquisition, supervision and writing-review. A.C.S.B: conceptualization, methodology, investigation, funding acquisition, supervision, formal analysis and writing - review.

Editors: Fernando Pelisser, José Luiz Antunes de Oliveira e Sousa, Guilherme Aris Parsekian.

Rev. IBRACON Estrut. Mater., vol. 13, no. 6, e13612, 2020

IBRACON Structures and Materials Journal
Revista IBRACON de Estruturas e Materiais
ISSN 1983-4195 ismj.org

ORIGINAL ARTICLE

Analysis of nodal stress on reinforced concrete two-pile caps supported on steel piles

Análise das tensões nodais em blocos de concreto armado apoiado sobre duas estacas metálicas

Rodrigo Gustavo Delalibera[a]
Marco Aurélio Tomaz[a]
Vitor Freitas Gonçalves[a]
José Samuel Giongo[b]

[a]Universidade Federal de Uberlândia, Faculdade de Engenharia Civil, Uberlândia, MG, Brasil
[b]Universidade de São Paulo – USP, Escola de Engenharia de São Carlos, Departamento de Estruturas., São Carlos, SP, Brasil

Received 14 June 2018
Accepted 04 May 2020

Abstract: Reinforced concrete pile caps may be designed trough plastic models (strut and tie model) or models based on bending theory. The formulae available for verifying the stress is based on caps supported on concrete piles, with few studies about the stress distribution on caps supported on steel piles. To analyze the structural behavior of caps supported on steel piles, as well as the stress on the superior and inferior nodal zones, four two-pile caps supported on steel piles were tested. The variables were the embedment length and in one of the specimens a steel plate was welded on top of both piles. It was observed that the embedment length has substantial influence on pile cap structural behavior. It was concluded that, to verify the stress on inferior nodal zone of the cap, aside from pile area, an area of concrete confined between the flaps of the pile must be considered.

Keywords: pile caps, steel piles, strut and tie model, nodal stress.

Resumo: Blocos de concreto armado sobre estacas podem ser dimensionados por meio de modelos plásticos (Modelo das bielas e tirantes) ou modelos baseados na teoria da flexão. A formulação disponível para a verificação das tensões é baseada em blocos apoiados sobre estacas de concreto, sendo que existem poucos estudos abordando a distribuição de tensões em blocos sobre estacas metálicas. Com o intuito de analisar o comportamento estrutural de blocos apoiados sobre estacas metálicas e as tensões que surgem nas zonas nodais superior e inferior, foram ensaiados quatro modelos de blocos sobre duas estacas metálicas. As variáveis foram o comprimento de embutimento do perfil dentro do bloco e em um dos modelos foi soldada uma chapa de aço quadrada no topo das estacas. Observou-se que o embutimento interfere de maneira significativa no comportamento estrutural do bloco. Concluiu-se que, para a verificação das tensões na zona nodal inferior do elemento deve ser considerada, além da área da estaca, uma área de concreto confinado entre as abas do perfil.

Palavras-chave: blocos sobre estacas, estacas metálicas, modelo de bielas e tirantes, tensões nodais.

How to cite: R. G. Delalibera, M. A. Tomaz, V. F. Gonçalves, and J. S. Giongo, "Analysis of nodal stress on reinforced concrete two-pile caps supported on steel piles," *Rev. IBRACON Estrut. Mater.*, vol. 13, no. 6, e13612, 2020, https://doi.org/10.1590/S1983-41952020000600012

1 INTRODUCTION

According to NBR 6118: 2014 [1], pile caps are volumetric structural elements whose function is to transfer the loads from the superstructure to the infrastructure. Despite being essential for the safety and durability of a structure, pile caps are generally buried elements and, therefore, do not allow visual inspection when in service. The dimensioning of these elements can be performed by three-dimensional calculation models (linear or not) or strut and tie models, the

Corresponding author: Rodrigo Gustavo Delalibera. E-mail: delalibera@ufu.br
Financial support: The company Gerdau S.A., for supporting research and FAPEMIG - Research Support Foundation of the State of Minas Gerais.
Conflict of interest: Nothing to declare.

latter being preferred by engineers due to the possibility of dimensioning in plastic regime. The strut and tie models, for the analysis of stresses in the nodal regions, were elaborated with the premise of reinforced concrete blocks supported on concrete piles. The works of Blévot and Frémy [2], Schlaich and Schäfer [3] and Fusco [4] can be highlighted, as a reference for the study of pile blocks.

According to Xiao and Chen [5] and Velloso and Lopes [6], the use of metal piles provides some advantages in relation to concrete piles, such as the possibility of driving in soils that are difficult to transpose, high resistance to bending and traction, ease of cutting, splicing and transport. Even though they are widely used in bridges, viaducts, ports and containment structures, few studies on the use of metal piles in concrete blocks are found in the technical literature. Therefore, there are still questions about how embedded the metal pile should be in the block, how the connection between block and pile should be made, how the tension in the nodal region should be calculated and what is the maximum allowed tension in this region.

According to the SODH [7] (State of Ohio Department of Highways), piles designs on metal piles have been carried out on the premise that it is necessary to use a steel plate on top of the piles to prevent a concentration of stresses in the connection region between the block and the piles. According to NBR 6122:2010 [8], this connection must be made by means of plates, chartering or rebar welding.

SODH [7] conducted a large number of pile caps tests on a centered metal pile. In total, 47 pile caps were tested, varying the concrete used, the cross section of the pile, the length of the pile embedded within the pile cap, the height of the pile cap, presence or not of a welded steel plate at the top of the pile, the type of the frame of the pile caps and the type of support. Reinforced concrete pile caps with stirrups were used according to the sides of the block, with circular stirrups and simple concrete blocks. The SODH [7] concluded that the use of a sheet at the top of the pile does not increase the bond strength and, in the tests in which failure occurred in the concrete, the main cause was the appearance of tensile stresses transversal to the compressive stresses (diagonal traction, also called connecting rod splitting), due to the partially loaded block effect.

Slutter [9] rehearsed two pile caps on six metal piles. The pile caps were in real scale and rectangular in shape, with frames only in the horizontal plane and in mesh. In one of the pile caps, the author welded steel plates welded on top of two of the six piles, also verifying that the plates do not influence the bearing capacity of the block or the length of penetration of the piles within the element. In addition, Slutter [9] observed failure in the reinforcement anchoring, concluding that the distance between the axis of the piles and the edge of the block must be sufficient to allow the fulfillment of the anchoring requirements.

Xiao and Chen [5] studied one pile caps on piles in metallic profile with horizontal forces or tensile forces acting on the tip of the piles, in order to assess the resistance of the connection between the piles and the block under a situation of earthquake. The tested block had mesh reinforcement and comprised 16 piles, and for the piles subject to tension, two types of connection were tested. Xiao and Chen [5] concluded that the ultimate horizontal force is directly related to the axes of inertia of the profile, with greater resistance when the force is applied in the direction perpendicular to the axis of greater inertia of the profile. Regarding the traction force, there was no significant difference between the types of anchorage tested. In order to analyze the behavior of pile caps supported on metal piles, as well as to verify the stresses that arise in the nodal regions of the element, four pile caps supported on two metal piles were tested. The variables of the models studied were the length of the pile embedded in the pile caps and, in one of the models, steel plates were welded on top of the piles. The use of a steel plate on the top of the piles was made to analyze the hypothesis that this plate increases the area of the top of the pile, decreasing the tension in this region and, consequently, improving the structural behavior of the pile cap.

2 CRITERIA USED FOR DESIGN

Four pile caps were tested on two metal piles, with inlay lengths equal to 10 cm, 20 cm and 30 cm. In one of the pile caps with 10 cm inlay, square steel plates with 25 cm edges and thickness equal to the thickness of the section web (39 mm) were welded on top of the piles. The name given to each of the four models is in accordance with the following:

- BEmb10sch: Pile cap with 10 cm inlay, without top plate;
- BEmb10cch: Pile cap with 10 cm inlay, with top plate;
- BEmb20sch: Pile cap with 20 cm inlay, without top plate;
- BEmb30sch: Pile cap with 30 cm inlay, without top plate.

The models were dimensioned in accordance with the criteria of Blévot and Frémy [2] and the recommendations of NBR 6118:2014 [1], with the proviso that no additional reinforcement was used in addition to the main traction reinforcement (in other words, tie), as recommended by the Brazilian standard. This was done with the objective of minimizing the interference of steel bars in nodal stresses.

NBR 6118:2014 [1] classifies the pile caps as rigid or flexible, considering if the rigid pile caps work with flexion in both directions, with concentrated tension in the line on the piles and shear in both directions, and transmits the column forces to the piles by means of compression connecting rods (or struts). As for the flexible pile caps, NBR 6118:2014 [1] recommends a more complete analysis because their rupture can be defined by the puncture effect. The use of flexible pile caps is not recommended, as there is a need to use transverse reinforcement to resist the tensile stresses caused by shear stresses.

The classification as to the rigidity of the pile caps, by NBR 6118:2014 [1] is geometric, which may lead to contradictory results, as for example, in a situation of an elongated pillar. According to the Brazilian standard, a block is considered rigid, if the total height of the block is greater than or equal to the difference in block length, minus the column dimension in the same direction, divided by three, $h \geq (a- a_p/3)$, with "a" dimension of the pile cap in a given direction, "a_p" the dimension of the column in the same direction and "h" the total height of the pile cap. Applying to the previous expression, for an elongated pillar, it is possible to have a block classified as rigid, for a height considered small for it. Therefore, it is suggested that the classification of the pile cap stiffness be made by the angle of inclination of the strut in relation to the horizontal plane of the pile cap.

The Brazilian standard, NBR 6118:2014 [1], suggests strut and tie models for the design of pile caps. Applying this model, contained in that standard, the inclination of the strut in relation to the horizontal plane must be between 29.7º and 63.4º. According to Blévot and Frémy [2], the pile cap is considered rigid if the angle formed between the strut and the horizontal plane of pile cap is between 45º and 55º.

Applying the Blévot and Frémy model [2], based on Figure 1, it was determined that the distance between the longitudinal axis of the pile up to the face of the column plus ¼ of its dimension is equal to 25 cm, and the useful height of the pile cap (measured from the top of the pile to the upper face of the block) is equal to 25 cm, thus forming an angle of 45º.

Thus, it is concluded that the pile caps tested are rigid, because the strut angle in relation to the horizontal plane of the pile cap, respects the recommendations of NBR 6118:2014 [1] and Blévot and Frémy [2].

The Brazilian standard does not present specific criteria for the design of pile cap or guidelines for the case of pile caps on metal piles, it only limits the compression stresses in the nodal regions. For pile caps on two piles, NBR 6118: 2014 [1] recommends that stresses in the upper (CCC Node) and lower (CCT Node) nodal zones should be limited by Equations 1 and 2, where: σ_{zns} is the tension in the upper nodal zone; σ_{zni} is the tension in the lower nodal zone; fc is the uniaxial compressive strength of concrete. CCC nodes are understood as nodes where there are only compression forces, CCT nodes are nodes where there are compression forces, a tensile force and σ_{zn} is the normal tension in the nodal region, defined by the ratio between the compression force and the area of the strut, see Figure 1.

$$\sigma_{zns} \leq 1.0 \cdot f_c \tag{1}$$

$$\sigma_{zni} \leq 0.847 \cdot f_c \tag{2}$$

where f_c is the compressive strength of concrete.

In this paper, the factors that reduced concrete strength related to creep and the α_{v2} coefficient were not considered. This procedure was adopted, as it was intended to measure the experimental results against the limits established by the referred norm. For the lower nodal zone, the existence of cracks crossing the connecting rods was considered (this effect is considered in NBR 6118: 2014 [1] by multiplying the value of f_c by 0.72). Thus, in order not to consider the effect of long-term loads in the lower zone, the value of f_c was multiplied by 0.847. It is worth mentioning that the values presented by NBR 6118:2014, for nodal stresses are: $\sigma_{zns} \leq 0.85 \cdot \alpha_{v2} \cdot f_{cd}$, for the upper zone and $\sigma_{zni} \leq 0.72 \cdot \alpha_{v2} \cdot f_{cd}$, for the inferior nodal zone. Disregarding the value of 0.85, related to long-term loads in the two equations, the tensions in the upper and inferred node regions are obtained, respectively.

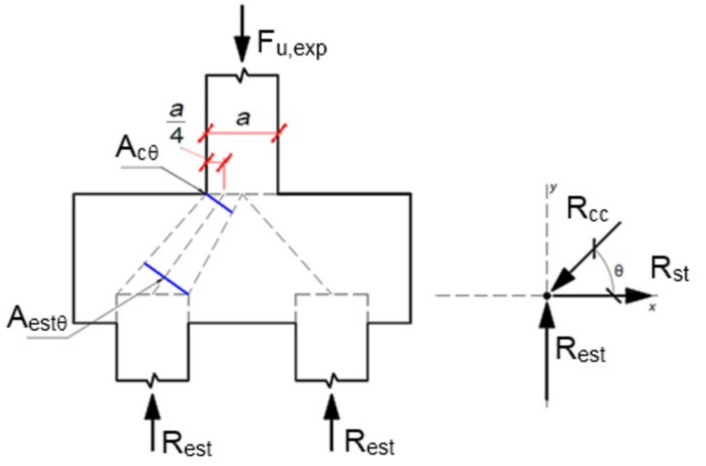

Figure 1. Strut and tie model proposed by Blévot and Frémy [2].

According to Blévot and Frémy [2], in the case of a pile cap supported on two piles, the axis of the strut is formed from the axis of the pile up to ¼ of the outer face of the column and, for the calculation of nodal stresses, the areas are considered of the pile and the column projected in the direction transverse to the strut. Figure 1 illustrates the model proposed by Blévot and Frémy [2] for the case of a pile cap supported on two piles, in which: $F_{u,exp}$ is the ultimate force applied to the column; "a" is the dimension of the column in the longitudinal direction of the pile cap, A_c is half the pillar area; A_{est} is the pile area; θ is the angle between the axis of the strut in relation to the horizontal plane; R_{est} is the reaction in the pile; R_{cc} is the compression force on the strut; R_{st} is the force in the tie. The stresses in the upper and lower nodal zones are calculated using Equations 3 and 4, respectively.

$$\sigma_{zns} = \frac{F_{u,exp}}{A_c \cdot sen^2(\theta)} \tag{3}$$

$$\sigma_{zni} = \frac{F_{u,exp}}{2 \cdot A_{est} \cdot sen^2(\theta)} \tag{4}$$

The force in the R_{st}, necessary for the dimensioning of the main reinforcement, is achieved through the static balance of forces of the lower nodal zone. Blévot and Frémy [2] recommend that the angle between the compression rod and the horizontal plane be 45º to 55º and that the stresses in the nodal regions should have the limits shown in Equations 5 and 6. In Equations 5 and 6, the concrete material lessening coefficients, the coefficient related to long-term loads and the confinement effect in CCC type nodes, caused by the concrete resistance in the multiaxial state of stresses, were not considered.

$$\sigma_{zns} \leq 0{,}60 \cdot f_c \tag{5}$$

$$\sigma_{zni} \leq 0{,}60 \cdot f_c \tag{6}$$

3 MECHANICAL AND GEOMETRIC PROPERTIES OF MODELS

The parameters fixed in all models were: the angle between the strut and the horizontal direction (θ) of 45º; height of 35 cm; width of 25 cm; 139.5 cm length; cross section of the 25×25 cm^2 column. For the piles, the W200×15 metal profile was used, positioned with the axis of greater inertia in the same direction as the pile cap width and cut so as to have the same length outside the pile cap in all models, varying only its embedded length. Table 1 shows the geometric properties of the models tested.

For the metallic profile, a yield stress of 345 MPa was considered, following the recommendations of NBR 8800:2008 [10]. As mentioned previously, reinforcement was used only on the tie, calculated so as not to reach the yield stress. For this, the balance of the lower nodal region was made considering the ultimate force supported by the metallic profile and under the premise that the force applied to the column is centered and the reactions in both piles are equal. The reinforcement was calculated considering the yield stress characteristic of CA-50 steel equal to 500 MPa, according to the guidance of NBR 6118:2014 [1]. Four bars of 20 mm in diameter were used, and the length of reinforcement anchoring, measured from the internal face of the piles to the external face of the pile cap, was verified according to the recommendations of NBR 6118:2014 [1]. In order to bring about the ruin to occur in the pile cap, the column was dimensioned considering the reduction coefficients of the strengths of the materials and increase of the soliciting efforts and, in addition, concrete with a compressive strength of 50 MPa was adopted. For the pile caps, 20 MPa was considered. Opted for concrete with a 20 MPa resistance to compression due to the support capacity of the reaction frame available at the Structural Laboratory of the Federal University of Uberlândia, where all tests were carried out. A height that was considered sufficient for the dissipation of tensions was adopted for the pillar, so that the second order effects could be neglected according to the Saint-Venant principle. The pillar was constructed with 8 bars of 10 mm in diameter and stirrups of 6.3 mm in diameter, spaced ever 2.5 cm. Figures 2 and 3 illustrate the geometric properties and the reinforcement arrangement of the models.

Table 1 - Geometric parameters of pile caps.

Model	Height (cm)	Pile axis distance (cm)	Pile cap length (cm)	Width (cm)	Column section (cm x cm)	Total pile length (cm)
BEmb10sch	35	62.5	139.5	25	25x25	35
BEmb10cch	35	62.5	139.5	25	25x25	35
BEmb20sch	35	62.5	139.5	25	25x25	45
BEmb30sch	35	62.5	139.5	25	25x25	55

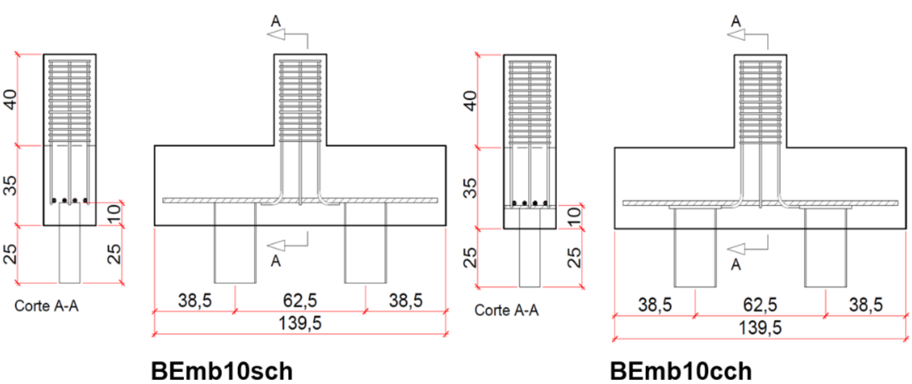

Figure 2. Models BEmb10sch and BEmb10cch (dimensions in cm).

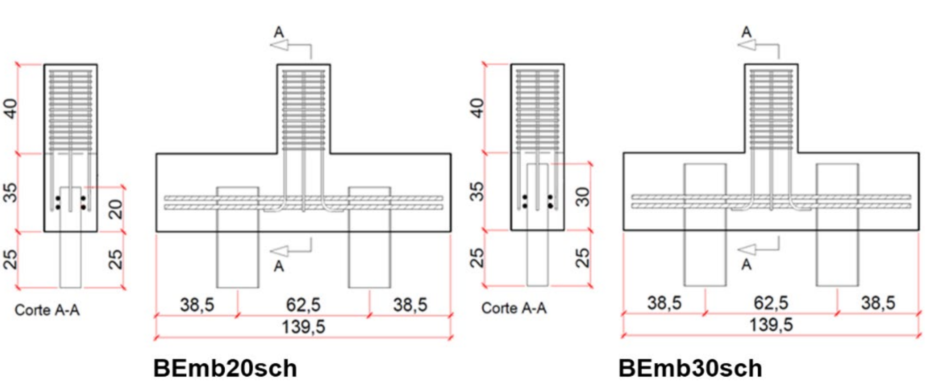

Figure 3. Models BEmb20sch and BEmb30sch (dimensions in cm)

4 CHARACTERIZATION OF MATERIALS AND EXPERIMENTAL TESTS

To define the properties of the metal profiles, each of the 8 pieces was weighed and its dimensions were obtained using a caliper. Figure 4 shows the dimensions measured in each profile and Table 2 shows the results of the measurements. For the calculation of the cross-sectional area of the profile, the circular sections, present between the flaps and the core of the part, were approximated to rectangular triangles of legs equal to 0.7 cm. Table 3 shows the geometric properties of the metal profiles, in which: $I_{x,cg}$ is the moment of inertia in relation to the horizontal axis that passes through the CG of the part; $I_{y,cg}$ is the moment of inertia in relation to the vertical axis that passes through the CG of the steel profile.

For the main frame of the pile caps and columns, CA-50 steel was used, characterized by tensile tests according to the recommendations of NBR 6892-1:2013 [11]. Table 4 shows the mechanical properties of the steel used, where: f_y is the yield strength; ε_y is strain deformation; f_u is stress ultimate; E it is the longitudinal strain module.

For 20 MPa concrete, cement with the addition of CPIV-32-RS pozzolan was used, with a mixture of 1:2.55:3.54:0.68 (cement, sand, crushed stone and a/c) and, for 50 MPa concrete, high-strength CPV initial cement was used, with mix proportion of 1:2.66:3.66:0.49 and 1.5% of superplasticizer additive. The characterization of the concrete used was carried out by means of compression tests, diametrical compression and test of determination of the initial tangent deformation module, following the recommendations of the standards NBR 5739:1994 [12], NBR 7222: 2011 [13] and NBR 8522:2008 [14]. For each model, 17 cylindrical specimens of 10 cm in diameter and 20 cm in height were molded, 8 specimens with concrete used in the pillars, and 9 specimens with concrete used in the pile caps.

Due to the volume of total concrete required, it was not possible to mold all models on the same day. The specimens remained in saturated cure until the test date and were tested on the same day as the pile caps. Table 5 presents the results of the compression tests, in which: fc is the compressive strength of the concrete; $f_{c,m}$ is the average of the compressive strengths presented by the specimens. It is noteworthy that there was a discrepancy in the results of the compressive strength of one of the tested pile caps, causing a decrease in the strength of the concrete. However, this did not harm the analysis, since the premise that the compressive strength of the columns is higher than that of the pile caps was verified. Table 6 shows the result of the diametrical compression tests, where: F is the maximum force; d is the diameter of the specimen; L is the height of the specimen; $f_{ct,sp}$ is the tensile strength by diametrical compression.

Table 2 - Cross section measurements of W200×15 steel profiles

Profile	Weight (kg)	Length (cm)	Linear mass (kg/m)	t_{f1} (mm)	t_{f2} (mm)	t_{f3} (mm)	t_{f4} (mm)	t_w (mm)	b_{f1} (mm)	b_{f2} (mm)	h_P (mm)
1	5.15	35.25	14.61	5.45	5.58	5.49	5.30	3.92	86.30	80.91	202.89
2	5.20	35.30	14.73	5.31	5.51	5.54	5.41	3.88	99.17	99.19	203.13
3	5.15	34.66	14.86	5.47	5.53	5.54	5.25	3.88	99.18	99.24	203.07
4	5.20	35.13	14.80	5.38	5.20	5.39	5.23	3.90	99.96	99.14	202.95
5	6.70	45.20	14.82	5.49	5.25	5.48	5.58	3.95	99.24	99.22	203.03
6	6.65	40.06	16.60	5.20	5.38	5.21	5.25	3.90	99.18	98.87	202.85
7	8.15	55.26	14.75	5.40	5.26	5.31	5.51	3.84	99.89	99.15	202.92
8	8.15	55.03	14.81	5.46	5.21	5.39	5.48	3.93	99.08	99.08	203.06
Medium values:			15.00	5.39	5.37	5.42	5.38	3.90	97.50	98.85	202.99

Table 3 - Geometric properties of W200×15 steel section

Profile	Area (cm²)	$I_{x,cg}$ (cm4)	$I_{y,cg}$ (cm⁴)
1	17.62	1205.40	53.66
2	19.24	1370.99	88.78
3	19.25	1371.17	88.94
4	19.04	1348.64	87.44
5	19.38	1375.13	89.07
6	18.90	1334.18	85.38
7	19.04	1355.99	88.48
8	19.20	1361.73	87.63
Medium values:	18.96	1340.41	83.67

Table 4 - Mechanical properties of CA-50 steel

Specimen	f_y (MPa)	ε_y (‰)	f_u (MPa)	E (GPa)
01	562.7	2.74	686.3	205.35
02	575.9	2.74	695.9	210.16
03	570.3	2.62	692.4	217.68
Medium values:	596.6	2.70	691.5	211.07

Table 7 presents the results of the tests for determining the initial longitudinal tangential deformation module of the concrete, where Eci,exp is the value of the tangential deformation module. The specimens 03 of the pile caps BEmb10cch and BEmb30sch, and the specimen 01 of the column presented different results and, therefore, were disregarded.

The models were instrumented with a displacement transducer, positioned in the middle of the pile cap span, and electrical resistance strain gages, installed on the flaps of the metal profiles and in different positions of the reinforcement. The reinforcement extensometers were placed only on one of the bars and, due to the symmetry of loading and dimensions of the models, it was decided to instrument only one side of the pile cap. Figure 5 shows the positioning of the extensometers in the models.

Table 5 - Concrete compressive strength

Element	Specimen	Age (days)	Slump test (mm)	f_c (MPa)	$f_{c,m}$ (MPa)
BEmb10sch	01	96	99	17.41	17.95
	02			15.47	
	03			20.97	
BEmb10cch	01	62	94	13.06	12.51
	02			10.96	
	03			13.50	
BEmb20sch	01	80	95	19.18	17.42
	02			16.55	
	03			16.52	
BEmb30sch	01	74	91	17.96	18.07
	02			18.45	
	03			17.79	
Column	01	37	37	36.85	43.85
	02			43.96	
	03			50.74	

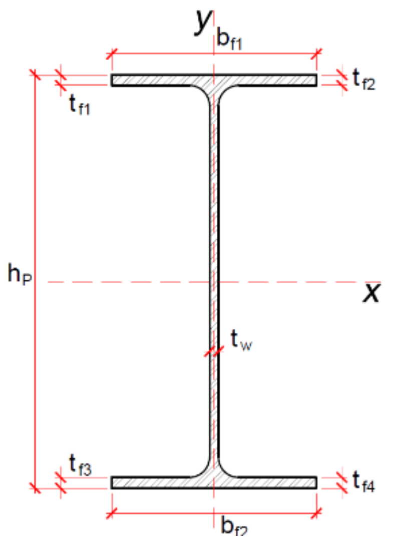

Figure 4. Cross section dimensions of steel profiles

Table 6 - Concrete tensile strength by diametrical compression

Element	Specimen	F (N)	d (mm)	L(mm)	$f_{ct,sp}$(MPa)	Medium values
Pile cap BEmb10sch	01	76920.71	100.49	200.11	2.44	2.17
	02	69114.43	100.02	199.16	2.21	
	03	58310.54	99.91	198.98	1.87	
Pile cap BEmb10cch	01	57864.14	100.45	198.65	1.85	1.86
	02	59154.89	100.43	198.27	1.89	
	03	57756.17	100.58	198.81	1.84	
Pile cap BEmb20sch	01	74405.11	99.72	199.58	2.38	2.40
	02	75952.50	99.75	199.15	2.43	
	03	74471.11	100.34	197.40	2.39	
Pile cap BEmb30sch	01	90474.68	100.07	199.74	2.88	2.77
	02	93251.93	100.53	200.48	2.95	
	03	79266.37	100.49	201.14	2.50	
Column	01	131625.94	100.07	200.25	4.18	4.43
	02	151606.49	101.82	202.53	4.68	

Table 7 - Longitudinal initial tangential deformation module of concrete

Element	Specimen	Eci,exp (MPa)	Medium values
Pile cap BEmb10sch	01	28.08	29.26
	02	31.33	
	03	28.36	
Pile cap BEmb10cch	01	22.39	23.06
	02	23.72	
	03	-	
Pile cap BEmb20sch	01	29.49	28.96
	02	29.51	
	03	27.87	
Pile cap BEmb30sch	01	33.82	31.98
	02	30.15	
	03	-	
Column	01	-	47.81
	02	58.53	
	03	37.09	

The intensity of the force applied to the column was measured by a load cell with a capacity of 2000 kN and, as a reaction structure, the metal frame and the reaction slab from the Structural Laboratory of the Federal University of Uberlândia were used. The column was placed on a support consisting of an elastomer layer and two layers of metal sheets. The pile caps were fixed to the reaction frame to guarantee their lateral stability during the tests. Figure 6 shows the test configuration of the models. More information about the experimental program can be found at Tomaz [15].

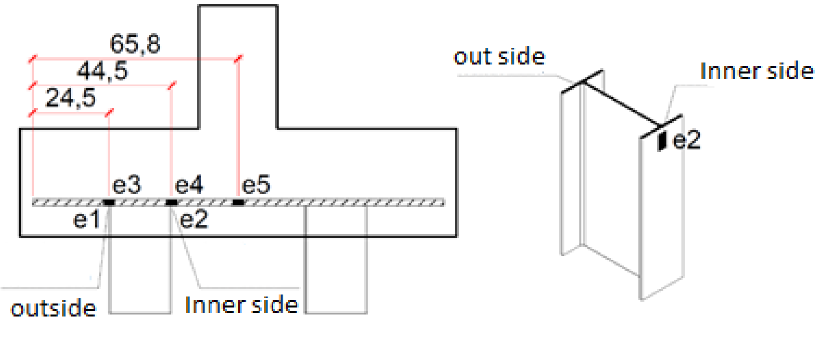

Figure 5. Position of extensometers on models.

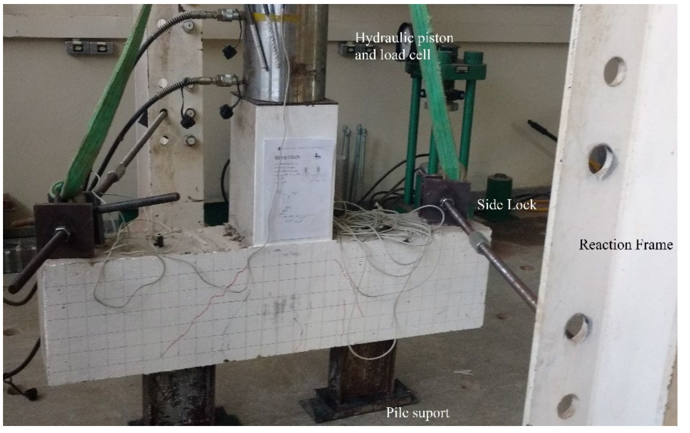

Figure 6. Test-system configuration.

5 RESULTS AND DISCUSSIONS

In all models the collapse occurred in the pile cap, that is, both the pillar and the metal post did not show signs of failure and, with the exception of the BEmb30sch model, all the pile caps presented ruin characterized by diagonal traction (strut cracking). The pile caps were tested at the same ages as the respective specimens, indicated in Table 5. Table 8 presents the experimental results, in which: F_r is the force related to the first crack; $F_{u,exp}$ is the ultimate force; δ is the vertical displacement measured in the middle of the pile cap's span. The ultimate forces were below expectations due to the low compressive strength of the concrete.

In both models with 10 cm inlay, BEmb10sch and BEmb10cch, the first crack occurred in the lower-central region of the pile and, subsequently, cracks appeared next cap to the internal face of the piles that propagated to the lateral face of the column, in the upper part the pile cap. Both models also had a high $F_r/F_{u,exp}$, that is, the rupture of the pile cap occurred after the first crack appeared. According to Delalibera and Giongo [16], this relationship can be reduced using horizontal stirrups or steel bars positioned diagonally, crossing struts.

The pile cap with a top plate reached 9% greater strength than the pile cap with the same inlay and without top plate, even with concrete with 30% lower strength. Therefore, the use of welded plate at the top of the profile improved the bearing capacity of the pile cap, in contrast to what was observed by Slutter [9], who states that the use of the top plate does not interfere with the structural behavior of the pile cap. Figures 7 and 8 demonstrate the rupture plans observed in the models BEmb10sch and BEmb10cch and, in highlight, the cracks observed next to the pile.

The BEmb20sch model presented two rupture planes, characterized by shear in the compression rod and vertical shear close to the profile flap. Figure 9 shows the rupture planes observed in the BEmb20sch model.

The BEmb30sch model, unlike the others, presented ruin characterized by shearing at the interface of the metallic profile with the upper face of the pile cap (punching), causing the concrete layer to unblock in this region. With this, it became evident that the bonding tension between the profile and the surrounding concrete was not effective and, due to the small thickness of the concrete layer located above the profile, it was not possible to form the compression rods. Consequently, the stresses arising from the reactions in the piles (R_{est}) were transmitted directly to the upper face of the pile cap. Figure 10 shows the cracks observed in the BEmb30sch model and Figure 11 shows a diagram of the rupture lines, similar to the rupture caused by the puncture effect.

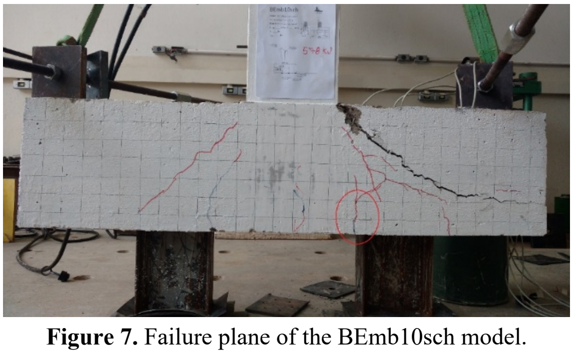

Figure 7. Failure plane of the BEmb10sch model.

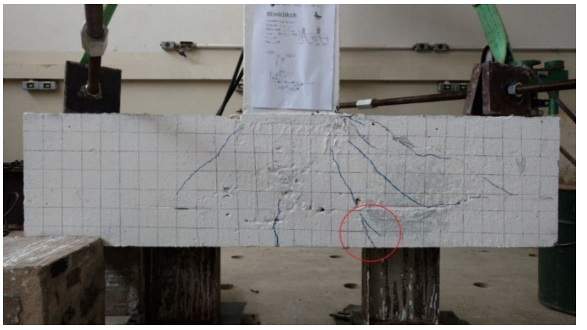

Figure 8. Failure plane of the BEmb10cch model.

Figure 9. BEmb20sch failure plans.

Figure 10. Cracks observed at the top of the model BEmb30sch.

Figure 12 shows the force curves versus vertical displacements of the models. The pile caps with 10 cm of embedding showed close displacements, indicating that the use of the top plate does not interfere with the rigidity of the pile caps.

The tested pile caps are classified as flexible, according to NBR 6118:2014 [1], which uses pile caps analogous to that of foundation (section 22.6.1). However, for pile caps, where the supports are discrete (piles), the best concept for the rigidity of the element is correlated with the angle of inclination of the strut in relation to the horizontal plane. This consideration was suggested a priori by Blévot and Fremy [2] and is described in section 22.3.1 of NBR 6118:2014 [1]. Thus, all tested models, with the exception of BEmb30sch, have rigid pile cap behavior. The BEmb30sch model presented a flexible pile cap behavior because it was not possible to observe the formation of struts experimentally, even though it is considered geometrically rigid. Therefore, the effect of embedding the piles in the inner part of the pile cap, changed its classification regarding rigidity.

In models with 10 cm inlay (embedded), the longitudinal reinforcement was positioned above the profile, which caused a pin effect. In this way, if the profile tends to penetrate the pile cap, the bars above it would prevent it. This contributed for the model without a plate to show stiffness close to the model with a plate. In the models with 20 and 30 cm inlay, the reinforcement was welded on the sides of the profiles and, therefore, this effect did not occur.

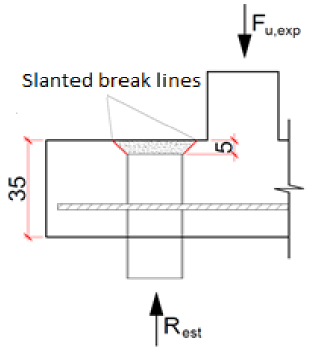

Figure 11. BEmb30sch break lines.

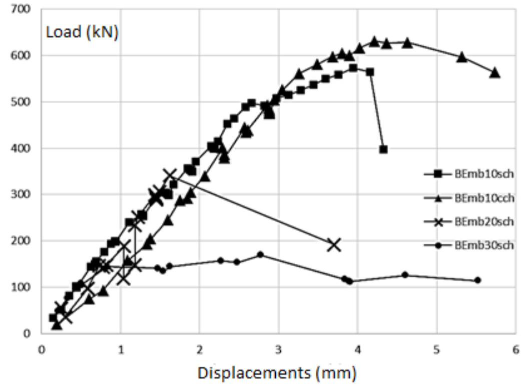

Figure 12. Load vs. displacements.

The deformations related to $F_{u,exp}$ in the bars and profiles, can be seen in Table 8, in which the extensometers are named according to Figure 5. Figures 13, 14, 15 and 16 show the deformations referring to F_r and $F_{u,exp}$ in the reinforcements and profiles. Some strain gauges, whose readings are not shown, showed defects during the tests.

Table 8 - Deformations in the reinforcement and profiles referring to $F_{u,exp}$

Pile cap	Steel profile		Steel bar		
	e1 (‰)	e2 (‰)	e3 (‰)	e4 (‰)	e5 (‰)
BEmb10sch	-0.182	-0.707	0.135	1.125	1.500
BEmb10cch	-0.416	-0.629	0.616	-	-
BEmb20sch	-0.045	-0.399	0.397	0.648	0.715
BEmb30sch	0.011	-0.031	0.041	-	0.244

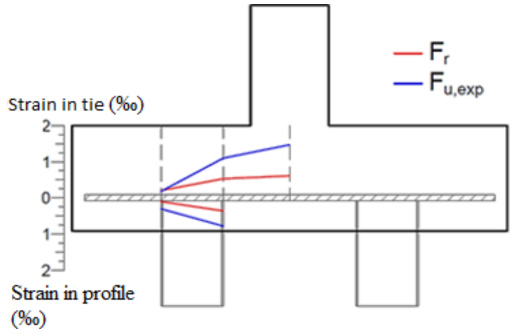

Figure 13. Strain in tie and profile of the BEmb10sch model.

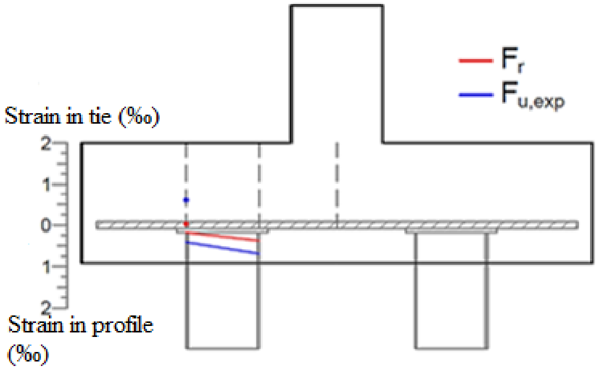

Figure 14. Strain in tie and profile of the BEmb10cch model.

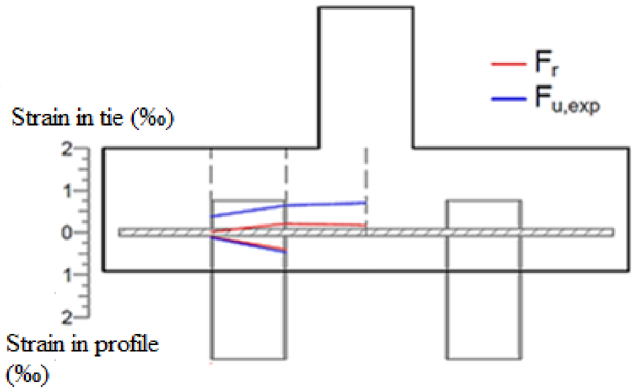

Figure 15. Strain in tie and profile of the BEmb20sch model.

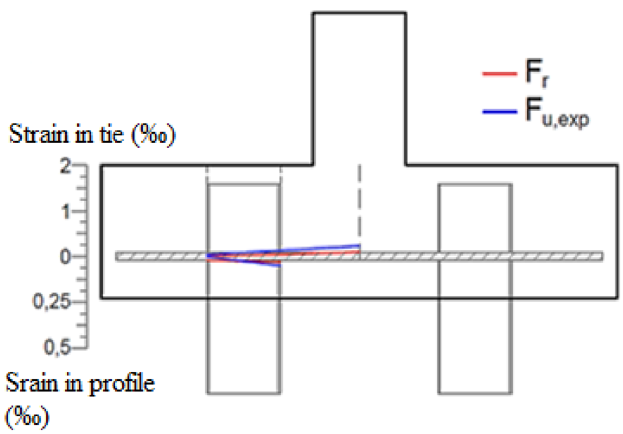

Figure 16. Strain in tie and profile of the BEmb30sch model.

It was found that the deformation is not constant along the tie (e3, e4 and e5 strain gages), which corroborates the observations of Delalibera and Giongo [16] and Adebar et al. [17], who experimentally analyzed pile caps on concrete piles, finding similar results regarding deformations in the main tensile reinforcement (tie), that is, in the central region of the pile caps, the tie deformation is practically constant, decreasing when the bars of the tie cross the strut (at this point, there is an increase in the normal force, increasing the frictional force and therefore decreasing the tension in the steel bars).

The flap closest to the end of the pile cap (strain gages e1) showed less deformation than the flap furthest from the end (strain gages e2). With this, it can be said that the profiles were not uniformly requested and, therefore, are subject to flexion-compression. Such behavior was also observed experimentally by Delalibera [18], Barros [19] and Munhoz [20].

As mentioned in item 2, it was considered that the connecting rod axis extends from ¼ of the column face to the geometric center of the pile section. The fact that the pile is subjected to flexion-compression indicates that the force from the strut does not act on the geometric center of the cross section of the pile, which alters the angle of inclination of the strut. This finding is most evident on the BEmb10sch and BEmb10cch models. In the BEmb30sch model, the profile obtained close deformations in the two flaps and in the tie, reinforcing the idea of ruin caused by punching.

Due to the difference in concrete strength of the tested pile caps, the analysis of the results obtained was based on the relative stress ($\sigma/f_{c,m}$). For models without a top plate, the stresses were calculated considering the cross-sectional area of the metal profile, while for the model with a top plate, the area of the plate was considered. Table 9 shows the results of nodal stresses related to the ultimate force.

The BEmb10cch model presented a relative tension, in the upper nodal zone, approximately 57% higher than the BEmb10sch model, with the same inlay. This value is significant because, in the formulation presented by Blévot and Frémy [2], the tension in the upper nodal zone does not depend on the shape and/or type of pile used. The low values of relative stresses, also in the upper nodal zone, presented by the models BEmb20sch and BEmb30sch, can be explained by the fact that the greater length of the embedding influenced the colapse mode of the pile caps.

Table 9 - Active nodal stresses and relative nodal stresses

Pile cap	$F_{u,exp}$ (kN)	$f_{c,m}$ (MPa)	A_{est} (cm²)	σ_{zni} (kN/cm²)	σ_{zns} (kN/cm²)	$\sigma_{zni}/f_{c,m}$	$\sigma_{zns}/f_{c,m}$
BEmb10sch	578.65	17.95	18.96	30.52	1.85	1.7003	0.1032
BEmb10cch	631.24	12.51	625	1.01	2.02	0.0807	0.1615
BEmb20sch	355.55	17.42	18.96	18.75	1.14	1.0765	0.0653
BEmb30sch	174.52	18.07	18.96	9.20	0.56	0.5094	0.0309

In the lower nodal zone, the relative stress of the BEmb10sch model was 2106% higher than that of the BEmb10cch model. This value is justified by the use, in the calculation of the relative stress in the lower nodal zone of the BEmb10sch block, of the effective area of the steel profile, which is approximately 33 times smaller than the area of the plate, however, this verification is only illustrative because this. The relative stress value does not match what was observed experimentally, since both models showed failure by diagonal traction and not by crushing the concrete in the nodal region. Therefore, the area considered in the lower nodal region must be greater than the area of the effective cross section of the profile.

ABNT NBR 6122:2019 [8] recommends, in its section 8.5.6.1, that the minimum diameter for isolated piles without locking is 30 cm, and for metal piles the diameter of the circle that circumscribes the cross section of the piles is considered. Thus, the stresses in the lower nodal zone were calculated again, considering the area defined by the circle circumscribed to the cross section of the profiles (A_{circ}). A collaborative concrete area was also considered equal to the area of confined concrete between the profile flaps, as illustrated by Figure 17, in which: $A_{sp,cc}$ is the total area to be considered; h_p is the average height of the profiles; b_{fm} is the average between b_{f1} and b_{f2}. Table 10 shows the stresses in the lower nodal zone, calculated with Equation 4, considering A_{est} equal to $A_{sp,cc}$ and A_{circ}.

As the upper nodal zone presents a confluence of compression stresses, the premise that this region is subject to the multiaxial state of stresses was verified. For that, the limit stress for concrete under multiaxial stress state was recommended by NBR 6118: 2014 [1], calculated by Equation 7.

$$\sigma_{zns} \leq 1.0 \cdot f_c + 0.9 \cdot f_{ct,sp} \quad (7)$$

Table 11 shows the limit stresses for the nodal regions, calculated according to NBR 6118:2014 [1] and with Blévot and Frémy [2], $\sigma_{zns,lim}$ is the limit stress for the upper nodal zone; $\sigma_{zni,lim}$ is the limit stress for the lower nodal zone.

Table 12 presents the relationship between the limit stresses and the stresses obtained experimentally, considering the stresses of the lower nodal zone calculated with the different areas $A_{sp,cc}$ and A_{circ}, where: $\sigma_{zns,exp}$ is the stress obtained experimentally for the superior nodal zone; $\sigma_{zni,exp}$ is the stress obtained experimentally for the lower nodal zone. Table 12 shows that the limit values of Blévot and Frémy [2] are very conservative and the normative values should be used only for models with 10 cm inlay of the metal profile, with and without the metal plate welded on top of it. In addition, in pile caps with 10 cm inlay, the values of nodal stresses in the lower zone were closer to the limit values when, in Equation 4, an area equal to is considered for A_{est}.

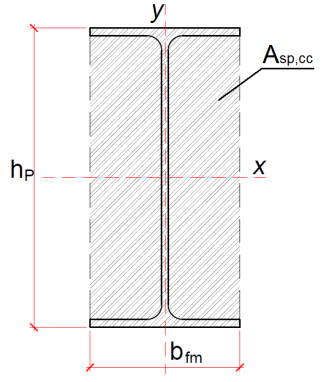

Figure 17. Collaborative concrete area to be considered

Table 10 - Tensions in the lower nodal region for A_{est} equal to $A_{esp,cc}$ and A_{circ}

Pile cap	A_{est} (cm^2)		σ_{zni} (kN/cm^2)		$\sigma_{zni}/f_{c,m}$	
	$A_{sp,cc}$	A_{circ}	$A_{sp,cc}$	A_{circ}	$A_{sp,cc}$	A_{circ}
BEmb10sch	199.29	399.4	2.90	1.45	0.1618	0.0807
BEmb10cch	625	399.4	1.01	1.01	0.0807	0.0807
BEmb20sch	199.29	399.4	1.78	0.89	0.1024	0.0511
BEmb30sch	199.29	399.4	0.88	0.44	0.0485	0.0242

Note: $A_{sp,cc}$ is the area of concrete defined by the area shown in Figure 17 and A_{circ} is the area of the circle circumscribed to the cross section of the steel profile

Table 11 - Stress limit for nodal regions.

Pile cap	NBR 6118:2014 [1]		Blévot and Frémy [2]		Multiaxial state
	$\sigma_{zns,lim}$ (kN/cm^2)	$\sigma_{zni,lim}$ (kN/cm^2)	$\sigma_{zns,lim}$ (kN/cm^2)	$\sigma_{zni,lim}$ (kN/cm^2)	$\sigma_{zns,lim}$ (kN/cm^2)
BEmb10sch	1.80	1.52	1.08	1.08	2.58
BEmb10cch	1.25	1.06	0.75	0.75	1.92
BEmb20sch	1.74	1.48	1.05	1.05	2.61
BEmb30sch	1.81	1.53	1.08	1.08	2.80

Table 12 - Relationship between observed stresses and limit stresses

Pile cap	NBR 6118:2014 [1]			Blévot and Frémy [2]			Multiaxial state
	$\sigma_{zns,exp}/\sigma_{zns,lim}$	$\sigma_{zni,exp}/\sigma_{zni,lim}$		$\sigma_{zns,exp}/\sigma_{zns,lim}$	$\sigma_{zni,exp}/\sigma_{zni,lim}$		$\sigma_{zns,exp}/\sigma_{zns,lim}$
		$A_{esp,cc}$	A_{circ}		$A_{esp,cc}$	A_{circ}	
BEmb10sch	1.03	1.91	0.95	1.72	2.70	1.35	0.72
BEmb10cch	1.61	0.95	0.95	2.69	1.35	1.35	1.05
BEmb20sch	0.65	1.21	0.60	1.09	1.71	0.85	0.44
BEmb30sch	0.31	0.57	0.29	0.52	0.81	0.40	0.20

Note: $A_{esp,cc}$ is the area of concrete defined by the area shown in Figure 17 and A_{circ} is the area of the circle circumscribed to the cross section of the steel section

6 CONCLUSIONS

The models BEmb10sch and BEmb10cch, with 10 cm inlay, presented ruin by diagonal traction. As the embedding value was increased, the rupture started to be defined by the shear effect. This behavior does not depend on the type of pile or its geometric shape. Shearing collapse in reinforced concrete pile caps is exclusively related to the value of the inlay.

The use of the welded top plate at the upper end of the profile increased the bearing capacity of the pile cap. Although the compressive strength of the concrete used in the BEmb10cch model showed less resistance, the block presented a final strength 9.18% greater than the ultimate strength of the BEmb10sch model. Therefore, it is concluded that the top plate in the pile, decreases the tension in the lower nodal region, thus increasing the ultimate resistance of the pile cap.

From the analysis of nodal stresses, it is recommended that for the lower nodal zone, at least the area of a rectangle should be considered, evolving the entire metallic profile, as suggested in Figure 17. It is worth mentioning, due to the limited number of experimental tests performed in this work and existing in the technical literature, these recommendations are applied only to pile caps on piles with the same characteristics as those tested in this work. It is also suggested that further studies on this topic be carried out, so that an analytical calculation model can be proposed.

The models with 10 cm inlay, presented rigid block behavior. Therefore, the use of metal piles did not affect the element's stiffness for this inlay. The small difference between the displacements of the BEmb10sch and BEmb10cch models proves that the steel plate did not interfere with the block stiffness. For models with 20 cm and 30 cm inlays, verification of the effect of bending and shear stress is necessary.

ACKNOWLEDGMENTS

The Faculty of Civil Engineering linked to the Federal University of Uberlândia, the company Gerdau S.A., for supporting research and FAPEMIG - Research Support Foundation of the State of Minas Gerais.

REFERENCES

[1] Associação Brasileira de Normas Técnicas, *Design of Concrete Structures – Procedure*, NBR 6118, 2014.

[2] Blévot, J., Frémy, R. “Semelles sur pieux. Analles de L’Institut Technique du Batiment.

[3] J. Schlaich and H. Schäfer, "Design and detailing of structural concrete using strut-and-tie models," *Struct. Eng.*, vol. 69, no. 6, pp. 113–125, 1991.

[4] P. B. Fusco, *Reinforcement Techniques for Concrete Structures*, 2. ed. São Paulo: PINI, 2013. Portuguese only..

[5] Y. Xiao and L. Chen, "Behavior of model steel H-pile-to-pile-cap connections," *J. Construct. Steel Res.*, vol. 80, no. 1, pp. 153–162, 2013.

[6] D. A. Velloso and F. R. Lopes, *Foundations, Deep Foundation, vol. 2*. São Paulo: Text Workshop, 2010. Portuguese only.

[7] Ohio. State of Ohio Department of Highways, *Investigation of the Strength of the Connection Between a Concrete Cap and the Embedded End of a Steel h-Pile* (Research Report 1). Ohio: SODH, 1947.

[8] Associação Brasileira de Normas Técnicas, *Design and Execution of Foundations*, NBR 6122, 2019.

[9] R. G. Slutter, “Full-scale pile cap tests and suggested design procedures,” in *Short Course-Semin. Anal. Des. Build. Found., vol. 1*, Bethlehem, 1976, pp. 567-581.

[10] Associação Brasileira de Normas Técnicas, *Design of Steel Structures and Mixed Steel and Concrete Structures for Buildings*, NBR 8800, 2008.

[11] Associação Brasileira de Normas Técnicas, *Metallic Materials – Tensile Test Part 1 – Test Method at Room Temperature*, NBR 6892, 2013.

[12] Associação Brasileira de Normas Técnicas, *Concrete – Cylindrical Specimen Compression Test*, NBR 5739, 1994.

[13] Associação Brasileira de Normas Técnicas, *Grout and Concrete – Determination of the Tensile Strength by Diametrical Compression of Cylindrical Specimens*, NBR 7222, 2011.

[14] Associação Brasileira de Normas Técnicas, *Concrete – Determination of the Elastic Modulus to Compression*, NBR 8522, 2008.

[15] M. A. Tomaz, “Analysis of nodal stress on two-pile caps supported on steel piles,” M.S. thesis, Esc. Eng. Civ., Univ. Fed. Uberlândia, Uberlândia, 2018.

[16] R. G. Delalibera and J. S. Giongo, "Deformation in diagonals in two piles caps," *Ibracon Struct. Mater. J.*, vol. 1, no. 2, pp. 121–157, 2008.

[17] P. Adebar, D. Kuchma, and M. P. Collins, "Strut-and-tie models for design of pile caps: an experimental study," *ACI J.*, vol. 87, no. 1, pp. 81–92, 1990.

[18] R. G. Delalibera “Numerical and experimental analysis of two pile caps subjected to the action of centered and eccent ric load,” Ph.D. dissertation, Esc. Eng. São Carlos, Univ. São Paulo, São Carlos, 2006.

[19] R. Barros, “Numerical and experimental analysis of two piles caps with external cup, partially embedded and embedded used in the column-pile caps connection,” Ph.D. dissertation, Esc. Eng. São Carlos, Univ. São Paulo, São Carlos, 2013.

[20] F. S. Munhoz, "Experimental and numerical analysis of rigid two pile caps with column of square and rectangular sections and different reinforcement rates," Ph.D. dissertation, Esc. Eng. São Carlos, Univ. São Paulo, São Carlos, 2014.

Author contributions: Delalibera, R. G. Orientation, writing, essays and analysis of results. Tomaz, M. A. writing, essays and analysis of results. Giongo, J. S. writing and analyzing the results. Gonçalves, V. F. writing and analyzing the results.

Editors: Osvaldo Luís Manzoli, José Luiz Antunes de Oliveira e Sousa, Guilherme Aris Parsekian.

IBRACON Structures and Materials Journal
Revista IBRACON de Estruturas e Materiais
ISSN 1983-4195 ismj.org

ORIGINAL ARTICLE

Concrete produced with recycled aggregate: a durability analysis for structural use

Concreto produzido com agregado reciclado: uma análise de durabilidade visando uso em estruturas

Lia Lorena Pimentel[a]
Giovanna Falzetta Rizzo[a]
Ana Elisabete Paganelli Guimarães de Avila Jacintho[a]
Patrícia Stella Pucharelli Fontanini[b]

[a]Pontifícia Universidade Católica de Campinas – PUC Campinas, Faculdade de Engenharia Civil, Programa de Pós-graduação em Sistemas de Infraestrutura Urbana, Campinas, SP, Brasil
[b]Universidade Estadual de Campinas – UNICAMP, Faculdade de Engenharia Civil Arquitetura e Urbanismo, Programa de Pós-graduação em Engenharia Civil, Campinas, SP, Brasil

Received 26 March 2018
Accepted 17 April 2020

Abstract: Construction and Demolition waste (CDW) is already used in many European countries as recycled aggregates to produce concrete for structural purposes. In Brazil, its use is still restricted to concretes with no structural function. The consumption of aggregates for the production of concrete is very large, and enabling the use of recycled aggregates in the production of concrete is essential to transform the civil construction industry into a more sustainable one. This work aimed to study the parameters that affect the durability of C30 grade concrete, produced with different types of recycled aggregate. We defined four types of coarse aggregates for carrying out this work: the natural (AN), the concrete (ARCO), the cementitious materials (ARCI) and the treated cementitious materials (ARCI Treated). We adopted 30% substitution content of natural aggregate for recycled aggregates. The treatment of the ARCI aggregate consisted of the application of water and cement solution, aiming to reduce its water absorption capacity. We determine the physical and mechanical characteristics of the concrete, in addition to carrying out indirect measurement tests of durability, by determining the permeability to air, penetration and migration of chloride ions, and determination of the carbonation depth. The results indicate that the concrete using the ARCO type aggregate, produced with 100% crushed concrete, presented characteristics like the reference concrete, indicating the possibility that it can be applied to reinforced concrete structures. As for the ARCI type aggregate, it presented inferior results when compared to the concrete reference for the tests of indirect measurement of durability, however, the concrete displayed good mechanical properties. The concrete produced with the treated ARCI did not perform better than the concrete with ARCI for most of the evaluated characteristics, indicating that the proposed treatment was not adequate.

Keywords: durability, construction waste, permeability.

Resumo: Os resíduos de construção civil (RCC) já são utilizados em muitos países da Europa como agregados reciclados para a produção de concreto com fins estruturais, no Brasil a sua utilização ainda é restrita a concretos sem função estrutural. O consumo de agregados para produção de concreto é muito grande, viabilizar a utilização de agregados reciclados na produção de concreto é fundamental para tornar a construção civil mais sustentável. Este trabalho teve como objetivo estudar os parâmetros que afetam a durabilidade do concreto de classe C30, produzido com diferentes tipos de agregado reciclado. Foram definidos quatro tipos de agregados graúdos para a realização deste trabalho, o natural (AN), o de concreto (ARCO), o cimentício (ARCI) e o cimentício tratado (ARCI Tratado) e foi fixado um teor de substituição do agregado natural pelos agregados reciclados de 30%. O tratamento do ARCI consistiu em aplicação de uma solução de água e cimento, visando a redução de sua capacidade absorção de água. Foram determinadas as características físicas e mecânicas dos concretos, além de ensaios de medição indireta da durabilidade, através da determinação da permeabilidade ao ar, penetração e migração de cloreto e carbonatação. Os resultados indicam que o concreto

Corresponding author: Lia Lorena Pimentel. E-mail: lialp@puc-campinas.edu.br
Financial support: São Paulo Research Foundation, grant 2014/20486-8.
Conflict of interest: Nothing to declare.

utilizando o agregado tipo ARCO, produzido com 100% de concreto britado, apresentou características similares ao concreto referência, indicando a possibilidade de ser aplicado em estruturas de concreto armado. Quanto ao ARCI, os resultados obtidos foram inferiores quando comparados ao concreto referência para os ensaios referentes a medição indireta da durabilidade, porém, o traço apresentou bom comportamento mecânico. O concreto produzido com o ARCI Tratado não apresentou melhor desempenho do que o concreto com ARCI para a maioria das características avaliadas, indicando que o tratamento proposto não foi adequado.

Palavras-chave: durabilidade, resíduo de construção, permeabilidade.

How to cite: L. L. Pimentel, G. F. Rizzo, A. E. P. G. A. Jacintho, and P. S. P. Fontanini, "Concrete produced with recycled aggregate: a durability analysis for structural use," *Rev. IBRACON Estrut. Mater.*, vol. 13, no. 6, e13613, 2020, https://doi.org/10.1590/S1983-41952020000600013

1 INTRODUCTION

Currently, the construction industry is one of the human activities that most affects the environment [1]. McGinnis et al. [2] stated that the production of natural aggregates is those that most impact the environment, since for the concrete mixture, about 50% of its total volume is natural aggregate.

The recycling of construction and demolition waste for use as aggregates in the production of concrete would not only decrease the consumption of natural aggregates, but also reduce energy consumption, transportation costs and, consequently, the emission of polluting gases [3], [4].

Civil construction waste is identified by the European Union as a priority for reuse and recycling, as it represents approximately 30% of the solid waste generated. The authors estimated that 46% of the waste resulting from civil construction is recycled and reused, but they point out large variations between different countries [5]. According to the Panorama of Solid Waste of the State of São Paulo [6], the percentage of civil construction waste within solid waste is variable and difficult to determine, as the percentage varies according to the characteristics of the construction and the economic development of each region. Due to the high variability in the composition of civil construction waste, which consequently generates different types of recycled aggregates, the use of these materials in the production of concrete for structural purposes is difficult, since the variability of recycled aggregates results in uncertainty about the characteristics of the concrete produced with this material.

Currently, each country generally has its regulatory standard for the use of recycled aggregates, with its own nomenclature, defining what the types of aggregates are, and the maximum and minimum levels of each material that comprise it. Some standards prescribe the contents of substitution of natural aggregates for recycled ones in the production of concrete. In the United Kingdom, recycled aggregates are divided into two groups (RA—recycled aggregate and RCA—recycled concrete aggregate), according to their composition. Aggregates classified as RA are limited to the production of concrete with a maximum strength class of 16 to 20 MPa. Aggregates classified as RCA, on the other hand, can be used for concretes with structural functionality, since the strength class varies from 40 to 50 MPa. However, the replacement of natural aggregates with recycled aggregates is restricted to 20% [7].

Also, according to Gonçalves and Brito [7], in Portugal the use standard for recycled aggregates is similar to that of Germany. There recycled aggregates are divided into three groups, namely: RCA (recycled construction aggregate), which presents in its constitution concrete and masonry elements, this aggregate can only be used for concrete without structural purposes. The ARB1 (recycled concrete aggregate with a minimum of 90% concrete in its composition) and ARB2 (recycled concrete aggregate with a minimum of 70% concrete in its composition), which can be partial substitutes, with a maximum replacement content of 25% and 20%, respectively, of natural aggregates. In addition to the replacement content, the standard establishes the maximum strength class of concrete at C40 / 50 MPa for ARB1 and C35 / 45 MPa for ARB2. The Australian Government allows the use of up to 30% recycled aggregates in the concrete mix for structural purposes [1]. In Brazil, the technical standard NBR 15116 [8] which regulates the quality and use of recycled aggregate, allows its use in mixing concrete that is not used for structural purposes. This same standard classifies recycled aggregates as aggregate of concrete waste (ARC), which in its large fraction, must have at least 90% by mass of fragments based on Portland cement and rocks, and mixed residue aggregate (ARM), which in its large fraction, must have less than 90% by mass of fragments based on Portland cement and rocks. The type of aggregate added to the concrete mix has a great influence on its properties. Modifying the physical and mechanical properties of the concrete, such as its strength, water absorption capacity and porosity, can influence its durability [9]. Therefore, the study of the characteristics of the recycled aggregates that will be used in the mixing of the concrete is necessary and extremely important.

According to Gonçalves and Brito [7], concrete produced from recycled aggregates presents different characteristics from concrete produced with natural aggregates, and these differences are linked to the type of recycled aggregate used in the mixture.

The mechanical properties of concrete produced from recycled aggregates decreases by 15 to 30% from the values obtained by conventional concrete, depending directly on the type of aggregate used. The greater the resistance of the concrete used in the production of the recycled aggregate, the better the quality of the aggregate and, consequently, the lesser the influence that these aggregates will have on the characteristics of the new concrete [10].

Initially, research on the effects caused by the replacement of natural aggregate with recycled aggregate was based only on the compressive strength that concrete using recycled aggregate could achieve, or on their economic viability. Since the beginning of such research, there has been increased interest in the mixing of recycled aggregate with concrete for structural purposes. For this reason, research has become more complex, introducing new variables, such as durability [11].

Durability refers to the ability of a structure to resist environmental influences of the installation site, throughout the expected life of the structure [12], i.e., “the effective period of time during the which structure meets the project's performance requirements, without unforeseen maintenance and repair actions” [13].

The durability of concrete can be attributed, for the most part, to the difficulty of penetrating aggressive agents in the concrete pore network [14].

The loss of the useful life of the reinforced concrete structure is due to the corrosion of the reinforcement, through attacks of deteriorating agents on the structure itself. Zhang and Shao [15] point out that corrosion of steel is one of the main problems in reducing the durability of the structure.

According to Santos [16], the durability of concrete is related to the mechanisms of fluid transport within the material since all possible mechanisms of deterioration of concrete structures involve gaseous or liquid transport processes. The dynamics of mass transport is determined by the interaction between the percolating fluid and the porous structure of the concrete. This interaction, depending on the fluid displacement by the pore structure, can occur in three different ways: diffusion (displacement due to a difference in concentration), capillarity (the result of capillary movements in the pores of the concrete opened to the medium) and permeability (flow under pressure differential).

Permeability is linked to the structure of the cement paste, to the aggregate and to the paste-aggregate interface, which determine the ease with which fluids and gases enter the structure. The lower the permeability of the concrete, the lower the penetration of aggressive agents into the interior concrete [17].

According to Ollivier and Vichot [14], the corrosion of concrete reinforcement is induced by two different phenomena: carbonation, the entry of carbon dioxide present in the atmosphere, and the penetration of chloride substances through the pores of the concrete, reaching the reinforcement.

The reduction in pH caused by carbonation accelerates corrosion of the reinforcements, since the chloride ions needed in the concrete to start the deterioration process are reduced [17].

Recycled aggregate generally has a greater water absorption capacity than natural aggregate due to its own porosity, which may change the properties of the concrete increasing its permeability, decreasing its mechanical resistance and, consequently, reducing its useful life.

To date, the mixing of recycled aggregates with concrete for structural purposes has been studied and has found that it is necessary to evaluate properties such as air permeability, water absorption capacity, among others [18]–[20].

The expansion in the field of consumption of the use of these materials is only possible through the development of continuous research to undo the negative concepts of the use of construction waste and to prove its full potential [21].

The objective of this work is to study the parameters that affect the durability of class C30 concrete that is produced with different types of recycled aggregate, to evaluate its mechanical and physical characteristics as well as the parameters that are directly linked to the durability of concrete structures after being exposed to adverse conditions. A treatment was also proposed for the recycled cementitious aggregate, aiming to reduce its water absorption capacity.

2 MATERIALS AND EXPERIMENTAL PROGRAM

The methodology for the development of the work was experimental and included the characterization of the materials, the dosage of the concrete, and the mechanical and physical evaluation. Indirect tests were used to evaluate durability.

2.1 Materials – preparation and characterization

We opted for the use of two types of recycled aggregate, one from the recycling plant and the other produced by crushing specimens in the laboratory. The recycled concrete aggregate (ARCO) was produced by crushing concrete specimens with strength classes between 30 to 50 MPa.

The recycled cement aggregate (ARCI) is the aggregate classified by NBR 15116 [8] as ARC, with a high percentage, more than 90% of particles based on Portland cement and rocks.

The treated cementitious recycled aggregate (ARCI-treated) is ARCI aggregate, which has undergone a treatment to reduce its water absorption capacity. This aggregate was an impregnated with a water and cement solution with the proportion of 45 kg of cement per cubic meter of recycled aggregate. The amount of water needed for the treatment was defined according to the water absorption capacity of the ARCI, to ensure that the entire cement paste was absorbed.

To carry out the treatment, the water and cement were mixed in a concrete mixer for 15 seconds, then the recycled ARCI aggregate was added, mixing it for another 120 seconds. After mixing, the treated recycled aggregate was maintained cured in a closed plastic bag for 28 days before use, and 24 hours after treatment, the bags were stirred to avoid conglomerate of particle. This procedure was proposed by Perea and Alvarado [22].

The other aggregates used were the natural fine aggregate, from rivers, and the natural coarse aggregate of basaltic origin (AN). The cement used was that of high initial strength (CPV—ARI). The ADVACAST 525 superplasticizer additive was used to maintain the consistency of all mixtures produced at 6.5 ± 1cm.

The characteristics of the aggregates were determined according to test procedures standardized by the NBR 7211 [23] and NBR 15116 [8] standards for natural and recycled aggregates. Table 1 presents the results obtained.

Table 1. Characteristics of the aggregates

Aggregates	Standard	Natural Sand	Natural Coarse	ARCO	ARCI	ARCI Treated
Specific mass (g/cm^3)	NBR NM 52 [24] / NBR NM 53 [25]	2.52	2.87	2.36	2.41	2.42
Water absorption (%)	NBR NM 52 [24]/ NBR NM 30 [26]	2.76	1.35	7.34	7.35	6.75
Crushing Strength (%)	NBR 9938 [27]	_	14.36	25.79	24.50	24.24
Max aggregate size (mm)	NBR NM 248 [28]	6.3	25	25	25	25

The natural sand had a fine modulus of 3.01. It was observed that the water absorption capacity of the recycled aggregates was much higher than that of the natural aggregate, and that the treatment applied to the recycled aggregate ARCI promoted a small reduction in the water absorption capacity. Regarding the crushing strength of the aggregate, the test showed that there was no difference between the recycled aggregates and they were all less resistant than the natural aggregate.

2.2 Concrete mix design

A concrete mix with a strength class of 30 MPa was defined using the IPT mix design method [29]. For this study, the replacement percentage of natural aggregate for recycled, 30%, was defined for each of the three types of recycled aggregates. The correction of aggregate volume was made according to the difference between the specific mass of the natural aggregate and that of the recycled aggregates.

The definition of the percentage content for this study was decided based on prior studies [30], [31] and the standards that were cited by [1], [7]. In some cases, authors [4], [32], [19] have used contents of 50% and 100% for replacement, but the results obtained in most cases have not been favorable, so the 30% replacement content was defined for this work.

Table 2 shows the unitary mixes—by mass, the nomenclature adopted for each mix, the cement consumption and the respective percentage of additive used.

Table 2. Concrete mass unit mix proportions

Concrete	Replacement content.	C	Natural Sand	Natural Coarse	Recycled aggregate	a/c	S. A.* (%)	Cc ** (kg/m^3)
T REF	0	1	2.71	3.79	0	0.6	0.4	308.5
T ARCO	30%	1	2.71	2.65	1.00	0.6	0.4	308.5
T ARCI	30%	1	2.71	2.65	1.02	0.6	0.3	308.5
T ARCI Treated	30%	1	2.71	2.65	1.02	0.6	0.5	308.5

*S.A. – Superplasticizer Additive; **Cement Consumption

After the production of the concrete, the specimens were kept in a humid chamber for 28 days. After that period, some of the specimens were placed outside to be exposed to the weather.

The other specimens were immersed in saline solution, with a concentration of 4% NaCl, the purpose of which was to evaluate the response of the concrete to chemical attack. The volume of liquid used inside the containers was four times greater than the volume of the specimens inserted into them. The specimens that were exposed to the weather and those submerged in saline solution remained in these conditions until the end of the test period.

2.3 Concrete properties

The consistency assessment was made through NBR NM 67 [33] and specific gravity through NBR 9833 [34]. Table 3 presents the concrete properties in the hardened state and the respective test standard method.

Table 3. Tests for characterization of concrete.

Tests performed	Standard Method
Resistance to axial compression	NBR 5739 [35]
Modulus of elasticity	NBR 8522 [36]
Water absorption capacity by immersion	NBR 9778 [37]
Capillary water absorption capacity	NBR 9779 [38]23
Chloride penetration	Adaptation of the methodologies used by Omrane et al. [3], França [39], Kim et al. [40], Real et al. [41]:
Air and water permeability (Porosiscope)	Manual *Porosiscope* [42]
Carbonation	Adaptation of the methodologies used by Perea and Alvarado [22], NBR 7211 [23], Valls and Vàzquez [43], Gandía-Romero [44]:
Chloride migration	According Medeiros [45]

2.4 Indirect durability indicators

2.4.1 Determination of carbonation depth

To determine the depth of carbonation, after 180 days of exposure to the weather, the specimens were cut and placed for one day in an oven for complete drying. Then, a phenolphthalein solution, with a concentration of 1%, was sprayed on the cutting surface. After spraying, photographic recording of the surfaces was performed and, as shown in Figure 1A, the distance from the camera to the specimen and the location lighting were standardized. This apparatus was also used to photograph the specimens used in the chloride penetration test. Figure 1B shows an example of a specimen after spraying phenolphthalein.

A B

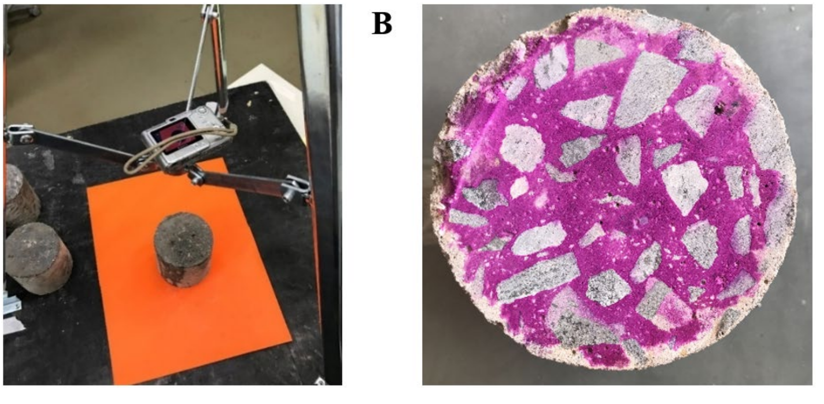

Figure 1. Test method of carbonation depth. **A.** Apparatus used to take the photographs. **B.** Specimen after spraying phenolphthalein.

The photographs were loaded into the AutoCAD® program, which facilitated the determination of the carbonated area. From this value, the average thickness of carbonation was calculated using Equations 1 and 2:

$$A_{carbonated} = A10 - A(10 - e) \tag{1}$$

$$0.786e^2 - 15.71e + A_{carbonated} = 0 \tag{2}$$

where A10 is the cross-sectional area of the specimen; and A (10 - e) is the area of the circle minus the carbonated thickness. With the carbonated area obtained in Equation 1, using the Bhaskára formula, the second-degree equation was defined for calculating the carbonation thickness (Equation 2).

2.4.2 Determination of the chloride penetration depth

After 180 days, the specimens immersed in saline solution were cut in half, repeating the procedure performed to determine the carbonation of the concrete. With the specimens at room temperature, a 0.3 M silver nitrate solution was sprayed onto the cutting surface. Photographic records of the surfaces were taken, and analysis of the images was also performed to determine the depth of chloride penetration. The average chloride penetration thickness was calculated according to Equations 1 and 2.

2.4.3 Determination of air permeability

After 210 days, the specimens were tested to determine the surface permeability using Porosiscope equipment, which is shown in Figure 2. The air was pressurized on a concrete surface with a pressure of 55 kPa. The equipment timer determined how many seconds it took for the pressure to drop to 50 kPa.

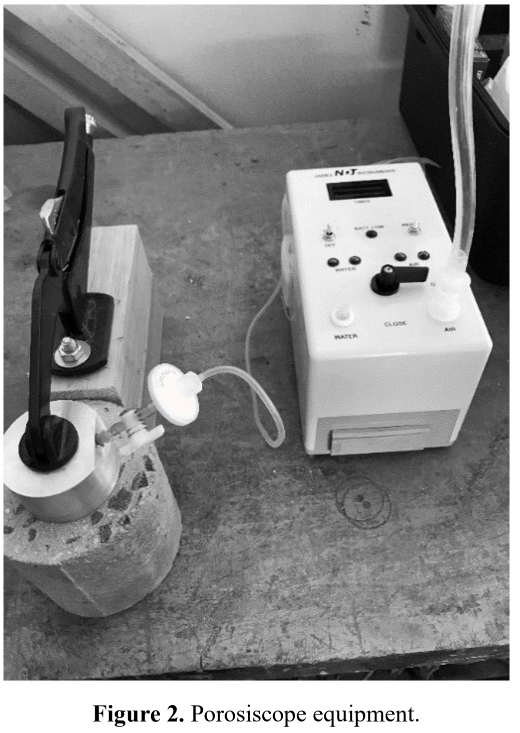

Figure 2. Porosiscope equipment.

The permeability was determined according to the time that the air took to travel through the pores and into the concrete, by decreasing the pressure in the device fixed on the surface of the specimen. The equipment manual determines the classification of concrete according to the time required to lose pressure [42], as shown in Table 4.

Table 4. Material classification according to permeability.

Quality Category	Time(s)	Protection Quality
0	< 30	Poor
1	30 - 100	Moderate
2	100 - 300	Satisfactory
3	300 - 1000	Good
4	> 1000	Excellent

Fonte: ASTM C 1202-05 [46]

2.4.4 Chloride migration

The chloride migration test was based on the methodology of Medeiros [45] and is outlined in Figure 3. The migration cells were assembled with PVC tubes, as this is a material resistant to aggressive media [42]. The two compartments, anodic and cathodic, were separated by a concrete sample with a thickness of 5 cm. Distilled water was placed in the anode compartment, and in the other, a solution with 1 M NaCl. A potential difference of 12 V was applied by an external voltage source, connected by electrodes with lengths of approximately 40 cm.

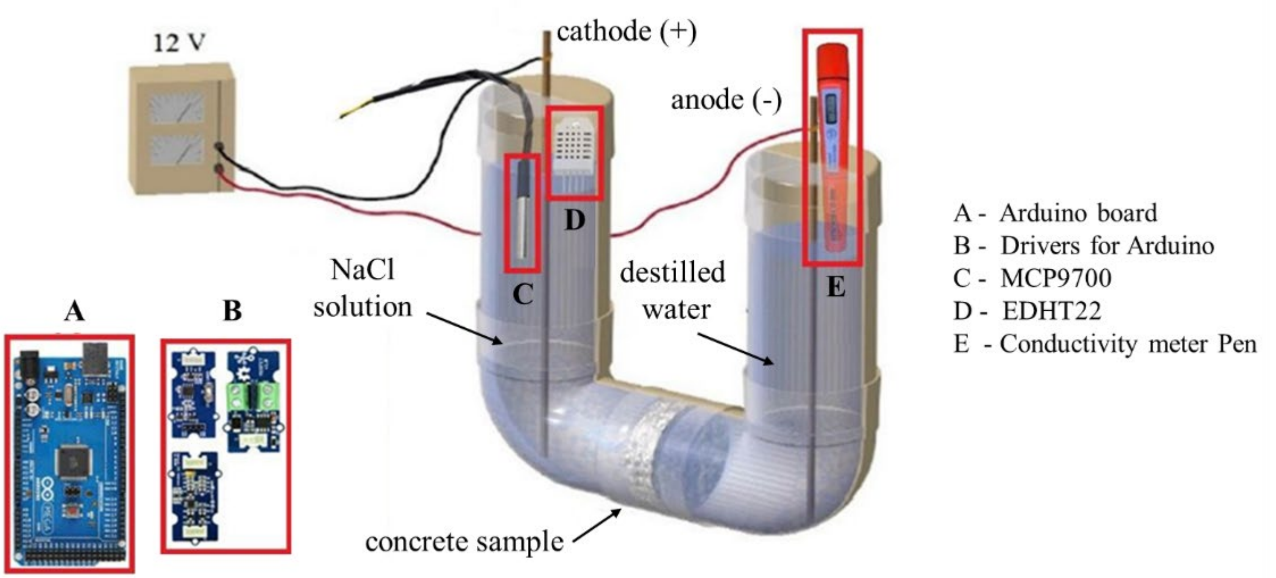

Figure 3. Scheme of chloride migration test adapted from Medeiros [45]

Like Medeiros [45], in addition to the concentration of chloride in the anode compartment, the temperature, electric current, conductivity and time necessary for the solutions to be chemically stabilized were also monitored. All data were collected by sensors and controlled by an Arduino board (A), which collects the data and transmits it to a memory card. Acting with the Arduino board (A), the drivers for Arduino (B) were: i) Current sensor, ii) Channel selector and iii) a digital device used to choose the channel.

The acquisition system selected the channel through digital outputs, and the SD card stored this data, which was made available in an Excel spreadsheet.

The electrical conductivity reading was performed using an Instrutherm model CD-880 Conductivity meter Pen (E). The internal temperature of the liquid was collected by the MCP 9700 sensor (C) and the DHT22 (D) sensor measured the humidity and temperature above the liquid level.

To make the correlation between chloride content and conductivity, a correlation curve was produced (Figure 4). The obtained R^2 was 0.9867, thus showing a strong correlation between conductivity and chloride concentration.

In this test, the peak current in mA and the concentration of chloride in the anode compartment—as a function of time (in seconds) were determined.

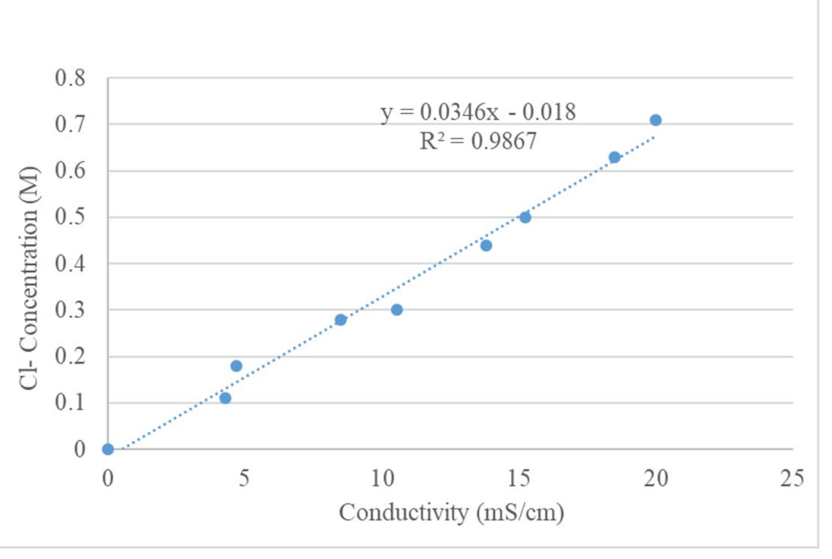

Figure 4. Calibration line between chloride concentration (M) and conductivity (mS /cm).

2.5 Results analysis

To carry out the statistical analysis of the mechanical characteristics of the concrete, some procedures were conducted. First, to verify whether the characteristics of the data met the assumptions of MANOVA (Multivariate Analysis of Variance), normality was assessed by the Shapiro-Wilk test, and homogeneity of variance by the Bartlett test. After verification and validation of the data, a MANOVA could be performed. This analysis was performed for the mechanical characteristics of the concrete, produced at 7, 28, 90, and 180 days after immersion in saline solution. Physical characteristics were also analyzed, including water absorption capacity by immersion and water absorption capacity by capillarity.

3 RESULTS AND DISCUSSIONS

3.1 Fresh concrete characteristics

Table 5 presents the results of the tests carried out on the concrete in its fresh state. The use of superplasticizer additive ensured 65 mm consistency, defined as standard. It was observed that the reference concrete (T REF) presented a specific gravity that was greater than the other concretes, which can be explained by the specific mass of the natural coarse aggregate, shown in Table 1 to be greater than that of the recycled coarse aggregates.

Table 5. Fresh concrete characteristics.

Concrete	*Slump Test* (cm)	Specific mass (g/cm^3)
T REF	6.5	2.50
T 30 ARCO	6.5	2.44
T 30 ARCI	7.0	2.44
T 30 ARCI Treated	6.5	2.37

3.2 Mechanical properties

The mechanical properties that were evaluated for concrete in the hardened state were the resistance to axial compression and the modulus of elasticity. Figure 5 shows the results of resistance to axial compression, through which all concrete mixtures reached the proposed strength class of 30 MPa.

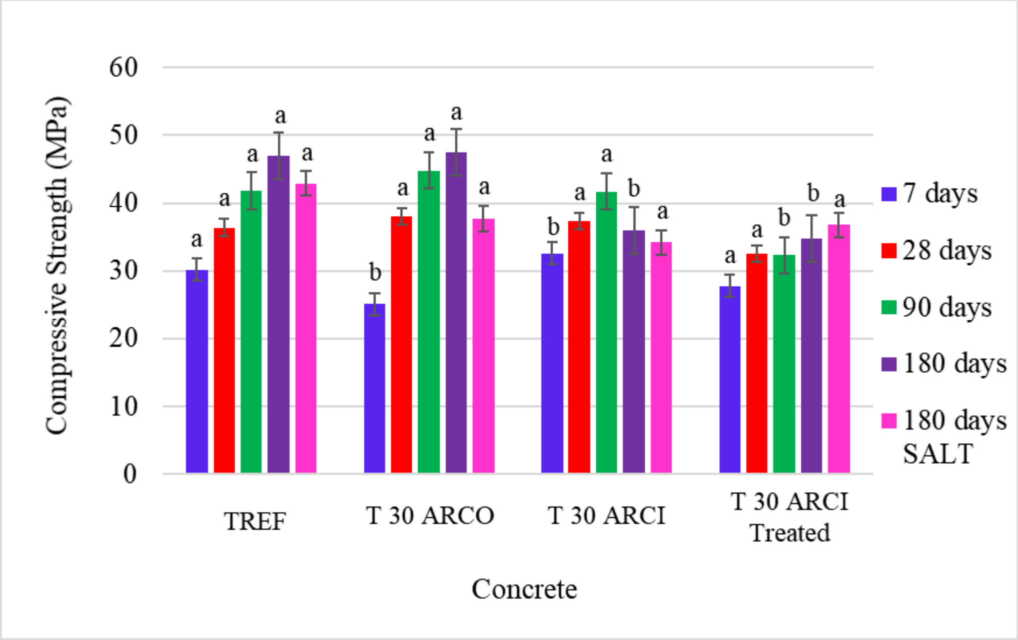

Figure 5. Results of resistance to axial compression.

At 28 days (post saline solution immersion), all concrete showed resistance to axial compression that were statistically similar to each other.

This behavior was not observed at 90 and 180 days. At 90 days, T 30 ARCO and T 30 ARCI showed similar behavior when compared to T REF, while T 30 ARCI Treated showed statistically different results and were thus inferior to the other concrete. At 180 days, T 30 ARCI showed a decrease in its resistance to axial compression, becoming statistically similar to T 30 ARCI Treated, whereas T REF and T 30 ARCO presented results that were statistically similar to each other.

After 180 days of saline immersion, all concrete showed similar behavior. It is worth mentioning that when the results of the resistance to axial compression after immersion in saline solution were compared with the results at 180 days, there were decreases in the results of resistance for T REF, T 30 ARCO and T 30 ARCI, a behavior that was not observed for T 30 ARCI Treated. Silva and Andrade [30] obtained loss in axial compression resistance for concretes that used only recycled aggregate when compared to the reference concrete; this behavior was improved by the addition of fly ash.

On the other hand, by crushing 80 MPa strength class concrete, Afroughsabet et al. [4] produced recycled aggregates when used in the production of concrete with a 50% substitution content, and showed results superior to the reference concrete. When this substitution content reached 100%, the results of resistance to axial compression obtained were similar to that of the reference concrete. The authors also point out that when the recycled aggregates produced started from a 40 MPa concrete, the same behavior was not observed, and the results of resistance to axial compression were lower than the reference concrete. In this study, the replacement of 30% of the natural aggregate with the recycled concrete aggregate (ARCO) produced from concrete with resistance between C30 and C50, did not affect the resistance to axial compression when compared to T REF. That is, the quality of the recycled aggregate can be linked to the type of crushed material.

Figure 6 shows the results obtained for the modulus of elasticity test. The concrete produced with ARCI showed a statistically inferior result when compared to the others at 28 days, approximately 17% lower than the T REF. However, at 90 and 180 days, this behavior was not observed. At these stages (90 and 180 days) all concrete variants showed statistically similar behavior. Only for the T 30 ARCI line could a decrease in the elasticity modulus of the concrete be observed after 180 days of immersion in saline solution.

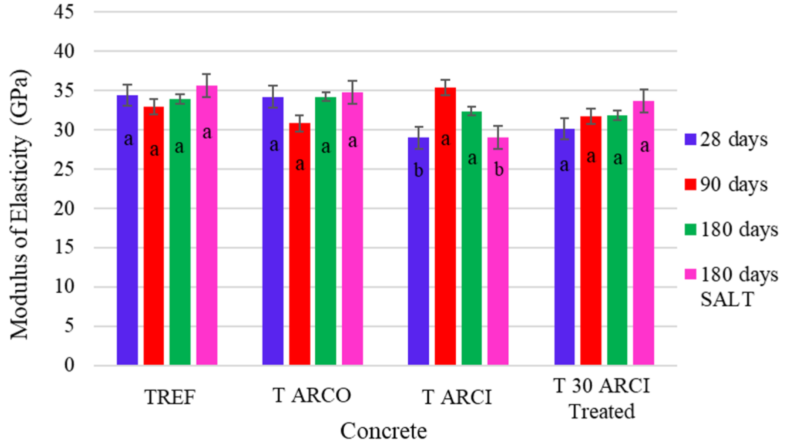

Figure 6. Results of modulus of elasticity.

McGinnis et al. [2] pointed out a 26.4% reduction in the modulus of elasticity for concrete produced with 50% recycled aggregate, and a 34.4% decrease for concretes with a 100% substitution content. The reduction observed by McGinnis et al. [2] was higher than that obtained in this study, but this is justified by the fact that the researchers used a higher percentage of substitution of the natural aggregate than that used in this research.

3.3 Indirect durability measurements tests

3.3.1 Water absorption capacity by immersion and capillarity

The main factor that affects the durability of concrete is the entry of gases and liquids into its interior. The ease of entry of deteriorating agents is linked to the useful life of the structure.

Figure 7 shows the water absorption capacity for all of the immersed concrete variants. It is observed that, at 28 days, the T REF showed a water absorption capacity by immersion higher than the concrete variants with recycled aggregate, and this behavior was not maintained at the later stages, when the water absorption capacity by immersion was higher for mixtures with recycled aggregates. It should be noted that the maximum absorption capacity obtained was 6%.

After 180 days of saline immersion, the concrete variants produced with recycled aggregate had a lower water absorption capacity than T REF. This behavior can be explained by the pore structure of the concrete, that is, the concrete variants produced with recycled aggregate are more porous, and when immersed in saline, they tend to absorb sodium chloride more easily and consequently, it solidifies and crystallizes inside the pores, filling voids and thus decreasing its water absorption capacity by immersion.

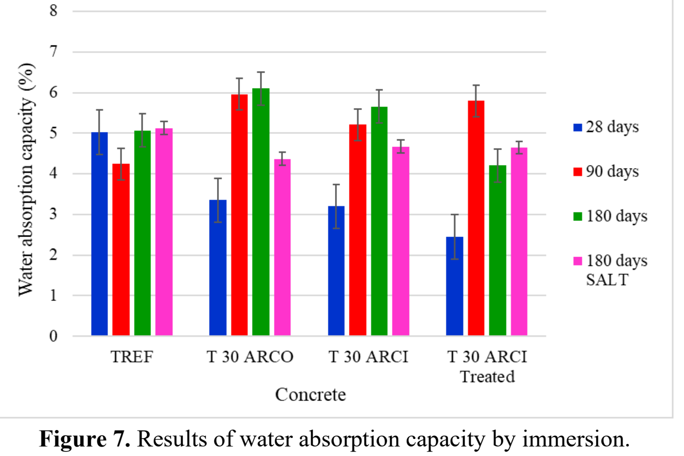

Figure 7. Results of water absorption capacity by immersion.

In this study it was observed that the water absorption capacities by immersion of the concrete variants using recycled aggregate were higher than those obtained for the reference concrete (TREF), consistent with the results of Troian [47].

Cenalmor et al. [19] pointed out that the substitution of natural aggregate for recycled aggregate should not be higher than 20%, since with this substitution content, the authors obtained a water absorption capacity by immersion of around 5.7%, a value close to the Instrucción Española del Hormigón Estructural (EHE-08). The water absorption capacity values for the present study reached a maximum value of 6%.

The results of water absorption by capillarity are shown in Figure 8, where the capillarity coefficient of 72 hours of each mix was observed at each test stage.

At the 28 days stage, the capacity of water absorption by capillarity of the T REF was greater than for the other variants. After this stage, the mixtures produced with recycled aggregate presented greater capillarity coefficients.

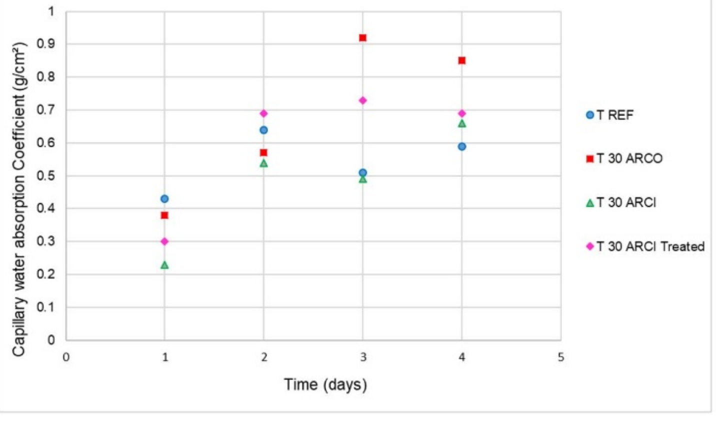

Figure 8. Results of capillary water absorption capacity.

3.3.2 Permeaability

The results of the air permeability test, performed with the Porosiscope equipment, are shown in Table 6.

In Table 6, it is possible to observe that even the concrete using natural aggregate (T REF) did not present a good classification regarding its permeability to air, being classified as moderate and presenting results between 30 and 100 s.

Table 6. Results of permeability test by the Porosiscope equipment.

	Permeability	
Concrete	Time (s)	Classification
T REF	55.5	Moderate
T 30 ARCO	21.5	Poor
T 30 ARCI	17.25	Poor
T 30 ARCI Treated	17.25	Poor

The results obtained in the present study are inferior to those obtained by Cenalmor et al. [19]. All other concrete mixes produced in the present study were classified as poor in terms of air permeability. However, the a/c ratio, used by Cenalmor et al. [19] (0.5), was lower than that used in this study (0.6). It is observed that the reference concrete (T REF) presented a better result than the mixtures using recycled aggregate, since it took the air approximately three times longer to flow through the pores compared to the mixtures produced with recycled aggregate.

When comparing the mixtures with recycled aggregate to each other, the T 30 ARCO showed the best behavior.

3.3.3 Determination of carbonation depth

Table 7 presents the results obtained from the carbonation test, with the results of carbonated area and average thickness of carbonation, the photographs of the specimen after the spraying of phenolphthalein, and the image drawn in the AutoCAD® program.

It can be observed that the carbonated area of the mixture produced with recycled concrete aggregate (T 30 ARCO) presented a better result, that is, it suffered less aggression than the mixture produced with recycled aggregate (T 30 ARCI and T 30 ARCI Treated). As expected, the reference concrete (T REF) obtained the smallest carbonated area.

In turn, when comparing T 30 ARCI and T 30 ARCI Treated, it is notable that for this determination, the treatment was effective.

Silva and Andrade [30] and Pedro et al. [31] note that concrete using recycled aggregates have a high porosity when compared to concretes that use natural aggregate, and that this characteristic has a significant influence on the carbonation process. According to the authors, at later stages, the depth of carbonation obtained was greater.

Pedro et al. [31] presented results of carbonation depth at 91 days. For concrete using natural aggregate, the depth reached 5.0 mm, while concrete using recycled aggregate had values between 6.2 to 10.6 mm. It is worth mentioning that the determination of the carbonation depth was defined by the authors as being measured after 91 days in a carbonation chamber, with a constant temperature of 20 ºC and carbon dioxide concentration of 5 +/- 1%. They [23] also found that even though the carbonation depths were greater for concrete variants produced with recycled aggregate, the differences in depth for the natural aggregate concrete variants were between 3 and 6 mm. In this work, the carbonation thickness of all mixtures did not exceed 6 mm, confirming the results obtained by NBR 7211 [23].

Table 7. Results of carbonation test.

Sample	Sample Photo	Image Analysis	Carbonated area (cm^2)	e (mm)
T REF		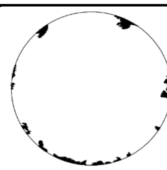	1.96	1.27
T 30 ARCO		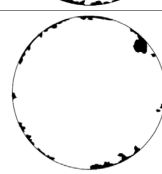	2.57	1.65
T 30 ARCI		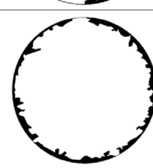	8.02	5.24
T 30 ARCI Treated		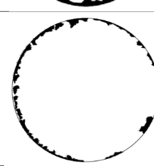	4.83	3.12

e: average carbonation thickness.

3.3.4 Determination of chloride penetration

The results of the chloride penetration test (area, thickness of penetration, photographs taken after spraying silver nitrate solution and the drawn images) are shown in Table 8.

In this case, T 30 ARCO and T 30 ARCI had an ion penetration area smaller than the T REF. It is noted that in neither case did the penetration thickness exceed 15 mm. It is worth mentioning that the concrete variants produced for this work meet the aggressiveness classes 1 and 2 of the NBR 12655 standard [48]. For these two classes of aggressiveness, NBR 6118 [12] defines respective minimum coverages of 20 and 25 mm for slabs, 25 and 30 mm for beam / columns, and 30 mm for structural elements in contact with the ground. In addition to the minimum coverage, the minimum coverage plus the execution tolerance, which must be at least another 10 mm, must also be added in the construction of the structure.

Table 8. Results of chloride penetration test.

Sample	Sample Photo	Image Analysis	Carbonated Area (cm^2)	e (mm)
T REF			17.60	11.89
T 30 ARCO			10.89	7.19
T 30 ARCI	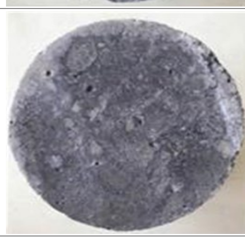		15.24	10.22
T 30 ARCI Treated	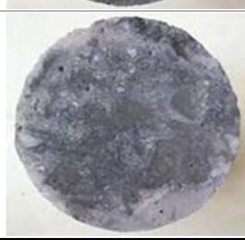	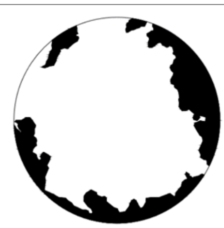	18.76	12.76

e: average carbonation thickness.

Thus, until the end of the 180-day period, none of the concrete variants had a greater carbonation thickness and chloride penetration thickness than the minimum coverage required by the Brazilian standard.

3.3.5 Chloride migration

Figure 9 shows the monitoring of electric current during the chloride migration test. It was observed that the behavior of the electric current in the chloride migration test was similar for all concrete variants. Initially, the current measured in the test was zero mA and gradually increased until it reached its peak, before then decreasing until the value reached was practically zero mA. Medeiros [45] found that the greater the peak of the current, the greater the ease with which the electrical current was able to travel through the concrete, meaning that the material has greater permeability. In this case, the highest peak current was presented by the T 30 ARCI, followed by the treated T 30 ARCI. As for the air permeability, carbonation and chloride penetration tests, the T 30 ARCO presented the best behavior, that is, the lowest current peak, even lower than the reference (T REF).

In addition to monitoring the electric current, this test also made it possible to calculate the concentration of chloride in the anode compartment, the results of which are shown in Figure 10. The concentration of chlorides showed a result similar to that obtained at peak current. The lowest concentration of chloride was obtained by T 30 ARCO, followed by T REF. The concrete variants with recycled aggregate type ARCI and ARCI Treated obtained similar and higher results, indicating greater permeability to the passage of ions. For the tests of indirect measurement of durability, it is notable that the T 30 ARCO variant presented the best behavior when compared to the other concrete variants that used recycled aggregates. In several tests, this behavior was even better than the reference concrete (T REF).

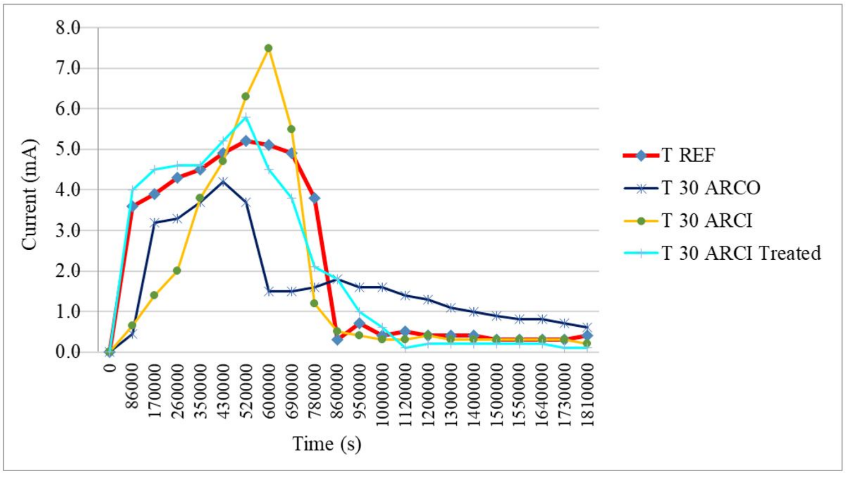

Figure 9. Monitoring of electrical current during chloride migration test.

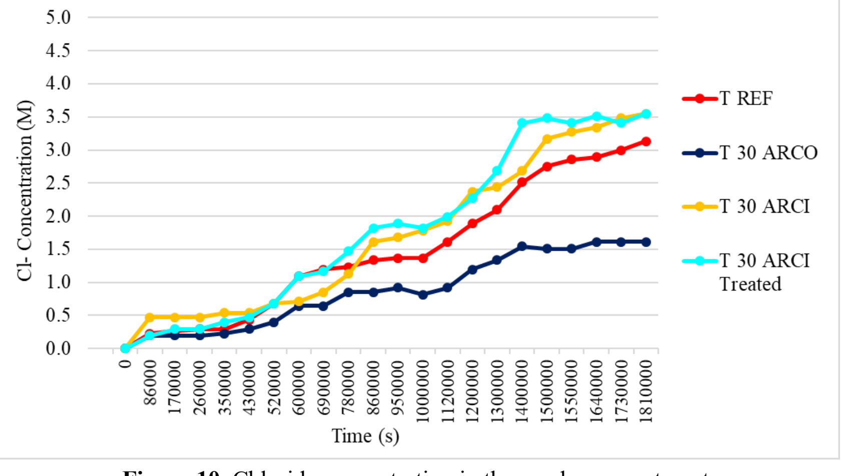

Figure 10. Chloride concentration in the anode compartment.

4 CONCLUSIONS

In view of the materials and test conditions of the present study, it can be concluded that:

- The use of coarse recycled concrete aggregate (ARCO) up to a content of 30% to replace natural aggregate does not change the resistance to axial compression.
- There is a decrease in the resistance to axial compression when using ARCI and ARCI-treated aggregates; however, all concrete types reached the desired strength class C30.
- The elastic modulus of all variants showed statistically equal values for the most advanced stages, from 90 and 180 days.
- Regarding the tests of indirect durability measurement, it is notable that the results obtained by the mix produced with recycled concrete aggregate (T 30 ARCO) presented better behavior in the face of attacks, including, in some cases, where the behavior of the T 30 ARCO was better than T REF.
- Regarding the migration of chloride ions, the T 30 ARCO concrete showed a lower index, showing better performance than the T REF.

- There was no improvement in the characteristics of the concrete produced with the treated cementitious aggregate (T 30 ARCI Treated) when compared to the concrete produced with cementitious aggregate (T 30 ARCI), indicating that this treatment is not viable.

Although the concrete produced with recycled concrete aggregate (ARCO) stood out over the others, this does not indicate that the use of cement aggregate (ARCI) is impracticable, and that this recycled aggregate does not guarantee adequate characteristics for concrete with structural functionality.

ACKNOWLEDGEMENTS

This work was carried out with the support of the Coordination for the Improvement of Higher Education Personnel—Brazil—CAPES and São Paulo Research Foundation (FAPESP).

REFERENCES

[1] World Business Council for Sustainable Development, *The Cement Sustainability Initiative*, 2009. Available: https://www.wbcsdcement.org/pdf/CSI-RecyclingConcrete-Summary.pdf (accessed Feb. 2, 2017).

[2] M. J. McGinnis, M. Davis, A. de la Rosa, B. D. Weldon, and Y. C. Kurama, "Strength and stiffness of concrete with recycled concrete aggregates," *Constr. Build. Mater.*, vol. 154, no. 15, pp. 258–269, Nov 2017, http://dx.doi.org/10.1016/j.conbuildmat.2017.07.015.

[3] M. Omrane, S. Kenai, E.-H. Kadri, and A. Aït-Mokhtar, "Performance and durability of self-compacting concrete using recycled concrete aggregates and natural pozzolan," *J. Clean. Prod.*, vol. 165, pp. 415–430, Nov 2017, http://dx.doi.org/10.1016/j.jclepro.2017.07.139.

[4] V. Afroughsabet, L. Biolzi, and T. Ozbakkaloglu, "Influence of double-hooked-end steel fibers and slag on mechanical and durability properties of high performance recycled aggregate concrete," *Compos. Struct.*, vol. 181, pp. 273–284, Dec 2017, http://dx.doi.org/10.1016/j.compstruct.2017.08.086.

[5] L. D. Poulikakos et al., "Harvesting the unexplored potential of European waste materials for road construction," *Resour. Conserv. Recycling*, vol. 116, pp. 32–44, Jan 2017, http://dx.doi.org/10.1016/j.resconrec.2016.09.008.

[6] São Paulo. Secretária do Meio Ambiente, *Plano de Resíduos Sólidos do Estado de São Paulo*. São Paulo: SMA, 2015. [Online]. Available: http://www.cetesb.sp.gov.br

[7] P. Gonçalves and J. Brito, "Recycled Aggregate Concrete (RAC) – comparative analysis of existing specifications," *Mag. Concr. Res.*, vol. 62, no. 5, pp. 339–346, May 2010, http://dx.doi.org/10.1680/macr.2008.62.5.339.

[8] Associação Brasileira de Normas Técnicas, *Agregados Reciclados de Resíduos Sólidos da Construção Civil – Utilização em Pavimentação e Preparo de Concreto Sem Função Estrutural – Requisitos*, ABNT NBR 15116, 2004.

[9] P. M. Mehta and P. M. J. Monteiro, *Concreto: Estrutura, Propriedades e Materiais*, 2nd ed. São Paulo: PINI, 2008.

[10] D. H. Nguyen, M. Boutouil, N. Sebaibi, F. Baraud, and L. Leleyter, "Durability of pervious concrete using crushed seashells," *Constr. Build. Mater.*, vol. 135, pp. 137–150, Mar 2017, http://dx.doi.org/10.1016/j.conbuildmat.2016.12.219.

[11] R. V. Silva and J. Brito, "Use of recycled aggregates from construction and demolition wastes in the production of structural concrete," in *EURO ELECS*, 2015, pp. 1-15.

[12] Associação Brasileira de Normas Técnicas, *Projeto de Estruturas de Concreto – Procedimento*, ABNT NBR 6118, 2014.

[13] International Organization for Standardization, *General Principles on the Design of Structures for Durability*, ISO 13.823, 2008.

[14] J. P. Ollivier and A. Vichot, *Durabilidade do Concreto – Bases Científicas para a Formulação de Concretos Duráveis de Acordo com o Ambiente*. São Paulo: Ed. Jean-Pierre Olivvier e Angélique Vichot, 2014.

[15] D. Zhang and Y. Shao, "Effect of early carbonatation curing on chloride penetration and weathering carbonation in concrete," *Constr. Build. Mater.*, vol. 123, pp. 516–526, Oct 2016, http://dx.doi.org/10.1016/j.conbuildmat.2016.07.041.

[16] T. C. Santos, "Otimização do método Cembureau de ensaio de permeabilidade ao gás para materiais cimentícios," Ph.D. dissertation, Prog. Pós-grad. Eng. Apl. Sust., Inst. Fed. Ed., Ciênc. Tecnol. Goiano, Rio Verde, 2019.

[17] G. F. Rizzo, "Durability of concretes with recycled aggregates," Ph.D. dissertation, Prog. Pós-grad. Sist. Infraestrut. Urb., Pontif. Univ. Catol. Campinas, Campinas, 2018.

[18] C. Medina, W. Zhu, T. Howind, M. I. Sánchez de Rojas, and M. Frías, "Influence of mixed recycled aggregate on the physical e mechanical properties of recycled concrete," *J. Clean. Prod.*, vol. 68, pp. 216–225, Apr 2014, http://dx.doi.org/10.1016/j.jclepro.2014.01.002.

[19] M. M. Cenalmor, D. Estévez, and M. C. Gonzalez, "Estudio de la durabilidad em hormigones con áridos reciclados procedentes de piezas pré-fabricadas," in *PATORREB*, 2015, pp. 1-15.

[20] C.-C. Fan, R. Huang, H. Hwang, and S.-J. Chao, "Properties of concrete incorporating fine recycled aggregates from crushed concrete wastes," *Constr. Build. Mater.*, vol. 112, pp. 708–715, Jun 2016, http://dx.doi.org/10.1016/j.conbuildmat.2016.02.154.

[21] A. Sucic and A. Lotfy, "Effect of new paste volume on performance of structural concrete using coarse and granular recycled concrete aggregate of controlled quality," *Constr. Build. Mater.*, vol. 108, pp. 119–128, Apr 2016, http://dx.doi.org/10.1016/j.conbuildmat.2015.10.064.

[22] M. Perea and A. Alvarado "Propriedades mecânicas en concretos fabricados con agregados gruesos reciclados tratados com lechadas," in *CONPAT*, 2015, pp. 1-14.

[23] Associação Brasileira de Normas Técnicas, *Agregados para Concreto – Especificação*, ABNT NBR 7211, 2009.

[24] Associação Brasileira de Normas Técnicas, *Agregado Miúdo – Determinação da Massa Específica e Massa Específica Aparente*, ABNT NBR NM 52, 2009.

[25] Associação Brasileira de Normas Técnicas, *Agregado Graúdo – Determinação da Massa Específica, Massa Específica Aparente e Absorção de Água*, ABNT NBR NM 53, 2009.

[26] Associação Brasileira de Normas Técnicas, *Agregado Miúdo – Determinação da Absorção de Água*, ABNT NBR NM 30, 2001.

[27] Associação Brasileira de Normas Técnicas, *Agregados – Determinação da Resistência ao Esmagamento de Agregados Graúdos*, ABNT NBR 9938, 1987.

[28] Associação Brasileira de Normas Técnicas, *Agregados – Determinação da Composição Granulométrica*, ABNT NBR NM 248, 2003.

[29] P. Helene and P. Terzian, *Manual de Dosagem e Controle do Concreto*. São Paulo: Pini, 1992.

[30] S. R. Silva and J. J. O. Andrade, "Investigation of mechanical properties and carbonation of concretes with construction and demolition waste and fly ash," *Constr. Build. Mater.*, vol. 153, pp. 704–715, Oct 2017, http://dx.doi.org/10.1016/j.conbuildmat.2017.07.143.

[31] D. Pedro, J. Brito, and L. Evangelista, "Structural concrete with simultaneous incorporation of fine and coarse recycled concrete aggregates: mechanical, durability and long-term properties," *Constr. Build. Mater.*, vol. 154, pp. 294–309, Nov 2017, http://dx.doi.org/10.1016/j.conbuildmat.2017.07.215.

[32] D. Xuan, B. Zhan, and C. S. Poon, "Durability of recycldes aggregate concrete prepared with carbonated recycled concrete aggregates," *Cement Concr. Compos.*, vol. 84, pp. 214–221, Nov 2017, http://dx.doi.org/10.1016/j.cemconcomp.2017.09.015.

[33] Associação Brasileira de Normas Técnicas, *Concreto – Determinação da Consistência pelo Abatimento do Tronco de Cone*, ABNT NBR NM 67, 1998.

[34] Associação Brasileira de Normas Técnicas, *Concreto Fresco – Determinação da Massa Específica, do Rendimento e do Teor de Ar pelo Método Gravimétrico*, ABNT NBR 9833, 2009.

[35] Associação Brasileira de Normas Técnicas, *Concreto – Ensaio de Compressão de Corpos de Prova Cilíndricos*, ABNT NBR 5739, 2007.

[36] Associação Brasileira de Normas Técnicas, *Concreto – Determinação do Módulo Estático de Elasticidade à Compressão*, ABNT NBR 8522, 2008.

[37] Associação Brasileira de Normas Técnicas, *Argamassa e Concreto Endurecidos – Determinação da Absorção de Água, Índice de Vazios e Massa Específica*, ABNT NBR 9778, 2005.

[38] Associação Brasileira de Normas Técnicas, *Argamassa e Concreto Endurecidos – Determinação da Absorção de Água por Capilaridade*, ABNT NBR 9779, 2012.

[39] C. B. França, "Avaliação de cloretos livres em concretos pelo método de aspersão de solução de nitrato de prata," Ph.D. dissertation, Univ. Catol. Pernambuco, Recife, 2011.

[40] M.-Y. Kim, E.-I. Yang, and S.-T. Yi, "Application of the colorimetric method to chloride diffusion evaluation in concrete structures," *Constr. Build. Mater.*, vol. 41, pp. 239–245, Apr 2013, http://dx.doi.org/10.1016/j.conbuildmat.2012.11.084.

[41] L. V. Real, D. R. B. Oliveira, T. Soares, and M. H. F. Medeiros, "Método colorimétrico por aspersão de nitrato de prata para avaliação da penetração de cloretos em concreto: estado da arte," *Rev. ALCONPAT*, vol. 5, no. 2, pp. 149–159, May 2015, http://dx.doi.org/10.21041/ra.v5i2.84.

[42] American Society for Testing and Materials, *Porosiscope™ Determines Air and Water Permeability in Concrete Both At and Below the Surface*, 2020. [Online]. Available: http://www.ndtjames.com/Porosiscope-p/c-p.htm

[43] S. Valls and E. Vàzquez, "Accelerated carbonatation of sewage sluge-cementsand mortars and its environmental impact," *Cement Concr. Res.*, vol. 31, no. 9, pp. 1271–1276, Sep 2001, http://dx.doi.org/10.1016/S0008-8846(01)00573-7.

[44] J. M. Gandía-Romero et al., "Potentiometric thick-film sensor for measuring the pH of concrete," *Cement Concr. Compos.*, vol. 68, pp. 66–76, Apr 2016, http://dx.doi.org/10.1016/j.cemconcomp.2016.02.006.

[45] R. A. Medeiros Jr., "Estudo da resistividade do concreto para proposta de modelagem de vida útil – corrosão das armaduras devido a penetração de cloreto," Ph.D. dissertation, Inst. Tecnol. Aeronáut., São José dos Campos, 2011.

[46] American Society for Testing and Materials, *Standard Test Method for Electrical Indication of Concrete Ability to Resist Chloride Ion Penetration*, ASTM C 1202-05, 2005.

[47] A. Troian, "Avaliação da durabilidade de concretos produzidos com agregado reciclado de concreto frente à penetração de cloreto," M.S. thesis, Univ. Vale do Rio dos Sinos, São Leopoldo, 2010.

[48] Associação Brasileira de Normas Técnicas, *Concreto de Cimento Portland – Preparo, Controle, Recebimento e Aceitação – Procedimento*, ABNT NBR 12655, 2015.

Author contributions: LLP: conceptualization, funding acquisition, supervision; GRF: writing; conceptualization, data curation; AEPGAJand PSPF: formal analysis, methodology.

Editors: José Luiz Antunes de Oliveira e Sousa, Guilherme Aris Parsekian.

IBRACON Structures and Materials Journal
Revista IBRACON de Estruturas e Materiais
ISSN 1983-4195 ismj.org

ORIGINAL ARTICLE

Numerical analysis of reinforced concrete shear walls with rectangular cross section

Análise numérica de pilares-parede de concreto armado com seção retangular

Maurício Castelo Branco de Noronha Campos[a]
Paulo Marcelo Vieira Ribeiro[b]
Romilde Almeida de Oliveira[c]

[a]Universidade Estadual do Piauí – UESPI, Centro de Tecnologia e Urbanismo, Teresina, Piauí, Brasil
[b]Universidade Federal de Pernambuco – UFPE, Centro de Tecnologia e Geociências, Recife, PE, Brasil
[c]Universidade Católica de Pernambuco – UNICAP, Centro de Ciências e Tecnologia, Recife, PE, Brasil

Received 03 April 2019
Accepted 12 May 2020

Abstract: This study addresses a numerical analysis of reinforced concrete columns in which the lengths are significantly larger than their widths with a rectangular cross section. Numerical simulations of 1,440 cases were performed, each case simulated with the single bar model, isolated bar model and mesh model, in addition, 3D model simulations were carried out. For the validation of 3D models and bar models, comparisons were made between the numerical simulation e experimental results of 24 reinforced concrete columns. Second order effects were analyzed on the vertical moment at the edge of the columns in which the lengths are significantly larger than the widths (localized second-order effects) and also the values of the horizontal moments along the cross sectional length in the mesh model. Influences of the main variables were observed influencing the behavior of the columns in which the lengths are significantly larger than their widths: the ratio between the cross sectional dimensions, the slenderness and the stresses (normal stress and bending moment around the axis of greatest inertia).

Keywords: shear walls, numerical analysis, nonlinear analysis, localized second-order effects.

Resumo: Neste trabalho foi feita uma análise numérica de pilares-parede de concreto armado com seção transversal retangular. Foram feitas simulações numéricas de 1.440 casos, onde cada caso foi simulado com o modelo de barra única, com o modelo de barras isoladas e com o modelo de malha, além disso, foram feitas simulações em modelos 3D. Para a validação dos modelos 3D e modelos de barra foram feitas comparações entre as simulações e resultados experimentais de 24 pilares de concreto armado. Foram analisados os efeitos de segunda ordem no momento vertical na extremidade do pilar-parede (efeitos localizados de segunda ordem) e também os valores dos momentos horizontais ao longo do comprimento da seção transversal no modelo com malha. Após as simulações numéricas foram feitas análises dos efeitos de segunda ordem no momento fletor ao longo da altura dos pilares-parede e dos momentos fletores na direção do comprimento da seção, observando as influências das principais variáveis que determinam o comportamento dos pilares-parede a relação entre as dimensões da seção transversal, a esbelteza e os esforços solicitantes (esforço normal e momento fletor em torno do eixo de maior inércia).

Palavras-chave: pilar-parede, análise numérica, análise não linear, efeitos localizados de segunda ordem.

How to cite: M. C. B. N. Campos, P. M. V. Ribeiro, and R. A. Oliveira, "Numerical analysis of reinforced concrete shear walls with rectangular cross section," *Rev. IBRACON Estrut. Mater*., vol. 13, no. 6, e13614, 2020, https://doi.org/10.1590/S1983-41952020000600014

INTRODUCTION

Shear walls are structural elements in which the cross sections are normally rectangular or consisting of rectangles where one of the dimensions is larger than the other, resulting in a column with an open or shut section with a slender wall. In accordance with ABNT NBR 6118:2014 [1], columns with a larger dimension of the cross section five times

Corresponding author: Maurício Castelo Branco de Noronha Campos. E-mail: mcbncampos@gmail.com
Financial support: None.
Conflict of interest: Nothing to declare.

more than the smaller dimension (b>5h) are called shear walls. Cross sections of shear walls can be single, rectangular, or consisting of two or more rectangles, having as a result sections in the shape of C, T, L and H, with high axial rigidity and high bending strength.

Similar to ABNT NBR 6118:2014 [1], the majority of international standards (for example, ACI-318 [2] and MC10 [3]) classify shear walls only according to the geometry as a result of the ratio between the sizes of the cross section, without considering the importance of the different effects from the existing demands.

Normally, shear walls act as bracing structures of the building and are placed in staircases and elevator shafts of tall buildings. They withstand both horizontal (due to wind or earthquakes) and gravitational loads.

According to Campos [4], the three key points to be observed when analyzing and sizing shear walls are: first, the distribution of the overall horizontal forces on the structural elements comprising the building; secondly, how these overall forces are absorbed by the cross section, and lastly, the possibility of localized effects.

Reinforced concrete shear walls with slender wall cross sections, when undergoing mainly compressive strengths due to the bending moment around the axis of greater inertia, are subject not only to localized effects along the stretch between cross bracing, but to concentrated effects at the ends of their cross section. These effects are termed by ABNT NBR 6118:2014 [1] as localized second order effects, see Figure 1.

The problem of buckling in concrete cross sections is more frequent now, mainly due to evolution of concrete technology, which has successfully produced stronger materials, resulting in cross sections with very high slenderness, which was not common in the shear walls of older buildings, when the strength of concrete used was not so high and, consequently, the cross sections were thicker, and therefore much more robust than those used today.

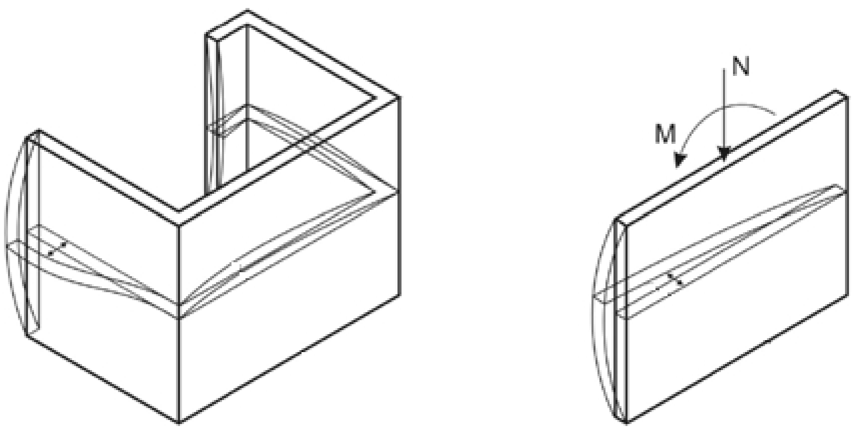

Figure 1. Localized second order effects (ABNT NBR 6118:2014 [1])

According to Wallace and Moehle [5], because of the significant progress in construction and design practice over the last 30 years and in order to optimize savings and safety, engineers made several modifications to the shear wall design boundaries. These modifications resulted in slimmer profiles undergoing stricter requirements that were confirmed in most laboratory tests or field experiments.

Failure due to buckling was observed in some laboratory tests (e.g., Thomsen and Wallace [6]. Detailed surveys carried out as part of the ATC-94, apud Wallace and Moehle [5], indicate that overall buckling of the wall was not caused by the shift in reinforcement (as had been initially suspected based on earlier studies), but instead, was a result of lateral instability of previously crushed edges.

Parra and Moehle [7] found two buckling mechanisms in the shear walls. The first occurs after the end of the shear wall had undergone a tensile plastic deformation that causes fissuring and, consequently, reduced rigidity. The second buckling mechanism begins with the detachment of the concrete from the reinforcement cover, resulting in a relatively slender core that tends to buckle. They conclude that the buckling mechanism is a form of secondary failure, which occurs after the reduction in rigidity of the end of the shear wall.

According to Wight and MacGregor [8], the main factors to be considered in the design of structural walls are the following: the structural function of the wall in relation to the rest of the structure, the wall may be supported and clamped to the structure, or the wall may act as a support and bracing for the rest of the structure; the types of load that the wall withstands; and the quantity and positioning of reinforcement in the cross section of the wall.

Based on the 2003 version, ABNT NBR 6118 implemented an item (15.9) specifically addressing the sizing of shear walls. In this item, ABNT NBR 6118:2014 [1] determines that: "*In order for shear walls to be able to be included as linear elements in the resistant assembly of the structure, it should be guaranteed that their cross section keeps its shape by proper bracing on the different floors and that the local second order effects are duly assessed*".

The local second order effects in shear walls must be analyzed in the same way as the conventional columns (b≤5h) and the localized second order effects may be considered according to an approximate process in which the shear wall is broken down into vertical strips that must be analyzed as separate columns. This approximate process of ABNT NBR 6118 was criticized in the technical sector, mainly with regard to analyzing the strips as if they were separate columns, since it is a situation very different from reality.

Campos [4] states that another item that has created lively discussion in the technical field is the quantity of transverse reinforcement in shear walls required by ABNT NBR 6118 since the edition in 2003. This transverse reinforcement is designed to combat buckling of the longitudinal reinforcement rods and to withstand the forces of horizontal bending from the localized second order effects.

In other international standards, namely, for example, ACI-318 [2] and MC10 [3], there is no reference to the consideration of the localized second order effects in the sizing of shear walls. However, the Brazilian situation is quite different from the rest. One of the major differences between what happens abroad and in Brazil is the occurrence of earthquakes. In Brazil, the main horizontal loading acting on buildings comes from wind force, contrary to what occurs in other countries, where the horizontal loading of the wind is secondary and the main horizontal demand originates in seismic waves.

This difference in loadings is reflected in the applied forces and, consequently, in how the shear walls are treated. Table 1 shows the sizes of the cross sections and the values of the dimensionless normal force of the shear walls analyzed by Araújo [9], França and Kimura [10], Arnott [11], Sritharan et al. [12], where a huge difference is found in the values of the design dimensionless normal force (v_d).

Table 1. Sections Dimensions and dimensionless normal force

	b (cm)	h (cm)	b/h	v_d
Araújo [9]	360	20	18	0.88
França and Kimura [10]	300	20	15	0.68
Anott [11]	600	20	30	0.04
Sritharan et al. [12]	229	15	15	0.00

Figure 2 shows the horizontal shake map in different parts of the world. The range of colors varies from white to brown, where the white represents the regions with low shake values and the brown representing regions with peak shake values.

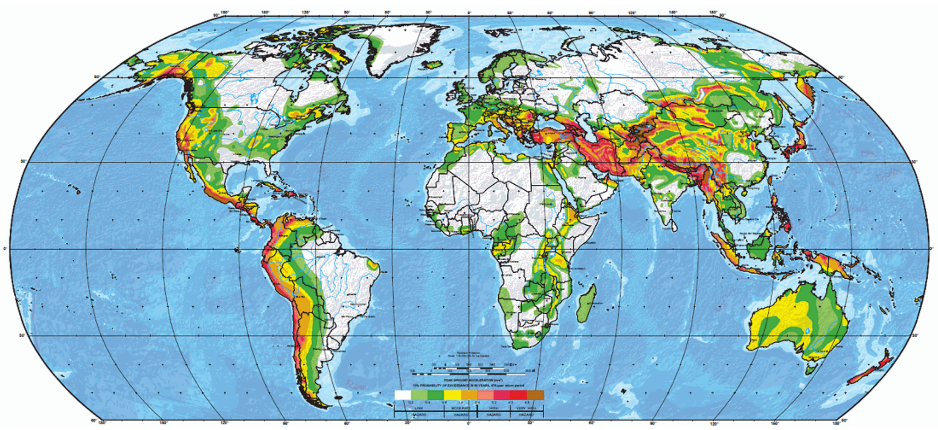

Figure 2. World horizontal shake map (http://www.maparelieve.com)

ABNT NBR 15421:2006 [13] sets the minimum requirements for checking the safety of the usual structures in civil construction in relation to the seismic actions and quantifying criteria of such actions and the strengths to be considered in the design of buildings' structures. To define the seismic actions to be considered in a design, this standard divides Brazil into five seismic zones (due to the design shake characteristic - g), as shown in Figure 3.

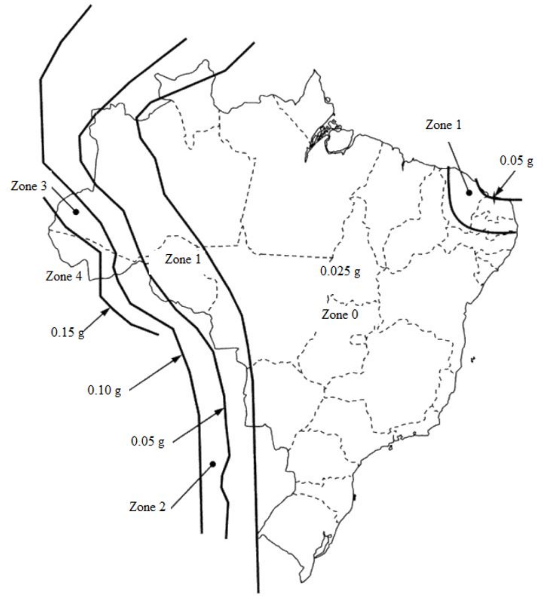

Figure 3. Characteristic horizontal shake map of Brazil (ABNT NBR 15421:2006)

Pursuant to item 7.3.1 of ABNT NBR 15421:2006 [13], for structures located in the seismic zone 0 there is no requirement of seismic resistance. Figure 3 shows that most Brazilian territory is within the seismic zone 0, especially the most densely populated regions and, therefore, with a higher quantity of buildings and where the highest are located, which are those that most suffer the effects of horizontal loads.

The region comprising the States of Ceará, Rio Grande do Norte and Paraíba has a relatively high population density (especially in the capitals) and are outside the seismic zone 0. This region is practically all within a seismic zone 1 where, and despite being necessary, low intensity seismic effects are considered since the value of the characteristic design shake is 0.025-0.05 (g). This is why the loading referring to seismic action in Brazil is not as important as in other countries.

1.1 Justification

Shear walls are structural elements very often used in bracing systems in modern buildings. The approximate process implemented by the ABNT NBR 6118:2003 [14] for sizing these elements has no similarity with what is presented by other standards that address this topic. The Brazilian situation is quite unique, however, especially concerning the loads that buildings will withstand throughout their working life, since very intense earthquakes are not to be found, at least in the more densely populated regions where there are the tallest buildings and more prone to suffer damages from horizontal loads. Therefore, we should really give a specific treatment to the shear walls in Brazilian buildings.

Although the approximate process implemented by ABNT NBR 6118:2003 [14] version has been widely criticized, it was kept in its 2014 version. The two key points that should be analyzed are the increase in the bending moment along the shear wall height, caused by the localized second order effects and the appearance of a bending moment along the length of the shear wall (largest dimension of the cross section).

Using this approximate process has resulted in a very high reinforcement rate (both longitudinal and transverse) in cases of shear walls with a rectangular section, and even in cases where the ratio between the largest and smallest size is close to the limit (b=5h).

A small sample will be presented here that could occur when sizing shear walls based on the recommendations of ABNT NBR 6118:2014 [1]. The data will be provided for eight buildings designed in the city of Teresina, Piauí State (PI). Table 2 shows some of the main characteristics of these buildings, namely the number of floors, total height, tower blueprint dimensions, slenderness (ratio between total height and smallest dimension on plan) and the existence or otherwise of a rigid core.

Table 2. Characteristics of buildings

Building	Nº Floors	Height (m)	Floor plan dimensions (m)		Slenderness		Rigid core
			Lx	Ly	H/Lx	H/Ly	
1	24	74.9	20.43	22.08	3.67	3.39	No
2	17	52.7	17.73	20.73	2.97	2.54	No
3	22	64.4	41.21	19.68	1.56	3.27	Yes
4	18	53.5	32.63	25.54	1.64	2.09	Yes
5	18	55.0	29.20	30.90	1.88	1.78	Yes
6	21	63.9	38.20	18.93	1.67	3.22	Yes
7	11	32.2	25.54	17.39	1.26	1.85	No
8	20	60.4	34.10	26.10	1.77	2.31	Yes

This is a fairly heterogeneous sample since, as can be seen from the above table, the number of floors varies from 11 to 24, total height from 32.2 to 74.9 meters and slenderness from 1.26 to 3.57.

Table 3 shows the characteristics of some columns of these buildings. It illustrates that the ratio between the largest and smallest size of the cross section is always equal to 5, which is the limit value between a conventional column and shear wall. This did not occur by chance, and became a design guideline whenever possible to prevent the use of sections in which a ratio between their dimensions is more than 5. Otherwise, it would be necessary to increase the quantity of reinforcement to comply with ABNT NBR 6118:2014 [1], since it recommends that in such cases the localized effects are considered and that the quantity of transverse reinforcement must be 25% or more of the longitudinal reinforcement (except in cases where a horizontal bending study has been undertaken).

Table 3. Characteristics of columns

Building	Column Nº	Transversion section	Longitudinal	Stirrup	
	Nº	section	reinforcement	Column	Shear wall
Jacarandá	P11	25x125	18 φ 25	Φ8 c/20	Φ8 c/5.7
	P15	25x125	18 φ 25	Φ8 c/20	Φ8 c/5.7
Jardim Fiesole	P2=P27	25x125	12 φ 25	Φ8 c/20	Φ8 c/8.5
	P5	20x100	8 φ 25	Φ8 c/20	Φ8 c/10
	P6=P7=P14	25x125	16 φ 25	Φ8 c/20	Φ8 c/6.4
	P18	30x150	28 φ 25	Φ8 c/20	Φ8 c/4.4
Chamonix	P2=P4=P25	30x150	26 φ 25	Φ8 c/20	Φ8 c/4.7
	P3=P26	30x150	38 φ 25	Φ8 c/20	Φ8 c/3.2
	P12	30x150	18 φ 25	Φ8 c/20	Φ8 c/6.8
Jardim Positano	P3=P23	30x150	32 φ 25	Φ8 c/20	Φ8 c/3.8
	P6	25x125	16 φ 12.5	Φ5 c/15	Φ5 c/10
	P7=P22	30x150	28 φ 25	Φ8 c/20	Φ8 c/3.8
	P8	20x100	22 φ 16	Φ5 c/19	Φ5 c/3.6
Savona Residence	P10=P13= P14=P18	30x150	18 φ 25	Φ8 c/20	Φ8 c/6.8
	P44=P68	25x125	16 φ 25	Φ8 c/20	Φ8 c/6.4
Maranhata	P9=P27	25x125	20 φ 25	Φ8 c/20	Φ8 c/5.1
	P13	30x150	18	Φ8 c/20	Φ8 c/3.4
	P16	25x125	20 φ 25	Φ8 c/20	Φ8 c/5.6
	P17	25x125	26 φ 25	Φ8 c/20	Φ8 c/4.7
	P20=P23	25x125	24 φ 25	Φ8 c/20	Φ8 c/4.3
	P22	25x125	16 φ 25	Φ8 c/20	Φ8 c/6.4

Table 3 also shows the longitudinal and transverse reinforcements obtained for sizing, considering a conventional column, in addition to the quantity of transverse reinforcement necessary to comply with ABNT NBR 6118:2014 [1] should the column be considered a shear wall and the relationship between these quantities as transverse reinforcement. This increase in transverse reinforcement was fairly high, varying from 2 to 6.2 times the necessary value for a conventional column, and without taking into account the localized effect that would probably result in an increase in longitudinal reinforcement and, consequently, in an even greater quantity of transverse reinforcement. This increase in reinforcement could result not only in a higher cost of the column but also its unfeasible implementation.

2 NUMERICAL SIMULATIONS

The first steps in performing a numerical simulation are to define the models to be used and to select the computer program. The main computer models used for numerical simulation of shear walls are three-dimensional models (solid elements), two-dimensional (plane stresses, plane deformations, shells), macro models and bar element models. In this study three-dimensional models were used as well as bar element models with a single bar (vertical) and bar element models consisting of a bar mesh (vertical and horizontal).

Two commercial computer programs were used, - MIDAS-FEA for numerical simulations with three-dimensional elements, and CAD-TQS for bar element models. It should be mentioned that it was only possible to use CAD-TQS by implementing some specific routines for this study, which are not available in the commercial version of the program. These routines were implemented by the courtesy of the TQS company technical team.

2.1 Single bar model

The models that use a single bar to represent a stretch of a column were used not only to simulate the entire section of the shear wall as if it were a single bar, but also to simulate isolated strips of shear walls obtained by using the approximate process in ABNT NBR 6118:2014 [1], each strip represented by an isolated bar. In this model each node has six degrees of freedom.

The geometric and physical nonlinearity were considered in models that use bar elements. The General Method was used in which the geometric nonlinearity was taken into account using the interactive P-δ process, through the load increment method. The total load was divided into 20 equal increments. The bars were divided into 12 equal parts and a finite element model was used to obtain the results. The physical nonlinearity was considered using the diagram M, N, 1/r, as described by Ribeiro [15].

The consideration of the physical nonlinearity was a point where it was necessary to request an adjustment to the mesh model available in CAD-TQS, since the drying rigidity obtained for the section by linearizing the diagram *M, N, 1/r* uses the design maximum moment value withstood by the section (M_{Rd}) and not the value of the design stress moment on the section (M_{Sd}). This is the procedure recommended by ABNT NBR 6118:2014 and can be adopted in designs, with no problem whatsoever, since it is conservative, but when using this procedure it may cause inconsistency in the results. This inconsistency was found in this study, which is why it was necessary to be adjusted in the CAD-TQS model.

2.2 Mesh model

This model consists of a mesh of horizontal and vertical bars. In it each vertical bar represents a strip of the shear wall obtained using the approximate process of ABNT NBR 6118:2014 [1]. Each vertical bar was divided into ten elements and their nodes were linked to the nodes of the adjacent strip by horizontal bars, to prevent a strip from being deformed independently of the others. As a result a point is eliminated, in which the approximate process of ABNT NBR 6118:2014 is widely criticized, perhaps the point most severely criticized of all.

In this model the geometric and physical linearity of the vertical bars are considered in the same way as in the single bar model and horizontal bars are considered elastic and linear with the characteristics of the gross concrete section, according to TQS [16].

2.3 Three-dimensional models

Three-dimensional models were made using the computer program MIDAS-FEA, in which the concrete was modeled using hexahedral solid elements, with eight nodes, and steel bars were modeled using the Line 3D element, in which the bar axis is defined and the program automatically converts the line into a solid element. To avoid problems when introducing loading, rigid blocks were created at the top and bottom of the columns and also modeled using hexahedral solid elements according to MIDAS [17].

The material used to represent the behavior of the concrete was Total Strain Crack, which describes the tensile and compressive behavior of a material with one stress-strain relationship. When the concrete undergoes tensile deformations the constituent ratio was defined using the Brittle function, which is a bilinear function whose diagram is represented in Figure 4a, where f_t is the concrete's tensile strength. In case of compressive deformation the constituent ratio was defined by the function of Thorenfeldt, which is a non-linear function whose diagram is represented in Figure 4b, where f_c is the concrete's compressive strength.

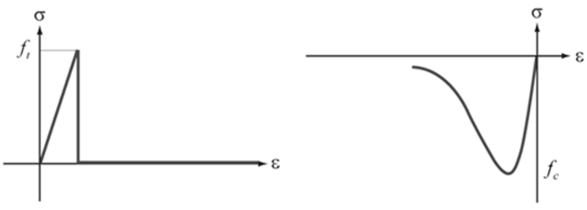

(a) Tensile (b) Compression

Figure 4. Stress-strain diagrams of concrete

The von Mises model was used to represent the behavior of the steel and rigid block, in which it is necessary to specify the elastic modulus, Poisson's ratio and the tensile elastic modulus, according to MIDAS [17].

2.4 Validation of computer models

To validate the computer models, results were used from the experimental work undertaken by Melo [18]. This study involved the experimental analysis of 24 reinforced concrete columns undergoing normal flexure and axial compression in the Structures Laboratory of the University of Brasília. The experimental program consists of three test series, with ten columns in Series 1, seven in Series 2 and seven in Series 3. The columns were identified as follows: PFN e-L, where:

PFN –column under flexure and axial compression normal stresses;

e – value of eccentricity toward least inertia, in millimeters;

L –length of column in meters.

Table 4 shows the characteristics of the tested columns. It is worth mentioning that the columns undergoing centered compression have the same name.

To validate the computer models, numerical simulations were made only in the cases where the section was actually submitted to the normal unsymmetrical bending, with a total of 21 cases since three cases were under centered compression (*PFN 0-3, PFN 0-2.5* and *PFN 0-2*). In these simulations the three-dimensional models and single bar models were used without considering transverse reinforcements.

Figure 6 illustrates the three-dimensional model of case *PFN 24-2*. It provides an overview of the finite element mesh (a), the lines representing the steel bars (b) and a detail of the rigid block when being loaded (c). The model consists of two rigid blocks with the same dimensions of 12 cm x 25 cm x 12 cm (x,y,z), one on top and another at the bottom, in addition to the middle stretch with dimensions equal to 12 cm x 25 cm x 176 cm (x,y,z).

The program automatically created a mesh, taking as reference a 4 cm dimension for the elements. Thus each rigid block consists of 128 elements and the central part comprises 1888 elements.

Loading was introduced by applying the concentrated loads to the nodes of the two rigid blocks (top and bottom). The vertical load was applied to the nodes along the axis towards *x* that is in the middle of the cross section and the moment was applied using a binary along the axes towards *x* that are on the edges of the cross section. In order for the concentrated loads to be standardized in a small stretch and for the deformations of these elements to be very small, a linear elastic material was used in the rigid blocks with a high elastic modulus value equal to 100,000 GPa.

The boundary conditions were introduced by applying restraints to the nodes of the rigid blocks. The boundary conditions represent an articulated column; to do so, restraints were imposed on the nodes placed along the axis towards *x* in the middle of the cross section. Shifts were prevented towards axes *x* and *y*, leaving the rotations free around the three axes (*x, y, z*) and the shift towards axis *z*.

The characteristics of the materials representing the concrete and steel were obtained from test samples performed by Melo [18]. In the *PFN 24-2* case, the concrete strength was equal to 38.5 MPa, the elastic modulus of the concrete was 20.6 GPa, the yield stress of steel was 595 MPa and the elastic modulus of the steel was 190 GPa. The slenderness ratio is 52.2 and a normal force is applied with relative eccentricity (*e/h*) of 0.20.

Table 4. Characteristics of tested columns [18]

Series	Column	e (mm)	e/h	λ	L (cm)	Ac (cm²)	As (cm²)	ρ (%)
	PFN 0-3	2	0.00					
	PFN 6-3	6	0.05					
	PFN 12-3	12	0.10					
	PFN 15-3	15	0.13					
	PFN 18-3	18	0.15					
1	PFN 24-3	24	0.20	92.7	300	300	4.71	1.57
	PFN 30-3	30	0.25					
	PFN 40-3	40	0.33					
	PFN 50-3	50	0.42					
	PFN 60-3	60	0.50					
	PFN 0-2.5	0	0.00					
	PFN 15-2.5	15	0.13					
	PFN 24-2.5	24	0.20					
2	PFN 30-2.5	30	0.25	71.5	250	300	4.71	1.57
	PFN 40-2.5	40	0.33					
	PFN 50-2.5	50	0.42					
	PFN 60-2.5	60	0.50					
	PFN 0-2	0	0.00					
	PFN 15-2	15	0.13					
	PFN 24-2	24	0.20					
3	PFN 30-2	30	0.25	52.2	200	300	4.71	1.57
	PFN 40-2	40	0.33					
	PFN 50-2	50	0.42					
	PFN 60-2	60	0.50					

All these columns have a cross section 12 cm x 25 cm, longitudinal reinforcement consisting of six CA-50 steel bars 10 mm in diameter and transverse reinforcement consisting of CA-60 steel stirrups 5 mm in diameter and 10 cm spacing between them, see Figure 5.

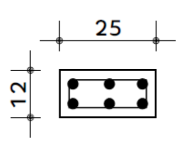

Figure 5. Cross section of columns

To validate the numerical models a comparison was made between the values of the maximum horizontal displacements. In the numerical models the failure load value (obtained in tests) was divided into 20 load increments and a nonlinear analysis was made with a maximum number of interactions equal to 100. Figure 7 shows the deformation of column *PFN 24-2* at the moment of collapse and the displacements towards *x* obtained by numerical simulations for the three-dimensional and bar element models.

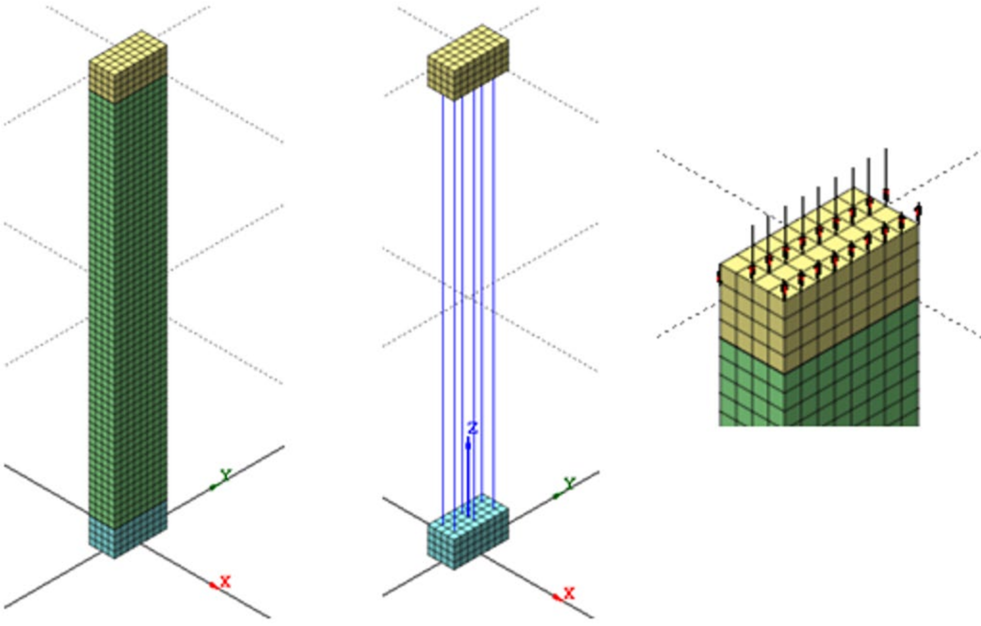

(a) (b) (c)

Figure 6. Three-dimensional model in the *PFN 24-2* case

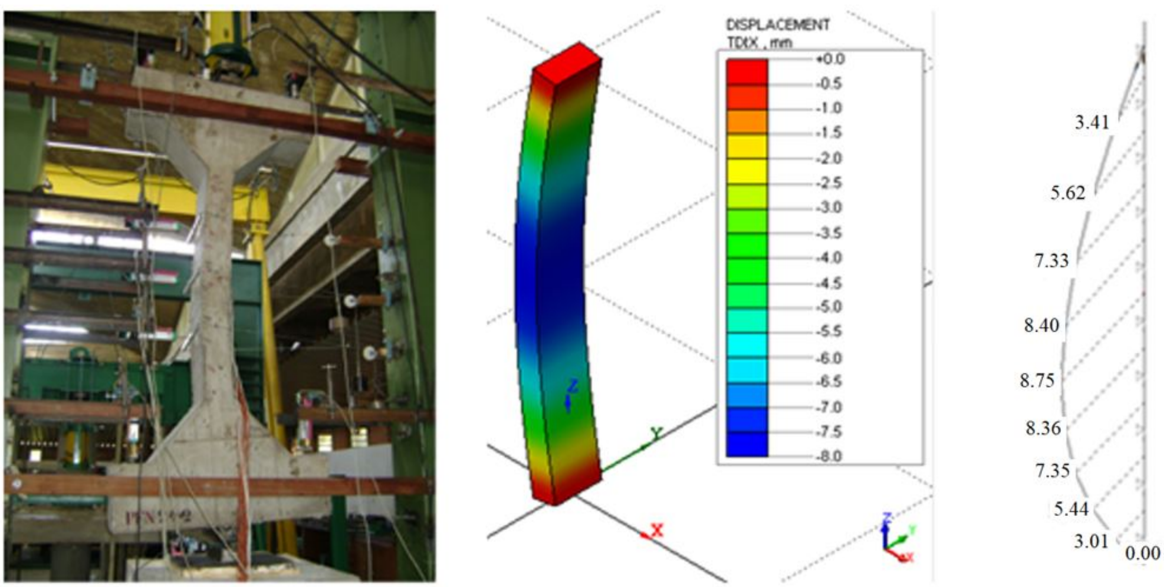

Figure 7. Displacements in column PFN 24-2

Figure 8 provides a diagram with the comparison of the results of the vertical load-horizontal displacement ratio obtained in the experimental analysis, numerical analysis with three-dimensional (3D) elements and numerical analysis with bar elements in the case of column *PFN 24-2*. This figure shows a good match between results. The resulting values for the horizontal displacements as the value of the force increases are practically the same for the three models until a vertical load value of 300 kN. From this point on the displacements in the 3D model are slightly smaller than in the other two models. There is a very good match between the bar model and the experimental model up to the conventional failure load of the bar model, which is determined by limiting the deformations in steel and concrete, 10‰

e 3.5‰, respectively. As the experimental model does not have this limitation, it reaches higher values for the breaking load and the corresponding displacement. The failure load values, and their displacements were: 440 kN and 14 mm for the experimental analysis; 456 kN and 8 mm for the 3D model; 410 kN and 9 mm for the bar model.

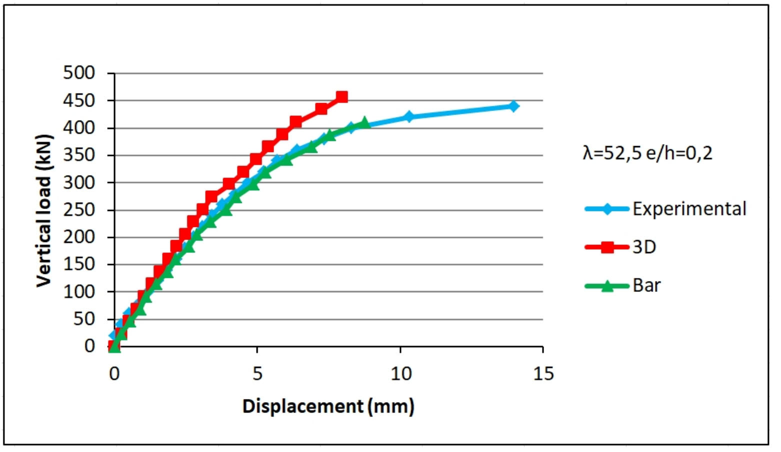

Figure 8. Diagram maximum load displacement - *PFN 24-2*

2.5 Definition of the analyzed cases

The definition of the analyzed cases was based on the main variables that might influence the behavior of the shear walls: a ratio between the cross section dimensions (*b/h*); value of the slenderness index (λ); value of the calculated dimensionless normal strain (ν_d); and the value of the calculated dimensionless bending moment around the axis of greatest inertia of the cross section (μ_{bd}).

Cross sections were studied with the following value of the ratio between the cross section dimensions: *b/h=5; b/h=7.5; b/h=10; e b/h=15.*For each *b/h* value six different numerical models were made, with the slenderness ratio varying between the limits specified by ABNT NBR 6118:2014 [1] for using the simplified process: $\lambda=36$; $\lambda=50$; $\lambda=60$; $\lambda=70$; $\lambda=80$; and $\lambda=90$.Thus, a total of 24 computer models were obtained.

Each model was processed for six different values of design dimensionless normal force, within limits normally used in preparing designs: $\nu_d=0.1$; $\nu_d=0.3$; $\nu_d=0.5$; $\nu_d=0.7$; $\nu_d=0.9$; $\nu_d=1.1$. Ten different values of μ_{bd} were applied for each value of ν_d.

The maximum value of the dimensionless bending moment applied to the section was determined by the rise of tensile strains caused by it. This value was obtained by multiplying the normal force value by an approximately 1/5 equal relative eccentricity (*e/b*), which is slightly higher than the relative eccentricity that defines the center core of inertia of a rectangular section. Therefore, although tensile strains appear on the outside surface of the cross section, they are low in intensity so that in every case analyzed the bar representing the strip at the end pulled by the bending moment remained with a normal compressive force. This maximum value of a dimensionless bending moment was divided into ten moment portions, totaling 1,440 analyzed cases.

Each of these cases was analyzed by three different bar models. In the first model the shear wall is analyzed as if it were a conventional column, being represented by a single vertical bar. In the second model the shear wall is analyzed according to the simplified model of ABNT NBR 6118:2014 [1]; that is, it is represented by a model consisting of separate vertical bars, in which each bar represents a strip of the shear wall. In the third model the shear wall is analyzed using the mesh model, in which horizontal bars connect the vertical bars representing the strips.

In every case design dimensionless bending moments were applied around the axis of the smallest inertia of the cross section (μ_{hd}) equal to the minimum moments specified by ABNT NBR 6118:2014 [1].

The geometry definitions of models, concrete strengths and covers of the reinforcements took into consideration the recommendations of ABNT NBR 6118:2014 [1]. With a view to using values coherent with design practice and that were somewhat conservative, the lowest value permitted by ABNT NBR 6118:2014 [1] was adopted for the smallest dimension of the shear walls, namely, $h=14$ cm. The characteristic strength adopted for the concrete was 25 MPa, which is the lowest value recommended by ABNT NBR 6118:2014 [1] for uncovered concrete structures in urban zones. The value of 3 cm was considered for covering reinforcements (c).

For these h and c values there is a relatively low efficient reinforcement, since the distance from the latter to the center of gravity of the section is small, confirming the conservative nature of this situation. However, the adopted value may be questioned for the covering of the reinforcements, since if the structure is located in a region where the environment is more aggressive, it would necessarily have a higher cover that would result in an even lower efficiency of the reinforcement. Yet in such situations h values equal to the minimum are seldom adopted.

With the definition of the h value, the b values were automatically defined as a result of the b/h ratio, as were the values of the buckling lengths as a result of the λ values. Having defined the sizes of the cross sections and concrete strength, the load forces were also automatically defined as a result of the dimensionless values of the normal force and bending moment.

Table 5 shows the characteristics of some of the models that were analyzed. The values of slenderness were 36, 50, 60, 70, 80 e 90 (this is the limit permitted for the use of the simplified process of ABNT NBR 6118:2014 [1]).

Table 5. Characteristics of models *PP1* to *PP6* (*b=0.71 m ; h=0.14 m; b/h=5*)

	ν_d	μ_{hd}	μ_{bd}									
			1	**2**	**3**	**4**	**5**	**6**	**7**	**8**	**9**	**10**
PP1	0.10	0.01	0.002	0.004	0.006	0.008	0.010	0.012	0.015	0.017	0.019	0.021
PP2	0.30	0.04	0.006	0.012	0.019	0.025	0.031	0.037	0.044	0.050	0.056	0.062
PP3	0.50	0.07	0.011	0.021	0.032	0.042	0.053	0.063	0.074	0.084	0.095	0.105
PP4	0.70	0.10	0.015	0.029	0.044	0.059	0.074	0.088	0.103	0.118	0.133	0.147
PP5	0.90	0.12	0.019	0.038	0.057	0.076	0.095	0.114	0.133	0.151	0.170	0.189
PP6	1.10	0.15	0.023	0.047	0.070	0.093	0.117	0.140	0.163	0.187	0.210	0.233

The methodology adopted to perform the numerical simulations was as follows: for each case, the first step was to determine the reinforcement, dimensioning the shear walls if it were a conventional column, taking into account only the local second order effects, that is without considering the localized second order effects. The second step analyzes the shear wall using the approximate process of ABNT NBR 6118:2014 [1], and in the third step, the shear wall was analyzed using the mesh model.

In every case the reinforcements determined in the first step were used, even though they were not enough to withstand the forces determined by the models in the second and third steps. Therefore, the localized second order effects for both the isolated bar model and the mesh model are always determined conservatively.

The type of steel used was CA-50 and the reinforcement rates adopted complied with the limits specified by ABNT NBR 6118:2014 [1]. The values of the reinforcement rates varied from a minimum value of 0.4% to a maximum of 8%.

3 RESULTS AND DISCUSSIONS

When analyzing the second order effects a comparison was made of the values of all moments (first order + second order) in the longest outside strip of the shear walls. The values obtained by the single bar model (conventional column) were compared to the values obtained by the isolated bar model, according to the approximate process of ABNT NBR 6118:2014 [1], and with the values obtained by the mesh model. To do so, the values for the single bar model were divided by the number of vertical bars of the other models.

In the simulations using the isolated bar model it was found in a number of cases that the end parts showed very different displacements from the displacements in the adjacent strip, a fact that it is impossible to occur in actual shear walls and that evidences the shortcoming of the simplified process. This behavior was observed in both the end strips compressed by the bending moment and the strips pulled by it. When using the mesh model, this defect is solved, as can be seen in Figures 9 and 10. In these figures the bars of the left end are compressed by the bending moment while the bars on the right end are pulled.

Figure 9 illustrates that for the independent bar model the maximum displacement of the longest bar is 53 mm, more than twice as long as the value of the adjacent bar, which is 26 mm and more than three times longer than the value of the bar at the opposite end which is 17 mm. In the mesh model case, the maximum displacement values are the same for all bars, equal to 23 mm.

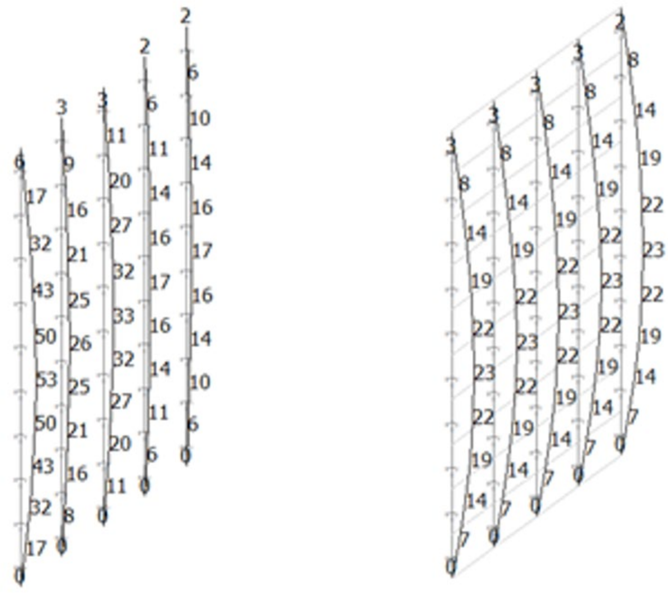

(a) (b)

Figure 9. Displacement (mm) - Case*PP21* (*λ=90; μ_{bd}=0.029*) - (a) Independent bars; (b) Mesh

Figure 10 shows that for the model of independent bars, the maximum displacement of the end pulled by the bending moment is 11 mm, more than five times more in value than that of the other bars, which are equal to 2 mm. In the mesh model case, every bar has the maximum displacement of 2 mm.

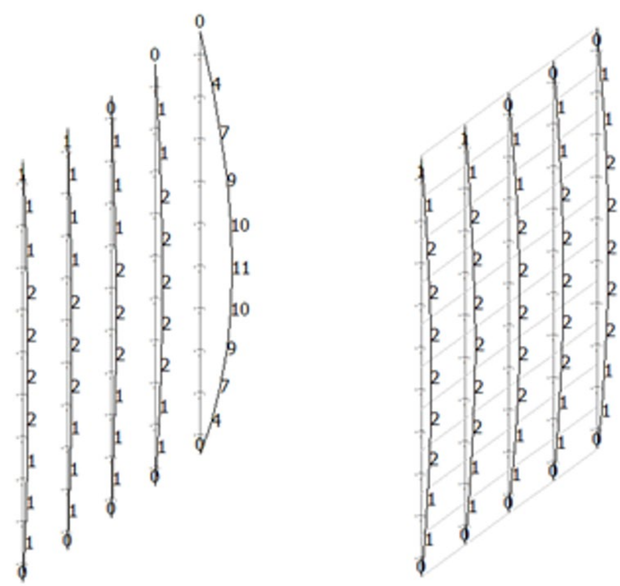

(a) Independent bars (b) Mesh

Figure 10. Displacement (mm) - Case*PP19* (*λ=80; μ_{bd}=0.020*)

In order to prove the results obtained by the mesh model, analyses were also made using three-dimensional models for these two cases. The results are shown in Figure 11.

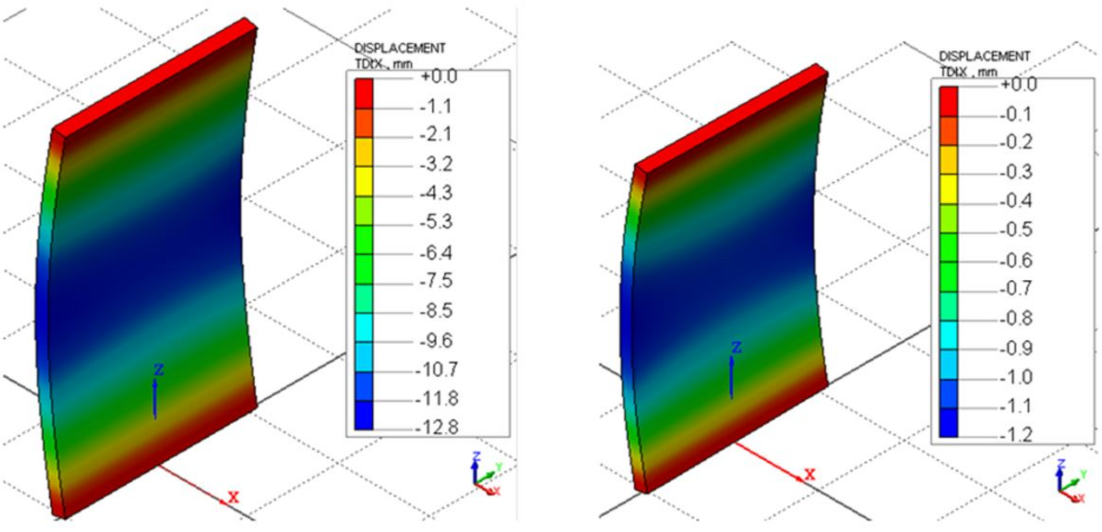

Figure 11. Displacement (mm) – 3D model

In the same way as in the mesh models, in the three-dimensional models the maximum displacement values are practically the same throughout the cross section. In case *PP21* ($\lambda=90;\ \mu_{bd}=0.029$) the result for the node situated in the axis of the cross section of the end compressed by the bending moment was 12.79 mm and the result for the node situated in the axis of the cross section of the end pulled by the bending moment was 12.81 mm. In case *PP19* ($\lambda=80;\ \mu_{bd}=0.020$) the result for the node situated in the axis of the cross section at the end compressed by the bending moment was 1.19 mm, and the result for the node situated in the axis of the cross section at the end pulled by the ending moment was 1.17 mm.

3.1 Bending moment in the vertical direction

To analyze the influence of the localized second order effects on the total bending moment value in the vertical direction of the shear walls, a comparison was made of the results obtained in three different ways. When the shear wall is analyzed by a single bar (as if it were a conventional column) there are no localized second order effects. When comparing the results of this model with the results from the isolated bar and mesh models it was possible to determine the influence of the localized second order effects. In other words, the differences in the values of the bending moments obtained from these last two models in relation to the values obtained from the first model come from the localized second order effects.

The results are presented in graphs showing the variation in the maximum bending moment in the bar with the longest end as a result of the main variables that can interfere in the results, as follows: the ratio between the dimensions of the cross section (*b/h*); slenderness (λ); the design dimensionless normal force (v_d); and design dimensionless bending moment around the axis with the highest inertia of the cross section (μ_{bd}).

It is obvious that in case *PP1*, shown in Figure 12, when there is little slenderness the bending moment values are only slightly altered as the μ_{bd} value increases, and that the bending moment values are practically the same for the three models. When the slenderness value increases, the bending moment values now increase as the μ_{bd} value increases, and the values determined by the three models now no longer coincide. The values of the isolated bar and mesh models (NBR) are higher than the values from the single bar model (column), indicating the existence of the localized second order effects.

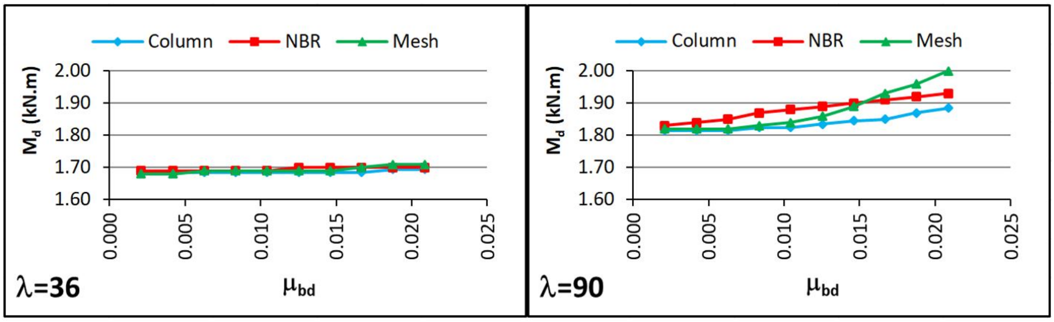

Figure 12. Diagrams M_d x μ_{bd} for the case*PP1 (b/h=5; ν_d=0.1)*

In order to quantify the localized second order effects, diagrams were built relating the values of the bending moments obtained from the single bar model with the values from the other two models, in which the vertical axes are the values of the bending moments obtained from the isolated bar and mesh models, divided by the values obtained from the single bar model ($M_d/M_{d,COLUMN}$).

It is possible when analyzing the diagrams in Figure 13 to confirm that when the slenderness is small the values from the three models are practically the same since the ratios between them are very close to 1.0. For higher slenderness values, as the value of μ_{bd} increases the ratio $M_d/M_{d,COLUMN}$ also increases, reaching a maximum value of 1.03 for the isolated bar model and 1.06 for the mesh model.

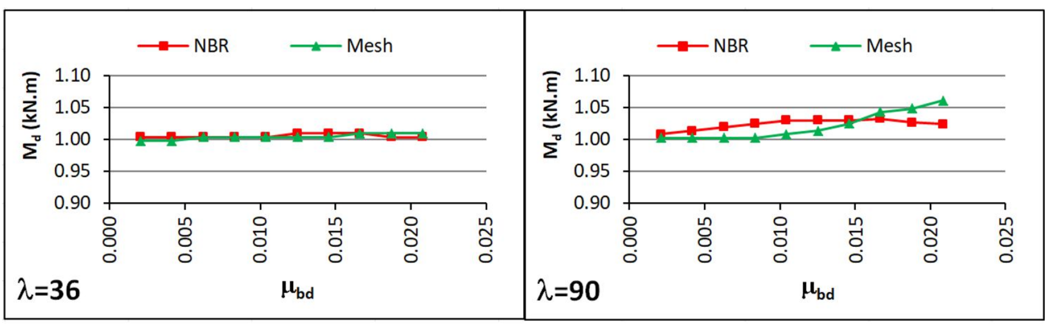

Figure 13. Diagrams $M_d/M_{d,COLUMN}$ x μ_{bd} for the case*PP1 (b/h=5; ν_d=0.1)*

To analyze the influence of the ratio *b/h* on the localized second order effects, the diagrams in Figure 14 were prepared. In those diagrams the vertical axis represents the ratio $M_{d,MESH}$ /$M_{d,COLUMN}$ and the horizontal axis represents the μ_{bd} values.

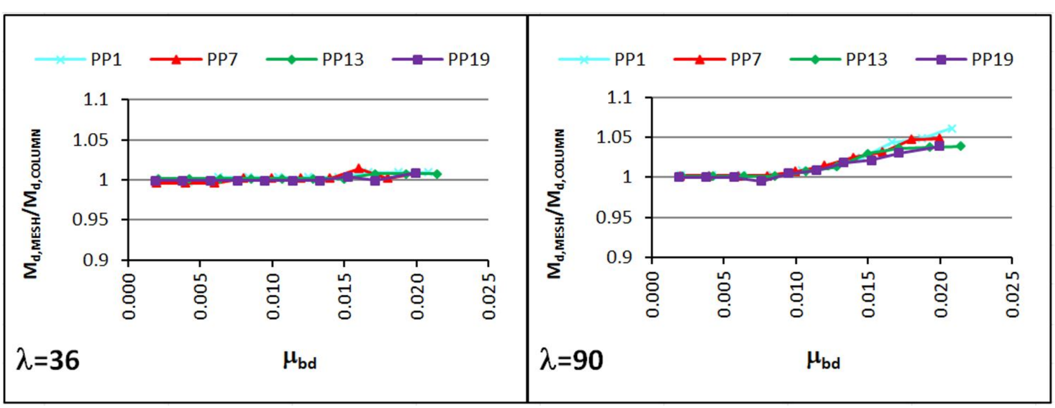

Figure 14. Diagrams $M_{d,MESH}/M_{d,COLUMN}$ x μ_{bd} in cases where ν_d=0.1

Figure 14 shows the results for cases *PP1 (b/h=5), PP7 (b/h=7.5), PP13 (b/h=10)* and *PP19 (b/h=15),* in which the value of the dimensionless normal force is 0.1. It is clear in this figure that in the cases of little slenderness the values of the ratios $M_{d,MESH}$ /$M_{d,COLUMN}$ are very close to 1.0, for any values of μ_{bd}. For more slenderness, as the value of μ_{bd} increases, the values of the ratios $M_{d,MESH}$ /$M_{d,COLUMN}$ also increase to reach a maximum value of 1.07.

Diagrams similar to those shown in Figures 12, 13 and 14 were made for all 1,440 cases analyzed with values of λ = 36, λ = 50, λ = 60, λ = 70, λ = 80 and λ = 90. Table 6 summarizes the maximum values obtained for the ratio $M_{d,MESH}/M_{d,COLUMN}$. Almost all cases have a low value for this ratio, except where v_d=0.3 that reaches a maximum value of 1.21.

Table 6. Summary of $M_{d,MESH}/M_{d,COLUMN}$ values

ν_d	$M_{dMESH}/M_{d.COLUMN}$				Maximum
	b/h				
	5	7.5	10	15	
0.10	1.06	1.05	1.04	1.04	1.06
0.30	1.21	1.16	1.13	1.13	1.21
0.50	1.08	1.10	1.09	1.13	1.13
0.70	1.04	1.06	1.08	1.07	1.08
0.90	1.04	1.03	1.03	1.07	1.07
1.10	1.01	-	1.01	1.05	1.05

Table 7 summarizes the maximum values obtained for the ratio $M_{d,BAR}$ /$M_{d,COLUMN}$. High values for this ratio are to be found, reaching a maximum of 1.89. By comparing the vales in those two tables, it is evident that the isolated bar model always presents higher values than the mesh model, in some cases with a significant difference.

Table 7. Summary of $M_{d,BAR}/M_{d,COLUMN}$ values

ν_d	$M_{dBAR}/M_{dCOLUMN}$				Maximum
	b/h				
	5	7.5	10	15	
0.10	1.03	1.05	1.06	1.07	1.07
0.30	1.10	1.25	1.35	1.55	1.55
0.50	1.61	1.61	1.89	1.56	1.89
0.70	1.52	1.33	1.45	1.46	1.52
0.90	1.24	1.10	1.35	1.29	1.35
1.10	1.09	-	1.13	1.07	1.13

3.2 Bending moment in the horizontal direction

Of the three different ways used to analyze the bending moment in the vertical direction, only simulation with the mesh model is able to detect the increase in the bending moment in the horizontal direction. In no analyzed case was there detected a bending moment on the horizontal with significant values.

Figures 15 and 16 show the displacements and diagram of a horizontal bending moment for cases *PP19* and *PP21*. These cases were chosen to demonstrate that there were no bending moments on the horizontal because they presented a huge difference in the maximum displacements of the vertical bars when they were analyzed by the isolated bar model. When they were analyzed with the mesh model, the maximum displacement values were the same as for all bars, as can be seen in Figures 9 and 10, suggesting that in such cases the horizontal bars should undergo greater forces to be able to equal the maximum displacements in all vertical bars.

In Figures 15 and 16 the bending moments in a horizontal direction are seen to be zero. Although the bending moment diagram is not presented in the three-dimensional models, it is possible to conclude that in those models the bending moments are also zero because, as can be seen in Figure 11, the horizontal displacement values are practically equal throughout a cross section, showing that there is no curvature on the horizontal. The fact there is no curvature on the horizontal means that the moment in the horizontal direction is zero.

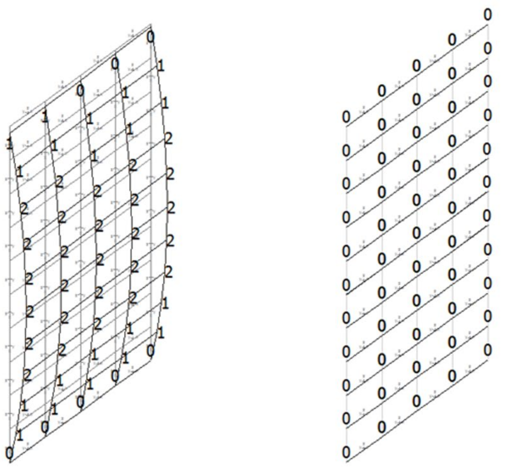

(a) Displacement (mm) (b) Bending moment on the horizontal (kN·m)

Figure 15. Case *PP19* ($\lambda=80; \mu_{bd}=0.020$) – Mesh model

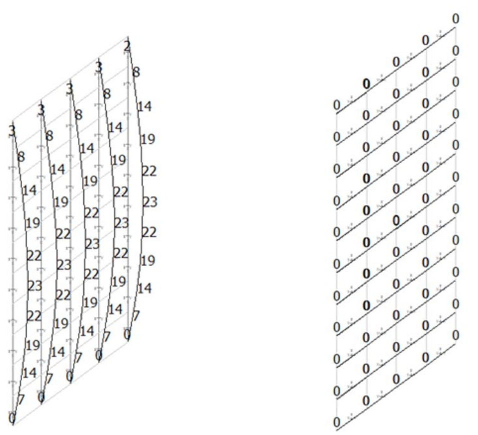

a) Displacement (mm) (b) Bending moment on the horizontal (kN·m)

Figure 16. Case*PP21* ($\lambda=90; \mu_{bd}=0.029$) – Mesh model

4 CONCLUSIONS

The principal conclusions from this study are:

The specifications for shear wall design in Brazil are quite different from the specifications for shear wall design in other countries of the Americas, Europe, Asia and Oceania, especially in relation to the loading forces. In most of these countries, shear walls must withstand seismic loads, while in Brazil most of its territory lies in a region where these loads are negligible.

Both the 3D model and the computer model consisting of a mesh of bars behaved properly. Therefore, the mesh model can be a good alternative for simulating shear walls, since its implementation is much simpler than that of the 3D model, in addition to requiring less computational effort. In this study, the computational effort was not of significant importance since isolated only one-floor shear walls were analyzed, however this may be a relevant factor when simulating an entire building.

The second order effects (local and localized) are negligible in the cases where slenderness is low, close to the limit of $\lambda=35$, confirming the ABNT NBR 6118:2014 recommendation to neglect these effects when the slenderness is equal to or less than 35.

The localized second order effects are strongly influenced by the slenderness, normal force and bending moment around the axis with greater inertia, but these effects are no influenced by the ratio between the cross section dimensions.

The values of the localized second order effects obtained from the mesh model are relatively low for the large majority of cases. The maximum values obtained for the ratio $M_d/M_{d,COLUMN}$ using this model were: *1.06* for the cases where $v_d=0.1$; *1.21* for the cases where $v_d=0.3$; *1.13* for the cases where $v_d=0.5$; *1.08* for cases where $v_d=0.7$; *1.07* for the cases where $v_d=0.9$; 1*.05* for cases where $v_d=1.1$.

The approximate process of ABNT NBR 6118:2014 provided much higher values for the localized second order effects that those obtained from the mesh model. The maximum values for the ratio $M_d/M_{d,COLUMN}$ with the approximate process of ABNT NBR 6118:2014 were: *1.07* for cases where $v_d=0.1$; *1.55* for cases where $v_d=0.3$; *1.89* for cases where $v_d=0.5$; *1.52* for cases where $v_d=0.7$; *1.35* for cases where $v_d=0.9$; and *1.13* for cases where $v_d=1.10$.

Regarding the consideration of the bending moment in the horizontal direction in shear walls with a rectangular section, bending moment in this direction was not observed in all cases analyzed. The results suggest that, in the case of shear walls with rectangular cross sections, there is no significant horizontal bending.

ACKNOWLEDGMENTS

The authors thank the Federal University of Pernambuco (UFPE), Piauí State University (UESPI) and the Federal Institute of Piauí (IFPI) for the opportunity they offered and for providing the necessary conditions to enable this study. They also thank TQS for the support in adapting a software version the requirements of this research.

REFERENCES

[1] Associação Brasileira de Normas Técnicas, *Projeto de Estruturas de Concreto – Procedimento*, NBR 6118, 2014.

[2] American Concrete Institute, *Building Code Requirements for Structural Concrete*, ACI-318, 2014.

[3] International Federation for Structural Concrete, *Model Code*, 2010.

[4] M. C. B. N. Campos, “Análise numérica de pilares-parede de concreto armado com seção retangular,” Ph.D. dissertation, Univ. Fed. Pernambuco, Recife, 2016.

[5] J. W. Wallace and J. P. Moehle, “Behavior and design of structural walls – lessons from recent laboratory tests & earthquakes,” in *Int. Symp. Eng. Lesson Learn. 2011 Great East Earthq.*, 2012.

[6] J. H. Thomsen 4th and J. W. Wallace, "Displacement-based design of slender reinforced concrete structural walls – experimental verification," *J. Struct. Eng.*, vol. 130, no. 4, pp. 618–630, 2004.

[7] P. F. Parra and J. P. Moehle, “Lateral buckling in reinforced concrete walls,” in *10NCEE - Tenth U.S. Nat. Conf. Earthq. Eng.*, 2014.

[8] J. K. Wight and J. G. MacGregor, *Reinforced Concrete: Mechanics and Design*, 5th ed. New Jersey: Pearson Prentice Hall, 2009.

[9] J. M. Araújo, "Análise do processo aproximado da NBR-6118 para consideração dos efeitos localizados de segunda ordem," *Rev. Teor. Prat. Eng. Civ.*, no. 10, pp. 1–10, 2007.

[10] R. L. S. França and A. E. Kimura, “Resultados de recentes pesquisas para o dimensionamento das armaduras longitudinal e transversal em pilares-parede,” in *An. 9º Enc. Nac. Eng. Consult. Estrut.*, 2006.

[11] K. Arnott, "Shear wall analysis – new modelling, same answer," *J. The Inst. Struct. Eng.*, vol. 83, no. 3, pp. 1–11, Feb 2005.

[12] S. Sritharan, J. Zhao, J. Waugh, S. Aaleti, *Nonlinear Analysis of Rectangular and t-Shaped Concrete Walls*. Ames: Dept. Civ. Constr. Environ. Eng., Iowa State Univ., 2008.

[13] Associação Brasileira de Normas Técnicas, *Projeto de Estruturas Resistentes a Sismos – Procedimento*, NBR 15421, 2006.

[14] Associação Brasileira de Normas Técnicas, *Projeto de Estruturas de Concreto – Procedimento*, NBR 6118, 2003.

[15] K. Ribeiro, “Diagramas para verificação de pilares retangulares em concreto armado submetidos à flexão composta normal,” M.S. thesis, Univ. Fed. Santa Catarina, Florianópolis, 2011.

[16] TQS Informática, *CAD/ TQS System – User’s Handbook*. São Paulo, 2010.

[17] MIDAS FEA, *Nonlinear and Detail FE Analysis System for Civil Structures*, Version 2.9.6, 2009.

[18] C. E. L. Melo, “Análise experimental e numérica de pilares birrotulados de concreto armado submetidos a flexo-compressão normal,” Ph.D. dissertation, Univ. Brasília, Brasília, 2009.

Author contributions: This study is based on the doctoral thesis of the author M. C. B. N. Campos, who wrote it under the guidance of the authors P. M. V. Ribeiro and R. A. Oliveira.

Editors: Osvaldo Luís Manzoli, José Luiz Antunes de Oliveira e Sousa, Guilherme Aris Parsekian.

Rev. IBRACON Estrut. Mater., vol. 13, no. 6, e13615, 2020

IBRACON Structures and Materials Journal
Revista IBRACON de Estruturas e Materiais
ISSN 1983-4195 ismj.org

ORIGINAL ARTICLE

Design considerations on the influence of slab continuity on punching resistance of flat slabs

Considerações de dimensionamento sobre a influência da continuidade na resistência à punção de lajes lisas de concreto armado

Fernanda Gabriella Batista Santos Oliveira[a]
Luis Fernando Sampaio Soares[a]
Robert Lars Vollum[b]

[a]Instituto Federal de Educação, Ciência e Tecnologia do Maranhão – IFMA, Departamento de Construção Civil, São Luís, MA, Brasil
[b]Imperial College London, Department of Civil and Environmental Engineering, London, UK

Received 24 June 2019
Accepted 12 May 2020

Abstract: This paper assesses the influence of slab continuity on the punching resistance of a realistically proportioned flat slab floor plate without shear reinforcement. The edge column punching resistance of a symmetric flat slab extending bays in each direction was assessed by means of NLFEA with TNO DIANA, MC2010 levels II, III, IV, Eurocode 2 and NBR 6118. Both Eurocode 2 and NBR 6118 are seen to give similar predictions for punching resistance, while MC2010, which is based on the Critical Shear Crack Theory and depends on how rotations are calculated and FE modelling assumptions, varies significantly with its levels of approximation with Level IV agreeing reasonably well with predictions from NLFEA. Direction for the critical rotations is shown to vary and can also be influenced by the reinforcement over the span. For EC2, NBR 6118 and MC2010 LoA II and III punching shear design are independent of span, unlike the results obtained with MC2010 LoA IV.

Keywords: punching shear, slab continuity, NBR 6118, Eurocode 2, MC2010.

Resumo: Este artigo avalia a influência da continuidade na resistência à punção de uma laje lisa de concreto armado com dimensões realísticas, sem armadura de cisalhamento. O estudo da resistência à punção teve enfoque em um pilar de borda avaliado por meio de análise não linear em elementos finitos com o TNO DIANA, MC2010 níveis II, III, IV, Eurocode 2 e NBR 6118. O Eurocode 2 e a NBR 6118 apresentaram resultados similares para a resistência à punção, enquanto o MC2010, baseado na Teoria da Fissura Crítica de Cisalhamento, que depende do método de cálculo das rotações e das premissas adotadas de modelagem em elementos finitos, apresentou variações em função dos níveis de aproximação, com o nível IV concordando razoavelmente bem com os resultados provenientes da análise não linear.A direção das rotações críticas também apresentou alterações, possivelmente influenciada pela taxa de armadura ao longo do vão. Para o EC2, NBR 6118 e MC2010 LoA II e III, o dimensionamento à punção independe da continuidade da laje, contrariamente aos resultados obtidos com o nível IV do MC2010.

Palavras-chave: punção, continuidade, NBR 6118, Eurocode 2, MC2010.

How to cite: F. G. B. S. Oliveira, L. F. S. Soares, and R. L. Vollum, “Design considerations on the influence of slab continuity on punching resistance of flat slabs,” *Rev. IBRACON Estrut. Mater.*, vol. 13, no. 6, e13615, 2020, https://doi.org/10.1590/S1983-41952020000600015

1 INTRODUCTION

Flat slabs are two way spanning slab directly supported by columns. Their thickness is typically governed by deflection control or punching shear resistance. The latter is influenced by many different factors, from concrete and reinforcement parameters, to more complex issues like size effect, slenderness, and boundary conditions (test set up).

Corresponding author: Fernanda Gabriella Batista Santos Oliveira. E-mail: fernandagbso@gmail.com
Financial support: This research was supported by the Science Without Borders Program, through the National Council for Scientific and Technological Development (CNPq) - 237859/2012-2.
Conflict of interest: Nothing to declare.

It is somewhat understandable that even after more than 100 years of research, and 50 years since the first rational model [1], there is still no consensus regarding a general theory.

The number of models available developed from different backgrounds, such as those described in the literature review of fib [2] (empirical control surface approaches, plasticity approaches, Kinnunen and Nylander [1]-like models, etc.), and dating as early as the 1910s [3], and as late as the 2010s [4], [5], shows that it is a very active field of research, and attempts are still being made in this regard.

The complexity of the phenomenon is reflected in the conflicting opinions expressed by researchers. For instance, depending on the test arrangement, conclusions can become conflicted regarding the influence of continuity, with works such as Sherif and Dilger [6] observing no difference between isolated and continuous specimens, whereas Chana and Desai [7] found an increase of around 40% on punching resistance from extending the panel beyond the line of contraflexure. The compressive membrane action is well recognized for contributing to punching resistance, which is influenced by a great number of factors leading to difficulties in quantifying the increase in resistance due only to continuity.

fib [2] states that when analyzing isolated specimens, the compressive membrane action is not considered, however in real slabs restrained shrinkage induces tensile stress which reduces the punching resistance. fib [2] also mentions that based on experimental results developed by Sherif [8] it can be concluded that the punching shear strength of an interior slab-column connection in a realistic slab is almost the same for a single column test specimen. Issues like this one led fib [2] to remark that, for design purposes, it is still not recommended to rely on compressive membrane action.

Another example is related to the shear reinforcement layout. Einpaul et al. [9] observed that cruciform and radial arrangements showed comparable performances regarding the punching strength as oppose to Vollum et al. [10], who concluded that stirrups in a cruciform layout increases the shear strength of flat slabs by a multiple up to 1.5, in comparison to multiples of 2.0 or more for well anchored radial arrangements.

Some of the assumptions of the different mechanical models differ significantly, while presenting reasonable predictions for punching shear capacity. Even models based on similar backgrounds such as the Critical Shear Crack Theory (CSCT) by Muttoni [11] and the Tangential Strain Theory (TST) by Broms [4] can present some discrepancy, like the impact of time dependent effects such as creep and drying shrinkage. The CSCT assumption that the critical shear width is proportional to the slab rotation implicates that punching capacity decreases with time due to the increased rotation resulting from concrete creep and drying shrinkage. However, Broms [4] stated, based on the experimental tests under sustained loading developed by Moe [12], that a slight enhancement of punching capacity (around 4%) can be observed even though both the width of flexural cracks and deflection increased by 80%. The TST can account for that minor increase by employing a creep factor $(1+\varphi)$ over the critical strain and Young's modulus of its model.

The CSCT by Muttoni [11] and Fernández Ruiz and Muttoni [13] was chosen as the physical theory behind the latest MC2010 [14]. Since its introduction, the model has been tested in many different situations (non-axis-symmetric slabs, steel fibre reinforced slabs, prestressing, post-installed shear reinforcement, continuity, etc.). However, the model is still not universally accepted, and works such as Ferreira et al. [15] and Broms [4] have already identified and discussed a few issues with the theory.

For instance, MC2010 Levels of Approximation (LoA) I to III do not consider the effect of moment redistribution on punching resistance. Consequently, they can give very conservative estimates of the shear resistance of slabs designed in accordance to UK practice using the equivalent frame method, where moments are typically redistributed downwards by 20% over columns. Both tests and the CSCT suggest that this inward movement of the line of radial contraflexure should lead to an increase in shear resistance. This increase is not accounted for in levels I to III of MC2010 which consequently underestimate the punching resistance of such slabs.

The interpretation of the size effect is also a subject that presents different approaches in normative codes and consequently divergences between researchers. Brazilian and European codes, for example, characterize the size effect through an empirical formulation, whereas MC2010 adopted the size effect equations based on the CSCT. However, Dönmez and Bažant [16] suggest that the CSCT derivation and calculation procedure obfuscates the mechanics of failure not leading to consistent results, based on their experimentally calibrated finite element simulations of crack path and width, of stress distributions and localizations during failure, and of strain energy release.

This paper addresses some of the theoretical issues regarding the punching shear resistance of flat slabs, while giving and comparing the amount of punching shear reinforcement required based on predictions of Brazilian's NBR 6118 [17], Eurocode 2 [18], and MC2010. The discussion is focused on a realistic flat slab according to the model developed by Sherif and Dilger [6], without shear reinforcement, in order to evaluate how the codes of practice consider the influence of in-plane restraint and flexural continuity in punching shear resistance and design. The analysis concentrates on edge columns. Punching at edge columns is much less researched than at internal columns, despite the fact that buildings typically have more edge than internal columns. Furthermore, practical experience shows that design for punching shear is frequently more critical at edge than internal columns.

This study also presents an evaluation of the directions of critical rotations for practical slabs, since MC2010 bases the shear resistance on the greater of the rotations about axes normal and parallel to the slab edge. As noted by Soares and Vollum [19] for example, different specimens such as those tested by Regan [20] and El-Salakawy et al. [21] all have shown critical rotations over the longitudinal direction. It also aims to discuss a few modelling assumptions adopted which are relevant on the interpretation of the results, such as the consideration of elastic columns in the numerical analyses required by MC2010 LoA III and IV in order to calculate the punching shear.

2 CODES OF PRACTICE

This paper includes comparisons of punching shear requirements between three codes of practice: Eurocode 2 (EC2), NBR6118, and MC2010. This section will provide the equations and general assumptions used in the studies extracted from the codes aforementioned.

2.1 Eurocode 2

BS EN 1992, Eurocode 2: Design of concrete structures, commonly abbreviated to EC2, is the current code adopted by the majority of European countries and by a few countries outside Europe. It allows flat slabs to be designed using a proven method of analysis such as Finite Element, Yield Line, Grillage, or Equivalent Frame. The analysis with Equivalent Frame divides the slab in both plane directions into frames consisting of columns and sections of the slab. The panels are divided into column and middle strips. The bending moment should be apportioned for the Column strip as 60-80% for negative, and 50-70% for positive moments and as 40-20% and 50-30% for negative and positive moments, respectively, in the middle strip. This code locates the control perimeter at a distance 2d from the column face and must be calculated in accordance with 6.4.2 section of EC2 [18]. The punching shear resistance without shear reinforcement is given by Equation 1

$$V_{Rd,c}=0.18\left(100\rho f_{ck}\right)^{\frac{1}{3}}(1+\sqrt{200/d})ud/\gamma_c \tag{1}$$

where $\rho=\left(\rho_{xl}\cdot\rho_{yl}\right)^{0.5}\leq 0.02$, in which ρ_{xl} and ρ_{yl} are the flexural tension reinforcement ratios A_{sl}/bd within a slab width equal to the column plus $3d$ to each side. For transfer of moment from slab edge to edge column, EC2 recommends that flexural reinforcement is placed in an effective width of c_2+y, though an increased width of c_2+2y is commonly adopted in UK practice [22], where c_2 is the column dimension parallel to the slab edge, and y is the perpendicular distance from the inner column face to the slab edge. f_{ck} is the characteristic concrete cylinder strength, d is the average effective depth of the tension reinforcement. The term $(1+\sqrt{200/d})$, which accounts for size effect, is limited to a maximum of 2.0, with d in mm.

EC2 multiplies the design shear force by β to account for the effects of uneven shear due to the support reaction being eccentric. The design shear stress is given by Equation 2.

$$v=\beta\frac{V}{ud} \tag{2}$$

EC2 also allows fixed values for β for structures where adjacent spans do not differ in length by more than 25% and the lateral stability does not depend on frame action between the columns and slabs. In such cases, $\beta=1.15$ for internal column, $\beta=1.4$ for edge columns and $\beta=1.5$ for corner columns can be adopted. The required area of shear reinforcement is calculated according to Equation 3

$$1.5A_{sw}\frac{d}{s_r}\geq\frac{V-0.75V_{Rd,c}}{f_{ywd,ef}} \tag{3}$$

where A_{sw} is the area of shear reinforcement in each perimeter, s_r is the radial spacing of the shear reinforcement and $f_{ywd,ef} = (250 + 0.25d) \le f_{ywd}$, where $f_{ywd,ef}$ and f_{ywd} are respectively the effective design strength and the design yield strength of the shear reinforcement.

2.2 MC2010

MC2010 punching shear recommendations are based on the CSCT [11], [13], and so it relates punching resistance to the rotation in the so-called critical shear crack. The basic control perimeter u is taken at a distance $0.5d$ from the column face, where d is the effective depth for shear considering support penetration, as illustrated in section 7.3.5.1. of MC2010 [14].

MC2010 reduces the design shear resistance by the multiple k_e to account for any eccentricity over the support. MC2010 allows k_e to be estimated as 0.9 for inner columns, 0.7 for edge columns and 0.65 for corner columns, for braced frames where the adjacent spans do not differ in length by more than 25%. k_e can also be calculated according to Equation 4

$$k_e = 1/(1 + e'/b_u) \tag{4}$$

where e' is the eccentricity of the shear forces resultant with respect to the centroid of the basic control perimeter, and b_u is the diameter of a circle with the same surface as the region inside the basic control perimeter. The punching shear resistance is calculated as $V_{Rd} = V_{Rd,c} + V_{Rd,s}$ where the design shear resistance attributed to the concrete, $V_{Rd,c}$, is calculated according to Equation 5

$$V_{Rd,c} = k_\psi k_e \frac{\sqrt{f_{ck}}}{\gamma_c} u d_v \tag{5}$$

in which f_{ck} is in megapascals (MPa). The parameter k_ψ, accounting for the opening of the shear critical crack and its roughness, depends on the maximum rotation ψ of the slab around the support region, and is calculated according to Equations 6 and 7

$$k_\psi = \frac{1}{1.5 + 0.9\psi d k_{dg}} \le 0.6 \tag{6}$$

$$k_{dg} = \frac{32}{16 + d_g} \ge 0.75 \tag{7}$$

where d_g is the size of the maximum aggregate particles. For high strength and lightweight concrete, the rupture may occur in the aggregate particles, in which case $d_g = 0$. The shear resistance provided by transverse reinforcement is calculated as Equation 8

$$V_{Rd,s} = \sum_d A_{sw} k_e \sigma_{sw} \tag{8}$$

where $\sum_d A_{sw}$ is the cross-sectional area of all shear reinforcement within the zone bounded by 0.35 d and d from the border of the support region. σ_{sw} is the stress that can be mobilized in the shear reinforcement.

The maximum punching resistance is limited by crushing of the concrete struts near the support region, according to Equation 9.

$$V_{Rd,max} = k_{sys} k_{\psi} \frac{\sqrt{f_{ck}}}{\gamma_c} u d_v \leq \frac{\sqrt{f_{ck}}}{\gamma_c} u d_v \tag{9}$$

The coefficient k_{sys} accounts for the performance of punching shear reinforcing systems, and is taken as 2.4 for stirrups and 2.8 for studs, provided the radial spacing to the first perimeter of shear reinforcement from the column face s_o is $\leq 0.5\,d$ and the spacing of successive perimeters of shear reinforcement s_1 is $< 0.6\,d_v$.

LoA II calculates the rotations as Equation 10

$$\psi = \alpha \frac{r_s}{d} \frac{f_{yd}}{E_s} \left(\frac{m_{Ed}}{m_{Rd}} \right)^{1.5} \tag{10}$$

where r_s denotes the position where the radial bending moment is zero with respect to the column axis and can be approximated as $0.22L_x$ or $0.22L_y$ if $0.5 \leq L_x/L_y \leq 2.0$, f_{yd} is the design yield strength of the flexural reinforcement, E_s is the modulus of elasticity of reinforcement, $\alpha = 1.5$, m_{Rd} is the design average flexural strength per unit width of the support strip, and m_{Ed} is the average bending moment per unit width in the support strip, which is assumed to be of width $b_s = 1.5\sqrt{r_{s,x} \cdot r_{s,y}} \leq L_{min}$. In LoA III, α from Equation 10 can be taken as 1.2, provided that both m_{Ed} and r_s are calculated with linear elastic finite-element analysis (LFEA), though r_s should not be taken as less than $0.67b_{sr}$ at edge and corner columns. Although not stated in MC2010, to account for twisting moments the reinforcement should be designed for the Wood moments [23] or equivalent.

Level IV of approximation allows the rotation ψ to be calculated with a nonlinear finite element analysis of the structure (NLFEA), accounting for tension stiffening, cracking, yielding of reinforcement, and any other significant non-linear effect that would help improving the simulation of the structure and its behaviour.

2.3 NBR 6118

Punching shear requirements according to Brazilian code NBR 6118 are very similar to those of EC2, previously described in section 2.1. Like EC2, the Brazilian code allows the use of equivalent frame method for the design of flat slabs when it is a reinforced concrete slab, in which the columns are arranged in regular orthogonal rows and with slightly different spans. The Brazilian code also locates the control perimeter at a distance 2d from the column face, as presented in section 19.5.2 of NBR 6118 [17]. The proportion of punching shear assumed to be resisted by concrete is calculated according to Equation 1. This portion is also reduced when shear reinforcement is considered, leading to Equation 11.

$$1.5 A_{sw} \frac{d}{s_r} \geq \frac{\left\{ V_{Sd} - 0.10 \left[\left(100 \rho f_{ck}\right)^{\frac{1}{3}} \left(1 + \sqrt{\frac{200}{d}} \right) \right] \right\} u_1 d}{f_{ywd,ef}} \tag{11}$$

However, the size effect term of $(1+\sqrt{200/d})$ is not limited to a maximum of 2.0, nor the flexural tension reinforcement ratio to a limit of 2% as recommended by EC2. NBR 6118 does not allow the use of fixed values, such as β (EC2) and k_e (MC2010), to account for eccentricity over the support in any circumstances, as opposed to the others codes under analysis. Therefore, the design shear stress is calculated based on Equation 12

$$v = \frac{V}{u^* d} + \frac{M_{Sd1} k}{W_p\, d} \tag{12}$$

Where u^* denotes the reduced control perimeter, k is a parameter dependent on the ratio between the column dimensions and provides the transferred moment to the column in punching shear, W_p is the plastic resistance module of the control perimeter and M_{Sd1} the design moment transferred from the slab to the edge column in the plane perpendicular to the free edge.

3 GENERAL ASPECTS

In order to assess the impact of continuity, a representative flat slab was designed using the equivalent frame method. The floor plate is 250 mm thick and consists of 9 square bays spanning 7500 mm between column centrelines. The internal columns are 400 mm square in cross section. Edge and corner columns are 250 mm x 400 mm in cross section. Figure 1 shows a plan view of the slab which, although not shown, is considered to be braced with shear walls or steel bracing. The slab was designed for a single load case of all spans fully loaded as permitted by the UK National annex to EC2 [24]. The resulting support bending moments were redistributed downwards by 30% at the edge columns and 20% at internal columns as required by the UK National annex to EC2 when designing for a single load case.

The characteristic concrete cylinder and reinforcement yield strength were taken as $f_{ck} = 30\ MPa$ and $f_{yk} = 500\ MPa$, respectively. The design loadings were slab self-weight = 6.25 kN/m^2, superimposed dead load = 1.5 kN/m^2, imposed load = 2.5 kN/m^2 and a perimeter load of 10 kN/m for external cladding.

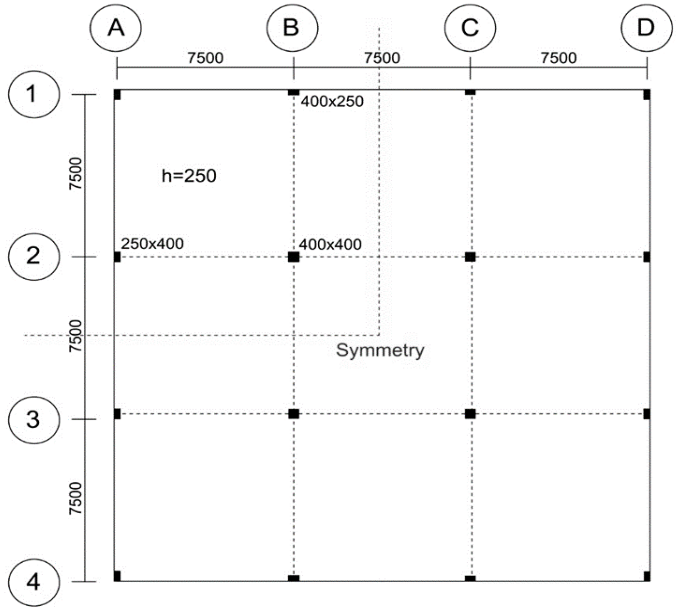

Figure 1. Plan view of the considered flat slab (Dimensions in mm).

The resulting uniformly distributed design ultimate load, calculated with load factors of 1.35 for dead load and 1.5 for imposed load, is 14.21 kN/m^2. The hogging flexural reinforcement was designed for the peak bending moments at the centreline of the columns. The slab was divided into column and middle strips and the design bending moments were proportioned between the strips in percentage as 75:25 for hogging, and 55:45 for sagging moments as allowed by the EC2 and NBR 6118. The additional reinforcement required by the cladding load was distributed across the entire edge column panel width in the same proportion as the UDL (Uniformly Distributed Load).

Surplus span rebar was provided for deflection control in accordance to EC2 span-to-effective-depth rules, which, for instance, increased the column strip sagging reinforcement ratio between columns A2 and B2 (refer to Figure 1) from 0.51% to 0.73%, or its middle strip sagging from 0.41% to 0.45%. Two thirds of the hogging reinforcement within the column strip was placed within a band over the columns of ¼ of the panel width. Details of the flexural reinforcement can be found in Soares [25]. The reinforcement effective depths were $d_1 = 212\ mm$ and $d_2 = 196\ mm$, calculated assuming 30 mm cover and 16 mm bars in both directions. A minimum area of 377 mm^2/m was provided, calculated in accordance with EC2 as $0.0013 b_t.d$, where b_t is the width of the tension zone. No shear reinforcement was designed at this stage, as a comparative study focusing on this parameter is carried out later on.

4 CONTINUOUS SLABS OF SHERIF AND DILGER [6]

Sherif and Dilger [6] tested two continuous flat slabs with a novel setup in which the panel extended to the points of zero shear, as shown in Figure 2. Further details of the test set up are given in Sherif [26]. The slabs measured 5000 mm x 7500 mm on plan and were 150 mm thick. Both slabs had the flexural reinforcement depicted in Figure 3, with No. 15 bars (200 mm^2) with $f_y = 444\ MPa$, and No. 10 bars (100 mm^2) with $f_y = 523MPa$. Slab S2 was reinforced with shear studs at both interior and edge columns in the arrangement shown in Figure 4. Slab S1 had no shear reinforcement.

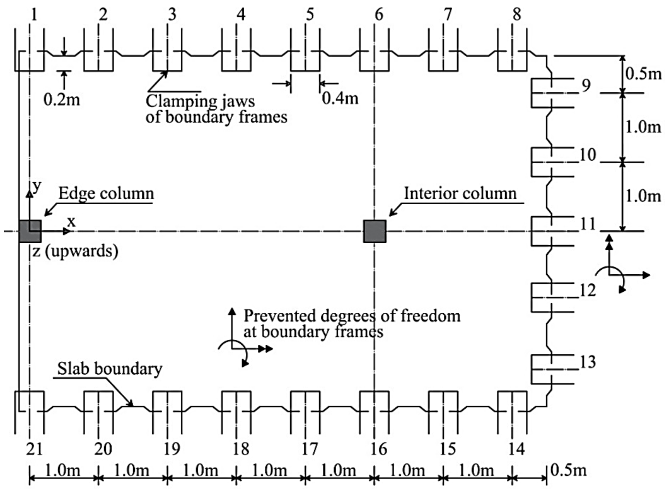

Figure 2. Specimen tested by Sherif and Dilger [6].

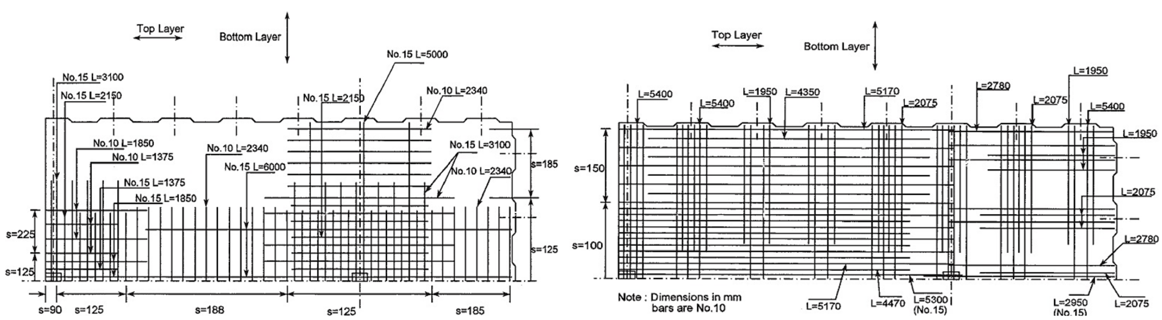

(a) (b)

Figure 3. Flexural reinforcement for the specimens tested by Sherif and Dilger [6].

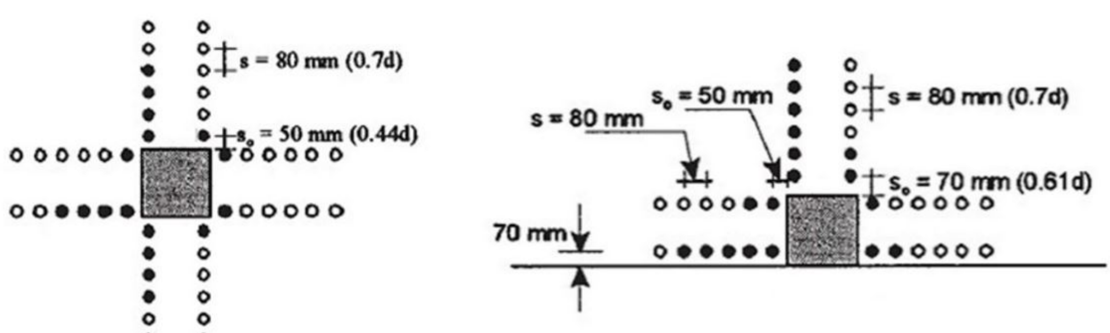

Figure 4. Shear reinforcement for slab S2 of Sherif and Dilger [6].

The load was applied to the specimen at 16 points on the full panel and 8 points on the half panel to simulate an UDL. The columns extended 1.5 m (around half of the story height) above and below the slab and were heavily reinforced with six No. 25 (500 mm^2) deformed bars. Table 1 gives more details of the specimens.

Table 1. Details of specimens tested by Sherif and Dilger [6].

Slabs	Column size (edge and internal) (mm)	h (mm)	d (mm)	ρ_{c2+3h}^{*} %	f_c (MPa)	Failure Load (kN/m^2)	Failure Mode and Location	Failure Shear Force (kN)	Remarks
S1	250x250	150	114	1.41	28	15.54	Punching at internal column	399	No Shear Studs
S2	250x250	150	114	1.41	33	19.97	Punching at edge column	164	Studs at edge and internal column

*: Reinforcement ratio within the width c2+3h

4.1 Numerical Modelling

The Sherif and Dilger [6] slabs were analysed with TNO Diana version 9.6 [27] using the following modelling assumptions: the slab was modelled with the eight-node quadrilateral isoparametric curved shell element. Reinforcement bars were modelled as embedded elements. The Von Mises yield criterion was adopted for reinforcement with no hardening. The integration scheme was 3 x 3 in plan with 9 points through the slab thickness as recommended by Vollum and Tay [28]. Concrete was modelled using the 'total strain fixed crack model' of Diana. Following the suggestion of Vollum and Tay [28], the concrete tensile was taken as 0.5 f_{ct} , where f_{ct} is the mean indirect tensile strength. Linear tension softening was adopted in which the tensile stress reduced to zero at a strain of 0.5 ε_y , where ε_y is the reinforcement yield strain.

Diana adopts the concept of a shear retention factor in its Total Strain Fixed crack models to account for the reduction in shear stiffness after cracking. Suidan and Schnobrich [29] suggests that it should lie around 0.1~0.2, which gives good results for shear dominant failure cases as shown in Sagaseta [30]. Trautwein [31], also using the commercial software Diana, developed analyses in axisymmetric models of slabs used in experimental studies, with a shear retention factor equal to 0.2. The value adopted for the shear retention factor in this analysis was also 0.2.

For behaviour in compression, the Thorenfeldt model [32] was adopted along with the four-parameter Hsieh-Ting-Chen failure surface to simulate the increase in concrete compressive strength with increasing isotropic stress. Concrete compressive strength reduction due to lateral cracking was modelled in accordance with Vecchio and Collins [33]. A Quasi-Newton iterative solution procedure was adopted in conjunction with an energy-based convergence criteria with 10^{-4} tolerance. The main aim of the NLFEA was to capture the deflected shape of the slab, allowing the punching resistance to be calculated with MC2010 LoA IV.

Around the columns, the mesh was refined using 50 mm square eight-node quadrilateral curved shell elements compared with 100 mm square elements elsewhere. The connection between the refined and coarse mesh was made with six-node triangular curved shell elements, shown in Figure 5. The final mesh is presented in Figure 5. The columns were modelled with the twenty-node brick and element size of 100 x 50 x 50 mm.

Figure 6 compares deflections from test data of Sherif [26] and NLFEA. The deflected shape was extracted along the slab centreline in the 7500 mm direction (Longitudinal), and the displacement was extracted at midway between the edge and internal column. Both slabs are reported to have failed in punching shear. The NLFEA gave very good estimates of the measured slab deflections up to failure. The analysis of S1 stopped fairly close to the flexural capacity as indicated by the yield line capacity in Figure 6.

Sherif and Dilger [6] reports that specimens S1 and S2 failed in punching at the internal and edge column, respectively. Figure 7 shows the prediction of MC2010 LoA IV, with resistances calculated from Equations 5 ($V_{Rd,c}$) and Equation 8 ($V_{Rd,s}$) using a $k_e = 0.9$ and $k_e = 0.7$ for internal and edge columns, respectively.

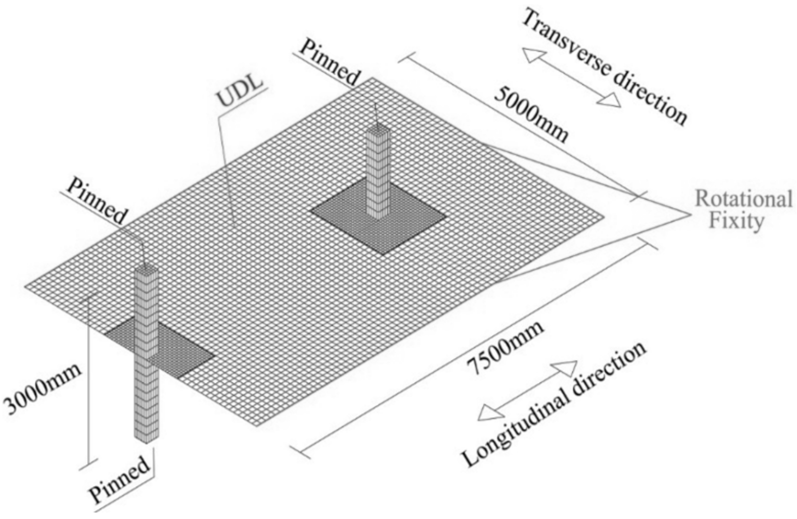

Figure 5. Mesh used for the NLFEA of Sherif and Dilger's [6] tests.

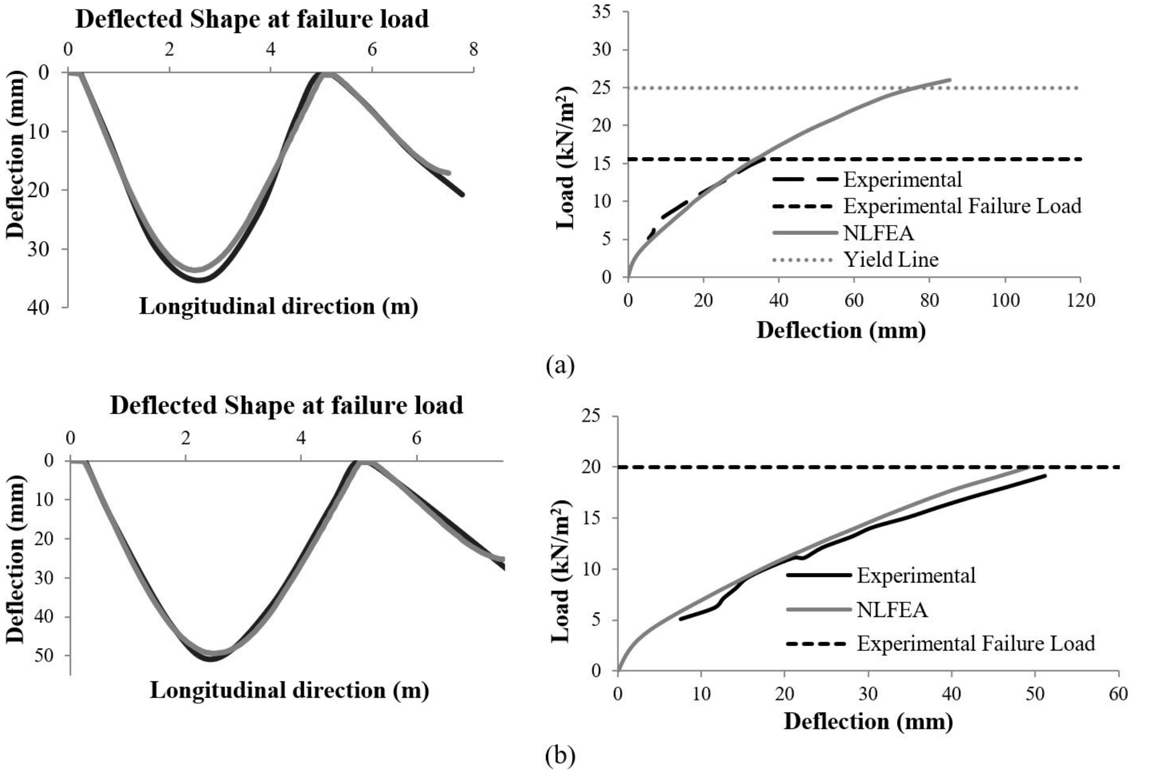

Figure 6. Comparisons between NLFEA results and experimental data from Sherif's (1996) slab (a) S1 and (b) S2.

In Figure 7, rotations relative to the column for both perpendicular directions on plan are depicted as 'Longitudinal' when calculated from the longitudinal deflected shape, and 'Transverse' (in this case, the transverse rotations are equal to either side of the column due to symmetry), when calculated from the deflected shape along the slab edge (see Figure 5). Previous analysis has already shown that there is no significant difference between extracting the rotations from the shell elements or calculating them from the corresponded deflected shape [25].

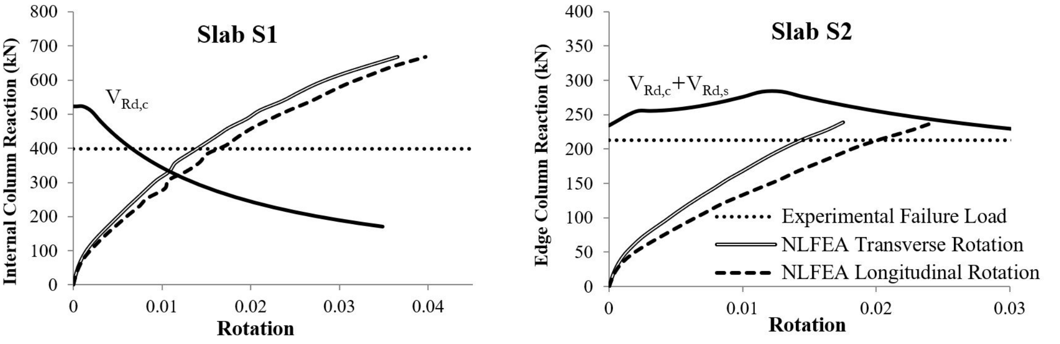

Figure 7. Column reaction-rotation relative to the column for the slabs of Sherif and Dilger [6] and resistance according to the CSCT.

The CSCT is seen to give reasonable predictions for punching failure for the slabs of Sherif and Dilger [6] when adopting a fixed k_e (0.9 and 0.7 for internal and edge column, respectively). A similar conclusion was found by Soares and Vollum [19], when comparing experimental punching shear failure load with those calculated with the CSCT for both isolated specimens of El-Salakawy et al. [21] and continuous specimens of Regan [20]. The longitudinal direction had the largest rotations, thus critical to calculate punching resistance according to MC2010 for all specimens aforementioned.

5 SUBASSEMBLY OF DESIGNED SLAB

A parametric analysis of the flat slab designed in Section 3 was carried out with Diana. The slab was modelled in a series of subassemblies similar to that tested by Sherif and Dilger [6]. The subassembly shown in Figure 8 includes edge column 2A and internal column 2B (refer to Figure 1).

The slab was modelled with eight-node quadrilateral curved shell elements with a size of around 50 mm square near the slab/column connection, and 150 mm square elsewhere. Six-node triangular curved shell elements were used to connect the refined mesh to the coarse mesh. The columns were modelled with elastic twenty-node brick elements measuring 150 x 50 x 50 mm, and were fully fixed at each end. Although unrealistic, this assumption has no significant influence on the NLFEA results since the columns were modelled elastically, which is representative of the lower levels of a tall building in which the axial column load is sufficient to prevent cracking.

The analysis modelled the full column height of 3.75 m above and below the slab. The adopted characteristic concrete compressive strength was 30MPa. Symmetry was simulated with only rotational fixities as done for the analysis in Soares and Vollum [34] to avoid any additional in-plane forces.

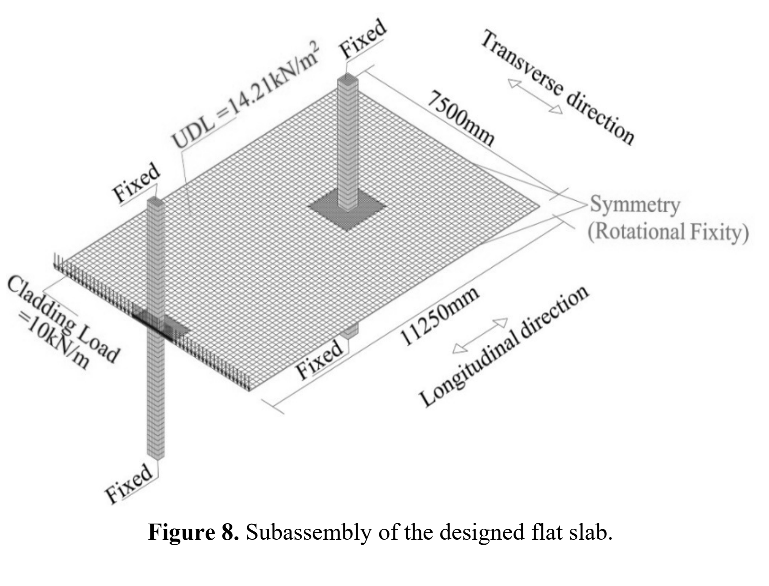

Figure 8. Subassembly of the designed flat slab.

5.1 Influence of Reinforcement arrangement

A parametric study was carried out to investigate the influence of varying the reinforcement in the slab of the subassembly shown in Figure 8. Columns were modelled as elastic and extended 3.75 m above and below the slab. The ends of the columns were fully fixed. Figure 8 gives further details on the slab dimensions and adopted boundary conditions. The objective was to determine whether the influence of varying the flexural reinforcement in the subassembly was similar to that predicted for slabs with the geometry tested by Regan [20], discussed in Soares and Vollum [19].

Figure 9 and 10 show the baseline reinforcement arrangement used in the subassembly which was determined from analysis of the full slab shown in Figure 1 using the procedure described in Section 3. A minimum reinforcement area of 377 mm^2/m was provided where no reinforcement is shown, calculated according to EC2. Loads were applied as shown in Figure 8. Both UDL and cladding loads were increased proportionately until failure. This load case is critical for the internal column, but not the edge column where pattern loading consisting of the full factored load on the end of span and factored dead load on the internal span is more critical. The all spans fully loaded load case was adopted since the main objective was to compare the punching resistances given by EC2, NBR 6118 and MC2010 Levels II to IV.

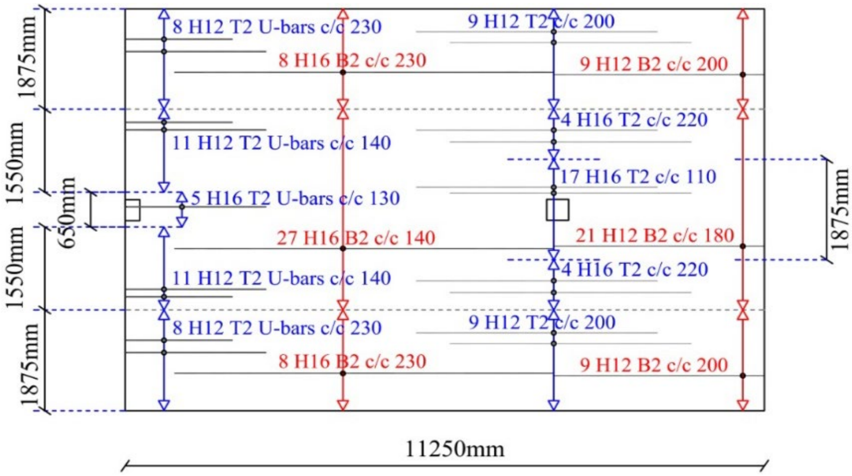

Figure 9. Longitudinal reinforcement designed for the subassembly.

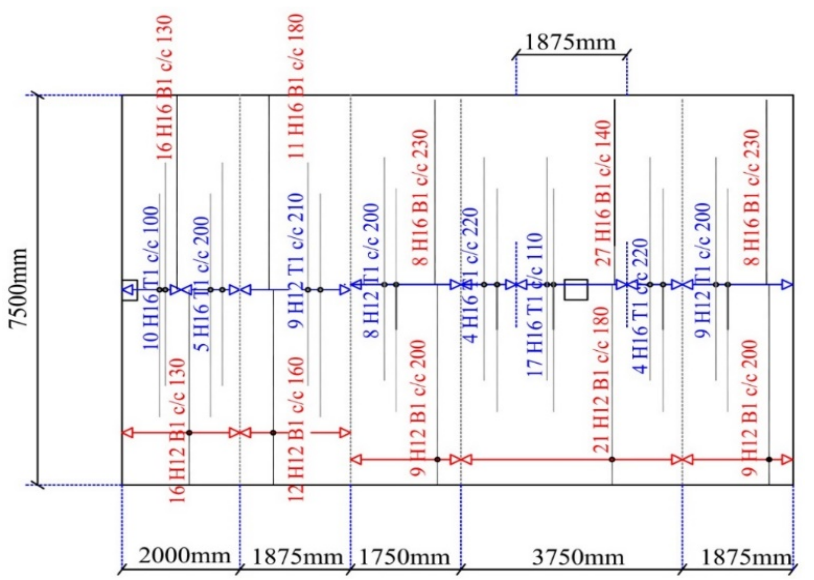

Figure 10. Transverse reinforcement designed for the subassembly.

In Figure 9, the support reinforcement ratio, normal to the free slab edge, is $\rho_{sup} = 0.8\%$ over a width of $c_2 + y$ (where y is the perpendicular distance from the slab edge to the inner column face and c_2 is the parallel column dimension). Analyses were also carried out with ρ_{sup} doubled to $\rho_{sup} = 1.0\%$ and halved to $\rho_{sup} = 0.5\%$. The span reinforcement ratio was also doubled from $\rho_{sup} = 0.6\%$ in to $\rho_{span} = 1.2\%$, and halved to $\rho_{span} = 0.3\%$. All nine slabs were loaded with a line load along the short external edge representing cladding. An additional analysis was carried out with reinforcement ratio of $\rho_{sup} = 0.8\%$ and $\rho_{span} = 0.6\%$ and no cladding load, making a total of ten analyses. Table 2 gives more details of the slabs.

Table 2. Details on the parametric study varying the reinforcement arrangement.

f_{ck}	**30 MPa**
γ_c	1.5
f_{yk}	500 MPa
E_s	200 GPa
γ_s	1.15
d_1 [a]	212 mm
d_2 [b]	196 mm
Self-weight	6.25 kN/m^2
Superimposed dead load	1.5 kN/m^2
Imposed load	2.5 kN/m^2
Cladding load	10 kN/m
Edge Column (2A)	250 mm x 400 mm
Internal Column (2B)	400 mm x 400 mm
k_e	0.7
k_{dg}	0.89

[a] Top and Bottom bars in the transverse direction. [b] Top and Bottom bars in the longitudinal direction.

Figure 11 shows the resulting longitudinal rotations relative to the column, calculated from the longitudinal deflected shape (such as that presented in Figure 6), and the design shear force at the external column extracted from LFEA. The rotations were calculated as previously described.

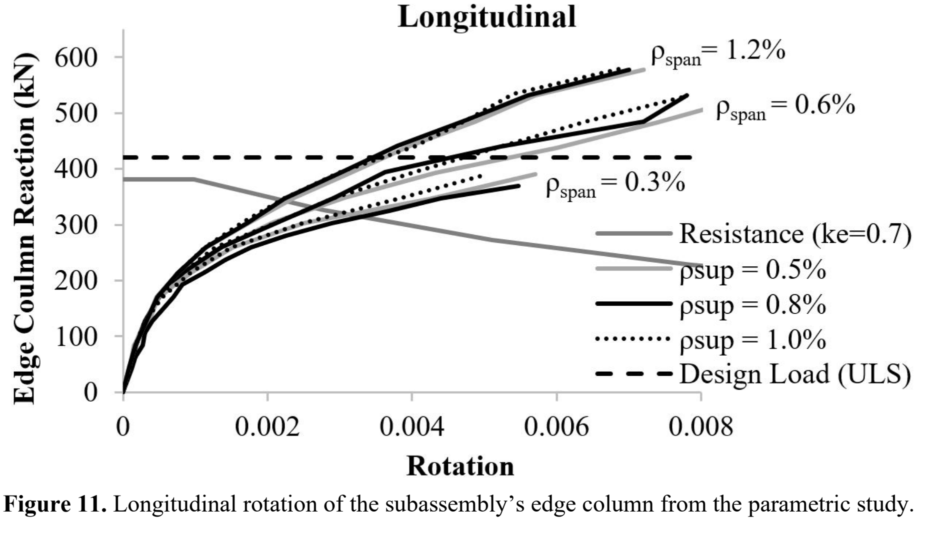

Figure 11. Longitudinal rotation of the subassembly's edge column from the parametric study.

Figure 11 shows that, as for Regan's [20] slabs (Soares and Vollum [19]) , longitudinal span reinforcement is predicted to have significantly greater influence on the longitudinal rotation at edge columns than longitudinal hogging reinforcement at the edge column. Figure 11 also shows the shear resistance provided by the concrete calculated according to MC2010 with $k_e = 0.7$, chosen on the basis of good results for previous analysis of continuous flat slabs tested by Regan [20] (Soares and Vollum [19]) and Sherif and Dilger [6].

Figure 12 shows that the calculated eccentricity M/V at the edge column increased with load. A similar outcome was observed in the specimens by Regan [20] (Soares [25]) where the increase in eccentricity for the elastic column is explained by its increased stiffness compared to the column in Regan's tests. In MC2010, the basic control perimeter is reduced by a multiple k_e to account for loading eccentricity. If k_e is calculated with Equation 4 of MC2010, the predicted punching resistance depends on the column flexural stiffness which depends on the column axial load. It is unclear whether this is the case in reality. In the limit, the maximum eccentricity is limited by the maximum moment that can be transferred to the column.

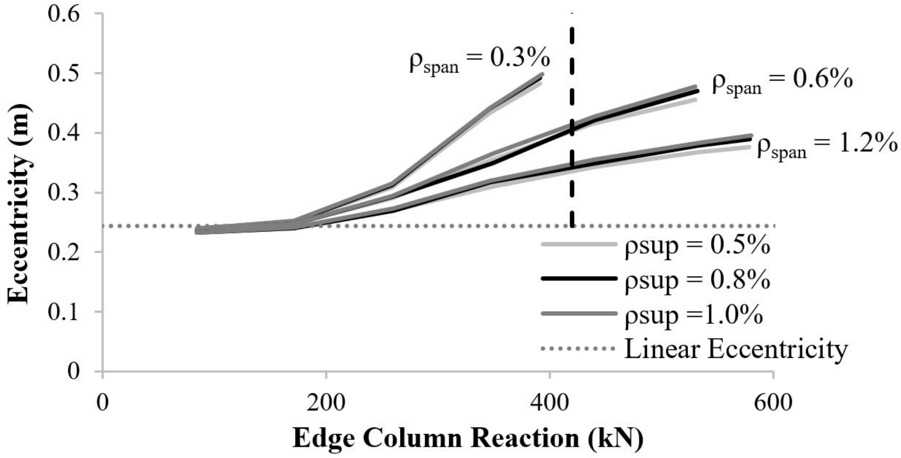

Figure 12. Influence of varying reinforcement arrangement in the eccentricity of the subassembly's edge column.

6 CODE PREDICTIONS

This section is used to compare predictions of levels II, III, IV of MC2010, NBR 6118, and EC2, for the slabs considered in the parametric study previously described.

6.1 Critical direction for rotations

According to MC2010, the punching resistance depends on the greater of the slab rotations relative to the column in the longitudinal and transverse directions. Soares and Vollum [19] show that longitudinal rotations (i.e. rotations calculated from longitudinal deflections) are critical for the specimens of El-Salakawy et al. [21] and Regan [20] in all cases. This finding is not true in general, and is partly a consequence of the specimen geometry and loading arrangement. Longitudinal rotations are also critical for the tests of Sherif and Dilger [6], but the difference between longitudinal and transverse rotations is much less than for Regan's [20] slabs, since the specimens have slightly more realistic dimensions ratio. The subassembly shown in Figure 8 realistically models the direction of span in both the longitudinal and transverse directions as for the Sherif and Dilger's [6] tests.

For practical slabs, the critical direction can vary and depends on parameters including the reinforcement arrangement and magnitude of the cladding load. Figure 13 compares the longitudinal and transverse rotations with and without cladding load for slab $\rho_{sup} = 0.8\%$ and $\rho_{span} = 0.6\%$. The reinforcement is the same for both cases and is designed for the case with cladding. Interestingly, the critical direction for rotations in Figure 13 changes from longitudinal to transverse when the cladding load is included. The resistances in Figure 13 are calculated with Equation 5 and $k_e = 0.7$. Table 3 summarizes the values of $V_{Rd,c}$ calculated at rotations corresponding to the design ULS (Ultimate Limit State) load at the edge column, which was calculated with LFEA.

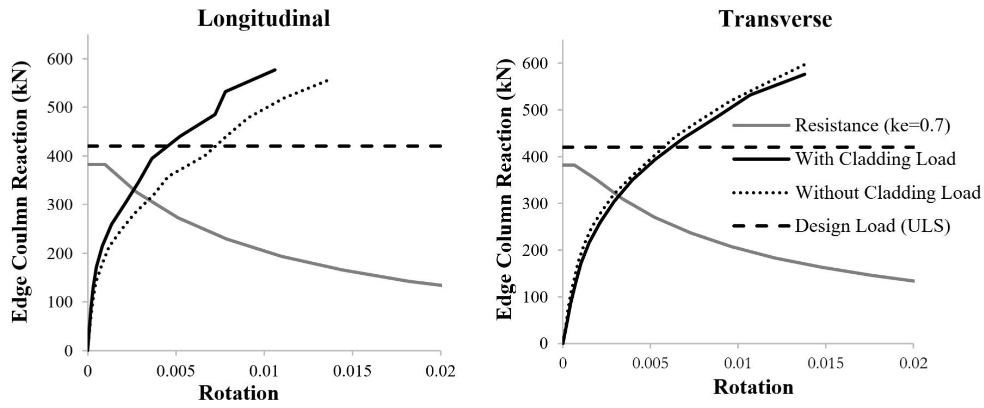

Figure 13. Comparison between longitudinal and transverse rotations with and without cladding loads for $\rho_{sup} = 0.8\%$ and $\rho_{span} = 0.6\%$.

Table 3. $V_{Rd,c}$ calculated with $k_e = 0.7$ with and without cladding load.

Slabs	$V_{Rd,c}$ (kN)	
	Longitudinal	**Transverse**
With Cladding Load	290	257
Without Cladding Load	240	260

Figure 14 compares longitudinal and right-hand side transverse rotations (greater than the left-hand side transverse rotation for all cases due to asymmetric transverse reinforcement), relative to the column, for all 9 slabs with cladding load. Also shown is the MC2010 punching resistance provided by the concrete calculated with Equation 5 for $k_e = 0.7$.

It can be seen in Figure 14 that transverse direction is critical for all cases. Neither the span nor the support longitudinal reinforcement seems to have a significant impact on these transverse rotations, as shown in Figure 15. Longitudinal flexural reinforcement (span/support) have no influence on transverse rotations, as can be seen in Figure 15, though it can still influence punching resistance owing to shear redistribution around the control perimeter, as stated by Sagaseta et al. [35], which suggests that the boundary conditions adopted in punching shear tests could have a greater influence than considered up to now.

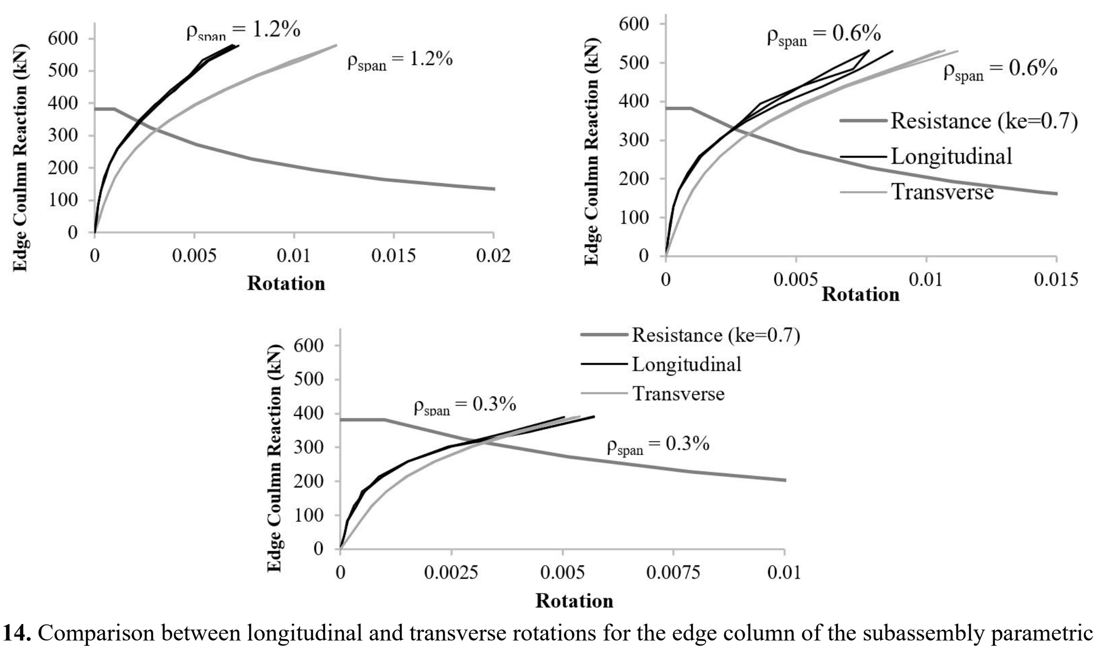

Figure 14. Comparison between longitudinal and transverse rotations for the edge column of the subassembly parametric study.

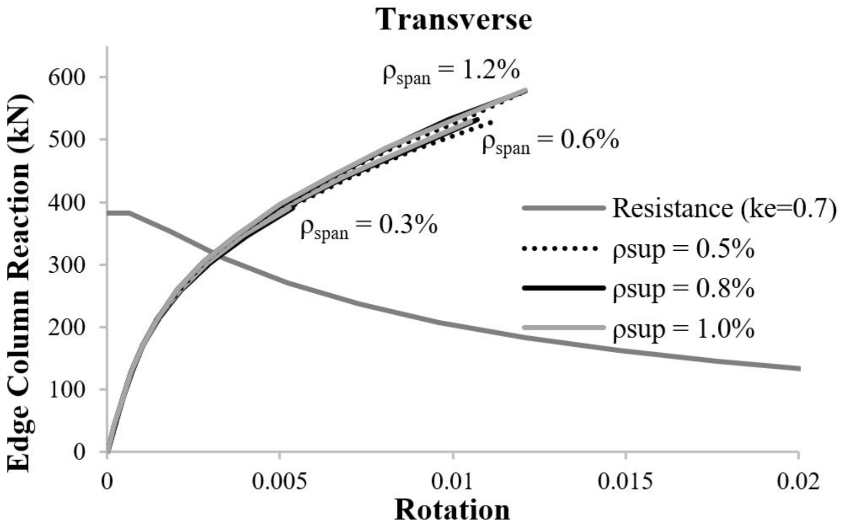

Figure 15. Transverse rotations of the subassembly's edge column from the parametric study.

6.2 Comparisons between MC2010 Levels II, III, IV, EC2 and NBR6118 for edge columns

The following section compares the areas of punching shear reinforcement required by the different levels of MC2010, NBR 6118 and EC2 for edge column A2 (refer to Figure 1). The effects of uneven shear were accounted for using the simplified $\beta = 1.4$ for EC2 and $k_e = 0.7$ for MC2010 as allowed for braced frames. NBR 6118 does not allows the use of a fixed value, as stated in section 2.3, so the design stress was calculated based on Equation 12. All three codes adopt partial factor of $\gamma_s = 1.15$ for reinforcement. For concrete, EC2 and MC2010 adopt $\gamma_c = 1.5$ and NBR 6118 adopts $\gamma_c = 1.4$. V_{flex} was calculated with yield line analysis.

For Level III, m_s and r_s were calculated in each direction with LFEA using the elements and mesh shown in Figure 8. Furthermore, m_s also included the twisting moments in accordance with Wood [23]. Figure 16 shows rotations for longitudinal and transverse directions from NLFEA, and calculated with LoA II and III of MC2010. It also shows $V_{Rd,c}$ from Equation 1 of EC2, which is similar for NBR 6118, and the resistance curve of Equation 5 from MC2010 using $k_e = 0.7$. MC2010, NBR 6118 and EC2 need $V_{Rd,c}$ to calculate the required amount of shear reinforcement. All three codes were used to design shear reinforcement within a zone of 1.5d around the column for the design shear force of 420 kN.

MC2010 requires a minimum area of reinforcement to satisfy $V_{Rd,s} > 0.5V_{Ed}$. This was overlooked for all the LoA IV calculations as it is intended for assessment. Figure 16 also shows the maximum punching resistance, limited by crushing of the concrete struts around the column, $V_{Rd,max}$, from Equation 9 ($k_{sys} = 2.8$). Table 4 shows $V_{Rd,c}$ for all LoA of MC2010 in both the longitudinal and transverse directions. The results in bold are the smallest, thus critical according to MC2010. Also shown in Table 4 are $V_{Rd,c}$ from Equation 1 of EC2 and NBR 6118, V_{flex} from yield analysis, and the shear reinforcement required by each code and LoA for MC2010.

Interestingly, the rotations in the transverse direction calculated with LoA III are slightly greater than LoA II. This is believed to be the result of the elastic shell elements overestimating torsion at the side of the column, which led to a greater $m_s = |M_{yy}| + |M_{xy}|$, and consequently greater rotations. Shear reinforcement requirements for LoA III almost double as a result of the transverse direction becoming critical. This issue merits further studies as reducing torsion stiffness in a LFEA of a shell-based model potentially reduces transverse rotations, but may affect rotations in the longitudinal direction.

As can be seen in Figure 16 and Table 4, the critical direction varies with the level of approximation. Figure 13 and Table 3 shows that the omission of cladding load in the NLFEA swapped the critical direction from transverse to longitudinal, which led to a slightly greater amount of shear reinforcement required according to MC2010 LoA IV (refer to Table 4).

In most of the LoA II and III designs, the design shear force is very close to the maximum possible shear capacity which is limited by crushing of concrete near the support region according to MC2010's limit of $k_{sys} = 2.8$ for double headed studs. For LoA II, the assumption of $r_s = 0.22L$ significantly overestimated the rotations for the analysis. LFEA suggests that the point of contraflexure is actually closer to $r_s = 0.15L$ in the longitudinal direction and $r_s = 0.18L$ in the transverse, which would result in smaller rotations. The overestimation of torsion from shell element-based models is enough to explain the poor performance of LoA III, as previously discussed. Analysis with LoA IV indicates that concrete crushing failure is not critical in reality for these slabs and that shear failure could be avoided through the provision of shear reinforcement as allowed by the UK National Annex to EC2 which limits $V_{R,max}$ to $2V_{Rd,c}$.

Though slabs with ρ_{span} = 0.3% would likely fail in flexure as suggested by V_{flex} from Yield Line, and NLFEA, which stopped before the design load could be reached, they are included in Figure 17 for comparative purposes.

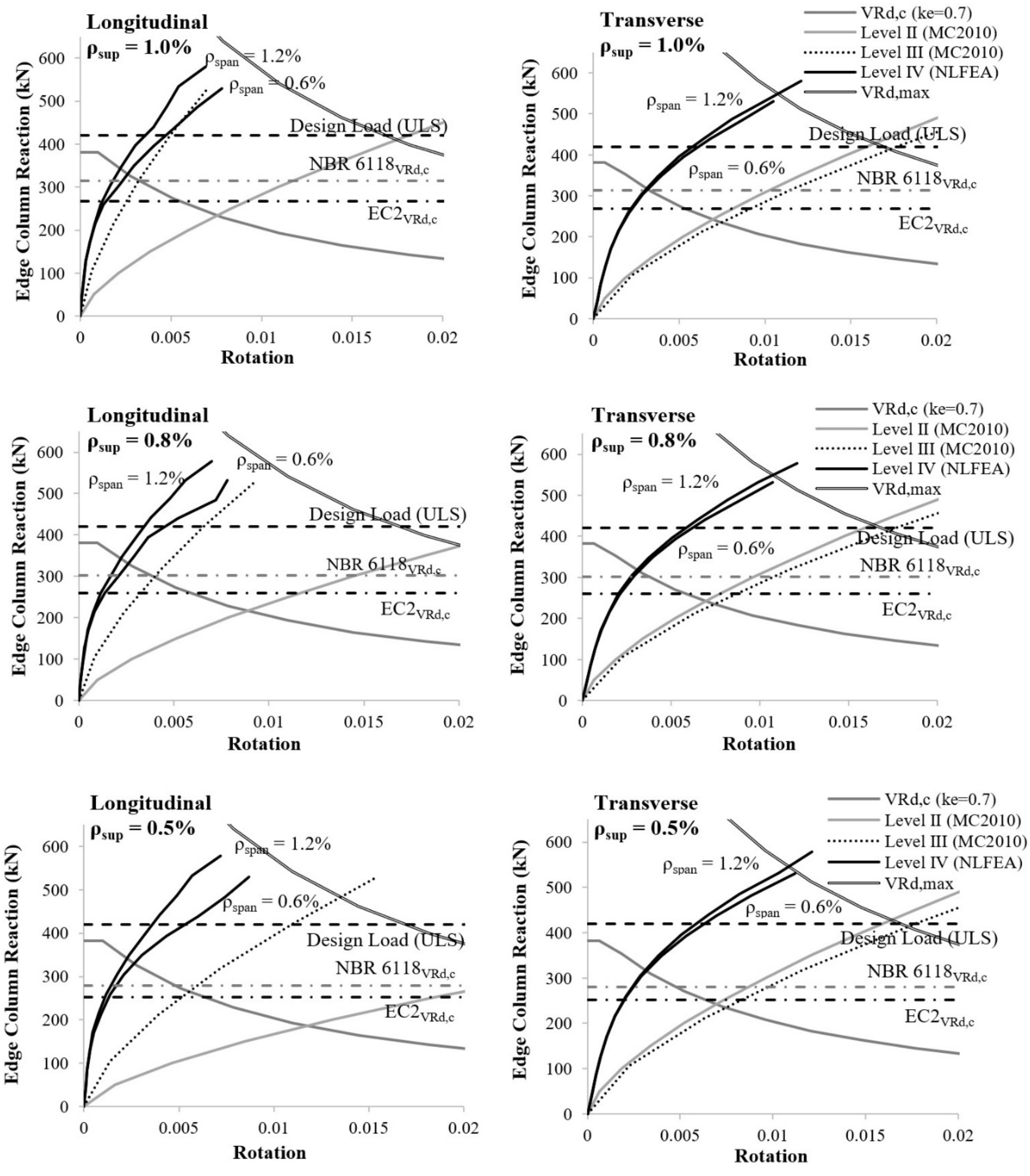

Figure 16. Longitudinal and Transverse rotations of the subassembly slabs from the parametric study. Note: Slabs with ρ_{span} = 0.3% didn't reach the design load as would likely fail in flexure, therefore they are not shown in the figure.

Table 4. $V_{Rd,c}$ and $\sum_{1.5d_v} A_{sw}$ from MC2010 LoA II to IV, EC2, NBR6118, and V_{flex}. Shear forces in kN.

	MC2010, $k_e = 0.7$: *Longitudinal/Transverse*			MC2010, $k_e = 0.7$: $\sum_{1.5d_v} A_{sw}$ [mm²]			EC2		NBR 6118		
	LoA IV	**LoA III**	**LoA II**	**LoA IV**	**LoA III**	**LoA II**	$V_{Rd,c}$	$\sum_{1.5d_v} A_{sw}$ **[mm²]**	$V_{Rd,c}$	$\sum_{1.5d_v} A_{sw}$ **[mm²]**	V_{flex}
$\rho_{sup} = 1.0\%$ $\rho_{span} = 0.3\%$	-/-			-							424.77
$\rho_{sup} = 1.0\%$ $\rho_{span} = 0.6\%$	285/**260**	274.44/**144.22**	**142.94**/155.48	788.18[b]	1358.52	1364.83	267.98	1107.72	313.97	1091.32	546.37
$\rho_{sup} = 1.0\%$ $\rho_{span} = 1.2\%$	310/**262**			778.33[b]							759.68
$\rho_{sup} = 0.8\%$ $\rho_{span} = 0.3\%$	-/-	246.43/**144.22**		-	1358.52						420.69
$\rho_{sup} = 0.8\%$ $\rho_{span} = 0.6\%$	290/**257**			802.96[b]							542.29
[a]$\rho_{sup} = 0.8\%$ $\rho_{span} = 0.6\%$	**240**/260	254.95/**172.55**	**117.80**/155.48	886.70[b]	1218.97	1488.67	260.09	1132.20	301.81	1126.4	542.29
$\rho_{sup} = 0.8\%$ $\rho_{span} = 1.2\%$	315/**262**	246.43/**144.22**		778.33[b]	1358.52						755.61
$\rho_{sup} = 0.5\%$ $\rho_{span} = 0.3\%$	-/-			-							414.34
$\rho_{sup} = 0.5\%$ $\rho_{span} = 0.6\%$	275/**255**	192.74/**144.22**	**79.59**/155.48	812.81[b]	1358.52	1676.90	252.21	1153.62	279.71	1190.19	535.95
$\rho_{sup} = 0.5\%$ $\rho_{span} = 1.2\%$	309/**262**			778.33[b]							749.25

[a] Without Cladding Load. [b] Smaller than the minimum reinforcement by MC2010 corresponding to $V_{Rd,s} > 0.5V_{Ed}$ (1034.48 mm²).

Figure 17 compares the amount of shear reinforcement within a zone of 1.5d around the column in relation to the longitudinal span reinforcement for all slabs with cladding load. According to MC2010 LoA II, III, NBR 6118, and EC2, the required area of punching shear reinforcement is independent of the span reinforcement ratio. However, Figure 17 shows that even though LoA IV captures the influence of span reinforcement, the impact on required shear reinforcement is minimal, especially for slabs with $\rho_{sup} = 1.0\%$. This is so since transverse rotations are critical for the considered slabs, which is not always the case.

The impact of longitudinal support reinforcement is significantly greater for LoA II of MC2010 than LoA III and IV, NBR 6118, or EC2. Both LoA II and III, which are intended for design, required significantly more punching shear reinforcement than NBR 6118, and in some cases double the reinforcement required by LoA IV, which is intended for assessment. LoA IV requirements are very close to those of EC2 when the minimum reinforcement rule of MC2010 is implemented.

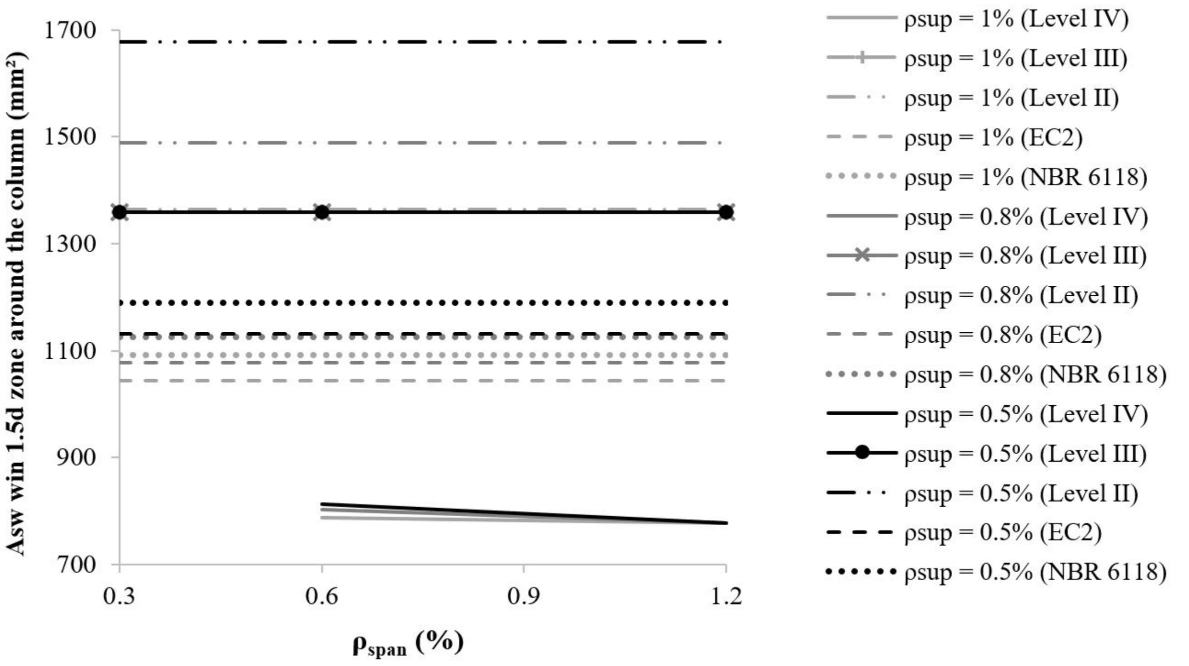

Figure 17. Shear reinforcement in 1.5d from the column required by MC2010, EC2 and NBR6118.

7 CONCLUSIONS

This paper investigated the impact of slab continuity through modelling assumptions, critical directions of rotations and code comparison on the punching resistance of an edge column from realistically proportioned flat slab floor plates. Elastic columns were considered in the punching shear assessments of the full-scale slab to simplify the analysis. The effect of this was to increase the moment transferred to the edge column but also to reduce longitudinal slab rotations calculated with NLFEA which were generally not critical for the considered slabs.

The increase in M/V with load, due to moment redistribution from span to support, presented in Figure 12 has little impact on the reactions at edge columns, as stated by Soares [25]. The reason being that edge column moment is relatively small compared with that at internal support. The parameter that characterizes the eccentricity by the MC2010, k_e, can be calculated according to Equation 4, therefore, different modelling assumptions can influence the moment transferred to the column, which leads to different values of k_e. In accordance to Soares and Vollum [19] the use of the constant parameter $k_e = 0.7$, recommended by MC2010 for edge columns, leads to reasonable results, justifying its use during the analysis. The average moment m_s to be adopted in MC2010 LoA III, which is calculated from LFEA with shell elements, requires further study since it depends on the shear modulus adopted in the analysis.

For the modelled full-scale flat slabs, longitudinal span reinforcement has a significantly greater impact on longitudinal rotations than longitudinal support reinforcement at the slab edge (Figure 11) as for Regan's [20] specimens. The direction of greatest rotation varies with reinforcement arrangement and between the LoA in MC2010. However, the longitudinal reinforcement could still affect punching resistance due to shear redistribution around the control perimeter of the type proposed by Sagaseta et al. [35] for slabs with non-axis-symmetrical reinforcement. The impact on punching resistance was significantly less than observed for Regan's specimens [20], partly because transverse rotations are critical for all cases. The analyses carried out in accordance with EC2, NBR 6118 and MC2010 LoA II and LoA III showed that results for punching shear reinforcement are independent of the longitudinal span reinforcement, unlike the results obtained with MC2010 LoA IV, which is capable of capturing the influence of continuity and flexural reinforcement ratio in the span. For the considered full-scale slab, the area of shear reinforcement required within $1.5\,d$ of the column face by MC2010 LoA IV is around 35% less than that by NBR 6118 and EC2. In some cases, the area of shear reinforcement required by MC2010 LoA IV is around half that required by LoA II and III, which are over conservative due to slab rotations being overestimated.

REFERENCES

[1] S. Kinnunen and H. Nylander, *Punching of Concrete Slabs Without Shear Reinforcement* (Transactions of the Royal Institute of Technology 158). Stockholm, Sweden: Royal Institute of Technology , 1960, 112 p.

[2] Fédération International du Béton, *Punching of Structural Concrete Slabs* (fib Bulletin 12), 2001.

[3] A. N. Talbot, *Reinforced Concrete Wall Footings and Column Footings* (Bulletin 67). Illinois: Engineering Experiment Station, University of Illinois, 1913.

[4] C. E. Broms, "Punching of flat plates – tangential strain theory for punching failure of flat slabs," *ACI Struct. J.*, vol. 113, pp. 95–104, Jan-Feb 2016, http://dx.doi.org/10.14359/51687942.

[5] L. C. Hoang and A. Pop, "Punching shear capacity of reinforced concrete slabs with headed shear studs," *Mag. Concr. Res.*, vol. 68, no. 3, pp. 118–126, 2016, http://dx.doi.org/10.1680/macr.15.00033.

[6] A. G. Sherif and W. H. Dilger, "Tests of full-scale continuous reinforced concrete flat slabs," *ACI Struct. J.*, vol. 97, no. 3, pp. 455–467, 2000.

[7] P. S. Chana and S. B. Desai, "Membrane action, and design against punching shear," *Struct. Eng.*, vol. 70, no. 19, pp. 339–343, 1992.

[8] A. G. Sherif, "Behaviour of reinforced concrete flat slabs", Ph.D. dissertation, Dept. Civ. Eng., Univ. Calgary, Calgary, Alberta, 1996.

[9] J. Einpaul, F. Brantschen, M. Fernández Ruiz, and A. Muttoni, "Performance of punching shear reinforcement under gravity loading: influence of type and detailing," *ACI Struct. J.*, vol. 113, no. 4, pp. 827–838, Jul-Aug 2016, http://dx.doi.org/10.14359/51688630.

[10] R. L. Vollum, T. Abdel-Fattah, M. Eder, and A. Y. Elghazouli, "Design of ACI-type punching shear reinforcement to Eurocode 2," *Mag. Concr. Res.*, vol. 62, no. 1, Jan 2010, http://dx.doi.org/10.1680/macr.2008.62.1.3.

[11] A. Muttoni, "Punching shear strength of reinforced concrete slabs without transverse reinforcement," *ACI Struct. J.*, vol. 105, no. 4, pp. 440–450, Jul-Aug 2008. [Online]. Available: https://infoscience.epfl.ch/record/116123

[12] J. Moe, *Shearing Strength of Reinforced Concrete Slabs and Footings under Concentrated Loads* (Development Department Bulletin D47). Skokie, IL: Portland Cement Association, 1961, pp. 130.

[13] M. Fernández Ruiz and A. Muttoni, "Applications of critical shear crack theory to punching of reinforced concrete slabs with transverse reinforcement," *ACI Struct. J.*, vol. 106, no. 4, pp. 485–494, 2009. [Online]. Available: https://infoscience.epfl.ch/record/134716

[14] Fédération International du Béton, *Model Code for Concrete Structures 2010*, 2013.

[15] M. P. Ferreira, G. S. Melo, P. E. Regan, and R. L. Vollum, "Punching of reinforced concrete flat slabs with double-headed shear reinforcement," *ACI Struct. J.*, vol. 111, no. 2, pp. 363–374, 2014., http://dx.doi.org/10.14359/51686535.

[16] A. Dönmez and Z. P. Bažant, "Critique of critical shear crack theory for fib Model Code articles on shear strength and size effect of reinforced concrete beams," *Struct. Concr.*, vol. 20, pp. 1451–1463, 2019., http://dx.doi.org/10.1002/suco.201800315.

[17] Associação Brasileira de Normas Técnicas, *Projeto de Estruturas de Concreto*, NBR 6118, 2014.

[18] British Standards Institution, *Eurocode 2, Design of Concrete Structures – Part 1-1 – General Rules and Rules for Buildings*, BS EN 1992-1-1:2004, 2004.

[19] L. F. S. Soares and R. L. Vollum, "Influence of continuity on punching resistance at edge columns," *Mag. Concr. Res.*, vol. 68, no. 23, pp. 1225–1239, 2016, http://dx.doi.org/10.1680/jmacr.16.00052.

[20] P. E. Regan, *Tests of Connections Between Flat Slabs and Edge Columns*. London: Sch. Archit. Eng., Univ. Westminster, 1993.

[21] E. F. El-Salakawy, M. A. Polak, and M. H. Soliman, "Reinforced concrete slab-column edge connections with shear studs," *Can. J. Civ. Eng.*, vol. 27, no. 2, pp. 338–348, 1998.

[22] The Institution of Structural Engineers, *Standard Method of Detailing Structural Concrete ISE*, 2006.

[23] R. H. Wood, "The reinforcement of slabs in accordance with a pre-determined field of moments," *Concrete (Lond.)*, vol. 2, no. 2, pp. 69–76, 1968.

[24] British Standards Institution, *UK National Annex to Eurocode 2 – Design of Concrete Structures – General Rules and Rules for Buildings*, EN 1992-1-1:2004, 2004.

[25] L. F. S. Soares, "Influence of slab continuity on punching resistance," Ph.D. dissertation, Imp. Coll. London, London, 2017.

[26] A. G. Sherif, "Behaviour of reinforced concrete flat slabs," Ph.D. dissertation, Dep. Civ. Eng., Calgary, Alberta, 1996.

[27] TNO Diana BV, *Finite-element Analysis User's Manual – Release 9.6*. TNO Diana BV, 2014.

[28] R. L. Vollum and U. L. Tay, "Modelling tension stiffening in reinforced concrete with NLFEA," *Concrete*, vol. 41, no. 1, pp. 40–41, 2007.

[29] M. Suidan and W. C. Schnobrich, "Finite element analysis of reinforced concrete," *J. Struct. Div.*, vol. 99, no. 10, pp. 2109–2122, 1973.

[30] J. Sagaseta, “The influence of aggregate fracture on the shear strength of reinforced concrete beams,” Ph.D. dissertation, Imp. Coll. London, London, 2008.

[31] L. M. Trautwein, “Punção em lajes cogumelo de concreto armado: análise experimental e numérica,” Ph.D. dissertation, Esc. Politéc., Univ. São Paulo, São Paulo, 2006.

[32] E. Thorenfeldt, A. Tomaszewicz, and J. J. Jensen, “Mechanical properties of high-strength concrete and applications in design,” in *Proc. Symp. Utilization of High-Strength Concr.*, Norway, 1987.

[33] F. J. Vecchio and M. P. Collins, "Compression response of cracked reinforced concrete," *J. Struct. Eng.*, vol. 119, no. 12, pp. 3590–3610, 1993, http://dx.doi.org/10.1139/l90-082.

[34] L. F. S. Soares and R. L. Vollum, "Comparison of punching shear requirements in BS8110, EC2 and MC2010," *Mag. Concr. Res.*, vol. 67, no. 24, pp. 1315–1328, 2015, http://dx.doi.org/10.1680/macr.14.00432.

[35] J. Sagaseta, A. Muttoni, M. F. Ruiz, and L. Tassinari, "Non-axis-symmetrical punching shear around internal columns of RC slabs without transverse reinforcement," *Mag. Concr. Res.*, vol. 63, no. 6, pp. 441–457, 2011, http://dx.doi.org/10.1680/macr.10.00098.

Author contributions: FGBSO: data curation, editing, formal analysis, methodology, writing, review, validation. LFSS: data curation, formal analysis, funding acquisition, investigation, methodology, review, software, validation, writing. RLV: conceptualization, project administration, resources, review, supervision.

Editors: Leandro Mouta Trautwein, José Luiz Antunes de Oliveira e Sousa, Guilherme Aris Parsekian.